FURTHER DEVELOPMENTS ON THEORETICAL AND COMPUTATIONAL RHEOLOGY

A Thesis submitted in partial fulfilment of the requirements for the degree of Doctor of Philosophy in Chemical and Biological Engineering by

ALEXANDRE MIGUEL PRIOR AFONSO

SUPERVISORS:
Professor Manuel António Moreira Alves
Professor Fernando Manuel Coutinho Tavares de Pinho

FEUP FACULDADE DE ENGENHARIA
UNIVERSIDADE DO PORTO

FCT Fundação para a Ciência e a Tecnologia
MINISTÉRIO DA CIÊNCIA, TECNOLOGIA E ENSINO SUPERIOR Portugal

Ciência.Inovação 2010 Programa Operacional Ciência e Inovação 2010
MINISTÉRIO DA CIÊNCIA, TECNOLOGIA E ENSINO SUPERIOR

POPH POTENCIAL HUMANO
UNIÃO EUROPEIA
FEDER

FURTHER DEVELOPMENTS ON THEORETICAL AND COMPUTATIONAL RHEOLOGY

ALEXANDRE MIGUEL PRIOR AFONSO

Philosophiæ Doctor (Ph.D.) in Chemical and Biological Engineering

Departamento de Engenharia Química

CEFT - Centro de Estudos de Fenómenos de Transporte

Faculdade de Engenharia da Universidade do Porto

September 2010

Alexandre Miguel Prior Afonso: *Further developments on theoretical and computational rheology,* Doctor of Philosophy Thesis in Chemical and Biological Engineering, © September 2010

SUPERVISORS:
Professor Manuel António Moreira Alves
Professor Fernando Manuel Coutinho Tavares de Pinho

LOCATION:
Faculdade de Engenharia da Universidade do Porto

September 2010

Dedicated to the loving memory of Bernardo Afonso.

1927 – 2009

ABSTRACT

The present thesis is aimed at increasing the current knowledge about several distinct, but complementary, subjects related with complex flows of complex fluids, and this is achieved both numerically and analytically.

This work involved, on one side, the incorporation of new features into an existing three-dimensional time dependent finite-volume method (FVM), for efficient and accurate viscoelastic flow calculations at high Weissenberg numbers and, on the other side, the investigation of various flows with an emphasis at exploring flow instabilities linked to viscoelasticity.

Given the hyperbolic nature of the constitutive equations used to represent the rheological behaviour of viscoelastic fluids, and the numerical problems typical of highly elastic flows, the simulations required the use of robust numerical methods. For this purpose, a recent numerical stabilization methodology, based on a logarithmic transformation of the conformation tensor, was used.

To assess the proposed implementation, and demonstrate the enhanced stability, some of the benchmark flows used in computational rheology were investigated, such as the flow around a confined cylinder and the 4:1 contraction flow.

Other work involved, on one side, the numerical implementation of the electrokinetic forcing term (the Poisson-Nernst–Planck equations) in the same FVM code and, on other side, the theoretical study of electro-osmotic flows of complex fluids. When the electrokinetic flow was used in combination with viscoelastic fluids, new types of flow instabilities appeared, as observed in the cross-slot flow.

Prior to the beginning of this work, there were no published analytical solutions for fully-developed electro-osmotic flows of non-linear viscoelastic fluids. In this thesis, a number of analytical solutions were derived for pressure/electro-osmosis flows of viscoelastic fluids in a channel under a variety of boundary conditions of practical relevance, such as those found in electro-osmotic pumps.

These analytical solutions were also of significant importance in order to test the proposed code implementation and demonstrate its high stability and accuracy.

KEYWORDS

Complex fluids (viscoelastic); high Weissenberg number problem; finite volume method; elastic instabilities; electro-osmotic flow.

RESUMO

Esta tese teve como objectivo aumentar o conhecimento actual sobre vários assuntos distintos, mas complementares, relacionados com o escoamento de fluidos complexos (viscoelásticos), tendo sido concretizado com recurso a ferramentas numéricas e analíticas.

Este trabalho envolveu, por um lado, a incorporação de novas funcionalidades num código numérico existente, baseado no método dos volumes finitos, para o tornar mais eficiente e preciso no cálculo do escoamento de fluidos viscoelásticos a elevados números de Weissenberg, e por outro lado, a investigação de vários tipos de escoamento, com particular ênfase na exploração de instabilidades induzidas pelas características viscoelásticas dos fluidos.

Dada a natureza hiperbólica das equações constitutivas utilizadas para representar o comportamento reológico de fluidos viscoelásticos, e as dificuldades numéricas observadas para escoamentos a elevados números de Weissenberg, foi necessária a utilização de métodos numéricos robustos e precisos. Para este efeito, foi utilizada uma metodologia de estabilização numérica proposta recentemente, e que se baseia numa transformação logarítmica do tensor conformação.

Para testar a implementação proposta e demonstrar a sua elevada estabilidade, estudaram-se alguns dos escoamentos de referência utilizados em reologia computacional, tais como o escoamento em torno de um cilindro confinado, bem como escoamentos numa contracção de razão 4:1.

Outros trabalhos envolveram, por um lado, a implementação numérica do termo eletrocinético (as equações de Poisson-Nernst-Planck) no código de volumes finitos e, por outro lado, o estudo teórico dos escoamentos electro-osmóticos de fluidos viscoelásticos. Quando o escoamento induzido por efeitos eletrocinéticos é usado em combinação com fluidos viscoelásticos, surgem novos tipos de instabilidades, como as observadas no escoamento numa junção em cruz de canais planos (*cross-slot*).

Até ao início deste trabalho, não existiam soluções analíticas publicadas para escoamentos electro-osmóticos de fluidos viscoelásticos, em condições de escoamento desenvolvido. Ao longo desta tese foram deduzidas diversas soluções analíticas para o escoamento electro-osmótico de fluidos viscoelásticos num canal sob distintas condições de contorno, de relevância prática, como no caso de bombas por electro-osmose.

Estas soluções analíticas foram também de grande utilidade no teste das implementações numéricas no código e na demonstração da sua elevada estabilidade e precisão.

PALAVRAS-CHAVE

Fluidos complexos (viscoelásticos); problema do elevado número de Weissenberg; método de volumes finitos; instabilidades elásticas; escoamento electro-osmótico.

RÉSUMÉ

La présente thèse vise l'accroître des connaissances actuelles sur plusieurs sujets différents, mais complémentaires, liés à l'écoulement de fluides complexes (viscoélastiques) et a été atteint en utilisant des outils numériques et analytiques.

Ce travail a impliqué, d'une part, l'incorporation de nouvelles fonctionnalités dans un code numérique existant basé sur la méthode des volumes finis, pour le rendre plus efficace et précis dans le calcul d'écoulements de fluides viscoélastiques à des nombres de Weissenberg élevés, et d'autre part, la recherche sur les différents types d'écoulement, avec un accent particulier sur l'exploitation des instabilités induites par la viscoélasticité des fluides.

Compte tenu de la nature hyperbolique des équations constitutives utilisées pour représenter le comportement rhéologique des fluides viscoélastiques, et les problémes numériques normalment observées aux écoulements à des nombres de Weissenberg élevés, il a été nécessaire d'utiliser des méthodes numériques robustes et précises. À cette fin, on a été utilisé une méthodologie de stabilisation numérique récemment proposée, qui est basée sur une transformation logarithmique du tenseur de conformation polymérique.

Pour tester l'implémentation proposée et démontrer sa grande stabilité, quelques-uns des écoulements de référence utilisés en rhéologie computationnel on été étudiés, telles que l'écoulement autour d'un cylindre confiné, et des écoulements dans une contraction de rapport 4:1.

D'autres travaux ont impliqué, d'une part, l'implémentation numérique du terme de force électrocinétique (équations de Poisson-Nernst-Planck) dans le même code de volumes finis et, par ailleurs, l'étude théorique de l'écoulement électro-osmotique des fluides viscoélastiques. Lorsque l'écoulement induit par l'effet électrocinétique est utilisé en combinaison avec des fluides viscoélastiques, de nouveaux types d'instabilités apparaissent, comme celles observées dans l'écoulement dans une jonction en croix de canaux plans (*cross-slot*).

Jusqu'au début de cette thèse, il n'y avait pas des solutions analytiques publiées concernant l'écoulement électro-osmotique des fluides viscoélastiques dans des conditions d'écoulement développées. Tout au long de ce travail ont été dérivées plusieurs solutions analytiques pour l'écoulement électro-osmotique de fluides viscoélastiques dans un canal sous différentes conditions de frontière, avec pertinence pratique, comme dans le cas des pompes par électro-osmose.

Ces solutions analytiques ont été également très utiles pour tester les implémentations numériques et la démonstration de sa grande stabilité et précision.

MOTS-CLÉS

Fluides complexes (viscoélastiques); problème du nombre élevé de Weissenberg, méthode des volumes finis; instabilités élastiques; écoulement électro-osmotique.

PUBLICATIONS

Some ideas and figures have appeared previously in the following publications:

- A. Afonso, PJ Oliveira, FT Pinho and MA Alves (2009). The log-conformation tensor approach in the Finite Volume Method framework, *Journal of Non-Newtonian Fluid Mechanics* **157** 55-65; on page 67
- A. Afonso M. A. Alves, F. T. Pinho and P. J. Oliveira (2008). Uniform flow of viscoelastic fluids past a confined cylinder, *Rheologica Acta*, **47** 325-348. on page 87
- A.M. Afonso, P.J. Oliveira, F.T. Pinho and M.A. Alves (2010), Dynamics of high Deborah number entry flows – a numerical study, accepted for publication in the *Journal of Fluid Mechanics*; on page 113
- A.M. Afonso, M.A. Alves, F.T Pinho (2010). Purely-Elastic flow instabilities in a 3D six arms cross slot geometry, *Journal of Non-Newtonian Fluid Mechanics* **165** 743–751; on page 143
- A.M. Afonso, M.A. Alves, R.J. Poole, P.J. Oliveira and F.T. Pinho (2010). Viscoelastic flows in mixing-separating cells, accepted for publication in the *Journal of Engineering Mathematics*; on page 157
- A.M. Afonso, M.A. Alves, F.T. Pinho (2009). Analytical solution of mixed electro-osmotic/ pressure driven flows of viscoelastic fluids in microchannels. *Journal of Non-Newtonian Fluid Mechanics* **159** 50-63; on page 171
- A.M. Afonso, M.A. Alves, F.T. Pinho (2010). Electro-osmotic flows of viscoelastic fluids in microchannels under asymmetric zeta potential, accepted for publication in the *Journal of Engineering Mathematics*; on page 197
- S. Dhinakaran, A.M. Afonso, M.A. Alves, F.T. Pinho (2010). Steady viscoelastic fluid flow in microchannels under electrokinetic forces: PTT model, *Journal of Colloid And Interface Science* **344** 513-520; on page 215
- A.M. Afonso, F.T. Pinho and M.A. Alves (2010), Two-fluid electro-osmotic flows of viscoelastic fluids, in preparation to submit to *Microfluidics and Nanofluidics*; on page 229
- A.M. Afonso, F.T Pinho and M.A Alves (2010). Electro-osmotic flows of viscoelastic fluids: a numerical study, in preparation to submit to *Journal of Non-Newtonian Fluid Mechanics,* on page 245.

Knowledge is in the end
based on acknowledgement.

— Ludwig Wittgenstein

ACKNOWLEDGMENTS

I acknowledge, and sincerely express my gratitude to CEFT, and the Portuguese Foundation for Science and Technology (FCT) for their financial support, through projects PTDC/EQU-FTT/70727/2006 and PTDC/EQU-FTT/71800/2006 and through the scholarship SFRH /BD28828 /2006, co-financed by the European Social Fund (ESF) under the Human Potential Operational Programme and National Strategic Reference Framework (NSRF).

During the last years I had the privilege of working with the most talented and hard-working people, my Professors and advisors: Manuel Alves and Fernando Pinho. From both, I learned the true meaning of scientific research, and the importance of detailed knowledge on fundamental questions. I am eternally grateful for their excellent and open-minded guidance, resulting from the powerful combination of distinct characteristics: Manuel was a always available advisor (he is a never-stop worker), a true source of clever and innovative ideas and his perfectionist approach to scientific production long precede him (his notes were my Books during my graduate years); Fernando's working capability is impressive, always providing a soothing presence and an astonishing clarity of vision, that saved me from possible hard times, by reformulating Buckminster Fuller's quote to "*Whenever you draw a circle, you immediately write about it*".

I sincerely acknowledge Paulo Oliveira and Rob Poole, for the help in some numerical and theoretical issues, and also for the pleasant exchange of ideias. I would also address a word of appreciation to João Rui Guedes de Carvalho, for the earlier taughts on good scientific writing.

I thank to all my co-workers in CEFT and FEUP, Adélio, Alexandre, Dhinakaran, Fabrice, Maria, Mónica, Patrícia, Resende (among others).

To all my closest friends a big *thank you!* for all the support and friendship, as well as a big *I'm sorry!* for all the unanswered phone calls. I dedicate Part I of this dissertation (or at least, the abstract) to the mazed expression on their faces when I tried to explain what I was doing during my PhD.

When I first saw her I had a Calculator in my back pocket. I still have that machine, but it does not have the necessary precision to display the 10^{googol} amount of love, companion and support during this years: Rita makes things easier.

Finally, I would like to express my gratitude to my lovely family. I thank my mother, Julieta, my brother, Rui, my sister, Paula, and the newborn elements (and all the others, new or not so new elements), for their support, patience, and love during all these years. I dedicate this work to my father, Bernado, I know he would be very proud of me.

CONTENTS

ACRONYMS

BEM Boundary Element Method

CMC Carboxymethyl cellulose

CFD Computational Fluid Dynamics

CUBISTA Convergent and Universally Bounded Interpolation Scheme for the Treatment of Advection

C14 Tetradecane

DEVSS-TG/SUPG Discrete Elastic-Viscous Split Stress, Traceless velocity Gradient interpolation, Streamline Upwind Petrov-Galerkin

DEVSS-G/SUPG Discrete Elastic-Viscous Split Stress, velocity Gradient interpolation, Streamline Upwind Petrov-Galerkin

DNS Direct Numerical Simulations

EDL Electric Double Layer

EOF Electro-osmotic flow

EVSS Elastic-Viscous Split Stress

FENE Finitely-Extensible Nonlinear Elastic model

FDM Finite Difference Method

FEM Finite Element Method

FVM Finite Volume Method

FDM Finite Difference Method

HDNP High Deborah Number Problem

HWNP High Weissenberg Number Problem

LDPE Low-density polyethylene

LDV Laser Doppler velocimetry

MIT Massachusetts Institute of Technology

PAA Polyacrylamide

PB Polybutene

PBDH Poisson-Boltzmann-Debye-Hückel

PDMS Polydimethylsiloxane

PIB Polyisobutylene

PIV Particle image velocimetry

PNP Poisson-Nernst-Planck

PTT Phan-Thien-Tanner

PVM Parallel Virtual Machine

SIMPLEC Semi-Implicit Method for Pressure Linked Equations Consistent

SEM Spectral Element Method

SPD Symmetric Positive Definite

UCM Upper-Convected Maxwell model

UCO Upper-Convected Oldroyd model

XPP eXtended Pom-Pom

Part I

PANTA RHEI

1

INTRODUCTION

[...] The Master stood by a river and said:
'Everything flows like this,
without ceasing, day and nigth' [...]

— Confucius (551–479 BC)

1.1 A STUDY ON COMPLEXITY: COMPLEX FLUIDS AND FLOWS

rheo *(From Greek rheos, stream, from rhein, to flow)* + logy *(Origin: Middle English -logie, from Old French, from Latin -logia, from Greek -logiā (from logos, word, speech))* *"Everything flows and nothing abides; everything gives way and nothing stays fixed."* *Heraclitus of Ephesus (540–475 BC)*

Who would think that the simplicity of Heraclitus of Ephesus (540–475 BC) philosophical statement "Panta rhei" (everything flows), could lead into an hypothesis of a study on complexity? But, as usual, simplicity always depends on the level of abstraction imposed by the observer. So let us start the present dissertation, descending (or ascending, following again Heraclitus's ideas "The road up and the road down is one and the same") by the road that, hopefully, will lead to a rather simple understanding of one specific and small part of the everything flows' complexity.

Simple questions (with rather complex answers) such as: does everything *really* flow? *why* everything flows? *how* everything flows? *where* everything flows? *when (or for how long)* everything flows?, were addressed in many other historical dissertations by many other world famous observers, such as Archimedes (200 BC), Newton (1687), Pascal (1663), Bernoulli (1738), Euler (1755), Navier (1822), Stokes (1845), Poiseuille (1841) and Maxwell (1867), among others. It is not the intention of this work to elaborate on these vast questions, although some of the answers given by our illustrious predecessors will be used along this dissertation.

In terms of simple questions, this contribution is somehow in between the *how* and *where* everything flows (although the *when (or for how long)* everything flows is also important). In terms of scientific (or mathematical modelling), the area of this investigation focus on both the complexity of the kind of *everything* that flows (related to the complexity of the material that flows, specifically, complex fluids), and on the complexity of the behaviour of the complex material that flows (related to complex flows of complex fluids).

In the next sections, a new level of abstraction on complex fluids and flows is presented. It is intended that, at the end of this introductory part, the reader will have a meaningful scientific and mathematic interpretation of these rather philosophical questions.

1.1.1 *Complex fluids: abstractions on* Panta (everything)

Heraclitus's "Panta rhei", is the motto of a scientific subject or discipline, the so called Rheology.

In this section some considerations related with the kind of *everything* that flows will be addressed. Since the 29th of April 1929 (Doraiswamy, 2002), Heraclitus's "Panta rhei", is the motto of a scientific subject or discipline, the so-called Rheology.

Rheology is, in fact, one of the few scientific subjects whose formal creation can be traced back to a specific date. Strictly speaking, the definition of Rheology is "the study of the flow and deformation of all forms of matter" (Denn, 2004). Rheology can also be defined from other points of view, as the scientific (through a mathematical, physical and phenomenological stand point) and the engineering (through an applied and industrial stand point) perspectives.

From a scientific point of view, it is related to that part in Classical Mechanics dealing with the interaction between the applied forces and the resulting deformations observed on the matter. Obviously, the precise nature of these interactions will depend on both the type (or duration) of the forces, as well as on the type of matter. Concerning the type of matter, and given the earthian thermodynamic conditions (standard pressure, volume and temperature), two extreme limiting boundary states can be assumed:

THE SOLID STATE OF MATTER: in an ideal approach, a rigid solid follows the Euclidean ideas, where a rigid body of mass does not deform under an applied force. However, real solids, even metals or minerals, have the capability to store energy and under applied forces present a spring-like elastic response, through a property known as elasticity. This phenomenon is described by Hooke's law, first introduced by Robert Hooke in 1678, and further improved by the subsequent works of Thomas Young (1807) and Augustin Cauchy (1827).

THE FLUID STATE OF MATTER: in a non-realistic approach, following the Pascalian definition of inviscid fluid (non viscous or frictionless fluid), even a very small applied force will give rise to a never ending flow, due to the inability of a fluid to resist forcing (for further classical studies of this kind of fluids, please refer to the works of Bernoulli (1738) and Euler (1755)). However, real fluids, such as water or air, dissipate energy when flowing because of a property known as the coefficient of viscosity (or simply viscosity). Those two fluids and others found in nature, are called Newtonian (or non-complex) fluids, defining the type of fluids that can be described by Newton's law of viscosity, first described in Sir Isaac Newton's (1687) *Principia*.

The principal subject in Rheology lies in the full range between these two extremes, i.e., between the Hookean elastic solid and the Newtonian viscous fluid models as well outside it. Indeed, these historical classical models do not depict the full behaviour of many real fluids, such as the observed non-linear and time dependent type of responses to deformation, usually referred to as VISCOELASTIC (or non-Newtonian) behaviour. These non-classical (or complex) viscoelastic behaviours are then the main interest of Rheology and of Rheologists.

An interesting and uncommon example of a complex fluid (or non-Newtonian) behaviour is the pitch drop experiment, the world's longest-running experiment. The experiment was started in the late 1920's by

Thomas Parnell and continues up to this day. A sample of pitch (a highly viscous non-Newtonian fluid which resembles a solid, most commonly bitumen) was poured into a glass funnel and let drip out due to gravity effects. The flow is so slow, that up to the present time, only eight drops have fallen!

The bitumen viscosity is almost 10^{11} times higher than the viscosity of water.

Time (or timescale) is then, to some extent, the essential core of complex fluids rheology. Indeed, any fluid can behave as an elastic solid or as a Newtonian fluid, depending on the magnitude of forces and on the deformation process that is imposed. Even argon will exhibit viscoelastic behaviour if the time scale of the applied deformation is comparable to the characteristic relaxation time of its molecular structure (Denn, 2004). In an after dinner talk at the Fourth International Congress of Rheology, Reiner (1964) presented an interesting (and almost theological) perspective on the relevance of timescale in Rheology, and on the implicit liquid/solid duality that each material may exhibit. Rescuing an Old testament famous song from the Prophetess Deborah of the book of Judges (5:5)*: "the mountains flowed before the Lord*", Reiner argued that, given a divine time observer (God himself), even a mountain would eventually flow and behave like a fluid. Obviously, in the time frame observation of a common mortal and under the same applied forces (or deformation), mountains behave essentially like a solid. Then, from Reiner's perspective, the difference between a solid and a fluid could be defined by the magnitude of a non-dimensional number, named appropriately as the Deborah number, defined as:

$$De = \frac{\text{material relaxation time}}{\text{time of observation}} = \frac{\lambda}{t_{obs}} \tag{1.1}$$

The Deborah number characterizes the interplay between the relaxation time of the material and the characteristic time of the applied forces (or deformations). Taking the biblical example cited above, to the divine entity the mountain Deborah number is zero ($De \to 0$), due to the infinite time of observation and Newtonian fluid behaviour is observed. In contrast, for a common mortal, the mountain Deborah number is very large ($De \to \infty$), since the time of observation is significantly lower than the characteristic mountain relaxation time. So, both limiting Deborah number cases, $De \to 0$ and $De \to \infty$, correspond to the two limiting situations of a Newtonian fluid and a perfectly elastic solid. It is time, then, that provides the closure to the *Panta* in Heraclitus motto, because it is the glue that brings together solid and fluids.

From an engineering point of view, both time and rheologists are restricted to more quotidian constrains, which limit the observation time to the representative or service time of the engineering (or industrial) application. So, rheology is of interest not only to mathematicians, chemists and physicists, but also to chemical, mechanical, material, food or civil engineers (the author of this dissertation is a chemical engineer), who have to deal with these complex fluid materials on a daily basis. The interest on complex fluids grew fast in the 1940's, motivated by the discoveries during the second world war, subsequently transformed into relevant industrial products, such as in the plastics industry, glass technology, painting industry and ink-jet printing (much later). Engineers deal regularly with CONSTITUTIVE EQUATIONS, that describe the rheological behaviour of the material as a relation between the stress (forces per unit area) and strain (a measure of deformation

history or rate of strain). These constitutive equations will depend on the structure of the complex fluid, and can be represented in the form of algebraic, differential, integral, or integro-differential equations (Bird et al., 1987a,b).

As a conclusion to this brief introduction, a final abstraction on the complexity of *Panta (everything)* is also introduced: this dissertation will focus specifically on VISCOELASTIC (or non-Newtonian) complex fluids, characterizing soft materials such as polymer solutions (materials containing polymer molecules which typically contain thousands to millions of atoms per macromolecule), colloidal suspensions, gels, emulsions, or surfactant mixtures.

1.1.2 *Complex fluids and flows: abstractions on* Rhei (flows)

Having started with the necessary considerations related to the kind of everything that flows, this section addresses the abstractions on the complexity of the behaviour of the complex material that *flows*, or in other words, on the complexity of the *transport* (or *motion*) of a complex fluid. So, here we will deal with the processes in the Mechanics of *continuum* media, which involve the transfer of mass, momentum and energy *through* and *with* matter. These processes are usually termed Transport Phenomena, and include diffusion processes, heat transport and fluid dynamics (Bird et al., 2002). This dissertation will focus primarily on fluid dynamics.

Fluid dynamics studies the motion of fluids, and was founded under the classical mechanics conservative axioms derived under the *continuum* hypothesis (here again, given the earthly thermodynamic standard PVT conditions, the quantum mechanics and general relativity theories are discarded):

conservation of mass;

. . . These axioms are well described by the Reynolds transport theorem.

conservation of momentum (Newton's Second Law of motion);

conservation of energy (First Law of Thermodynamics).

From a discrete point of view and following the kinetic theory, fluid dynamics is treated from a molecular perspective, in which a fluid is composed by molecules that collide with each other and with the molecules of the solid boundaries, while exhibiting random motion (Bird et al., 2002). If a *continuum* assumption can be considered, fluid dynamics can be treated from a macroscopic point of view, in which the fact that a fluid is made of discrete molecules is ignored and the properties of the fluid (as density or viscosity) are taken to vary continuously from one point to another. The concept of point is here a small control volume that contains the minimum number of molecules such that the fluid properties become independent of the number of molecules considered. This perspective is at the core of *continuum* mechanics and, under the specific subject of FLUID DYNAMICS, has been used for a long time.

The history of fluid dynamics is somehow interrelated with the historical definition of fluid itself (as addressed in the last Section). In the seventeenth century, Newton (1687) presented the equations for the flux of momentum in his *Principia*, where he described the universal law of gravitation and the three laws of motion, showing that the motion of

objects on earth and celestial bodies are governed by the same set of natural laws. The equations of motion for a frictionless, non-viscous fluid were presented in the eighteenth century by Bernoulli (1738) and Euler (1755), and were extensively used in the following two centuries by one theoretical branch of fluid dynamics called Hydrodynamics, and from an almost empirical and experimental perspective in another engineering branch called Hydraulics. The pioneering work of Ludwig Prandtl (1904), showed that the approach of using the non-viscous equations in industrial applications of the two most common and available fluids on earth (air and water) was very limited and unrealistic in most cases. Prandtl (1904) showed, experimentally and theoretically, the problems of neglecting viscous forces in the thin region near the solid walls, the so-called *boundary layer* and he was the fundamental contributor of the *boundary layer theory*. This theory was very important in aeronautics, especially for estimating drag forces and analysing flows with separation. On the nineteenth century Navier (1822) and Poisson (1831) derived, from a molecular perspective, a non-linear set of differential equations that described the flow of a fluid whose stress depend linearly on the velocity gradients. The same equations (although derived independently from another perspective) were presented later by Saint-Venant (1843) and George Stokes (1845). These equations are today commonly referred to as the Navier-Stokes equations (although a fairer name should be the Navier-Poisson-Saint-Venant-Stokes equations, or the easier, but fair, Navier-Saint-Venant equations), and are considered as the theoretical foundation of modern fluid dynamics.

Stokes (1851) is also responsible for an important consideration in fluid flow problems, when he introduced the concept of the ratio between inertial and viscous forces, i.e., the importance of the ratio between the change in momentum due to fluid acceleration and due to frictional forces exerted by the fluid deformations. Actually, this relation is well known as the Reynolds number, named after Osborne Reynolds (1883), who extensively used it in the characterization of the law of resistance to the flow of water in pipes and parallel channels. The Reynolds number is a dimensionless parameter, defined as

$$Re = \frac{\text{inertial forces}}{\text{viscous forces}} = \frac{\rho U^2 L^2}{\mu U L} = \frac{\rho U L}{\mu} \tag{1.2}$$

where μ and ρ are the fluid viscosity and density, respectively, U is the fluid velocity and L is a characteristic length scale of the flow geometry. For small Reynolds number flows, also called *laminar* flows, viscous effects are dominant and the prevailing mechanism of momentum transport is due to diffusion. For large Reynolds number flows, also called *turbulent* flows, viscous effects can be neglected except close to walls and elsewhere the dominant mechanism of momentum transport is advection. Additionally, at very high Reynolds numbers laminar flows are unstable to infinitesimal perturbations and the flows become turbulent, but even here viscous effects cannot be neglected close to walls, in the boundary layers. In this case momentum transport is also occurring by the turbulent fluctuations which is also an advection mechanism. In the complex flows of complex fluids analysed in this dissertation, the Reynolds numbers are usually sufficiently small so that inertial effects can largely be neglected. Here the flows are mostly dominated by viscous forces and (inertial) turbulence is not encountered.

The study of flows of complex fluids (as the ones introduced in the last section, viscoelastic fluids) really started in earnest after the second world war and led to a new branch of fluid dynamics, which may be called Viscoelastic (or more appropriately non-Newtonian) fluid dynamics. This was mainly due to the growing awareness that the majority of the substances encountered in industrial applications, natural or synthetic, were polymeric melts or solutions which do not satisfy the Newtonian postulate of the linear relationship between the stresses and rates of deformation.

Wilhelm Weber (1835), a German physicist inventor of the first electromagnetic telegraph (together with Carl Gauss), reported, in the first rheological experiments on biological specimens – spider silk, a power-law time dependent stress relaxation. Later, Wilhelm Weber (1841) undertook the first attempt to describe that complex behaviour theoretically.

Nevertheless, there were earlier seminal experimental and theoretical works, as those on the mechanical response of spider silk threads performed by Wilhelm Weber (1835; 1841), considered as the first and irrefutable example of a biological material that behaves outside the classical extremes. Other seminal theoretical works, mostly related with the general subject of linear viscoelasticity, were presented by Ludwig Boltzmann (1874), Oskar Meyer (1874), Woldemar Voigt (1889), William Thomson (Lord Kelvin) (1865) and the interesting work of James Clerk Maxwell (1867). Maxwell's (1867) work on the elastic collisions of gas molecules in the dynamic theory of gases is now seen as the introduction to fluid materials that present some solid-like characteristics. The relevance and actuality of that work is remarkable, and such models as the Upper-Convected Maxwell model (UCM) are still well established in the 21st century works on *continuum* mechanics. Related to theoretical works on non-linear viscoelasticity, the earlier contributions at the beginning of the 20th century by S. Zaremba (1903) and Gustav Jaumann (1905), introduced what is now generally known as the corotational derivative. In the middle of the 20th century, James Oldroyd (1950), a Professor of Applied Mathematics at the University of Liverpool, presented a seminal work using convected coordinates to derive permissible processes of time differentiation and time integration in constitutive modelling (Walters, 1999). Oldroyd (1950) was also responsible for the definition of the Upper-Convected Oldroyd model (UCO), also known as the Oldroyd-B constitutive equation, another well established model nowadays. Subsequent works focused on simple extensions of classical results obtained with Newtonian fluids, as the theory of matched asymptotic expansions for singular perturbation problems, using Prandtl's boundary layer theory. Most of these works considered inelastic fluids of variable viscosity such as Metzner's studies seeking to extend flow correlations to fluids with non-Newtonian viscosities (Metzner and Reed, 1955; Metzner and Otto, 1957), or the Falkner-Skan solution for laminar boundary layer flow over a wedge of purely viscous fluids with a power-law viscosity (Schowalter, 1960; Acrivos et al., 1960). However, there were also early contributions using viscoelastic constitutive equations, such as the Falkner-Skan problem for weakly viscoelastic fluid of Denn (1967) or many others as can be found in the first volumes of *Rheology Acta* and of the *Journal of Rheology* (formerly called *Transactions of the Society of Rheology*).

The Falkner-Skan (1931) equation is a generalization of the Blasius (1908) equation, a simple nonlinear boundary layer problem describing viscous flow over a flat plate, and because of its application to fluid flow, has fascinated physicists, engineers, mathematicians and numerical analysts.

Text books that deal broadly with non-Newtonian fluid dynamics, with widely differing emphases and perspectives, include Astarita and Marrucci (1974), Schowalter (1978), Crochet et al. (1984), Bird et al. (1987a,b), Joseph (1990), Leonov and Prokunin (1994), Huilgol and Phan-Thien (1997), Tanner and Walters (1998), Larson (1998, 1999) and Owens and Phillips (2002), amongst many others. Most texts on rheology discuss non-Newtonian fluid mechanics, but generally in the

context of flows used for measurement of fluid properties, the so-called rheometric flows. Viscoelastic fluid dynamics is distinct from rheology on the simple fact that rheology focuses on the material properties from molecular theories, while viscoelastic fluid dynamics focuses on the flow of complex fluids that are not necessarily suitable for direct measurement of material properties (Denn, 2004). In fact, ideally, the rheometric flows are controllable flows, i.e., flows whose kinematics is independent of the fluid as happens with plane Couette flow.

A photo gallery of interesting flow phenomena exhibited by non-Newtonian fluids is presented by Boger and Walters (1993). Bird and Curtiss (1984) presented a collection of TEN STRANGE FLOWS of liquids containing very large molecules, which presented the opposite behaviour of the expect from the daily experience with *normal* fluids. Some of the fascinating *counter-intuitive* flow behaviours are (see Figure 1.1 for illustration):

THE WEISSENBERG EFFECT: this phenomenon shows a polymeric fluid climbing a rotating rod. For a Newtonian fluid, the fluid surface is depressed near the rod due to inertia, whereas a polymeric fluid climbs the rod. This effect is due to an up/down force produced by a non-zero difference between the normal components of the stress tensor of the fluid motion due to the turning rod.

THE VISCOELASTIC RECOIL: this phenomenon illustrates the *fading memory* of a viscoelastic fluid. Following a fluid element while flowing down a duct, it can be seen that once the flow is stopped, the Newtonian fluid comes to rest, while the polymeric fluid shows a partial *recoil*, in which the fluid does not return all the way to their initial configuration (as a purely elastic band would after being stretched in the purely elastic regime).

THE DIE SWELL: is a common observed phenomenon in polymer extrusion processes, in which the polymeric fluid swells when emerging from a tube or slit. The swell of the polymeric fluid jet can increase by as much as a factor of five and needs to be properly accounted for to avoid distorted extruded material in industry.

THE SIPHON EFFECT: this phenomenon is also called a *tubeless siphon* or *self-siphon*. One can siphon polymeric fluids even if there is a gap of several centimetres between the surface of the fluid and the end of the aspirating tube, while for a Newtonian fluid siphons only work as long as the suction tube is beneath the surface of the fluid.

A final abstraction on the complexity of *Rhei (flow)* concludes this section: this dissertation will be focused specifically on LAMINAR VISCOELASTIC FLUID DYNAMICS, and on the standard problem of solving the resulting set of coupled field equations that define the continuum *constitutive equations* relating the stress and the strain history, for a specified geometry and well defined boundary conditions.

1.1.3 *Challenges on* Panta Rhei

Despite the historical effort on understanding the complexity of *Panta Rhei*, there are still plenty of challenges to unravel. This Section presents some abstractions on the actual challenges in order to clearly formulate the work objectives in the next section and, hopefully, attain our goals.

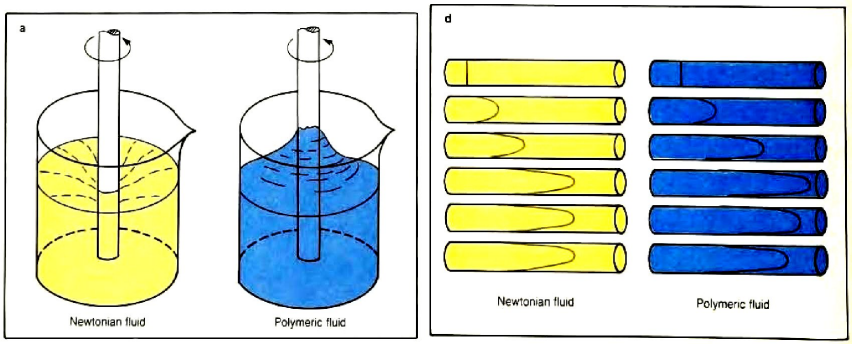

(a) the Weissenberg effect.

(b) the viscoelastic recoil.

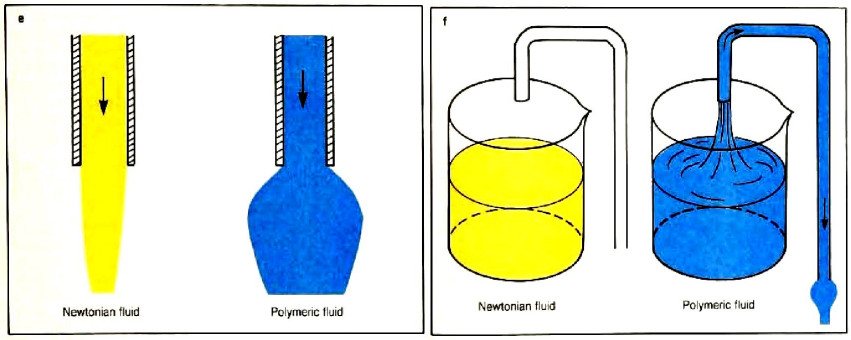

(c) the die swell.

(d) the siphon effect.

Figure 1.1: Selection of some of Bird and Curtiss (1984) collection of STRANGE FLOWS (reprinted with permission from the publisher).

For non-complex fluids and despite of the linearity of the relationship between the rate of deformation and the stress field, classical fluid dynamics is rich in complex nonlinear problems, most of them defying the goal of obtaining exact solutions. Somewhat surprisingly, even when analytical techniques are applied to the Navier–Stokes equations, the mathematicians have not yet been able to prove that the solution always exist in generic three dimensional problems, and when the solution does exist the smoothness could be questionable, i.e., the solution could contain any singularity or discontinuity. These interrogations are usually called the Navier–Stokes existence and smoothness problems, and remain one of the seven most important open problems in mathematics selected by the Clay Mathematics Institute.

In the Millennium Prize Problems, *the Clay Mathematics Institute offers a US$1,000,000 prize for demonstration of the existence and uniqueness of the solution of the Navier–Stokes equations. Interestingly, one of the seven problems selected was solved recently by Dr. Grigoriy Perelman (Poincaré conjecture) and in March 2010 one of the* Millennium Prizes *was awarded to him, but he refused to receive the prize.*

Due to restrictions on the purely analytical approach to solve the full complexity of the flow dynamic problems, scientists and especially engineers often rely on modern computational tools and particularly on COMPUTATIONAL FLUID DYNAMICS (CFD) to calculate the flow in many geometries.

Computational Fluid Dynamics is today a well established and growing scientific branch of fluid dynamics, in which a new level of abstraction and simplification is introduced, with the motto "divide to conquer" being an easy way to explain it. A very schematic view on how the solution is determined in a simple flow problem is the following: the physical domain of the flow dynamic problem is "divided" in very small sub-domains, meaning that the physical domain is "discretised" into a so-called computational grid consisting of very small computational cells; the governing transport equations are also reformu-

lated into a discrete formulation at each computational cell, including the boundary regions, following some simplifications; the solution of the resulting system of discrete equations is achieved via an iterative algorithm, solved with the help of a computer, where the inherent non-linearities of the algebraic equations are dealt with adequately.

Obviously, the smaller the sub-domains the better the level of the approximation to the "true" solution of the flow dynamic problem, and in order to achieve the invariance of the computational results with respect to the temporal and spacial discretization, some computational grid and time refinements are needed. The most usual types of numerical procedures to reformulate the governing transport equations in a flow dynamic problem are:

FINITE DIFFERENCE METHOD (FDM, Roache, 1972);

FINITE VOLUME METHOD (FVM, Patankar, 1980);

FINITE ELEMENT METHOD (FEM, Zienkiewicz and Taylor, 1989);

BOUNDARY ELEMENT METHOD (BEM, Becker, 1992).

There are also some recent procedures that combine some of the above methods, such the hybrid FEM/FVM method (Sato and Richardson, 1994) or the spectral element method (SEM, Patera, 1984), in which a high order finite element method is combined with spectral techniques. Additionally, and instead of this Eulerian philosophy, there are other methods that follow a Lagrangian approach, i.e., particles are introduced into the flow and the governing equations for each particle are solved as they evolve inside the flow domain, such the Smoothed Particle Hydrodynamics (SPH, Monaghan, 1988), or the Lattice Boltzmann methods (LBM, McNamara and Zanetti, 1988), based on microscopic models and mesoscopic kinetic equations. The Arbitrary-Lagrangian-Eulerian (ALE, Hirt et al., 1974) is a re-meshing technique that combines both the Lagrangian and Eulerian philosophy.

The use of atomistic constitutive equations is extremely expensive and with today's resources they are restricted to very simple molecular-sized computational domains. Some coarse-graining is required to be able to compute macroscopic flows, and micro-macro numerical methods have been devised to allow calculations with these mesoscale constitutive equations. These numerical methods, reviewed by Keunings (2004), are still computationally very expensive and difficult to perform in complex geometries of engineering interest, especially considering the need for very refined meshing and time stepping for accurate viscoelastic predictions. Hence, the majority of engineering calculations, such as those mentioned above, rely on macroscopic constitutive equations some of which have been derived using more or less sophisticated closures of the mesoscale models. These derived closures invariably use decoupling and some form of pre-averaging (Bird et al., 1980; Lielens et al., 1999) that remove or change some rheological characteristics of the original mesoscale models (Van Heel et al., 1998; Zhou and Akhavan, 2003). Needless to say the mesoscale closures have their own simplifications, hence they require improvements of their own.

Micro-macro *methods couple mesoscopic scale of kinetic theory to the macroscopic scale of* continuum mechanics, *and have been introduced in the pioneering works by Biller and Petruccione (1987; 1988).*

The above sketched solution procedure seems simple enough, and one might expect that the flow properties can easily be calculated with the aid of a suitable computer. However, there are numerous complications, and the CFD field remains a treasure trove of challenging

and important areas of research. These complications are intrinsically related with the level of complexity on the abstractions on how a complex fluid is flowing.

Even for simple fluids, the flow may actually be too complicated to be solved on a computer on a suitable time scale. This is particularly true when the complexity of the flow equipment is evident, such as in extruders, mixers, fluidized beds, reactors, etc. Some simplifications are necessary to handle these problems, as reducing the degrees of freedom by reducing the number of spacial dimensions, or decrease the level of complexity of the geometry. For instance, one can look at a flow in an extruder as combining flows in simpler geometries such as:

DIE SWELL FLOW

FLOW AROUND AN OBSTACLE (E.G., CYLINDER)

FLOW IN A CONTRACTION

so that a method that cannot solve any of this is unlikely to be able to solve correctly the whole problem and another complex flows.

These simpler flows were selected as BENCHMARK FLOWS and have been studied independently by several research groups, in order to obtain consistently more accurate numerical solutions. These benchmark flows are today standard in the assessment of code performance as well as uncertainty quantification of new numerical methods for viscoelastic fluids.

If numerical methods are applied to flows of complex fluids, as in the fairly recent scientific branch of CFD called COMPUTATIONAL RHEOLOGY, the difficulties are even more challenging and demanding. In this thesis, COMPUTATIONAL RHEOLOGY relates particularly to the numerical simulation of laminar flows of viscoelastic fluids and not to the direct measurement of the rheological properties of the fluid (rheometry). However, in the broad sense Computational Rheology also includes the use of computational tools to assist rheometry.

The debate around the most appropriate designation, Deborah or Weissenberg number, is endless and not terribly helpful (McKinley, 2005) and in the XVIth *International Workshop on Numerical Methods for Non-Newtonian Fluids in 2010, Bruce Caswell declared, in a pacifist and ironic tone, that the term Deborah-Weissenberg number is the better one. Recently, in the Rheology Bulletin (2010), Roland Keunings (cited in Dealy 2010) ironically comments that "changing from* HIGH WEISSENBERG NUMBER PROBLEM *to* HIGH DEBORAH NUMBER PROBLEM (HDNP) *won't make the problem any simpler."*

Historically, after a rather short initial period of optimism, in which it was thought that the direct application of techniques developed for the simulation of Newtonian flows would also be efficient for computational rheology, it was found that the results obtained by different research groups suffered from a common problem, namely the loss of convergence at very low values of Deborah or Weissenberg numbers (Weissenberg number, $We = \lambda\dot{\epsilon}$, named after Karl Weissenberg by White (1964), is like the Deborah number, a non-dimensional parameter that measures the elasticity of a fluid and indicates the degree of anisotropy or orientation generated by the deformation). Then, Crochet and Walters (1983) stated, in a pessimistic tone, that the maximum limit of elasticity achieved in the results published between the 1950's up to the 1980's were so low that solutions were mere perturbations around the Newtonian solutions. Thus, it was proved that computational rheology, particularly the numerical calculation of viscoelastic flows, was a more complex task to deal with than the Newtonian fluid CFD, exhibiting iterative problems of convergence and accuracy, and leading to higher computation time and demanding computing resources, such as memory and processing time. This defined and identified the infamous puzzling problem presented to computational rheology, that became known as the HIGH WEISSENBERG NUMBER PROBLEM (HWNP). This problem on numerical calculations of laminar viscoelastic fluid flows can be

better understood by consulting several reference works, particularly Keunings (1986) and Owens and Phillips (2002), but it can shortly be explained as the existence of a limit in the Weissenberg number above which numerical methods diverge. The critical value of the Weissenberg number depends on the flow geometries as well on the constitutive equation, but geometric singularities are usually associated with more severe problems.

Another intellectual as well practical challenging aspect of fluid dynamics is related to Flow Instabilities. Flow instabilities (here related to physical instabilities rather than to the non-linearities of the mathematical approximations to the physical problem) take place in many different situations, depending on fluid type, velocity field and geometry, as well as the presence of other physical phenomena, such as temperature or concentration variations, surface tension gradients and electrokinetic body forces. One classical example of a simple fluid flow instability is the inertial driven transition from laminar to turbulent flow (Reynolds, 1883; Manneville, 2004).

Instabilities in viscoelastic fluids in the absence of inertial effects and under isothermal conditions, are also a puzzling challenge. These purely elastic instabilities, due solely to the viscoelasticity of the fluids, depend on the corresponding flow conditions. For simple linear shear flows instability studies have been done, such as the effects of parallel flow superpositions presented by Ramanan and Graham (2000), the instabilities in free-surface flows by Graham (2003), the instabilities in square cavity flows by Kim et al. (2000) and in parallel plate flows by McKinley et al. (1991a), and the industrially relevant extrusion instabilities at high flow rates, reviewed recently by Denn (2001) and Morozov and van Saarloos (2007). For curvilinear shear flow instabilities, studies on linear stability theory were extensively reviewed by Shaqfeh (1996), and works in the Taylor-Couette, Dean, Taylor-Dean and cone-plate instabilities were presented by Muller et al. (1989), McKinley et al. (1991a), Muller et al. (1993) and Larson et al. (2006). For extension dominated flows, and in particular in flows containing stagnation points at solid-liquid and liquid-gas interfaces, as one finds in flow around solid bodies or bubbles, or on contraction flows, instabilities have been known to take place for quite a long time (Cable and Boger, 1978a,b, 1979; Giesekus, 1968). For interior stagnation point flows, such as the flow in the opposed jet (Chow et al., 1988), in Taylor's four-roll mill (Giesekus, 1962) or in the cross-slot channel (Gardner et al., 1982), instabilities are also observed at high Deborah number flows.

There are also some theoretical developments on the criteria for the onset of these elastic instabilities, such as the work by Shaqfeh (1996) and McKinley and co-workers (McKinley et al., 1996; Pakdel and McKinley, 1996), that presented a dimensionless criterion for the onset of elastic instabilities based on the local flow curvature and the tensile stress acting along the streamlines. However, despite the recent efforts and progress on the understanding of the complexity of these flow instabilities, this is still a contemporary challenge to *Panta Rhei*.

Microfluidics *emerged in the beginning of the 1980's and even though it is still in a state of exploratory research, there are practical applications where its advantages stand out clearly, such as in screening for protein crystallization, bioanalyses or the manipulation of multiphase flows.*

The level of complexity also increases with the complexity of the practical applications, as when the Navier–Stokes equations are combined with the equations of energy and mass conservation, or when New Forcing Terms are taken into account in order to deal with other physical phenomena. Usually, these new forcing terms become important when they scale with surface area and the fluid transport

design strategies are scaled down to micron or sub-micron scales, as in MICROFLUIDIC devices. At such scales, surface-dominated physical forces/phenomena (e.g., capillary, wetting, electrokinetic effect), which usually can be neglected in macroscale flow processes, become important and in some cases dominant (Squires and Quake, 2005). The widespread use and low cost of microfluidic techniques is fostering a wealth of new practical applications involving complex fluids, often associated with complex phenomena. These are the cases of the study on magnetohydrodynamics or electrohydrodynamics (also known as electro-fluid-dynamics or electrokinetic phenomena) such as electro-osmotic flow, where the Navier–Stokes equations are coupled with the Maxwell's and the Poisson-Nernst-Planck (PNP) (also called Smoluchowski equation), respectively. The Poisson-Nernst–Planck equations are a conservation of species equation used to describe the motion of ions in a fluid medium, in which the diffusing species are also in motion with respect to the fluid by electrostatic forces.

Walther Nernst, German chemist that studied under Ludwig Boltzmann; Max Planck, German physicist and mathematician. Planck reformulated Nernst's theorem, which later came to be known as the third law of thermodynamics.

Electro-osmosis is a basic electrokinetic phenomenon, where the flow is induced by a new body force term, the applied external electric field. The interaction between the channel walls and the polar fluid creates near-wall layers of ions, and these layers move under the action of the applied electric field, whereas the neutral core is dragged by viscous forces and moves as a solid body. The principle was first demonstrated by Ferdinand Reuss (1809), in an experimental investigation using porous clay. This was followed by the theoretical work on the Electric Double Layer (EDL) by Hermann von Helmholtz (1879), which related the electrical and flow parameters for electrokinetically driven flows. In the early 1900's Marian von Smoluchowski (1903) contributed to the understanding of electrokinetically driven flows, especially for conditions where the EDL thickness is much smaller than the channel height.

For Newtonian fluids, rigorous modelling and analytical solutions of simple shear electro-osmotic flow has been the subject of several studies, and a thorough review on this and on various other aspects of electro-osmosis can be found in Karniadakis et al. (2005). On the other hand, the theoretical study of electro-osmotic flows for complex fluids is fairly recent and most works have been restricted to simple inelastic fluid models, such as the power-law, due to the inherent difficulties introduced by more complex constitutive equations. It was clear that there were no analytical solutions for fully-developed electro-osmotic flows of quasi-linear and non-linear viscoelastic fluids, and even less so when in combination with pressure gradient before the work done in this thesis (Afonso et al., 2009c). Also, the numeric approach to more complex geometry flows for complex fluids with electrokinetic effects are scarce, and are one of the actual challenges on *Panta Rhei*.

To conclude this section, a final overview is presented on some of the actual challenges on *Panta Rhei* that drives this thesis and more specifically on the actual challenges on COMPUTATIONAL RHEOLOGY: the *infamous* HIGH WEISSENBERG NUMBER PROBLEM, the *eccentric* purely elastic FLOW INSTABILITIES and the *puzzling* increase in complexity introduced by NEW FORCING TERMS associated with electro-osmosis and due to the small scale of fluid transport in microfluidic systems.

1.2 OBJECTIVES

This study aims to increase the current knowledge about several distinct, but complementary, subjects. This is accomplished in a numerical and theoretical investigation addressing the following four main objectives/questions:

OBJ. 1 Is it possible to develop robust and highly accurate numerical schemes to overcome the of HIGH WEISSENBERG NUMBER PROBLEM?

OBJ. 2 Is it possible to use these robust and highly accurate numerical schemes to simulate complex flows of complex fluids that originate purely elastic FLOW INSTABILITIES?

OBJ. 3 Is it possible to use these robust and highly accurate numerical schemes to simulate complex flows of complex fluids driven by NEW FORCING TERMS, such electro-osmosis, and do these flows lead to elastic FLOW INSTABILITIES?

OBJ. 4 Is it possible to obtain analytical solutions for simple flows of complex fluids driven by NEW FORCING TERMS, such as electro-osmosis?

The proposed objectives 1 and 2 involved, on one side, the incorporation of new features into an existing code for efficient and precise viscoelastic flow calculations at high Weissenberg numbers and, on the other side, the investigation of various flows with an emphasis at exploring flow instabilities linked to viscoelasticity.

The in-house code used is a three-dimensional time dependent finite-volume code developed by Oliveira et al. (1998), with improvements described later in Oliveira and Pinho (1999a,b) and Alves (2004). The FVM code uses collocated non-orthogonal meshes, central differences for discretization of diffusive terms, a second order backward implicit time discretization through the SIMPLEC algorithm (Patankar, 1980) to ensure simultaneously the momentum balance and mass conservation. The CUBISTA high resolution scheme, introduced by Alves et al. (2003a), is used to discretize the advection terms of the governing equations.

Given the hyperbolic nature of the constitutive equations used to represent the rheological behaviour of viscoelastic fluids, and given the inherent HWNP, the simulations require the use of robust numerical methods. For this purpose, the numerical stabilization methodology recently proposed by Fattal and Kupferman (2004) was implemented, the so-called matrix-logarithm or log-conformation formulation for the viscoelastic constitutive equations, which is based on a reformulation of the constitutive law in terms of the matrix logarithm of the conformation tensor. To test the proposed implementation and demonstrate the enhanced stability, some of the benchmark flows used in computational rheology will be investigated.

The proposed objectives 3 and 4 involved, on one side, the numerical implementation of the new terms and equations related to the electrokinetic phenomenon in the in-house FVM code and, on other side, the theoretical study of electro-osmotic flows for complex fluids.

To compute flows driven by electro-osmosis the Poisson-Nernst–Planck equations were incorporated into the code to calculate the electric charge distribution required to quantify the electric field forcing of the momentum equation. This new code feature is of extreme relevance in microfluidics. When electro-osmosis flow is used in combination with viscoelastic fluids, new phenomena emerges, such as new types of flow instabilities.

Up to the beginning of this thesis, there were no analytical solutions for fully-developed electro-osmotic flows for non-linear viscoelastic fluids. In order to test the proposed code implementation and demonstrate its high stability and accuracy, we carried out several theoretical studies on the development of analytical solutions for channel and pipe flows of viscoelastic fluids under the mixed influence of electro-osmosis and pressure forces. These studies were performed for different constitutive models and for different boundary conditions at the walls.

1.3 DISSERTATION OUTLINE

The present dissertation falls into the category of *multi-paper (or paper-based) dissertations*, built up as a collection of ten peer-review journal papers, published (or under evaluation) in international scientific journals. A complete list of the included papers can be found in Section Publications (on page xi). The included papers were prepared in the course of this PhD thesis and correspond to specific stages and parts of the above mentioned objectives.

The present dissertation is divided in four main parts:

Part I: Introduction (Panta Rhei)

Part II: Developments on theoretical and computational rheology

Part III: (Further) Developments on theoretical and computational rheology

Part IV: Conclusions and Outlook

The present section closes the introductory part (Part I). In Part II, "Developments on theoretical and computational rheology", the main contributions of each paper will be described, on the following topics: High Weissenberg Number Problem, purely elastic instabilities and viscoelastic electro-osmotic flows.

The papers presented in Part III are integral versions of the work already published or in the process of submission or review.

In Part IV, the main conclusions are presented. The outlook of the Thesis is presented at the final section of Part IV, including suggestions for future work.

Part II

DEVELOPMENTS ON THEORETICAL AND COMPUTATIONAL RHEOLOGY

INTRODUCTION TO PART II

... all the difficulty of philosophy seems to consist in this:
from the phenomena of motions to investigate the forces of Nature,
and then from these forces to demonstrate the other phenomena.

— Sir Isaac Newton

In the present Part II of this dissertation, called "Developments on theoretical and computational rheology", detailed insights into the achieved numerical and analytical developments will be presented. Each contribution related to the work objectives, presented in Section 1.2, will be explained in detail. Given that the present dissertation falls into the category of *multi-paper dissertations*, and in order to keep repetition of information at a minimum level, the majority of the governing equations, figures, tables, numerical algorithms and other published information will be addressed in Part III of this dissertation.

Part III, called "(Further) Developments on theoretical and computational rheology" includes a complete and integral version of the papers written during this PhD work.

Part II is further divided into three main chapters. In Chapter 2, the High Weissenberg Number Problem is described in more detail, with a brief historical revision. Possible causes and solutions are also addressed, such as the encouraging results obtained by our numeric FVM code.

Chapter 3, is reserved for the developments and achievements in the *eccentric* features of elastic flow instabilities. Numerical results in a three-dimensional cross-slot geometry and in the mixing-separating geometry, will be also presented. These numerical results were obtained with the code implementations presented in Chapter 2.

Finally, in Chapter 4, the analytical and numerical developments related to the treatment of electro-osmosis will be briefly discussed. The various analytical solutions presented in this Chapter, were useful for testing the correct implementation of the Smoluchowski diffusion equation. The numerical solutions revealed that a mixture of elastic/electrokinetic instabilities are present in the flow of viscoelastic fluids in microfluidic devices.

2

THE *INFAMOUS* HIGH WEISSENBERG NUMBER PROBLEM

INFAMOUS :: *having an extremely bad reputation*

To err is human,
and to blame it on a computer is even more so.

— Robert Orben

The *bad reputation* posed by the High Weissenberg Number Problem (HWNP) has long faced those who wish to perform numerical simulations of complex flows of complex fluids. This problem was first identified by the breakdown of the numerical schemes for macroscopic continuum mechanics constitutive equations, such as the Upper-Convected Maxwell or Oldroyd-B models. This numerical failure at moderately low Weissenberg/Deborah numbers ($De \sim 1$), was accompanied by numerical inaccuracies and lack of mesh-convergent solutions, particularly when geometrical corners or stagnation point singularities are present, due to the exponential growth of the normal stresses at such locations.

The mathematical description of the UCM and Oldroyd-B models, is presented on page 91 for the extra stress tensor representation, $\boldsymbol{\tau}$, and on page 70 for the conformation tensor representation, $\mathbf{A}$.

Given the endless debate around the most appropriate use of Deborah or Weissenberg numbers (see more on page 12), we use De throughout this dissertation.

Several plausible explanations for the so-called HWNP have been identified along the past decades. However, and despite some recent progress, there is not yet a full understanding of its origin and possible solution. The main arguments put forward point essentially to each one of the following branches:

MODEL PROBLEMS: in computational rheology, the momentum and mass conservation equations (see equations (5.14) and (5.14), on page 91) are inherently coupled with macroscopic constitutive equations for the extra stress, $\boldsymbol{\tau}$ (or conformation tensor, $\mathbf{A}$). The adequate choice of the constitutive equation depends on the physical characteristics of the *real* working fluid. For instance, models presenting constant shear viscosity, such the UCM, Oldroyd-B or FENE-CR (Chilcott and Rallison, 1988) models, should not be used when the viscosity of the real fluid varies with the shear rate, such as for shear-thickening (also termed dilatant) or shear-thinning (known also as pseudoplastic) fluids. These types of fluids should be described instead by the PTT (Phan-Thien and Tanner, 1977; Phan-Thien, 1978), Giesekus (Giesekus, 1982) or FENE-P (Bird et al., 1980) models, amongst others. Therefore, ideally, for each fluid, there should be a model describing correctly its fluid rheological properties. The development of efficient, more realistic models is still a fertile ground in rheology (Boger and Walters, 2000), and so far no model is physically exact. The UCM and Oldroyd-B models are definitely not good physical models even for dilute polymer fluids. In particular, both can be derived

The mathematical description of the FENE-CR model, is presented on page 91.

The mathematical description of the Phan-Thien-Tanner (PTT) model, of the FENE-P model, based on the kinetic theory for finitely extensible dumbbells with a Peterlin approximation for the average spring force, and for the Giesekus model, is presented on page 91.

from a kinetic theory, with dumbbells modelling ensembles of polymer molecules that are assumed to be infinitely extensible. Some works relate this model assumption to the inherently more severe HWNP when these models are used. However, a bad physical model can be a good mathematical model, and the UCM and Oldroyd-B models remain, nevertheless, a good first approximation to the rheological behaviour of many viscoelastic fluids. Indeed, they already present mathematical difficulties common to most of the viscoelastic models and its equivalence with a kinetic model allows also for a deep understanding of this set of equations.

NUMERICAL PROBLEMS: the inclusion of the constitutive equations does not only increase the total number of degrees of freedom but also modifies the mathematical type of the resulting system of governing equations (Joseph, 1990). Several authors (Keunings, 1986; Renardy, 2000; Alves et al., 2001b; Fattal and Kupferman, 2004; Alves, 2004) claimed that the HWNP is related to the numerical discretization method, because the exact form of the constitutive equation indeed admits regular solutions at the continuous level. Other issues related to the divergence of the numerical methods are simply due to the fact that, for any model under consideration, no stationary state always exists. Steady state solutions for viscoelastic models in complex flows, as the flow past submerged solid bodies (cylinders, spheres, etc) and in contraction flows, were not computed yet at high Deborah numbers, a situation which is very similar to what happens with Newtonian fluids, in which the flow becomes time dependent at high Reynolds numbers, so imposing a steady solution may result in loss of convergence. Moreover, the evolutionary character of the constitutive models and the hyperbolic nature of the equations are usually dependent on the positive definiteness of the conformation tensor (Dupret and Marchal, 1986; Joseph, 1990), and numerical discretization errors could, eventually, lead to the loss of such positive definiteness, resulting in a loss of topological evolutionarity that can trigger Hadamard instabilities (Joseph, 1990).

Jacques Hadamard (1902) introduced the mathematical concept of well-posed problems*, in which the mathematical description of physical phenomena should present existing unique solutions that depend continuously on the data, in some reasonable topology.*

In this work the second group of arguments is favoured, subscribing to the idea that, for defying challenging problems, the weapons should be *clever,* and usually simple*, approaches* to numerical flow solutions.

2.1 CLEVER APPROACHES

For over twenty years, an abundant literature has been discussing issues of numerical stability and seeking to devise *clever* numerical schemes in order to achieve more efficient, accurate, and stable solutions.

Some of these *clever* approaches were not exclusively presented for low Reynolds number, or inertialess, computational rheology, but also for turbulent flows of Newtonian fluids. The near wall thin boundary layers and sharp velocity gradients developed in the turbulent flow regime, and the inherent numerical difficulties, motivated the experts of this field to develop new numerical methods and use near-wall laws. Numerical improvements were then introduced, such the design of

special upwind-based finite volume schemes (Yang and Shih, 1993), the linearization and implicit treatment of source terms (Jacon and Knight, 1994), high-resolution central schemes for nonlinear conservation laws (Kurganov and Tadmor, 2000), high-resolution non-oscillatory advection methods (Drikakis, 2001), and a logarithm transformation used in turbulence modelling within the k-ε formalism (Ilinca et al., 1998). Ilinca et al. (1998) re-wrote the k-ε model in terms of the variables $\log(\kappa)$ and $\log(\varepsilon)$, so that when κ and ε are recovered they are always positive. This transformation also results in improved accuracy in regions of sharp gradients of turbulent quantities such as in boundary layers near the walls and in stagnation points.

This kind of simple logarithm transformation was also used in mass transfer problems by Miranda and Campos (2001) and Afonso et al. (2009a), who applied a scalar logarithmic transformation to the solute concentration to solve the laminar flow and solute transport in a parallel plate device with permeable walls, improving the FDM and allowing for the use of a larger grid spacing without loss of accuracy.

For turbulent flow of viscoelastic fluids, early attempts to perform numerical simulations of polymer induced drag reduction were unsuccessful. The difficulty resulted from the ill-posed problem identified by Hadamard (1902), in which the cumulative errors arising from the numerical discretization, eventually could lead to the loss of positive definiteness of the conformation tensor, $\mathbf{A}$, and trigger evolutionarity Hadamard instabilities (Joseph, 1990). The conformation tensor is a variance–covariance, Symmetric Positive Definite (SPD) tensor, and should remain SPD when evolving in time. To overcome these ill-posed instabilities, Sureshkumar and Beris (1995) introduced an artificial stress diffusion term into the evolution equation for the conformation tensor, leading to successful results when used with spectral evaluation of all variables. Vaithianathan et al. (2006) developed another method that also guarantees positive eigenvalues of the conformation tensor (remaining SPD), while preventing over-extension for dumbbell models, such as the Oldroyd-B, FENE-P and Giesekus models. The FDM code was coupled with a pseudo-spectral scheme for homogeneous turbulent shear flow, and it extended the Kurganov and Tadmor (2000) scheme, with the resulting spectra of the numerical simulations presenting no signs of aliasing errors. Recently, Housiadas et al. (2010) presented a new numerical method for the simulation of the flow of complex fluids with internal microstructure applied in Direct Numerical Simulations (DNS) of viscoelastic turbulent channel flow. This method was based on the log-conformation (Fattal and Kupferman, 2004) and was implemented in a full 3D spectral representation for the spatial variables and a backward differentiation second order scheme for time integration. Here again, numerical diffusion was added to the hyperbolic constitutive equation for the conformation tensor via the implementation of a second order finite difference multigrid diffusion scheme, with the main advantage (compared with a spectral method implementation used in Housiadas and Beris 2004) of preserving the positive definiteness of the conformation tensor.

A symmetric matrix $\mathbf{A}$ is positive defined (SPD) if $\mathbf{X}\cdot\mathbf{A}\cdot\mathbf{X}^{T} > 0$, for arbitrary $\mathbf{X}$.

In the framework of laminar flow computational rheology, and specifically for the inertialess (negligible inertia, $Re \sim 0$) HWNP case, theoretical nonlinear (energy) estimates for the stress and velocity components in a general setting, for an Oldroyd-B fluid, where presented by Lozinski and Owens (2003). They worked with the configuration tensor, $\mathbf{c}$, and derived a method that guarantees a well-posed evolutionarity Hadamard problem (Joseph, 1990). Alves et al. (2003a) proposed a new high-resolution non-oscillatory advection scheme, especially designed to be used with differential viscoelastic constitutive equations, referred to as the Convergent and Universally Bounded Interpolation Scheme for the Treatment of Advection (CUBISTA). This high resolution scheme

The symmetric configuration tensor, $\mathbf{c}$ was defined as $\mathbf{c} = \boldsymbol{\tau} + \frac{1}{We}\mathbf{I}$, for an Oldroyd-B fluid.

is formally third-order accurate on uniform meshes for smooth flows, and proved to be a good scheme to predict accurately viscoelastic flows.

Fattal and Kupferman (2004) also proposed a *clever* idea for viscoelastic constitutive equations, based on a reformulation of the constitutive law in terms of the matrix logarithm of the conformation tensor. According to Fattal and Kupferman (2004), this formulation introduces a better polynomial interpolation of the logarithm of the variables that exhibit an exponential growth near stagnation points, with the added advantage of preserving the positive definiteness of the conformation tensor. From a numerical point of view, the tensor-logarithmic transformation requires the determination of eigenvectors and eigenvalues of the conformation tensor at every computational cell and instant of time. Fattal and Kupferman (2004) also reported a breakthrough in the HWNP in their numerical simulations with the FENE-CR model (Chilcott and Rallison, 1988) in a two-dimensional lid-driven cavity flow. Later, Fattal and Kupferman (2005) extended the log-conformation approach to an Oldroyd-B fluid in the same geometry using a multigrid solver, providing the possibility to perform stable simulations at very large values of the Weissenberg number. They also reported on a stability condition and stated that it may be very restrictive when convection is weak, as in creeping flows, and in the presence of large deformation rates , as in the flow around sharp corners, showing the benefit of using the tensor-logarithmic transformation.

This matrix-logarithm or log-conformation *formulation (denomination used henceforth), is as the name implies, a simple logarithmic transformation of the conformation tensor in the constitutive differential equations of viscoelastic fluids.*

Jacopo Riccati, an Italian mathematician, looked at the approximation to the second order differential equations, in the form: $\frac{dy}{dx} = P(x) + Q(x)y + R(x)y^2$.

Lee and Xu (2006) presented a class of positivity preserving discretization schemes applied for rate-type viscoelastic constitutive equations, using a semi-Lagrangian approach and FEM, based on the observation that the rate-type constitutive equations can be cast into the general form of the Riccati differential equations and demonstrated that their method is second-order accurate for both time and space. Cho (2009) proposed a vector decomposition of evolution equations of the conformation tensor of Maxwell-type. In this transformation, the vectorized equations were considered as the sum of dyadics of the conformation tensor. This vector decomposition preserved the positive definiteness of the conformation tensor and did not require the solution of the eigenvalue problem at every calculation step, decreasing the computation cost. Nevertheless, in a generic 3D simulation, the vector decomposition required the calculation of nine components instead of the six independent components of the log-conformation tensor approach, thus limiting its efficiency in 3D numerical calculations, when compared with the log-conformation transformation approach.

A dyad $\mathbf{A}$ *is formed by the dyadic product (or external product) of two vectors* $\mathbf{a}$ *and* $\mathbf{b}$: $\mathbf{A} = \mathbf{a} \otimes \mathbf{b}$.

Balci et al. (2010) proposed, very recently, a method in which the square root of the conformation tensor is used for Oldroyd-B and FENE-P models. They derive an evolution equation for the positive-definite square root of the conformation, by taking advantage of the fact that the positive definite symmetric polymer conformation tensor possesses a unique symmetric square root that satisfies a closed-form evolution equation. Balci et al. (2010) claimed that their method can be easily implemented in numerical simulations, because it does not require the determination of eigenvectors and eigenvalues of the conformation tensor at every calculation step, resulting in significant practical advantages in terms of both accuracy and stability. This *square-root* formalism was very recently implemented in the in-house FVM code (Afonso et al., 2010a), but the results are still very preliminary, therefore this topic will be discussed later (See the Outlook section on page 267).

If the above mentioned *clever* approaches were independent of the numerical procedures used to discretize the system of governing equations, and so suitable for FVM, FEM, FDM or other procedures, a note should be addressed on the large amount of literature on stabilization schemes within the FEM and hybrid FEM/FVM frameworks for viscoelastic flows. For a more detailed description of these stabilization methods the works of Baaijens (1998); Baaijens et al. (2004) and Coronado (2009) are recommended.

As stated earlier (Section 1.1.3), there are specific BENCHMARK FLOWS that have been set to help the development and assessment of the behaviour of all these numerical techniques in computational rheology, and which have been studied independently by several research groups, in order to obtain consistently high accurate numerical solutions. These benchmark flows are very useful to measure the accuracy and assess the performance of the implementation of new numerical methods.

Among the proposed benchmark flows in computational rheology over the past years (Brown and McKinley, 1994; Hassager, 1988), it is now possible to conclude that the favourite geometries are the flow around a cylinder or a falling sphere and the 4:1 contraction flow (Owens and Phillips, 2002). In the next sections these two interesting type of flows will be reviewed in some detail.

2.2 CYLINDER FLOWS

The flow around a confined cylinder in a planar Poiseuille flow is a usual benchmark test-case in computational rheology (Brown and McKinley, 1994). It is representative of fundamental flow dynamics of viscoelastic fluids around submerged solid bodies and it can be encountered in many engineering processes, namely in the food industry (Xia and Sun, 2002), in composite and textile coating operations (Liu et al., 1998) and flows through porous media (McKinley et al., 1993).

From a numerical point of view, this flow is considered a smooth flow, due to the absence of geometrical singularities, such as a re-entrant or salient corner found in entry flows. However, it also introduces some difficulties associated with the development of thin stress layers on the cylinder sidewall and along the centreline in the cylinder rear wake, imposing a limiting value to the critical Deborah number, De_{crit}, for which steady solutions can be obtained.

For all these reasons, in the VIIIth international workshop on numerical methods for non-Newtonian flows, this flow was selected as a benchmark problem in computational rheology (Brown and McKinley, 1994). Another reason for the success of this choice was the suitability of this benchmark flow to experimental investigations, especially for birefringence studies.

A schematic view of the flow past a confined cylinder in a planar channel is shown in Figure 2.1. The ratio of channel height h to cylinder radius R is set equal to 2, which corresponds to the benchmark 50% blockage ratio case (Brown and McKinley, 1994). The Deborah number for this benchmark flow, based on the fluid relaxation time, λ, the mean inlet velocity, U, and the cylinder radius, R, can be defined as

$$De = \frac{\lambda U}{R}. \tag{2.1}$$

A Boger fluid is an elastic liquid with a constant viscosity. The first Boger fluid was introduced over 30 years ago by David V. Boger in a note entitled "A Highly Elastic Constant Viscosity Fluid" (Boger, 1977). Boger's purpose was to create an optically clear, highly viscous and highly elastic fluid which exhibits a nearly constant viscosity and which can be processed at room temperature.

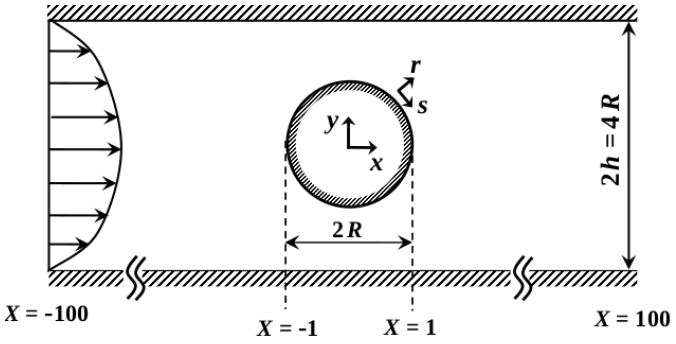

Figure 2.1: Schematic representation of the flow past a confined cylinder geometry ($X = x/R$)

This computational benchmark flow described by Brown and McKinley (1994) was based on the experimental results of McKinley et al. (1992, 1993). The fluid used in this work was a constant viscosity Boger fluid, a highly viscous and highly elastic polymeric solution consisting of a mixture of 0.31% (w/w) Polyisobutylene (PIB) dissolved in Polybutene (PB) and Tetradecane (C_{14}), with a relaxation time of $\lambda = 0.794$ s. The rheological properties of this Boger fluid, also known as the Massachusetts Institute of Technology (MIT) Boger fluid, are documented in detail by Quinzani et al. (1990).

For the inertialess flow around a confined cylinder it is also necessary to define a second dimensionless number, the ratio between the Newtonian solvent viscosity, η_s, and the total viscosity, η_o, defined as

$$\beta = \frac{\eta_s}{\eta_o} = \frac{\eta_s}{\eta_s + \eta_p}, \tag{2.2}$$

where η_p is the polymeric contribution to the shear viscosity.

The value $\beta = 0.59$ characterizes the MIT Boger fluid used in the experiments of McKinley et al. (1992, 1993), and has been used since then in most of the numerical works for this flow (Liu et al., 1998; Fan et al., 1999; Dou and Phan-Thien, 1999; Alves et al., 2001b; Owens et al., 2002; Kim et al., 2004; Hulsen et al., 2005; Afonso et al., 2008, 2009b).

For the cylinder problem, two possible configurations are commonly used in computational rheology:

- the cylinder is fixed relative to the confining channel walls and a planar Poiseuille flow emerges from an imposed pressure gradient (the common *computational benchmark flow* described by Brown and McKinley (1994));

- the cylinder moves as in the case of a cylinder falling freely along the middle of a channel, which is equivalent to a uniform flow approaching a fixed cylinder with channel walls moving with the fluid (this case is a *work in progress*, and several contributions were reported in the recent past).

During this work, several detailed studies (five presentations in international and national conferences and two published papers, Afonso et al. (2008, 2009b)) were performed on both cylinder flow cases. In the

next sections both the common *computational benchmark flow* and the freely falling cylinder cases are discussed in more detail.

2.2.1 *Flow around a cylinder*

2.2.1.1 *Brief review: experimental work*

For Newtonian fluids, the first approach to solve the flow around submerged solid bodies was made by Stokes (1851), who obtained the analytical solution for creeping (or inertialess) flow around a sphere and the corresponding expression for the drag force. Oseen (1910) obtained an approximate analytical solution for the flow around a cylinder at low Reynolds numbers, and later, Proudman and Pearson (1957) derived the complete solution, using asymptotic expansions.

For laminar, transition and turbulent flow regimes (ranging from Reynolds numbers from 50 to $9{\times}10^3$) of non-Newtonian fluids around a cylinder, a detailed experimental study was presented by Coelho and Pinho (2003a,b, 2004). Using 0.1 to 0.6% (w/w) aqueous solutions of Carboxymethyl cellulose (CMC) and tylose, two cylinders with an aspect ratio of 12 and 6 and blockages of 5 and 10%, respectively, results were presented for the various vortex shedding regimes as a function of the Reynolds and elasticity numbers (Coelho and Pinho, 2003a), for the particular flow characteristics within each of those flow regimes (Coelho and Pinho, 2003b), and for the pressure field on the cylinder surface, such as the drag coefficient, the pressure rise coefficient and the wake angle (Coelho and Pinho, 2004).

For low Reynolds numbers or inertialess flows of complex fluids, and even before the establishment of the computational benchmark flow, Dhahir and Walters (1989) performed extensive experimental drag force measurements on a cylinder, by considering the effect of wall confinement (using a 50% blockage ratio). Several types of fluids were used, such as a Newtonian fluid (a mixture of corn syrup in water), a Boger fluid (a mixture of Polyacrylamide (PAA) in water and corn syrup), an inelastic shear-thinning solution (xanthan gum in water) and a viscoelastic fluid with elastic and shear thinning effects (PAA in water). The drag force on the cylinder was found to decrease for all non-Newtonian fluids, when compared with the Newtonian case, with the higher reduction obtained for the viscoelastic shear thinning fluid and the lower for the Boger fluid, by approximately 55% and 20% as compared to Newtonian fluid, respectively.

Using Laser Doppler velocimetry (LDV) and video flow visualization McKinley et al. (1992, 1993) documented a series of flow transitions for creeping flow past a circular cylinder confined between two parallel channels, using a highly viscous viscoelastic PIB-based Boger fluid. For low Deborah numbers ($De < 1$) the flow field remained steady and two-dimensional, but for higher Deborah numbers ($De > 1$) a transition from steady 2D to steady three-dimensional flow was reported, with the secondary flow in the downstream wake region periodically moving in the axial direction of the cylinder. Because this transition occurred at low Reynolds numbers, inertial effects could be ruled out, suggesting that these instabilities are purely elastic. The critical Deborah number (De_{crit}) for the onset of these purely elastic instabilities depends on the blockage ratio, increasing with the increase of this aspect ratio.

McKinley et al. (1992, 1993) also described a steady to unsteady 3D flow transition at higher Deborah numbers.

The elastic flow transitions for viscoelastic flow past a confined circular cylinder under creeping flow conditions were also studied experimentally in several subsequent works, such as the experiments of Byars et al. (1995), Byars (1995), McKinley et al. (1996) and Shiang et al. (1997, 2000). Byars (1995) examined the nonlinear dynamics of the secondary flows for a wide range of aspect ratios and the effect of the upstream conditions on the spatial and temporal characteristics of the secondary flow structures. Shiang et al. (1997) also worked with the PIB-based Boger fluid characterized by Quinzani et al. (1990), and investigated the influence of elasticity and geometry eccentricity effects on the dynamics and kinematics of the inertialess, viscoelastic flow past a confined circular cylinder, using Particle image velocimetry (PIV) to measure the whole-field of instantaneous velocity, at a fixed aspect ratio of 16. Due to this high aspect ratio, Shiang et al. (1997) did not observe the 3D transition from steady to unsteady flow, as reported by McKinley et al. (1992, 1993). Shiang et al. (2000) extended the work, using PIV and long-exposure streak line photography to investigate creeping viscoelastic flow past a circular cylinder, with a fixed aspect ratio of 2. The critical Deborah number determined by Shiang et al. (2000) was $De_{crit} \approx 0.21$, significantly lower than the values reported by McKinley et al. (1993), $De_{crit} = 1.3$, for a channel width to cylinder radius aspect ratio of two. Shiang et al. (1997, 2000) also identified experimentally a periodic vortical structure for $De_{crit} \approx 0.66$.

From these works it seems that the elastic instabilities are related to the extension of the high molecular network and the large stresses developed in the wake of the cylinder. McKinley and co-workers (McKinley et al., 1996; Pakdel and McKinley, 1996) proposed a criterion that defines and unifies the critical conditions for the appearance of elastic instabilities in these systems, where the streamlines have curvature. Recently, a new criterion (semi-empirical) specifically for the viscoelastic flow past a confined cylinder was presented by Dou and Phan-Thien (2008), and the trigger mechanism for the onset of the elastic instabilities was related to an inflection of the velocity profile originated by the normal stress near the cylinder surface. This criterion is consistent with that proposed by McKinley et al. (1996) and Pakdel and McKinley (1996), with De_{crit} increasing with the aspect ratio h/R, and scaling with $O\left[1/\sqrt{1-\beta}\right]$.

Other type of fluid that was studied in several experimental works (and simulations, see next section 2.2.1.2), was the shear-thinning mixture of 5% (w/w) PIB in C14. Baaijens and co-workers (Baaijens et al., 1994, 1995) performed accurate measurements of the velocity and the stress fields, using LDV and flow induced birefringence, respectively, for several flow rates and cylinder eccentricity. Later, Baaijens et al. (1997), changed the working fluid to a Low-density polyethylene (LDPE) melt and the aspect ratio to 8 and also investigated the case of the flow around an asymmetrically confined cylinder.

2.2.1.2 *Brief review: numerical work*

Along with the experimental work, Baaijens and co-workers (Baaijens et al., 1994, 1995, 1997, 2004) also performed numerical predictions for shear thinning viscoelastic flow past a confined circular cylinder under creeping flow conditions, using a mixed FEM code. Baaijens et al. (1994)

used a PTT model in the numerical simulations to compare with the experimental results obtained at $De = 0.216$, with the numerical results describing accurately the velocity field but failing to predict the normal stresses in the wake of the cylinder. The use of a multimode PTT model allowed Baaijens et al. (1995) to obtain a good agreement between the numerical and experimental normal stress fields, including the results for the eccentric cylinder. Later in Baaijens et al. (1997), the numerical predictions for the wake normal stress for the LDPE fluid, were not in agreement with the experimental works, when using a four mode PTT model with exponential kernel for the stress coefficient function and also a multimode Giesekus model.

For the flow of an Oldroyd-B fluid in the Stokes regime for a 50% blockage ratio and $\beta = 0.59$ (as in the experimental work of McKinley et al., 1993), an extensive list of investigations were performed over the last years (e.g. Dhahir and Walters, 1989; Hu and Joseph, 1990; Huang and Feng, 1995; Liu et al., 1998; Fan et al., 1999; Phan-Thien and Dou, 1999; Dou and Phan-Thien, 1999; Caola et al., 2001; Alves et al., 2001b; Oliveira, 2001a; Owens et al., 2002; Kim et al., 2004; Alves, 2004; Oliveira and Miranda, 2005; Hulsen et al., 2005; Gerritsma, 2006; Coronado et al., 2007; Sahin and Wilson, 2007; Guénette et al., 2008; Afonso et al., 2008; Kane et al., 2009; Afonso et al., 2009b; Damanik et al., 2010; Jafari et al., 2010). From this vast list, three sets of works can be selected as *milestones* in the process of defying the cylinder HWNP. The main reason, besides its clear relevance, to select these specific papers over other equally interesting works, is to helping establish an organized review of this subject (and avoid the possible repetition with the reviews made at the paper presented in Part III, Section 5.1). These *milestones* works are:

- Fan et al. (1999) and Alves et al. (2001b). Prior to these works, there was a significant discrepancy in the results presented by various research groups. Surprisingly this limitation is observed even at low De values, where all the methods converge to a stable solution. For instance, and taking as comparison the dimensionless drag coefficient, C_D, the results for $De > 0.7$ are not in agreement between the C_D values proposed by Fan et al. (1999), Caola et al. (2001) and Owens et al. (2002), with the exception of the results from Alves et al. (2001b) and Fan et al. (1999), as illustrated in Figure 2.2(a). It was the first time that two different numerical codes yield independent similar results, not only in the good agreement for the C_D values (although it is an important parameter, the C_D is not the better indicator of the quality or accuracy of the numerical solutions, since it is an integral quantity), but also for the unambiguous results for the profiles of normal stresses along the centreline downstream of the cylinder, at $De = 0.7$, shown in Figure 2.2(b).

The mathematical description of the dimensionless drag coefficient, C_D, is presented in equation (5.22), on page 93. In other notations, the dimensionless drag coefficient is designed as K (see equation (5.12), on page 74, for a mathematical description).

- Fattal and Kupferman (2004). After the presentation of this work on the log-conformation methodology, the scenario changed significantly, at least in respect to the C_D data. The first numerical implementation of this method was performed in the finite difference framework by the authors (Fattal and Kupferman, 2004, 2005), later in the finite element framework in a joint work with Hulsen (Hulsen et al., 2005) (and only two months later, by Kwon, 2004), in the finite volume method framework by Afonso et al.

(2009b) (see more detail in the next section), and recently in the spectral elements framework by Jafari et al. (2010).

Hulsen et al. (2005) tested the log-conformation method in the benchmark flow of Oldroyd-B and Giesekus fluids past a confined circular cylinder and reported an apparent unbounded convergence limit for the Giesekus model, whereas for the Oldroyd-B fluid the solution became unsteady at high Deborah numbers while exhibiting a strong mesh dependency, particularly for the normal stresses on the wake of the cylinder. Kwon (2004) extended the log conformation formulation to viscoelastic flows around asymmetric arrays of cylindrical obstacles confined in a channel and the results agreed qualitatively with the flow characteristics. Coronado et al. (2007) presented a simple alternative implementation of the log-conformation formulation and their results demonstrated that the method works well for a generalized constitutive model improving the numerical stability at high De, especially in the flow past a confined cylinder, where the maximum De was extended to 1.0, as compared to 0.7 obtained with the standard DEVSS-TG/SUPG method. Their results were also in good agreement with those presented by Hulsen et al. (2005). Guénette et al. (2008) performed simulations of the flow of a viscoelastic fluid around a confined cylinder using the Oldroyd-B and Giesekus models. They used a FEM, with an anisotropic adaptive remeshing method, based on the log-conformation formulation, and showed that convergence with mesh refinement was possible for the Oldroyd-B model up to at least $De = 0.7$. Kane et al. (2009) compared four different FEM treatments for the convective term of the log-conformation evolution equation and performed a comparative study on the cylinder benchmark flow. Jafari et al. (2010) presented a spectral element algorithm based on the log-conformation with the aim of removing the instabilities observed in the simulation of unsteady viscoelastic fluid flows, and surprisingly, at least for FENE-P, the results obtained with the log-conformation did not converge for higher Deborah numbers flows. Damanik et al. (2010) used a fully coupled monolithic multigrid finite element approach with consistent edge-oriented stabilization technique. Stress convergence was attained up to $De \approx 0.7$ in the cylinder flow, and converged solutions were obtained up to $De \approx 2.1$, with the drag coefficient comparable with the data presented by Hulsen et al. (2005) and Afonso et al. (2009b). Nevertheless, the monolithic edge-oriented FEM presented by Damanik et al. (2010), used a direct steady approach which could dissipate the expected unsteady behaviour of the flow at high Deborah numbers. The use of only half of the computational domain (i.e. imposing symmetry boundary conditions along the centreline), eliminates the possibility to capture possible symmetry-breaking steady/unsteady phenomena.

The Discrete Elastic-Viscous Split Stress, independent Traceless velocity Gradient interpolation, Streamline Upwind Petrov-Galerkin (DEVSS-TG/SUPG) are stabilization schemes used within the FEM framework.

If, on one hand, Alves et al. (2001b) clearly identified the necessity to use very refined meshes and accurate schemes for the advection terms of the governing equations, on the other hand, Fattal and Kupferman (2004) provided a glimpse into the possible results for $De \geqslant 0.8$ in the cylinder case, opening the doors to the supposed unsteady viscoelastic flows at high Deborah numbers and its inherent instabilities, as the

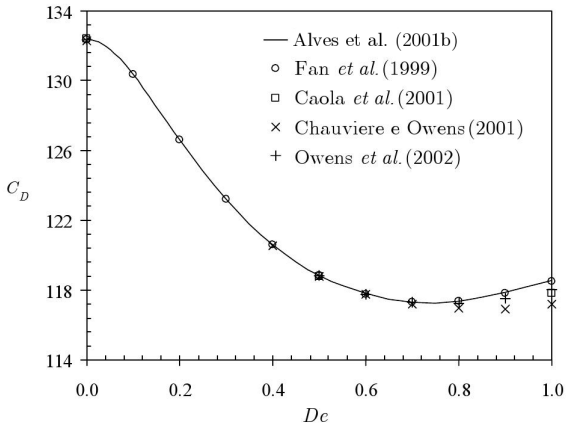

(a) Drag force coefficient, C_D.

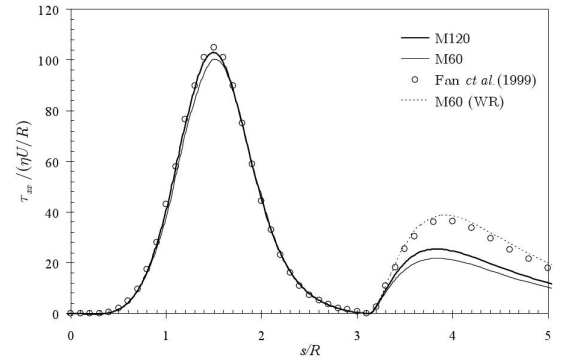

(b) Stress profiles.

Figure 2.2: Flow of an Oldroyd-B fluid ($\beta = 0.59$) past a cylinder: (a) drag force coefficient, C_D and (b) stress profiles along cylinder wall and downstream centreplane at $De = 0.7$. Figures adapted from Alves (2004) with the permission of the author.

ones reported in the investigations of Afonso et al. (2009b), detailed in the next section.

2.2.1.3 *Contribution from this work*

In Afonso et al. (2009b) (see the integral version of this investigation on Section 5.1, on page 67), the log conformation methodology was implemented within the finite volume method framework for the first time. This was achieved via the discretization of the log-conformation evolution equation (see equation (5.9), on page 71) into the existing FVM code.

The flow around a confined cylinder with a blockage ratio of 0.5 was chosen as the test geometry and detailed comparison between the results obtained by both the standard formulation (based on the extra stress tensor, see equations (6.3) and (6.5), on page 70, and called abbreviately as *StrT*) and the log-conformation tensor approach (called *LogT*) was presented.

The results for the *StrT* formulation obtained in the refined mesh (mesh $M60_{WR}$, with WR standing for *wake refined*) with a minimum cell size of the order $O(10^{-4} : 10^{-3})$ diverged at low $De \approx 0.9$, while for the *LogT* there was no limiting bound for the attained Deborah number, although only simulations up to $De = 1.9$ were performed.

This represents an increase of about 90% in the maximum attainable De when the *LogT* is used instead of the *StrT* formulation.

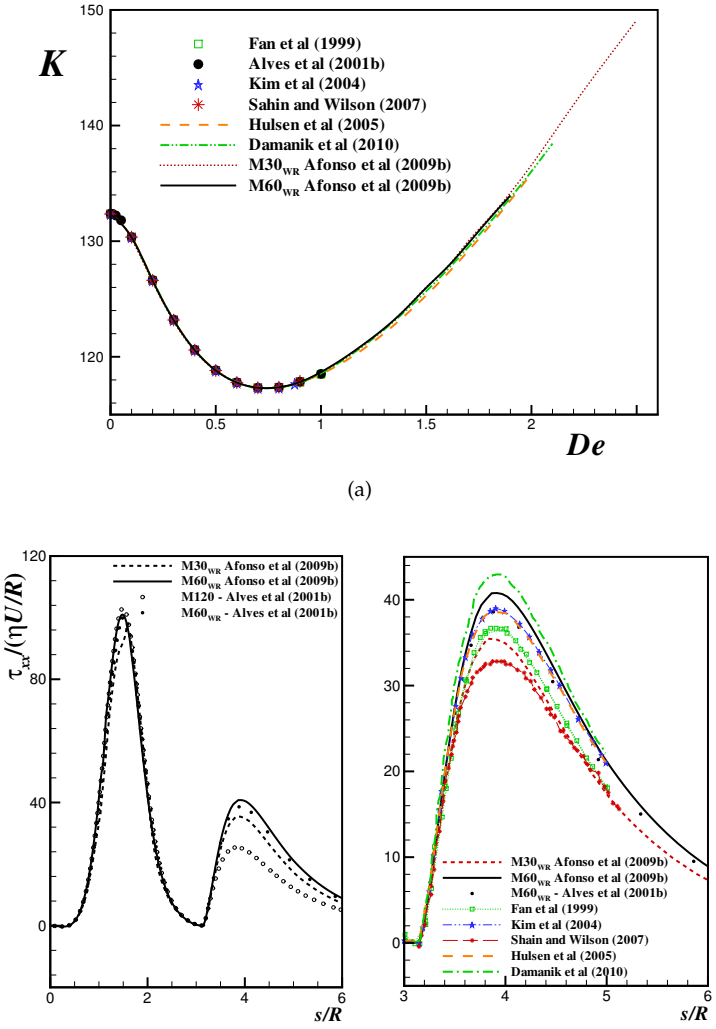

Figure 2.3: Flow of an Oldroyd-B fluid ($\beta = 0.59$) past a cylinder: (a) drag force coefficient, K and (b) stress profiles along cylinder wall and (c) downstream centreplane at $De = 0.7$.

For the Oldroyd-B model it is expected that $\det(\mathbf{A})_{min} \geqslant 1$ *(Hulsen, 1988).*

The divergence of the simulations performed with the *StrT* formulation was related with the loss of positive definiteness of $\mathbf{A}$ (Figure 5.2, on page 75), with the time evolution of $\det(\mathbf{A})_{min}$ at the rear stagnation point region becoming negative. For the *LogT* formulation the value of $\det(\mathbf{A})_{min}$ is, by design, always positive, thus showing no signs of violating the positive definiteness criterion.

The predictions for the drag coefficient K, obtained by Afonso et al. (2009b), along with the data published after that work, are presented in Figure 2.3a. Up to $De = 1$ the results agree and follow the trend data of Alves et al. (2001b), Fan et al. (1999), Kim et al. (2004) and Sahin and Wilson (2007). For higher Deborah numbers (up to $De = 1.9$), the drag coefficient predictions are in good agreement with the data presented by Hulsen et al. (2005) and Damanik et al. (2010). The underprediction presented by Hulsen et al. (2005) can be explained by the fact that for $De > 1$ no steady state could be attained, and in Afonso et al. (2009b)

the K values were the time-average values, while for Hulsen et al. (2005), K is assumed right after the onset of the transient behaviour. The direct steady approach and the use of only half of the computational domain, did not allowed Damanik et al. (2010) to obtain the expected unsteady behaviour of the flow at high Deborah numbers.

Concerning the normal stress convergence along the cylinder surface and the rear wake, mesh independent results were obtained up to $De = 0.7$, and in agreement with the values obtained by Alves et al. (2001b) (see Figures 2.3b and 2.3c). At $De = 0.9$ stress convergence was not achieved by any published work. The mesh dependence can be even more important given the observations by Afonso et al. (2009b) on the specific location of peak stress, x_{max}, where the maximum normal stress, $(\tau_{xx})_{max}$, along the centreline of the rear wake region occurs (see Figure 5.7). For high Deborah numbers the location of x_{max}/R shifts back towards the rear stagnation point, while the maximum normal stress, $(\tau_{xx})_{max}$ is increasing. This upstream shift in x_{max}/R at large Deborah numbers certainly contributes to numerical difficulties, as the size of the region of peak normal stress may eventually become smaller than the local streamwise mesh resolution.

Afonso et al. (2009b) also performed simulations using the PTT model, with a linear kernel for the stress function and two different extensional parameters ($\varepsilon = 0.02$ and 0.25), in order to better understand the main differences between the results obtained with a constant viscosity viscoelastic fluid (represented by the Oldroyd-B model) and a viscoelastic shear-thinning fluid (PTT model). The extensional parameter ε imposes an upper limit to the elongational viscosity ($\eta_E \propto 1/\varepsilon$ for low ε) and allowed the study of the effect of polymer concentration, ranging from dilute ($\varepsilon = 0.02$) to concentrated ($\varepsilon = 0.25$) polymer solutions.

When $\varepsilon \to 0$ the PTT model reduces to the Oldroyd-B model.

For lower values of ε ($\varepsilon = 0.02$), and on the most refined mesh, the standard formulation diverged at $De \approx 1.2$, again with signs of negative values of $\det(\mathbf{A})_{min}$, while for the log-conformation approach, converged solutions could be attained up to $De \approx 10$. This breakthrough in the critical Deborah number for steady flow clearly shows the advantage of using the *LogT* formulation. For high values of ε ($\varepsilon = 0.25$), the scenario was outstanding, with the *LogT* presenting no bound for the limiting Deborah number, while the *StrT* presented signs of ill-posed problems at $De \approx 30$.

For the PTT model, and for both ε values investigated, the mesh refinement effect for the profiles of τ_{xx} at the cylinder sidewalls and in the near wake region is negligible (see Figure 5.10, on page 82), even for so high Deborah numbers.

2.2.2 *Freely falling cylinder*

The freely falling cylinder in the middle of a channel is equivalent (by means of a Galilean transformation) to an uniform flow approaching a fixed cylinder with channel walls moving with the fluid. This configuration is different from the situation discussed in the previous section, in which the cylinder is fixed relative to the confining channel walls and a planar Poiseuille flow emerges from an imposed pressure gradient.

The freely falling cylinder case gives rise to the interesting phenomenon of *negative wakes* (Hassager, 1979), essentially consisting of fluid in the wake of the cylinder moving faster and in the opposite direction to the wake-generating object. In a frame of reference fixed

to the cylinder, this correspond to velocities in the wake that are faster and in the same direction as the uniform approach flow, a situation that arises only with viscoelastic fluids. The origin of negative wakes is not yet well understood, and one of the motivations for this work was numerical quantification of conditions for its formation.

2.2.2.1 *Brief review: experimental work*

For some viscoelastic fluids, the steady flow behind a cylinder is characterized by the appearance of a *negative wake* which strongly depends on fluid rheology. *Negative wakes* are overshoots of the streamwise velocity seen by the moving body along the centreline and have been found in wake of cylinders, spheres and rising bubbles, and is schematically represented in Figure 2.4.

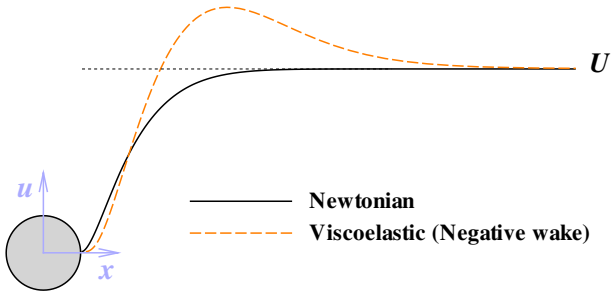

Figure 2.4: Schematic representation of a negative wake. Velocity profiles along the rear wake of the cylinder (reference attached to the cylinder).

One of the most extensive early investigations of this phenomenon were the visualizations of the sedimentation of a sphere in shear-thinning PAA solutions by Arigo and McKinley (1998), who also made an extensive literature survey review. For Boger fluids, however, McKinley et al. (1993) were unable to detect the appearance of negative wakes downstream of a cylinder and up to the present time there is no experimental evidence of negative wake formation with constant viscosity elastic fluids.

The specific physical conditions under which the negative wake arises and the possible mechanisms involved in their formation are still not fully understood in spite of several studies that have focused on these issues. In the sphere/cylinder geometries, Bush (1993) attributed the negative wake behaviour to the relative proportion between elongational stresses in the downstream region and fluid elasticity, and suggested that the upstream shift in streamlines and the formation of negative wake are a result of having a Deborah number much greater than the Trouton ratio. For the sphere flow case, Harlen (2002) proposed that the origin of negative wake was related to the circumferential gradient of shear stress along the centreline, and in particular with the competition of shear and normal stress distributions. Based on the suggestions of Bush (1993) and Harlen (2002), Arigo and McKinley (1998) proposed a criterion for the formation of negative wake based on the ratio of axial tensile stress to shear stress. Dou and Phan-Thien (2004) also studied this phenomenon and proposed a different criterion, this time based on the ratio between the gradient and the magnitude of

elongational viscosity, to predict the critical De marking the onset of negative wake for several constitutive models (PTT, FENE-CR, FENE-P and Giesekus models).

2.2.2.2 *Brief review: numerical work*

The settling of a cylinder in a confined viscoelastic fluid is still a *work in progress* in computational rheological, and several contributions have come forward in the recent past. Huang and Feng (1995) investigated the steady settling of a cylinder through quiescent Newtonian and Oldroyd-B fluids in a vertical channel, employing FEM with the Elastic-Viscous Split Stress (EVSS) scheme. For their higher blockage case (50%), Huang and Feng (1995) predicted a negative wake at high Deborah numbers, but this unusual phenomenon was not replicated by Oliveira et al. (1998) in their numerical work based on the FVM. The predictions of Oliveira et al. (1998) for the unbounded flow case and the confined case with blockage area of 33% were in agreement with those of Huang and Feng (1995), but discrepancies were found in the wake velocities for the higher blockage case (50%). These discrepancies were attributed to the response of viscoelastic fluids to intense local shear and elongational flows at the proximity of the channel wall. Dou and Phan-Thien (2004) carried out simulations of the uniform flow of a viscoelastic fluid past a cylinder in a moving channel using the UCM, PTT, Oldroyd-B and the FENE-CR models. They used a control volume finite element method with a DEVSS-ω formulation under a distributed computing environment through a Parallel Virtual Machine (PVM) library. Again, a negative wake was not observed with the UCM and Oldroyd-B fluids for various retardation ratios ($\beta = 0.125, 0.4, 0.6, 0.8$), thus corroborating the predictions of Oliveira et al. (1998) in contrast to the results of Huang and Feng (1995). However, for the PTT and FENE-CR models a negative wake appeared at a critical De. Regarding drag coefficient, C_D, predictions, the early calculations of Dou and Phan-Thien (2003) found a monotonic decrease of C_D with De for the FENE-CR fluid with lower extensibility parameter ($L^2 = 10$). For a higher extensibility parameter ($L^2 = 100$), however, they predicted a non-monotonic behaviour, with an initial decrease followed by an increase for approximately $De > 0.6$, related to the strong increase of the extensional effects. The numerical investigation of Kim et al. (2005a) focused on the comparison of negative wake generation in both uniform and Poiseuille flows past a cylinder, and on the influence of the FENE-CR model parameters upon this flow feature: viscosity ratio, β, and polymer extensibility, L^2. By employing a DEVSS-G/SUPG formulation with an efficient iterative solution method developed for the mixed FEM by Kim et al. (2004), they found that the drag coefficient monotonically decreased for both $L^2 = 10$ and $L^2 = 100$, in contrast with the results obtained by Dou and Phan-Thien (2003). They also found that, for all flow conditions and model parameters, the negative wake generation is more pronounced when the approach flow is uniform than when it is a Poiseuille flow.

The EVSS (Elastic-Viscous Split Stress) is stabilization scheme used within the FEM framework.

The DEVSS-ω is an independent interpolation of the vorticity version of the DEVSS FEM stabilization scheme.

The Discrete Elastic-Viscous Split Stress, velocity Gradient interpolation, Streamline Upwind Petrov-Galerkin (DEVSS-G/SUPG) is another FEM stabilization scheme.

Negative wakes in the settling sphere problem have also been extensively studied using numerical methods (Harlen, 2002; Dou and Phan-Thien, 2003; Kim et al., 2005a; Satrape and Crochet, 1994). These works lead to the general conclusion that both shear-thinning and elastic effects are necessary for the formation of a negative wake. In contrast, the numerical simulations by Satrape and Crochet (1994) and Harlen

(2002) showed that a negative wake can be present for constant viscosity elastic fluids, such as those represented by the FENE-CR model.

2.2.2.3 *Contribution from this work*

In Afonso et al. ((2008) (see the integral version of this investigation on Section 5.2, on page 87), the flow of viscoelastic fluids past a cylinder settling between two parallel plates was numerically investigated using a finite-volume technique.

Five different constitutive models are used (UCM, Oldroyd-B, FENE-CR, PTT and Giesekus), in order to properly assess the effect of various rheological properties and models. For the 50% blockage case, the steady flow behind the cylinder is characterized by a negative wake, which strongly depends on the fluid rheology. "Negative wakes" were visualized in past experimental work and have been extensively studied in very recent numerical work, especially with view to find the conditions under which they arise.

Simulations were carried out under creeping flow conditions, using very fine meshes, especially in the wake of the cylinder, where large normal stress gradients are observed for high Deborah number flows. Numerical solutions could be obtained up to Deborah numbers in excess of those reported previously in the literature, especially in the case of the PTT, FENE-CR and Giesekus models. Special care was exercised in order to guarantee that all solutions are well converged iteratively, with the L_2 norm of the residuals of the equations to be less than a tolerance of 10^{-6}, and that sufficient mesh convergence is also provided, with the minimum normalized cell spacing along the radial and azimuthal directions of 0.002 and 0.0003, respectively, allowing estimation of drag coefficients which are exact up to the first decimal place, corresponding to an accuracy of around 0.1 - 0.3 % on average.

Understanding the origin and other factors that influence the negative wake phenomenon thus appears as the main motivation for the present work. In terms of outcome, this study leads to three important contributions:

- clarify the significant discrepancies in the predicted drag coefficient of a FENE-CR fluid obtained by Dou and Phan-Thien (2003) and Kim et al. (2005a),
- progress towards the development of theory for the formation of negative wake, and
- confirmation of some sets of results in the literature by different numerical methods.

For the UCM and the Oldroyd-B fluids with low solvent viscosity contribution ($\beta = 0.125$), the drag coefficient on the cylinder decreases monotonically with increasing Deborah number. When the solvent viscosity contribution is high ($\beta = 0.8$) the drag coefficient first decreases with De followed by a levelling out and marginal, very slight increase, for $De \geqslant 1.1$. For all retardation ratios, our results are well below the predictions of Dou and Phan-Thien (2003), with agreement only between the Newtonian cases up to $De \approx 0.3$. For the other models with bounded extensional viscosity, the FENE-CR, PTT and Giesekus, the latter two being shear-thinning, the drag coefficient decreases monotonically with increasing Deborah number. For the FENE-CR model,

good agreement was found with the C_D results of Kim et al. (2005a) for both extensibility parameters, $L^2 = 10$ and $L^2 = 100$, whereas the predictions of Dou and Phan-Thien (2003) with $L^2 = 10$ lie well below both sets of results, close to the predictions for the $L^2 = 100$ case. For $L^2 = 100$, the results from Dou and Phan-Thien (2003) show a non monotonic behaviour, diverging from both our predictions and those of Kim et al. (2005a), with agreement only for $De \leqslant 0.6$.

Regarding the existence of negative wake these sets of simulations have shown that models with unbounded or bounded but very large extensional viscosities do not exhibit this feature. For the UCM and Oldroyd-B fluids there was no sign of a negative wake regardless of the values of β, with the velocity profiles presenting an upstream shift close to the back of the cylinder ($x/R \leqslant 1.5 - 2$) followed by a downstream shift for $De > 0.5$. For the FENE-CR model with $L^2 = 100$, there is a negative wake for $De > 1.5$, starting about 3 radii from the rear of the cylinder and extending up to $x/R \approx 16$. The magnitude of the negative wake increases with De and is approximately 11.7% at $De = 5.0$. For the FENE-CR fluid with $L^2 = 10$, there is no upstream shift of the velocity and the negative wake is more intense and clearly marked appearing at $De > 0.5$, and formed at about one radius distance behind the cylinder. For $L^2 = 10$ the magnitude of the negative wake is larger than for $L^2 = 100$, being 32.8% at $De = 7.8$, whereas its length is actually smaller, with $x/R \approx 10$ for$L^2 = 10$ and $x/R \approx 16$ for $L^2 = 100$. For the PTT fluid with the highest elongational parameter $\varepsilon = 0.25$, a negative wake in the velocity overshoot is found at $De > 0.5$, starting at $x/R \approx 2$ and extending to approximately $x/R \approx 9$. The relative velocity overshoot increases with De up to $De \approx 5$ and then asymptotes to a constant value of about 34%, while its location shifts further downstream. For lower values of the ε parameter, the flow behaviour becomes similar to that seen with the UCM model. The Giesekus model produces an initial upstream shift followed by a downstream shift and a negative wake for $De \geqslant 2$, starting at $x/R \approx 5.5$ and extending in the axial direction up to $x/R \approx 25$. The negative wake magnitude increases with De, attaining a maximum value of about 3% for $De = 8$.

2.3 CONTRACTION FLOWS

Entry flows *are accelerative flows from a large cross-section via an abrupt or angular entry into a smaller cross-section (Keunings, 1989).*

Contraction flow (also called *entry flow*) of viscoelastic fluids is an established benchmark flow in computational rheology from almost three decades. It does not only serve as a demanding and *cut of the edge* numerical validation geometry, as also entails the possibility of predicting the correct kinematic and pressure distribution of flow, enabling the practical design of efficient applications, in which undesirable vortex structures are suppressed and high stress regions are eliminated to prevent material damage.

The simplicity of this flow geometry combined with the extremely numerical complexity, mainly due to the stress singularity in the re-entrant corner, lead to the recognition that the low Reynolds number Maxwellian fluid flow in a 4:1 contraction, was one of the most important numerical problems for viscoelastic fluids.

This classification occurred in the V^{th} International Workshop on Numerical Methods in Non-Newtonian Flows (Hassager, 1988), held in Lake Arrowhead in the US. The leitmotif for this choice were the precedent pessimistic mismatch between the experimental and numeric

Right before Hassager's (1988) report, the 4:1 sudden contraction flow was a predominant theme in the IVth *International Workshop on Numerical Methods for Non- Newtonian Flows, held in 1985 in Spa, Belgium (e.g. Debbaut and Crochet, 1986; Dupret and Marchal, 1986; Joseph and Saut, 1986; Josse et al., 1986; Keunings, 1986, Marchal and Crochet, 1986).*

results (Crochet and Walters, 1983), here again blamed on the *infamous* HWNP. This problem is well documented in the review works condensed by Boger (1987) and White et al. (1987). Further extensive literature reviews of experiments in this flow were presented by McKinley et al. (1991b) and Owens and Phillips (2002), while reviews on related numerical work can be found in Keunings (1989), Baaijens (1998), Oliveira and Pinho (1999a), Walters and Webster (2003), Owens and Phillips (2002), Rodd et al. (2005) and Alves et al. (2008).

The schematic representation of the 4:1 contraction flow geometry is illustrated in Figure 2.5. The fluid accelerates from one channel (or pipe) to another, causing a complex flow that includes regions of predominantly shear flow (near the walls) as well as regions where the flow is essentially extensional (along the central axis).

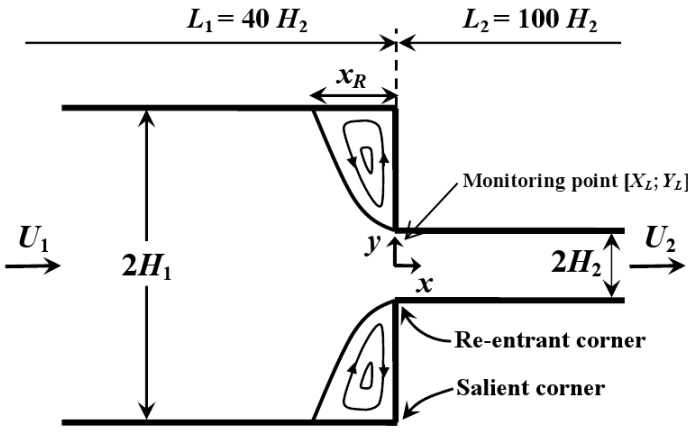

Figure 2.5: Schematic representation of the 4:1 planar contraction geometry.

The half-width of the downstream channel, H_2, is taken as the characteristic length scale and the mean velocity in that channel, U_2, is the characteristic velocity. For the Newtonian case, the flow only depends on the Reynolds number, $Re = \rho U_2 H_2/\eta$, and on the contraction ratio, $C_r = H_1/H_2$. For a viscoelastic fluid, the flow becomes also dependent on the Deborah number, usually defined for this flow by

$$De = \frac{\lambda U_2}{H_2}, \tag{2.3}$$

where λ is the relaxation time of the fluid.

In the computational benchmark, the flow was explicitly assumed two-dimensional, in order to simplify the simulations. In the experimental works, several distinct types of entry flows were studied over the last decades.

The geometric characteristics of the *entrance* in which the fluid evolves defines if the contraction is abrupt (or sudden, in which the salient corner makes a 90º degree angle) or smooth. The characteristic of the *neutral* direction (spanwise direction, in opposition of the main stream direction of the fluid, usually called streamwise direction), defines wether the contraction is axisymmetric (also called circular or tubular), planar (or quasi-planar in which the neutral direction is not contracted, and usually three-dimensional can be assumed negligible) and squared

(in which the spanwise direction is also contracted and the flow can be considered fully three-dimensional).

In some cases, such as in microfluidic geometries, the planar configuration can become markedly three dimensional, due to wall effects and reduced characteristic aspect ratios, defined as the ratio of the two spanwise lengths, $A_r = L_y/L_z$ (assuming that the streamwise direction is x). The true three-dimensional nature of a real microfluidic contraction flows depends on the characteristic aspect ratio of the geometry, and by varying the depth of the spanwise direction different flow configurations can be attained ranging from a quasi Hele-Shaw flow, at very small aspect ratios, up to quasi 2D flows, at large aspect ratios.

Hele-Shaw (1898) flow (named after H.S. Hele-Shaw) is defined as a highly viscous flow between two parallel flat plates separated by a small gap, and is important in microfluidics due to its shallow planar configurations and typically low Reynolds numbers. Interestingly Hele-Shaw flows have streamline patterns identical to the corresponding potential (irrotational) flow of ideal (inviscid) fluids.

During this work, several detailed studies (twelve presentations in international and national conferences and three peer-review journal papers, Afonso and Pinho, 2006; Poole et al., 2007d; Afonso et al., 2010e) were performed on the contraction flow problem[1]. In the next sections this benchmark flow is analysed at in more detail.

2.3.1 *Brief review: experimental work*

In the literature on entry flows of viscoelastic fluids, interest has focussed mainly on the following aspects (Owens and Phillips, 2002; Rodd et al., 2005):

- corner vortex characteristics (vortex size, as measured by the distance it extends up the wall of the large channel, X_R, and intensity of recirculation, Ψ_R,) and behaviour (vortex regimes: growth, diverging flow, and unstable);
- lip vortex characteristics (length and behaviour);
- pressure drop across the contraction (usually defined by means of the Couette correction coefficient, C_{corr}).

The Couette correction coefficient, C_{corr}, represents a dimensionless extra pressure drop due to flow redevelopment at the entrance to the smaller channel. The mathematical description is presented in equation (5.39), on page 132.

Pioneering visualization studies with viscoelastic fluids in contractions were carried out by Cable and Boger (1978a,b, 1979) and Nguyen and Boger (1979). Cable and Boger (1978a,b, 1979) performed visualizations in axisymmetric contractions with ratios of $C_r = 2$ and 4, using high viscous shear-thinning solutions of dilute PAA in a glucose syrup. These experiments reported a sequence of distinct flow regimes:

- Newtonian-like vortex flow regime at very low flow rates, where the corner vortex is strictly a result of the Newtonian stresses caused by the kinematical constraints of the corner and its presence is predicted by applying the similarity solution of Moffatt (1964) to the analysis of the local flow in this region.
- elastic vortex growth regime with steady recirculating vortex at moderate flow rates;
- diverging flow regime at higher flow rates with the streamlines diverging away from the centreline;
- unstable flow regime above a critical Deborah number, with large vortex either pulsating symmetrically or moving in an asymmetric and spiral flow fashion.

Divergent flow *is characterised by a strong curvature of the streamlines away from the centreline towards the duct walls some distance upstream of the contraction: almost as if some "invisible obstacle" has been placed in the liquid's path (Alves and Poole, 2007).*

1 In Afonso and Pinho, 2006 and Poole et al., 2007d, *smooth* (or gradual) contraction flows were numerically and experimentally analysed.

Fluid inertia was found to stabilize the flow, requiring higher values of the Deborah number for the onset of flow instabilities. Nguyen and Boger (1979) also used axisymmetric contraction with contraction ratios of $C_r = 4$ and 14.6. They used Boger (highly viscous, elastic fluids with viscosities that remain nearly constant over many decades of shear rate) and shear-thinning fluids, and also mapped a rich sequence of flow regimes ranging from essentially Newtonian-like flow up to unsteady asymmetric flow, with rotating and helical flow, for higher elasticity.

Walters and Webster (1982) used several different constant viscosity dilute solutions of PAA in a water/maltose syrup mixture in the flow through a planar 4:1 contraction. In contrast with the observations of the results obtained in the axisymmetric 4.4:1 contraction, no significant vortex enhancement was observed. In the axisymmetric configuration vortex enhancement was clearly noticeable when elasticity was increased, up to the point in which inertia played an important role. Evans and Walters (1986, 1989) performed experimental visualisations for both Boger fluids and shear-thinning PAA solutions in planar contraction flows, and investigated the effect of both contraction ratio ($C_r = 4$, 16 and 80) and rounding of the re-entrant corner. Divergent flow behaviour for low PAA concentrations was observed, when both inertia and shear-thinning became important.

A variety of contraction ratios ranging ($4 < C_r < 16$) were used in the axisymmetric contraction experiments performed by Boger et al. (1986). Using two different Boger fluids (PAA/corn syrup and PIB/PB solutions) designed to present similar dynamic and steady rheological properties, the results obtained in the 4:1 contraction, showed a wide difference in the vortex growth behaviour within the fluids. From these results, Boger et al. (1986) concluded that using only the steady and dynamic shear rheological properties was insufficient to predict the behaviour of the fluid in axisymmetric contraction geometries. Later, Boger (1987) related the different extensional viscosities of the two Boger fluids as the possible explanation for the wide different observed behaviour, and subsequently the transient shear flows experiments performed by Mackay and Boger (1987) and Quinzani et al. (1990) also showed that in order to correctly model the rheological behaviour of Boger fluids, a spectrum of relaxation over a wide range of shear rates times is needed.

McKinley et al. (1991b) performed a experimental study in the axisymmetric contraction using highly elastic PIB/PB Boger fluid for a variety of contraction ratios ($2 < C_r < 8$). These authors found that at a critical Deborah number for contraction ratios in the range 2:1 to 5:1, the flow near the lip of the contraction became time-dependent, with periodic motion. This unsteady becomes quasi-periodic and aperiodic when elasticity increases. A three-dimensional unstable flow revealing small-scale instabilities throughout the entry region was also presented by Cartalos and Piau (1992), in the flow visualizations of low concentration solutions of partially hydrolysed polyacrylamide (HPAA) through an axisymmetric contraction ($C_r = 16.4$).

The experimental investigations by Rothstein and McKinley (1999, 2001) in axisymmetric contraction/expansion used Boger fluids and a variety of contraction ratios ($4 < C_r < 8$), corroborate the important role of the extensional viscosity on the vortex growth and associated measured enhanced pressure drop. They found that in the axisymmetric case, the size of the salient corner vortex formed was smaller than in

the planar case, due to different experienced Hencky strains as the flow changes from uniaxial to planar.

The evidence that the flow behaviour of the same constant viscosity dilute polymer solution in both planar and axisymmetric contractions is dramatically different was provided by Nigen and Walters (2002). Using two Boger fluids based on dilute solutions of PAA in a water/glucose syrup mixture, for a variety of contraction ratios ($2 < C_r < 32$), they reported that the vortex enhancement was dominant in the axisymmetric contraction whereas absent for planar contractions.

Poole et al. (2007d) reported experimental observations and numerical simulations, based upon the PTT model, for the laminar flow of a series of viscoelastic liquids 0.05%, 0.1%, and 0.4% concentrations of a PAA over a smooth contraction. As the flow progresses through the contraction, velocity overshoots develop adjacent to the flat sidewalls of the contraction that, due to their appearance, were dubbed as *cat's ears*. There is an abrupt change from the nearly two-dimensional flow in the central region of the contraction with extremely high velocity gradients evident in the velocity overshoots. The exact shape and magnitude of the cat's ears are found to be Reynolds number and Deborah number dependent.

Cat's ears *were study in a systematic parametric investigation by Afonso and Pinho (2006) with the single mode PTT model, and by Poole and Alves (2009) using the UCM model.*

Experiments with Newtonian and Boger fluids in 3D square-square contraction flows were reported by Alves et al. (2005) and Sousa et al. (2009), where extensive flow visualizations are presented at the middle plane of a 4:1 contraction using a streak line photography technique. These experiments revealed the formation of a lip vortex at high Deborah numbers for the more concentrated Boger fluid (aqueous solution of polyacrylamide at 300 ppm) and related this lip vortex with the increase of the role of shear induced normal stresses due to the secondary flow in the cross section of the rectangular channel. An interesting fluid dynamics feature caused by elasticity was identified experimentally in this geometry by Alves et al. (2008), in a work which also included 3D numerical simulations using a 4 mode PTT model with a Newtonian solvent contribution. Their experimental and numerical results showed the expected significant vortex growth, measured on longitudinal midplanes, and revealed the occurrence of an inversion in the direction of rotation of the recirculation flow inside the vortices due to elastic effects. When elastic effects are strong the fluid particles enter the vortices through the horizontal (or vertical) planes of symmetry and leave through the diagonal planes, whereas in the absence of elasticity the fluid elements enter the vortices through the diagonal symmetry planes and exit at the horizontal (vertical) mid planes of symmetry. A similar finding was reported by Sirakov et al. (2005) in 3D 4:1 square to circular cross-section contraction simulations with a finite element method using the eXtended Pom-Pom (XPP) model to analyse the viscoelastic flow of branched LDPE solutions.

With the advent of microfluidics, some literature in microfabricated contraction geometries has been published, allowing the exploration of conditions (very low Re and very high De) not accessible in the corresponding macro-scale experiments.

Rodd et al. (2005) performed pressure drop measurements and flow visualization of the flow of dilute aqueous polyethylene oxide (PEO) solutions through microfabricated planar abrupt contraction/expansion ($C_r = 16$). For all polymer solutions used, the onset of elastic instabilities at the contraction entry occurred at a critical Deborah number of

50. Later, Rodd et al. (2007) investigated the role of inertia with similar experiments using a constant concentration of PEO, while varying the viscosity of the solvent with four different glycerol-water solutions. Four flow regimes were identified, such as the Newtonian-like flow, steady viscoelastic flow, diverging flow, and elastic corner vortex growth.

Oliveira et al. (2008) presented a detailed study of the flow of a Newtonian fluid through 3D-planar microgeometries containing a hyperbolic contraction followed by an abrupt expansion, aimed at assessing its potential application as an extensional micro-rheometer. They reported important 3D effects, which depend on the aspect ratio and a simple 2D approach is often inadequate, even qualitatively, to describe the flow patterns. For geometries with very low-aspect ratios, a Hele–Shaw flow approximation is appropriate and, therefore, the flow patterns resemble those of 2D-potential flow and not planar 2D viscous flow, as often assumed erroneously in numerical works in microfluidic devices. Gulati et al. (2008) performed an experimental study on the viscoelastic flow in a micro-contraction ($C_r = 2$) using a shear thinning semi-dilute DNA solution. For the entire range of flow visualization, $3.9 < De < 193.3$, the corner vortex grew symmetrically, while the lip vortex was observed. The microfluidic flow of DNA solutions in a 4:1 contraction was very recently performed by Hemminger et al. (2010). This work examined the contraction deformation/flow behaviour of a model system for entangled polymeric liquids using DNA solutions in a micro-fluidic setup, enabling the direct correlation of molecular responses to continuum flow profiles.

The main picture emerging from the experiments in contraction flows is that the flow characteristics depends on both the geometrical properties and on fluid rheology. Specifically for the 2D 4:1 contraction flow, for some shear-thinning fluids there is corner vortex enhancement following the formation of a lip vortex, which initially grows and subsequently merges with the corner vortex, whereas for Boger fluids the lip vortex mechanism is absent (it does exist, however for large contraction ratios) and the corner vortex keeps growing with De. At larger Deborah numbers the single existing corner vortex still grows with De and the flow is still steady. For all fluids the flow becomes unsteady above a critical Deborah number.

2.3.2 *Brief review: numerical work*

In order to organize the review of this subject (and avoid the possible repetition with the reviews made at the paper presented in Part III, Section 5.3), the literature on this computational benchmark is organized in three different periods:

- pioneer FEM works and their relevance on the HWNP:

  the identification of the HWNP appeared in the earlier FEM numerical works (Cochrane et al. (1981), Walters and Webster (1982), Debbaut and Crochet, 1986; Dupret and Marchal, 1986; Joseph and Saut, 1986; Josse et al., 1986; Keunings, 1986 and Marchal and Crochet, 1986), performed even previously to the contraction computational benchmark (Hassager, 1988). An excellent review on those pioneering FEM works can be found in Keunings (1989);

- advent of FVM and other methods and the possibility of framework-independent benchmark results:

  in the early 1990's some numerical investigations in the contraction benchmark flow were performed within the FVM framework (Yoo and Na, 1991, Xue et al., 1998b,a, Oliveira and Pinho, 1999a, Alves et al., 2000 and Phillips and Williams, 2002), within the hybrid FEM/FVM framework (Sato and Richardson, 1994, Matallah et al., 1998 and Aboubacar and Webster, 2001) and within the BEM framework (Meng et al., 2002).

  Alves et al. (2003b) used a new convection scheme (CUBISTA, Alves et al., 2003a) with the Oldroyd-B fluid, achieving convergence up to $De = 2.5$ on their finest mesh. Their results in terms of vortex size were not much different from those previously obtained by Aboubacar and Webster (2001) using a hybrid finite volume/finite element scheme, although some differences were discernible (cf. Figure 2.6). Later, high resolution results obtained by Kim et al. (2005b) in the same geometry with an Oldroyd-B model were also close to those of Alves et al. (2003b), but somewhat below even for Newtonian fluids. It is surprising that for this particular limiting case of Newtonian fluid ($De = 0$), the results of Aboubacar and Webster (2001) and Belblidia et al. (2006) are also underpredicting the vortex size compared to Alves et al. (2003b). Kim et al. (2005b) used a transient numerical algorithm based on the four-step fractional step method and DEVSS-G/DG with equal-order linear interpolation functions and also obtained converged solutions up to $De = 2.5$ with their finest mesh. Recently, the benchmark results of Alves et al. (2003b) were also confirmed by Belblidia et al. (2006), in their steady-state investigation with the Oldroyd-B model using different stabilisation methodologies embedded within a time-marching incremental pressure-correction formulation;

"In particular, the present results are in good agreement with the predictions of the high-resolution finite volume method of *Alves et al. (2003b)*. This may be the first case that quantitative agreement is obtained between studies using different numerical methods for the benchmark problem of 4:1 planar contraction flow" *(cited from Kim et al., 2005b)*

- the log-conformation methology (Fattal and Kupferman, 2004):

  up to the beginning of this thesis, the log-conformation was not applied to the 4:1 contraction benchmark flow, with the Oldroyd-B model.

  Kwon (2004) investigated numerically the planar 4:1 contraction flow using the Leonov constitutive equation and found stabler computations when using the log-conformation method than with the conventional approach. Kwon (2004) also concluded that this new method may only work efficiently for constitutive equations that are proven globally stable and that the stability constraint has to be taken into serious consideration. In a sequel, Yoon and Kwon (2005) obtained solutions for Deborah numbers in excess of 100 using finer meshes. These authors also presented solutions for the 4:1:4 contraction/expansion flow and obtained converged solutions for Deborah numbers above 10. However, in both geometries the convergence limits decreased with mesh refinement.

In the paper by Fattal and Kupferman (2005) a reference was made to an upcoming paper in the JNNFM on the contraction flow, but this paper was never published: this maybe an indication of the extreme difficulty of this computational rheology benchmark flow.

It is clear that this viscoelastic flow is notoriously difficult to simulate numerically at levels of elasticity above a (rather small) critical Deborah number, where the numerical results exhibit symptoms of mesh

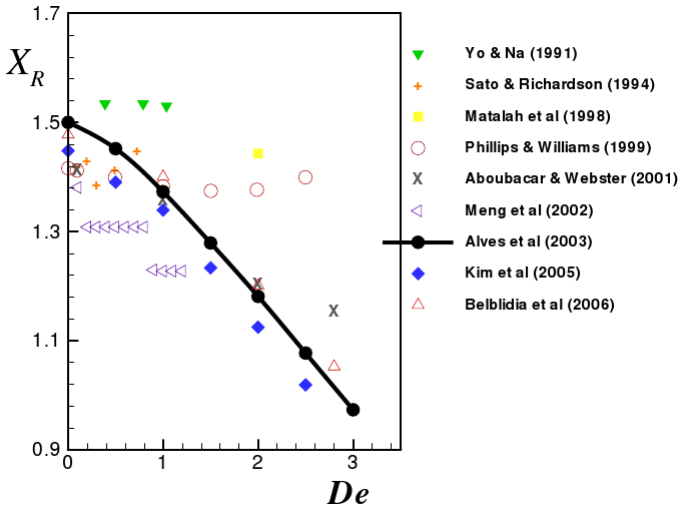

(a) 2006 scenario.

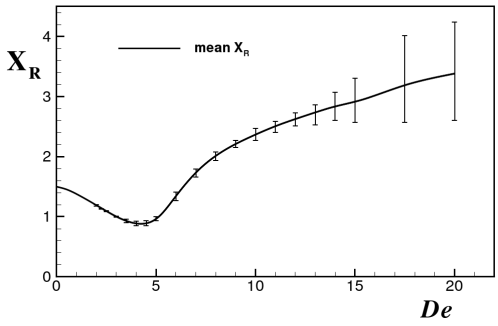

(b) 2010 scenario.

Figure 2.6: Flow of an Oldroyd-B fluid ($\beta = 1/9$) in a 4:1 contraction: (a) vortex size, X_R in the beginnig of this thesis (b) actual vortex size, X_R , for the recent work of Afonso et al. (2010e).

dependency even with refined meshes and usually have a tendency to diverge.

The scenario at the beginning of this thesis was not promising, as evidenced in Figure 2.6a. Even for the Newtonian case, the vortex size, X_R was not correctly predicted by the works from different numerical frameworks. Not surprisingly, at high Deborah numbers the agreement between results from different numerical methods is harder to achieve than at low Deborah numbers and there are also important differences between predictions and experiments.

For instance, the majority of numerical studies on entry flows with Boger fluids have been restricted to the range of parameters where the size of upstream vortices is still decreasing and the pressure drop is smaller than the corresponding Newtonian pressure drop (Alves et al., 2003b; Aboubacar and Webster, 2001). These predictions were obtained using continuum mechanics/ macroscale constitutive equations and are in contrast with experimental results employing constant-viscosity polymer solutions and melts, which invariably show increased pressure drop and enhanced vortex formation (Cable and Boger, 1978a,b, 1979; McKinley et al., 1991b; Chiba et al., 1990). The discrepancies are rooted both on the physics of the constitutive equations and on the HWNP numerical issues (Owens and Phillips, 2002).

Figure 2.6b illustrates the current situation for the X_R prediction, and clearly a significant improvement was achieved, as reported in the next section.

2.3.3 *Contribution from this work*

In Afonso et al. (2010e, see the integral version of this investigation on Section 5.3, on page 113), high elasticity simulations of 2D and 3D entry flows were performed. These were possible due to the use of the log-conformation formulation technique of Fattal and Kupferman (2004) in combination with a high-resolution finite volume method.

For this flow, again no limiting bound for the attained Deborah number was observed, with stable solutions obtained up to $De = 100$ in the 2D case with the Oldroyd-B model and up $De \approx 10000$ in the 3D square/square contraction with the PTT model. The dynamic behaviour for the 2D and 3D contraction flows was attained at much higher De than previously, and demonstrate a rich succession of dynamical transitions, from steady to unsteady flow with lip and corner vortex enhancement, and from symmetric to asymmetric patterns with alternating vortex pulsation, up to almost chaotic regime of back-shedding upstream of the contraction plane, in the author knowledge, for the first time reported in the literature. Fast Fourier transform (FFT) of velocity signal at a monitoring point to determine the dominant frequencies was used, which show a characteristic frequency doubling regime at high De. Qualitatively these results are comparable to the experimental data of McKinley et al. (1991b), who studied viscoelastic vortex dynamics in an axisymmetric contraction.

The time average evolution of the vortex size and pressure drop revealed, for the first time, that after an initial decreasing tendency with De, there is an upturn followed by considerable enhancement at higher elasticity. Thus, the trends of the available experimental results are well captured by the present simulations (qualitatively), except the rise of pressure drop above the corresponding Newtonian value.

For the 2D 4:1 abrupt contraction flow of the Oldroyd-B fluid, which has a constant shear viscosity as in real Boger fluids, the flow becomes unstable at a relatively low critical De of about 2.5, which is of the same order attained in most previous works. On increasing De the flow exhibits local unsteadiness which tends to grow as elasticity is further increased, eventually leading to an asymmetric flow regime with alternate back-shedding of vorticity from the two pulsating recirculating eddies formed on the top and bottom walls of the upstream channel. Dominant frequencies were determined via FFT of velocity signals, showing a tendency for a frequency doubling mechanism at high De eventually leading to a chaotic regime. Average vortex size and overall pressure drop were computed from the time evolution of the predicted data and show the typical upturn shape seen in experimental data and in the recent multiscale simulations of Koppol et al. (2009), with an initial steep decrease followed by strong enhancement when plotted against De. However, the doubling of the excess pressure drop above the Newtonian value was not predicted with the present Oldroyd-B simulations, presumably because of its physical limitations regarding the transient extensional viscosity behaviour.

The energy losses in the flow of the Oldroyd-B fluid through the abrupt contraction, evaluated by the Couette correction coefficient

(C_{corr}) that represents a dimensionless extra pressure drop due to flow redevelopment at the entrance of the smaller channel, presented a non-monotonic behaviour with the elasticity increase. The increase in C_{corr} occurred for $De > 20$, as had been seen in earlier studies for the PTT fluid (Alves et al., 2003b) and in close agreement with the experimental findings of McKinley et al. (1991b) and Rothstein and McKinley (2001).

3

THE *ECCENTRIC* PURELY ELASTIC INSTABILITIES

ECCENTRIC ::
suggests a wide divergence from the usual or normal, especially in behaviour

A viscoelastic fluid can be considered *eccentric*, since its behaviour presents a *wide divergence from the usual or normal behaviour*. From the opposite behaviour of the expected from the daily experience with *normal* fluids and the fascinating *counter-intuitive* flow examples presented in Section 1.1.2 (cf. Figure 1.1, on page 10), passing throught numerical and experimental elastic instabilities observed in the cylinder and contraction flows (presented in the previous Chapter), up to an eventual inertialess turbulent regime (elastic turbulence), viscoelastic fluids are a true source of eccentricity.

Elastic turbulence, *named based on similarities to the inertia driven turbulence (Larson, 2000; Groisman and Steinberg, 2000), identifies a path to a chaotic flow in a form of irregular flow patterns, occurring above the purely elastic instability.*

3.1 ELASTIC INSTABILITIES

Flow instabilities are a challenging topic of research both intellectually as well as of practical engineering interest. They take place in many different ways and situations, depending on fluid type, flow velocity and geometry as well as the in presence of other physical phenomena (such as variable density due to temperature or concentration variations or surface tension gradients), the classical example being transition to turbulence (Reynolds, 1883; Manneville, 2004). Of concern here are instabilities in non-Newtonian fluids in the absence of inertial effects and under isothermal conditions, which are due to the viscoelasticity of the fluids.

There are various types of elastic instabilities depending on the corresponding flow conditions. The most common and more extensively investigated are found in shear flows, one industrially relevant example being the extrusion instabilities at high flow rates, and its relation to wall slip, reviewed recently by Denn (2001). An early review on instabilities with non-Newtonian fluids was carried out by Pearson (1976), who clearly concentrated on shear flows and distinguished between instabilities in non-Newtonian flows that are mere modifications of Newtonian instabilities and those that are genuinely of elastic origin.

In the subsequent twenty years major progress took place in measuring, understanding and linking elastic instabilities in curvilinear shear flows (Taylor-Couette, Dean, Taylor-Dean, parallel plate and cone-plate flows) with linear stability theory and rheological constitutive modelling, as extensively reviewed by Shaqfeh (1996). In all these cases it was found that elastic instabilities are related to hoop stresses and hoop stress gradients in high Deborah number flows. Work has continued on viscoelastic instabilities in essentially creeping shear flows

and some examples of subsequent research are on the effects of parallel flow superpositions by Ramanan and Graham (2000), instabilities in free-surface flows Graham (2003) and square cavity flows by Kim et al. (2000), amongst others. Naturally, instabilities in viscoelastic flows in the presence of inertia effects have always been a relevant topic of research, as the work on cylinder flows by Cadot and Kumar (2000) and Coelho and Pinho (2003a,b, 2004), but these are not so important in the present context.

Extension dominated flows are on a different class and this work concerns their instabilities, in particular those of flows containing a stagnation point. Here we are concerned with single-phase stagnation flows, i.e., excluding flows with stagnation points at solid-liquid and liquid-gas interfaces as one finds in flows around solid bodies or bubbles. Elastic instabilities can also arise from the high molecular extension and stresses developed in the wake of the cylinder, as observed by McKinley and co-workers (McKinley et al., 1996; Pakdel and McKinley, 1996), who proposed a criterion that defines and unifies the critical conditions for the appearance of elastic instabilities in these systems. Dou and Phan-Thien (2008) presented a semi-empirical criterion specifically for the viscoelastic flow past a confined cylinder, and the trigger mechanism for the onset of the elastic instabilities was related to the inflection of the velocity profile originated by the normal stresses near the cylinder surface. This criterion is consistent with that proposed by McKinley et al. (1996) and by Pakdel and McKinley (1996).

Elastic instabilities were also often encountered in experimental studies of entry flows, as the jetting instability upstream of a 4:1:4 axisymmetric contraction–expansion (Rothstein and McKinley, 2001), the *bent-elbow shape* streak lines close to the re-entrant corner of a 12:1 square-square contraction (Sousa et al., 2009) and the local instability associated with the formation and decay of a dip of the vortex boundary at the lip corner of a 4:1 circular contraction (Chiba et al., 2004).

Most research on extension dominated flows has concentrated on contraction flows, where instabilities have been known to take place for quite a long time (Cable and Boger, 1979, Giesekus, 1968). In stagnation point flows, such as the flow in the opposed jet (Cogswell, 1978), in Taylor's four-roll mill (Giesekus, 1962) or in the cross-slot channel (Gardner et al., 1982), high stresses develop during the flow compression and subsequent extension, forming a birefringent strand which lasts longer the higher the flow Deborah number.

Such high stress development represent a challenge to numerical predictions, and during this PhD work, several investigations in stagnation point flows were performed, such as in the cross-slot channel (ten presentations in international and national conferences and a peer-review journal paper, Afonso et al., 2010b) and in the mixing-separating geometry (two presentations in international conferences and a peer-review journal paper, Afonso et al., 2010d), as addressed in the following section.

3.2 CROSS-SLOT FLOW

The schematic representation of the Cross-slot geometry is presented in Figure 3.1. This cross-slot is bounded by flat top and bottom walls, but other configurations can also be designed, such as the 3D six arms cross flow geometry.

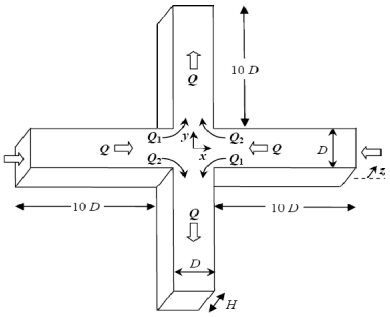

Figure 3.1: Schematic representation of the Cross-slot geometry.

The central region of the cross-slot, corresponding to the intersection of the two arms, defines a square with side length H. The length of the inlet and outlet "arms" is $L = 20H$. The Deborah number is here defined as $De = \lambda U/H$ and the Reynolds number as $Re = \rho U H/\eta$.

3.2.1 *Brief literature review*

The use of the cross-slot and other similar extensional flows, such as the four roll mill and opposed jet apparatus, has gained momentum in the 1980's, because of the need to develop methods for measuring the extensional viscosity of dilute polymer solutions (Fuller et al., 1987), the investigations on coil-stretch transition and on retraction by Gardner et al. (1982), the works on polymer scission by extensional flow in the cross-slot of Keller and co-workers (for instance in Odell et al., 1990) and more recently in the numerical work of Hsieh et al. (2005). These scission works are reviewed in more detail by Pathak and Hudson (2006), who have also used the cross slot for scission experiments of wormlike micelles. Earlier, Remmelgas et al. (1999) had investigated numerically the symmetric flow of FENE fluid models in the cross-slot channel at low Weissenberg numbers, so it can be said that the subcritical flows of viscoelastic fluids in the cross-slot are well known. Instabilities in the opposed-jet flow of viscoelastic fluids have been observed by Chow et al. (1988).

The stability analysis of Öztekin et al. (1997) with Oldroyd-B fluids concerned a stagnation flow in the vicinity of a wall and found an analogy between the onset of time-dependent instabilities here and that in other complex flows of elastic fluids having curved streamlines. Clearly, none of the instabilities found in these studies resembles the asymmetric flow visualized by Arratia et al. (2006) in their sub-millimitre cross flow geometry, see Figure 3.2(a-b). The advent of soft-lithography has opened up the possibility of manufacturing very small geometries, where the flows of viscoelastic fluids reach high Deborah numbers at negligible inertia. Since these flows are dominated by diffusion, mixing is severely limited unless enhanced by flow instabilities (Stroock et al., 2002). The addition of minor amounts of polymers to fluids, imparting viscoelastic rheological characteristics, opens up the possibility of enhanced mixing due to the onset of elastic flow instabilities (Squires and Quake, 2005).

Of particular relevance to the study of elastic instabilities is the experimental observation of instabilities in a "quasi two-dimensional" cross-slot microchannel flow by Arratia et al. (2006), which motivated

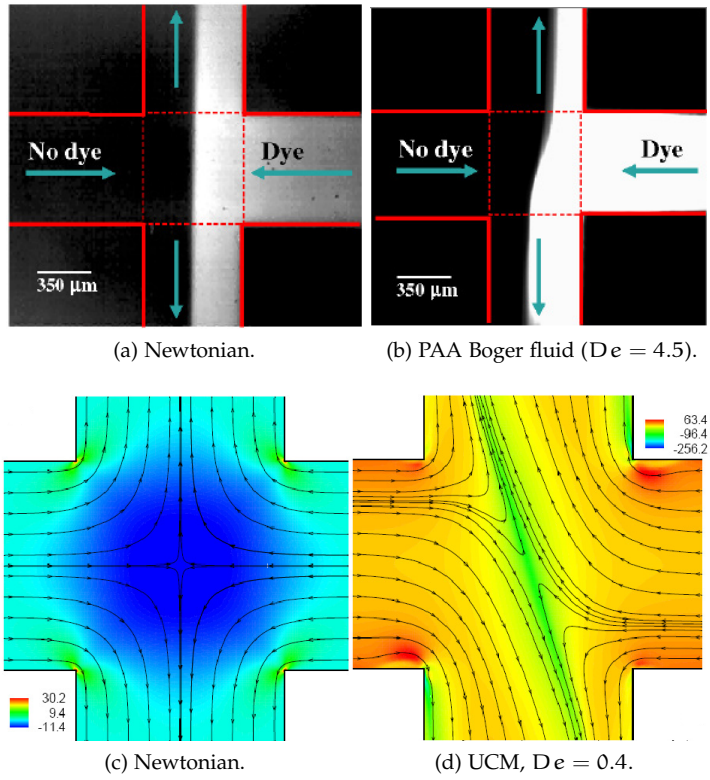

(a) Newtonian. (b) PAA Boger fluid ($De = 4.5$).

(c) Newtonian. (d) UCM, $De = 0.4$.

Figure 3.2: Comparison of experimental and numeric results in a Cross-slot geometry flow at low Reynolds number ($Re < 10^{-2}$). The experimental results (a) and (b) were obtained by Arratia et al. (2006), and the numerical results (c) and (d) were obtained by Poole et al. (2007c), with permission from the publisher.

the numerical work by Poole et al. (2007c) on the two-dimensional cross-slot flow of an upper-convected Maxwell fluid under low Reynolds flow conditions. Poole et al. (2007c) were the first to predict the first type of flow instability (asymmetric flow) in a two-dimensional cross-slot channel flow of an UCM fluid (cf. Figure 3.2(c-d)), which in this case led to a corresponding reduction of pressure loss, and reported also the stabilizing effect of inertia. Their findings are here explored in much more detail and complemented by other effects not previously reported. Poole et al. (2007c) have shown numerically that inertia stabilizes the flow of UCM fluids by delaying the onset of the steady bifurcation to higher Deborah numbers, as well as by decreasing the magnitude of flow asymmetry.

The calculations of Poole et al. (2007b) in a 3D cross-slot, have shown the destabilizing role of the bounding walls in the spanwise direction. The stability map presented in Poole et al. (2007b) revealed the existence of the two asymmetric flow regions for two-dimensional and weakly three-dimensional flow and the disappearance of the asymmetric steady flow regime as the Hele-Shaw condition is approached while simultaneously the critical Deborah number for the periodic instability decreases.

Later, Poole et al. (2007a) incorporated the effect of solvent viscosity ($\beta \neq 0$ in the Oldroyd-B model) and finite extensibility ($\varepsilon \neq 0$ in the sPTT model), presenting $\beta - Re - De$ and $\varepsilon - Re - De$ maps of flow pattern types (cf. Figure 3.3), showing the existence of a narrow region

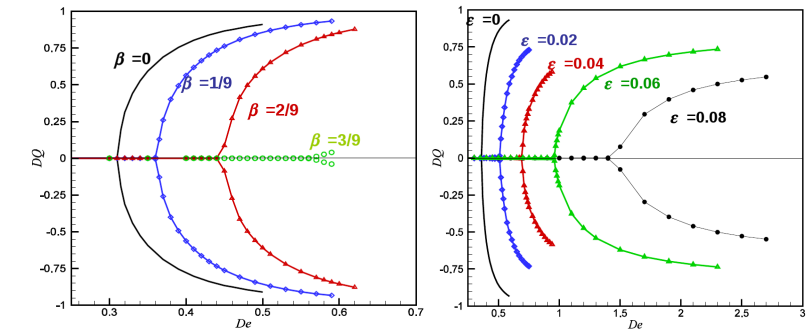

(a) $\beta - De$ map. (b) $\varepsilon - De$ maps

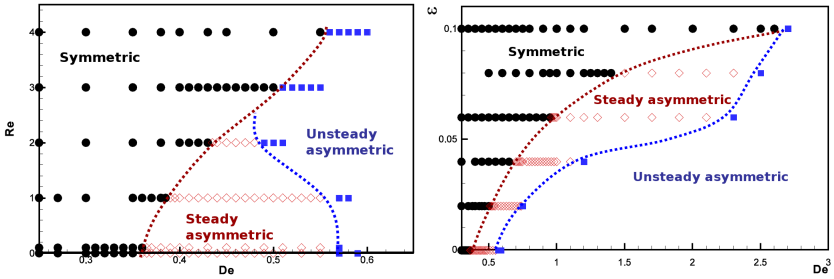

(c) $Re - De$ stability map. (d) $\varepsilon - De$ stability maps

Figure 3.3: $\beta - Re - De$ and $\varepsilon - Re - De$ maps of flow pattern types (Poole et al., 2007a).

where steady asymmetric flow can emerge, and identified the limiting De for onset of time dependent flow. The effect of finite extensibility was studied numerically by Rocha et al. (2009) and analytically by Becherer et al. (2008), using FENE models.

3.2.2 *Contribution from this work*

In Afonso et al. (2010b) (see the integral version of this investigation on Section 6.1, on page 143), the previous investigations for planar geometries (Poole et al., 2007c,b,a) are extended to three-dimensional cross-slot flows with inlets and outlets in the three orthogonal directions.

A 3D finite-volume numerical method is used to study the viscoelastic flow inside a 3D six arms cross flow geometry considering two symmetric flow configurations that lead to uniaxial and biaxial extensional flows, respectively, and represented schematically in Figure 3.4. The influence of the ratio of inlet to outlet flow rates and of the Deborah and Reynolds numbers on the onset of the flow instability are investigated numerically in order to demonstrate its purely elastic nature.

The influences of Deborah and Reynolds numbers and different types of extensional flow near the stagnation point were analysed, namely for biaxial and uniaxial extensional flows.

The uniaxial extensional flow configuration is prone to the onset of steady flow asymmetries at $De_{crit} \approx 0.22$ and at a higher Deborah number there is a second transition from steady asymmetric to unsteady flow, as in the corresponding two-dimensional cross slot geometry. This steady asymmetric flow is predominantly a shear type flow, where transition to unsteady flow is associated with large hoop

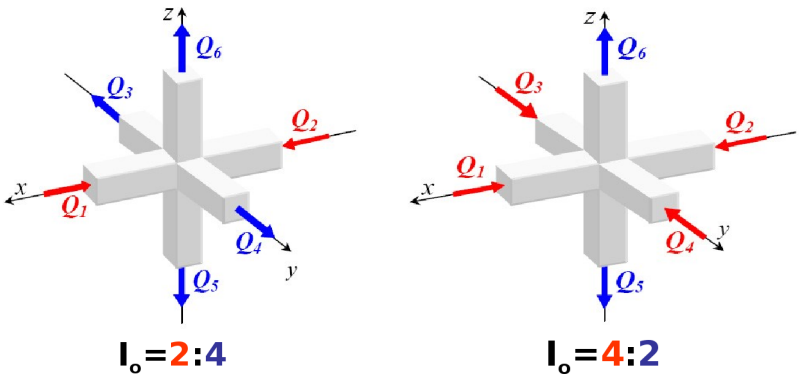

Figure 3.4: Biaxial extension configuration ($I_o = 2:4$) and uniaxial extension configuration ($I_o = 4:2$), obtained in the 3D six arms cross flow geometry.

stresses developing in curved streamlines, as explained by McKinley et al. (1996). In this mechanism the curved streamlines become unstable at hoop stresses that vary inversely with their curvature. Most likely the instability appears first at the curved streamlines near the re-entrant corners, but it could also appear elsewhere closer to the stagnation point, where the streamlines are also curved. By raising the Reynolds number the curvature of the streamlines in the region of interest increase and the same critical level of hoop stress is attained at a lower Deborah number. It is easy to visualize that higher inertial forces push the flow towards the central region of the cross-slot and this forces the fluid to turn direction closer to the geometric centre of the cross-slot, thus increasing locally the curvature of the streamlines.

Explaining the stabilizing effect of the Reynolds number for the first transition is more difficult, since we do not even know yet what is the primary cause for the first transition in creeping flow. Even though it is tempting to consider the unbounded normal stresses as its cause, there are indications that this is not the case given the fact that Poole et al. (2007c), Rocha et al. (2009) and Becherer et al. (2008) found such transitions to occur for PTT and FENE fluids for the equivalent 2D cross-slot flow. Clearly, understanding the causes of both types of transition in the 2D and 3D cross-slot flows is an important research topic.

On the other hand, for the 3D biaxial extensional flow configuration a perfectly symmetric flow has been observed up to $De \approx 0.61$ and above this critical Deborah number the flow becomes unsteady and asymmetric without transitioning to a steady asymmetric flow. Inertia was found to stabilize the first type of transition (for the uniaxial extensional flow) and to destabilize the second transition in both flow configurations, although to a much lesser degree in the biaxial extensional flow configuration.

3.3 MIXING-SEPARATING FLOW

The schematic representation of the mixing-separating geometry is presented in Figure 3.5. A mixing-separating geometry is formed by two opposed channels interacting through a gap of nondimensional width $\theta = g/H$, in the middle of a thin separating wall of nondimensional

thickness $\alpha = a/H$. It can also be seen as a cross-slot after rotation of two opposing arms into the other two remaining arms.

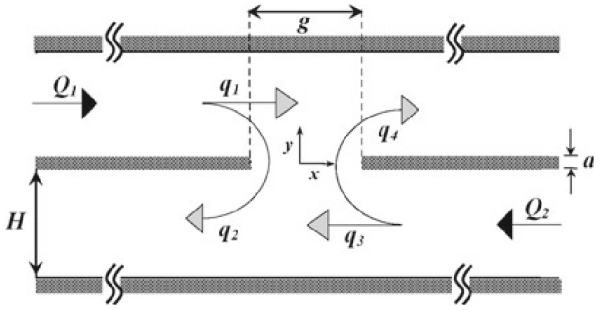

Figure 3.5: Schematic representation of the Mixing-Separating geometry.

The Deborah number represents the ratio between the relaxation time of the fluid, λ, and a characteristic time scale of the flow, here chosen as g/U. Consequently, for the present geometry the Deborah number is defined as $De = \lambda U/g$. For flows with non-negligible inertia the Reynolds number is also important, and is here defined as $Re = \rho U H/\eta$.

The degree of flow reversal relative to the unidirectional flow that would exist in the absence of a gap in the middle wall, is quantified using the parameter $R_r = q_2/Q_1 = q_4/Q_2$, where q_2 and q_4 correspond to the partial flow rates per unit depth that reverse from each inlet arm and $Q_1 = Q_2 = UH$ are the total flow rates per unit depth at each inlet channel

3.3.1 *Brief literature review*

There are very few published data for the mixing-separating geometry, and up to the beginning of this thesis, none on the elastic instabilities had been observed.

Some investigations were performed however, both experimentally and numerically by Cochrane et al. (1981), Walters and Webster (1982), Humphrey and Li (1981) and Humphrey et al. (2008). Baloch et al. (1995) and Fiétier (2002) analysed this flow numerically under different conditions.

Cochrane et al. (1981) employed a finite-difference method and selected the UCM model to describe the rheological behaviour of a highly-elastic constant-viscosity "Boger" fluid (Boger, 1977). These investigators analysed the effects of gap width using two different flow configurations: (*i*) matching flow rates in the two inlet channel arms and (*ii*) unbalanced inlet flow rates. In a follow-up work (Walters and Webster, 1982), thin insert plates with rounded edges were used. For both experimental studies it was found that the flow displayed distinctive Newtonian and viscoelastic behaviours, with the occurrence of unidirectional and reversed flows in varying extents.

Later, Baloch et al. (1995) selected the PTT model (Phan-Thien and Tanner, 1977) to describe the rheological behaviour, and simulated this flow also using thin insert plates with rounded edges, for the case of equal flow rates at the inlet channels. Fiétier (2002) simulated the flow of a FENE-P model (Bird et al., 1980) using a spectral element method, and considered the case with a thick insert plate with rounded edges.

The numerical results obtained captured qualitatively the experimental results presented by Walters and Webster (1982).

Humphrey and Li (1981) used a dye visualization technique, which revealed the time-evolution of pairs of transversely aligned vortices in a confined counter-current shearing flow configuration, for moderate Reynolds numbers ($Re = 100 - 1000$).

More recently, Humphrey et al. (2008) simulated the time-dependent flow of a Newtonian fluid in a counter-current shearing flow configuration, for $100 < Re < 300$.

3.3.2 *Contribution from this work*

In Afonso et al. (2010d) (see the integral version of this investigation on Section 6.2, on page 157) a numerical investigation is presented aimed to expand the limited knowledge available on the viscoelastic fluid flow behaviour in the mixing and separating geometry, clarifying and mapping different flow behaviours as a function of gap size under conditions of low inertia and different elasticity levels. The occurrence and extent of purely-elastic flow instabilities was also assessed. These instabilities usually arise in extensionally-dominated flows with strong streamline curvature, such as flows with a stagnation point (e.g. cross-slot flow: Arratia et al., 2006; Poole et al., 2007c,a), or the opposed jet apparatus (Chow et al., 1988).

This investigation focused on the mixing-separating flow geometry with thin insert plates and equal flow rates at the two channel inlets under low-Re flow conditions. For a combination of critical flow parameters, it was possible to identify a new steady and stable bifurcation in the flow patterns at low inertia and high elasticity, depending on the gap sizes:

- For large dimensionless gap sizes, but below a critical value ($\theta \leqslant 1.6$), the reversed flow is initially slightly enhanced with elasticity, followed by a significant decrease towards zero when Deborah number further increases. This behaviour is characterized by a significant departure from streamline parallelism in the mixing-separating gap region, although with the fluid still tending to flow unidirectionally in agreement with experiments (Cochrane et al., 1981; Walters and Webster, 1982).

- For a supercritical dimensionless gap size ($\theta \geqslant 1.84$), elasticity is responsible for a continuous increase of flow reversal relative to the unidirectional flow with Deborah number. This type of supercritical pattern has not yet been observed experimentally primarily due to the stabilising effect of inertia.

- At a well-defined intermediate gap width range ($1.6 \leqslant \theta \leqslant 1.84$), a steady bifurcation flow pattern emerges, with a sudden jump between two widely different flow configurations, ranging from almost unidirectional to almost fully reversed flows, at Deborah numbers slightly higher than the critical Deborah number. The bifurcation between these two flow patterns is due to a purely-elastic instability since inertia has no role ($Re = 0$) in the present simulations (we have also observed such purely elastic instabilities in the works of Poole et al., 2007c,a and Rocha et al., 2009). Further stability analysis suggested that in this bifurcation flow pattern,

although both flow configurations are steady and stable, the unidirectional configuration is preferred.

Flow inertia was found to increase the critical Deborah number for the steady flow bifurcation. Inertia naturally enhances the straight flow configuration and at $Re = 5$, R_r always decreased with Deborah number for $De \leqslant 0.6$ and for the investigated gap sizes. The interplay between inertia and elastic effects is clarified using the elasticity number, El, instead of Re and De separately.

Essentially the viscoelastic fluid adjusts itself so as to avoid changes in the flow direction and when the streamline curvature imposed by the geometry (increasing θ) is large, the elastic normal stresses become so strong, with consequent high energy loss coefficient, that the reversed flow pattern can no longer be sustained. There is then a sudden jump from reversed flow (large curvature) to unidirectional flow (small curvature), accompanied by a reduction of the energy loss associated with the flow. In addition, for a limited range of flow parameters, a pair of extreme flow patterns might co-exist as a solution of the governing equation, an indication of a steady bifurcation phenomenon.

These results suggest the need for experiments with highly viscous and elastic fluids (or at microscale where Re is naturally reduced and De is enhanced) in order to identify the supercritical behaviour, which has so far not been reported in the literature.

4

A *PUZZLING* DRIVING FORCE: VISCOELASTIC ELECTRO-OSMOTIC FLOWS

PUZZLING :: *difficult to understand or solve;*
to ponder or study over some perplexing problem or matter;
to solve by careful study or effort.

Usually fluid transport design strategies cannot be easily scaled down to micron or sub-micron scales because at such lenght scales, surface-dominated physical forces/phenomena (e.g., capillary, wetting, electrokinetic effect), which can usually be neglected in macroscale flow processes, become important. These microchannel flows are often used in the separation of biological or chemical components, such as the separation of DNA in genetic engineering. Some of these fluids present different rheological behaviour from the Newtonian fluids, and to the authors knowledge, analytical solutions of electroosmotically-driven flow of viscoelastic fluids in microchannels have rarely been found in the open literature.

The widespread use and low manufacturing cost of microfluidic chips (or circuits) is fostering a wealth of new industrial applications involving complex fluids, often associated with complex phenomena. Even though microfluidics is still in a state of exploratory research, there are industrial applications where its advantages stand out clearly, such as in screening for protein crystallization, bioanalyses or the manipulation of multiphase flows.

In simple geometries, where the flow is essentially parallel to walls and these are unpatterned, numerical investigations of electroosmosis flows can be carried out with simple models, such as the Poisson- Boltzmann equation. However, for general flow systems and time-dependent three-dimensional flows the numerical solution of the base governing Nernst-Planck equations are required for the accurate computation of the electric charge distribution. This is essentially a convection-diffusion equation, which can be easily incorporated into existing numerical methods. The main difficulty of these computations is the overhead cost associated with the very thin electric double-layer (EDL) at the walls, where steep velocity and potential gradients are found.

Most numerical solutions of electro-osmotic flows concern simplified electrokinetic models and Newtonian fluids, but there are already some simple implementations for viscoelastic fluids, which avoided calculations inside the EDL by bridging it with the Helmholtz-Smoluchowski velocity for the Phan-Thien—Tanner fluid (Park and Lee, 2008b). This approach needs further research to assess whether it can be generalized as in the similar law of the wall problem for turbulent flows and considering also the Nernst-Planck equation.

4.1 ELECTRO-OSMOTIC FLOW (EOF)

Electro-osmosis is a basic electrokinetic phenomenon, where the flow is induced by a new body force term, the applied external electric field, acting on ions that spontaneously formed near walls and other interface.

The principle was first demonstrated by Reuss (1809), in an experimental investigation using porous clay. This was followed by the theoretical work on the Electric Double Layer (EDL) by von Helmholtz (1879), which related the electrical and flow parameters for electrokinetically driven flows. Later von Smoluchowski (1903) contributed to the understanding of electrokinetically driven flows, especially for conditions where the EDL thickness is much smaller than the channel height.

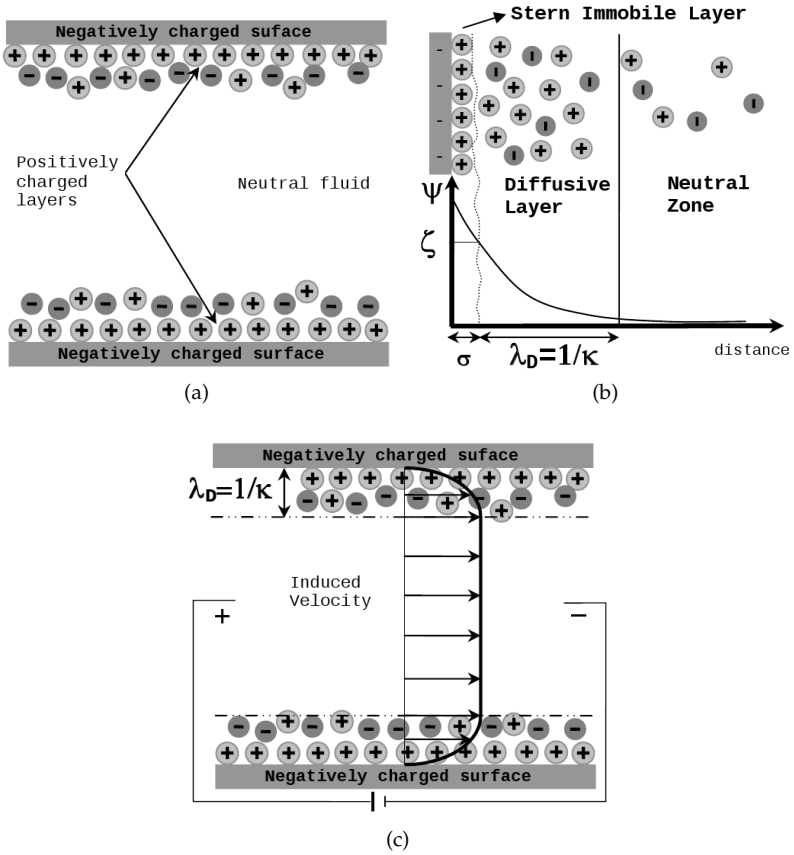

Figure 4.1: Schematic representation of the electro-osmotic flow mechanism.

A possible schematic view of an electro-osmotic flow in microchannels can be sketched as follows. A natural migration of ions arises due to the interaction between the dielectric charged wall and the polar fluid (cf. Figure 4.1a). Here, the two negatively charged walls of the microchannel attract counter-ions forming layers of positively charged fluid near the walls and repel the co-ions. Very thin layers of immobile counter-ions cover the walls, known as the Stern layers, σ, followed by thicker more diffuse layers of mobile counter-ions, called the Debye layer, λ_D. The two near wall layers form what is called the Electrical Double Layer (EDL), as observed in Figure 4.1b.

The global charge of the conducting fluid remains neutral, but since the EDL is thin the core of the conducting fluid is essentially neutral. Applying a DC potential difference between the two electrodes at the inlet and outlet of thechannel, generates an external electric field that exerts a body force on the counter-ions of the EDL, which move along the channel dragging the neutral conducting fluid core above by viscous forces, as observed in Figure 4.1c.

For Newtonian fluids, rigorous modelling and analytical solutions of simple shear electro-osmotic flow has been the subject of several studies, and a thorough review on this and on various other aspects of electro-osmosis can be found in Karniadakis et al. (2005). The theoretical study of electro-osmotic flows for viscoelastic fluids is fairly recent and most works have been restricted to simple inelastic fluid models, such as the power-law, due to the inherent difficulties introduced by more complex constitutive equations.

It was clear that there were no analytical solutions for fully-developed electro-osmotic flows of quasi-linear and non-linear viscoelastic fluids, and even less so when in combination with pressure gradient (at the start of this thesis). Also, the numerical approach to more complex geometry flows of complex fluids with electrokinetic effects were scarce.

Since then, several studies were performed on both theoretical and computational EOF of viscoelastic fluids, such as (Das and Chakraborty, 2006; Park and Lee, 2008b; Berli and Olivares, 2008; Zhao et al., 2008; Sousa et al., 2010a; Bryce and Freeman, 2010) and Afonso et al., 2009c, 2010c,f,g and Dhinakaran et al., 2010. This set (seven presentations in international and national conferences and five published papers) is discussed in detail in the next sections.

4.1.1 *Analytical contribution from this work*

Various analytical solutions were derived during this PhD, such as Afonso et al. (2009c, 2010c,f,g) and Dhinakaran et al. (2010).

In Afonso et al. (2009c) an analytical solution is presented for the flow of viscoelastic fluids in micron sized ducts, namely between parallel plates and pipes, under the combined influence of electrokinetic and pressure forces using the Debye–Hückel approximation, including the limit case of pure electro-osmotic flow. The viscoelastic fluids used are described by the simplified Phan-Thien–Tanner model (sPTT), with linear kernel for the stress coefficient function, and zero second normal stress difference, and the FENE-P model, based on the kinetic theory for finitely extensible dumbbells with a Peterlin approximation for the average spring force. The combined effects of fluid rheology, electro-osmotic and pressure gradient forcings on the fluid velocity distribution and fluid stresses are also discussed.

In the absence of an imposed pressure gradient, the electro-osmotic flow exhibits a pluglike velocity profile, as found previously for Newtonian fluids, but with the maximum velocity plateau increasing quadraticaly with $\sqrt{\bar{\varepsilon}}De_\kappa$, for all $\bar{\kappa}$ values. When the viscoelastic flow is induced by a combination of both electrical and pressure potentials, in addition to the single contributions from these two mechanisms there is an extra term in the velocity profile that simultaneously combines both, which is absent for the Newtonian case where the superposition principle applies. This non-linear term can contribute significantly to

the total flow rate, depending on the value of $\bar{\kappa}$. Under conditions of favourable pressure gradient it thus acts as a drag reducer, but for adverse pressure gradients it changes its role to become a drag increaser. Its existence invalidates the superposition principle and is associated with the non-linearity of the rheological model, with this analytical solution indicating that for quasi-linear viscoelastic equations the superposition principle still applies. Under favourable pressure gradients, the velocities increase significantly with $\sqrt{\varepsilon}De_\kappa$, with the profiles at higher values of $\bar{\kappa}$ exhibiting large shear rates within the electric double layer. As for Newtonian fluids, adverse pressure gradients lead to local velocity peaks at the edge of the electric double layer. Regarding the streaming potential problem, viscoelasticity increases the amount of electrical streaming current, which asymptotes to a constant value at high $\sqrt{\varepsilon}De_N$. The amount of electrical streaming current decreases with the increase of Υ_1, due to the lower $E_{x,sp}$ required to establish the conduction current for good conductors and the consequent lower streaming potential as found for Newtonian fluids.

Afonso et al. (2010c) extended the previous work by considering asymmetric boundary conditions, namely different zeta potentials at the walls. The fluids are assumed $z-z$ symmetric electrolytes. The analytic solutions of the electrical potential, velocity distributions and streaming potential are based again on the Debye-Hückel approximation for weak potential. The viscoelastic fluids used are modelled by the simplified Phan-Thien—Tanner constitutive equation, with linear kernel for the stress coefficient function, and the Finitely Extensible Non-linear Elastic dumbbells model with a Peterlin approximation for the average spring force. The combined effects of fluid rheology, electrical double-layer thickness, ratio of the wall zeta potentials and ratio between the applied streamwise gradients of electrostatic potential and pressure on the fluid velocity and stress distributions are discussed.

Later, Dhinakaran et al. (2010) studied analytically the pure electro-osmotic flow between parallel plates of a viscoelastic fluid, described by the complete form of the Phan-Thien-Tanner model. This model uses the Gordon-Schowalter convected derivative, which leads to a non-zero second normal stress difference in pure shear flow. A nonlinear Poisson-Boltzmann equation governing the electrical double-layer field and a body force generated by the applied electrical potential field are included in the analysis. Results are presented for the velocity and stress component profiles in the microchannel for different parametric values that characterize this flow. Equations for the critical shear rates and maximum electrical potential that can be applied to maintain a steady fully developed flow are derived and discussed. Some of the important results can be summarised as follows:

- Comparison with the analytical solution for the flow of Newtonian fluids, available in the literature was consistent.
- Dimensionless velocities profiles in the channel are invariant with De_κ below $De_\kappa = 0.1$.
- When the shear rate and Deborah number exceed a critical value a constitutive flow instability occurs for $\xi, \neq 0$. Expressions for these critical values of shear rate and Deborah number are reported. The critical shear rate is found to be dependent of ε and ξ, whereas

the critical Deborah number is only dependent on ξ, for large $\overline{\kappa}$. The critical Deborah number increases with decrease in ξ, tending to infinity as ξ tends to zero.

- Normal and shear stresses are approximately zero near the centreline and rise rapidly near the channel walls. At low Deborah numbers both these quantities are almost negligible. At higher De_κ the values of these quantities rise rapidly with increasing microchannel height ratio.

In Afonso et al. (2010f) (see the integral version of this investigation on Section 7.4, on page 229) an analytical model that describes a two-fluid electro-osmotic flow of stratified viscoelastic fluids is present. This is the principle of operation of an EO two-fluid pump, presented by Brask et al. (2003), in which an electrically nonconducting fluid is transported by the interfacial dragging viscous force of a conducting fluid that is driven by electro-osmosis. The electric potential in the conducting fluid and the analytical steady flow solution of the two-fluid electro-osmotic stratified flow in a planar microchannel are presented by assuming a planar interface between the two viscoelastic immiscible fluids.

The effects of fluid rheology, dynamic viscosity ratio, holdup and interfacial zeta potential are analysed to show the viability of this technique, where an enhancement of the flow rate is observed as the shear-thinning effects are increased. This work demostrated that higher volumetric flow rates of a nonconducting Newtonian fluid can be acheived in EOF pumping when the conducting fluid is viscoelastic rather than Newtonian, due to the increasing of the shear-thinning effects.

4.1.2 *Numeric contribution from this work*

In Afonso et al. (2010g) (see the integral version of this investigation on Section 7.5, on page 245), three different implementations of electro-osmosis physical models, depending on the desired level of approximation, were introduced.

In the first implementation, the Poisson-Nernst–Planck (PNP) equations were incorporated into the code and the electric charge distribution required to quantify the electric field forcing of the momentum equation is calculated without approximations. The second implementation is an approximation in which a stable Boltzmann distribution of ions in the electric double layer can be assumed. Here, the Poisson-Boltzmann equations were implemented. Finally, the so-called Debye-Hückel approximation was implemented in the Poisson-Boltzmann-Debye-Hückel (PBDH) version, for cases with small ratio of electrical to thermal energies. To test each one of the numerical implementations, some predictions are compared with existing analytical solutions for the flow in a two-dimensional microchannel under symmetric and asymmetric boundary conditions for the zeta potential at the walls (Afonso et al., 2009c, 2010c).

New types of flow instabilities, a mixture between electrokinetic and elastic instabilities, were obtained in the electro-osmosis flow in combination with viscoelastic fluids, such as in the cross-slot flow. For the UCM fluid flow above a critical Deborah number ($De_H = 0.275$) the

flow becomes asymmetric, and the differences between the results for the cross slot with pure EOF and pure pressure gradient flows by Poole et al. (2007c), were related with the role of the amount of stabilizing shear flow in the stagnation point region which is less important in the case of EOF. This difference may also be important for understanding the onset of the purely-elastic instabilities. At higher Deborah numbers the flow becomes unsteady, with the formation of vortical structures in the central region of the cross-slot.

Part III

(FURTHER) DEVELOPMENTS ON THEORETICAL AND COMPUTATIONAL RHEOLOGY

INTRODUCTION TO PART III

The shortest answer
is doing the thing.

— Ernest Hemingway

The present dissertation falls into the category of *multi-paper dissertations*, and in the Part III of this dissertation, called "(Further) Developments on theoretical and computational rheology", includes the complete and integral version of the papers written in the course of this PhD work. These papers where explained and contextualized in the previous Part II, in Chapters 2, 3 and 4.

Part III is further divided into three main chapters. In Chapter 5, the following papers, related with the High Weissenberg Number Problem, are presented:

- A. Afonso, PJ Oliveira, FT Pinho and MA Alves (2009). The log-conformation tensor approach in the Finite Volume Method framework, *Journal of Non-Newtonian Fluid Mechanics* **157** 55-65, in Section 5.1, on page 67;
- A. Afonso M. A. Alves, F. T. Pinho and P. J. Oliveira (2008). Uniform flow of viscoelastic fluids past a confined cylinder, *Rheologica Acta*, **47** 325-348, in Section 5.2, on page 87;
- A.M. Afonso, P.J. Oliveira, F.T. Pinho and M.A. Alves (2010), Dynamics of high Deborah number entry flows – a numerical study, accepted for publication in the *Journal of Fluid Mechanics*, in Section 5.3, on page 113.

Chapter 6, is reserved for the papers related with the *eccentric* features of elastic flow instabilities:

- A.M. Afonso, M.A. Alves, F.T Pinho (2010). Purely-Elastic flow instabilities in a 3D six arms cross slot geometry, *Journal of Non-Newtonian Fluid Mechanics* **165** 743–751, in Section 6.1, on page 143;
- A.M. Afonso, M.A. Alves, R.J. Poole, P.J. Oliveira and F.T. Pinho (2010). Viscoelastic flows in mixing-separating cells, accepted for publication in the *Journal of Engineering Mathematics*, in Section 6.2, on page 157.

Finally, in Chapter 7, the following analytical and numerical papers related with viscoelastic electro-osmotic flows are presented:

- A.M. Afonso, M.A. Alves, F.T. Pinho (2009). Analytical solution of mixed electro-osmotic/ pressure driven flows of viscoelastic fluids in microchannels. *Journal of Non-Newtonian Fluid Mechanics* **159** 50-63, in Section 7.1, on page 171;
- A.M. Afonso, M.A. Alves, F.T. Pinho (2010). Electro-osmotic flows of viscoelastic fluids in microchannels under asymmetric zeta potential, accepted for publication in the *Journal of Engineering Mathematics*, in Section 7.2, on page 197;

- S. Dhinakaran, A.M. Afonso, M.A. Alves, F.T. Pinho (2010). Steady viscoelastic fluid flow in microchannels under electrokinetic forces: PTT model, *Journal of Colloid And Interface Science* **344** 513-520, in Section 7.3, on page 215;
- A.M. Afonso, F.T. Pinho and M.A. Alves (2010), Two-fluid electro-osmotic flows of viscoelastic fluids, in preparation to submit to *Microfluidics and Nanofluidics*, in Section 7.4, on page 229;
- A.M. Afonso, F.T Pinho and M.A Alves (2010). Electro-osmotic flows of viscoelastic fluids: a numerical study, in preparation to submit to *Journal of Non-Newtonian Fluid Mechanics,* in Section 7.5, on page 245.

5

THE *INFAMOUS* HIGH WEISSENBERG NUMBER PROBLEM AND *(FURTHER)* DEVELOPMENTS

5.1 THE LOG-CONFORMATION TENSOR APPROACH IN THE FINITE VOLUME METHOD FRAMEWORK

Abstract[1]
The log-conformation formulation, proposed by Fattal and Kupferman (2004), has helped to provide further insights into the High-Weissenberg Number Problem. In this work, we investigate the performance of the log-conformation formulation in the Finite Volume Method (FVM) framework for creeping flows of viscoelastic fluids in steady and unsteady flows around a confined cylinder. The Oldroyd-B and Phan-Thien– Tanner (PTT) constitutive equations were used to assess the effect of different rheological behaviour on the flow patterns and solution stability. The calculation of the polymer stress contribution is carried out with both the standard technique and with the log- conformation methodology. For all test cases, up to the critical conditions when both methods converge to a steady solution, the use of the log-conformation technique provides solutions with similar accuracy as the standard approach. In terms of stability the log-conformation formulation is found to be significantly more robust, and solutions could be obtained at higher Deborah number flows.

Keywords: Finite-volume method; Log-conformation tensor; Viscoelastic fluid; Cylinder flow.

5.1.1 *Introduction*

A Finite Volume method (FVM) is applied to the numerical simulation of laminar viscoelastic flow around a confined cylinder using the Oldroyd-B model (Bird et al., 1987a) and the Phan-Thien–Tanner model (Phan-Thien and Tanner, 1977; Phan-Thien, 1978) (PTT) with linear stress coefficient kernel. The Oldroyd-B fluid was selected for this study, in order to allow direct comparison with previous works (e.g. Alves et al., 2001b), and also to analyze the applicability and benefits of using the matrix logarithm transformation (Fattal and Kupferman, 2004) for Maxwell-type models in a smooth flow (i.e., without geometric singularities).

The flow around a confined cylinder is a usual benchmark test-case in computational rheology. It is representative of fundamental flow dynamics of viscoelastic fluids around solid bodies and it can

1 A. Afonso, PJ Oliveira, FT Pinho and MA Alves (2009). The log-conformation tensor approach in the Finite Volume Method framework, *Journal of Non-Newtonian Fluid Mechanics* **157** 55-65.

be encountered in many engineering processes. This flow has been studied experimentally by McKinley et al. (1993), Baaijens et al. (1994) and Shiang et al. (1997, 2000). Owens and Phillips (2002) documented and summarized the main numerical results, focusing primarily on the Oldroyd-B model. Although the flow around a confined cylinder is classified as a smooth flow, its numerical calculation presents some difficulties associated with the development of thin stress layers on the cylinder sidewall and along the centreline in the cylinder rear wake, imposing a limiting value to the Deborah number for which steady solutions can be obtained. In fact, the simulations for the cylinder flow with the Upper-Convected Maxwell (UCM) or Oldroyd-B fluids are somehow limited by the so called High-Weissenberg Number Problem (HWNP; like the Deborah number, the Weissenberg number measures the flow elasticity). A breakdown in the calculations is found at a limiting Deborah number below 1 for the UCM fluid whereas for the Oldroyd-B fluid the breakdown occurs at higher Deborah numbers depending on the solvent viscosity ratio.

In order to get further insights into the HWNP, this work implements the methodology recently proposed by Fattal and Kupferman (2004), the so called matrix-logarithm or log-conformation formulation (nomenclature used heretoforth) of the viscoelastic constitutive equations. This is based on a reformulation of the constitutive law in terms of the matrix logarithm of the conformation tensor. According to Fattal and Kupferman (2004), taking the logarithm of the conformation tensor reduces its very large (often exponential) variation. (e.g. in stagnation points, or near the walls). The new variable can be more accurately approximated by a polynomial interpolation, and the method also preserves the positive definiteness of the conformation tensor (Fattal and Kupferman, 2004, 2005; Pan and Hao, 2007; Hulsen et al., 2005; Kwon, 2004; Yoon and Kwon, 2005; Kwon, 2006; Coronado et al., 2007; Guénette et al., 2008). A similar logarithm transformation was used previously for scalar quantities in mass transfer problems by Miranda and Campos (2001), who applied a simple logarithmic variable transformation of the solute concentration in the solution of laminar flow and solute transport equations in a parallel plate device with permeable walls. This variable transformation improved their finite difference method allowing the use of a larger grid spacing without loss of accuracy. A logarithm transformation has also been used in turbulence modelling using the k-ε formalism (Ilinca et al., 1998). The model is rewritten in terms of the variables $\log(k)$ and $\log(\varepsilon)$, and when k and ε variables are recovered the result is always positive.

Fattal and Kupferman (2004) reported a breakthrough in the HWNP in their numerical simulations with the Finitely-Extensible Nonlinear Elastic model using the Chilcott-Rallison approximation (FENE-CR) in a two-dimensional lid-driven cavity flow. Later, Fattal and Kupferman (2005) applied the log-conformation scheme to the flow of an Oldroyd-B fluid in the same geometry, using a multigrid solver, and reported the ability to perform stable simulations at large values of the Weissenberg number. They proposed a stability criterion and stated that this condition may be very restrictive when convection is weak and in the presence of large deformation rates, as in the flow around sharp corners. Recently, Pan and Hao (2007) performed numerical simulations of the lid-driven cavity creeping flow for an Oldroyd-B fluid, using the finite element method (FEM). They also relied on the log-conformation tech-

nique, and found that this methodology is stable at higher Weissenberg numbers, and presented solutions up to $De = 3$.

Hulsen et al. (2005) were the first to implement the log-conformation methodology within the FEM framework and applied it to the benchmark flow of Oldroyd-B and Giesekus fluids past a confined cylinder. They reported an almost unbounded convergence limit for the Giesekus model, whereas for the Oldroyd-B fluid the solution became unsteady at higher Deborah numbers, while exhibiting symptoms of strong mesh dependency particularly in the stress fields near the cylinder. Kwon (2004) investigated numerically the planar 4:1 contraction flow using the Leonov constitutive equation and found stabler computations when using the log-conformation method than with the conventional approach. Kwon (2004) also concluded that this new method may only work efficiently for constitutive equations that are proven globally stable and that the stability constraint has to be taken into serious consideration. In a sequel, Yoon and Kwon (2005) obtained solutions for Deborah numbers in excess of 100 using finer meshes. These authors also presented solutions for the 4:1:4 contraction/expansion flow and obtained converged solutions for Deborah numbers above 10. However, in both geometries the convergence limits decreased with mesh refinement. More recently, Kwon (2006) extended the log conformation formulation to the calculations of flows of viscoelastic fluids in a channel obstructed by an asymmetric array of cylindrical obstacles. The Leonov model was employed, and stable solutions were obtained with an apparent unbounded convergence limit when the retardation parameter that specifies the solvent viscosity contribution was 0.5. In contrast, in the absence of a solvent contribution to the Leonov model, the limiting Deborah number becomes finite, between 4.5 and 20.

Coronado et al. (2007) used an alternate implementation of the log-conformation formulation in their simulations of the planar Couette flow and flow past a cylinder in a channel, for several viscoelastic fluids. These were modelled by a generalized constitutive equation formulated in terms of the conformation tensor. Their results demonstrated that this methodology works well and improves the numerical stability at higher De, especially in the flow past a confined cylinder, where the maximum De limit was extended to 1.0 as compared to 0.7 obtained with the standard DEVSS-TG/SUPG method. The results were also in good agreement with those presented by Hulsen et al. (2005). Recently, Guénette et al. (2008) performed simulations of the flow of a viscoelastic fluid around a confined cylinder using the Oldroyd-B and Giesekus models. They used a FEM, with an anisotropic adaptive remeshing method, based on the log-conformation formulation, and showed that convergence with mesh refinement is possible for the Oldroyd-B model up to at least $De = 0.7$, although at $De = 0.8$ mesh convergence was lost.

The remaining of this paper is organised as follows: after presenting the governing equations, the log-conformation modified constitutive equation is described. Then, we explain how the positive definiteness of the conformation tensor is assessed. Prior to the presentation of results the numerical method is briefly described and the geometry and computational meshes used are presented. The paper ends with the main conclusions.

5.1.2 *Governing Equations*

To simulate the steady incompressible flow of viscoelastic fluids, the following set of governing equations needs to be solved: conservation of mass,

$$\nabla \cdot \mathbf{u} = 0, \tag{5.1}$$

conservation of momentum,

$$\rho \frac{D\mathbf{u}}{Dt} = -\nabla p + \beta \eta_o \nabla^2 \mathbf{u} + \frac{\eta_o}{\lambda}(1-\beta)\ \nabla \cdot \mathbf{A}, \tag{5.2}$$

containing an additive term which either obeys the Oldroyd-B or the PTT model and a constitutive equation describing the evolution of the conformation tensor, $\mathbf{A}$,

$$\lambda \overset{\nabla}{\mathbf{A}} = -Y(\mathrm{tr}\mathbf{A})(\mathbf{A}-\mathbf{I}) \tag{5.3}$$

where $\mathbf{I}$ is the unit tensor, $\mathbf{u}$ is the velocity vector, p is the pressure, λ is the relaxation time of the polymer, and $\overset{\nabla}{\mathbf{A}}$ represents Oldroyd's upper-convected derivative of $\mathbf{A}$, given by

$$\overset{\nabla}{\mathbf{A}} = \frac{D\mathbf{A}}{Dt} - \mathbf{A}\cdot\nabla\mathbf{u} - \nabla\mathbf{u}^T\cdot\mathbf{A} \tag{5.4}$$

The total fluid extra-stress is the sum of the solvent and polymer stress contributions, and the viscosity ratio, β, is defined as the ratio between the Newtonian solvent viscosity, η_s, and the total zero shear-rate viscosity, η_0,

$$\beta \equiv \frac{\eta_s}{\eta_0} = \frac{\eta_s}{\eta_s + \eta_p} \tag{5.5}$$

where η_p is the coefficient of viscosity of the polymer.

In its general form function $Y(\mathrm{tr}\mathbf{A})$ for the PTT model is exponential (Phan-Thien, 1978) but in this work we use its linear form, $Y(\mathrm{tr}\mathbf{A}) = 1 + \varepsilon(\mathrm{tr}\mathbf{A} - 3)$ (Phan-Thien and Tanner, 1977). When $Y(\mathrm{tr}\mathbf{A}) = 1$ (i.e. for $\varepsilon = 0$) the Oldroyd-B model is recovered. The non-unitary form of $Y(\mathrm{tr}\mathbf{A})$ for the PTT model with a Newtonian solvent imparts shear-thinning behavior to the shear viscosity of the fluid and bounds its extensional viscosity. The constitutive law written in terms of the conformation tensor $\mathbf{A}$, can be explicitly formulated as a function of the polymer contribution to the extra-stress tensor, $\boldsymbol{\tau}$, with the following relation valid for both models,

$$\tau = \frac{\eta_p}{\lambda}(\mathbf{A}-\mathbf{I}). \tag{5.6}$$

The use of these governing equations in terms of $\boldsymbol{\tau}$ was followed in previous works (Alves et al., 2001b; Oliveira et al., 1998; Alves et al., 2000, 2003a; Afonso et al., 2008; Oliveira and Miranda, 2005), where the numerical methodology was extensively validated in the framework of FVM. This approach is known as the standard method, and is not used here except in some comparisons to assess the performance of the new log-conformation method. In such comparison the standard method will be based on the polymer stress given by equations (5.3) and (5.6).

5.1.2.1 *The log-conformation representation*

As mentioned above, Fattal and Kupferman (2004) suggested a simple tensor-logarithmic transformation of the conformation tensor for differential viscoelastic constitutive equations, which can be applied to a wide variety of constitutive laws. The core feature of the transformation is the decomposition of the velocity gradient, $\nabla \mathbf{u}^T$, into a traceless extensional component, $\mathbf{E}$, and a pure rotational component, $\mathbf{R}$. With this decomposition, the evolution equation (5.3), can be re-written as (Fattal and Kupferman, 2004)

$$\frac{\partial \mathbf{A}}{\partial t} + (\mathbf{u}\cdot\nabla)\mathbf{A} - (\mathbf{RA} - \mathbf{AR}) - 2\mathbf{EA} = \frac{Y(\mathrm{tr}\mathbf{A})}{\lambda}(\mathbf{A} - \mathbf{I}) \tag{5.7}$$

In the log-conformation representation the evolution equation (5.7) is replaced by an equivalent evolution equation for the logarithm of the conformation tensor, $\mathbf{\Theta} = \log \mathbf{A}$, benefiting from the fact that $\mathbf{A}$ is a symmetric positive definite (SPD) matrix, and thus can be diagonalized into the form (Fattal and Kupferman, 2004)

$$\mathbf{A} = \mathbf{\Omega}\ \mathbf{D}\ \mathbf{\Omega}^T, \tag{5.8}$$

where $\mathbf{\Omega}$ is an orthogonal matrix that consist of the eigenvectors of matrix $\mathbf{A}$, and $\mathbf{D}$ is a diagonal matrix made with the corresponding three distinct eigenvalues of matrix $\mathbf{A}$. The transformation from equation (5.7) to an equation for $\mathbf{\Theta} = \log \mathbf{A}$ is described in Fattal and Kupferman (2004), and leads to

$$\frac{\partial \mathbf{\Theta}}{\partial t} + (\mathbf{u}\cdot\nabla)\mathbf{\Theta} - (\mathbf{R\Theta} - \mathbf{\Theta R}) - 2\mathbf{E} = \frac{Y\left[\mathrm{tr}(e^{\mathbf{\Theta}})\right]}{\lambda}(e^{-\mathbf{\Theta}} - \mathbf{I}). \tag{5.9}$$

To recover $\mathbf{A}$ from $\mathbf{\Theta}$ the inverse transformation $\mathbf{A} = \mathrm{e}^{\mathbf{\Theta}}$ is used when necessary. The positive definiteness of the conformation tensor is crucial for the well posedness of the evolution equation. In this work, the positive definiteness is assessed by checking if the determinant of $\mathbf{A}$ is positive (a necessary condition for $\mathbf{A}$ being positive definite. For the Oldroyd-B model, $\det(\mathbf{A}) \geqslant 1$ as shown by Hulsen, 1988).

5.1.3 *Numerical method and computational meshes*

In the past, our group adapted a Newtonian FVM to calculate viscoelastic flows where the polymer contribution to the extra-stress tensor was described by one of various differential rheological constitutive equations (Alves et al., 2001b; Oliveira et al., 1998; Alves et al., 2000, 2003a; Afonso et al., 2008; Oliveira and Miranda, 2005). This fully-implicit FVM is based on a time-marching pressure-correction algorithm, formulated with the collocated variable arrangement, as explained in detail in Oliveira et al. (1998) and Alves et al. (2000, 2003a). Here, the methodology is adapted to the log-conformation procedure and the corresponding modifications are explained below.

The governing equations are first transformed to a non-orthogonal system, but keeping the Cartesian velocity and conformation/log-conformation components. The log-conformation tensor evolution equa-

tion (5.9) can thus be written into a general non-orthogonal coordinate system $(\sigma_1, \sigma_2, \sigma_3)$ as,

$$\frac{\partial J\Theta_{ij}}{\partial t} + \frac{\partial}{\partial \sigma_l}\left(u_k \beta_{lk} \Theta_{ij}\right) = J\left(R_{ik}\Theta_{kj} - \Theta_{ik}R_{kj}\right) + 2JE_{ij} + Y\left(A_{kk}\right)\frac{J}{\lambda}\left(e^{-\Theta_{ij}} - \delta_{ij}\right) \tag{5.10}$$

where J is the Jacobian of the transformation $x_k = x_k(\sigma_l)$ and β_{lk} are metric coefficients, defined by the cofactor of $\partial x_k/\partial\sigma_l$. After integration over the control volumes forming the computational mesh, and in time over a time step (δt), the β_{lk} metric coefficients are replaced by area components (index k) of the surface whose normal vector points towards direction l, the Jacobian J is replaced by the computational cell volume V, and the derivatives $\partial/\partial\sigma_l$ become differences between values along direction l. More details can be found in Oliveira et al. (1998).

After the discretization, the various terms are assembled, to obtain a system of algebraic equations of the form

$$a_P^{\Theta}\Theta_{ij,P} - \sum_F a_F^{\Theta}\Theta_{ij,F} = S_{\Theta_{ij}} + \frac{\lambda_P V_P}{\delta t}\Theta_{ij,P}^{0}, \tag{5.11}$$

where $\Theta_{ij,P}^{0}$ refers to the ij component of the log-conformation tensor at the previous time level, a_P^{Θ} represents the central coefficient, a_F^{Θ} represents the coefficients of the neighbouring cells (with F spanning the near-neighbouring cells of cell P) and $S_{\Theta_{ij}}$ is the source term.

The numerical procedure used in the standard method to solve for the extra-stress - equations (5.3) and (5.6)- was modified for the new form of stress equation based on the log-conformation tensor, equation (5.9), so that now the algorithm contains the following steps:

1. Initially, the conformation tensor A_{ij}, obtained from the extra-stress components τ_{ij} - from equation (5.6) - is used to calculate the log-conformation tensor, θ_{ij}. For each computational cell, A_{ij} is diagonalized according to equation (5.9), and all eigenvalues and eigenvectors are computed, which are used in the calculation of the orthogonal matrix, Ω_{ij}, and the diagonal matrix, D_{ij}. The tensor θ_{ij} is then calculated using the relation $\boldsymbol{\Theta} = \boldsymbol{\Omega}^{T}\left(\log \mathbf{D}\right)\boldsymbol{\Omega}$.

2. Following the appropriate decomposition (Fattal and Kupferman, 2004) of the velocity gradient, $\nabla\mathbf{u}$, and using the values of Ω_{ij}, and D_{ij}, the traceless extensional components, E_{ij}, and the pure rotational component, R_{ij}, are calculated at each cell;

3. The evolution equation for θ_{ij} - equation (5.10) - is solved to obtain θ_{ij} at the new time level;

4. The conformation tensor A_{ij} is recovered and the extra-stress τ_{ij} is calculated from the newly computed conformation field using equation (5.6);

5. The momentum equations are solved for each velocity component, u_i;

6. As generally the velocity components do not satisfy the continuity equation, this step of the algorithm involves a correction to u_i and to the pressure field p, so that the updated velocity field u_i and the corrected pressure field p satisfy simultaneously the continuity

and the momentum equations. This part of the algorithm remains unchanged and is described in detail in Oliveira et al. (1998);

7. Steps 1 to 6 are repeated until convergence is reached (steady state calculations), or until the desired final time is reached (unsteady calculations).

The advective term in equation (5.10) is discretised with the CUBISTA high-resolution scheme (Alves et al., 2003a), formally of third-order accuracy and especially designed to deal with differential constitutive relations.

5.1.4 *Results*

In order to analyse the performance of the log-conformation formalism in comparison with the standard formulation of the extra-stress tensor, the flow past a confined circular cylinder was calculated with both formulations. For conciseness henceforth we denote by ***StrT*** and ***LogT*** the results obtained with the standard and log-conformation methods, respectively. In all cases the L_1-norm of the residuals of the governing equations was required to be less than a tolerance of 10^{-6} in order to stop the time stepping procedure. In all test cases this convergence criterion was found to be sufficient to attain a converged steady-state solution.

5.1.4.1 *Flow geometry and computational meshes*

The geometry of the viscoelastic fluid flow past a confined cylinder in a channel is shown in Figure 5.1. The ratio of channel half-height h to cylinder radius R is set equal to 2, which corresponds to the benchmark 50% blockage case (Brown and McKinley, 1994). The computational domain is $200R$ long, with $99R$ upstream and $99R$ downstream of the forward and rear stagnation points of the cylinder, respectively. The downstream length is sufficient for the flow to become fully-developed and to avoid any effect of the Neumann outflow boundary condition upon the flow in the vicinity of the cylinder. Vanishing axial gradients are applied to all variables, including the pressure gradient, at the outlet plane. No-slip conditions are imposed at both the cylinder surface ($r = R$: $u = 0$, $v = 0$) and the channel wall ($y = \pm h$: $u = 0$, $v = 0$).

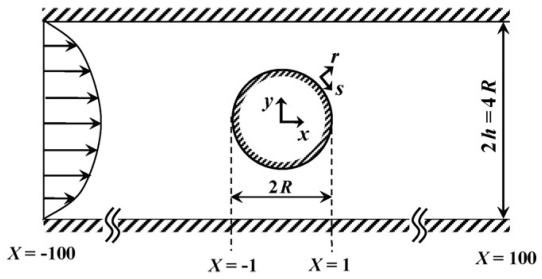

Figure 5.1: Schematic representation of the flow past a confined cylinder geometry ($X = x/R$).

The main characteristics of the meshes $M30_{WR}$ and $M60_{WR}$ used in this work are given in Table 5.1, including the total number cells (NC), the number of control volumes around the surface of the cylinder (NS),

Table 5.1: Main characteristics of the computational meshes.

	NC	NR	NS	$(\Delta r/R)_{min}$	$(\Delta s/R)_{min}$
$M30_{WR}$	11280	30	260	0.008	0.0012
$M60_{WR}$	45120	60	520	0.004	0.0006

the number of cells placed radially from the cylinder to the channel wall (NR), and the minimum cell spacing normalized with the cylinder radius along the radial (Δr) and the azimuthal ($\Delta s = R\Delta\theta$) directions. All the computational meshes mapped the complete flow domain (i.e. no symmetry boundary condition was imposed along the centreline), in order to capture possible symmetry-breaking steady/unsteady phenomena (Poole et al., 2007c; Rocha et al., 2009). The subscript WR (for *wake-refined*) is added to the mesh designation to denote highly refined meshes along the wake. For mesh $M30_{WR}$ the minimum normalized cell spacing along the azimuthal direction is 0.0012 compared with 0.0314 for the equivalent mesh M30 used in Alves et al. (2001b). Mesh $M60_{WR}$ has twice the number of cells along both directions as mesh $M30_{WR}$, with a total of 45120 cells. The number of cells along the cylinder sidewall with that mesh is 520 and the minimum normalized cell spacing along the radial and azimuthal directions is 0.004 and 0.0006, respectively.

Results of computations are presented in two ways: as a scalar integral quantity representative of the whole flow; and as detailed profiles of stress components in the vicinity of the cylinder. The integral quantity is the dimensionless drag coefficient, K, calculated as

$$K = \frac{1}{\eta_0 U} \int_S (\boldsymbol{\tau}_{tot} - p\mathbf{I}) \cdot \mathbf{n} \cdot \mathbf{i} \; dS \tag{5.12}$$

where $\mathbf{I}$ is the unit tensor, $\mathbf{n}$ is the unit vector normal to the cylinder surface and $\mathbf{i}$ is the unitary vector aligned with the streamwise direction. Stress profiles are shown along the cylinder wall and on the downstream rear wake, in order to ascertain the quality of the predictions.

All the calculations were carried out at a vanishing Reynolds number, $Re = \rho U R/\eta = 0$ (creeping flow conditions - imposed by dropping out the convective term in the momentum equation) and we studied the effect of the Deborah number, here defined as

$$De = \frac{\lambda U}{R} \tag{5.13}$$

where U and R represent average velocity and the cylinder radius, respectively. This definition of Deborah number is the same used in previous works (eg. McKinley et al. (1993); Baaijens et al. (1994); Shiang et al. (1997, 2000); Oliveira et al. (1998); Afonso et al. (2008); Fan et al. (1999), and is consistent with taking U for velocity scale and R for length scale. However we note that sometimes the same dimensionless group is called Weissenberg number (eg. Hulsen et al., 2005; Coronado et al., 2007), and that a distinction between the notion of De and Wi is irrelevant (except perhaps for a constant multiplicative factor) when the blockage ratio ($b = R/h$) is not varied. When such a distinction is required it is appropriate to define $Wi = \lambda\dot{\gamma}_c$ with the characteristic shear rate based on velocity and length scales existing in the gap

between the cylinder and the channel walls, thus $\dot{\gamma}_c = U_{gap}/h_{gap} = (3/2)U[h/(h=R)]/[(h=R)/2]$, giving $Wi = 3Deb/(1=b)^2$ (with $b = 0.5$ as in the present study, $Wi = 6De$). The fact that our numerical results show either a steady/unsteady flow transition or difficulties to achieve mesh convergence when $De \sim 1$, gives further support to base the level of elasticity on this definition.

The results for the Oldroyd-B model are presented in Section 5.1.4.2 and for the PTT model in Section 5.1.4.3.

5.1.4.2 *Oldroyd-B fluid*

In this section we use the Oldroyd-B model with a solvent viscosity ratio $\beta = 0.59$. Normalization of the data is done as follows: coordinates in the x and y directions were normalized by the cylinder radius, R, the velocity components by the average velocity, U, and the extra stress tensor τ and the pressure p are scaled with a viscous stress, $\eta_0 U/R$.

The simulations with the ***StrT*** formulation diverged at $De = 0.9$ with mesh $M60_{WR}$. The loss of positive definiteness of $\mathbf{A}$ precedes the onset of divergence of the numerical method, as observed in Figure 5.2, where the time evolution of the minimum value of the determinant of the conformation tensor along a calculation is plotted. After approximately two relaxation times, the simulation with the ***StrT*** formulation begins to present negative values of $\det(\mathbf{A})_{min}$. For the ***LogT*** formulation the value of $\det(\mathbf{A})_{min}$ is, by design, always positive, thus showing no signs of violation of the positive definition criteria. We also observe that with the ***LogT*** formulation $\det(\mathbf{A})_{min} \geqslant 1$, as expected for the Oldroyd-B model (Hulsen, 1988). It can also be observed that the location where loss of positive definiteness evolution occurs is in the rear stagnation point region, as depicted in the inset of Figure 5.2. This agrees with the results of Afonso et al. (2008) for uniform flow of viscoelastic fluids past a cylinder, where $\det(\mathbf{A})$ values were minimum in the rear stagnation point at all Deborah numbers.

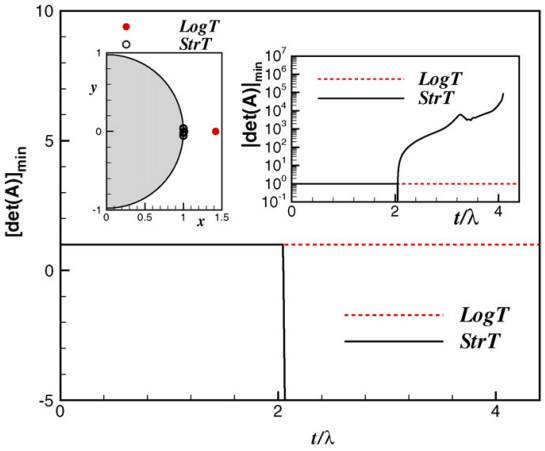

Figure 5.2: Time evolution of $\det(\mathbf{A})_{min}$ for creeping flow of an Oldroyd-B fluid (β= 0.59) past a cylinder. Comparison between *StrT* and *LogT* formulations at $De = 0.9$, calculated in mesh $M60_{WR}$. The circles in the inset figure indicate the location where the minimum value of $\det(\mathbf{A})$ is observed.

Drag coefficient results

The literature data for the dimensionless drag coefficient (K) show some discrepancies, especially for Deborah numbers above 0.7. Alves et al. (2001b) used the standard method, employing highly refined non-orthogonal meshes, and the predicted drag force agrees well with values from other simulations in the literature (Hulsen et al., 2005; Coronado et al., 2007; Guénette et al., 2008; Fan et al., 1999; Kim et al., 2004). In particular, their predictions of K were nearly identical to those of the FEM simulations of Fan et al. (1999). The predictions of drag force of Kim et al. (2004) also agreed well with the previous results up to $De = 0.9$.

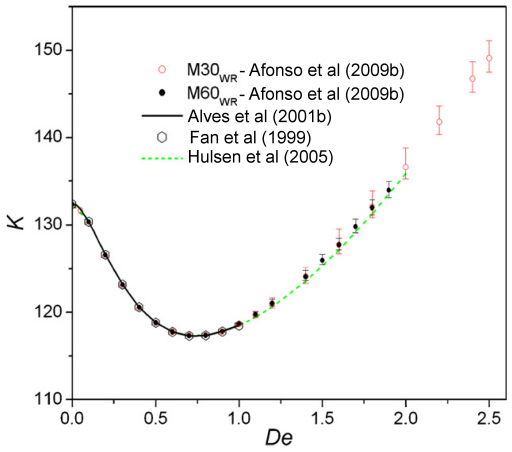

Figure 5.3: Drag force coefficient for the creeping flow of an Oldroyd-B fluid (β= 0.59) past a cylinder. Results obtained with the *LogT* formulation with meshes $M30_{WR}$ and $M60_{WR}$, and comparison with data from Alves et al. (2001b), Hulsen et al. (2005) and Fan et al. (1999).

Table 5.2: Drag force coefficient for the Oldroyd-B model with $\beta = 0.59$ (data in brackets indicate time-average values).

	StrT		*LogT*	
De	$M30_{WR}$	$M60_{WR}$	$M30_{WR}$	$M60_{WR}$
0.5	118.772	118.821	118.781	118.818
0.6	117.768	117.776	117.778	117.774
0.7	117.370	117.324	117.350	117.323
0.8	117.441	117.370	117.380	117.364
0.9			117.797	117.817
1.0			(118.662)	(118.680)
1.1			(119.740)	(119.780)
1.2			(120.985)	(121.051)
1.4			(124.129)	(124.092)
1.5			(126.022)	(125.972)
1.6			(127.759)	(127.751)
1.7			(130.012)	(129.802)
1.8			(132.024)	(131.937)
1.9			(134.188)	(133.952)
2.0			(136.580)	-
2.2			(141.801)	-
2.4			(146.730)	-
2.5			(149.112)	-

The predictions of K obtained in the present work are presented in Figure 5.3 and in Table 5.2. Up to $De = 0.9$ the results agree well with the accurate data of Fan et al. (1999), Alves et al. (2001b), Kim et al.

(2004) and Hulsen et al. (2005). For higher Deborah numbers, no steady state could be attained, with the K values oscillating in time with the amplitude marked as error bars in Figure 5.3. Here, instead of using the value of K right after the onset of the transient behaviour, as used by Hulsen et al. (2005), the plotted quantity is the time-average K value. Although the mean values for both meshes are slightly higher than the predictions of Hulsen et al. (2005), the lower bound of the oscillations are in agreement with their predictions.

Stress convergence

In terms of stress convergence with mesh refinement, it is well known that for $De > 0.7$ significant discrepancies are found among the results from the literature (Alves et al., 2001b; Hulsen et al., 2005; Coronado et al., 2007; Guénette et al., 2008; Fan et al., 1999; Kim et al., 2004), especially in the maximum peak of normal stresses at the rear wake. Even the predictions of the extra-stresses obtained with highly refined meshes at the rear stagnation region and using high order methods are not conclusive in this respect.

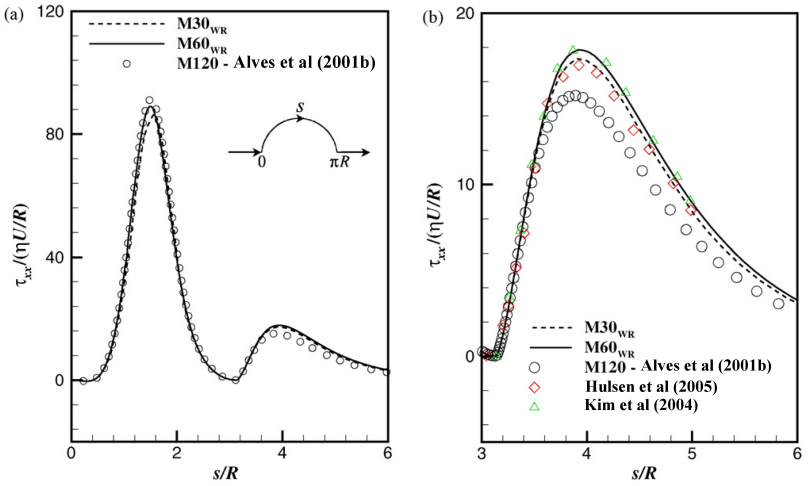

Figure 5.4: Effect of mesh refinement: (a) stress profiles along cylinder wall and downstream centreplane for Oldroyd-B fluid at $De = 0.6$. *LogT* formulation with meshes $M30_{WR}$ and $M60_{WR}$ and comparison with data from Alves et al. (2001b); (b) closer view in the rear wake of the cylinder and comparison with data from the literature.

Figure 5.4 shows normal stress profiles along the cylinder surface and the rear wake as obtained with different meshes at $De = 0.6$; the results are essentially mesh independent, but in the rear wake they are slightly above those of Alves et al. (2001b) using the ***StrT*** formulation (in this section, we use the results of Alves et al. (2001b) in their refined mesh (M120) to represent the ***StrT*** formulation). This difference is due to the refinement of the mesh in the wake allowing the stresses to be better resolved in meshes $M30_{WR}$ and $M60_{WR}$ than in mesh M120, thus showing the advantage of wake refined meshes. At $De = 0.7$ the corresponding normal stress profiles obtained with our wake refined meshes are plotted in Figure 5.5, and are in good agreement with those of Alves et al. (2001b) obtained with the ***StrT*** formulation. In the rear wake zone there is now a more noticeable mesh dependency, with the present results obtained with the ***LogT*** formulation exhibiting higher

stress peaks. The results of Alves et al. (2001b), Kim et al. (2004) and Hulsen et al. (2005) are all in close agreement, except for the maximum peak values in the wake that are slightly below those calculated here on the finest mesh.

Further increase in Deborah number to $De = 0.9$ enhances the discrepancies in the rear wake zone, as shown in Figure 5.6. Although on the cylinder surface the normal stress peaks obtained with the ***LogT*** and mesh $M60_{WR}$ are in close agreement with the ***StrT*** results of Alves et al. (2001b) for mesh M120, in the rear wake the differences are large. There is also a noticeable discrepancy in relation to the data of Fan et al. (1999) and Coronado et al. (2007).

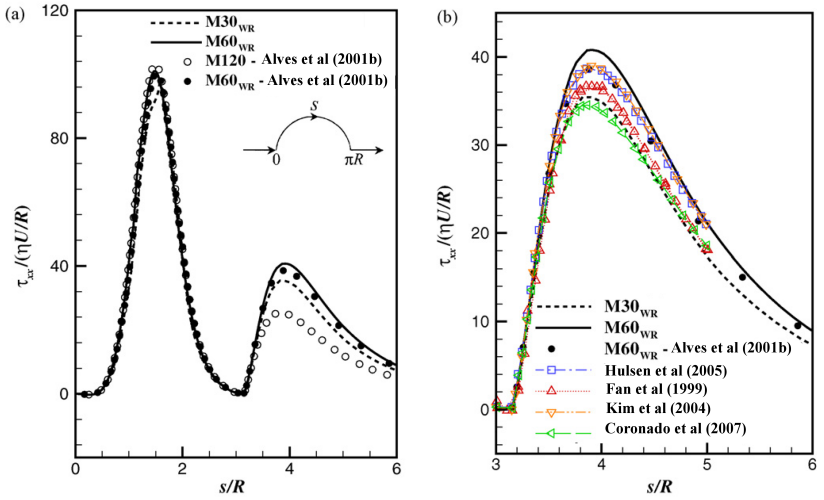

Figure 5.5: Effect of mesh refinement: (a) stress profiles along cylinder wall and downstream centreplane for Oldroyd-B fluid at $De = 0.7$. *LogT* formulation with meshes $M30_{WR}$ and $M60_{WR}$ and comparison with data from Alves et al. (2001b); (b) closer view in the rear wake of the cylinder and comparison with data from the literature.

Another useful observation concerns the relation between the maximum normal stress, $(\tau_{xx})_{max}$, along the centreline of the rear wake region and the location of peak stress, x_{max}. These data are plotted in Figure 5.7, and the value of $(\tau_{xx})_{max}$ increases nearly exponentially with De and the location x_{max}/R shows a non-monotonic behaviour, moving downstream from the rear stagnation point (from $(x-R)/R \approx 0.42$ to $(x-R)/R \approx 0.78$) for $De < 0.6$, and shifting back towards the stagnation point at higher Deborah numbers. This upstream shift in x_{max}/R at large Deborah numbers certainly contributes to numerical difficulties, as the size of the region of peak normal stress may eventually become smaller than the local streamwise mesh resolution. Also, as x_{max}/R approaches the rear stagnation point, higher residence times are observed in regions with higher strain rates, thus leading to a strong increase in the $(\tau_{xx})_{max}$ values as the fluid stresses are allowed to build up.

High Deborah number results

The question of whether a steady solution for cylinder flow can be attained at high De by improving numerical method accuracy and stability, is still open to debate. Fan et al. (1999) and Owens et al. (2002)

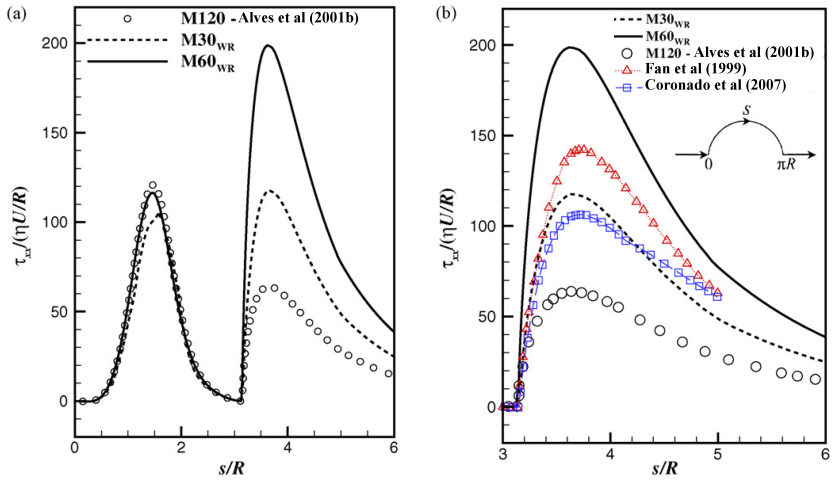

Figure 5.6: Effect of mesh refinement: (a) stress profiles along cylinder wall and downstream centreplane for Oldroyd-B fluid at $De = 0.9$. *LogT* formulation with meshes $M60_{WR}$ and $M60_{WR}$ and comparison with data from Alves et al. (2001b); (b) closer view in the rear wake of the cylinder and comparison with data from the literature.

argued that steady numerical solutions for the Oldroyd-B fluid flow at Deborah numbers above 0.8 are probably numerical artifacts. Recently, Bajaj et al. (2008) studied the cylinder flow problem with ultra-dilute and dilute polymer solutions, modelled by the Oldroyd-B and FENE-P models, and estimated that the number of finite elements required to achieve convergence is unfeasible to obtain solutions for the Oldroyd-B model above $De = 1$, due to the steep increase in the normal stresses in the thin boundary layer in the vicinity of the cylinder. On the other hand, experimental work in this geometry with a constant-viscosity PIB polymer solution showed a first transition from steady 2D to a steady 3D flow at $De \approx 1.3$, followed by a transition to a periodic time dependent flow at $De \approx 1.85$ (McKinley et al., 1993). Shiang et al. (1997, 2000) also identified experimentally a cellular structure in the cross-flow plane over a confined cylinder at $De_{crit} \approx 0.21$, with a periodic vortical structure obtained for $De_{crit} \approx 0.66$. The fluid used in these experiments has no noticeable shear-thinning for the range of tested shear-rates. Inspired by the experiments of McKinley et al. (1993), Oliveira and Miranda (2005) performed numerical simulations using the FENE-CR model and conjectured that the predicted pulsating small vortex attached to the rear stagnation point, could be the triggering mechanism leading to the formation of 3D cellular structures in the wake of the cylinder. If this is the case, then numerical results computed at high De assuming 2D flow are not representative of the real flows.

In this work, unsteady solutions were obtained for Deborah numbers from 1.0 up to 3.0 and 1.9, for meshes $M30_{WR}$ and $M60_{WR}$, respectively. This represents an increase of about 90% in the maximum attainable De as one changes from the ***StrT*** to the ***LogT*** formulation. Using the ***LogT*** approach the stability requirements were always attained, as per design. Figure 5.8a illustrates that the minimum value of det($\mathbf{A}$) is always positive, and above one (Hulsen, 1988). As described in the last Section, the unsteady flow was also reflected in the K results, and Figure 5.8b shows the time oscillations for several De, as predicted with mesh $M60_{WR}$. The range of these oscillations increase with De

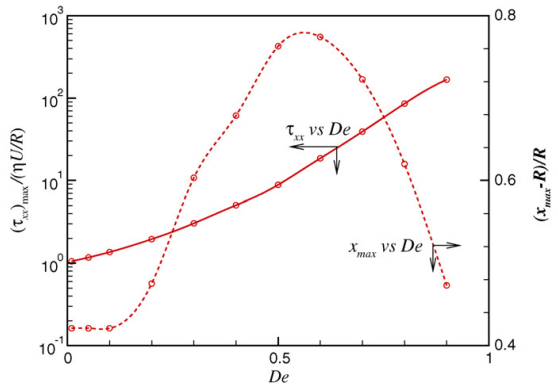

Figure 5.7: Maximum value of τ_{xx} along the downstream centreline and location of peak stress, x_{max}, as function of De. Results obtained with the Oldroyd-B fluid in mesh $M60_{WR}$.

and decrease with mesh refinement. Mesh independent results will be pursued in future work but those calculations are very time consuming. Nevertheless, even for $De = 1.9$ the relative amplitude of the oscillations is only of about 1.4% of the time-average value.

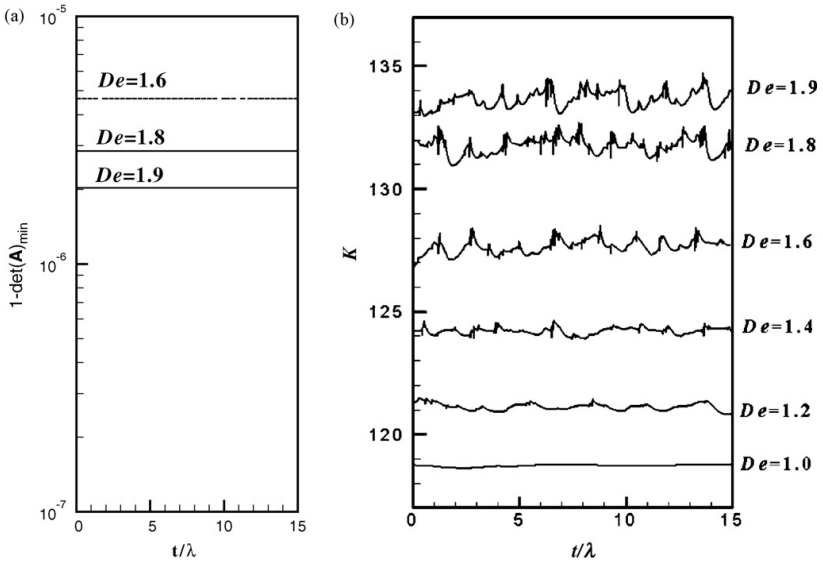

Figure 5.8: Time evolution of (a) $1-\det(\mathbf{A})_{min}$ and (b) drag force coefficient, calculated in mesh M60WR.

To obtain further insights into the time-dependent flow, calculations were carried out using a second-order time discretization scheme (Oliveira, 2001a) in order to improve time accuracy. Figure 5.9a shows the time evolution of K using different time steps for $De = 1.2$ and mesh $M30_{WR}$. The solutions obtained with the smaller time steps ($\Delta t/\lambda = 4x10^{-5}$ and $\Delta t/\lambda = 2x10^{-5}$) collapse and are independent of Δt, showing good time accuracy even if no characteristic frequency could be estimated from the numerical results of K *vs* t. The normal stress profiles at four instants plotted in Figure 5.9b show sharp increases in τ_{xx} near the rear stagnation point at some moments, thus breaking the smoothness of the stress profile in this viscoelastic flow. This reveals the major importance of the minimum mesh size in the

axial direction in the stagnation point region. Although stable results were obtained up to $De = 1.8$ by Hulsen et al. (2005) they also reported symptoms of stress convergence problems for $De > 0.7$, suggesting that a possible reason was that the length scale associated with the changes of the velocity gradient near the rear stagnation point was much smaller than the minimum mesh size in their most refined mesh. Hulsen et al. (2005) also questioned the existence of a smooth solution near the cylinder and recently Renardy (2006) argued that at high Deborah number flows the smoothness of viscoelastic stresses could be expected to deteriorate.

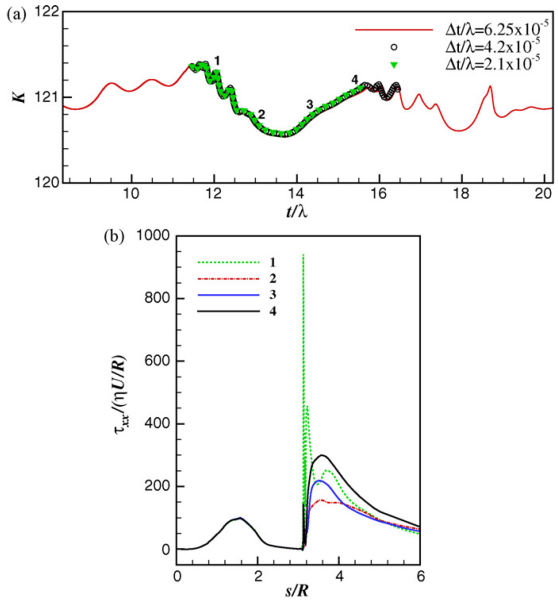

Figure 5.9: Creeping flowof an Oldroyd-B fluid (β= 0.59) past a cylinder at $De = 1.2$ (Mesh $M30_{WR}$). (a) Time evolution of the drag force coefficient for different time steps, $\Delta t/\lambda$. (b) Axial normal stress profiles along cylinder wall and downstream centreline at the four instants marked in (a).

5.1.4.3 *PTT fluid*

The evolution equation for the log-conformation tensor, equation (5.9), includes the PTT model (Phan-Thien and Tanner, 1977; Phan-Thien, 1978) with linear stress coefficient kernel, $Y(\mathrm{tr}\mathbf{A}) = 1 + \varepsilon(\mathrm{tr}\mathbf{A} - 3)$; when $\varepsilon = 0$ the Oldroyd-B model is recovered ($Y(\mathrm{tr}\mathbf{A})$= 1). This function brings in a new parameter ε that imposes an upper limit to the elongational viscosity ($\eta_E \propto 1/\varepsilon$ for low ε), and here the PTT model is employed with two typical values of $\varepsilon = 0.02$ and 0.25, and with solvent viscosity contribution ($\beta = 0.59$). The PTT model is shear-thinning in viscosity, in contrast to the Oldroyd-B model used in the previous Sections, and has been employed in several numerical works of flow past a cylinder with both uniform and Poiseuille inlet conditions (Afonso et al., 2008; Phan-Thien and Dou, 1999; Dou and Phan-Thien, 2003).

Stability and Drag coefficient results

For lower values of ε ($\varepsilon = 0.02$), the simulations with the ***StrT*** formulation diverged at $De \approx 3$ and $De \approx 1.2$ with meshes $M30_{WR}$ and

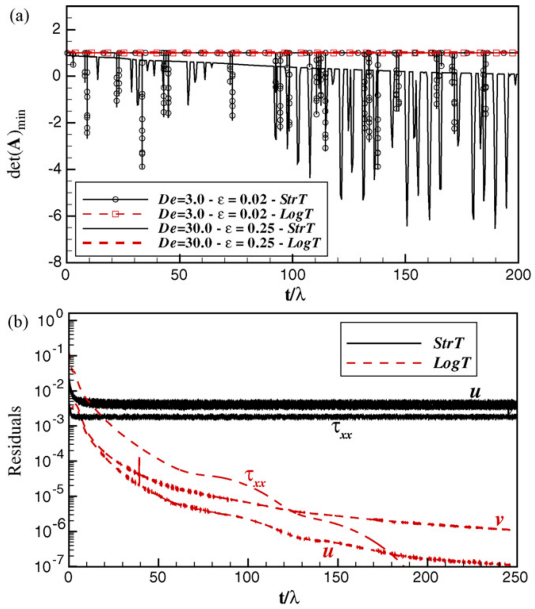

Figure 5.10: Time evolution of $\det(\mathbf{A})_{min}$ and residuals of the governing equations for the creeping flow of a PTT fluid (β= 0.59) past a cylinder calculated in mesh $M30_{WR}$. (a) Comparison of $\det(\mathbf{A})_{min}$ between ***StrT*** and ***LogT*** formulations at $De = 3$ (ε= 0.02) and $De = 30$ (ε= 0.25); (b) Comparison of iterative convergence between *StrT* and *LogT* formulations at $De = 30$ (ε= 0.25).

$M60_{WR}$, respectively. Note that when $\varepsilon \to 0$ the PTT model reduces to the Oldroyd-B model and, as observed for this latter model, a probable cause for divergence is the loss of positive definiteness, as observed in Figure 5.10a, where the determinant of the conformation tensor is presented for the near critical value of $De = 3$. The simulation with the ***StrT*** formulation has at least one negative eigenvalue of $\mathbf{A}$, leading to negative values of $\det(\mathbf{A})_{min}$ and this takes place near the rear stagnation point. For the ***LogT*** formulation with $\varepsilon = 0.02$, the value of $\det(\mathbf{A})_{min}$ is always positive, as per design, and converged solutions up to $De \approx 20$ and $De \approx 10$ were obtained with meshes $M30_{WR}$ and $M60_{WR}$, respectively. This breakthrough in the critical Deborah number for steady flow clearly shows the advantage of using the ***LogT*** formulation. This scenario is even more outstanding in the simulations for higher values of ε ($\varepsilon = 0.25$), where the ***LogT*** formulation shows no signs of convergence problems, while for the ***StrT*** formulation positive definiteness is no longer observed for $De \approx 30$ with mesh $M30_{WR}$, as shown in Figure 5.10b. The simulations with the ***StrT*** formulation with mesh $M30_{WR}$ still converged up to $De \approx 200$, but the value of $\det(\mathbf{A})_{min}$ was always negative with its magnitude increasing with De, and with the L_1-norm of the residuals of the governing equations not attaining the required tolerance while the residuals for the equivalent ***LogT*** simulation converging up to the prescribed tolerance of 10^{-6}, as shown in Figure 5.10b for $De = 30$ and ε = 0.25.

The predictions of K are displayed in Figure 5.11 and in Table 5.3. Since there is no available data in the literature for a PTT fluid at $\beta = 0.59$, a direct comparison with results from both formulations is presented. Up to the critical Deborah number, the results from both approaches and values of ε agree very well. For higher De the predic-

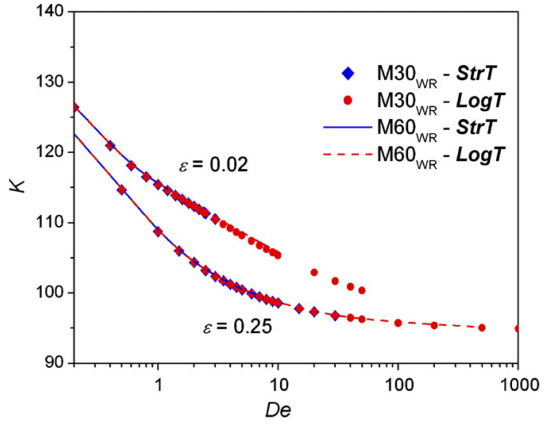

Figure 5.11: Drag force coefficient for the inertialess flow of a PTT fluid (β= 0.59) past a cylinder. Results obtained with the ***LogT*** and ***StrT*** formulations with meshes $M30_{WR}$ and $M60_{WR}$.

Table 5.3: Drag force coefficient for the PTT model with $\beta = 0.59$ (data in brackets indicate that full convergence was not achieved).

	$\varepsilon = 0.02$					$\varepsilon = 0.25$			
	StrT		***LogT***			***StrT***		***LogT***	
De	$M30_{WR}$	$M60_{WR}$	$M30_{WR}$	$M60_{WR}$	***De***	$M30_{WR}$	$M60_{WR}$	$M30_{WR}$	$M60_{WR}$
0	132.231	132.345			0	132.231	132.345		
0.1	130.095	130.256	130.094	130.256	0.1	128.370	128.567	128.369	128.566
0.2	126.428	126.613	126.427	126.613	0.5	114.640	114.805	114.635	114.805
0.4	120.961	121.160	120.959	121.158	1.0	108.789	108.929	108.784	108.928
0.6	118.112	118.312	118.112	118.310	1.5	106.022	106.151	106.024	106.150
0.8	116.498	116.699	116.500	116.698	2.0	104.359	104.481	104.362	104.481
1.0	115.405	115.611	115.409	115.612	2.5	103.227	103.344	103.232	103.345
1.2	114.566	114.781	114.572	114.785	3.0	102.396	102.510	102.402	102.511
1.4	113.878		113.883	114.107	4.0	101.243	101.351	101.247	101.352
1.6	113.290		113.289	113.529	5.0	100.465	100.570	100.469	100.572
1.8	112.772		112.769	113.023	6.0	99.898	100.001	99.901	100.002
2.0	112.306		112.302	112.571	7.0	99.462	99.564	99.464	99.565
2.5	111.322		111.320	111.614	8.0	99.114		99.115	99.216
3.0	110.523		110.505	110.832	9.0	98.828		98.829	98.929
4.0			109.222	109.605	10	98.588		98.588	98.688
5.0			108.243	108.662	20	97.324		97.319	97.420
6.0			107.425	107.905	50	(96.261)		96.244	96.351
8.0			106.273	106.746	100			95.724	95.831
10			105.386	105.888	500			95.057	95.152
20			102.902		1000			94.905	

tions of K exhibit a slight mesh dependency, of approximately 0.46% ($De = 10$) and 0.11% ($De = 100$) for $\varepsilon = 0.02$ and $\varepsilon = 0.25$, respectively.

Stress convergence and high Deborah number results

Previous works with constitutive models exhibiting shear-thinning or bounded extensional viscosity, such as FENE-CR, PTT or Giesekus models (Oliveira et al., 1998; Afonso et al., 2008; Oliveira and Miranda, 2005), have shown mesh refinement not to be so crucial as with UCM and Oldroyd-B models. This observation is also valid for the predictions of τ_{xx} presented here, as shown in Figure 5.12**.** For lower values of ε, the normal stress profiles along the cylinder sidewalls and in the rear region at near critical conditions ($De = 1$ and $De = 1.2$) are similar for all meshes and formulations, with a slightly mesh dependency of τ_{xx} profiles in the rear region at $De = 1.2$ (c.f. Figure 5.12a). The mesh convergence dependency weakens when the value of ε is increased

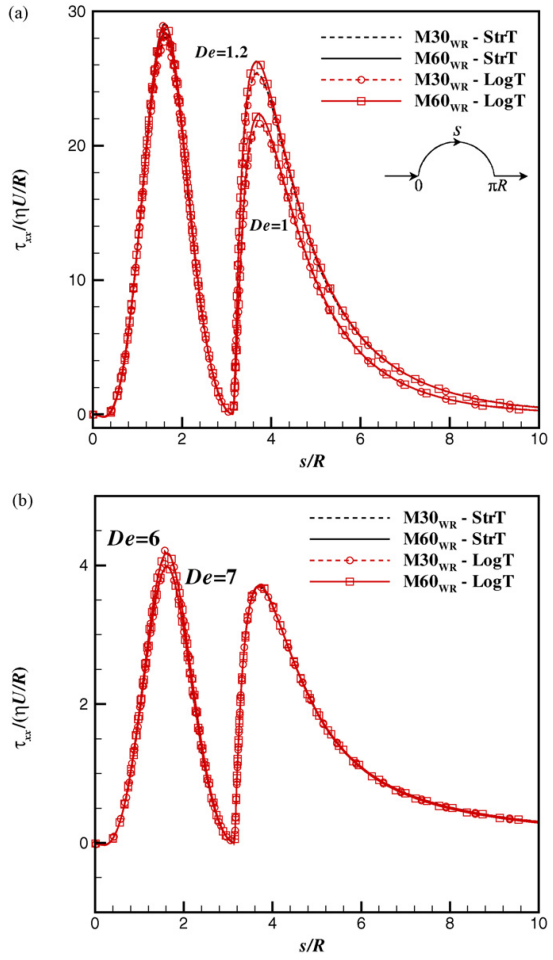

Figure 5.12: Effect of mesh refinement: stress profiles along cylinder wall and downstream centreline for PTT fluid with meshes $M30_{WR}$ and $M60_{WR}$ at (a) $De = 1$ and $De = 1.2$ with $\varepsilon = 0.02$; (b) $De = 6$ and $De = 7$ with $\varepsilon = 0.25$.

to 0.25, as illustrated in Figure 5.12b, with the predictions of τ_{xx} at $De = 6$ and $De = 7$ becoming indistinguishable for all meshes and formulations, even in the rear region.

As observed in previous Section, the simulations for the PTT model using the ***LogT*** formulation exhibit a significant breakthrough in the HWNP, with stable and convergent results obtained up to significantly higher Deborah numbers. In terms of convergence with mesh refinement, we were able to obtain mesh-independent results at low values of the extensional parameter (c.f. Figure 5.13a), these corresponding to situations where shear-thinning is weaker. The profiles of τ_{xx} exhibit a progressive increase in magnitude and width with De, both at the cylinder sidewalls and in the near wake region. For all plotted profiles, corresponding to $De = 1.4$, 2.2, 5 and 10, the results obtained in meshes $M30_{WR}$ and $M60_{WR}$ are similar.

The high De results of Figure 5.13b, obtained with $\varepsilon = 0.25$, show some new features not seen with the Oldroyd-B model. At the cylinder sidewalls for high De, all τ_{xx} profiles decrease with an increase of Deborah number due to shear-thinning. This behaviour was also observed by Afonso et al. (2008) for a PTT fluid in an uniform flow

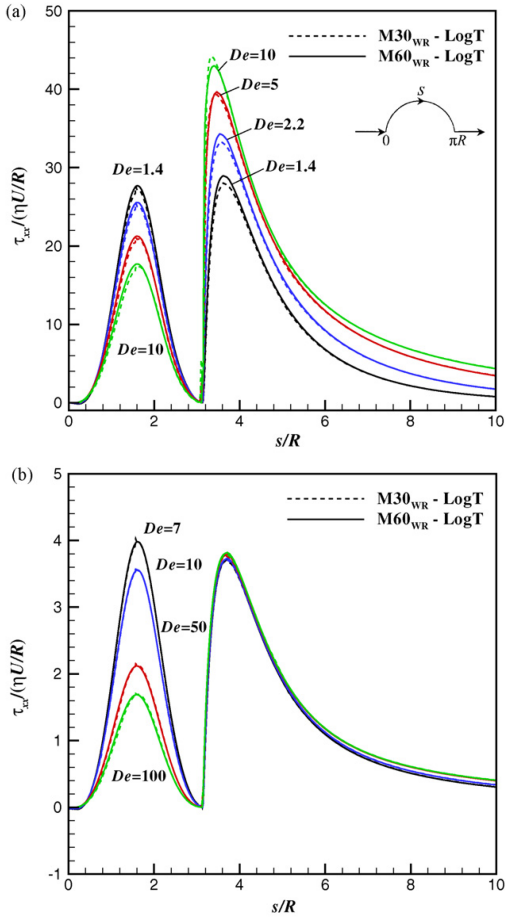

Figure 5.13: Stress profiles along cylinder wall and downstream centreline for PTT fluid with meshes $M30_{WR}$ and $M60_{WR}$ at (a) $De = 1.4$, 2.2, 5 and 10 with $\varepsilon = 0.02$; (b) $De = 7$, 10, 50 and 100 with $\varepsilon = 0.25$.

past a cylinder. In the near wake region the τ_{xx} profiles at high De, corresponding to $De = 7$, 10, 50 and 100, exhibit a small decrease in magnitude and a small increase in width downstream the cylinder. At this extensional parameter, the mesh refinement effect is negligible, in spite of the very high Deborah numbers.

5.1.5 *Conclusions*

In this work a finite-volume method was adapted to use the log-conformation formulation of Fattal and Kupferman (2004) and was applied to the simulation of 2D laminar viscoelastic fluid flow around a confined cylinder, using both the Oldroyd-B and the PTT models.

In spite of the usual stress convergence problems in the confined cylinder geometry using the Oldroyd-B model, calculations with the log-conformation approach enable results to be obtained at higher Deborah numbers, as compared to the standard stress formulation, with the critical De for divergence raising from $De \approx 1.0$ to either 1.9 or 2.5 depending on the mesh. At Deborah numbers higher than ~ 1 the results are unsteady without a well defined frequency, and sharp profiles are observed for τ_{xx} near the rear stagnation point breaking the smoothness of the stress profile and revealing the major importance

of refinement in the axial direction at the rear stagnation region of the cylinder.

With the PTT model the stabilizing benefits of the log-conformation approach are more clearly established since the range of the allowable Deborah numbers raises significantly without visible physical destabilization of the flow, which remains steady and symmetric about the x-axis. Quantitatively, the ***LogT*** formulation for the higher value of ε tested ($\varepsilon = 0.25$) showed no signs of convergence problems on any of the meshes employed, while for the ***StrT*** formulation the violation of positive definiteness of the conformation tensor occurred at $De \approx 7$ on the finest mesh $M60_{WR}$. On this same mesh, and for smaller value of ε tested ($\varepsilon = 0.02$), which increases the elongational viscosity and approaches the Oldroyd-B model, the critical De raised from 1.2 with the ***StrT*** formulation to 10 with the ***LogT*** formulation.

5.1.6 *Acknowledgements*

Funding from Fundação para a Ciência e a Tecnologia (FCT, Portugal) and FEDER under program POCI 2010 is gratefully acknowledged (projects POCI/EQU/59256/2004, POCI/EQU/56342/2004 and PTDC/EME-MFE/70186/2006). A. Afonso also thanks FCT for financial support through scholarship SFRH/BD28828/2006.

Abstract[2]
Uniform steady flow of viscoelastic fluids past a cylinder placed between two moving parallel plates is investigated numerically with a finite-volume method. This configuration is equivalent to the steady settling of a cylinder in a viscoelastic fluid, and here, a 50% blockage ratio is considered. Five constitutive models are employed (UCM, Oldroyd-B, FENE-CR, PTT and Giesekus) to assess the effect of rheological properties on the flow kinematics and wake patterns. Simulations were carried out under creeping flow conditions, using very fine meshes, especially in the wake of the cylinder where large normal stresses are observed at high Deborah numbers. Some of the results are compared with numerical data from the literature, mainly in terms of a drag coefficient, and significant discrepancies are found, especially for the constant-viscosity constitutive models. Accurate solutions could be obtained up to maximum Deborah numbers clearly in excess of those reported in the literature, especially with the PTT and FENE-CR models. The existence or not of a negative wake is identified for each set of model parameters.

Keywords: Falling Cylinder; Viscoelastic; UCM; Oldroyd-B; FENE-CR; PTT; Giesekus; Negative Wake; Numerical simulations.

5.2.1 *Introduction*

The flow of a viscoelastic fluid past a cylinder has been extensively studied both experimentally (Manero and Mena, 1981; Bush, 1993; McKinley et al., 1993; Broadbent and Mena, 1974) and numerically (Bush, 1993; Hu and Joseph, 1990; Huang and Feng, 1995; Liu et al., 1998; Oliveira et al., 1998; Fan et al., 1999; Sun et al., 1999; Alves et al., 2001b; Caola et al., 2001; Owens et al., 2002; Phan-Thien and Dou, 1999; Kim et al., 2004, 2005a; Oliveira and Miranda, 2005; Gerritsma, 2006). The large number of works in this geometry may be explained from two major motivations: (1) it is representative of the fundamental flow dynamics of viscoelastic fluids around solid bodies, and (2) it is intrinsically related to many processes in chemical engineering, namely flows through porous media (McKinley et al., 1993), enhanced oil recovery, composite and textile coating operations (Liu et al., 1998) and food processes. From a numerical point of view the flow past a cylinder is a *smooth flow* because it does not introduce any geometrical singularity, in contrast, for instance, with the salient corner in entry flows. Nonetheless the development of thin stress boundary layers on the cylinder sidewalls and especially the high normal stress developed along the rear wake centerline, remain a challenge and impose a limiting value on the Deborah number (De), at least as far as a symmetric steady flow is concerned.

Two configurations are possible for flow around a cylinder: either the cylinder is fixed relative to the confining channel walls and a planar Poiseuille flow emerges from an imposed pressure gradient, or it moves as in the case of a cylinder falling freely along the middle of a channel, which is equivalent to a uniform flow approaching a fixed cylinder

2 A. Afonso M. A. Alves, F. T. Pinho and P. J. Oliveira (2008). Uniform flow of viscoelastic fluids past a confined cylinder, *Rheologica Acta*, **47** 325-348.

with channel-walls moving with the fluid. The present paper deals with the second situation which gives rise to the interesting phenomenon of "negative wakes" (Sigli and Coutanceau, 1977; Hassager, 1979), to be discussed further down in this section but essentially consisting of a fluid in the wake of the cylinder moving faster and in the opposite direction to the wake-generating object. In a frame of reference fixed to the cylinder this correspond to velocities in the wake that are faster and in the same direction as the uniform approach flow, a situation that arises only with viscoelastic fluids. The nature of negative wakes is not yet well understood and one of the motivations for this work was numerical quantification of conditions for its formation.

The case of confined flow around a fixed cylinder has been investigated more often than the settling of a cylinder in bounded or unbounded domains, and Owens et al. (2002) documented and summarized the main results in their book, focusing primarily on the Oldroyd-B model. Phan-Thien and Dou (1999) carried out simulations of confined cylinder flows with the upper-convected Maxwell (UCM), Oldroyd-B and PTT models where the flow was fully developed well upstream of the cylinder. They found negative wakes behind the cylinder for this flow at high Deborah numbers and only for the PTT model. Alves et al. (2001b) implemented classical high-resolution interpolation schemes for convection (the MINMOD and SMART schemes) in the general collocated finite-volume method (FVM) procedure for viscoelastic flows developed by Oliveira et al. (1998). This implementation enhanced numerical accuracy and was tested with the benchmark problem of the flow past a confined cylinder with blockage ratio of 0.5, using the UCM and the Oldroyd-B models. Highly refined non-orthogonal meshes were used which allowed a good comparison of the predicted drag force on the cylinder (the benchmark result) with values from other simulations in the literature (Liu et al., 1998; Fan et al., 1999; Sun et al., 1999; Caola et al., 2001; Owens et al., 2002; Phan-Thien and Dou, 1999; Kim et al., 2004). In particular, predictions of the drag coefficient up to $De \approx 0.7$ were consistent with the finite element method (FEM) simulations of Fan et al. (1999). More recently, Gerritsma (2006) presented results obtained with a spectral element method and again excellent agreement with the numerical results obtained by Fan et al. (1999) and Alves et al. (2001b) was found.

The settling of a cylinder in a confined viscoelastic fluid is still a *work in progress* in rheological engineering, and several contributions have come forward in the recent past. Huang and Feng (1995) investigated the steady settling of a cylinder through quiescent Newtonian and Oldroyd-B fluids in a vertical channel, employing FEM with the elastic-viscous stress split scheme (EVSS). For their higher blockage case (50%), Huang and Feng (1995) predicted a negative wake at high Deborah numbers, but this unusual phenomenon was not replicated by Oliveira et al. (1998) in their numerical work based on the FVM. The predictions of Oliveira et al. (1998) for the unbounded flow case and the confined case with blockage area of 33% were in agreement with those of Huang and Feng (1995), but discrepancies were found in the wake velocities for the higher blockage case (50%). These discrepancies were attributed to the response of viscoelastic fluids to intense local shear and elongational flows at the proximity of the channel wall. Dou and Phan-Thien (2004) carried out simulations of the uniform flow of a viscoelastic fluid past a cylinder in a moving channel using the UCM, PTT, Oldroyd-B and the

FENE-CR models. They used a control volume finite element method (CVFEM) with a DEVSS-*w* formulation under a distributed computing environment through a Parallel Virtual Machine (PVM) library. Again, a negative wake was not observed with the UCM and Oldroyd-B fluids for various retardation ratios ($\beta = 0.125, 0.4, 0.6, 0.8$), thus corroborating the predictions of Oliveira et al. (1998) in contrast to the results of Huang and Feng (1995). However, for the PTT and FENE-CR models a negative wake appeared at a critical De. Regarding drag coefficient (C_D) predictions, the early calculations of Dou and Phan-Thien (2003) found a monotonic decrease of C_D with De for the FENE-CR fluid with lower extensibility parameter ($L^2 = 10$). For a higher extensibility parameter ($L^2 = 100$), however, they predicted a non-monotonic behaviour, with an initial decrease followed by an increase for approximately $De > 0.6$, related to the strong increase of the extensional effects. The numerical investigation of Kim et al. (2005a) focused on the comparison of negative wake generation in both uniform and Poiseuille flows past a cylinder, and on the influence of the FENE-CR model parameters upon this flow feature: viscosity ratio (β) and polymer extensibility (L^2). By employing a discrete elastic viscous split stress (DEVSS-G)-streamline upwinding/Petrov–Galerkin (G/SUPG) formulation with an efficient iterative solution method developed for the mixed FEM by Kim et al. (2004), they found that the drag coefficient monotonically decreased for both $L^2 = 10$ and $L^2 = 100$, in contrast with the results obtained by Dou and Phan-Thien (2003). They also found that, for all flow conditions and model parameters, the negative wake generation is more pronounced when the approach flow is uniform than when it is a Poiseuille flow.

So, for some viscoelastic fluids, the steady flow behind a cylinder is characterized by the appearance of a *negative wake* which strongly depends on fluid rheology. Negative wakes are overshoots of the streamwise velocity seen by the moving body along the centreline and have been found in the wake of cylinders, spheres and rising bubbles (Sigli and Coutanceau, 1977; Hassager, 1979). One of the most extensive early investigations of this phenomenon was the visualization of the sedimentation of a sphere in shear-thinning polyacrylamide (PAA) solutions by Arigo and McKinley (1998), who also made an extensive review of the literature. Early, however, McKinley et al. (1993) had been unable to detect the appearance of negative wakes downstream of a cylinder for Boger fluids and up to the present time there is no experimental evidence of negative wake formation with constant viscosity elastic fluids. Negative wakes in the settling sphere problem have also been extensively studied using numerical methods (Jin et al., 1991; Zheng et al., 1991; Bush, 1994). These works lead to the general conclusion that both shear thinning and elastic effects are necessary for the formation of a negative wake, but the numerical simulations by Satrape and Crochet (1994) and Harlen (2002) showed that a negative wake can also be present for constant viscosity elastic fluids, such as those represented by the FENE-CR model. The predicted velocity profiles along the centreline downstream of the sphere wake were intimately linked to the extensional properties of the constitutive model, especially the extensibility parameter L^2. For small values of L^2 a negative wake was predicted even at low De values. On the other hand, increasing the strain-hardening character of the model (by increasing L^2) the negative wake was reduced and eventually eliminated.

The physical conditions under which the negative wake arises and the mechanisms involved in its formation are still not fully understood in spite of several studies that have focused on these issues. In the sphere/cylinder geometries, Bush (1994) attributed the negative wake behaviour to the relative proportion between elongational stresses in the downstream region and fluid elasticity, and suggested that the upstream shift in streamlines and the formation of negative wake are a result of having a Deborah number much greater than the Trouton ratio. For the sphere flow case, Harlen (2002) proposed that the origin of negative wake was related to the circumferential gradient of shear stress along the centreline, and in particular with the competition of shear and normal stress distributions. Based on the suggestions of Bush (1994) and invoking also arguments later used by Harlen (2002), Arigo and McKinley (1998) proposed a criterion for the formation of negative wake based on the ratio of axial tensile to shear stresses. Dou and Phan-Thien (2004) also studied this phenomenon numerically and proposed a different criterion, this time based on the ratio between the gradient and the magnitude of elongational viscosity, to predict the critical De marking the onset of negative wake for several constitutive models (PTT, FENE-CR, FENE-P and Giesekus models).

Identifying the conditions that lead to the onset of a negative wake is one of the motivations for the present work. In terms of outcome, this study leads to two important contributions: (1) clarify the significant discrepancies in the predicted drag coefficient of a FENE-CR fluid obtained by Dou and Phan-Thien (2003) and Kim et al. (2005a), and (2) confirmation of some sets of results available in the literature which were obtained by different numerical methods. It should thus be clear that the present work is essentially numerical and aims at clarifying the conditions under which negative wakes are formed for the most common differential constitutive models, and giving reliable data for the drag coefficient on the falling cylinder. A detailed matching of existing experimental measurements requires close fitting of the rheology of the fluids, most certainly through the incorporation of a multimode model, and as such it should be left for a future work.

The paper is organized as follows: in Sections 5.2.2 and 5.2.3 we briefly describe the general flow problem, present the governing equations and outline the numerical method used to simulate the settling of the cylinder in a confined viscoelastic fluid. In Section 5.2.4, results are presented for all constitutive models, encompassing the predicted drag coefficient, detailed profiles of velocity and stress components in the vicinity of the cylinder and stability criteria. A summary of the main findings closes the paper in Section 5.2.5.

5.2.2 *Governing equations and numerical method*

The flow is assumed to be steady, laminar and the fluid is incompressible. The governing equations are those expressing conservation of mass:

$$\nabla \cdot \mathbf{u} = 0 \tag{5.14}$$

and momentum balance:

$$\rho \frac{\partial \mathbf{u}}{\partial t} + \rho \nabla \cdot \mathbf{u}\mathbf{u} = -\nabla p + \nabla \cdot \boldsymbol{\tau} + \eta_s \nabla^2 \mathbf{u} \tag{5.15}$$

where $\mathbf{u}$ is the velocity vector, p the pressure, t the time, ρ the fluid density, η_s the Newtonian solvent viscosity and $\boldsymbol{\tau}$ the polymeric extra stress contribution. Five constitutive equations are employed: the upper-convected Maxwell model (UCM), the Oldroyd-B model (Bird et al., 1987a), the linear form of the simplified PTT model (Phan-Thien and Tanner, 1977; Phan-Thien, 1978), the modified FENE-CR model (Chilcott and Rallison, 1988) and the Giesekus model (Giesekus, 1982). For an isothermal flow these five rheological equations of state can be written in a compact form as:

$$P(\mathrm{tr}\,\boldsymbol{\tau})\boldsymbol{\tau} + \frac{\lambda}{F}\left[\frac{\partial \boldsymbol{\tau}}{\partial t} + \mathbf{u}\cdot\nabla\boldsymbol{\tau} - \nabla\mathbf{u}\cdot\boldsymbol{\tau} - \nabla\mathbf{u}^{T}\cdot\boldsymbol{\tau}\right] = 2\eta_p\mathbf{D} + \mathbf{G} \quad (5.16)$$

$$F = \frac{L^2 + \frac{\lambda}{\eta_p}\mathrm{tr}(\boldsymbol{\tau})}{L^2 - 3} \quad (5.17)$$

$$P(\mathrm{tr}\,\boldsymbol{\tau}) = 1 + \frac{\varepsilon\lambda}{\eta_P}\mathrm{tr}(\boldsymbol{\tau}) \quad (5.18)$$

$$\mathbf{G} = \alpha\boldsymbol{\tau}^2 \quad (5.19)$$

where λ is a relaxation time, η_p is the polymer viscosity coefficient, $\mathbf{D}$ the rate of deformation tensor, F is the stretch function that depends on the extensibility parameter L^2, representing the ratio of the maximum to equilibrium average dumbbell extensions. The stress coefficient function, $P(\mathrm{tr}\,\tau)$, depends on the trace of $\boldsymbol{\tau}$ and $\mathbf{G}$ is the non-linear term of the Giesekus model, with α representing a dimensionless "mobility factor". The stress coefficient function of the PTT model, $P(\mathrm{tr}\,\tau)$, introduces the dimensionless parameter ε which is closely related to the steady-state elongational viscosity in extensional flows ($\eta_E \propto 1/\varepsilon$ for low ε).

The viscosity ratio is defined here as the ratio of the solvent to total viscosities (note that in some works β is instead defined as η_p/η_0 (e.g. Dou and Phan-Thien, 2003 and Kim et al., 2005a):

$$\beta = \frac{\eta_s}{\eta_s + \eta_P} = \frac{\eta_s}{\eta_0} \quad (5.20)$$

A specific constitutive model can be chosen by an appropriate selection of parameters α, L^2, ε and β, and the range of all parameters used in this work is listed in Table 5.4.

Table 5.4: Range of the model parameters used in this work.

Models	ε	β	α	L^2
UCM	0	0	0	∞
Oldroyd-B	0	0.125; 0.4 and 0.8	0	∞
PTT	0.02 and 0.25	0	0	∞
FENE-CR	0	0.1	0	10 and 100
Giesekus	0	0.59	0.02	∞

Elastic effects are quantified by a non-dimensional Deborah number, defined here as

$$De = \frac{\lambda U}{R} \tag{5.21}$$

with U representing the bulk velocity in the channel and R the cylinder radius. In the numerical simulations the inlet bulk velocity and the cylinder radius were kept constant, therefore the Deborah number was varied by changing the value of the relaxation time. Of course in an experiment with a given fluid and geometry the elasticity number $E = \lambda\eta_0/\rho R^2$ is kept constant and the Deborah number is varied by changing the flow rate, that is U, and consequently the Reynolds number. However, since we force the Reynolds number to be zero and are concerned with steady flows, the only parameter left is De and it is theoretically irrelevant whether it is λ or U that is varied.

All the calculations were carried out with a finite-volume method (for details see Oliveira et al., 1998 and Alves et al., 2000, 2001b, 2003a) for the limiting case of $Re = 0$, which was imposed numerically by neglecting the convective terms of the momentum equation. Accurate representation of the convective terms in the constitutive equation is of extreme importance in viscoelastic simulations and the CUBISTA high-resolution scheme developed by Alves et al. (2003a) was applied for this purpose. The CUBISTA scheme has the advantage over classical high-resolution schemes (e.g. the SMART scheme by Gaskell and Lau (1988) of promoting better iterative convergence when employed in conjunction with implicit methods. It is a simpler alternative to Lagrangian approaches whose implementation in conjunction with finite element methods is addressed in the review of Baaijens (1998). Additional details of the present method regarding the implementation of the Giesekus model so that numerical stability is improved can be found in Oliveira (2001b).

5.2.3 *Problem description and computational meshes*

A Galilean transformation shows that the settling of a cylinder in a medium confined by two parallel plates is equivalent to the steady uniform flow of a fluid around and past a cylinder in a channel, whose walls move at the same velocity of the approach flow, as shown in Figure 5.14. The ratio of channel half-height h to cylinder radius R is set equal to 2 which corresponds to a 50% blockage case. The computational domain is $80R$ long, with $19R$ upstream and $59R$ downstream of the forward and rear stagnation points of the cylinder, respectively. The downstream length is sufficient for the flow to become fully-developed and to avoid any effect of the outflow boundary condition upon the flow in the vicinity of the cylinder. Vanishing axial gradients are applied to all variables, including the pressure gradient, at the outlet plane. No-slip conditions are imposed at both the cylinder surface ($r = R$: $u = 0, v = 0$) and the channel wall ($y = \pm h$: $u = U$).

The main characteristics of the meshes used in this work are given in Table 5.5, including the total number cells (NC), the number of control volumes around the surface of the cylinder (NS), the number of cells placed radially from the cylinder to the channel wall (NR), and the minimum cell spacing along the radial (Δr) and the azimuthal ($\Delta s = r\Delta\theta$) directions both normalized with the cylinder radius. The

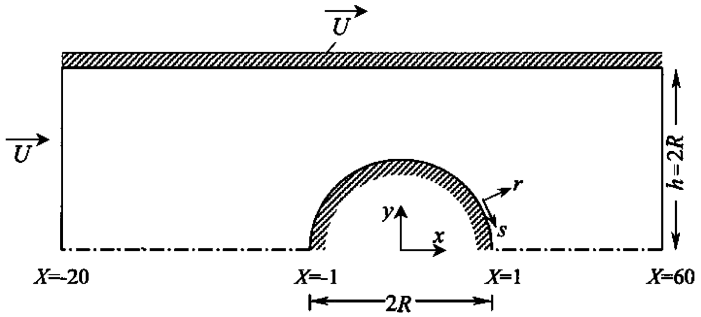

Figure 5.14: Schematic representation of the flow geometry.

Table 5.5: Main characteristics of the computational meshes.

	NC	DOF	NR	NS	$(\Delta r/R)_{min}$	$(\Delta s/R)_{min}$
M60	17400	104400	60	200	0.00481	0.0157
$M60_{WR}$	22560	135360	60	260	0.004	0.0006
$M120_{WR}$	90240	541440	120	520	0.002	0.0003

first numerical simulations were carried out with mesh M60 of our previous work (for complete details see Alves et al., 2001b).

Mesh $M60_{WR}$ has the same number of cells in the radial direction as mesh M60, but is more refined along the wake (hence the subscript WR for *wake-refined*). The total number of cells is 22560. The high degree of refinement in the rear wake region of the cylinder of mesh $M60_{WR}$ leads to a minimum normalized cell spacing along the azimuthal direction of 0.0006 compared with 0.0157 for mesh M60. Mesh $M120_{WR}$ was used to check the convergence with mesh refinement at Deborah numbers near the critical value. This mesh has twice the number of cells along both directions as mesh $M60_{WR}$ with $NC = 90240$ cells. The number of cells on the cylinder surface of mesh $M120_{WR}$ is 520 and the minimum normalized cell spacing along the radial and azimuthal directions is 0.002 and 0.0003, respectively.

5.2.4 *Results and discussion*

Results of computations are presented as a scalar integral quantity representative of the flow and as detailed profiles of velocity and stress components in the vicinity of the cylinder. The integral quantity selected was the dimensionless drag coefficient, C_D, calculated as:

$$C_D = \frac{1}{\eta_0 U} \int_S (\boldsymbol{\tau}_{tot} - p\mathbf{I}) \cdot \mathbf{n} \cdot \mathbf{i} \; dS \tag{5.22}$$

where $\mathbf{I}$ is the unit tensor, $\mathbf{n}$ is the unit vector normal to the cylinder surface and $\mathbf{i}$ is the unitary vector in the x-direction (streamwise direction). Stress profiles are shown in the thin stress boundary-layer around the cylinder and on the thin high normal stress region downstream the rear wake, in order to ascertain the quality of the predictions.

For the UCM and Oldroyd-B models we used two different criteria to assess numerical stability. One method consisted simply in examining the positive definiteness of the conformation tensor, $\mathbf{A}$, that is $\det \mathbf{A} > 0$; in addition, Hulsen (1988) demonstrated that for the Oldroyd-B model

one should have det $\mathbf{A} \geqslant 1$. The conformation and polymer stress tensors are related by

$$\boldsymbol{\tau} = \frac{\eta_P}{\lambda}(\mathbf{A} - \mathbf{I}). \tag{5.23}$$

The other criterion for judging the performance of the numerical discretization is to determine whether the elastic tensor, $\mathbf{T}$,

$$\mathbf{T} = \boldsymbol{\tau} + \frac{\eta_P}{\lambda}\mathbf{I} = \frac{\eta_P}{\lambda}\mathbf{A}, \tag{5.24}$$

is positive definite (Dupret and Marchal, 1986). Alternatively the system condition number, S, can also be used to indicate a temporal loss of evolution (Kim et al., 2005b). For a 2D flow, S is given by (Kim et al., 2005a),

$$S = 2\frac{\lambda_1\lambda_2}{\lambda_1^2 + \lambda_2^2} = 2\frac{\det T}{\mathrm{tr}(T^2)}, \tag{5.25}$$

where λ_1 and λ_2 are the non-trivial eigenvalues of the elastic tensor, $\mathbf{T}$. In order to guarantee no loss of evolution S needs to be positive.

In this work, x and y Cartesian coordinates are normalized with the cylinder radius, R, the velocity components (u and v) with the characteristic velocity U, and the extra stress tensor $\boldsymbol{\tau}$ and the pressure p by $\eta_0 U/R$.

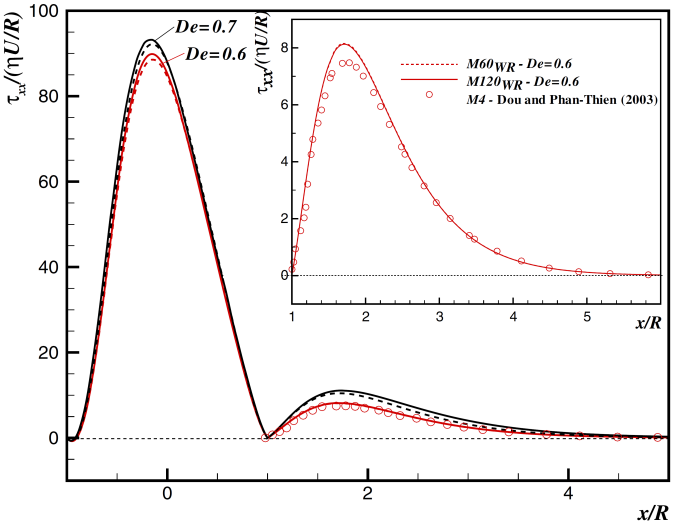

Figure 5.15: Effect of mesh refinement: stress profiles along cylinder wall and downstream centreplane for UCM fluid. Mesh $M60_{WR}$ (dashes); $M120_{WR}$ (lines). Symbols (empty circles) from Dou and Phan-Thien (2003) for $De = 0.6$.

5.2.4.1 *Mesh refinement studies*

It is recognized that this flow problem is difficult to solve accurately, because in order to resolve the very thin stress boundary layer at the cylinder wall and the normal stresses downstream of the rear stagnation point, very refined meshes are required in these regions. The effect of mesh refinement for the UCM model is shown in Figure 5.15, where the normalised streamwise normal stresses along the cylinder

sidewalls and wake centreline are plotted for $De = 0.6$ and 0.7. In the region of maximum stresses on the cylinder sidewall and the rear wake there is a small mesh dependency, especially at $De = 0.7$. For comparison, Figure 5.15 also presents the τ_{xx} profile along the rear wake centreline predicted by Dou and Phan-Thien (2003) with their mesh M4 at $De = 0.6$. A small inaccuracy might result from extracting their data from the original figures, however their maximum value of τ_{xx} in the wake still deviates approximately by 9.2% from our predictions (cf. zoom included in Figure 5.15), and such differences are probably related to the insufficient mesh refinement of Dou and Phan-Thien (2003). In fact, their mesh M4 has only a typical hp mesh size of $O(10^{-2})$, compared with our mesh size $O(10^{-3}; 10^{-4})$ in mesh $M120_{WR}$.

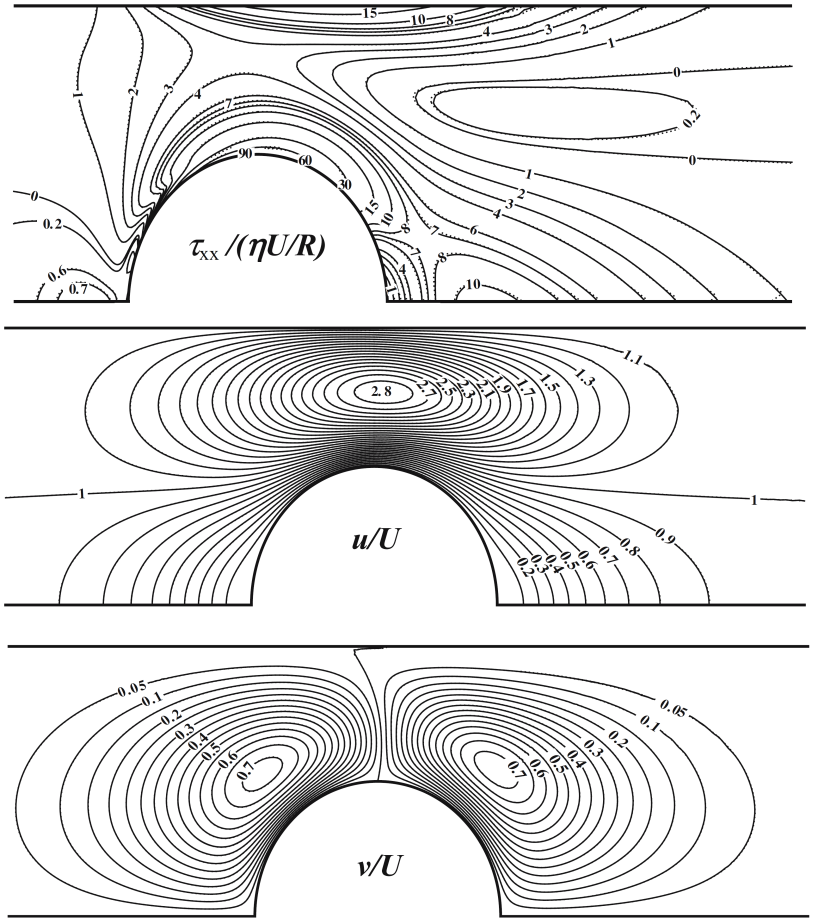

Figure 5.16: τ_{xx}, u and v contour plots for UCM fluid at $De = 0.7$. Mesh $M60_{WR}$ (lines) and $M120_{WR}$ (dashes).

Slight differences present in the results obtained with meshes $M60_{WR}$ and $M120_{WR}$ may be observed in the stress contour plot maps in Figure 5.16, whereas the velocity contours are visually indistinguishable. In contrast to the Newtonian case, the inertialess UCM flow is clearly asymmetric about the $x = 0$ plane, particularly the stress fields, with τ_{xx} exhibiting maxima along the cylinder sidewall and at the centreline downstream of the cylinder. For the Oldroyd-B model, Figure 5.17 shows normal stress profiles along the cylinder sidewalls and centreline under nearly critical conditions. These profiles are for $\beta = 0.125$ ($De =$

1.0), $\beta = 0.4$ ($De = 1.1$), and $\beta = 0.2$ ($De = 1.4$). Small differences between the solutions on the two meshes are visible near the points of maximum stress, but it should be emphasized that these flow conditions are close to the critical De, when the differences are more discernible. In fact, for lower De discrepancies in the normal stress profiles, and also in the corresponding peak values, are significantly smaller and even negligible. It has been checked that iteratively converged numerical solutions can still be obtained when De is increased by 0.1 for the above three cases but the discrepancies in the predicted peak normal stresses in the wake region with the $M60_{WR}$ and $M120_{WR}$ meshes tended to accentuate. Figure 5.17 also shows a comparison between our predictions of τ_{xx} along the rear wake centreline with those of Dou and Phan-Thien (2003) on their mesh M4; a significant difference of the order of 50% is observed due to the high level of azimuthal refinement of $M120_{WR}$ mesh.

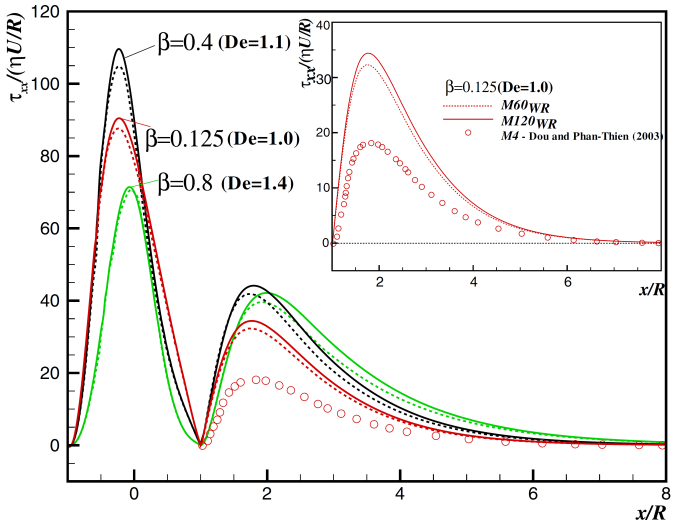

Figure 5.17: Effect of mesh refinement: stress profiles along cylinder wall and downstream centreplane for Oldroyd-B fluid. Mesh $M60_{WR}$ (dashed line); $M120_{WR}$ (full line). Symbols (empty circles) from Dou and Phan-Thien (2003) for $De = 1.0$.

Previous works have shown mesh refinement not to be so crucial with constitutive models exhibiting shear-thinning or bounded extensional viscosity (Oliveira et al., 1998; Oliveira, 2001b; Oliveira and Miranda, 2005; Alves et al., 2000, 2001b, 2003a), such as FENE-CR, PTT or Giesekus models, and therefore we decided not to use the finer mesh $M120_{WR}$ and restrict the simulations with these models to meshes M60 and $M60_{WR}$. This decision is corroborated by the comparisons shown in Figure 5.18 for the FENE-CR model, where τ_{xx} predictions are presented near critical Deborah numbers of 5.0 and 4.0 for $L^2 = 10$ and $L^2 = 100$, respectively, using meshes M60 and $M60_{WR}$. Both meshes yield normalized normal stress profiles in good agreement, and also of the corresponding peak stresses, an indication of the good accuracy achieved by M60 with the FENE-CR model. This mesh independence is also confirmed in the comparison with Kim et al. (2005a) results presented in the inset of Figure 5.18. Their predictions at $De = 2.5$ with $L^2 = 10$ were obtained with their mesh UM3 having a minimum mesh size of $O(10^{-4})$ whereas mesh M60 is only $O(10^{-2})$ and yet has similar

level of accuracy. Those authors also employed a "high resolution" FEM and the matching against our data is excellent.

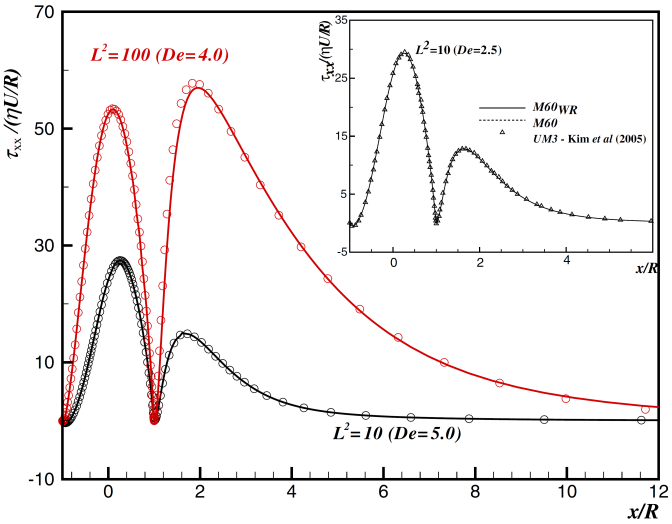

Figure 5.18: Effect of mesh refinement: normal stress profiles along cylinder wall and downstream centreplane for FENE-CR fluid. Mesh M60$_{WR}$ (empty circles) and M60 (lines). Symbols (empty triangles) in the inset are from Kim et al. (2005a).

After demonstrating the accuracy of our predictions, in the following sections we present and discuss separately the results for each constitutive model.

5.2.4.2 *UCM and Oldroyd-B models*

We start with the two *simpler* quasi-linear differential constitutive models, the upper-convected Maxwell (UCM) and Oldroyd-B models. Evidence from the literature on viscoelastic flow past a confined cylinder shows that an increase in viscoelasticity tends to reduce the drag force. As shown in Figure 5.19 and Table 5.6, this tendency is replicated by our predictions for the case of sedimentation of a cylinder in a viscoelastic fluid medium obeying the UCM and Oldroyd-B models. Figure 5.19 also compares the C_D values obtained using meshes M60$_{WR}$ and M120$_{WR}$ with those of Dou and Phan-Thien (2003) obtained with a CV/FEM method. All sets of data show a decrease in C_D with Deborah number but, in contrast to the present data, the drag coefficient predicted by Dou and Phan-Thien (2003) always show an increase at high De numbers whereas our data only exhibits this increase for large values of β. Another important difference is that for all retardation ratios, the results are well below the predictions of Dou and Phan-Thien (2003), with agreement only in the range $De \leqslant 0.3$. Since higher values of drag coefficient are usually associated with coarse meshes (Alves et al., 2001b) or insufficient accuracy, the discrepancies in Figure 5.19 are an indication of loss of accuracy in the results of Dou and Phan-Thien (2003). With the UCM model, stable and iteratively converged simulations could be obtained up to $De = 0.85$ with mesh M60$_{WR}$ and $De = 0.7$ with mesh M120$_{WR}$. For $De = 0.85$ and mesh M60$_{WR}$ a periodic solution leading to oscillating drag force values was observed.

Figure 5.20 presents the two stability factors discussed above, the system condition number and the determinant of the conformation

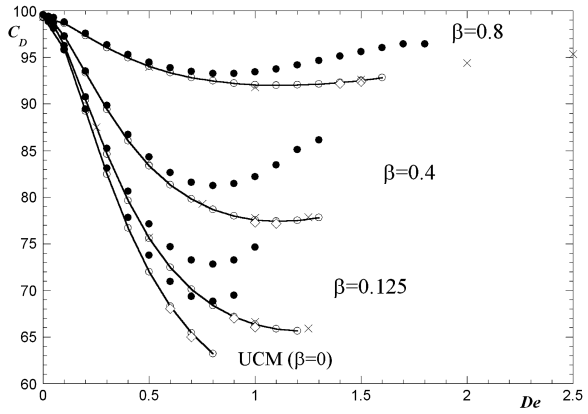

Figure 5.19: Drag force coefficient for UCM and Oldroyd-B fluids. Mesh M60 (×); Mesh $M60_{WR}$ (-o-); Mesh $M120_{WR}$ (empty diamonds) and Dou and Phan-Thien (2003) data (filled circles).

Table 5.6: Drag force coefficient for the UCM and Oldroyd-B models.

	Oldroyd-B β = 0.8			Oldroyd-B β = 0.4			Oldroyd-B β = 0.125			UCM	
De	M60	M60WR	M120WR	M60	M60WR	M120WR	M60	M60WR	M120WR	M60WR	M120WR
0.0	99.393	99.366		99.393	99.366		99.393	99.366		99.366	
0.1		98.653			97.290			96.286		95.896	
0.2		97.354			93.354			90.477		89.225	
0.3		96.059			89.407			84.625		82.476	
0.4		94.955			86.057			79.622		76.676	
0.5	93.988	94.067		83.960	83.384		75.702	75.607		71.981	
0.6		93.378			81.327			72.495		68.286	68.047
0.7		92.858			79.797			70.142		65.420	64.993
0.8		92.483			78.707			68.410		63.242	
0.9		92.230			77.989			67.178	66.992		
1.0	91.807	92.081		77.767	77.573	77.293	66.633	66.354	66.045		
1.1		92.024			77.429	77.187	65.925	65.860			
1.2		92.049			77.508			65.654			
1.3		92.149			77.885						
1.4		92.317	92.207								
1.5	92.633	92.541									
1.6		92.842									
2.0	94.425										
2.5	95.953										

tensor, along the cylinder surface and the downstream centreline for a range of Deborah numbers. For all simulations the minimum values of S and det**A** are always positive, showing no loss of evolution when the flow is steady. It can also be observed that the determinant of the conformation tensor increases with Deborah number both on the cylinder sidewall and in the rear wake zone, indicating strong normal stress effects (in shear and extension, respectively), while S behaves inversely (the two quantities are seen to have symmetric shapes relative to S= det**A**=1 line when plotted in a log-scale). In the rear stagnation point, both system condition numbers S and det**A** tend to unity. The results in Figure 5.20 suggest S as being a better indication of loss of evolution.

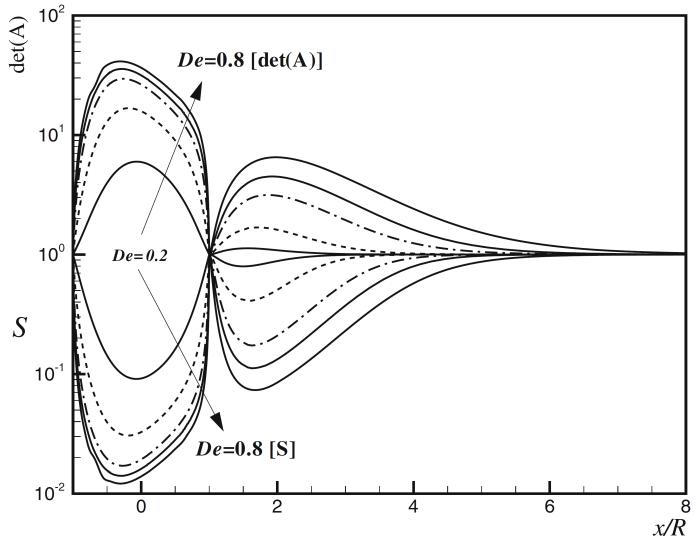

Figure 5.20: Stability factors [S factor and det(**A**)] on the centreline for UCM fluid and increasing Deborah numbers ($De = 0.2$, 0.4, 0.6, 0.7 and 0.8).

Figure 5.21 presents normal stress and velocity profiles along the cylinder surface and the centreline downstream of the cylinder as function of Deborah number for the UCM model. The τ_{xx} profiles in Figure 5.21a show increasing stresses and peak values with Deborah number, with the maximum at the cylinder sidewall larger than the peak at the wake. Near the critical Deborah number ($De = 0.8$) the wake maximum normal stress is only 20% of the larger normal stress at the cylinder wall, in contrast to the related problem with stationary channel walls where the wake normal stress maxima attains similar values to the cylinder peak.

According to Oliveira et al. (1998), Alves et al. (2001b) and Dou and Phan-Thien (2003, 2004), there is no "negative wake" with UCM fluids for both Poiseuille and uniform approach flows. This is confirmed here for uniform flow in Figure 5.21b, where no velocity overshoots in the wake are observed. A small global upstream shift in the velocity profiles with respect to the Newtonian case is seen up to $De \approx 0.5$ (the inset shows the difference, $\Delta u/U = (u=u_{Newt})/U$). Then, for $De > 0.5$ the behaviour observed becomes more complex with the velocity profiles exhibiting both an upstream shift near the rear stagnation point followed by a downstream shift further downstream of the cylinder. Similar observations of a downstream shift in the elastic wake behind a cylinder in a channel were reported by McKinley et al. (1993). This phenomenon has been found to increase monotonically with De in all experimental studies to date.

For the Oldroyd-B model the results are globally similar to those obtained with the UCM model, with slight differences discussed below. Using three different viscosity ratio values ($\beta = 0.125$, $\beta = 0.4$ and β=0.8), stable and converged simulations on mesh $M60_{WR}$ could be obtained up to $De = 1.2$, $De = 1.3$ and $De = 1.6$, respectively. In terms of the normalized velocity components and the normal stress contour maps for these cases the behaviour follows closely Figure 5.16 for the UCM, and the plots are therefore not shown here for conciseness. An important difference between Oldroyd-B and UCM fluids can be

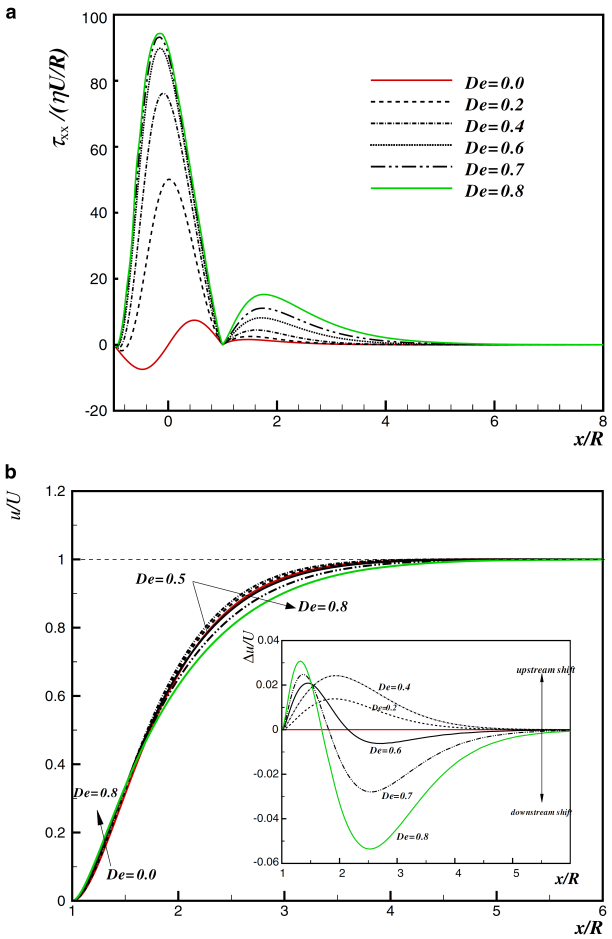

Figure 5.21: (a) τ_{xx} and (b) u centreline profiles for UCM fluid. The inset shows the wake velocity difference, $\Delta u/U = (u - u_{Newt})/U$.

observed by comparing the normal stress profiles for $\beta = 0.125$ in Figure 5.22a with those for $\beta = 0$ in Figure 5.21b. At low elasticity and as for the UCM model, the normal stress on the cylinder sidewall increases significantly with Deborah number up to $De = 0.9$, however above $De = 1.0$ there is a change of trend for the Oldroyd-B fluid and τ_{xx} starts decreasing with De. The behaviour in the rear wake zone is also noteworthy: for the Oldroyd-B model the normal stress increases strongly with De and near the critical value the maximum value of τ_{xx} in the rear wake is higher than in the cylinder sidewall, whereas for the UCM model the rear peak values are well below the cylinder peak values. This feature occurs for all models except for the UCM fluid, probably because for this model we cannot obtain steady results for De above unity.

The velocity profiles presented in Figure 5.22b illustrate the absence of negative wake for the Oldroyd-B model, and show the same trends seen previously with the UCM model, i.e., an upstream shift at all De near the rear stagnation point followed by a downstream shift for $De \geqslant 0.5$. The axial position where the transition from upstream to downstream shift occurs decreases with Deborah number from $x/R \approx 2.2$ at $De = 0.6$ to $x/R \approx 1.6$ at $De = 1.2$.

Decreasing polymer concentration of the Oldroyd-B model (increasing the viscosity ratio factor to $\beta = 0.4$ and $\beta = 0.8$), the global be-

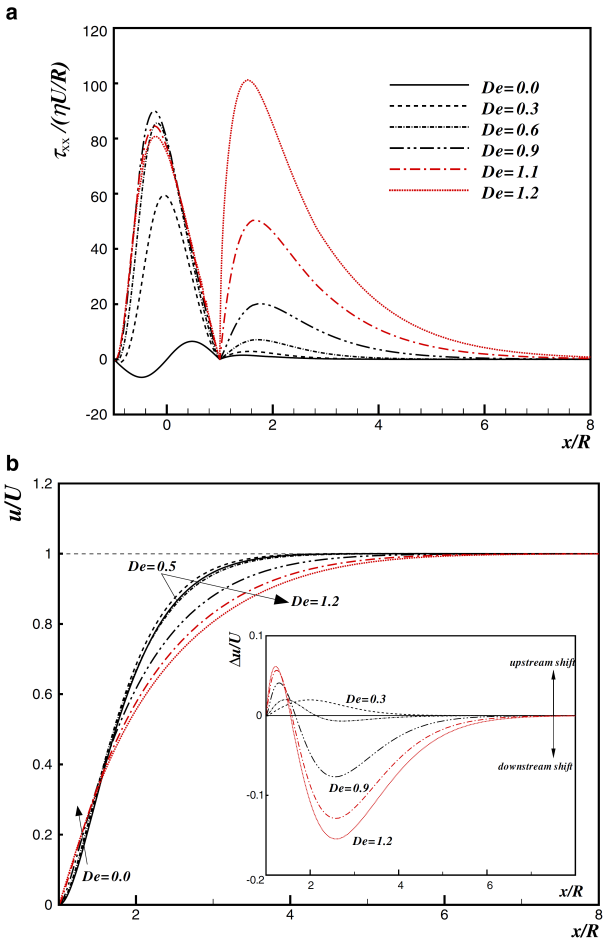

Figure 5.22: (a) τ_{xx} and (b) u centreline profiles for Oldroyd-B fluid with β=0.125. The inset shows the wake velocity difference, $\Delta u/U = (u - u_{Newt})/U$.

haviour for all variables remains qualitatively similar to that of the $\beta = 0.125$ case discussed above. Figure 5.23a shows the normalized normal stress profiles at high Deborah numbers ($De = 1.2$, 1.3 for $\beta = 0.4$ and $De = 1.5$, 1.7 for $\beta = 0.8$). The peak values on the cylinder sidewalls saturate and then decrease, whereas in the wake the second peak exceeds the first at high De. Since the critical De has increased with the increase of β, the peaks values of τ_{xx} in the wake, due to viscoelastic extensional effects, can rise to higher values than before (smaller β). Regarding the profile at $De = 1.7$ and $\beta = 0.8$ in Figure 5.23a, although some oscillations are visible on the cylinder wall zone and in the total drag force, the corresponding simulation did not show signs of iterative divergence, presenting positive values of min(S) and min(det **A**). These results are not shown here for conciseness; anyway, the waviness of τ_{xx} is most certainly the first indication that the maximum allowable De is about to be reached.

5.2.4.3 *FENE-CR Model*

A slightly modified version of the FENE-CR model was proposed and used by Coates et al. (1992) and later by a number of other authors in a variety of studies, such as in cylinder and sphere problems, both with uniform and Poiseuille approach flow conditions (McKinley et al., 1993;

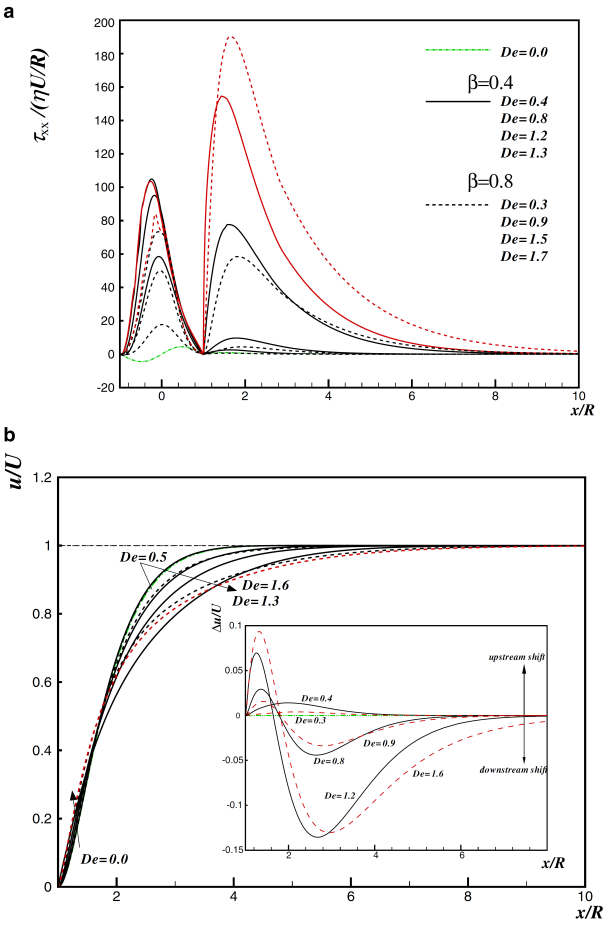

Figure 5.23: (a) τ_{xx} and (b) u centreline profiles for Oldroyd-B fluid with β=0.4 and β=0.8. The inset shows the wake velocity difference, $\Delta u/U = (u=u_{Newt})/U$.

Kim et al., 2005a; Oliveira and Miranda, 2005; Satrape and Crochet, 1994; Harlen, 2002; Dou and Phan-Thien, 2004). In all these works, the constant viscosity FENE-CR model predicted the onset of negative wake in the velocity profiles for sufficiently low levels of the extensibility parameter. In the present investigation the FENE-CR model was applied with $\beta = 0.1$ and two extensibility values, $L^2 = 10$ and $L^2 = 100$, in order to assess the influence of this model parameter on the negative wake phenomenon.

Figure 5.24 compares the values of C_D obtained in this work with those of Kim et al. (2005a). Our simulations were carried out on meshes M60 and $M60_{WR}$, the data are given in Table 5.7, and it was found that the drag force coefficient decreases monotonically with the Deborah number. Iterative convergence was possible up to $De = 7.8$ and $De = 5.0$ for $L^2 = 10$ and $L^2 = 100$, respectively. Remarkably good agreement was found with the recent results of Kim et al. (2005a) for the two extensibility parameters considered, but values of De three times higher could be attained here. In contrast, the predictions of Dou and Phan-Thien (2003) with $L^2 = 10$ are well below our results, in fact rather close to our predictions for the $L^2 = 100$ case; with $L^2 = 100$ their predictions agree with ours. These discrepancies can be attributed

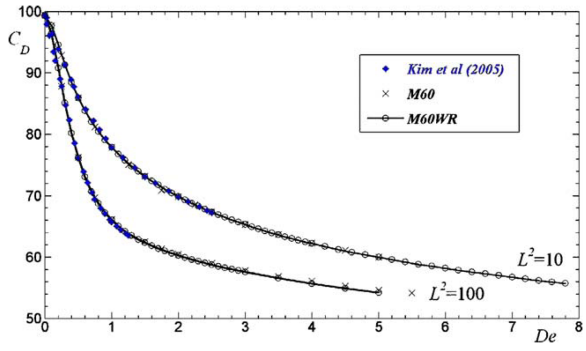

Figure 5.24: Drag force coefficient for for the FENE-CR fluid. Mesh M60 (×); Mesh $M60_{WR}$ (-◯-); Kim et al. (2005a) data (filled diamonds) Mesh $M120_{WR}$ (empty diamonds).

Table 5.7: Drag force coefficient for the FENE-CR model.

	FENE-CR $L^2 = 10$		FENE-CR $L^2 = 100$	
De	M60	$M60_{WR}$	M60	$M60_{WR}$
0.1	97.715	97.709		96.426
0.2		94.575		90.775
0.3		91.308		85.072
0.4		88.419		80.178
0.5	85.988	85.935	76.263	76.218
1.0	77.902	77.881	66.144	66.037
1.5	73.188	73.156	62.502	62.343
2.0	69.875	69.862	60.458	60.261
2.5	67.380	67.329	59.009	58.769
3.0	65.341	65.306	57.839	57.578
3.5	63.679	63.629	56.846	56.618
4.0	62.273	62.222	56.119	55.796
5.0	60.017	59.968	54.612	55.069
6.0		58.199		
7.0		56.764		
7.8		55.716		

to either inadequate mesh refinement or lower-order discretization schemes.

Figures 5.25a and 5.25b show axial velocity and stress contour plots for the FENE-CR model with $\beta = 0.1$, $De = 3.0$ at two values of extensibility, $L^2 = 10$ and $L^2 = 100$, respectively. For $L^2 = 100$ (Figure 5.25a), i.e., when the F term in eq. (5.17) tends to unity and the FENE-CR model approaches the Oldroyd-B model, the maximum values of the normal stress are located along the cylinder sidewall, due to shear flow and in the birefringent strand in the centreline downstream of the cylinder, here due to extensional flow. The birefringent strand at higher value of extensibility $L^2 = 100$, is much longer and exhibits higher stress values than the corresponding case with a lower value of extensibility, $L^2 = 10$, as shown in Figure 5.25b. In both cases the fore-aft asymmetry is more pronounced than was the case with the previous models (cf. Figure 5.16) and a negative wake downstream of the cylinder is now visible (contours of $u/U > 1$).

As briefly discussed in the Introduction, the onset and strength of the negative wake depends strongly on the extensibility parameter L^2 of the FENE-CR model and for uniform approach flow several

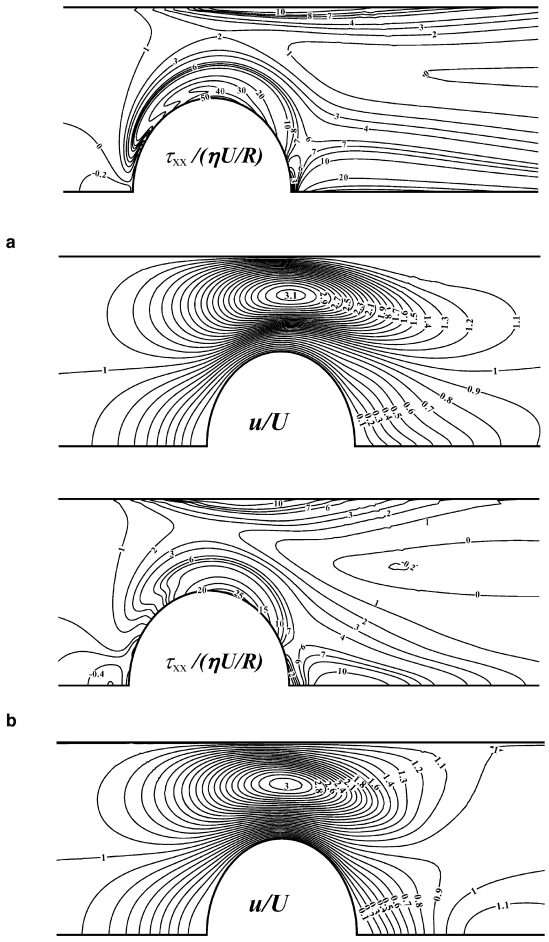

Figure 5.25: τ_{xx}, u and v contour plots for FENE-CR with (a) $L^2 = 10$ and (b) $L^2 = 100$ at $De = 3$ on mesh $M60_{WR}$.

authors (Satrape and Crochet, 1994; Harlen, 2002; Dou and Phan-Thien, 2004) indicated the absence of a negative wake for high values of L^2, as the fluid behaviour approaches that of the Oldroyd-B model. Dou and Phan-Thien (2003) suggested that the absence of negative wake in the experiments of McKinley et al. (1993) can be attributed to the high extensibility of the fluid (which was modelled with the FENE-CR having $L^2 = 144$ based on rheological measurements). This trend is also observed in our results, when comparing Figures 5.26a and 5.26b. For the FENE-CR model with $L^2 = 100$ (Figure 5.26b), and for small values of De (< 1.5) no negative wake is observed. Only upstream, followed by downstream shifts ($0.5 < De < 1.5$) in the velocity profiles are observed with respect to the Newtonian case, and these variations are similar to those reported for the Oldroyd-B fluid in Figure 5.23. Then, for $De > 1.5$ there is also an initial small upstream shift, followed by a downstream shift extending to $x/R \approx 4.5$ and finally a negative wake appears that extends further downstream to $x/R \approx 16$. The magnitude of the negative wake, measured by the relative velocity overshoot $\Delta u/U = (u=u_{Newt})/U$, increases with De and is approximately 11.7% at $De = 5.0$. When the extensibility parameter is reduced, the wake behaviour changes significantly, as illustrated in Figure 5.26b. Now, for all values of De no initial upstream shift is observed and the negative wake appears earlier at $De > 0.5$, following a small downstream shift

of the velocity profile near the rear stagnation point. The magnitude of the negative wake is higher than for the $L^2 = 100$ case, increasing with De from approximately 1% at $De = 1.0$ to 32.8% at $De = 7.8$. However, the negative wake is shorter for $L^2 = 10$ ($x/R \approx 10$) than for $L^2 = 100$ ($x/R \approx 16$).

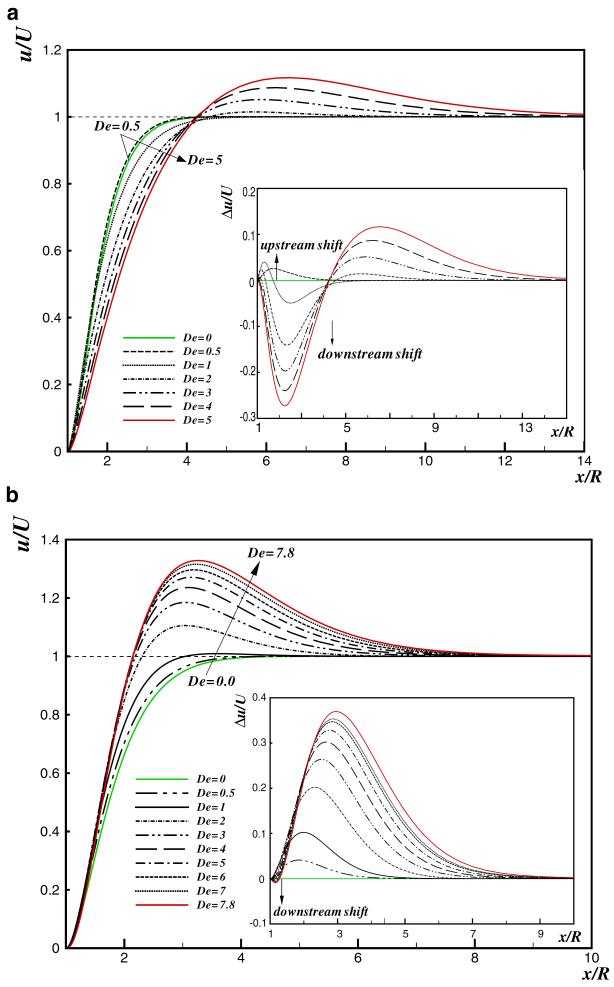

Figure 5.26: u centreline profiles for FENE-CR with (a) $L^2 = 10$ and (b) $L^2 = 100$. The inset shows the wake velocity difference, $\Delta u/U = (u - u_{Newt})/U$.

5.2.4.4 *PTT Model*

The PTT model includes the stress coefficient function, see Eq. (5.18), bringing in a new parameter ε that imposes an upper limit to the elongational viscosity ($\eta_E \propto 1/\varepsilon$ for low ε). This model is shear-thinning in viscosity, in contrast with the FENE-CR of the previous section, and was used in several numerical works of flow past a cylinder with both uniform and Poiseuille inlet conditions (Alves et al., 2001b; Phan-Thien and Dou, 1999; Dou and Phan-Thien, 2003). Here the PTT model is employed without a solvent viscosity ($\beta = 0$), for two typical parameters $\varepsilon = 0.02$ and 0.25. Note that when $\varepsilon \to 0$ the PTT model approaches the UCM model.

Figure 5.27 (and on Table 5.8) compares the computed of C_D values with those obtained by Dou and Phan-Thien (2003). The present

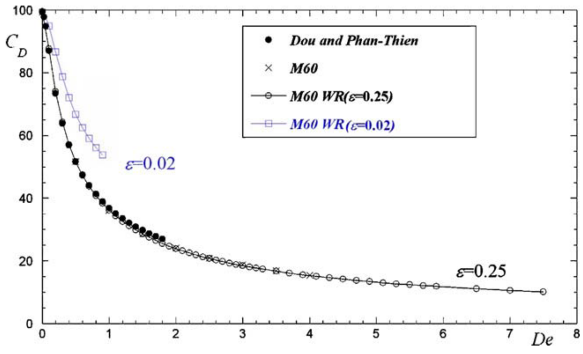

Figure 5.27: Drag force coefficient for a PTT fluid with β=0. Mesh $M60_{WR}$ (-◯- or squares); Mesh M60 (×); and Dou and Phan-Thien (2003) data (filled circles).

Table 5.8: Drag force coefficient for the PTT model.

	PTT $\varepsilon = 0.25$		PTT $\varepsilon = 0.02$
De	M60	$M60_{WR}$	$M60_{WR}$
0.1		87.672	94.948
0.2		74.035	86.716
0.3		64.257	78.760
0.4		57.133	72.102
0.5	51.681	51.690	66.814
0.6		47.370	62.540
0.7		43.839	59.115
0.8		40.886	56.147
0.9		38.372	53.763
1.0	36.227	36.202	
1.5	28.655	28.584	
2.0	24.081	23.936	
2.5	20.970	20.774	
3.0	18.788	18.462	
3.5	16.836	16.713	
4.1		15.082	
5.1		13.061	
6.5		11.151	
7.0		10.626	
7.5		10.158	

predictions obtained on meshes M60 and $M60_{WR}$ are virtually indistinguishable and show the drag coefficient to decrease monotonically with the Deborah number, up to limiting values of $De = 0.9$ and $De = 7.5$, for $\varepsilon = 0.02$ and $\varepsilon = 0.25$, respectively. Generally, numerical simulations are easier the highest the value of ε and the lower the Deborah number, and this is borne out in the good agreement observed in Figure 5.27 for $\varepsilon = 0.25$ against with the results of Dou and Phan-Thien (2003), to be contrasted with the poor comparison involving constant viscosity models ($\varepsilon = 0.0$) in Figure 5.19. Above $De \approx 0.9$ our results are below those of Dou and Phan-Thien (2003) and furthermore we could attain a maximum Deborah number four times higher.

Figures 5.28 and 5.29 present our predictions of axial normal stress and streamwise velocity along the cylinder wall and rear centreline for the two cases $\varepsilon = 0.25$ and $\varepsilon = 0.02$, respectively. Generally speaking, the stress levels are much lower than those of previous models on

account of shear-thinning which affects both the shear viscosity and the normal stresses. For the PTT model with the higher value of extensional parameter ($\varepsilon = 0.02$) the τ_{xx} predictions present some features not previously seen. Figure 5.28a shows that, on the cylinder sidewalls for $De > 0.5$, all τ_{xx} profiles decrease with an increase of Deborah number due to shear-thinning, this decrease being more intense at smaller De values. For small values of De, not shown here, the profiles of τ_{xx} exhibit a progressive increase with De, these corresponding to situations where the shear-thinning is very weak and the effect of elasticity prevails. This is actually seen to a larger extent in Figure 5.29a where the low value of ε imparts a weaker shear-thinning. Above $De \approx 5$ the decrease in the normal stress peak at the cylinder sidewalls is not so intense, with a constant maximum normalized value of approximately 7 to 8. In the near wake region the τ_{xx} profiles increase with De up to $De \approx 5$ and then a small decrease and shift to downstream locations occurs for higher De values.

For the PTT model with a low value of ε ($\varepsilon = 0.02$) the behaviour of the τ_{xx} profiles is akin to that obtained with the UCM model (cf. Figures 5.29a and Figure 5.21a). The τ_{xx} profiles increase with De up to $De \approx 0.5$ and then decrease up to the critical value ($De = 0.9$). In the rear wake zone there is a slow monotonic increase in τ_{xx} on account of extensional effects and the small amounts of shear-thinning.

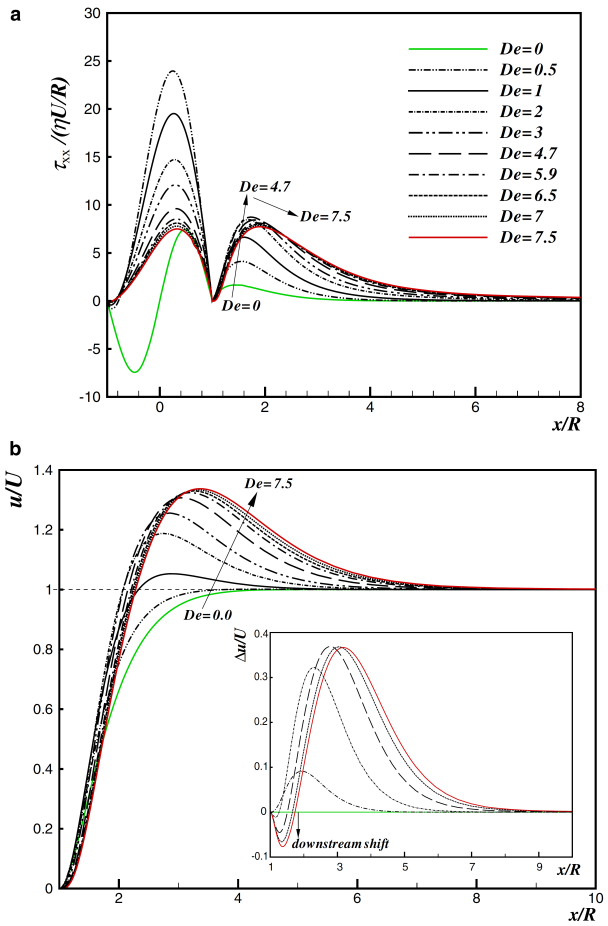

Figure 5.28: (a) τ_{xx} and (b) u centreline profiles for the PTT model (ε=0.25). The inset shows the wake velocity difference, $\Delta u/U = (u=u_{Newt})/U$.

As expected, the formation of a negative wake depends on the ε parameter, with an absence of this flow feature for low values of ε. These behaviours are illustrated by our results presented in Figures 5.28b and 5.29b. The formation of a negative wake for $De \geqslant 1$ with $\varepsilon = 0.25$ is obvious in Figure 5.28b, as well as a small downstream shift in the velocity profiles with respect to the Newtonian condition near the rear stagnation point. The negative wake seen with $\varepsilon = 0.25$ extends to approximately $x/R \approx 9$ for $De = 7.5$. The relative velocity overshoot increases with De up to $De \approx 5$, then asymptotes to a constant value of about 34% and shifts further downstream. With the reduction of the parameter ε, the flow behaviour becomes similar to that seen with the UCM model, as observed in Figure 5.29b. For $\varepsilon = 0.02$ there is an upstream shift in the velocity profiles with respect to the Newtonian profile up to $De \approx 0.6$. At higher Deborah numbers, the velocity profiles also exhibit an upstream shift near the stagnation point in the rear wake of the cylinder, followed by a downstream shift further downstream of the cylinder, but no negative wake appears regardless of the value of ε.

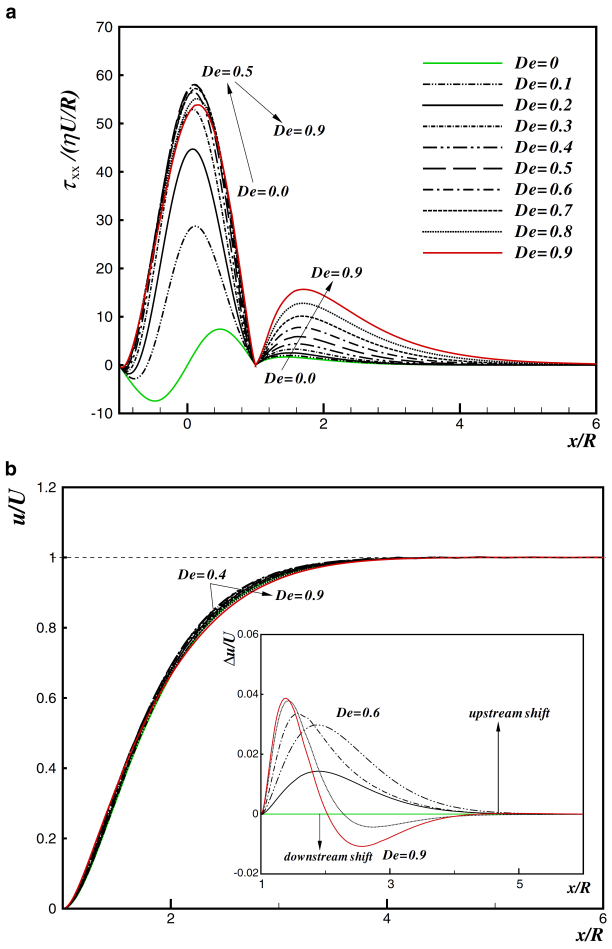

Figure 5.29: (a) τ_{xx} and (b) u centreline profiles for the PTT model (ε=0.02). The inset shows the wake velocity difference, $\Delta u/U = (u - u_{Newt})/U$.

5.2.4.5 *Giesekus Model*

In this section we discuss the results obtained with the Giesekus model for $\alpha = 0.02$ and $\beta = 0.59$. This viscosity ratio, β, is frequently used in

numerical works and can be traced back to the value adopted in the experimental work of McKinley et al. (1993) for the Boger fluid used in their experiments. Hulsen et al. (2005) applied an implementation of the log-conformation methodology with a finite element method to the benchmark flow of Oldroyd-B and Giesekus fluids past a fixed confined cylinder. An almost unbounded convergence limit for the Giesekus model was reported, whereas for the Oldroyd-B the solution became unsteady at high Deborah numbers while exhibiting symptoms of mesh dependency.

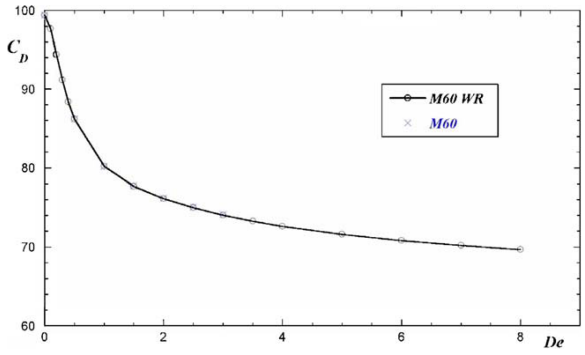

Figure 5.30: Drag force coefficient for a Giesekus fluid (α=0.02 and β=0.59). Mesh $M60_{WR}$ (-◯-); Mesh M60 (×).

Table 5.9: Drag force coefficient for the Giesekus model.

	Giesekus	
De	M60	$M60_{WR}$
0.1		97.672
0.2		94.394
0.3		91.151
0.4		88.401
0.5	86.190	86.178
1.0	80.217	80.198
1.5	77.739	77.713
2.0	76.192	76.160
2.5	75.040	75.002
3.0	74.114	74.063
3.5		73.300
4.0		72.652
5.0		71.623
6.0		70.837
7.0		70.201
8.0		69.684

Figure 5.30 presents the C_D values obtained with meshes M60 and $M60_{WR}$ for the Giesekus model (quantified in Table 5.9). The drag force coefficient decreases monotonically with the Deborah number, and convergent simulations could be obtained up to $De \approx 8$. A direct comparison cannot be made against the results of Hulsen et al. (2005) because these are for the flow around fixed-cylinder problem, but it is clear that the log-conformation formulation offers a much larger range of allowable Deborah numbers.

Figure 5.31a shows the τ_{xx} profiles for the Giesekus model, where it can be observed that along the cylinder sidewalls all profiles decrease

with increasing Deborah number ($De \geqslant 2$), again a consequence of shear-thinning. As for the PTT case, this decrease is more intense at low Deborah numbers (up to $De \approx 6$) than at higher De. On the other hand, in the rear wake zone the τ_{xx} profiles increase for all De and the maximum value is greater than in the cylinder sidewalls above $De = 1$. Although the simulations were stable and convergent, some oscillations in the stress profiles are observed in the cylinder sidewalls and in the rear wake zone at high De.

The formation of a negative wake at $De \geqslant 1$ is also seen for the Giesekus model in Figure 5.31b, where initially an upstream shift in the velocity profiles, with respect to the Newtonian profile, is present near the rear stagnation point, and is followed by a downstream shift that extends to approximately $x/R \approx 5$. The length of the negative wake increases with De so that at $De = 8$ it extends in the axial direction up to $x/R \approx 25$. Even though the relative velocity overshoot increases with De, its magnitude is not as large as seen with the previous models, attaining a maximum value of only about 3% at $De = 8$.

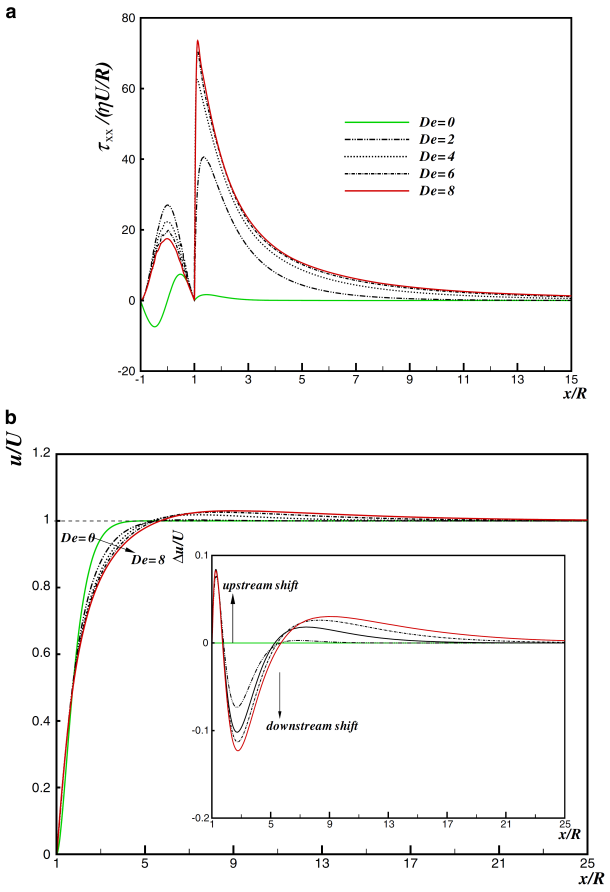

Figure 5.31: (a) τ_{xx} and (b) u centreline profiles for the Giesekus model (α=0.02 and β=0.59). The inset shows the wake velocity difference, $\Delta u/U = (u - u_{Newt})/U$.

5.2.5 *Conclusions*

In this work we present detailed results of a numerical investigation of the flow of viscoelastic fluids past a confined cylinder settling between

two parallel plates with a 50% blockage ratio, using a finite-volume method. In order to properly assess the effect of various rheological properties, five constitutive models have been used: UCM, Oldroyd-B, FENE-CR, PTT and Giesekus models.

Simulations were carried out under creeping flow conditions, using very fine meshes, especially in the wake of the cylinder where large normal stress gradients are observed for high Deborah number flows. Numerical solutions could be obtained up to Deborah numbers in excess of those reported previously in the literature, especially in the case of the PTT, FENE-CR and Giesekus models. Special care was exercised in order to guarantee that all solutions are well converged iteratively, with stopping tolerances of around 10^{-4}, and that sufficient mesh convergence is also provided, with smaller mesh spacing of order $\Delta r = 0.002$, allowing estimation of drag coefficients which are exact up to the first decimal place, corresponding to an accuracy of around 0.1 - 0.3 % on average. Besides providing reliable data for the drag coefficient variation and graphs of velocity and normal stress profiles along the wake, we reached some other conclusions worth mentioning:

1. Drag coefficient: For the UCM and the Oldroyd-B fluids with low solvent viscosity contribution ($\beta = 0.125$), the drag coefficient on the cylinder decreases monotonically with increasing Deborah number. When the solvent viscosity contribution is high ($\beta = 0.8$) the drag coefficient first decreases with De followed by a levelling out and marginal, very slight increase, for $De \geqslant 1.1$. For all retardation ratios, our results are well below the predictions of Dou and Phan-Thien (2003), with agreement only between the Newtonian cases up to $De \approx 0.3$. For the other models with bounded extensional viscosity, the FENE-CR, PTT and Giesekus, the latter two being shear-thinning, the drag coefficient decreases monotonically with increasing Deborah number. For the FENE-CR model, good agreement was found with the C_D results of Kim et al. (2005a) for both extensibility parameters, $L^2 = 10$ and $L^2 = 100$, whereas the predictions of Dou and Phan-Thien (2003) with $L^2 = 10$ lie well below both sets of results, close to the predictions for the $L^2 = 100$ case. For $L^2 = 100$, the results from Dou and Phan-Thien (2003) show a non monotonic behaviour, diverging from both our predictions and those of Kim et al. (2005a), with agreement only for $De \leqslant 0.6$.

2. Negative wake: Regarding the existence of negative wake these sets of simulations have shown that model with unbounded or bounded but very large extensional viscosities do not exhibit this feature. Figure 5.32 summarizes our findings on the maximum magnitude of the negative wake for all models tested. For the UCM and Oldroyd-B fluids there was no sign of a negative wake" regardless of the values of β, with the velocity profiles presenting an upstream shift close to the back of the cylinder ($x/R \leqslant 1.5 - 2$) followed by a downstream shift for $De > 0.5$. For the FENE-CR model with $L^2 = 100$, there is a negative wake for $De > 1.5$, starting about 3 radii from the rear of the cylinder and extending up to $x/R \approx 16$. The magnitude of the negative wake increases with De and is approximately 11.7% at $De = 5.0$, as seen in Figure 5.32. For the FENE-CR fluid with $L^2 = 10$, there is no upstream shift of the velocity and the negative wake is more

intense and clearly marked appearing at $De > 0.5$, and formed at about one radius distance behind the cylinder. For $L^2 = 10$ the magnitude of the negative wake is larger than for $L^2 = 100$, being 32.8% at $De = 7.8$, whereas its length is actually smaller, with $x/R \approx 10$ for$L^2 = 10$ and $x/R \approx 16$ for $L^2 = 100$. For the PTT fluid with the highest elongational parameter $\varepsilon = 0.25$, a negative wake in the velocity overshoot is found at $De > 0.5$, starting at $x/R \approx 2$ and extending to approximately $x/R \approx 9$. The relative velocity overshoot increases with De up to $De \approx 5$ and then asymptotes to a constant value of about 34%, while its location shifts further downstream, as seen in Figure 5.32. For lower values of the ε parameter, the flow behaviour becomes similar to that seen with the UCM model. The Giesekus model produces an initial upstream shift followed by a downstream shift and a negative wake for $De \geqslant 2$, starting at $x/R \approx 5.5$ and extending in the axial direction up to $x/R \approx 25$. The negative wake magnitude increases with De, attaining a maximum value of about 3% for $De = 8$.

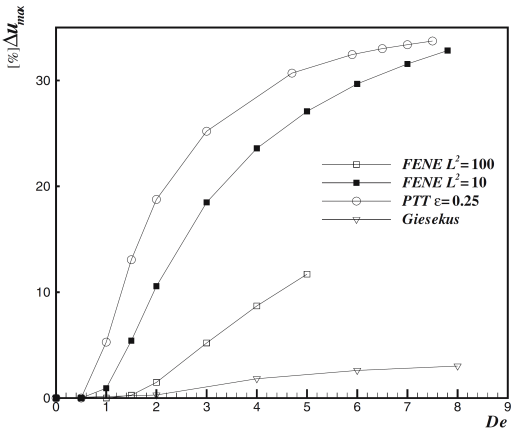

Figure 5.32: Maximum negative wake magnitude $(u_{max}=U)/U$ (%) for the FENE-CR, PTT and Giesekus models.

5.2.6 *Acknowledgements*

The authors acknowledge funding from FEDER and FCT through projects POCI/EQU/59256/2004, POCI/EQU/56342/2004 and POCI/E-ME/59338/2004. A. Afonso would also like to thank FCT for financial support through the scholarship SFRH/BD28828/ 2006. We appreciate helpful conversations with Dr. R. J. Poole and thank him for proof-reading this manuscript.

Abstract[3]
*High elasticity simulations of flows through a two-dimensional 4:1 abrupt contraction and a 4:1 three-dimensional square-square abrupt contraction were performed with a finite volume method implementing the log-conformation formulation, proposed by Fattal and Kupferman (2004) to alleviate the High Weissenberg Number Problem. For the 2D simulations of Boger fluids, modelled by the Oldroyd-B constitutive equation, local flow unsteadiness appears at a relatively low Deborah number (*De*) of 2.5. Predictions at higher* De *were only possible with the log-conformation technique and show that the periodic unsteadiness grows with* De *leading to an asymmetric flow with alternate back-shedding of vorticity from pulsating upstream recirculating eddies. This is accompanied by a frequency doubling mechanism deteriorating to a chaotic regime at high* De*. For the 3D contraction, calculations were restricted to steady flows of Oldroyd-B and Phan-Thien-Tanner (PTT) fluids and very high* De *were attained (*$De \approx 20$ *for PTT with* $\varepsilon = 0.01$ *and* $De \approx 10000$ *for PTT with* $\varepsilon = 0.25$*), with prediction of strong vortex enhancement. For the Boger fluid calculations there was inversion of the secondary flow at high* De *as observed experimentally by Alves et al. (2008). The log-conformation technique gave solutions of similar accuracy to the thoroughly tested standard finite volume method under steady flow conditions and the onset of a time-dependent solution occurred approximately at the same Deborah number for both formulations. Nevertheless, for Deborah numbers higher than the critical Deborah number, and for which the standard iterative technique diverges, the log conformation technique continues to provide stable converged solutions up to quite (impressively) high Deborah numbers, demonstrating its advantages relative to the standard methodology.*

Keywords: Finite-volume method; Log-conformation tensor; Viscoelastic fluids; Planar contraction; Square/Square contraction.

5.3.1 *Introduction*

Viscoelastic entry flows and in devices with geometric singularities, such as flows through contractions or contraction/expansions, are important in polymer processing and in the emerging field of viscoelastic microfluidics, while posing a great challenge to the numerical methods, especially at high elasticity, as measured by the Weissenberg (*Wi*) or Deborah (*De*) numbers (here the latter will be used). Due to the geometrical simplicity and known numerical difficulty, the planar 4:1 sudden contraction was established as a benchmark flow problem in 1987 (Hassager, 1988), and gave rise to several experimental studies in both planar and axisymmetric geometries: Cable and Boger (1978a,b, 1979), McKinley et al. (1991b), Chiba et al. (1990) and Yesilata et al. (1999), just to cite a few. Owens and Phillips (2002), McKinley et al. (1991b) and Boger (1987) present extensive literature reviews of experiments in this flow, while reviews on related numerical work can be found in Keunings (1989), Baaijens (1998), Walters and Webster (2003), Owens and Phillips (2002) and Oliveira and Pinho (1999a). The picture

3 A.M. Afonso, P.J. Oliveira, F.T. Pinho and M.A. Alves (2010), Dynamics of high Deborah number entry flows – a numerical study, accepted in the *Journal of Fluid Mechanics.*

emerging from experiments in 2D 4:1 contractions depends on fluid rheology. For some shear-thinning fluids there is corner vortex enhancement following the formation of a lip vortex, which initially grows and subsequently merges with the corner vortex, whereas for Boger fluids the lip vortex mechanism is absent (it does exist, however for large contraction ratios, not dealt with in this paper) and the corner vortex keeps growing with De. At larger Deborah numbers the single existing corner vortex still grows with De and the flow is still steady. For all fluids the flow becomes unsteady above a critical Deborah number.

Experiments with Newtonian and Boger fluids in 3D square-square contraction flows were reported by Alves et al. (2005) and Sousa et al. (2009), where extensive flow visualizations are presented at the middle plane of a 4:1 contraction using a streak line photography technique. These experiments revealed the formation of a lip vortex at high Deborah numbers for the more concentrated Boger fluid (aqueous solution of polyacrylamide at 300 ppm) and related this lip vortex with the increase of the role of shear induced normal stresses due to the secondary flow in the cross section of the rectangular channel. An interesting fluid dynamics feature caused by elasticity was identified experimentally in this geometry by Alves et al. (2008), in a work which also included 3D numerical simulations using a 4 mode Phan-Thien-Tanner (PTT) model with a Newtonian solvent contribution. Their experimental and numerical results showed the expected significant vortex growth, measured on longitudinal mid-planes, and revealed the occurrence of an inversion in the direction of rotation of the recirculation flow inside the vortices due to elastic effects. When elastic effects are strong the fluid particles enter the vortices through the horizontal (or vertical) planes of symmetry and leave through the diagonal planes, whereas in the absence of elasticity the fluid elements enter the vortices through the diagonal symmetry planes and exit at the horizontal (vertical) mid planes of symmetry. A similar finding was reported by Sirakov et al. (2005) in 3D 4:1 square to circular cross-section contraction simulations with a finite element method using the eXtended Pom–Pom model to analyze the viscoelastic flow of branched LDPE solutions.

These viscoelastic flows are notoriously difficult to simulate numerically at levels of elasticity above a critical Deborah number, where the numerical results exhibit symptoms of mesh dependency even with refined meshes and usually have a tendency to diverge. Not surprisingly, at high Deborah numbers the agreement between results from different numerical methods is harder to achieve than at low Deborah numbers and there are also important differences between predictions and experiments. For instance, the majority of numerical studies on entry flows with Boger fluids have been restricted to the range of parameters where the size of upstream vortices is still decreasing and the pressure drop is smaller than the corresponding Newtonian pressure drop (Alves et al., 2003b; Aboubacar and Webster, 2001). These predictions were obtained using continuum mechanics/ macroscale constitutive equations and are in contrast with experimental results employing constant-viscosity polymer solutions and melts, which invariably show increased pressure drop and enhanced vortex formation (Cable and Boger, 1978a,b, 1979; McKinley et al., 1991b; Chiba et al., 1990). The discrepancies are rooted both on the physics of the constitutive equations and on numerical issues (Owens and Phillips, 2002).

The use of atomistic constitutive equations is extremely expensive and with today's resources they are restricted to very simple molecular-sized computational domains. Some coarse-graining is required to be able to compute macroscopic flows, and micro-macro numerical methods have been devised to allow calculations with these mesoscale constitutive equations. These numerical methods, reviewed by Keunings (2004), are still computationally very expensive and difficult to perform in complex geometries of engineering interest, especially considering the need for very refined meshing and time stepping for accurate viscoelastic predictions. Hence, the majority of engineering calculations, such as those mentioned initially, rely on macroscopic constitutive equations some of which have been derived using more or less sophisticated closures of the mesoscale models. These derived closures invariably use decoupling and some form of pre-averaging (Bird et al., 1980; Lielens et al., 1999) that remove or change some rheological characteristics of the original mesoscale models (Van Heel et al., 1998; Zhou and Akhavan, 2003). Needless to say the mesoscale closures have their own simplifications, hence they require improvements of their own.

Using mesoscale modeling Koppol et al. (2009) predicted the viscoelastic flow in a 4:1:4 axisymmetric contraction/expansion and were able to show simultaneously the correct upstream vortex patterns and qualitatively the growth of the normalized pressure drop with Deborah number above that for Newtonian fluids, as in the experiments of Rothstein and McKinley (1999). However, their simulations with the FENE-P model failed to observe the growth of the pressure drop above that for Newtonian fluids at high Deborah numbers and the justification was the inadequacy of the FENE-P model at predicting correctly the transient extensional viscosity growth along the centerline region, which required at least a mesoscale approach. So, there is clearly the need for better closures of the mesoscale models leading to new macroscale constitutive equations for improved predictions.

In addition to improvements in the physical modeling of the rheological behavior of fluids, there is also the need to improve classical computational methods, i.e., methods applied to macroscale constitutive equations in order to enable engineering calculations at high Deborah numbers.

In the present work we explore the dynamics of 2D and 3D contraction flows up to much higher De than previously attained, and demonstrate a succession of dynamical transitions, from steady to unsteady flow with lip and corner vortex enhancement, and from symmetric to asymmetric patterns with alternating vortex pulsation, up to almost chaotic regime of back-shedding upstream of the contraction plane. We use the fast Fourier transform (FFT) of velocity signal at a monitoring point to determine the dominant frequencies, which show a characteristic frequency doubling regime at high De. Qualitatively these results are comparable to the experimental data of McKinley et al. (1991b), who studied viscoelastic vortex dynamics in a axisymmetric contraction. Finally, the time average evolution of the vortex size and pressure drop from the present simulations reveal, for the first time, that after an initial decreasing tendency with De, there is an upturn followed by considerable enhancement at higher elasticity. Thus the trends of the available experimental results are well captured by the present simulations, except the raise of pressure drop above the corresponding Newtonian value.

To accomplish this we use the log-conformation technique within the finite volume method. We show first that this numerical technique allows computations of viscoelastic 2D and 3D entry flows at very high Deborah numbers, provided the rheological equations of state are transformed and re-written on the basis of the matrix-logarithmic of their conformation tensors. This technique, originally proposed by Fattal and Kupferman (2004) in the context of computational rheology, introduces a better polynomial interpolation of the stresses when these exhibit an exponential growth, such as near stagnation points, and has been tested in the recent past in a number of viscoelastic flow problems and shown to enable computations at higher Deborah numbers than usual. An additional benefit of the log-conformation formulation is that it forces positive-definiteness of the conformation tensor (Pan and Hao, 2007; Hulsen et al., 2005; Kwon, 2004; Yoon and Kwon, 2005; Kwon, 2006; Coronado et al., 2007; Kane et al., 2009; Afonso et al., 2009b), thus avoiding a kind of Hadamard instability plaguing the numerical simulation once the flow becomes inherently unstable, which invariably leads to quick divergence of iterative numerical procedures.

There are a number of works in the literature implementing the log-conformation formulation in the scope of the finite-element method (FEM) (Fattal and Kupferman, 2005; Pan and Hao, 2007; Hulsen et al., 2005; Kwon, 2004; Yoon and Kwon, 2005; Kwon, 2006) and showing its advantages relative to the classical methods with a variety of flows and constitutive equations. Others were aimed at formulating less computer-intensive alternative log-conformation algorithms (Coronado et al., 2007; Kane et al., 2009). Even though they all have shown that it was possible to achieve a converged solution at high Deborah numbers, they have not investigated in detail the dynamics of unsteady viscoelastic flows as done here for the sudden contraction flows.

In a previous work (Afonso et al., 2009b), the original log-conformation formulation was implemented in the FVM framework and applied to a benchmark flow problem without geometrical singularities, creeping viscoelastic flow past a confined cylinder. Here we wish to apply that formulation to the contraction flow problem to be able to predict the rich dynamical transitions that unfold when the elasticity is sufficiently high and that were observed experimentally and described by McKinley et al. (1991b).

The remainder of this paper is organised as follows: after presenting the governing equations, the constitutive equations are modified to incorporate the log-conformation formalism. This is followed by a brief description of the numerical method, then the geometries and computational meshes used for each flow problem are given and finally the results of the simulations are presented and discussed.

5.3.2 *Governing Equations and numerical method*

In this section we provide the set of differential equations that need to be solved, encompassing the flow and the constitutive equations, explain succinctly how they are transformed to the log-formulation, and give a short description of the numerical method, which has been explained in detail in a number of previous papers (e.g. Oliveira and Pinho, 1999a; Alves et al., 2003b; Afonso et al., 2009b).

5.3.2.1 *Base equations*

To simulate steady incompressible flow of viscoelastic fluids, conservation equations for mass,

$$\nabla \cdot \mathbf{u} = 0, \tag{5.26}$$

and momentum,

$$\rho \frac{D\mathbf{u}}{Dt} = -\nabla p + \beta \eta_o \nabla^2 \mathbf{u} + \frac{\eta_o}{\lambda} (1-\beta) \ \nabla \cdot \mathbf{A}, \tag{5.27}$$

need to be solved. The two last terms on the right-hand-side of the momentum equation describe the rheology of the fluid: the Laplacian operator corresponds to a Newtonian solvent contribution and the divergence of the conformation tensor ($\mathbf{A}$) is an additive viscoelastic term which follows here either the Oldroyd-B (Oldroyd, 1950) or the PTT (Phan-Thien and Tanner, 1977; Phan-Thien, 1978) models. To complete the constitutive equation describing the additive term, an evolution equation for the conformation tensor needs also to be solved,

$$\lambda \overset{\nabla}{\mathbf{A}} = -Y(\mathrm{tr}\mathbf{A}) (\mathbf{A} - \mathbf{I}) . \tag{5.28}$$

In these equations, $\mathbf{I}$ represents the unitary tensor, $\mathbf{u}$ is the velocity vector, p is the pressure, λ is the relaxation time of the polymer, and $\overset{\nabla}{\mathbf{A}}$ represents Oldroyd's upper-convected derivative of $\mathbf{A}$, given by

$$\overset{\nabla}{\mathbf{A}} = \frac{D\mathbf{A}}{Dt} - \mathbf{A} \cdot \nabla \mathbf{u} - \nabla \mathbf{u}^T \cdot \mathbf{A}. \tag{5.29}$$

The fluid total extra-stress is the sum of solvent and polymer stress contributions. The viscosity ratio, β (cf. Eq. 5.30), is defined as the ratio between the Newtonian solvent viscosity, η_s, and the total zero shear-rate viscosity, η_0:

$$\beta \equiv \frac{\eta_s}{\eta_0} = \frac{\eta_s}{\eta_s + \eta_P}, \tag{5.30}$$

where η_P is the coefficient of viscosity of the polymer.

In its general form function $Y(\mathrm{tr}\mathbf{A})$ for the PTT model is exponential (Phan-Thien, 1978) but in this work we use its linear form, $Y(\mathrm{tr}\mathbf{A}) = 1 + \varepsilon (\mathrm{tr}\mathbf{A} - 3)$ (Phan-Thien and Tanner, 1977). When $Y(\mathrm{tr}\mathbf{A}) = 1$ (i.e. for $\varepsilon = 0$) the Oldroyd-B model is recovered. The non-unitary form of $Y(\mathrm{tr}\mathbf{A})$ for the PTT model with a Newtonian solvent imparts shear-thinning behavior to the shear viscosity of the fluid and bounds its extensional viscosity. The constitutive law written in terms of the conformation tensor $\mathbf{A}$, can be explicitly formulated as a function of the polymer contribution to the extra-stress tensor, $\boldsymbol{\tau}$, with the following relation valid for both models,

$$\tau = \frac{\eta_p}{\lambda} (\mathbf{A} - \mathbf{I}) . \tag{5.31}$$

When the governing equations are written in terms of the fluid extra-stress by combining equations (5.28) and (5.31) and writing $\mathbf{A}$ explicitly in terms of $\boldsymbol{\tau}$, so that the momentum equation will have a divergence of the extra stress term, instead of a divergence of conformation tensor,

we end up with the "standard formulation", described in detail and extensively validated within the FVM framework in (Oliveira and Pinho, 1999a; Alves et al., 2008, 2003a,b, 2000; Oliveira et al., 1998). This "standard formulation", based on the polymer extra-stress given by equations (5.28) and (5.31), will not be followed here except in some comparison test-cases in order to assess the performance of the new log-conformation method.

5.3.2.2 *The log-conformation representation*

As already described, Fattal and Kupferman (2004) proposed a tensor-logarithmic transformation of the conformation tensor for differential viscoelastic constitutive equations, which can be applied to a wide variety of constitutive laws. The core feature of this transformation is the decomposition of the velocity gradient, $\nabla\mathbf{u}$, into a traceless extensional component, $\mathbf{E}$, and a pure rotational component, $\mathbf{R}$. With this decomposition, the evolution equation (5.29), can be re-written as Fattal and Kupferman (2004)

$$\frac{\partial \mathbf{A}}{\partial t} + (\mathbf{u}\cdot\nabla)\mathbf{A} - (\mathbf{R}\mathbf{A} - \mathbf{A}\mathbf{R}) - 2\mathbf{E}\mathbf{A} = \frac{Y(\mathrm{tr}\mathbf{A})}{\lambda}(\mathbf{A} - \mathbf{I})\,. \tag{5.32}$$

In the log-conformation representation the evolution equation (5.32) is replaced by an equivalent evolution equation for the logarithm of the conformation tensor, $\mathbf{\Theta} = \log \mathbf{A}$, benefiting from the fact that $\mathbf{A}$ is a symmetric positive definite (SPD) tensor, and thus can be diagonalized into the form Fattal and Kupferman (2004),

$$\mathbf{A} = \mathbf{\Omega}\,\mathbf{\Lambda}\,\mathbf{\Omega}^{T}, \tag{5.33}$$

where $\mathbf{\Omega}$ is an orthogonal tensor that consists of the eigenvectors of matrix $\mathbf{A}$ and $\mathbf{\Lambda}$ is a diagonal matrix assembled with the corresponding three distinct eigenvalues of $\mathbf{A}$. The transformation from Eq. (5.32) to an equation for $\mathbf{\Theta}$ is described in detail by Fattal and Kupferman (2004), and leads to

$$\frac{\partial \mathbf{\Theta}}{\partial t} + (\mathbf{u}\cdot\nabla)\mathbf{\Theta} - (\mathbf{R}\mathbf{\Theta} - \mathbf{\Theta}\mathbf{R}) - 2\mathbf{E} = \frac{Y\left[\mathrm{tr}(e^{\mathbf{\Theta}})\right]}{\lambda}(e^{-\mathbf{\Theta}} - \mathbf{I}). \tag{5.34}$$

To recover $\mathbf{A}$ from $\mathbf{\Theta}$ the inverse transformation $\mathbf{A} = e^{\mathbf{\Theta}}$ is used when necessary. So, instead of solving numerically equation 5.29), it is the evolution equation for log $\mathbf{A}$ (equation 5.34) that is solved. Then, the inverse transformation is used to calculate the stress field prior to solving the momentum and mass conservation equations.

5.3.2.3 *Overview of solution method*

A complete description of the steps required to adapt our FVM to the log-conformation procedure and the main modifications to the solution algorithm is presented in Afonso et al. (2009b). It is important to emphasize that the advective term in equation (5.34) was discretized with two distinct differencing schemes: the first-order accurate upwind differencing scheme (UDS) and the CUBISTA high-resolution scheme (Alves et al., 2003a). This latter scheme is formally of third-order accuracy and was especially designed for differential constitutive relations. The UDS scheme is only first-order accurate, but highly stable, and will only be used in some test cases.

The positive definiteness of the conformation tensor is crucial for the well-posedness of the evolution equation. In this work, the positive definiteness is assessed by checking if the determinant of $\mathbf{A}$ is positive, and the more strict condition that $\det(\mathbf{A}) = 1$ is satisfied (Hulsen et al., 2005). A useful parameter to analyse the numerical results is the following scalar used to classify the local flow type (Lee et al., 2007):

$$\xi = \frac{|\mathbf{D}| - |\boldsymbol{\Omega}|}{|\mathbf{D}| + |\boldsymbol{\Omega}|}. \tag{5.35}$$

where $|\mathbf{D}|$ and $|\boldsymbol{\Omega}|$ represent the magnitudes of the rate of deformation and vorticity tensors, respectively

$$\mathbf{D} = \frac{1}{2}\left[\nabla\mathbf{u} + (\nabla\mathbf{u})^{T}\right], \quad \boldsymbol{\Omega} = \frac{1}{2}\left[\nabla\mathbf{u} - (\nabla\mathbf{u})^{T}\right], \tag{5.36}$$

which can be calculated as

$$\begin{aligned} |\mathbf{D}| &= \sqrt{\frac{1}{2}\left(\mathbf{D} : \mathbf{D}^{T}\right)} = \sqrt{\frac{1}{2}\sum_{i}\sum_{j} D_{ij}^{2}} \\ |\boldsymbol{\Omega}| &= \sqrt{\frac{1}{2}\left(\boldsymbol{\Omega} : \boldsymbol{\Omega}^{T}\right)} = \sqrt{\frac{1}{2}\sum_{i}\sum_{j} \Omega_{ij}^{2}}. \end{aligned} \tag{5.37}$$

The flow type parameter varies from -1, which corresponds to solid-like rotation, up to 1, for pure extensional flow. Pure shear flow is characterized by $\xi = 0$.

5.3.3 *Results*

Most simulations were carried out with the log-conformation tensor formulation (***LogT)*** just explained, while a few simulations for comparison purposes used the standard formulation (***StrT***), which has the extra stress tensor as dependent variable (i.e. without using the conformation tensor). In both cases iterative convergence to steady solution required the L_2 norm of the residuals of the equations to be less than a tolerance of 10^{-6}, when the time stepping procedure was stopped and convergence assumed. All steady and unsteady calculations for both formulations were obtained with the same time step increment (Δt).

In section 5.3.3.1 we present results for the viscoelastic flow in the planar 4:1 contraction and in section 5.3.3.5 the results for a 4:1 square-square three-dimensional abrupt contraction.

5.3.3.1 *Abrupt 4:1 contraction*

This section is organized in three parts: first we present a few details about the computational meshes employed in the simulations and the non-dimensionalization of the results (section 5.3.3.2); then we deal with the low-Deborah number range of flows (section 5.3.3.3), basically for $De = 3$ under conditions for which accurate steady results were obtained in previous studies (Alves et al., 2003b). The purpose is to demonstrate the correctness of the log-conformation implementation and that this formulation is able to achieve the same accuracy as the standard formulation, an important aspect since the accuracy of the log-conformation has often been cast in doubt (Coronado et al., 2007;

Guénette et al., 2008). Finally in section 5.3.3.4 we present the most interesting results, for the high-Deborah number range, where the standard stress formulation fails. These are new results predicted with the differential macroscopic Oldroyd-B model, comprising the unsteady dynamics of the asymmetric vortical structures formed upstream of the contraction plane and exploring numerically, for the first time, the range of elasticity for which the pressure drop increases and the vortex size is strongly enhanced, as usually observed in the experiments using Boger fluids. To be able to capture asymmetric flows, the mesh had to map the complete contraction domain and not just half of it, as it is usual by invoking symmetry arguments.

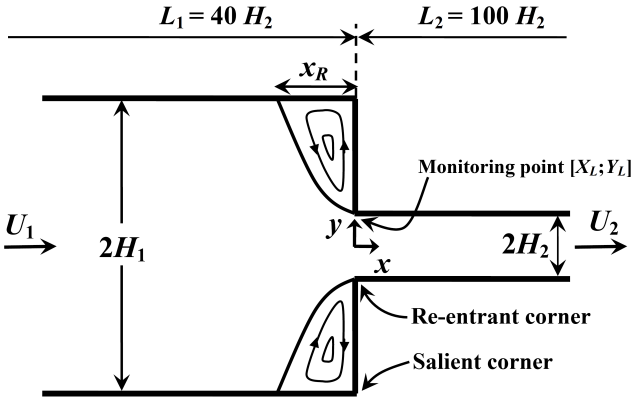

Figure 5.33: Schematic representation of the 4:1 planar contraction geometry.

5.3.3.2 *Computational meshes*

The planar abrupt contraction is sketched in Figure 5.33. In the first set of simulations, only half of the two dimensional domain is used in the computations, with symmetry conditions imposed at the centre-line, $y = 0$. However, in a second set of simulations at high Deborah numbers, calculations were performed using the complete flow domain, so that possible symmetry-breaking flows and instabilities could be captured. All calculations were carried out at zero Reynolds number, $Re = \rho U H/\eta = 0$ (creeping flow), and at varying Deborah numbers, here defined as

$$De = \frac{\lambda U_2}{H_2}, \tag{5.38}$$

where H_2 and U_2 represent the half-width of the downstream channel and the corresponding average velocity (Figure 5.33). These variables are used as length and velocity scales. An inlet length $L_1 = 40H_2$ and an outlet length $L_2 = 100H_2$ were used to ensure complete flow development upstream and downstream of the contraction. At the inlet the velocity and stress profiles are prescribed by the analytical solutions, whereas at the outlets Neumann boundary conditions are imposed for all computed variables, except pressure which is linearly extrapolated from the two adjacent upstream cells. Calculations with the Oldroyd-B model were carried out with three meshes M1, M2 and M3, whose major characteristics are listed in Table 5.10. Mesh M3C maps the whole physical domain, but has the same characteristics of mesh M3, which relies on symmetry. All computational meshes are

orthogonal but non-uniform, and the concentration of cells is higher near the corner of the contraction and the walls (in such a way that $\Delta x_{min} = \Delta y_{min}$), where the stress/conformation tensor gradients are expected to be higher.

Table 5.10: Main characteristics of the 4:1 contraction computational meshes.

	NC	DOF	$\Delta x_{min}/H_2; \Delta y_{min}/H_2$
M1	5282	31692	0.020
M2	10587	63522	0.014
M3	42348	254088	0.0071
M3C	84696	508176	0.0071

5.3.3.3 *Low Deborah number flows*

In this section we analyse and compare the performance of the standard and the log-conformation formulations at low Deborah number flows, using the Oldroyd-B model as the constitutive equation and a viscosity ratio of $\beta = 1/9$. In this range of elasticity ($De = 3$) the flow is expected to be steady and this study is a standard benchmark problem serving as a precursor study to the unsteady flows of the next section.

Alves et al. (2000) used high order spatial discretization schemes and fine meshes to predict accurately the flow of UCM fluids in the 4:1 planar contraction, thus improving on earlier predictions of Oliveira and Pinho (1999a). Subsequently, Alves et al. (2003b) used a new discretisation scheme (CUBISTA) and simulated the flow of an Oldroyd-B fluid, achieving high accuracy and convergence up to $De = 2.5$ on their finest mesh. Their results in terms of vortex size were not much different from those previously obtained by Aboubacar and Webster (2001) using a hybrid finite volume/finite element scheme, although some differences were discernible. Later, high resolution results obtained by Kim et al. (2005b) in the same geometry with an Oldroyd-B model were also close to those of Alves et al. (2003b), but somewhat below even for Newtonian fluids. It is surprising that for this particular limiting case of Newtonian fluid ($De = 0$), the results of Aboubacar and Webster (2001) and Belblidia et al. (2006) are also underpredicting the vortex size compared to Alves et al. (2003b). Kim et al. (2005b) used a transient numerical algorithm based on the four-step fractional step method and DEVSS-G/DG with equal-order linear interpolation functions and also obtained converged solutions up to $De = 2.5$ with their finest mesh. More recently, the benchmark results of Alves et al. (2003b) were also confirmed by Belblidia et al. (2006), in their steady-state investigation with the Oldroyd-B model using different stabilisation methodologies embedded within a time-marching incremental pressure-correction formulation.

The results obtained in the present investigation for the corner vortex length ($X_R = x_R/H_2$), using the Oldroyd-B model with both ***StrT*** and ***LogT*** formulations, are presented in Table 5.11 for all meshes and are plotted in Figure 5.34 for the refined mesh M3. These results, irrespective of the formulation are graphically undistinguishable from the benchmark data of Alves et al. (2003b) and follow the trends of the recent data (Aboubacar and Webster, 2001; Kim et al., 2005b; Belblidia et al., 2006), with the length of the corner vortex decreasing with elasticity up to $De \approx 3$. We have then a quantitative confirmation that the

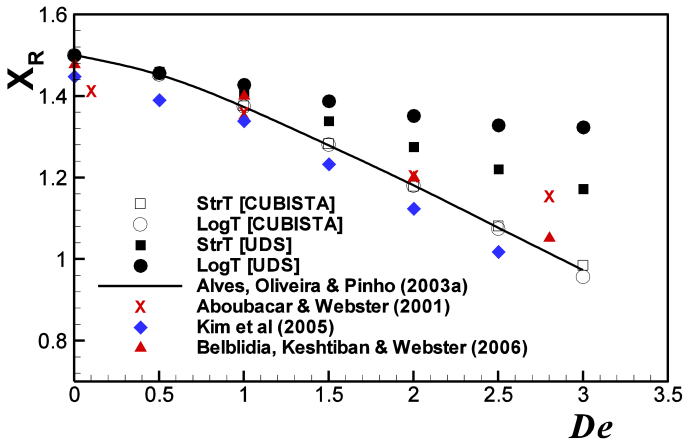

Figure 5.34: Dimensionless length of primary vortex ($X_R = x_R/H_2$) as function of Deborah number in mesh M3 (Oldroyd-B model). Comparison of two differencing shemes (UDS and CUBISTA) and results from various sources. The results of *StrT* and *LogT* methodologies were obtained with mesh M3.

Table 5.11: Dimensionless length of primary vortex (X_R) as a function of Deborah number, mesh, differencing scheme and stress formulation (Oldroyd-B model).

	M1				M2				M3			
	CUBISTA		UDS		CUBISTA		UDS		CUBISTA		UDS	
De	StrT	LogT	StrT	LogT	StrT	LogT	StrT	LogT	StrT	LogT	StrT	LogT
0.0	1.495	-	-	-	1.497	-	-	-	1.499	-	-	-
0.5	1.456	1.457	1.466	1.477	1.457	1.458	1.466	1.475	1.454	1.454	1.460	1.457
1.0	1.397	1.395	1.453	1.488	1.389	1.387	1.435	1.468	1.379	1.378	1.407	1.428
1.5	1.322	1.315	1.456	1.513	1.308	1.302	1.410	1.466	1.289	1.286	1.339	1.388
2.0	1.238	1.230	1.478	1.552	1.215	1.207	1.404	1.477	1.188	1.185	1.276	1.352
2.5	1.149	1.159	1.512	1.596	1.121	(1.117)[a]	1.414	1.503	1.091	(1.102)[a]	1.221	1.329
3.0	1.071	(1.056)[a]	1.569	1.652	1.026	(1.037)[a]	1.439	1.545	1.008	(1.065)[a]	1.173	1.324

[a] - X_R oscillates with harmonic periodicity.

log-conformation offers similar accuracy as the standard formulation, for steady state solutions, provided the CUBISTA scheme is used in the discretization of the convective term. Figure 5.34 also illustrates the detrimental effect in accuracy brought about by the highly diffusive upwind differencing scheme (UDS), in spite of allowing steady (but inaccurate) converged simulations to be obtained up to higher Deborah numbers ($De = 5.0$ on mesh M3). It is important to mention at this point that the ***LogT*** formulation, but not the ***StrT***, is able to predict an elastic instability, manifested as an unsteady behaviour at $De \approx 2.5$. This unsteadiness is captured with the CUBISTA scheme and a mesh that still relies on computations with flow symmetry imposed at the centre plane. To indicate unsteady flow, the values of X_R inside brackets in Table 5.11 represent the time-average value of X_R along the cycle of such harmonic oscillation. Note that Aboubacar and Webster (2001) have also reported the onset of time oscillations at $De \approx 2.5$ when using their finest mesh.

Figure 5.35 shows the coupled effect of mesh refinement and differencing scheme on the streamline patterns at $De = 2.5$, for both formulations. At this Deborah number simulations with the CUBISTA scheme on meshes M2 and M3 present the unsteady features just

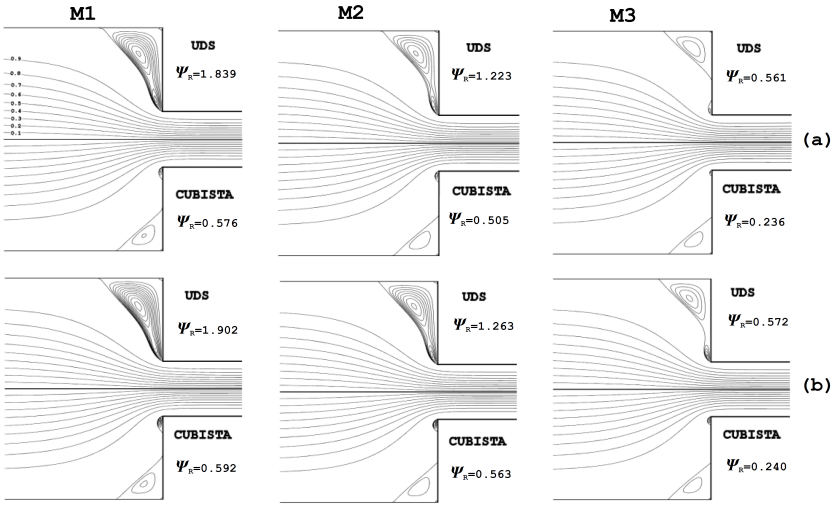

Figure 5.35: Coupled effect of mesh refinement and differencing scheme on the streamline patterns at De=2.5 for the Oldroyd-B model: (a) *StrT*; (b) *LogT*. Note: streamline spacing. Ψ_R= 0.2 × 10^{-3} inside the recirculations; Ψ_R multiplied by 10^3.

mentioned. All simulations with ***LogT*** result in higher values of the dimensionless intensity of recirculation, Ψ_R, than the ***StrT*** simulations, but in both cases those values tend to decrease with mesh refinement. The dimensionless intensity of the recirculation is defined as $\Psi_R = (\psi_{max} - \psi_{inl})/\psi_{inl} = \Psi_{max} - 1$, where ψ_{max} is the stream function value at the centre of the vortex and ψ_{inl} is the inlet value at the upper wall (assuming $\psi_{sym} = 0$ at the symmetry axis), which corresponds to the inlet flow rate per unit depth. The lip vortices in all ***LogT*** simulations are larger than those calculated with ***StrT***, but as refinement of the mesh increases both formulations converge towards the same solution.

Figure 5.36 displays streamlines and contour maps of the flow classification parameter x for increasing values of Deborah number, based on predictions with both ***LogT*** and ***StrT*** formulations, on the finest mesh M3. As the Deborah number was raised, the salient corner vortex decreased in size and strength while the lip vortex grew in intensity, with these lip vortices appearing at around $De \approx 1.5$ for both formulations. The comparison of **Figure 4** essentially confirms that no major differences exist between predictions with the ***StrT*** and ***LogT*** formulations at low Deborah number flows. However, a careful examination of the data in Figure 5.36 reveals that at $De \approx 2$ the simulations with the ***StrT*** formulation violate the minimum stability criteria, with the occurrence of negative values of det(**A**), while for the ***LogT*** simulations the minimum value of det(**A**) remains positive and greater than unity as it should (Hulsen et al., 2005). This constitutes a major advantage of the ***LogT*** formulation in high Deborah number simulations, because negative values of det(**A**), beside being physically incorrect, rapidly lead to numerical divergence of iterative methods, following an Hadamard kind of instability, a situation eventually occurring with the ***StrT*** formulation but not with the ***LogT*** formulation.

In the flow type contour maps presented in Figure 5.36, the three limiting types of flow are clearly identified: the region of plane shear flow, where $\xi \approx 0$ as indicated by point 3, in the vicinity of the walls

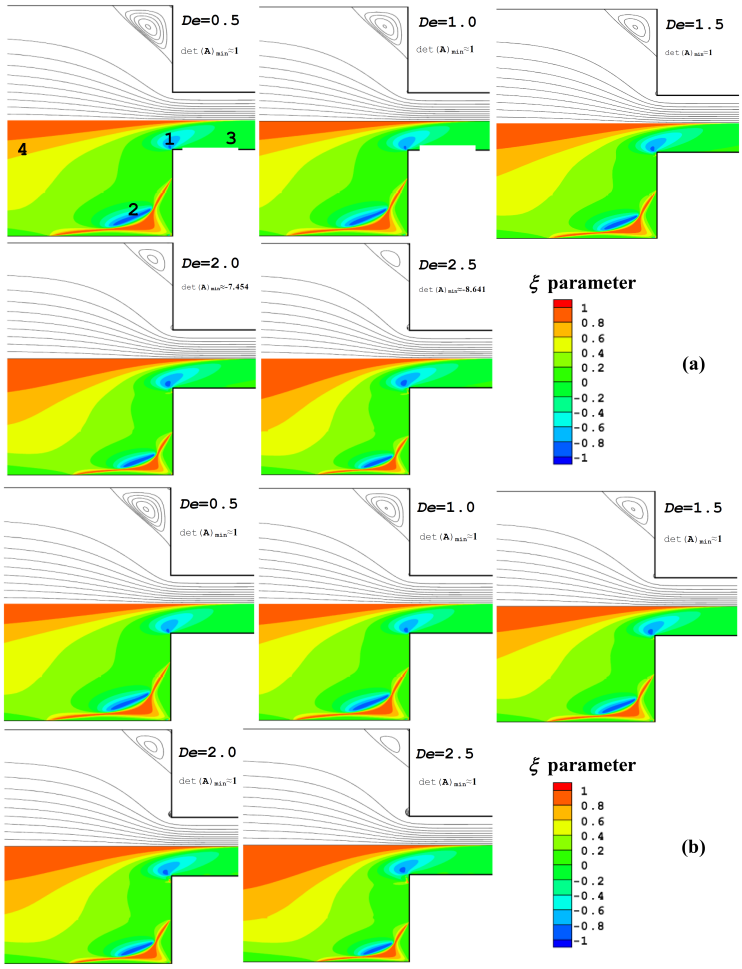

Figure 5.36: Flow patterns (top half) and maps of flow-type parameter (bottom half) as predicted on mesh M3 (Oldroyd-B model). (a) *StrT*; (b) *LogT*. (The values of $\det(\mathbf{A})_{min}$ are indicated beside each map).

especially in the smaller channel and elsewhere in the contraction zone; extensional flow ($\xi \to 1$, point 4) just upstream of the contraction plane and near the corner; and nearly rigid-body rotation flow, in two demarked zones of rotation ($\xi \to -1$; points 1 and 2). As De increases, the location and relative sizes of these zones evolves (irrespective of formulation): the size of the rotational region near the re-entrant corner increases; extensional flow in the corner decreases, and in the contraction entrance the region of extensional flow increases.

Figure 5.37 presents the longitudinal distribution of the first normal stress difference along the centreline and near the downstream channel wall, predicted on mesh M3 with the CUBISTA high-resolution scheme. As expected, there are no visible differences between the two formulations along the symmetry axis for the range of De at which the flow remains steady. This is especially clear for the profiles near the wall (at $y/H_2 = 0.993$) and in the vicinity of the salient corner where stresses grow intensively. However, significant discrepancies in the first normal stress difference, N_1, arise near the downstream duct wall at $De \approx 2.5$, which are related to the intensification of the flow unsteadiness predicted with the log-conformation method at high Deborah numbers, as discussed in the next section.

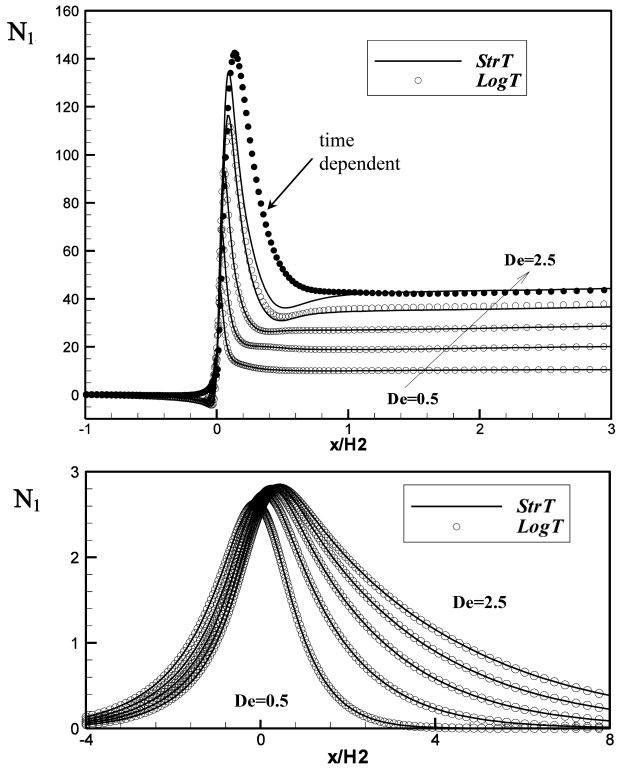

Figure 5.37: Distribution of the axial first normal stress differences near the downstream duct wall at $y/H_2 = 0.993$ (top) and along the centreline (bottom), calculated for increasing De (0.5, 1, 1.5, 2 and 2.5) on mesh M3 with *LogT* and *StrT* formulations (Oldroyd-B model).

5.3.3.4 *Non-linear dynamics at high Deborah number flows*

Time-dependent behaviour in the 4:1 abrupt contraction flow, associated to a pure elastic instability, has been observed in many experimental works (e.g. McKinley et al. 1991b; Chiba et al. 1990; Boger 1987) and some numerical investigations (Aboubacar and Webster, 2001; Oliveira, 2001c). Oliveira (2001c) reported velocity oscillations in his computations of creeping flow with the PTT and Giesekus models at high Deborah numbers ($De \approx 5$) using half the physical domain. In a numerical study of planar contraction flow with the Oldroyd-B model, El Hadj and Tanguy (1990) and Fortin and Esselaoui (1987) compared the solutions obtained using meshes mapping half and the full geometries, and reported the existence of multiple-solution families and the existence of an oscillatory flow in the contraction region at high Deborah number flows. Their simulations with the full contraction domain yielded stable as well as periodic solutions, with the frequency of the oscillations being roughly inversely proportional to the square root of the relaxation time.

We report now the most interesting results of the work, related to the dynamical aspects of the vortex motion and unsteady flow patterns formed upstream of the contraction plane at high De. Such flow features have never been reported before in numerical studies and it is only the ability of the log-conformation approach to maintain the positive definiteness of $\mathbf{A}$ and enhance numerical stability that makes these predictions possible. So, in order to obtain further insight into the fluid

dynamics of the flow, and in particular its inherent unsteadiness, a new set of simulations was performed using the mesh mapping the full physical domain M3C.

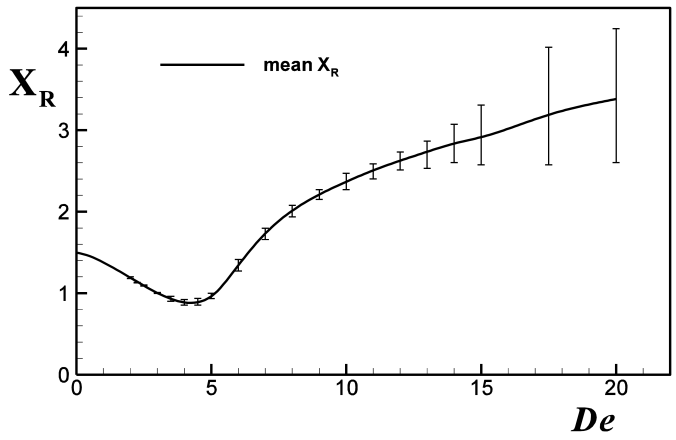

Figure 5.38: Time average dimensionless length of primary vortex (X_R) as function of Deborah number obtained with mesh M3C. Error bars represent the amplitude of the oscilations.

Convergent and steady results were obtained up to $De \approx 2.5$ for both the ***strT*** and ***LogT*** formulations. For $De > 2.5$ the flow became unsteady, and simulations with ***StrT*** diverged at $De = 3$. Simulations with ***LogT*** were not carried out beyond $De = 100$, due to computational time limitations and also due to insufficient inlet length to ensure complete flow development and corner vortex extension. In these unsteady simulations the number of time-steps per relaxation time is of the order of 5 000 and 25 000, at low and high Deborah numbers, respectively. Due to numerical simplicity and high stability, a first-order implicit Euler scheme for the time integration was used. Even though small times steps were used, time accuracy needs to be further investigated in the future, preferably using second-order time schemes.

Table 5.12: Mean dimensionless length of primary vortex (X_R) obtained with mesh M3C using the CUBISTA scheme.

De	StrT	LogT
0.5	1.454	1.454
1.0	1.380	1.378
1.5	1.290	1.287
2.0	1.191	1.191
2.5	1.086	1.093
3.0	-	1.002
3.5	-	0.931
4	-	0.887
5	-	0.889
6	-	0.962
7	-	1.342
8	-	1.732
9	-	2.012
10	-	2.210
15	-	2.915
20	-	3.383

The results obtained for the time-average corner vortex length (X_R), using the Oldroyd-B model with both ***StrT*** and ***LogT*** formulations and for mesh M3C, are presented in Table **5.12** and plotted in Figure 5.38 for ***LogT***. A non-monotonic evolution is observed, with a minimum value of X_R attained at $De \approx 4.5$ and then more than doubling at $De = 20$ relative to the Newtonian value. The error bars in Figure 5.38 indicate the amplitude of the X_R oscilations. A similar non-monotonic behaviour was recently reported by Howell (2009), using a continuation algorithm for the discontinuous Galerkin finite element approximation of the viscoelastic fluid flow in a 4:1 abrupt contraction. Their measured quantity was the solution norm, and for their refined mesh ($\Delta x_{min} \approx 0.125$ and $\Delta x_{min}/H = \Delta y_{min} \approx 0.03125$), they obtained a minimum value at $De \approx 5.7$. Otherwise, all other works we are aware of were confined to the range $De = 5$ and therefore the minimum and the upturning portions of the X_R.*vs*.De variation could not be anticipated.

Concerning the dynamics of the viscoelastic fluid, a variety of different flow regimes could be observed from our predictions while increasing the Deborah number. At low Deborah numbers ($De < 1.0$) the corner vortex decreases in size, and the fluid behaves as a highly viscous Newtonian fluid flowing through an abrupt contraction, with the fluid in the upstream duct converging and accelerating directly towards the downstream duct (*steady flow* regime). At $De_{lip} \approx 1.5$, a very weak elastic lip vortex can be observed at the edge of the re-entrant corner, as previously depicted in Figure 5.36. This lip vortex increases in size as the elasticity is further increased, while the length of the corner vortex still decreases. Up to this point the two vortices remain separated and their flow features are steady up to $De_{osc} \approx 2.5$, when very small oscillations are detected near the re-entrant corner.

Dynamical flow features in the next figures will be shown with help of instantaneous streamline plots and velocity history traces at a specific position, namely at the first internal node near the re-entrant corner at $x_L = x_{min}/2$ and $y_L = H_2 - y_{min}/2$ (cf. Figure 5.33). Improved understanding of the dynamic processes described below can be gained from observation of the movies which are deposited in the following web-address: `http://www.fe.up.pt/~mmalves/jfm2010/index.htm`.

Figure 5.39a presents an instantaneous plot of the flow pattern at $De = 3.0$, where the lip vortex is noticeable. At this Deborah number, the amplitude of the oscillations is still quite small as reported in Figure 5.40a, showing a time trace of the dimensionless axial velocity component (u_L/U_2) predicted next to the re-entrant corner at the monitoring location mentioned above. The corresponding fast Fourier transform is also represented in Figure 5.40a and we observe a dimensionless frequency spectrum with combined features of sub-harmonic period-doubling (with frequencies of half of the fundamental frequency, λf_1) as well as some harmonic frequencies (the peak at $2\lambda f_1$). To resume, for $2.5 \leqslant De \leqslant 4.5$ a regime of flow unsteadiness with periodicity sets in with lip vortex growth (*unsteady periodic* or *lip vortex growth* regime).

As the Deborah number is further increased, the elastic lip vortex increases in size (*lip vortex growth* regime), eventually reaching the corner vortex region, and merging with it in a fairly complex dynamic process. The beginning of this *merging-growth* regime occurs at $De_{merg} \approx 4.5$, corresponding to the minimum value of X_R shown in Figure 5.38. It is characterized by a complex interaction between very weakly pulsating lip and corner vortices, which tend to approach and separate. The

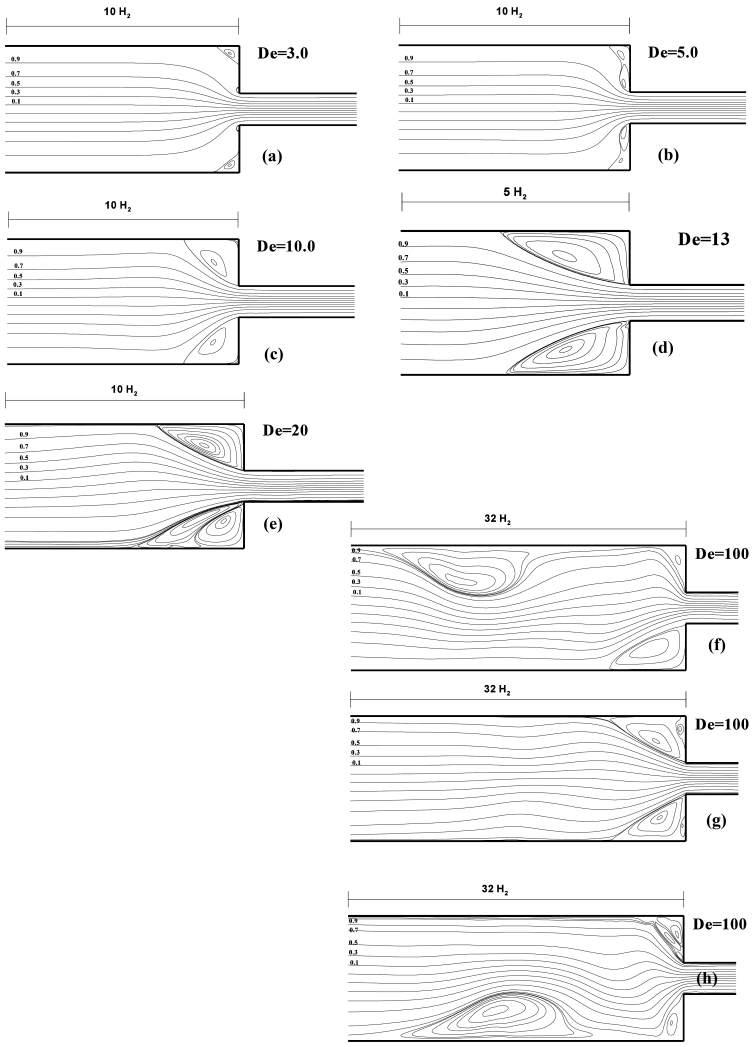

Figure 5.39: Illustration of the unsteady flow patterns at high Deborah numbers (mesh M3C and CUBISTA scheme).

variation of the corner vortex size is given by the error bars in Figure 5.38. In this process there is a mechanism of stress release whereby the first normal stress difference, N_1, near the downstream duct wall also varies between a maximum value, when the two vortices are more separated and a minimum when the vortices are closer. The shape of the boundary engulfing the two vortices is concave and there is also a top-bottom asymmetry, which is weak as seen in the instantaneous streamline plots of Figure 5.39b for $De = 5.0$, showing the formation of the large concave elastic vortex. As a consequence of the loss of symmetry the vortices become dissimilar in size and the longer vortex can appear on either wall. At this Deborah number, the dimensionless axial velocity component (u_L/U_2) oscillations are stronger, and higher harmonics of the dimensionless oscillation frequency ($2\lambda f_1$, $3\lambda f_1$) appear in the corresponding frequency spectrum presented in Figure 5.40b. Sub-harmonic period-doubling features (with $\lambda f_2 \approx \frac{1}{2}\lambda f_1$) are still observed and a very small symptom of quasi-periodicity emerges as a small peak of energy that can be identified as a linear combination of λf_1 and λf_2 (i.e., $m_1\lambda f_1 + m_2\lambda f_2$, with m_1 and m_2 integers).

For higher Deborah numbers, the dynamics and shape of the flow patterns change, exhibiting only a single large corner vortex with a convex boundary shape for $De_{cc} = 8$, as presented in the still image of Figure 5.39c pertaining to $De = 10$. This convex curvature of the vortex boundary is accompanied by *divergent flow streamlines* upstream of the abrupt contraction, a typical phenomenon usually observed in high De contraction flows (Alves and Poole, 2007). Simultaneously, the vortex increases in size and the unsteady flow behaviour becomes more noticeable. The top-bottom asymmetry continues to exist with the longer vortex alternating from the bottom to the top wall and vice-versa, as at lower De. Although the variation in X_R is not very large, as measured by the error bars of Figure 5.38, the process is clearly more complex exhibiting a wider range of characteristic frequencies as observed in Figure 5.40c, which plots the fundamental dimensionless frequencies of the oscillations of the axial velocity at the edge of the re-entrant corner. Again, quasi-periodic oscillations are evident, with dimensionless frequency peaks identified as multiple linear combinations of λf_1 and λf_2.

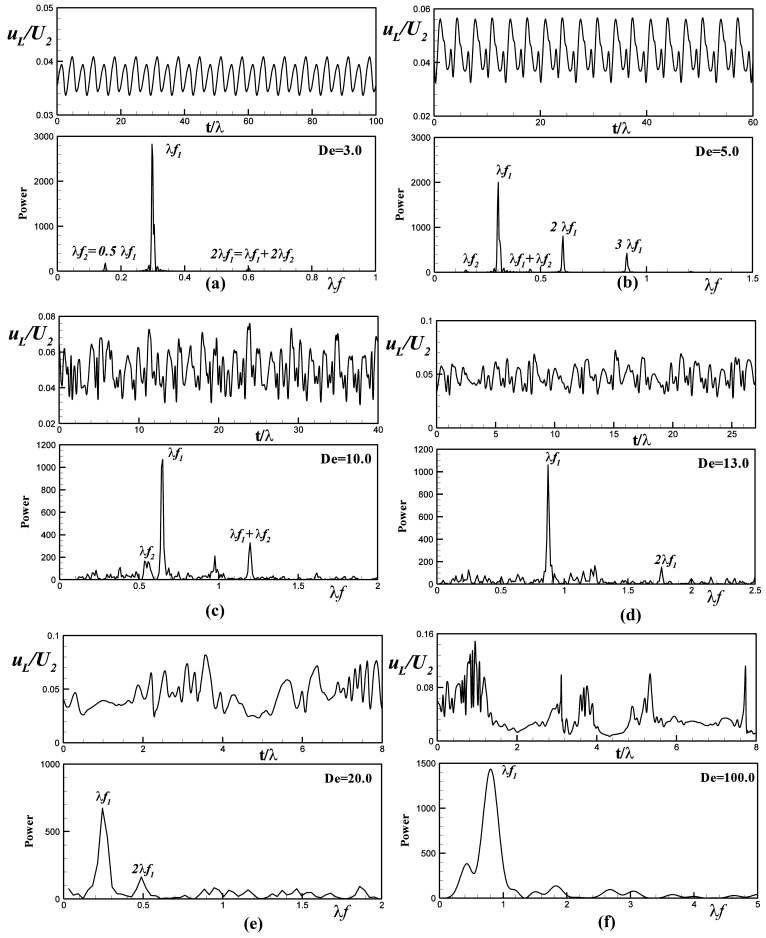

Figure 5.40: Velocity trace at $x_L = [x = x_{min}/2; y = H_2 - y_{min}/2]$ and FFT spectrum for: (a) $De = 3.0$; (b) $De = 5.0$; (c) $De = 10$ (d) $De = 13$, (e) $De = 20$ and (f) $De = 100$.

Further increasing the Deborah number after the elastic vortex enhancement ($De_{3rd} = 12$), a new kind of time-dependent instability arises, particularly near the re-entrant corner of the contraction, with

the appearance of a *third vortex* inside the larger corner vortices. This kind of elastic instability is often encountered in experimental studies, as the jetting instability upstream of a 4:1:4 axisymmetric contraction–expansion (Rothstein and McKinley, 2001), the *bent-elbow shape* streak lines close to the re-entrant corner of a 12:1 square-square contraction (Sousa et al., 2009) and the local instability associated with the formation and decay of a dip of the vortex boundary at the lip corner of a 4:1 circular contraction (Chiba et al., 2004). This is well shown by the instantaneous flow pattern obtained at $De = 13$ in Figure 5.39d. The amplitude of the oscillations is equivalent to those reported at $De = 10$, while the corresponding dimensionless fundamental frequencies have grown, as presented in the frequency spectrum of Figure 5.40d.

By increasing even more the elasticity of the fluid ($De_{bs} = 15$), there is an intensification of the third vortex, and the time-dependent nature of the flow undergoes a new transition into the so-called *third vortex growth and back-shedding regime*. The flow has large corner vortices, which have different sizes and hence the flow is asymmetric as well as periodic. Inside the existing shorter vortex, a new lip vortex is periodically generated in the vicinity of the re-entrant corner. This inner lip vortex grows first very quickly inside the original vortex eventually forcing it to elongate. As this elongation takes place, the inner lip vortex decreases in size and vanishes when the enveloping outer vortex reaches its maximum length. Simultaneously, the large vortex at the opposite wall decreases in size. This is shown in the instantaneous flow pattern obtained at $De = 20$ in Figure 5.39e. The dimensionless amplitude of the oscillations are now stronger and the top-bottom asymmetry is very clear and stronger than at lower De. As shown in the frequency spectrum presented in Figure 5.40e the corresponding dimensionless fundamental frequencies are now smaller than at lower De, no longer sharply defined but exhibiting a broader range of frequencies (broad-based peak) and there are still higher harmonics of the oscillation frequency $2\lambda f_1$.

As the Deborah number goes well beyond a value of 20, elastic effects become even more dramatic, and the inner lip vortex that we saw developing inside the large corner vortex at lower De, is now stronger and forces a detachment of the vorticity, which is shed in the upstream flow direction (*back-shedding*). This *back-shedding* of vorticity is sketched at three different times in the instantaneous flow patterns of Figures 5.39(fgh) for $De = 100$. The corresponding oscillations of the dimensionless velocity have large amplitudes, as presented in Figures 5.40(fgh) together with the FFT plot showing the predominant broad-based back-shedding frequency. Although at this Deborah number the ratio between the time step employed in the simulations and the relaxation time is $1/25000$, the spatial and temporal resolutions may not be sufficient for the same level of accuracy as before (in fact mesh M3C was shown to be well suited at small De, cf. Figure 5.34 and Table **5.11**), therefore these results at high De should be regarded as qualitative, meaning that this data is not of benchmark quality. In addition, accurate results in the back-shedding regime require the use of longer computational domains upstream of the contraction (and possibly downstream) than was the case here. Finally, as for other flows with a sequence of transitions (for instance, inertial transitions in the Newtonian fluid flow around a cylinder (Williamson, 1996) or elastic transitions in Taylor-Couette flow (Shaqfeh, 1996)) it is expected

that at some stage the flow becomes three-dimensional, thus requiring expensive full three-dimensional time dependent computations.

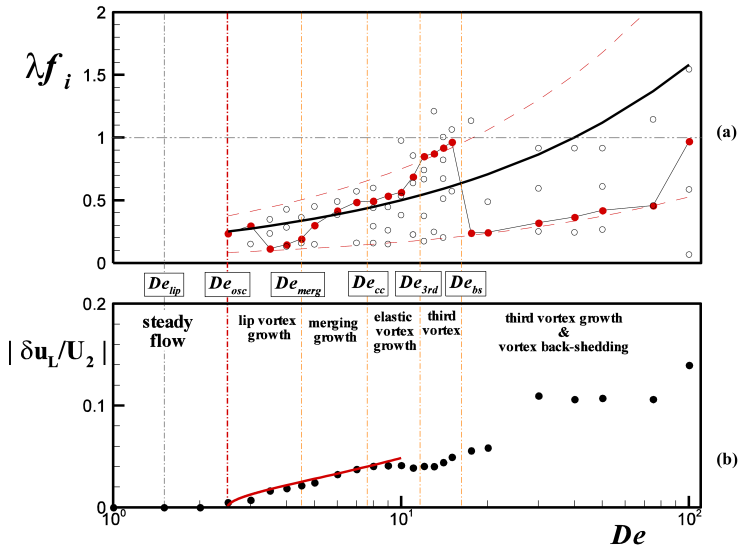

Figure 5.41: Dominant frequencies (a) and velocity amplitude at location $x_L = [x = x_{min}/2,\ y_L = H_2 - y_{min}/2]$ (b) as function of Deborah number obtained with mesh M3C. Lines in the frequencies graph are $\lambda f_i \propto a\sqrt{De}$ (with $a = 0.0527$, 0.1581 and 0.23715), as predicted by El Hadj and Tanguy (1990) and Fortin and Esselaoui (1987). Line in the amplitude graph represents the fitting to identify the critical Deborah number for the Hopf bifurcation to unsteady flow $|\delta_{u_L}| \propto \sqrt{De - De_{osc}}$.

Variations of the dominant frequencies and velocity amplitudes traced at the monitoring location X_L close to the corner are presented in Figure 5.41 as a function of Deborah number. The vertical lines refer to tentative values of characteristic Deborah numbers marking the onset of the various flow regimes described in the precedent discussion. The full thick line in Figure 5.41a represents the functional dependence $\lambda f_i = a\sqrt{De}$ with $a = 0.1581$, giving the dimensional frequency as inversely proportional to the square root of relaxation time (El Hadj and Tanguy, 1990; Fortin and Esselaoui, 1987) and the lower and upper dashed lines correspond to $\lambda f_i = a\sqrt{De}/3$ and $\lambda f_i = 3a\sqrt{De}/2$, respectively. Our predicted frequencies, with the dominant frequencies represented with full symbols and the other frequencies with open symbols, agree with $\lambda f_i = 0.1581\sqrt{De}$ at small and intermediate Deborah numbers ($De = 3$ and $5 \leqslant De \leqslant 11$), but fall below this line at higher Deborah numbers ($De = 20$), where the predicted data tend to agree better with the correlation of the lower dashed line, $\lambda f_i = a\sqrt{De}/3$. In the region $11 < De < 20$ the data agree with the upper line and we note that the beginning of the back-shedding regime ($De_{bs} \approx 15$) is characterized by a period of oscillation roughly equal to the fluid relaxation time, i.e., the product of Strouhal and Deborah numbers is unity ($St\ De = t_{flow} f_i$), which is in agreement with $\lambda f_i = 3a\sqrt{De}/2$. In the amplitude graph (Figure 5.41b), the full line represents the fit to identify the critical Deborah number for the Hopf bifurcation to unsteady flow ($|\delta u_L| \propto \sqrt{De - De_{osc}}$).

To quantify the energy losses in the flow of the Oldroyd-B fluid through the abrupt contraction, we evaluated the variation of the Cou-

ette correction coefficient (C_{corr}) with De. The Couette correction is the normalized pressure drop between inlet and outlet after discounting for the fully-developed pressure drop along the channels (i.e., it represents a dimensionless extra pressure drop due to flow redevelopment at the entrance of the smaller channel), and is calculated as:

$$C_{corr} = \frac{\Delta p - \Delta p_{FD}}{2\tau_w}, \tag{5.39}$$

where Δp is the pressure difference between the inlet and the outlet, Δp_{FD} is the pressure drop required to drive fully-developed flow in the inlet and outlet straight channels, as in the absence of the abrupt planar contraction, and τ_w is the wall shear stress under fully-developed flow conditions. In Figure 5.42 we plot C_{corr} on the basis of the time-average pressure differences, but error bars accounting for the dynamic process are included. In the literature there are only data for the steady flow regime (mainly for $De = 3$) and the present predictions agree with those of Alves et al. (2003b) and Aboubacar and Webster (2001) in the low De range. The plot shows that the energy losses for the Oldroyd-B fluid evolve non-monotonically with De, with an increase in C_{corr} occurring for $De > 20$, as had been seen in earlier studies for the PTT fluid (Alves et al., 2003b). It is interesting to notice, by comparing Figures 5.38 and 5.42 that the pressure drop is still decreasing when the vortex sizes are already growing, showing that both quantities are not directly related.

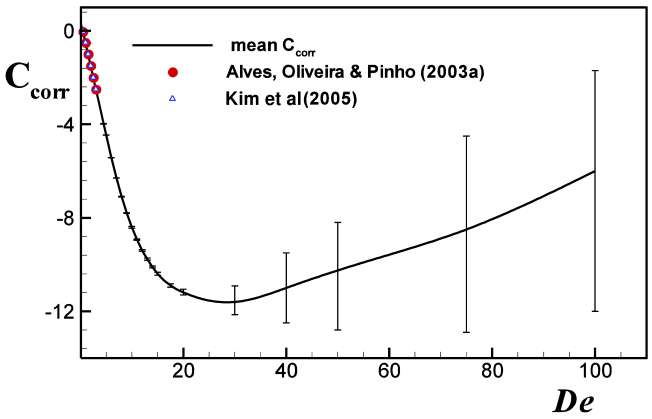

Figure 5.42: Time average Couette correction (C_{corr}) as function of Deborah number obtained with mesh M3C. Error bars represent the amplitude of the oscilations.

5.3.3.5 *Square-square three-dimensional abrupt contraction*

Flow geometry and computational meshes

The flow geometry is illustrated in Figure 5.43a. In this case, the full domain is used in all the simulations in order to be able to capture elastic flow asymmetries or instabilities that may arise. Inlet and outlet lengths are the same used for the two-dimensional problem, $L_1 = 40H_2$ and $L_2 = 100H_2$, which are long enough for complete flow development upstream and downstream of the contraction, as will be demonstrated. However, a difference relative to the 2D problem is that now, at the entrance of the inlet duct a uniform velocity profile is imposed, since for the PTT model the analytical solution for a square duct is not known;

at the exit Newmann boundary conditions are used as in the planar contraction flow.

Calculations with the Oldroyd-B and PTT models were carried out at a vanishing Reynolds number $Re = \rho U_2 H_2/\eta = 0$ (creeping flow) using the two meshes M40 and M56, characterised in Table 5.13. The mesh data in Table 5.13 includes the total number of control volumes in the meshes (NC), the number of degrees of freedom (DOF) and the minimum sizes near the re-entrant corners. Meshes M40 and M56 have 40 and 56 cells, respectively, in both transverse directions at the upstream channel. A zoomed view of mesh M56 near the contraction plane is depicted in Figure 5.43b. Another difference with the previous problem is that only steady-state results are reported here, and any detected sign of unsteadiness in the calculations will serve to identify the critical Deborah number. We restrict our analysis to steady flows due to the large CPU times that would be required for accurate unsteady flow calculations using viscoelastic models in a 3D geometry.

a)

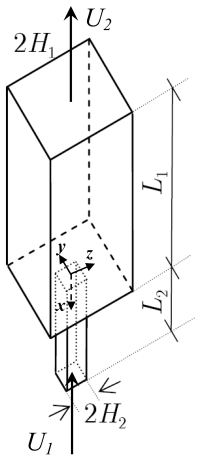

b)

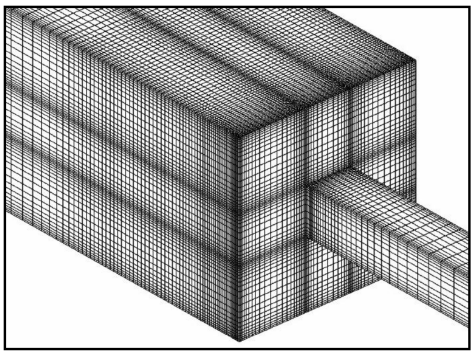

Figure 5.43: (a) Schematic representation of the 3D Square/Square 4:1 contraction geometry and (b) detailed view near the contraction plane for Mesh M56.

Table 5.13: Computational meshes used for the 4:1 3D square/square contraction flow.

	NC	DOF	$\Delta x_{min}/H_2$	$\Delta y_{min}/H_2$	$\Delta z_{min}/H_2$
M40	51000	510000	0.104	0.10	0.10
M56	312816	3128160	0.051	0.054	0.054

In the next sections we present qualitative (flow patterns on the symmetry planes and 3D streak lines) and quantitative results (vortex size measured along the diagonal plane and the central plane; distribution of the normalized first normal stress difference along the centreline and downstream channel wall; stability criteria). In section 5.3.3.6 we present results obtained for the Oldroyd-B model and in section 5.3.3.7 the results for the PTT fluid.

5.3.3.6 *Oldroyd-B model*

In this section we analyse the results obtained with the Oldroyd-B model having a viscosity ratio of $\beta = 0.59$. We start by comparing, in Figure 5.44, the theoretical and the numerical axial velocity profiles for fully developed flow at the inlet and outlet square channels. These predictions are for both ***StrT*** and ***LogT*** formulations at a Deborah number of 4.8, taken in the mid symmetry planes as a function of the transverse direction coordinates, y and z. The theoretical and numerical profiles match at this Deborah number, indicating that the assumed inlet and outlet lengths (L_1 and L_2) of the computational meshes are sufficient for complete flow development upstream before the flow reaches the contraction plane, and flow redevelopment downstream of the contraction. The theoretical velocity profile was calculated using the analytical solution for a Newtonian fluid in a square channel (White, 1991), which is also applicable for constant viscosity viscoelastic fluids (Boger fluids) such as those described by the Oldroyd-B model.

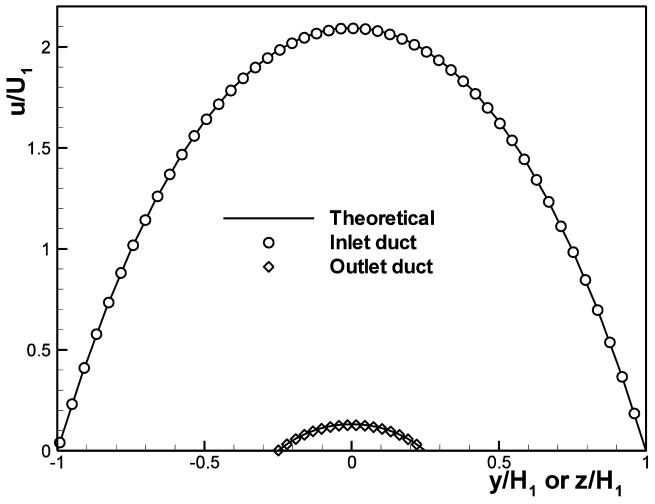

Figure 5.44: Theoretical and numerical axial velocity profiles along the transverse directions for the Oldroyd-B model at $De = 4.8$ (mesh M56).

Results for the normalized vortex lengths measured along the diagonal ($X_{DR} = x_{DR}/H_1$) and horizontal/vertical ($X_{HR} = x_{HR}/H_1$) planes, for both the ***StrT*** and ***LogT*** formulations, are presented in Figure 5.45. These data are now scaled with the upstream channel half-width, for consistency with previous works (Alves et al., 2005, 2008; Sousa et al., 2009), and were predicted on meshes M40 and M56 with two different interpolating schemes for the convective terms in the constitutive equation (UDS and CUBISTA). Again, numerical diffusion introduced by the upwind scheme allows much higher De numbers to be reached, at the expense of a loss in accuracy indicated by the significant tendency

to over predict the vortex size. Steady solutions having similar accuracy were obtained up to $De \approx 4.8$ with both formulations, when the finest mesh and the CUBISTA scheme are employed. For these conditions, the simulations with the ***StrT*** formulation diverged at $De \approx 5$ while the simulations with the ***LogT*** formulation continue to converge up to $De \approx 22$, with noticeable unsteady behaviour, particularly for $De = 20$. The normalized vortex lengths measured along the diagonal and the horizontal/vertical planes increase significantly with Deborah number (cf. Figure 5.45), and there is close agreement between results calculated using the two formulations. On the coarse mesh M40, the critical Deborah number for onset of time-dependent flow raised to $De \approx 6.4$ and $De \approx 8.0$ for the ***strT*** and ***LogT*** formulations, respectively, raising even further to $De \approx 6.9$ and $De \approx 48$ when using the UDS scheme with the ***StrT*** and ***LogT*** formulations, respectively. This is, once again, an unambiguous demonstration of the stabilising effect of the numerical diffusion inherent to the upwind scheme (Alves et al., 2000, 2003b), which comes, unfortunately, accompanied by a significant loss of accuracy, as observed from the ***StrT*** results, with both X_{DR}, and X_{HR} deviating significantly from the accurate predictions obtained on a finer mesh with the CUBISTA scheme. Even though Figure 5.45 shows that for this particular flow UDS in conjunction with the ***LogT*** formulation provides results closer to those obtained with both a precise interpolation (CUBISTA) scheme and the finest mesh M56 (especially for X_{HR}, cf. Figure 5.45), showing that this formulation is not so sensitive with respect to the interpolation scheme as is the standard formulation, we cannot conclude that the ***LogT*** formulation is more accurate than the ***StrT*** methodology, or otherwise. Indeed, a different trend was observed in the planar contraction flow (cf. Figure 5.34).

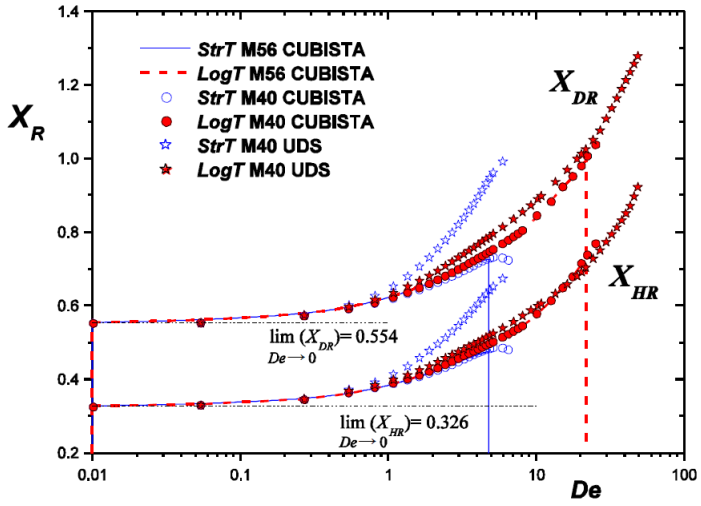

Figure 5.45: Dimensionless vortex length measured along the diagonal ($X_{DR} = x_{DR}/H_1$) and horizontal/vertical ($X_{HR} = x_{HR}/H_1$) planes as a function of Deborah number obtained with M40 and M56. Oldroyd-B model.

Figure 5.46 shows maps of stream trace patterns taken in the mid symmetry plane ($y = 0$ or $z = 0$) and the diagonal plane ($z = \pm y$) with both formulations (for each case, the top half shows ***StrT*** and the bottom half shows ***LogT*** predictions) up to the critical Deborah number

for the ***StrT*** formulation. These predictions were based on mesh M56 and the CUBISTA scheme.

The flow patterns displayed in Figure 5.46 predicted with the two formulations are quite similar at each De, except for a slight difference observed at $De \approx 4.8$, when a small "lip vortex" near the re-entrant corner in the horizontal plane becomes visible in the predictions with the ***StrT*** formulation. The minimum value of the stability criterion, $\det(\mathbf{A})$, is approximately equal to one for all simulations, therefore no problems of lack of numerical convergence and stability occurred in these simulations. Regarding the flow type, Figure 5.46 shows a contour plot of ξ, demonstrating that the flow in the central part of the geometry is essentially of extensional nature, except near the walls where the expected shear flow is observed. However, in contrast to the 2D case, we do not observe the small regions of solid-body rotation near the re-entrant and salient corners, presumably because of the extra shear introduced by the secondary flow along the third coordinate, which is typical in this geometry, as discussed below. When increasing the Deborah number, there is an important increase in the extensional nature of the flow in the recirculation zone, visible in both the diagonal and lateral symmetry planes. At $De = 4.8$ we see the first instances of some differences between predictions by the ***StrT*** and ***LogT*** formulations, especially in the diagonal symmetry plane where the lengths of the vortices become noticeably different. These differences are better seen in Figure 5.47, which plots the streamwise variation of the normalized first-normal stress difference (N_1) close to the downstream channel wall as predicted by the ***StrT*** and ***LogT*** formulations.

The three-dimensional nature of the open recirculations for Newtonian and viscoelastic flows through square-square abrupt contractions was previously reported and analysed by Alves et al. (2008), where a good agreement with experiments was also shown. As commented in the introduction, they also reported a flow inversion due to elastic effects in the 3D 4:1 square-square contraction using shear-thinning fluids. Sirakov et al. (2005) commented upon a similar flow inversion in their 3D simulations of a square to circular cross-section contraction flow. This fluid dynamical inversion was also observed experimentally by Sousa et al. (2009) using Boger fluids, thus confirming that the effect is due to elasticity and not to the shear-thinning nature of the fluid.

To corroborate the flow visualizations of Sousa et al. (2009), in this work we present the first numerical evidence that the fluid dynamical inversion for Boger fluids can be predicted with the Oldroyd-B model. Figure 5.48 shows streamline plots and the corresponding flow-type classification maps (ξ) calculated in the symmetry planes for the flow of Oldroyd-B fluids at $De \geqslant 7.5$, predicted on mesh M56 and with the ***LogT*** formulation. For the Newtonian case (cf. Figure 5.46a for $De = 0$) and low De, the fluid particles departing from the top corner of the diagonal plane ($z = \pm y$, Figure 5.48b) enter the recirculation in the diagonal plane, rotate toward its centre and then flow towards the horizontal/vertical plane vortex ($y = 0$ or $z = 0$, Figure 5.48a), where they rotate back from the eye of the recirculation to the outside before exiting the contraction near the re-entrant corner. At high Deborah numbers (e.g. $De = 15$ or 20 in Figure 5.48) the flow direction inside the recirculation inverts, and the fluid particles enter the recirculating region at the middle plane vortex ($y = 0$ or $z = 0$, Figure 5.48a winding

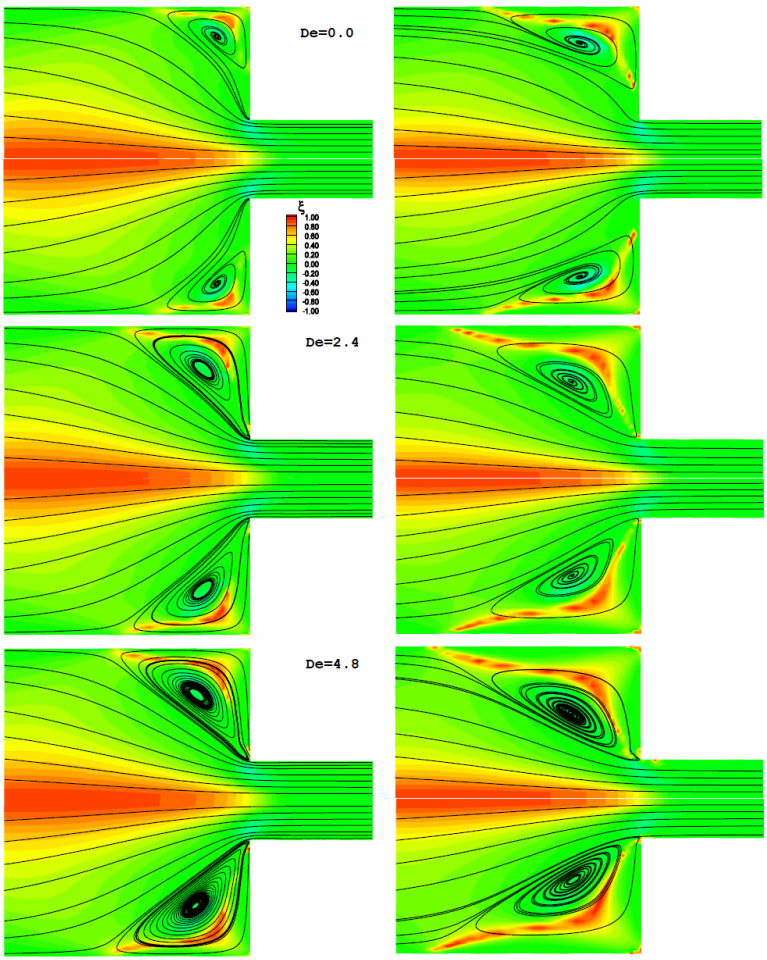

Figure 5.46: Flow patterns and 3D flow-type parameter (ξ) predicted for the Oldroyd-B model on mesh M56. (top half) *StrT*; (bottom half) *LogT*;. Left column: mid symmetry plane ($y = 0$ or $z = 0$) and right column: diagonal plane ($z = \pm y$).

through its eye and drifting from here to the diagonal vortex ($z = \pm y$, Figure 5.48b where they unwind to exit the contraction. That is, we have now exactly the opposite behaviour of that seen at low De, as far as the secondary flow in the recirculation region is concerned. Regarding the flow type classification contours, also plotted in Figure 5.48, increasing the Deborah number leads to a significant increase in the extensional nature of the flow in the central part of the geometry as well as inside the recirculation zone, in both the mid ($y = 0$ or $z = 0$) and diagonal symmetry planes ($z = \pm y$). At the highest Deborah numbers there is also an enhancement of the Moffatt recirculation (Moffatt, 1964) at the salient corner of the contraction particularly noticeable at the diagonal mid plane.

5.3.3.7 *PTT model*

In this section we analyse the results obtained with the PTT model having a viscosity ratio of $\beta = 1/9$. The PTT model is shear-thinning in viscosity and in the first normal stress coefficient, in contrast to the Oldroyd-B model used in the previous Sections. The extensional viscosity is bounded due to the non zero value of the new parameter

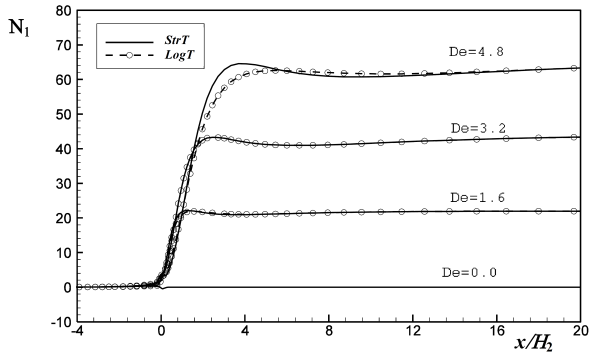

Figure 5.47: Axial first normal stress difference along a line close and parallel the downstream duct wall for the Oldroyd-B model on mesh M56 and using the CUBISTA scheme. Comparison of the results from the two formulations.

ε appearing in the stress coefficient function, since the steady-state extensional viscosity is inversely proportional to ε, at low ε values. If this extensional parameter is set to 0, then $Y(\mathrm{tr}\mathbf{A}) = 1$ and the Oldroyd-B constitutive equation is recovered. In this work we perform computations for $\varepsilon = 0.02$ and $\varepsilon = 0.25$, typical of dilute and concentrated polymer solutions, respectively.

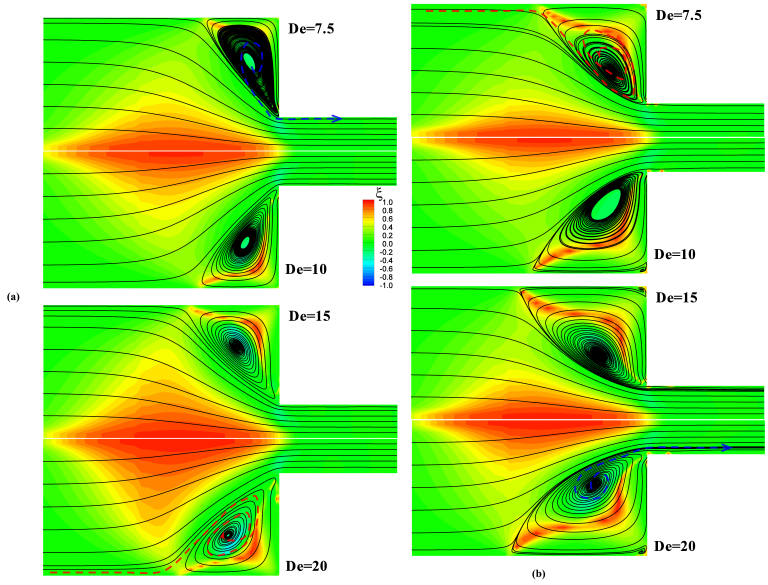

Figure 5.48: Flow patterns and 3D flow-type parameter (ξ) predicted at high Deborah numbers for the Oldroyd-B model on mesh M56. (a) mid symmetry plane ($y = 0$ or $z = 0$) and (b) diagonal plane ($z = \pm y$).

Results for the vortex length along the diagonal (X_{DR}) and horizontal/vertical (X_{HR}) symmetry planes for both the ***StrT*** and ***LogT*** formulations, are presented in Figure 5.49. These predictions were obtained on meshes M40 and M56 with the CUBISTA high-resolution scheme for the two extensibility parameters, $\varepsilon = 0.25$ and $\varepsilon = 0.02$. For the lower value of ε ($\varepsilon = 0.02$), the simulations with the ***StrT*** formulation diverged at $De \approx 2$ and $De \approx 4$ with meshes M56 and M40, respectively. Note that when $\varepsilon \to 0$ the PTT model reduces to the Oldroyd-B model and, as remarked before, a probable cause for divergence is the loss of

positive definiteness of the conformation tensor. For the ***LogT*** formulation with $\varepsilon = 0.02$, the value of $\det(\mathbf{A})_{min}$ was always positive, as per design of the ***LogT*** methodology, showing no sign of loss of evolution up to $De \approx 20$ and $De \approx 30$ with meshes M56 and M40, respectively (cf. Figure 5.49a). Such significant increase in the critical Deborah number for steady flow by almost an order of magnitude clearly shows the advantage of using the ***LogT*** formulation in a flow problem possessing a geometrical singularity. At the higher value of ε ($\varepsilon = 0.25$), the superiority of the ***LogT*** formulation shows even more clearly with no signs of loss of evolution or divergence up to $De \approx 10000$, while for the ***StrT*** formulation loss of evolution occurs at $De \approx 90$ and $De \approx 60$ with meshes M40 and M56, respectively, as shown in Figure 5.49b. We further note that the two formulations provide similar results up to the point where the standard stress formulation is unable to provide an adequate numerical solution.

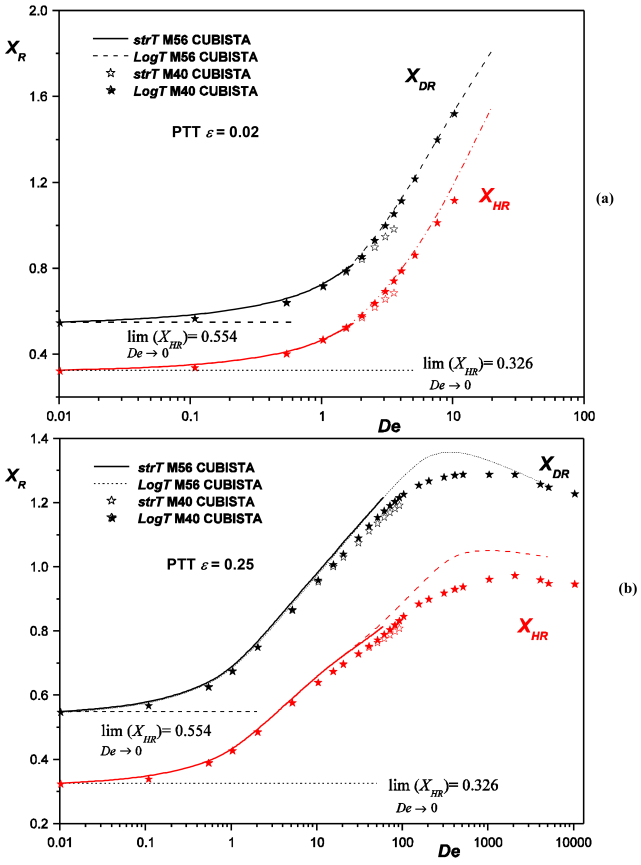

Figure 5.49: Dimensionless vortex length measured along the diagonal ($X_{DR} = x_{DR}/H_1$) and horizontal/vertical ($X_{HR} = x_{HR}/H_1$) planes as a function of Deborah number obtained with M40 and M56. PTT model with (a) ε=0.02 and (b) ε=0.25.

Figure 5.50 presents the flow patterns and contours of the flow-type classification parameter (ξ) predicted with the PTT model ($\varepsilon = 0.25$) on mesh M56 with the ***LogT*** formulation. For this shear-thinning fluid, both the vortex lengths along the diagonal diagonal (X_{DR}) and horizontal/vertical (X_{HR}) symmetry planes increase up to $De \approx 100$, and then the value remains almost constant, as shown in Figure 5.49b. As for the Oldroyd-B fluid increasing the Deborah number leads also

to a significant increase in the extensional nature of the flow in the central part of the geometry and also in the recirculation zones in both symmetry planes ($y = 0$ or $z = 0$ in Figure 5.50a) and $z = \pm y$ in Figure 5.50b)). Looking more carefully at the flow patterns in the diagonal plane ($z = \pm y$ in Figure 5.50b) at large De ($De = 100$), we see the growth of a second recirculation at the salient edge of the contraction, which could explain the stabilisation of the length of the main vortex. As for the Oldroyd-B fluid, the elasticity-driven inversion of the secondary flow is clearly apparent for higher Deborah numbers ($De = 100$), as previously reported by Alves et al. (2008).

5.3.4 *Conclusions*

High elasticity simulations of 2D and 3D entry flows are reported, and were possible due to the use of the log-conformation formulation technique of Fattal and Kupferman (2004) in combination with a high-resolution finite volume method.

For the 2D 4:1 abrupt contraction flow of the Oldroyd-B fluid, which has a constant shear viscosity as in real Boger fluids, the flow becomes unstable at a relatively low critical De of about 2.5, which is of the same order attained in most previous works. On increasing De the flow exhibits local unsteadiness which tends to grow as elasticity is further increased, eventually leading to an asymmetric flow regime with alternate back-shedding of vorticity from the two pulsating recirculating eddies formed on the top and bottom walls of the upstream channel. Dominant frequencies were determined via FFT of velocity signals, showing a tendency for a frequency doubling mechanism at high De eventually leading to a chaotic regime. Average vortex size and overall pressure drop were computed from the time evolution of the predicted data and show the typical upturn shape seen in experimental data and in the recent multiscale simulations of Koppol et al. (2009), with an initial steep decrease followed by strong enhancement when plotted against De. However, the doubling of the excess pressure drop above the Newtonian value was not predicted with the present Oldroyd-B simulations, presumably because of its physical limitations regarding the transient extensional viscosity behaviour.

For the 4:1 square-square 3D abrupt contraction, simulations were carried out both with the Oldroyd-B and the PTT models, but they were restricted to steady flows. Very high Deborah numbers were attained ($De \approx 20$ for PTT model with $\varepsilon = 0.02$ and $De \approx 10000$ for PTT model with $\varepsilon = 0.25$), with prediction of strong vortex enhancement and inversion of the sense of rotation of fluid particles inside the vortices, previously observed experimentally with Boger fluids, but not reported numerically with constant viscosity model fluids.

These high Deborah number calculations could only be performed with the log-conformation technique, whereas the standard stress formulation systematically diverged beyond a critical low De. When both methods converge to a steady solution, the use of the log-conformation technique provides results of global and local quantities, such as eddy size and stress profiles that cannot be distinguished visually from those of the standard approach when refined meshes and accurate discretization schemes are used. Thus, these computations show well that at least in the scope of the finite volume procedure the log conformation for-

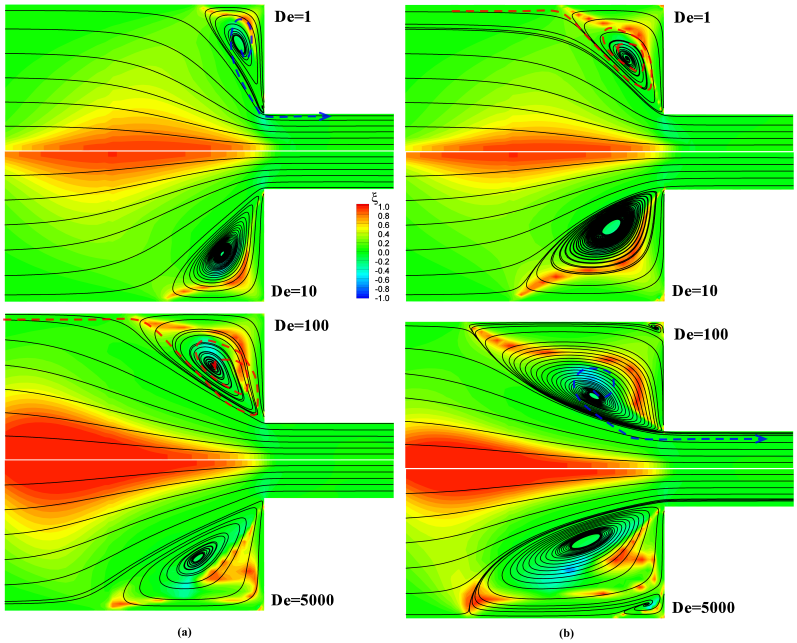

Figure 5.50: Flow patterns and 3D flow-type parameter (ξ) predicted at high Deborah numbers for the PTT model (ε=0.25) on mesh M56. (a) mid symmetry plane ($y = 0$ or $z = 0$) and (b) diagonal plane ($z = \pm y$).

mulation is superior to the standard approach that uses the extra-stress tensor as dependent variable.

5.3.5 *Acknowledgements*

The authors acknowledge funding from Fundação para a Ciência e a Tecnologia (FCT), placecountry-regionPortugal, through projects PTDC/EQU-FTT/70727/2006 and PTDC/EQU-FTT/ 71800/2006. A.M. Afonso is grateful to FCT for financial support through scholarship SFRH/BD28828/2006. P.J. Oliveira also acknowledges a sabbatical leave conceded by Universidade da Beira Interior.

6

THE *ECCENTRIC* PURELY ELASTIC INSTABILITIES AND *(FURTHER)* DEVELOPMENTS

6.1 PURELY-ELASTIC FLOW INSTABILITIES IN A 3D SIX ARMS CROSS SLOT GEOMETRY

Abstract[1]
The creeping flow of an upper-convected Maxwell (UCM) fluid is investigated numerically in a three-dimensional orthogonal cross-slot geometry. We analyse two different flow configurations corresponding to uniaxial extension and biaxial extension, and assess the effects of extensional flow type, Deborah and Reynolds numbers on flow dynamics near the interior stagnation point. Using these two flow arrangements the amount of stretch and compression near the stagnation point can be varied, providing further insights on the viscoelastic flow instability mechanisms in extensionally-dominated flows with an interior stagnation point. The uniaxial extensional flow arrangement leads to the onset of a steady flow asymmetry, followed by a second purely elastic flow instability that generates an unsteady flow at higher flow rates. On the other hand, for the biaxial extension flow configuration a symmetric flow is observed up to the critical Deborah number when the time-dependent purely-elastic instability sets in, without going through the steady symmetric to steady asymmetric transition. **Keywords:** 3D Cross-slot; Elastic instability; UCM model; Flow bifurcation; Finite-Volume method.

6.1.1 *Introduction*

The occurrence of purely-elastic instabilities in several canonical viscoelastic fluid flows is now a recognized fact. These instabilities are often present in extensionally-dominated viscoelastic flows containing an interior stagnation point, such as the opposed jet devices (Chow et al., 1988), the four roll mill apparatus (Lagnado et al., 1984) and cross-slot geometry (Lagnado et al., 1984; Poole et al., 2007c). Purely elastic instabilities have also been observed in shear flows with or without extensional flow contributions. Examples of the former are found in the flow in the mixing-separating geometry investigated by (Afonso et al., 2010d) and in converging flows in abrupt contractions (Alves et al., 2008; Sousa et al., 2009) or in T-like geometries (Oliveira et al., 2009; Soulages et al., 2009). The Taylor-Couette instability is an example of a shear flow without extensional flow contributions in which elastic instabilities arise (Muller et al., 1989; Larson et al., 2006; Muller et al.,

1 A.M. Afonso, M.A. Alves, F.T Pinho (2010). Purely-Elastic flow instabilities in a 3D six arms cross slot geometry, *Journal of Non-Newtonian Fluid Mechanics* **165** 743–751.

1993), but other shear flows with streamline curvature also originate elastic instabilities (Pakdel and McKinley, 1996; McKinley et al., 1996), which can eventually lead to elastic turbulence as argued by Groisman and Steinberg Groisman and Steinberg (2000, 2004), and provided the instability threshold is independent of the wave number. These pure shear flows of viscoelastic fluids with streamline curvature are linearly unstable, as quantified by various criteria (Larson et al., 2006; Joo and Shaqfeh, 1992), and summarized by the Pakdel-McKinley criterion (Pakdel and McKinley, 1996). Theoretical modeling of extension dominated flows and its instabilities and singularities have also been extensively investigated, as in the works of Rallison and Hinch (1988), Renardy (2006), Thomases and Shelley (2007, 2009) and Becherer et al. (2008). These flows have received particular attention recently due to their potential use in the measurement of the extensional viscosity of dilute polymer solutions in micro systems, where the elastic nature of the fluid is amplified by the small scales (Squires and Quake, 2005).

Of particular relevance to this study is the experimental observation of instabilities in a "quasi two-dimensional" cross-slot microchannel flow by Arratia et al. (2006) (this cross-slot is bounded by flat top and bottom walls), which motivated the numerical work by Poole et al. (2007c) on the two-dimensional cross-slot flow of an upper-convected Maxwell (UCM) fluid under low Reynolds flow conditions. These authors were able to predict the onset of a bi-stable steady asymmetric flow above a critical Deborah number (De), followed by a second transition to a time dependent flow at higher De. These numerical results were qualitatively in agreement with the experimental observations of the quasi two-dimensional flow of Arratia et al. (2006). Subsequently, Poole et al. (2007b) considered the true three-dimensional nature of a real microfluidic cross-slot flow and investigated the effect of the aspect ratio of the geometry, by varying the depth of the slot channel from a quasi-Hele-Shaw flow configuration up to large aspect ratios (quasi-2D flow). Later, Poole et al. (2007a) incorporated the effect of solvent viscosity ($\beta \neq 0$ in the Oldroyd-B model) and finite extensibility ($\varepsilon \neq 0$ in the sPTT model), presenting $\beta - Re - De$ and $\varepsilon - Re - De$ maps of flow pattern types, showing the existence of a narrow region where steady asymmetric flow can emerge, and identified the limiting De for onset of time dependent flow. The effect of finite extensibility was also studied numerically by Rocha et al. (2009) and analytically by Becherer et al. (2008), using FENE models.

In this work the previous investigations for planar geometries (Poole et al., 2007c,b,a) are extended to three-dimensional cross-slot flows with inlets and outlets in the three orthogonal directions. A 3D finite-volume numerical method is used to study the viscoelastic flow inside a 3D six arms cross flow geometry considering two symmetric flow configurations that lead to uniaxial and biaxial extensional flows, respectively. The influence of the ratio of inlet to outlet flow rates and of the Deborah and Reynolds numbers on the onset of the flow instability are investigated numerically in order to demonstrate its purely elastic nature.

The remaining of this paper is organized as follows: in Section 6.1.2 we present the governing equations and briefly describe the numerical method used in their solution. Section 6.1.3 presents the computational meshes and describes the flow problem under analysis. The numerical

results are presented and discussed in Section 6.1.4, before ending the paper with the main conclusions of this study.

6.1.2 *Governing equations and Numerical Method*

The equations to be solved are those of conservation of mass

$$\nabla \cdot \mathbf{u} = 0, \tag{6.1}$$

and momentum

$$\rho \frac{\partial \mathbf{u}}{\partial t} + \rho \nabla \cdot \mathbf{u}\mathbf{u} = -\nabla p + \nabla \cdot \boldsymbol{\tau}, \tag{6.2}$$

of an incompressible fluid, together with an appropriate constitutive equation for the extra-stress, $\boldsymbol{\tau}$. In this work, for reasons of rheological simplicity, the UCM model is used

$$\boldsymbol{\tau} + \lambda \left(\frac{\partial \boldsymbol{\tau}}{\partial t} + \nabla \cdot \mathbf{u}\boldsymbol{\tau} \right) = \eta \left(\nabla \mathbf{u} + \nabla \mathbf{u}^T \right) + \lambda \left(\boldsymbol{\tau} \cdot \nabla \mathbf{u} + \nabla \mathbf{u}^T \cdot \boldsymbol{\tau} \right), \tag{6.3}$$

where λ and η are the relaxation time and shear viscosity of the fluid, respectively. An alternative formulation of this constitutive law writes the extra-stress tensor as an explicit function of the conformation tensor $\mathbf{A}$, which for the UCM model reads as,

$$\boldsymbol{\tau} = \frac{\eta_p}{\lambda} \left(\mathbf{A} - \mathbf{I} \right). \tag{6.4}$$

Then, the conformation tensor $\mathbf{A}$ is described by an evolution equation which for the UCM is

$$\lambda \left(\frac{D\mathbf{A}}{Dt} - \nabla \mathbf{u} \cdot \mathbf{A} - \mathbf{A} \cdot \nabla \mathbf{u}^T \right) = \left(\mathbf{A} - \mathbf{I} \right). \tag{6.5}$$

The main advantage of this transformation is on its numerical solution since it provides the possibility of using the log-conformation technique, introduced by Fattal and Kupferman (2004), which has been shown to lead to a significant increase of numerical stability (Kwon, 2004; Hulsen et al., 2005; Coronado et al., 2007; Afonso et al., 2009b; Kane et al., 2009). In this technique a simple tensor-logarithmic transformation is performed on the conformation tensor for differential viscoelastic constitutive equations. This technique can be applied to a wide variety of constitutive laws and in the log-conformation representation the evolution equation (6.5) is replaced by an equivalent evolution equation for the logarithm of the conformation tensor,$\boldsymbol{\Theta} = \log \mathbf{A}$, benefiting from the fact that $\mathbf{A}$ is a symmetric positive definite matrix, and thus can be diagonalized into the form (Fattal and Kupferman, 2004)

$$\mathbf{A} = \mathbf{O}\mathbf{X}\mathbf{O}^T, \tag{6.6}$$

where $\mathbf{O}$ is an orthogonal matrix generated with the eigenvectors of matrix $\mathbf{A}$ and $\mathbf{X}$ is a diagonal matrix created with the corresponding three distinct eigenvalues of $\mathbf{A}$. The transformation from equation (6.5) to an equation for Θ is described by Fattal and Kupferman (2004), and leads to

$$\frac{\partial \boldsymbol{\Theta}}{\partial t} + (\mathbf{u} \cdot \nabla)\boldsymbol{\Theta} - (\mathbf{R}\boldsymbol{\Theta} - \boldsymbol{\Theta}\mathbf{R}) - 2\mathbf{E} = \frac{1}{\lambda} \left(e^{-\boldsymbol{\Theta}} - I \right). \tag{6.7}$$

In Eq. (6.7) $\mathbf{R}$ and $\mathbf{E}$ are a pure rotational tensor and a traceless extensional tensor, respectively, which combine to form the velocity gradient tensor (Fattal and Kupferman, 2004). To recover $\mathbf{A}$ from $\boldsymbol{\Theta}$ the inverse transformation $\mathbf{A} = e^{\boldsymbol{\Theta}}$ is used when necessary. The extra-stress tensor can be obtained, if necessary, using Eq. (6.4).

A fully-implicit finite-volume method was used to solve Equations (6.1) – (6.7). This fully-implicit FVM is based on a time marching pressure-correction algorithm and is formulated with the collocated variable arrangement. The numerical method used to solve the log-conformation evolution equation is explained in detail in Afonso et al. (2009b) and in some papers therein. The advective terms were discretized with the CUBISTA high-resolution scheme (Alves et al., 2003a), formally of third-order accuracy. Along with inertial effects, in this work we will also focus on creeping-flow conditions, in which case the advective term in the momentum equation is neglected.

6.1.3 *Flow problem and computational meshes*

The three-dimensional cross-slot geometry is illustrated in Figure 6.1, for the two flow configurations studied in this work.

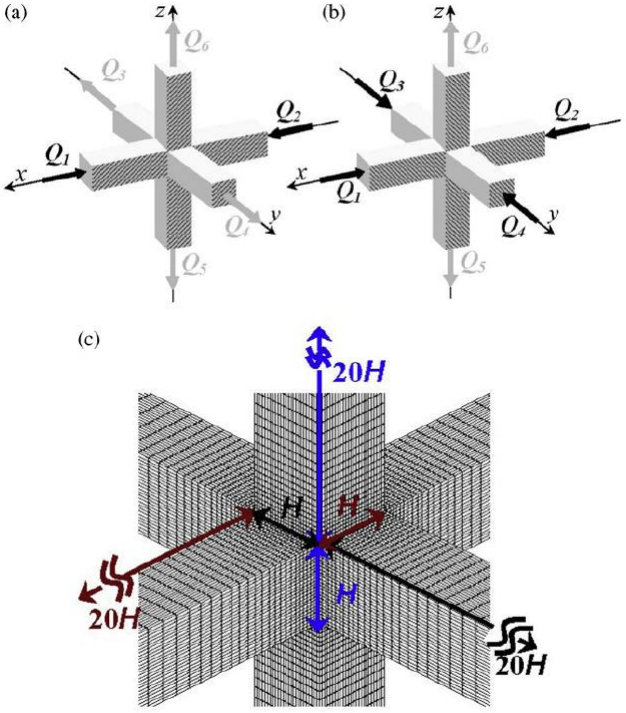

Figure 6.1: Schematic view of the cross-slot geometry: (a) biaxial extension configuration ($I_o = 2 : 4$); (b) uniaxial extension configuration ($I_o = 4 : 2$) and (c) zoomed view of the mesh near the center.

The geometries are identified by the ratio of the number of inlets to the number of outlets (I_o): the biaxial extension configuration ($I_o = 2 : 4$) has two inlets (Q_1 and Q_2) and four outlets (Q_3 to Q_6) and the uniaxial extension configuration ($I_o = 4 : 2$) has four inlets (Q_1 to Q_4) and two outlets (Q_5 and Q_6).

These configurations generate different degrees of stretch and compression near the stagnation point, providing new insights into the

viscoelastic flow instability mechanism in cross-slot flows. For the coordinate system illustrated in Figure 6.1, and using the definition of strain rate tensor (Walters et al., 2009), its components at the stagnation point are given by

$$\dot{\varepsilon}_{ij} = \dot{\varepsilon}_0 \begin{bmatrix} -(m+1) & 0 & 0 \\ 0 & m & 0 \\ 0 & 0 & 1 \end{bmatrix} \tag{6.8}$$

Depending on the value of the parameter m, different types of extensional flow can be observed near the interior stagnation point. For the biaxial extension configuration ($I_o = 2:4$), represented in Figure 6.1a, $m = 1$, while for the uniaxial extension configuration ($I_o = 4:2$), sketched in Figure 6.1b, $m = -1/2$. In general, for extensional flows m is in the range $-1/2 \leqslant m \leqslant 1$.

The central region of the cross-slot, corresponding to the intersection of the six arms, defines a cube with side length H. The length of the inlet and outlet "arms" is $L = 20H$. Fully-developed velocity (with an average value U) and stress profiles are imposed as inlet boundary conditions, while at outlets Neumann boundary conditions are imposed to all variables, i.e. $\partial\varphi/\partial x = 0$, including the pressure gradient. Previous works for 2D flow (Poole et al., 2007c,b,a) confirm that further increases in the inlet and outlet arms lengths have a negligible effect on the critical Deborah number for elastic instabilities and on the flow patterns. The Deborah number is here defined as $De = \lambda U/H$ and the Reynolds number as $Re = \rho UH/\eta$.

The mesh used in the numerical simulations has a total of 203,125 cells, corresponding to 2,031,250 degrees of freedom. A zoomed view of the mesh at the central region of the cross-slot is also presented in Figure 6.1c, along with a description of relevant dimensions. The central cubic region of the cross-slot has 25 cells along each direction (x, y and z), corresponding to minimum cell sizes of $\Delta x_{min}/H = \Delta y_{min}/H = \Delta z_{min}/H = 0.04$. Increasing the mesh refinement leads to significant increases in the CPU times, due to the three-dimensional nature of the flow, therefore more detailed three-dimensional mesh refinement studies will be undertaken in the future. For this particular mesh, we can estimate the numerical uncertainty of the results to be less then 5% from the investigation of the corresponding 2D flows of (Oliveira et al., 2009; Rocha et al., 2009), where extensive mesh refinement studies were carried out. These three dimensional simulations were carried out in a AMD dual core with 2 GHz and 2 GB of RAM and each complete simulation for steady state flow conditions took on average from 12 to 24 hours of CPU time at low De, going up to about 340 hours of CPU time at the highest De, where the flow is asymmetric.

6.1.4 *Results*

Due to the complex three dimensional flow dynamics it is more difficult to quantify the flow asymmetry than for two-dimensional flows. For that purpose we used the main direction angles of the rate of deforma-

tion tensor at the interior stagnation point. To obtain such angles we decomposed the deformation rate tensor,

$$\mathbf{D} = \frac{1}{2}\left[\nabla\mathbf{u} + (\nabla\mathbf{u})^{T}\right], \tag{6.9}$$

into its eigenvalues and corresponding right eigenvectors,

$$\mathbf{D}v_i = \lambda_i v_i \qquad i = 1,2,3 \ \text{(no summation on } i\text{)}. \tag{6.10}$$

The eigenvectors v_1, v_2, and v_3 are the principal directions of the deformation rate tensor, i.e. the shear-free directions, and the corresponding eigenvalues λ_1, λ_2, and λ_3 are the principal strain rates, thus quantifying the elongations in the principal directions. Finally, we define the *direction angles* as the angles between the principal directions of the deformation rate tensor and the versors that define the coordinate system $(\hat{\mathbf{e}}_j)$, $\kappa_{ij} = \arccos\left(v_i \cdot \hat{\mathbf{e}}_j / \|v_i\|\right)$ (no summation over identical indices). In particular, we are interested in the *main direction angles*, which are obtained when $i = j$.

Results are presented in section 6.1.4.1 for the flow in the biaxial extension configuration ($I_o = 2:4$) and in section 6.1.4.2 for uniaxial extensional flow ($I_o = 4:2$).

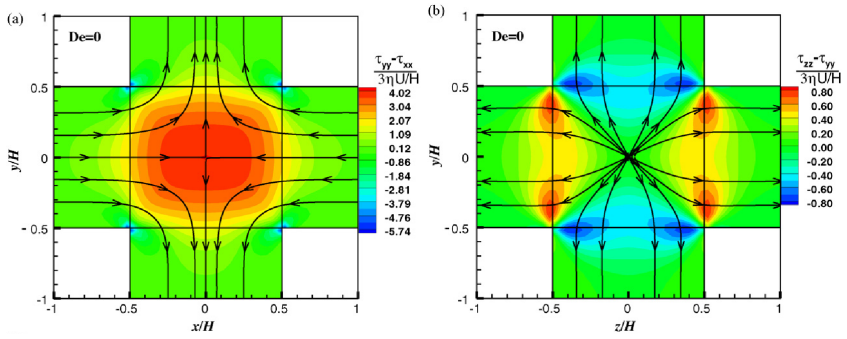

Figure 6.2: Flow patterns and contour plots of normalized first normal-stress differences for Newtonian flow for $I_o = 2:4$ at centre planes (a) xy and (b) yz.

6.1.4.1 *Biaxial extension configuration* ($I_o = 2:4$)

The creeping-flow simulations for the biaxial extension flow ($I_o = 2:4$) did not present any signs of asymmetry up to $De \approx 0.61$. The principal angle directions calculated in the vicinity of the central stagnation point, show that the three ii remain constant with the increase of the Deborah numbers up to $De \approx 0.61$, with $\kappa_{11} = \kappa_{22} = \kappa_{33} = \pi/4$. Under these conditions the flow is shear free in this central region as can be observed in Figures 6.2 and 6.3, where the flow characteristics are shown via stream traces and contour plots of normalized normal-stress differences, $(\tau_{jj} - \tau_{ii}) / (3\eta U/H)$, for Newtonian and $De = 0.6$ flows, respectively (no summation over repeated indices and $i \neq j$). It is clear that the flow remains symmetric for these two cases. At $De \approx 0.3$ we start to observe the appearance of symptoms of diverging streamlines (Alves and Poole, 2007) in the yz centreplane, the plane where the strain rate is positive,

but the flow remains symmetric in relation to all planes (no change in ii).

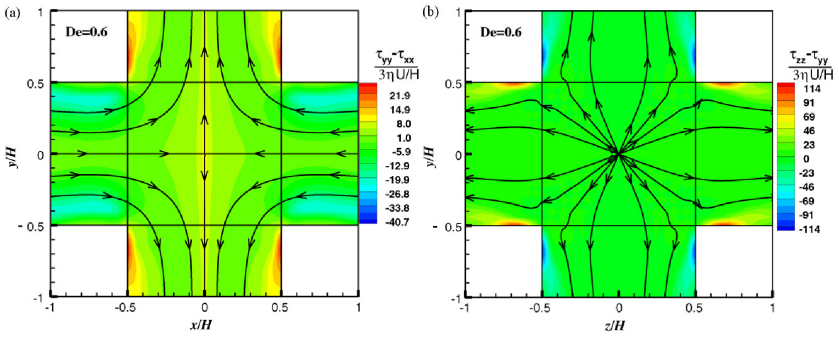

Figure 6.3: Flow patterns and normalized first normal-stress differences contours at $De = 0.6$ for $I_o = 2 : 4$ at centre planes (a) xy and (b) yz.

The *diverging streamlines* phenomenon is seen when we also observe the waved stream traces near the corners of the two exit ducts, especially at higher De, as shown in Figure 6.3. Then, above a critical Deborah number, $De = 0.62$, the flow becomes unsteady, with oscillations occurring in all directions. Thus, in the biaxial extension flow, the first transition is directly from a steady symmetric flow to a time dependent flow, not showing the intermediate regime of a bi-stable steady asymmetric flow, as reported by Arratia et al. (2006); Poole et al. (2007c,b) for a planar cross-slot geometry.

Becherer et al. (2008) argued that a transition from a steady to a time dependent 2D flow in a cross-slot geometry is a purely elastic instability of a highly elastic flow with curved streamlines (McKinley et al., 1996) and usually is a Hopf bifurcation. However, that referred to a steady asymmetric flow that had previously transitioned from being-extensional dominated to being shear-dominated. This earlier transition has not been observed here in this biaxial extensional flow, which evolves directly from the steady symmetric to an unsteady flow, even though the Reynolds number is zero. So, a question arises as to whether the generalization of Becherer et al. (2008) can be extended to any extensional 3D flow or just to uniaxial extension, where there is a transition from steady symmetric to steady asymmetric flow, as will be shown in the next section.

For the biaxial extensional flow ($I_o = 2 : 4$) the effect of inertia is very small for the studied Re range [$Re \leqslant 2$], with the critical Deborah number for the onset of unsteady behavior being nearly constant, as observed in the $Re - De$ stability map of Figure 6.4, i.e. inertia has a very small destabilizing effect regarding this transition in biaxial extensional flow. Further research into this problem requires the use of finer meshes. For all simulations with $I_o = 2 : 4$, the results in planes xy and xz were similar.

6.1.4.2 *Uniaxial extension configuration* ($I_o = 4 : 2$)

For the uniaxial extensional flow case ($I_o = 4 : 2$) a transition from steady symmetric flow in all planes (cf. Figure 6.5) to a steady asymmetric flow was observed at a rather small critical Deborah number ($De_{crit} \approx 0.22$). Figures 6.5 and 6.6 show the flow patterns and contour

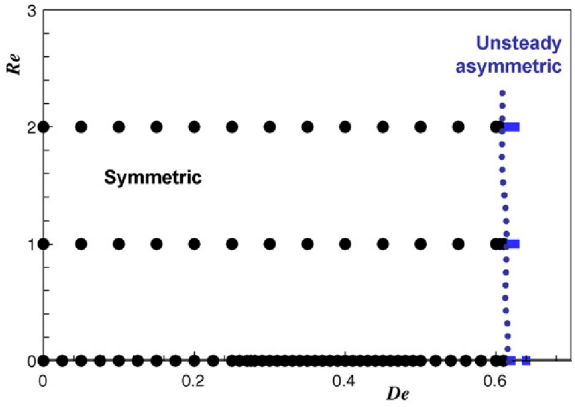

Figure 6.4: Re–De stability map for the biaxial extension flow configuration ($I_o = 2:4$).

plots of normal stress differences for $I_o = 4:2$ at $De = 0$ and $De = 0.3$ at centre planes xy and yz (similar to the flow pattern at plane xz), respectively. The asymmetric flow is clear with the inlet flow dividing by different amounts into the two z-direction channels and in the distortion of the stress contour levels at the centre (the stress contours are antisymmetric when the flow is symmetric). We note that in Figure 6.6 we are plotting the projected streamtraces since the visualized planes are no longer symmetry planes. When the flow is symmetric (as in Figure 6.5) the real streamtraces are plotted.

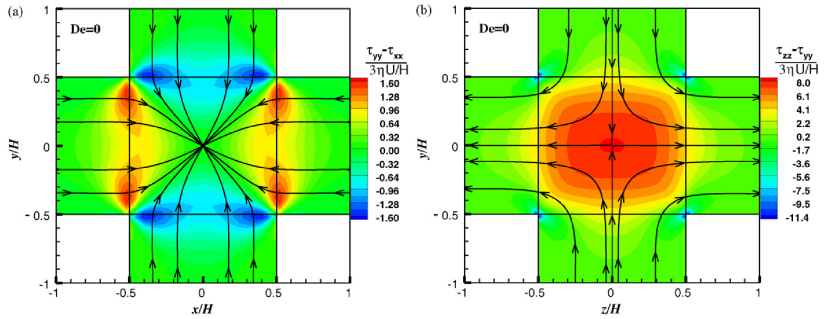

Figure 6.5: Flow patterns and contour plots of normal-stress differences for Newtonian flow for $I_o = 4:2$ at centre planes (a) xy and (b) yz.

When the flow is asymmetric, the flow distortion can be quantified using the main direction angle in the z-direction (κ_{33}), as presented in Figure 6.7. This clearly shows that an asymmetric flow exists and that the flow at the center is no longer purely extensional, but is a combination of shear and extension. This is more evident in the flow type plots presented in Figure 6.8, where the following parameter is used to quantify the local flow type:

$$\xi = \frac{|\mathbf{D}| - |\mathbf{\Omega}|}{|\mathbf{D}| + |\mathbf{\Omega}|}. \tag{6.11}$$

where $|\mathbf{D}|$ and $|\mathbf{\Omega}|$ represent the magnitudes of the rate of deformation tensor -equation (6.9) - and vorticity tensor,

$$\mathbf{\Omega} = \frac{1}{2}\left[\nabla\mathbf{u} - (\nabla\mathbf{u})^{T}\right], \tag{6.12}$$

which can be calculated as

$$\begin{aligned} |\mathbf{D}| &= \sqrt{\frac{1}{2}\left(\mathbf{D}:\mathbf{D}^{T}\right)} = \sqrt{\frac{1}{2}\sum_{i}\sum_{j} D_{ij}^{2}} \\ |\mathbf{\Omega}| &= \sqrt{\frac{1}{2}\left(\mathbf{\Omega}:\mathbf{\Omega}^{T}\right)} = \sqrt{\frac{1}{2}\sum_{i}\sum_{j} \Omega_{ij}^{2}}. \end{aligned} \tag{6.13}$$

this flow type parameter has previously been used by Lee et al. (2007) and Mitsoulis and Hatzikiriakos (2009) and apparently much earlier by Fuller and Leal (1980), amongst others.

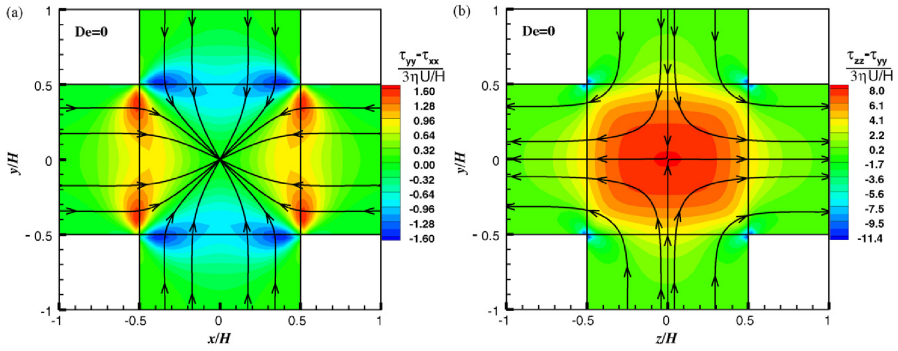

Figure 6.6: Projected stream lines at centre planes (a) xy and (b) yz. Also shown are the contour plots of normal-stress differences for $De = 0.3$ ($I_o = 4:2$).

The flow type parameter varies from $\xi = -1$, which corresponds to solid-like rotation, up to $\xi = 1$, which corresponds to extensional flow. A shear flow is identified when $\xi \to 0$. As observed in Figure 6.8, for the Newtonian fluid the flow in the central part of the geometry is essentially of extensional nature, except near the walls where the expected shear flow is observed. On the other hand, for $De = 0.3$ we can observe an important shear region near the stagnation point, thus showing that the transition to asymmetric flow is accompanied by a flow type transition, from an extensionally dominated flow to a situation where shear effects become dominant. In order to better understand this transition, we plot in Figure 6.9 the variation with De of the local Weissenberg number, $Wi = \lambda\dot{\varepsilon}$, calculated at the stagnation point. The strain rate at the stagnation point can be calculated from the second and third invariants of the rate of deformation tensor (Bird et al., 1987a; Walters et al., 2009),

$$\dot{\varepsilon} = 3\frac{I_3(D)}{I_2(D)} = \frac{6\ \det(D)}{\mathrm{tr}(D^2)}. \tag{6.14}$$

As observed in Figure 6.9, for low Deborah numbers ($De < 0.05$) there is a linear relation between Wi and De. As the coil stretch transition

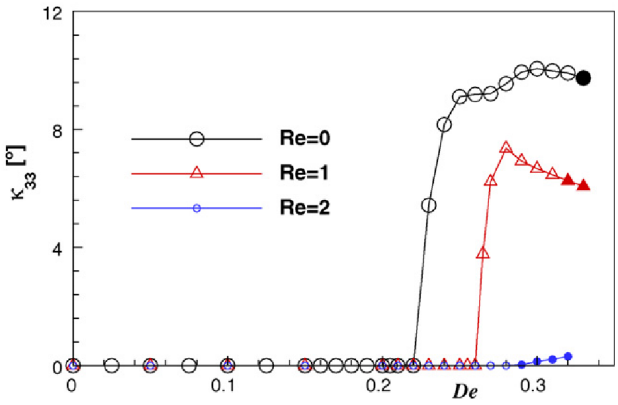

Figure 6.7: Variation of main direction angle κ_{33} with Deborah number at the center of the cross-slot for uniaxial extension flow ($I_o = 4:2$). Full symbols represent unsteady simulations.

is approached ($Wi = 0.5$) Wi tends to a plateau. We note, however, that for $De > 0.1$ the local Weissenberg number at the stagnation point exceeds the critical value ($Wi = 0.5$) and the stream wise normal stress becomes unbounded. As also found for the planar cross slot flow, it is not the unbounded nature of the normal stress at the stagnation point that drives the first instability (Poole et al., 2007c). Indeed, for the planar cross slot this instability is also observed with models that have bounded extensional viscosities, such as the FENE-CR model used by Rocha et al. (2009). However, until the critical De, the local Weissenberg number at the stagnation point does not increase further, otherwise the singularity of the normal stress field would become more severe (Becherer et al., 2008). When the asymmetric flow sets in, we observe a significant decrease of ξ at the stagnation point, with a transition to a shear-dominated flow, as also shown in Figure 6.9.

Becherer et al. (2008) analytically studied the effect of the boundary conditions for the normal and shear components of the stress tensor at the inflow boundaries of the central region of the cross-slot flow geometry. The authors argued that the first instability observed in the cross-slot geometry (Arratia et al., 2006; Poole et al., 2007c,b) corresponds to a switching from elongational-dominated to shear-dominated velocity field, whereas the second transition is that of a shear-dominated flow with curved streamlines, in agreement with the present results. In Figure 6.9 we also plot the variation of Wi at the stagnation point with De for the biaxial extension configuration ($I_o = 2:4$), and it is clear that the asymmetric steady flow configuration is not observed because of the lower Wi values attained before the onset of the unsteady instability. Presumably, for the $I_o = 2:4$ when the extensional flow becomes unstable any asymmetric steady shear flow is inherently unstable and the transition is directly from steady extensional to unsteady flow.

We have also undertaken simulations in a geometry consisting of one eighth of the full domain (for $I_o = 4:2$), and imposing symmetry at the geometric xy, xz and yz symmetry planes crossing the origin of the Cartesian system of coordinates. For lower Deborah number conditions ($De < De_c$) the results with the full geometry and the geometry with imposed symmetry coincide. However, above the critical De the artificially imposed symmetry will be representative of the flow field that would be obtained if there was no perturbation in the flow

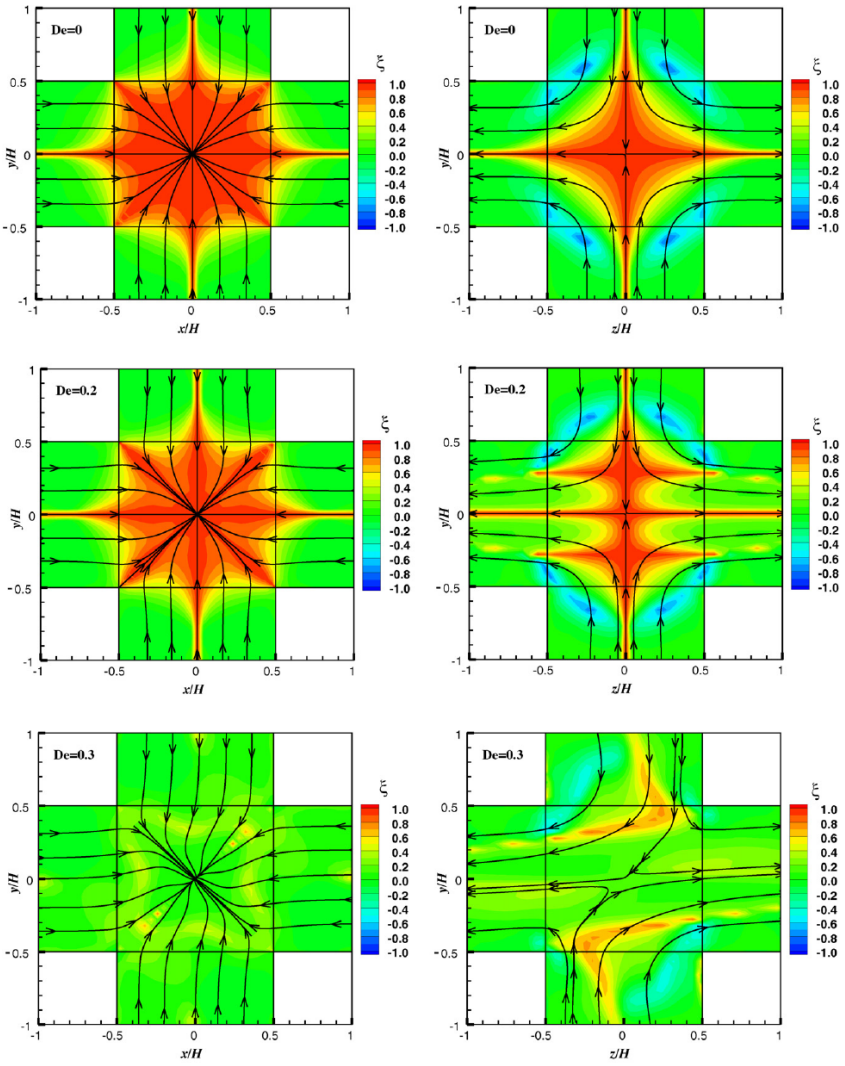

Figure 6.8: Flow type parameter and projected stream lines at centre planes xy and yz for $De = 0$, 0.2 and 0.3.

that drives the asymmetry. As shown in Figure 6.9, in this case the flow at the stagnation point is still extensionally dominated ($\xi \approx 1$), in contrast with the full mesh simulations where the transition to a quasi shear flow is observed, with a simultaneous increase of the local deformation rate.

Further increasing the Deborah number leads to a second flow transition from a steady asymmetric flow to an unsteady asymmetric flow as in the experiments of Arratia et al. (2006) and in the 2D numerical works of Poole et al. (2007c,b) for "quasi 2D" and 2D cross slot flows, respectively. This is seen in the stability map of Figure 6.10 for $Re = 0$, where the two Deborah numbers for the first and second transitions are approximately 0.22 and 0.32, respectively.

Regarding the effect of flow inertia, the trends are different for the first and second transitions: whereas inertia has a stabilizing effect for the first transition from steady symmetric to steady asymmetric flow (the first critical Deborah number increases with Re), for the second transition from steady asymmetric to unsteady flow inertia helps destabilize the flow and the second Deborah number decreases

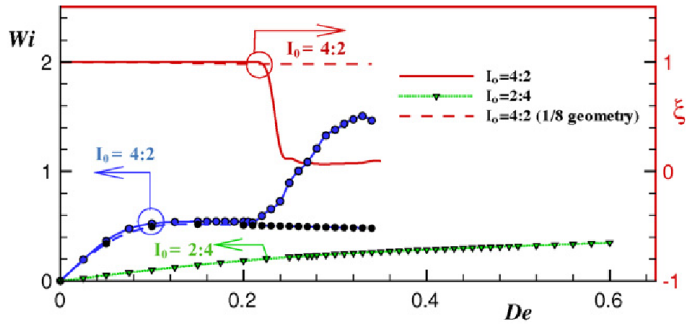

Figure 6.9: Variation with De of the local Weissenberg number (*Wi*) and flow type parameter (ξ) at the stagnation point for the biaxial ($I_o = 2:4$) and uniaxial ($I_o = 4:2$) extensional flow configurations. Values for the symmetry-imposed flow also included for the uniaxial configuration.

with Re, as is also observed for the transition in the $I_o = 2:4$ flow configuration, although to a much lesser degree. Hence, at $Re = 0$, the second transition takes place at $De_{crt} \approx 0.32$, for $Re = 1$ $De_{crt} \approx 0.31$ and at $Re = 2$ $De_{crt} \approx 0.29$. These changes can be observed both in the main direction angle plot (Figure 6.7) as well as in the Re–De stability map represented in Figure 6.10. Finally, for Reynolds numbers in excess of around 2, the transition associated with elasticity is directly from a steady symmetric to an unsteady flow, as is also observed for the transition in the $I_o = 2:4$ flow configuration for all Reynolds numbers studied.

As we have seen above in Figs. 6.9 and 6.10, the steady asymmetric flow is predominantly a shear type flow, where transition to unsteady flow is associated with large hoop stresses developing in curved streamlines, as explained by McKinley et al. (1996). In this mechanism the curved streamlines become unstable at hoop stresses that vary inversely with their curvature. Most likely the instability appears first at the curved streamlines near the reentrant corners, but it could also appear elsewhere closer to the stagnation point, where the streamlines are also curved. By raising the Reynolds number the curvature of the streamlines in the region of interest increase and the same critical level of hoop stress is attained at a lower Deborah number. It is easy to visualize that higher inertial forces push the flow towards the central region of the cross-slot and this forces the fluid to turn direction closer to the geometric centre of the cross-slot, thus increasing locally the curvature of the streamlines. It is not so easy to understand on simple terms why there is an increase of streamline curvature with Reynolds number near the reentrant corner, but this possibility is open.

Explaining the stabilizing effect of the Reynolds number for the first transition is more difficult, since we do not even know yet what is the primary cause for the first transition in creeping flow. Even though it is tempting to consider the unbounded stresses as its cause, we suspect that is not the case given the fact that Poole et al. (2007c), Rocha et al. (2009) and Becherer et al. (2008) found such transitions to occur for PTT and FENE fluids for the 2D equivalent cross-slot flow. Clearly, understanding the causes of both types of transition in the 2D and 3D cross-slot flows is an important research topic.

As argued by Oliveira et al. (2009), the existence of a symmetry-breaking bifurcation is likely to be related with a stress relief mechanism, and this can be assessed by comparing the energy losses in the real flow, with those predicted in the symmetry-imposed flow configuration. For creeping flow conditions, the power dissipation can be calculated from:

$$\Delta \dot{W}_{real} = \sum_i Q_{in,i} p_{in,i} - \sum_j Q_{out,j} p_{out,j}, \tag{6.15}$$

where the subscript 'in' refers to inlet boundaries and the subscript 'out' refers to the outflow boundaries. For both flow configurations analyzed in this work one obtains

$$\Delta \dot{W}_{real} = (p_{in} - p_{out}) \sum_i Q_{in,i}. \tag{6.16}$$

The power dissipation $\Delta \dot{W}_{real}$ can be compared to that of an ideal flow where fully developed shear flow conditions would be observed everywhere along the channels, and no energy dissipation would take place in the central region of the cross slot. For this ideal flow configuration the power dissipation can be estimated as

$$\Delta \dot{W}_{ideal} = \sum_{i=1}^{6} Q_i \, |dp/ds|_i \, L_i, \tag{6.17}$$

where $|dp/ds|_i$ represents the stream wise pressure gradient under fully-developed flow conditions in arm *i*. The extra power dissipation due to the extensional flow in the cross slot geometry can be estimated as (and is independent of the length of the arms, when they are sufficiently long for achieving fully developed flow conditions at inlets and outlets) $\Delta \dot{W}_{exc} = \Delta \dot{W}_{real} - \Delta \dot{W}_{ideal}$. In order to generalize the results, it is useful to work with a dimensionless extra power dissipation, K, here defined as:

$$K = \frac{\Delta \dot{W}_{real} - \Delta \dot{W}_{ideal}}{\sum_j Q_{out,j} \, |dp/ds|_j \, H} = \frac{\Delta p_{real} - \Delta p_{ideal}}{4\tau_w} \tag{6.18}$$

where Δp_{real} is the pressure difference between one of the inlets and one of the outlets, Δp_{ideal} is the pressure drop required to drive fully-developed flow in the inlet and outflow straight channels, as in the absence of the interference of the central region, and τ_w is the *average* wall shear stress under fully-developed conditions at any of the outflow channels ($\tau_w = |dp/ds|_j \, H/4$).

In Figure 6.11 we present the variation of K with De, together with data from a set of additional calculations with imposed flow symmetry, i.e., simulations with only 1/8 of the geometry. As was also observed in previous works (Poole et al., 2007c; Afonso et al., 2010d; Soulages et al., 2009), K is reduced above the critical Deborah number, showing that the steady asymmetric flow dissipates less energy than the symmetric flow configuration. This is an interesting observation, similar to previous works in the planar cross-slot and flow focusing geometries (Poole et al., 2007c; Afonso et al., 2010d; Soulages et al., 2009), but it does not necessarily imply a minimum energy loss principle as the cause for the flow transition.

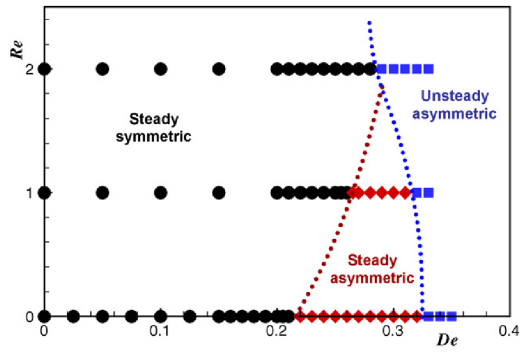

Figure 6.10: Re–De stability map for the uniaxial extension configuration ($I_o = 4 : 2$).

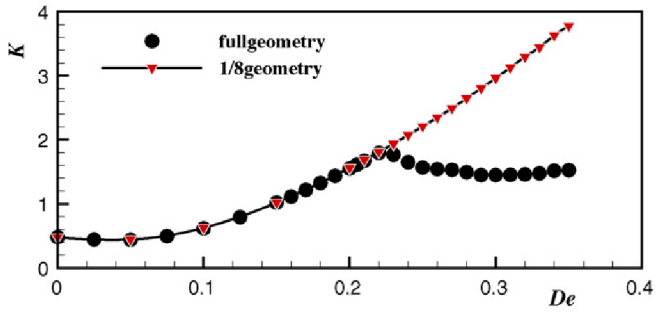

Figure 6.11: Effect of Deborah number on the dimensionless extra power dissipation (K) for the uniaxial extension configuration ($I_o = 4 : 2$). Simulations with full geometry (•) and 1/8 of the geometry (imposed flow symmetry) (-∇-).

6.1.5 *Conclusions*

A numerical study of creeping flow of an UCM fluid in three-dimensional cross-slot geometries with six arms was undertaken. The influences of Deborah and Reynolds numbers and different types of extensional flow near the stagnation point were analyzed, namely biaxial and uniaxial extensional flow. The uniaxial extensional flow configuration is prone to the onset of steady flow asymmetries at $De_{crit} \approx 0.22$ and at a higher Deborah number there is a second transition from steady asymmetric to unsteady flow, as in the corresponding two-dimensional cross slot geometry. On the other hand, for the biaxial extensional flow configuration a perfectly symmetric flow has been observed up to $De \approx 0.61$ and above this critical Deborah number the flow becomes unsteady and asymmetric without transitioning to a steady asymmetric flow. Inertia was found to stabilize the first type of transition (for the uniaxial extensional flow) and to destabilize the second transition in both flow configurations, although to a much lesser degree in the biaxial extensional flow configuration.

6.1.6 *Acknowledgments*

The authors acknowledge the financial support from FEDER and FCT through projects PTDC/EQU-FTT/ 70727/ 2006, PTDC/EQU-FTT/71800/2006 and scholarship SFRH/BD /28828/2006 (A.M. Afonso).

Abstract[2]
The flow of Newtonian and viscoelastic fluids in a mixing-separating geometry that consists of two opposed channel flows interacting through a gap in the common separating wall is investigated. The flow in this type of geometry was studied experimentally by Cochrane et al. (1981) using Newtonian and viscoelastic fluids at low Reynolds numbers ($\mathrm{Re} < 50$*). In this numerical study, by use of a finite-volume method, the effects of Deborah (*De*) and Reynolds numbers and gap size on the two-dimensional flow dynamics are assessed. The normalized gap size varies between 0 and 5,* Re *varies between 0 and 50 and* De *varies between 0 and the maximum attainable value. Due to the anti-symmetry of the fully developed inlet conditions and the symmetry of the flow geometry, the Newtonian creeping flow is anti-symmetric. Increasing the gap size of the separating walls leads to an increase of the reversed flow-rate ratio (*$\mathrm{R_r}$*), which is defined as the ratio of the reversed and the total flow rate. For creeping flow of viscoelastic fluids, here described by the upper-convected Maxwell model, two distinct flow patterns are observed. Below a critical gap size, the reversed flow is slightly enhanced when the Deborah number increases. Further increase of* De *leads to a subsequent decrease in* $\mathrm{R_r}$ *towards zero. For a supercritical gap size, increasing the Deborah number leads to a monotonic increase in* $\mathrm{R_r}$*.*

Keywords: Mixing-separating, viscoelastic fluids, UCM model, elastic instabilities, flow bifurcation.

6.2.1 *Introduction*

In this work we investigate the flow in a mixing and separating geometry (Cochrane et al., 1981) for low Reynolds number flow conditions, including the limit of vanishing inertia (creeping flow). The simplest differential constitutive equation describing viscoelastic behaviour, the upper-convected Maxwell (UCM) model, is used in the present numerical study. The flow in this geometry was also investigated experimentally and numerically by Cochrane et al. (1981), Walters and Webster (1982), Humphrey and Li (1981) and Humphrey et al. (2008). Baloch et al. (1995) and Fiétier (2002) analysed this flow numerically under different conditions.

Cochrane et al. (1981) employed a finite-difference method and selected the UCM model to describe the rheological behaviour of a highly-elastic constant-viscosity "Boger" fluid (Boger, 1977). These investigators analysed the effects of gap width (g) using two different flow configurations: (*i*) matching flow rates in the two inlet channel arms and (*ii*) unbalanced inlet flow rates. In a follow-up work (Walters and Webster, 1982), thin insert plates with rounded edges were used. For both experimental studies it was found that the flow displayed distinctive Newtonian and viscoelastic behaviours, with the occurrence of unidirectional and reversed flows in varying extents. Later, Baloch et al. (1995) selected the Phan-Thien-Tanner (PTT) model (Phan-Thien and Tanner, 1977) to describe the rheological behaviour, and simulated

2 A.M. Afonso, M.A. Alves, R.J. Poole, P.J. Oliveira and F.T. Pinho (2010). Viscoelastic flows in mixing-separating cells, accepted for publication in the *Journal of Engineering Mathematics*.

this flow also using thin insert plates with rounded edges, for the case of equal flow rates at the inlet channels. Fiétier (2002) simulated the flow of a FENE-P model (Bird et al., 1980) using a spectral element method, and considered the case with a thick insert plate with rounded edges. The numerical results obtained captured qualitatively the experimental results presented by Walters and Webster (1982). Humphrey and Li (1981) used a dye visualization technique, which revealed the time-evolution of pairs of transversely aligned vortices in a confined counter-current shearing flow configuration, for moderate Reynolds numbers ($Re = 100 - 1000$). More recently, Humphrey et al. (2008) simulated the time-dependent flow of a Newtonian fluid in a counter-current shearing flow configuration, for $100 < Re < 300$.

In the present numerical investigation we expand the limited knowledge available on the viscoelastic fluid flow behaviour in the mixing and separating geometry, clarifying and mapping different flow behaviours as a function of gap size under conditions of low inertia and different elasticity levels. The occurrence and extent of purely-elastic flow instabilities is also assessed. These instabilities usually arise in extensionally-dominated flows with strong streamline curvature, such as flows with a stagnation point (e.g. cross-slot flow Arratia et al., 2006; Poole et al., 2007c,a), or the opposed jet apparatus (Chow et al., 1988). In their numerical investigation, Poole et al. (2007c) studied the two-dimensional cross-slot flow of an UCM fluid for creeping and low Re flow conditions, and reproduced qualitatively the occurrence of a steady bi-stable asymmetric flow, above a critical Deborah number. Further increase of De led to a second transition to a time-dependent flow as observed in the experimental work of Arratia et al. (2006). Later, Poole et al. (2007a) included the effects of solvent viscosity and finite extensibility (using the Oldroyd-B and PTT models), and delimited different flow patterns in $\beta - Re - De$ and $\varepsilon - Re - De$ maps. These flow maps showed the existence of a narrow region of steady asymmetric flow in the $\varepsilon - \beta - Re - De$ parameter space and identified the critical De for occurrence of time-dependent flow.

Elastic instabilities are not restricted to extensional flows and are found in shear flows, as widely documented by Morozov and van Saarloos (2007). Earlier investigations on elastic instabilities in Poiseuille and Couette flows were reported in Ho and Denn (1977) and Joo and Shaqfeh (1992), and criteria for their onset were proposed by Shaqfeh (1996) and McKinley et al. (1996).

In this investigation we focus on the mixing-separating flow geometry with thin insert plates and equal flow rates at the two channel inlets under low-Re flow conditions. Newtonian and viscoelastic fluids, described using UCM model, are used. This flow combines, under certain conditions, regions of extensional flows with shear flows, but shear effects play an important role under all conditions.

The remainder of this paper is organised as follows: initially the governing equations are presented, followed by a brief description of the finite-volume method used in the simulations. Afterwards, we describe the flow geometry and the computational meshes used before presenting the numerical results obtained. The paper ends with the main conclusions.

6.2.2 *Governing equations and numerical method*

The equations we need to solve are those of conservation of mass and momentum of an incompressible fluid,

$$\nabla \cdot \mathbf{u} = 0, \tag{6.19}$$

$$\rho \frac{\partial \mathbf{u}}{\partial t} + \rho \nabla \cdot \mathbf{u}\mathbf{u} = -\nabla p + \nabla \cdot \boldsymbol{\tau}, \tag{6.20}$$

coupled with a constitutive equation for the extra-stress tensor, $\boldsymbol{\tau}$. For reasons of rheological simplicity, we use the UCM model which is described by the evolution equation

$$\boldsymbol{\tau} + \lambda \left(\frac{\partial \tau}{\partial t} + \mathbf{u} \cdot \nabla \boldsymbol{\tau} \right) = \eta \left(\nabla \mathbf{u} + \nabla \mathbf{u}^T \right) + \lambda \left(\boldsymbol{\tau} \cdot \nabla \mathbf{u} + \nabla \mathbf{u}^T \cdot \boldsymbol{\tau} \right), \tag{6.21}$$

where λ and η are the relaxation time and shear viscosity of the fluid, respectively.

A fully-implicit finite-volume method was used to solve Equations (6.19) – (6.21). The method is based on a time marching pressure-correction algorithm formulated with the collocated variable arrangement, as described in detail in previous works (Oliveira et al., 1998; Alves et al., 2003a). Recently, this numerical method was adapted to use the *log-conformation* methodology proposed by Fattal and Kupferman (2004), and this technique is used here due to the enhanced numerical stability. The main modifications implicated in the use of the log-conformation method are described in detail by Afonso et al. (2009b), therefore are not here repeated. In summary, the governing equations are initially transformed to a non-orthogonal coordinate system, but keeping the dependent variables in a Cartesian coordinate system. Afterwards, the equations are integrated in space over the control volumes of the computational mesh, and in time over a small time step (δt), leading to sets of linearised algebraic equations of the general form:

$$a_P u_{i,P} = \sum_{F=1}^{6} a_F u_{i,F} + S_{u_i}, \tag{6.22}$$

to be solved for the velocity components, and

$$a_P^{\Theta} \Theta_{ij,P} = \sum_{F=1}^{6} a_F^{\Theta} \Theta_{ij,F} + S_{\Theta_{ij}} \tag{6.23}$$

to be solved for the logarithm of the conformation tensor, Θ_{ij}. In Eqs. (6.22) and (6.23) a_F represents coefficients accounting for advection and diffusion (only advection in Eq. 6.23) and S contains the source terms with all contributions that are not included in the terms with coefficients. The subscript P denotes a generic cell and subscript F the corresponding neighbour cells. The central coefficient of the momentum equation, a_P, is given by

$$a_P = \frac{\rho V_P}{\delta t} + \sum_{F=1}^{6} a_F. \tag{6.24}$$

The sets of linear equations (6.22) are solved sequentially for the Cartesian velocity components. This newly-computed velocity field usually does not satisfy the continuity equation and needs to be adjusted by an adequate correction of the pressure field that drives it. This adjustment is accomplished through a pressure-correction field determined from a Poisson pressure equation, following the ideas of the SIMPLEC algorithm (Van Doormaal and Raithby, 1984). Once a velocity field that satisfies the continuity equation has been obtained, the implicitly-discretized constitutive equations (i.e. Eq. 6.23) are solved sequentially. To formulate the advective fluxes of the constitutive equation, we use the CUBISTA high-resolution scheme, a third-order method specifically designed for differential rheological constitutive equations (Alves et al., 2003a). In this work we will focus primarily on creeping-flow conditions, in which case the advective term of the momentum equation (i.e. the left side of equation 6.20) is neglected. When inertial flows are considered, we include the advective term of the momentum equation, and also use the CUBISTA high-resolution scheme in the evaluation of the advective fluxes.

6.2.3 *Flow geometry and computational meshes*

The flow under investigation is that of two opposed channels interacting through a gap of nondimensional width $\theta = g/H$, in the middle of a thin separating wall of nondimensional thickness $\alpha = a/H$, as illustrated in Figure 6.12. The two inlet and outlet channels have the same width (H) and lengths $L = 20H$.

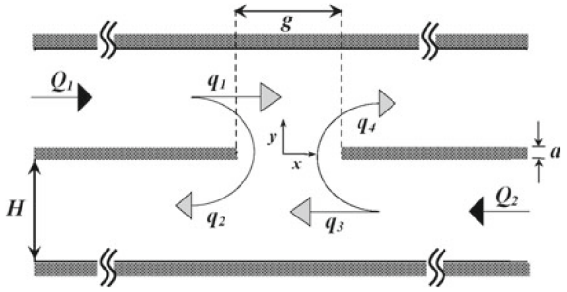

Figure 6.12: Schematic diagram of the mixing-andseparating flow geometry.

Fully-developed velocity and stress profiles are imposed at the two inlets. Preliminary studies confirmed that the inlet and outlet channel lengths are sufficiently long to avoid interference of the inlet and/or outflow boundary conditions upon the flow in the central region. At all channel walls, no-slip boundary conditions are imposed. At the outlet planes Neumann boundary conditions ($\partial\varphi/\partial x = 0$) are applied to all variables including the pressure gradient.

For all gap values analysed the computational domain was mapped using six orthogonal blocks, one in each of the four channels and two blocks in the central region. The main characteristics of the three consecutively refined meshes used in this work are presented in Table 6.1, for the case with $\theta = 1$.

Table 6.1 includes the information regarding the total number cells of the meshes (NC), the number of control volumes in the central region in both x and y directions (NCS), and the minimum cell spacing (Δx_{min} and Δy_{min}), which also occurs in the central region. For other

Table 6.1: Main characteristics of the computational meshes ($\theta = 1$).

	NC	DOF	NCS_x	NCS_y	$\Delta x_{min}/H$	$\Delta y_{min}/H$
M25($\theta = 1$)	6300	37800	26	25	0.0385	0.04
M51($\theta = 1$)	25704	154224	52	51	0.0186	0.0196
M101($\theta = 1$)	102212	613272	104	101	0.0093	0.0099

plate thicknesses and gap values, the meshes were adapted in order to have the same minimum cell spacing at the central region of the meshes. For each value of θ investigated, different meshes were generated with different number of cells in the x and y directions, but always ensuring consistent mesh refinement and that the minimum cell spacing in both directions remained essentially the same (i.e. square control volumes in the region of interest). Consequently, in all meshes the central region of the mesh is uniform, and progressively refined from $\Delta x_{min}/H = \Delta y_{min} \approx 0.04$ to 0.02 and 0.01 for meshes M25, M51 and M101, respectively. These two-dimensional meshes contain 102212 and 122816 cells (M101) corresponding to 613272 and 736896 degrees-of-freedom (DOF), for low and large nondimensional gap widths, respectively.

The results discussed in the next section are presented in dimensionless form, unless otherwise stated. Velocities are normalised using the bulk velocity in the inlet channels (U) and the extra-stresses are normalised using a characteristic viscous stress, $\eta U/H$. The Deborah number represents the ratio between the relaxation time of the fluid (λ) and a characteristic time scale of the flow, here chosen as g/U. Consequently, in the present investigation we define the Deborah number as $De = \lambda U/g$.

For flows with non-negligible inertia the Reynolds number is also important, and is here defined as $Re = \rho U H/\eta$. The degree of flow reversal relative to the unidirectional flow that would exist in the absence of a gap in the middle wall, is quantified using the parameter $R_r = q_2/Q_1 = q_4/Q_2$, where q_2 and q_4 correspond to the partial flow rates per unit depth that reverse from each inlet arm and $Q_1 = Q_2 = UH$ are the total flow rates per unit depth at each inlet channel, as shown in Figure 6.12.

6.2.4 *Results and discussion*

6.2.4.1 *Assessment of numerical accuracy*

In this section we estimate the numerical uncertainty analysing the convergence with mesh refinement. In Figure 6.13 we plot the transverse profiles of the dimensionless velocity and shear stress along the vertical line ($x = 0$) that crosses the stagnation point located at the middle of the gap. The data from all the meshes correspond to the creeping flow of an UCM fluid at $De = 0.35$, for a dimensionless gap and for a separating wall with negligible thickness ($\alpha = 0$). The velocity profiles calculated in meshes M51 and M101 exhibit excellent agreement. The stress profiles show a slight mesh dependency near the stagnation point, due to the high stress gradients that occur in that region, but elsewhere the agreement between all meshes is very good.

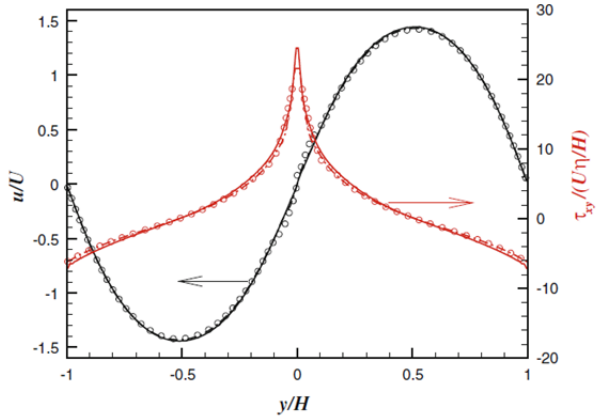

Figure 6.13: Transverse profiles of the normalised velocity and shear stress at $x/H = 0$, for $De = 0.35$ ($Re = 0$, $\theta = \sqrt{2}$ and $\alpha \to 0$), on mesh M25 (*open circle*), mesh M51 (*dashed line*) and mesh M101 (*full line*).

Table 6.2: Quantification of numerical uncertainty for some representative cases: Couette correction.

		C_{corr}				Error (%)		
De	θ	M25	M51	M101	Extr.	M25	M51	M101
0.42	1.414	1.496	1.486	1.482	1.480	1.069	0.369	0.127
0.26	1.740	2.348	2.194	2.180	2.179	7.768	0.674	0.059
0.30	2.000	2.475	2.396	2.378	2.373	4.303	0.980	0.223

Additional information on the accuracy of the numerical results is presented in Table 6.2, where the estimated error for the Couette correction (C_{corr}) coefficient (discussed in Section 6.2.4.4 and defined in Eq. 6.25) is provided for all three meshes and for three different nondimensional gap widths ($\theta = \sqrt{2}$, 1.74 and 2) for a range of Deborah numbers. The uncertainties were estimated by comparison with the C_{corr} extrapolated using Richardson's extrapolation technique (Ferziger, 1981). As can be observed, the uncertainties estimated for meshes M51 and M101 are always below 1%, showing again the high level of accuracy of the numerical results. Therefore, in the remainder of the paper, unless otherwise stated, the results presented were obtained with the intermediate mesh M51.

6.2.4.2 *Newtonian fluid flow*

Geometrically, the mixing-and-separating geometry can be idealized as a cross-slot device (Arratia et al., 2006) with one pair of aligned arms rotated by 90° towards the other pair, leading to a nondimensional gap size of and a vanishing thickness of the separation plate ($\alpha \to 0$). If during this transformation the flow type wouldn't change, the ratio between the reversed to unidirectional flow would be $R_r = 0.5$, in order to keep full similarity with the cross-slot. Obviously, this is not the case as illustrated in Figure 6.14, where R_r is plotted as a function of normalized gap width, θ, for various plate thicknesses, α, for creeping flow of a Newtonian fluid. For this shear dominated flow we obtain $R_r = 0.29$ for $\theta = \sqrt{2}$. In order to achieve $R_r = 0.5$ the normalized gap should be about $\theta \approx 1.75$. From Figure 6.14 we conclude that the effect of plate thickness for thin plates is small in agreement with

experiments (Cochrane et al., 1981; Walters and Webster, 1982). Figure 6.14 also highlights that the transition from a straight unperturbed no-reverse-flow situation at low θ to a full flow reversal occurs when the dimensionless gap size becomes large.

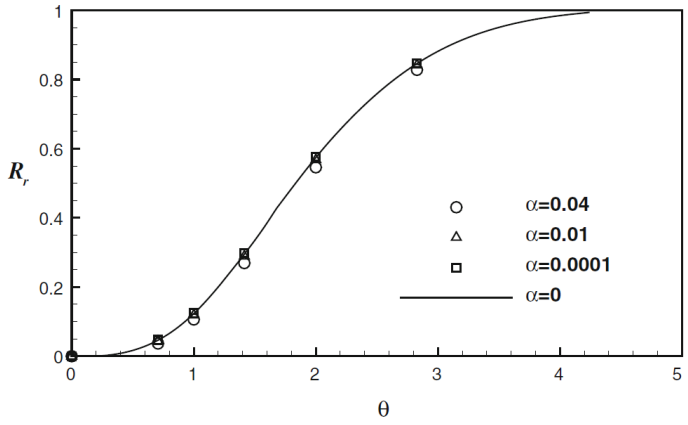

Figure 6.14: Degree of reverse flow as function of gap width, θ, and plate thickness, α, for the Newtonian case at $Re = 0$.

The differences between the results for the cross-slot and the mixing-and-separating geometries can be explained from the different angles of the approaching flows in the vicinity of the stagnation points. In the mixing-and-separating geometry these approach flows are not aligned with the channels and are not orthogonal as occurs in the cross-slot flow. Consequently, in the mixing-and-separating geometry the shear flow is important in the stagnation point region, being absent in the cross-slot flow geometry which is purely extensional in character, except in the vicinity of the channel walls. This difference may also be important for understanding the onset of purely-elastic instabilities in the cross-slot geometry (Morozov and van Saarloos, 2007; Afonso et al., 2010b). These observations are better understood analysing the streamline plots presented in Figure 6.15 , which correspond to creeping flow of Newtonian fluids at low, medium and large dimensionless gap widths ($\theta = 1$, 2 and 2.83). These patterns correspond to the $\alpha = 0$ curve represented in Figure 6.14, where the corresponding reversed flow rate ratios take the numerical values of 0.123, 0.575 and 0.846, i.e., increasing with gap size.

Figure 6.16 illustrates the influence of flow inertia on R_r for Newtonian fluids as a function of the dimensionless gap width, θ. For all Reynolds numbers analysed, R_r varies from 0 to 1 as the gap sizes increases in agreement with experiments (Cochrane et al., 1981; Walters and Webster, 1982). For conditions of low inertia (say, $Re \leqslant 1$) the variation of R_r with θ is independent of Reynolds number. However, when inertial effects are significant, flow reversal is enhanced. In Figure 6.16 we plot data of R_r at some representative Reynolds numbers as function of θ for each of the three meshes, and once again, mesh dependency is barely noticeable.

6.2.4.3 *Viscoelastic and Inertial effects*

Figure 6.17 illustrates an interesting bifurcation which depends on the gap width and occurs with UCM fluids under creeping flow conditions. For large dimensionless gap sizes, but below a critical value

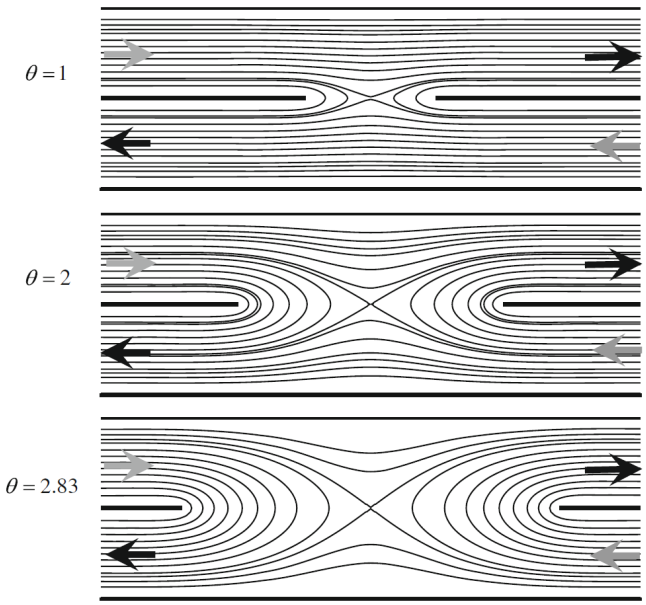

Figure 6.15: Streamlines for the mixing-and-separating geometry for several gap widths, θ, and plate thickness, α, for the Newtonian case at $Re = 0$.

($\theta \leqslant 1.6$), the reversed flow is slightly enhanced initially as viscoelasticity increases, followed by a significant decrease towards zero when *De* further increases. This behaviour is characterized by a significant departure from streamline parallelism in the gap region, although with the fluid still tending to flow unidirectionally in agreement with experiments (Cochrane et al., 1981; Walters and Webster, 1982). This situation is illustrated by the flow pattern of Figure 6.18a.

In contrast, for a supercritical dimensionless gap size ($\theta \geqslant 1.84$) we find that viscoelasticity is now responsible for a continuous increase of R_r with De, and the corresponding flow patterns are similar to those illustrated in Figure 6.18b. It is important to emphasize that this supercritical pattern has not yet been observed experimentally primarily due to the stabilising effect of inertia, to be discussed below.

For creeping flow and at a definite intermediate gap width range ($1.6 \leqslant \theta \leqslant 1.84$, cf. Figure 6.17 for $\theta = 1.74$) a steady bifurcation flow pattern emerges, with a sudden jump between two widely different flow configurations, ranging from almost unidirectional to almost fully reversed, at Deborah numbers slightly higher than the critical Deborah number. The corresponding streamline plots are illustrated in Figure 6.18 for $De = 0.345$ and $\theta = 1.74$. On the upper plot the flow is almost unidirectional ($R_r = 0.047$) while at the bottom plot the flow is highly reversed ($R_r = 0.85$). The bifurcation between these two flow patterns is due to a purely-elastic instability since inertia has no role ($Re = 0$) in the present simulations (we have also observed such purely elastic instabilities in Poole et al., 2007c,a; Rocha et al., 2009). Incidentally, when $\theta = 1.74$ we find a maximum value of $R_r = 0.5$ before bifurcation (at $De \approx 0.2$) and this corresponds to the situation where the approach flows at the stagnation point tend to be closer to perpendicular. Here, we found that the critical Deborah number for the onset of the bifurcation of UCM fluids is $De_{crit} = 0.316$, a similar value to that reported for

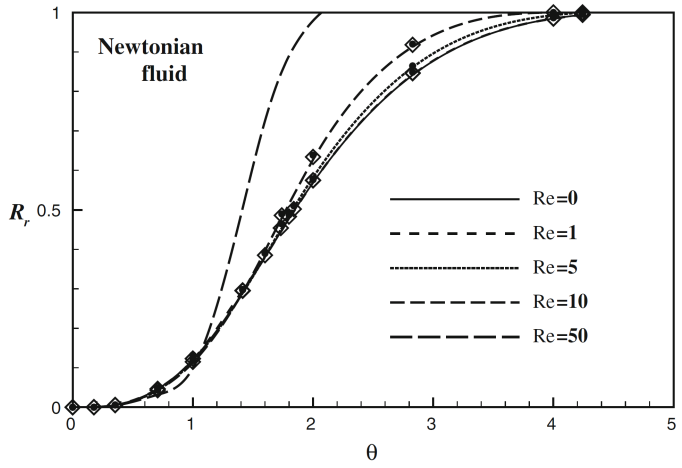

Figure 6.16: Degree of reverse flow as function of gap width, θ, for several Reynolds numbers. Newtonian case on meshes M25 (diamond), M51 (lines) and M101 (closed circle).

the instability in the cross-slot geometry ($De_{crit} \approx 0.31$, Poole et al. 2007c) with this De defined as θDe. The predictions also indicated that in this intermediate region of bifurcated flow the critical De decreases in inverse proportion to θ.

Regarding the influence of flow inertia, the critical De for the steady bifurcation is found to increase with Re, as illustrated in Figure 6.19 for $\theta = 1.74$ and $Re = 1$. Here, R_r is plotted as a function of De for three different dimensionless gap widths ($\theta = \sqrt{2}$, 1.74 and 2) and for Re up to 10. As observed for the Newtonian fluids, the degree of flow reversal is essentially independent of Reynolds number for $Re \leqslant 1$. At higher Reynolds numbers (e.g. $Re = 5$ and 10) and $\theta = 2$ we observe an inversion in the flow configurations: whereas at low Re viscoelasticity was seen to be responsible for an increase in R_r (the typical supercritical behaviour), at large Reynolds numbers R_r decreases with De (the typical subcritical behaviour). Thus, strong inertial effects eliminate the elastic bifurcation and the flow becomes more unidirectional. This behaviour is also in contrast with the Newtonian case where for the same value of $\theta = 2$ an increase in the Reynolds number increased the reversed flow. This opposed effect of flow inertia at low and high elasticity explains why the supercritical behaviour has not yet been observed in experiments and suggests the need for further experimental work, using a highly viscous and elastic fluid, to attain low Reynolds numbers flow at high Deborah numbers. An interesting alternative is to use microfluidic geometries, in which the small sizes lead to a decrease of flow inertia and to a significant enhancement of viscoelasticity (note that De increases when the length scale decreases) (Stone et al., 2004).

In order to clarify the trends in Figure 6.19 and mimic the procedure of experiments, we conducted an additional set of simulations with constant Elasticity number ($El = De/Re = \lambda\eta/\rho H^2\theta$), a situation that better reproduces the experimental scenario, where an increase of the flow rate leads to a proportional increase of Re and De, without altering the elasticity number (which is independent of flow rate). Using such an approach, the combined effects of elasticity and inertia are quantified by the Elasticity number, and these effects are presented in Figure 6.20 ,

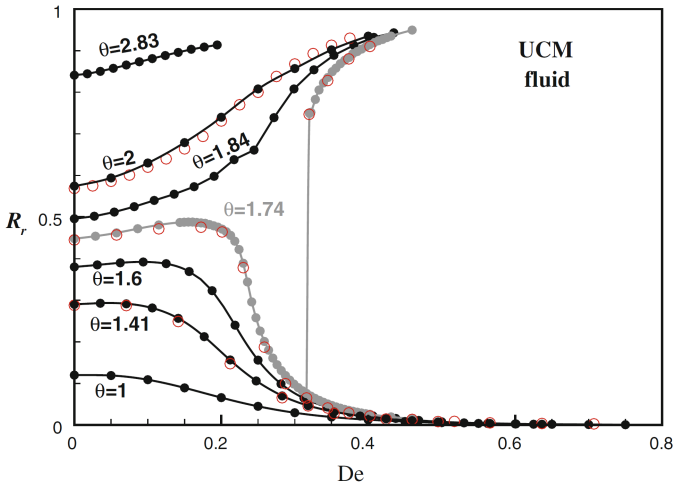

Figure 6.17: Degree of reverse flow as function of Deborah number for several gap widths, θ, and $Re = 0$ (closed symbols—Mesh M51 and open symbols—Mesh M101).

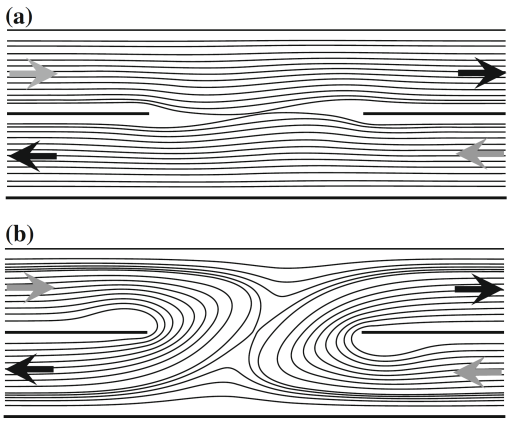

Figure 6.18: Streamlines for $\theta = 1.74$, $\alpha = 0$, $Re = 0$ and $De = 0.345$ in mesh M101: the two bifurcated solutions have (a) $R_r = 0.041$ and (b) $R_r = 0.83$.

where R_r is plotted as a function of De for three different gap widths ($\theta = \sqrt{2}$, 1.74 and 2) and for three different values of El ($El = 0.1$, 1 and 5). For a subcritical gap size ($\theta = \sqrt{2}$) the effect of El is small, with the reversed flow slightly attenuated by viscoelasticity, followed by a strong decrease in R_r towards zero as De further increases. For the intermediate gap width ($\theta = 1.74$), the steady bifurcation flow patterns are not observed for low Elasticity numbers ($El = 0.1$), and the critical Deborah number increases as El decreases, showing the stabilising effect of inertia. Finally, for a supercritical gap size ($\theta = 2$) we can observe again an inversion in the flow configurations for low El, with R_r decreasing with De, thus the flow becomes more unidirectional.

6.2.4.4 *Steady bifurcation flow stability*

As discussed in the previous sections, for intermediate gap widths ($1.6 \leqslant \theta \leqslant 1.84$) a steady bifurcation flow pattern is observed. For Deborah numbers higher than a critical value, two different steady flow

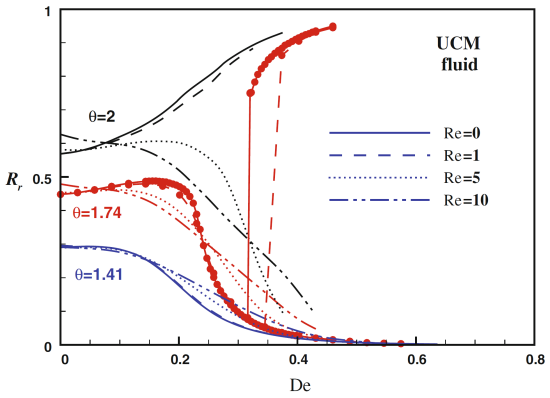

Figure 6.19: Degree of reverse flow as function of Deborah number for several gap widths, θ, and $Re = 0$, 1, 5 and 10.

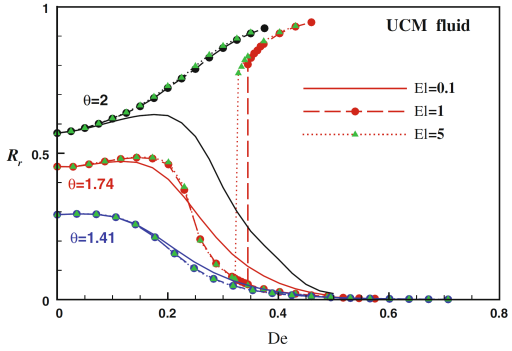

Figure 6.20: Degree of reverse flow as function of Deborah number for several gap widths, θ, and elasticity numbers ($El = 0.1$, 1 and 5).

patterns with different flow configurations can be observed. In order to access the stability of these dual configurations we performed a simple test for $\theta = 1.74$, the results of which are shown in Figure 6.21. Time-dependent flow simulations were performed for a periodic variation of Deborah number, departing from a De near the critical value ($De = 0.322$, corresponding to a highly reversed configuration flow, $R_r = 0.75$), down to $De = 0.316$ (corresponding to a quasi unidirectional configuration flow, $R_r = 0.076$), using a second-order time discretization scheme (Oliveira, 2001a) with a small time step ($\Delta t/\lambda = 2x10^{-5}$), for good accuracy in time. After one cycle of De, the flow configuration shifts from a reversed to a unidirectional configuration, remaining in this configuration along the rest of the pulsating variation. This observation suggests that, although both flow configurations are steady and stable, the unidirectional configuration is preferred.

An alternative explanation to this behaviour is based on the energy losses of the two flow configurations, here quantified using a Couette correction coefficient (C_{corr}), evaluated as the normalized pressure drop between inlet and outlet after discounting for the fully-developed

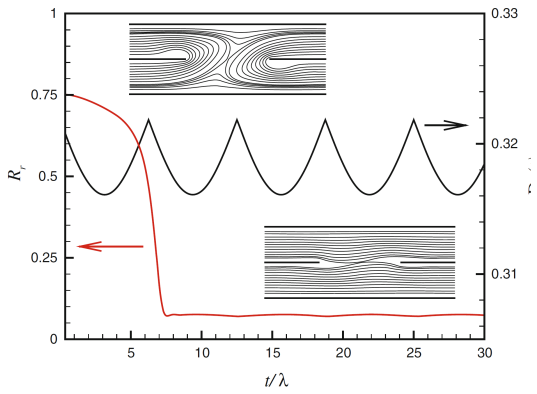

Figure 6.21: Stability analysis for $\theta = 1.74$, with $\alpha = 0$, $Re = 0$ and $De = [0.316, 0.322]$.

pressure drop along the channels (i.e. C_{corr} represents a dimensionless extra pressure drop):

$$C_{corr} = \frac{\Delta p - \Delta p_{FD}}{2\tau_w}, \tag{6.25}$$

where Δp is the pressure difference between any of the inlets and one of the outlets, Δp_{FD} is the pressure drop required to drive fully-developed flow in the inlet and outflow straight channels, as in the absence of the interference of the gap, and τ_w is the wall shear stress under fully-developed conditions (given by $\tau_w = 6\eta U/H$ for the UCM model). The value of C_{corr} for Newtonian fluids as function of the non-dimensional gap size is presented in Figure 6.22a, showing that C_{corr} increases asymptotically to about 1.3 as θ increases beyond 2, corresponding to increased levels of reversed flow. So, extrapolating these findings to the viscoelastic case we conclude that the preferred configuration (unidirectional flow) corresponds to the less dissipative flow field, a situation that has been reported in other similar instabilities in cross slot and flow focusing geometries (Poole et al., 2007c; Rocha et al., 2009; Oliveira et al., 2009). This difference is also clear in the results for C_{corr} obtained for an intermediate gap width ($\theta = 1.74$) and plotted as a function of De in Figure 6.22b. The reversed flow is initially slightly enhanced up to $De = 0.25$ (recall Figure 6.17) and mainly because strong hoop stresses are established due to fluid elasticity and flow curvature, the value of C_{corr} increases significantly above the Newtonian level, and this is followed by a decrease of the Couette correction when the flow starts to become more unidirectional as De is further increased. At Deborah numbers above the De_{crit}, and for the reversed configuration flow, it is clear that the energy losses are significantly higher than for the corresponding unidirectional flow configuration, correlating with the results presented in Figure 6.21.

6.2.5 *Conclusions*

The UCM model was used to simulate viscoelastic fluid flows in a mixing-separating geometry (Cochrane et al., 1981). For a combination

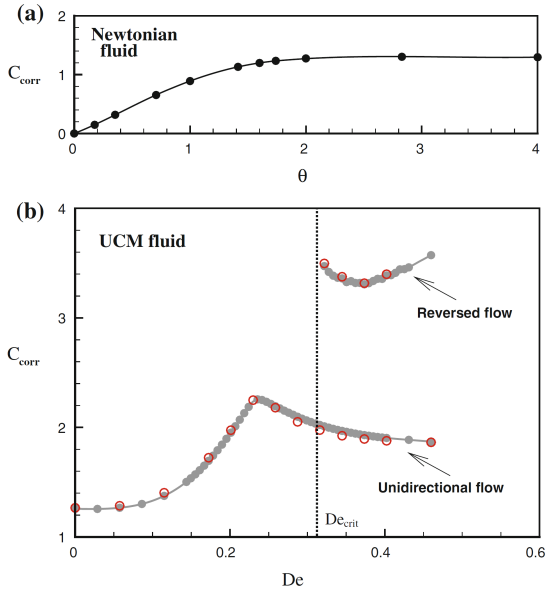

Figure 6.22: Couette correction coefficient under creeping flow conditions and zero thickness ($Re = 0$ and $\alpha = 0$) as function of: (a) dimensionless gap size, θ, in Newtonian flow ($De = 0$); (b) Deborah numbers for UCM fluid flow ($\theta = 1.74$). (closed circle Mesh M51; open circle M101).

of critical flow parameters, it was possible to identify a new steady bistable bifurcation in the flow patterns at low inertia and high elasticity.

Under creeping flow conditions the UCM model exhibited two distinct flow patterns. For normalized gap sizes below a critical value, the reversed flow is slightly enhanced as De increases, followed by a strong decrease towards zero of the reversed flow rate as De further increases. In contrast, above a supercritical gap size increasing De leads to a monotonic increase in R_r. For near-critical flow geometries it was possible to observe a sudden transition between the two flow conditions at slightly different Deborah numbers. Flow inertia was found to increase the critical Deborah number for steady flow bifurcation. Inertia naturally enhances the straight flow configuration and at $Re = 5$, R_r always decreased with Deborah number for $De \leqslant 0.6$ and for the investigated gap sizes. The interplay between inertia and elastic effects is clarified using the elasticity number, El, instead of Re and De separately. Essentially the viscoelastic fluid adjusts itself so as to avoid changes in the flow direction and when the streamline curvature imposed by the geometry (increasing θ) is large, the elastic normal stresses become so strong, with consequent high energy loss coefficient, that the reversed flow pattern can no longer be sustained. There is then a sudden jump from reversed flow (large curvature) to unidirectional flow (small curvature), accompanied by a reduction of the energy loss associated with the flow. In addition, for a limited range of flow parameters, a pair of extreme flow patterns might co-exist as a solution of the governing equation, as an indication of a steady bifurcation phenomenon.

These results suggest the need for experiments with highly viscous and elastic fluids (or at microscale where Re is naturally reduced and De is enhanced) in order to identify the supercritical behaviour, which has so far not been reported in the literature.

6.2.6 *Acknowledgements*

The authors acknowledge the financial support from FEDER and FCT through projects PTDC/EQU-FTT/70727/2006 and PTDC/EQU-FTT/71800/2006, and scholarship SFRH/BD/28828/2006 (A.M. Afonso).

7

A *PUZZLING* DRIVING FORCE AND *(FURTHER)* DEVELOPMENTS

7.1 ANALYTICAL SOLUTION OF MIXED EO/PRESSURE DRIVEN FLOWS

Abstract[1]
Analytical solutions are presented for the flow of viscoelastic fluids in micron sized ducts, namely between parallel plates and pipes under the combined influence of electrokinetic and pressure forces using the Debye–Hückel approximation, including the limit case of pure electro-osmotic flow. The viscoelastic fluids used are described by the simplified Phan-Thien–Tanner model (sPTT), with linear kernel for the stress coefficient function, and zero second normal stress difference, and the FENE-P model, based on the kinetic theory for finitely extensible dumbbells with a Peterlin approximation for the average spring force. The solution is non-linear with a significant contribution arising from the coupling between the electric and pressure potentials. This term acts as a drag reducer and a drag increaser under favorable and adverse pressure gradients, respectively and contrasts with the Newtonian flow case, for which it does not exist, demonstrating that the superposition principle valid for Newtonian fluids no longer applies when non- linear viscoelastic fluid models are considered. The combined effects of fluid rheology, electro-osmotic and pressure gradient forcing on the fluid velocity distribution and fluid stresses are also discussed. The analysis of the streaming potential is also included.

Keywords: Electro-osmotic/pressure driven flows; PTT model; FENE-P model; viscoelastic fluids; microchannels; streaming potential.

7.1.1 *Introduction*

Pressure-driven fully developed pipe and channel flows of Newtonian fluids are simple flows described in most classical books on viscous fluid mechanics (Lamb, 1932). For non-Newtonian fluids the corresponding flow characteristics are also well known when their rheological descriptions are inelastic and rely on such simple models as the power-law or Bingham equations (Skelland, 1967). In contrast, the corresponding flows for complex materials described by quasi-linear and non-linear viscoelastic constitutive equations have only been the subject of research over the last 30 years, except for a few simple cases which have been known for a longer time. For the Phan-Thien–Tanner (PTT)

1 A.M. Afonso, M.A. Alves, F.T. Pinho (2009). Analytical solution of mixed electro-osmotic/pressure driven flows of viscoelastic fluids in microchannels. *Journal of Non-Newtonian Fluid Mechanics* **159** 50-63.

model (Phan-Thien and Tanner, 1977; Phan-Thien, 1978) there are several recent analytical solutions in the literature for non-homogeneous shear flow under fully-developed conditions in pipes, channels and annuli (Oliveira and Pinho, 1999c; Pinho and Oliveira, 2000; Alves et al., 2001a; Cruz and Pinho, 2004; Mirzazadeh et al., 2005). For the FENE-P fluid (Bird et al., 1980), Oliveira (2002) investigated analytically the solution for slit and pipe flows and some of these solutions for PTT and FENE-P fluids were extended by Cruz et al. (2005) to account for the presence of a Newtonian solvent and the use of multimode models (Cruz and Pinho, 2007). For the Giesekus fluid an earlier solution was derived by Schleiniger and Weinacht (1991) and for the Johnson-Segalman constitutive equation the reader is referred to Van Schaftingen and Crochet (1985) and Fyrillas et al. (1999). Issues of flow stability in these flows have also been investigated as reported discussed in the introduction of Cruz and Pinho (2007).

The overall impact of surface forces on flow characteristics increases as the flow scale decreases (Stone et al., 2004). Therefore, capillary and electrokinetic effects, which may be negligible in macroscale flow processes, can become dominant or be used on purpose for flow control in microchannels and microfluidic devices (Stone et al., 2004). The latter are relevant in the present context and arise when dielectric surfaces are brought in contact with polar fluids further enhanced by the application of external electric potentials. It is the case of separation and synthesis of biological or chemical components, such as the separation and manipulation of DNA molecules (Jendrejack et al., 2003), biopolymers and large proteins.

Electro-osmosis is a basic electrokinetic phenomenon, where the flow of an electrolyte in a channel is induced by an external electric field applied between the inlet and outlet, after the interaction between the dielectric channel walls and the polar fluid has created near-wall layers of counter-ions within the fluid. These layers of liquid move under the action of the applied electric field whereas the neutral core is dragged and moves as a solid body (Bruss, 2008). The principle was first demonstrated by Reuss (1809), in an experimental investigation using porous clay. This was followed by the theoretical work on the Electric Double Layer (EDL) of von Helmholtz (1879), which related the electrical and flow parameters for electrokinetically driven flows. In the early 1900s von Smoluchowski (von Smoluchowski, 1903) contributed to the understanding of electrokinetically driven flows, especially for conditions where the EDL thickness is much smaller than the channel height.

For Newtonian fluids, rigorous modeling of the electro-osmotic flow in microchannels has been the subject of several studies. Burgreen and Nakache (1964) studied the effect of the surface potential on liquid transport through ultrafine slits relying on the Debye–Hückel linear approximation to the electrical potential distribution under an imposed electrical field. Rice and Whitehead (1965) discussed the same problem in a circular capillary and Levine et al. (1975) extended the Rice and Whitehead model (Rice and Whitehead, 1965) to a higher surface potential. Dutta and Beskok (2001) obtained analytical solutions for the velocity distribution, mass flow rate, pressure gradient, wall shear stress, and vorticity in mixed electro-osmotic/pressure driven flows for two-dimensional straight channels, under conditions of small EDL thickness, with application to microfluidic devices where the wall-to-

wall distance was one to three orders of magnitude larger than EDL thickness. Arulanandam and Li (2000) and Wang et al. (2007a) presented a two-dimensional analytical model for the electro-osmotic flow in a microchannel with rectangular cross-section. A thorough review on various other aspects of electro-osmosis can be found in Karniadakis et al. (2005).

The theoretical study of electro-osmotic flows of non-Newtonian fluids is recent and most works have been limited to simple inelastic fluid models, such as the power-law, due to the inherent analytical difficulties introduced by more complex constitutive equations. Examples are the recent works of Das and Chakraborty (2006) and Chakraborty (2007), who presented explicit analytical solutions for velocity, temperature and concentration distributions in electro-osmotic microchannel flows of a non-Newtonian bio-fluid described by the power-law model. Other purely viscous models were analytically investigated by Berli and Olivares (2008), who considered the existence of a small wall layer depleted of additives (the skimming layer) and behaving as a Newtonian fluid under the combined action of pressure and electrical fields, thus restricting the non-Newtonian behaviour to the electrically neutral region outside the EDL. Investigations on other relevant phenomena in microfluidics, such as surface tension effects and its relation to non-Newtonian properties also rely on the inelastic power law viscosity model (Chakraborty, 2005).

Very recently these studies were extended to viscoelastic fluids by Park and Lee (2008b), who derived the Helmholtz-Smoluchowski velocity for pure electro-osmotic flow of PTT fluids and provided a simple numerical procedure to calculate its value. It is clear that there are no analytical solutions for fully-developed electro-osmotic flows of quasi-linear and non-linear viscoelastic fluids, and even less so when in combination with pressure gradient, where some new non-linear coupled terms arise. This work aims to partially fulfill this gap by presenting the analytical solutions for the flows of PTT and FENE-P fluids between two parallel plates under the mixed influence of electrokinetic and pressure forces, including the limit case of pure electro-osmosis. The PTT fluid (Phan-Thien and Tanner, 1977) obeys the simplified model, with a linear kernel for the stress coefficient function (Phan-Thien, 1978) and a zero second normal stress difference, thus it includes the solution for Upper-Convected model (UCM) fluids. The FENE-P fluid is also used, and this model is based on the kinetic theory for Finitely Extensible Non-linear Elastic dumbbells with a Peterlin approximation for the average spring force (cf. Bird et al., 1980). The viscoelastic fluids are assumed to have the same properties in the whole domain including the EDL. Bio-fluids are usually complex in their structure leading to equally complex constitutive equations to describe their rheology and the ensuing flows. In particular they often exhibit normal stresses, shear-thinning viscosity and memory effects and their rheological behaviour can be described by differential viscoelastic constitutive equations that are related to the PTT and FENE-P form, as in the case of blood (Owens, 2006; Moyers-Gonzalez et al., 2008), saliva (Vissink et al., 1984), synovial fluid (Thurston and Greiling, 1978; Fam et al., 2007) or other biofluids containing long chain molecules. The flows of relevance here would be in micron-size geometries as in chips for chemical and biological analysis and in micro-rheometers (Rodd et al., 2007).

The paper starts with the set of governing equations including the nonlinear Poisson –Boltzmann equation governing the EDL field and the added body force to the momentum equation caused by the applied electrical potential field. The simplifications required to obtain the analytical solution are discussed, the solutions are presented, including the particular case of streaming potential, and a discussion of the effects of the various relevant nondimensional parameters upon the flow characteristics closes this work.

7.1.2 *Governing equations*

The steady, fully-developed flow of the incompressible viscoelastic fluid under investigation is sketched in Figure 7.1. The flow direction in the conditions illustrated is from left to right, but it can be reversed if either the polarity at the walls or of the electrodes at each end of the channel are reversed. In both cases, the solutions here described remain valid.

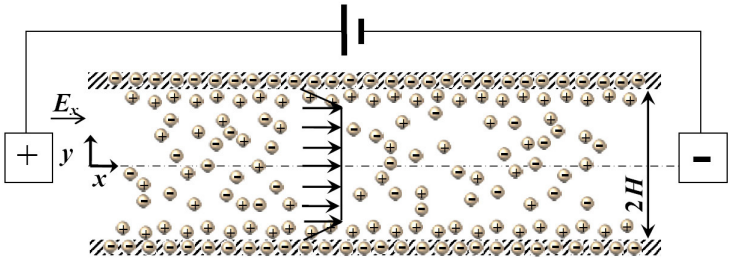

Figure 7.1: Schematic of the flow in a microchannel.

The migration of ions naturally arises due to the interaction between the dielectric walls and the polar fluid. Here, the two negatively charged walls of the microchannel of height $2H$, length l and width w, with $w \gg 2H$, attract counter-ions forming layers of positively charged fluid near the walls and repel the co-ions. Very thin layers of immobile counter-ions cover the walls, known as the Stern layers, followed by thicker more diffuse layers of mobile counter-ions, the two layers near the wall forming what is called the Electrical Double Layer (EDL). The global charge of the flow domain remains neutral, but since the two EDLs are thin the core is essentially neutral. Applying a DC potential difference between the two electrodes at the inlet and outlet generates an external electric field that exerts a body force on the counter-ions of the EDL, which move along the channel dragging the neutral liquid core. The pressure difference that can also be applied between the inlet and outlet can act in the same direction of the electric field or in the opposite direction. Alternatively, the potential difference is not imposed, but results from the accumulation of ions at the end of the channel due to the flow created by the pressure difference. This particular case, known as streaming potential, implies a specific relation between the favorable pressure gradient and the ensuing adverse external electric field (Yang and Li, 1997), which will be quantified later in this paper.

The basic field equations describing this fully-developed flow for incompressible fluids are the continuity equation,

$$\nabla \cdot \mathbf{u} = 0 \tag{7.1}$$

and the modified Cauchy equation,

$$-\nabla p + \nabla \cdot \boldsymbol{\tau} + \rho_e \mathbf{E} = 0 \tag{7.2}$$

where $\mathbf{u}$ is the velocity vector, p the pressure, ρ the fluid density and $\boldsymbol{\tau}$ the polymeric extra-stress contribution. The $\rho_e \mathbf{E}$ term of equation (7.2) represents a body force per unit volume, where $\mathbf{E}$ is the applied external electric field (or resulting from the streaming potential) and ρ_e is the net electric charge density in the fluid.

7.1.2.1 *Constitutive equations*

7.1.2.2 *PTT model*

The polymer extra-stress $\boldsymbol{\tau}$ is described by an appropriate constitutive equation, and in this work we consider two models. The first model describes the viscoelastic behaviour following the ideas of Phan-Thien and Tanner (Phan-Thien and Tanner, 1977; Phan-Thien, 1978), who derived the PTT model - equation (7.3) - from network theory arguments,

$$f(\boldsymbol{\tau}_{kk})\boldsymbol{\tau} + \lambda \overset{\nabla}{\boldsymbol{\tau}} = 2\eta \mathbf{D} \tag{7.3}$$

where $\mathbf{D} = \left(\bigtriangledown \mathbf{u}^T + \bigtriangledown \mathbf{u}\right)/2$ is the rate of deformation tensor, λ is the relaxation time of the fluid, η is a polymer viscosity coefficient and $\overset{\nabla}{\boldsymbol{\tau}}$ represents the upper-convected derivative of $\boldsymbol{\tau}$, defined as

$$\overset{\nabla}{\boldsymbol{\tau}} = \frac{D\boldsymbol{\tau}}{Dt} - \bigtriangledown \mathbf{u}^T . \boldsymbol{\tau} - \boldsymbol{\tau} . \bigtriangledown \mathbf{u} \tag{7.4}$$

The stress coefficient function, $f(\boldsymbol{\tau}_{kk})$, is given by the linear form (Phan-Thien and Tanner, 1977)

$$f(\boldsymbol{\tau}_{kk}) = 1 + \frac{\varepsilon\lambda}{\eta}\boldsymbol{\tau}_{kk} \tag{7.5}$$

where $\boldsymbol{\tau}_{kk}$ represents the trace of the extra-stress tensor and ε is a parameter that imposes an upper limit to the elongational viscosity. For $\varepsilon = 0$ the upper-convected Maxwell model (UCM) is recovered.

7.1.2.3 *FENE-P model*

The second viscoelastic model used in this work is the FENE-P equation, based on the kinetic theory for finitely extensible dumbbells with a Peterlin approximation for the average spring force. In this case the polymer extra-stress is given by (Bird et al., 1980):

$$Z(\boldsymbol{\tau}_{kk})\boldsymbol{\tau} + \lambda \overset{\nabla}{\boldsymbol{\tau}} - \lambda \left(\boldsymbol{\tau} - \frac{b}{b+2} n k_B T \mathbf{I}\right) \frac{D \ln Z}{Dt} = 2\eta \left(\frac{b+5}{b+2}\right) \mathbf{D} \tag{7.6}$$

where $\mathbf{I}$ is the identity tensor, b is a parameter that measures the extensibility of the dumbbell, k_B is the Boltzmann constant, T is the absolute temperature and n is a parameter of the model (Bird et al., 1980). The stress coefficient function, $Z(\boldsymbol{\tau}_{kk})$, can be expressed by (Bird et al., 1980):

$$Z(\boldsymbol{\tau}_{kk}) = 1 + 3\left(\frac{1}{b+2} + \frac{\lambda}{3\eta}\frac{\boldsymbol{\tau}_{kk}}{(b+5)}\right) \tag{7.7}$$

Note that for fully-developed flows $^{D\ln Z}/_{Dt} \approx 0$ and equation (7.7) becomes considerably simplified.

7.1.2.4 *Poisson–Boltzmann equation*

Contact between the dielectric walls of the channel with the electrolyte fluid spontaneously results in the formation of two electric double layers (EDL), one near each wall, as seen in Figure 7.1. They are sufficiently far from each other to allow us to consider them as independent. In the case of pipe flow there is a single EDL around the wall, so that EDL's at opposite sides of a diameter do not interfere. The potential field (ψ) of these electric double layers can be expressed by means of a Poisson–Boltzmann equation:

$$\nabla^2\psi = -\frac{\rho_e}{\epsilon} \tag{7.8}$$

where ϵ is the dielectric constant of the solution, assumed constant. The Poisson- Boltzman equation can be integrated subjected to adequate boundary conditions, to be given in the next section. Prior to that it is necessary to quantify the electric charge density in order to have a closed-form equation. According to Bruss (2008) the electric charge density, ρ_e, for an electrolyte in equilibrium near a charged surface is given by

$$\rho_e = -2n_o ez \sinh\left(\frac{ez}{k_B T}\psi\right) \tag{7.9}$$

here n_o is the ionic density, e is the elementary electronic charge and z is the valence of the ions.

7.1.2.5 *Boundary conditions and other assumptions*

The coordinate system is represented in Figure 7.1. Due to the symmetry of the geometry only half of the channel ($0 \leqslant y \leqslant H$) is considered in this analysis. For the pipe geometry, H is the pipe radius. At the wall the no-slip condition applies whereas on the centreplane/axis, $y = 0$, the condition of symmetry applies. Since the flow is fully-developed the velocity and stress fields only depend on the transverse coordinate y. This coordinate represents the radial position for the pipe flow.

As described above, the contact between the dielectric wall and the electrolyte fluid results in a spontaneous charge transfer between wall and fluid by ionization, ion adsorption or ion dissolution that leads to an opposite charge distribution at the wall and fluid, which depends on the chemical composition of both materials, while maintaining global charge neutrality. Then, electro-osmotic flow results from the motion of the charged fluid species when subjected to an externally applied electric field between the channel/pipe inlet and outlet. The thickness of the EDL depends on the ionic concentration, thermal energy and electrical properties of the liquid, ranging from nanometers for high ionic concentration solutions to several microns for pure water and pure organic liquids. Here, we assume that the ionic charge distribution across the channel/pipe is such that the two EDL are thin. Under these conditions and provided the applied electric field is weak, i.e., that $\triangle\phi/l \ll \psi_0/\xi$, where $\triangle\phi$ is the potential difference of the applied electric field, l is the channel length and ξ is the Debye layer thickness,

the charge distribution is essentially independent of the external electric field and is determined from the potential at the wall, ψ_0, frequently called the zeta potential. If the local electro-osmotic flow velocities are small, which is the case for thin EDL, the effect of fluid motion on the charge redistribution can also be neglected. These assumptions are all part of the so-called standard electrokinetic model.

The electric double layer is thin when the potential at the wall is small. For small values of $ez\psi_0/k_BT$, synonymous of a small ratio of electrical to thermal energies, equation (7.9) can be linearized, $\sinh x \approx x$. This is called the Debye-Hückel approximation and is invoked in this work. At room temperature this limits the zeta potential to values much smaller than 26 mV. Under these conditions, each wall only affects the charge distribution in its vicinity and does not interfere with the charge distribution near the other wall of the channel. For thin layers in a pipe this also means that there is no need to account for wall curvature effects, when deriving the potential and electric charge distributions for the pipe flow solution.

The boundary conditions for the Poisson-Boltzmann equation are $\partial\psi/\partial y = 0$ at the symmetry plane/axis and zeta potential at the wall, $\psi_{wall} = \psi_0$, which takes the sign of the fluid charges at the wall.

Regarding the non-Newtonian fluid, the assumption is made that there is a well mixed fluid behaviour uniformly distributed across the channel/pipes. An alternative assumption, sometimes invoked for solutions and suspensions, including non-Newtonian fluids (Berli and Olivares, 2008), is that there is depletion of additives very close to the wall, where the fluid essentially behaves as a Newtonian fluid. This is currently under investigation and the corresponding solution is considerably more eleaborate. Besides there are here possibilities that need to be considered, and this matter is left for future work.

7.1.3 *Analytical solution*

7.1.3.1 *PTT constitutive equation*

The extra-stresses for the PTT model in these fully-developed flows, for which $\mathbf{u} = \{u(y), 0, 0\}$, can be obtained from equations (7.3-7.5), which reduce to

$$f(\boldsymbol{\tau}_{kk})\tau_{xx} = 2\lambda\dot{\gamma}\tau_{xy} \tag{7.10}$$

$$f(\boldsymbol{\tau}_{kk})\tau_{yy} = 0 \tag{7.11}$$

$$f(\boldsymbol{\tau}_{kk})\tau_{xy} = \eta\dot{\gamma} + \lambda\dot{\gamma}\tau_{yy} \tag{7.12}$$

where $\boldsymbol{\tau}_{kk} = \tau_{xx} + \tau_{yy}$ is the trace of the extra-stress tensor. Equation (7.11) implies $\tau_{yy} = 0$, $\tau_{kk} = \tau_{xx}$, and the stress coefficient function becomes an explicit function of the streamwise normal stress $f(\tau_{xx})$ as in Phan-Thien and Tanner (1977). Then, upon division of equation

(7.10) by equation (7.12) the specific function $f(\tau_{xx})$ cancels out, and a relation between the normal and shear stresses is obtained,

$$\tau_{xx} = 2\frac{\lambda}{\eta}\tau_{xy}^2 \tag{7.13}$$

7.1.3.2 *FENE-P constitutive equation*

For the FENE-P fluid in fully developed shear flow between two parallel plates and in a pipe, i.e., subjected to $\mathbf{u} = \{u(y), 0, 0\}$, equations (7.6) and (7.7) reduce to

$$Z(\boldsymbol{\tau}_{kk})\tau_{xx} = 2\lambda\dot{\gamma}\tau_{xy} \tag{7.14}$$

$$Z(\boldsymbol{\tau}_{kk})\tau_{xy} = \left(\frac{b+5}{b+2}\right)\eta\dot{\gamma} \tag{7.15}$$

Again, the trace of the extra-stress tensor becomes $\boldsymbol{\tau}_{kk} = \tau_{xx}$, thus

$$Z(\tau_{xx}) = \left(\frac{b+5}{b+2}\right)\left[1 + \frac{\lambda}{\eta}\frac{(b+2)}{(b+5)^2}\tau_{xx}\right] \tag{7.16}$$

The relation between the normal and shear stresses is,

$$\tau_{xx} = 2\frac{\lambda}{\eta}\left(\frac{b+2}{b+5}\right)\tau_{xy}^2 \tag{7.17}$$

7.1.3.3 *Potential field across the channel*

The potential field only depends on y, $\nabla^2\psi = d^2\psi/dy^2$, which can be used in equation (7.8). Substituting the distribution of the net charge density (ρ_e) by equation (7.9) and invoking the assumptions discussed in Section 7.1.2.5, the following form of the Poisson- Boltzmann equation for the potential across the half channel is obtained:

$$\frac{d^2\psi}{dy^2} = \kappa^2\psi \tag{7.18}$$

where $\kappa^2 = \frac{2n_0e^2z^2}{\epsilon k_B T}$ is the Debye-Hückel parameter, related to the thickness of the Debye layer, $\xi = \frac{1}{\kappa}$ (also referred to as the EDL thickness). This approximation is valid when the Debye thickness is small but finite, i.e., for $10 \lesssim H/\xi \lesssim 10^3$, and it is also used here for pipe flow neglecting wall curvature effects in the Laplacian.

Equation (7.18) can be solved subjected to the boundary conditions (cf. Section 7.1.2.5) to give,

$$\psi = \frac{\psi_0\cosh(\kappa y)}{\cosh(\kappa H)} \tag{7.19}$$

for $0 \leqslant y \leqslant H$. Finally, the net charge density distribution, equation (7.9), in conjunction with equations (7.19) reduces to

$$\rho_e = -\epsilon\psi_0\kappa^2\frac{\cosh(\kappa y)}{\cosh(\kappa H)} \tag{7.20}$$

which is a positive quantity for a wall charged negatively ($\psi_0 < 0$).

7.1.3.4 *Analytical solution for the PTT model*

Henceforth, the analytical solution and the subsequent discussions are for channel flow, thus avoiding unnecessary complications. The full solution for pipe flow is presented in Appendix A without any discussion because the trends are similar to those found for the slit flow.

Under fully developed conditions, the momentum equation (7.2), reduces to

$$\frac{d\tau_{xy}}{dy} = -\rho_e E_x + p_{,x} \tag{7.21}$$

where $p_{,x} \equiv dp/dx$, $E_x \equiv -d\phi/dx$ and ϕ is the electric potential of the applied external field, which is characterized by a constant streamwise gradient under fully-developed flow conditions. Note that in this flow the external electrical field is positive according to Figure 7.1, and negative otherwise.

Using equation (7.20) and noting that the shear stress at the centerline is zero, Eq. (7.21) can be integrated to yield the following linear contribution of electro-osmotic and pressure gradient contributions to the shear stress distribution

$$\tau_{xy} = \epsilon\psi_0 E_x \kappa \frac{\sinh(\kappa y)}{\cosh(\kappa H)} + p_{,x} y \tag{7.22}$$

Using the relation between the normal and shear stresses - equation (7.13), the following explicit expression for the normal stress component is obtained,

$$\tau_{xx} = 2\frac{\lambda}{\eta}\left(\epsilon\psi_0 E_x \kappa \frac{\sinh(\kappa y)}{\cosh(\kappa H)} + p_{,x} y\right)^2 \tag{7.23}$$

The square term in equation (7.23) introduces a contribution to the normal stress from the combined electro-osmotic and pressure forces.

To determine the velocity gradient, equations (7.12), (7.22) and (7.23) are combined to give

$$\dot{\gamma} \equiv \frac{du}{dy} = \left[1 + 2\varepsilon\lambda^2\left(\frac{\kappa\epsilon\psi_0 E_x}{\eta}\frac{\sinh(\kappa y)}{\cosh(\kappa H)} + \frac{p_{,x}}{\eta} y\right)^2\right]\left(\frac{\kappa\epsilon\psi_0 E_x}{\eta}\frac{\sinh(\kappa y)}{\cosh(\kappa H)} + \frac{p_{,x}}{\eta} y\right) \tag{7.24}$$

Equation (7.24) can be integrated subject to the no-slip boundary condition at the wall ($u_{\|y=H} = 0$) and the resulting velocity profile is

$$u = u^E + u^P + u^{EP} \tag{7.25}$$

with

$$u^E = \left(\frac{\epsilon\psi_0 E_x}{\eta} - 2\overline{C}\kappa^2\varepsilon\lambda^2\left[\frac{\epsilon\psi_0 E_x}{\eta}\right]^3\right)(\overline{A} - 1) + \frac{2}{3}\kappa^2\varepsilon\lambda^2\left[\frac{\epsilon\psi_0 E_x}{\eta}\right]^3(\overline{A}^3 - 1) \tag{7.26}$$

$$u^P = \frac{1}{2}\left[\frac{p_{,x}}{\eta}\right](y^2 - H^2)\left[1 + \varepsilon\lambda^2\left[\frac{p_{,x}}{\eta}\right]^2(y^2 + H^2)\right] \tag{7.27}$$

$$\begin{aligned} u^{EP} = {} & \frac{3}{2}\varepsilon\lambda^2\left[\frac{\epsilon\psi_0 E_x}{\eta}\right]^2\left[\frac{p_{,x}}{\eta}\right]\left[1 - \overline{A}^2 + (\kappa^2 H^2 - \kappa^2 y^2)\overline{C} + 2\kappa\overline{D}(y\overline{A}\,\overline{B} - H)\right] \\ & + 12\frac{\varepsilon\lambda^2}{\kappa^2}\left[\frac{\epsilon\psi_0 E_x}{\eta}\right]\left[\frac{p_{,x}}{\eta}\right]^2\left[\kappa\overline{D}(H - y\overline{B}) + (1 + \frac{1}{2}\kappa^2 y^2)\overline{A} - (1 + \frac{1}{2}\kappa^2 H^2)\right] \end{aligned} \tag{7.28}$$

where $\overline{A} = \frac{\cosh(\kappa y)}{\cosh(\kappa H)}$, $\overline{B} = \frac{\sinh(\kappa y)}{\sinh(\kappa H)}$, $\overline{C} = \frac{1}{\cosh^2(\kappa H)}$ and $\overline{D} = \tanh(\kappa H)$.

As suggested by equation (7.25) there are three contributions to the velocity profile: u^E represents the pure electro-osmotic flow for a viscoelastic fluid and is given by equation (7.26); u^P is the contribution due to the pressure gradient for a viscoelastic fluid and is given by equation (7.27); finally, the third contribution couples the Poiseuille and electro-osmotic flows and this is given by u^{EP} expressed by equation (7.28), which is simultaneously proportional to $p_{,x}$ and E_x. This last contribution only exists because the fluid is nonlinear, i.e., no such effect is present if the fluid is Newtonian or a quasi-linear viscoelastic fluid, such as UCM fluid. Indeed, u^{EP} is proportional to ε, which is non-zero for the PTT fluid but is zero for UCM/Oldroyd-B fluids. Equation (7.25) shows that the superposition principle valid for Newtonian and quasi-linear viscoelastic fluids is no longer valid for the PTT and FENE-P fluids and suggests that the same applies to other non-linear viscoelastic models.

It is often more convenient to work with the dimensionless form of equation (7.25). Introducing the normalizations $\bar{y} = y/H$ and $\bar{\kappa} = \kappa H$, the dimensionless velocity profile can be written as

$$\begin{aligned}\frac{u}{u_{sh}} &= (1-2\overline{C}\varepsilon De_\kappa^2)(1-\overline{A}) + \frac{2}{3}\varepsilon De_\kappa^2(1-\overline{A}^3) \\ &\quad - \frac{1}{2}\Gamma\left(1-\bar{y}^2\right)\left[1+\frac{\varepsilon De_\kappa^2}{\bar{\kappa}^2}\Gamma^2\left(1+\bar{y}^2\right)\right] \\ &\quad + \frac{3}{2}\frac{\varepsilon De_\kappa^2}{\bar{\kappa}^2}\Gamma\left[1-\overline{A}^2+(\bar{\kappa}^2-(\bar{\kappa}\bar{y})^2)\overline{C}+2\bar{\kappa}\overline{D}\left(\bar{y}\overline{A}\,\overline{B}-1\right)\right] \\ &\quad - \frac{12\varepsilon De_\kappa^2}{\bar{\kappa}^4}\Gamma^2\left[\bar{\kappa}\overline{D}\left(1-\bar{y}\overline{B}\right)+(1+\frac{1}{2}(\bar{\kappa}\bar{y})^2)\overline{A}-(1+\frac{1}{2}\bar{\kappa}^2)\right]\end{aligned} \tag{7.29}$$

where $De_\kappa = \frac{\lambda u_{sh}}{\xi} = \lambda\kappa u_{sh}$ is the Deborah number based on the EDL thickness and on the Helmholtz-Smoluchowski electro-osmotic velocity, defined as $u_{sh} = -\frac{\epsilon\psi_0 E_x}{\eta}$ (von Smoluchowski, 1903; Park and Lee, 2008b). In Poiseuille flows a different Deborah number is usually defined (Oliveira and Pinho, 1999c; Pinho and Oliveira, 2000) based on the cross-sectional average velocity for the Newtonian flow under the sole influence of pressure gradient and the channel half-height, $De_N = \frac{\lambda U_N}{H}$ with $U_N = -\frac{H^2 p_{,x}}{3\eta}$. A third alternative Deborah number for electro-osmotic flow is based again on u_{sh}, but considers the channel half-height, $De_{sh} = \frac{\lambda u_{sh}}{H}$. These three Deborah numbers are related by $De_\kappa = \bar{\kappa} De_{sh} = -\frac{3}{\Gamma}\bar{\kappa} De_N$, where parameter $\Gamma = -\frac{H^2}{\epsilon\psi_0}\frac{p_{,x}}{E_x}$ represents the ratio of pressure to electro-osmotic driving forces.

Flow problems are usually of direct or indirect/inverse type. In a direct problem the pressure gradient $p_{,x}$ and the applied electric potential gradient E_x are known (or instead the ratio of pressure to electro-osmotic driving forces is known) and the flow rate, or the cross-sectional average velocity, is required. The flow rate can be determined from integration of the velocity profile of equation (7.25). Here, this integration was carried out using the normalized velocity profile, equation (7.29), thinking ahead on the benefit this brings to the inverse problem,

where the aim is the determination of Γ for a given dimensionless flow rate. The expression for the normalized flow rate is

$$\begin{aligned}
\overline{Q} &= \frac{Q}{2Hu_{sh}} = \frac{\overline{u}}{u_{sh}} = \int_{-1}^{1} \frac{u}{u_{sh}} d\overline{y} = 2\int_{0}^{1} \frac{u}{u_{sh}} d\overline{y} = \overline{Q}^{E} + \overline{Q}^{P} + \overline{Q}^{EP} \\
\overline{Q}^{E} &= 2\left(1 - 2\overline{C}\varepsilon D e_{\kappa}^{2}\right)\left(1 - \frac{\overline{D}}{\bar{\kappa}}\right) + \frac{4}{3}\varepsilon D e_{\kappa}^{2}\left(1 - \frac{1}{3}\frac{\overline{D}}{\bar{\kappa}}\left(1 + 2\overline{C}\right)\right) \\
\overline{Q}^{P} &= -2\Gamma\left(\frac{2}{5}\frac{\varepsilon D e_{\kappa}^{2}}{\bar{\kappa}^{2}}\Gamma^{2} + \frac{1}{3}\right) \\
\overline{Q}^{EP} &= 3\frac{\varepsilon D e_{\kappa}^{2}}{\bar{\kappa}^{2}}\Gamma\left(2 - \frac{\overline{D}}{\bar{\kappa}} - \overline{C} + \frac{2}{3}\overline{C}\bar{\kappa}^{2} - 2\bar{\kappa}\overline{D}\right) \\
&\quad - \frac{24\varepsilon D e_{\kappa}^{2}}{\bar{\kappa}^{4}}\Gamma^{2}\left(-3 + 3\frac{\overline{D}}{\bar{\kappa}} + \frac{3}{2}\bar{\kappa}\overline{D} - \frac{1}{2}\bar{\kappa}^{2}\right)
\end{aligned} \tag{7.30}$$

This is a cubic equation on Γ and the solution of the inverse problem (calculation of Γ for a given $\overline{Q}$) involves the determination of Γ, which can be done using the Cardan-Tartaglia solution for cubic algebraic equations. Within the assumptions invoked in Section 7.1.2.5, the analysis in this section is general, but relies on the Debye-Hückel approximation. Here, as in many practical applications the finite electric double layer is very small, about 1 to 3 orders of magnitude smaller than the thickness of the microfluidic channel ($10 \lesssim \bar{\kappa} \lesssim 10^{3}$). In these circumstances $\cosh(\bar{\kappa}) \gg 1$ and $\overline{D} = \tanh(\bar{\kappa}) \approx 1$, so the above equations for the velocity profile can be further simplified. In particular the normalized flow rate becomes

$$\begin{aligned}
\overline{Q} &\simeq 2\left(\frac{\bar{\kappa} - 1}{\bar{\kappa}}\right) + \frac{4}{3}\varepsilon D e_{\kappa}^{2}\left(\frac{3\bar{\kappa} - 1}{3\bar{\kappa}}\right) - 2\Gamma\left(\frac{2}{5}\frac{\varepsilon D e_{\kappa}^{2}}{\bar{\kappa}^{2}}\Gamma^{2} + \frac{1}{3}\right) \\
&\quad + 3\frac{\varepsilon D e_{\kappa}^{2}}{\bar{\kappa}^{2}}\Gamma\left(\frac{2\bar{\kappa} - 1 - 2\bar{\kappa}^{2}}{\bar{\kappa}}\right) - \frac{24\varepsilon D e_{\kappa}^{2}}{\bar{\kappa}^{4}}\Gamma^{2}\left(\frac{\bar{\kappa}}{2}(3 - \bar{\kappa}) + \frac{3 - 3\bar{\kappa}}{\bar{\kappa}}\right)
\end{aligned} \tag{7.31}$$

which is simpler than equation (7.30), but still cubic in Γ. This expression can be written in compact form as

$$\Gamma^{3} + a_{1}\Gamma^{2} + a_{2}\Gamma + a_{3} = 0 \tag{7.32}$$

The explicit solution of the inverse problem, giving the ratio of pressure to electro-osmotic driving forces as a function of the non-dimensional flow rate, viscoelastic model parameters and relative microchannel ratio is obtained using the Cardan-Tartaglia solution,

$$\begin{aligned}
\Gamma &= \sqrt[3]{-\frac{b_{1}}{2} + \sqrt{\frac{b_{1}^{2}}{4} + \frac{a^{3}}{27}}} + \sqrt[3]{-\frac{b_{1}}{2} - \sqrt{\frac{b_{1}^{2}}{4} + \frac{a^{3}}{27}}} - \frac{a_{1}}{3} \\
a &= a_{2} - \frac{a_{1}^{2}}{3} \\
b_{1} &= a_{3} - \frac{a_{1}a_{2}}{3} + \frac{2a_{1}^{3}}{27}
\end{aligned} \tag{7.33}$$

with

$$\begin{aligned}
a_{1} &= 15\left(\frac{3 - \bar{\kappa}}{\bar{\kappa}}\right) + 30\left(\frac{3 - 3\bar{\kappa}}{\bar{\kappa}^{3}}\right) \\
a_{2} &= \frac{5}{6}\frac{\bar{\kappa}^{2}}{''De_{»}^{2}} + \frac{15}{4}\left(\frac{2\bar{\kappa}^{2} - 2\bar{\kappa} + 1}{\bar{\kappa}}\right) \\
a_{3} &= \frac{5}{4}\frac{\bar{\kappa}^{2}}{''De_{»}^{2}}\left(\overline{Q} - 2\left(\frac{\bar{\kappa} - 1}{\bar{\kappa}}\right) - \frac{4}{3}\varepsilon D e_{\kappa}^{2}\left(\frac{3\bar{\kappa} - 1}{3\bar{\kappa}}\right)\right)
\end{aligned} \tag{7.34}$$

The explicit expressions for the dimensionless shear and normal stress components are obtained from normalization of equations (7.22) and (7.23),

$$\frac{\tau_{xy}}{3\eta u_{sh}\kappa} = \frac{1}{3}\left[\Gamma\frac{\overline{y}}{\bar{\kappa}} - \frac{\sinh(\bar{\kappa}\overline{y})}{\cosh(\bar{\kappa})}\right] \tag{7.35}$$

$$\frac{\tau_{xx}}{3\eta u_{sh}\kappa} = \frac{2}{3}De_{\kappa}\left(\Gamma\frac{\overline{y}}{\bar{\kappa}} - \frac{\sinh(\bar{\kappa}\overline{y})}{\cosh(\bar{\kappa})}\right)^2 \tag{7.36}$$

The normalized shear rate is

$$\frac{\dot{\gamma}}{u_{sh}\kappa} = \left[1 + 2\varepsilon De_{\kappa}^2\left(\Gamma\frac{\overline{y}}{\bar{\kappa}} - \frac{\sinh(\bar{\kappa}\overline{y})}{\cosh(\bar{\kappa})}\right)^2\right]\left(\Gamma\frac{\overline{y}}{\bar{\kappa}} - \frac{\sinh(\bar{\kappa}\overline{y})}{\cosh(\bar{\kappa})}\right) \tag{7.37}$$

and the viscosity profile is given by

$$\mu(\dot{\gamma}) \equiv \frac{\tau_{xy}}{\dot{\gamma}} \Rightarrow \frac{\mu(\dot{\gamma})}{\eta} = \left[1 + 2\varepsilon De_{\kappa}^2\left(\Gamma\frac{\overline{y}}{\bar{\kappa}} - \frac{\sinh(\bar{\kappa}\overline{y})}{\cosh(\bar{\kappa})}\right)^2\right]^{-1} \tag{7.38}$$

Wall values for all these quantities are useful and are obtained after setting $\overline{y} = 1$ (and $\tanh(\bar{\kappa}) \approx 1$ for $\bar{\kappa} \gtrsim 10$):

$$\begin{aligned}
\left.\frac{\tau_{xy}}{3\eta u_{sh}\kappa}\right|_w &\simeq \frac{1}{3}\left(\frac{\Gamma}{\bar{\kappa}} - 1\right) \\
\left.\frac{\tau_{xx}}{3\eta u_{sh}\kappa}\right|_w &\simeq \frac{2}{3}De_{\kappa}\left(\frac{\Gamma}{\bar{\kappa}} - 1\right)^2 \\
\left.\frac{\mu(\dot{\gamma})}{\eta}\right|_w &\simeq \left[1 + 2\varepsilon De_{\kappa}^2\left(\frac{\Gamma}{\bar{\kappa}} - 1\right)^2\right]^{-1}
\end{aligned} \tag{7.39}$$

The dimensionless locci of the local velocity profile maximum (or minimum), $\overline{\delta}$, can be obtained by setting the shear rate equation (7.37) to zero. Since the first term on the right hand side of equation (7.37) is always positive, $\overline{\delta}$ requires the multiplicative factor to be null and is given by,

$$\overline{\delta} = \frac{\bar{\kappa}}{\Gamma}\frac{\sinh(\bar{\kappa}\overline{\delta})}{\cosh(\bar{\kappa})} = \frac{\bar{\kappa}}{\Gamma}\overline{B(\overline{\delta})} \tag{7.40}$$

This is an interesting equation, because it is independent of the fluid rheology. Recalling equation (7.35) it implies that $\tau_{xy\|\overline{y}=\overline{\delta}} = 0$, and obviously $\overline{\delta} = 0$ is a natural solution of equation (7.40) required by the centerline symmetry condition. However equation (7.40) must have a second solution for $\overline{\delta}$ for positive values of Γ as will become apparent in Section 7.1.4 (cf. Figure 7.3).

7.1.3.5 *Streaming potential solution*

In the solution of the previous section, the electrical field E_x can be applied externally or be a consequence of electric potentials created by the flow. In the absence of an externally applied electrical field, the imposed pressure difference causes a flow containing ions in motion, hence it causes an electrical current, called the streaming current, I_s'. The streaming current accumulates counterions at the end of the channel

therefore setting up an electric field, $E_{x,sp}$ which is associated with the so-called streaming potential, ϕ_{sp} via $E_{x,sp} = -\Delta\phi_{sp}/l$. Therefore, this induced electric field opposes the flow and creates an opposite current, I'_c, called conduction corrent. The net electrical current, I', is the sum of the streaming current and the electrical conduction corrent and in steady-state should be zero:

$$I' = I'_s + I'_c \equiv 0 \tag{7.41}$$

The electrical streaming current (per unit of of width) is of the form:

$$I'_s = 2\int_0^H u(y)\rho_e(y)dy \tag{7.42}$$

which for the particular case of the PTT fluid leads to

$$\begin{aligned}\frac{I'_s}{\epsilon\psi_0} = {} & \kappa\left[\frac{\epsilon\psi_0 E_{x,sp}}{\eta}\right]\left[\overline{D} - \kappa H\overline{C} + \kappa^2\varepsilon\lambda^2\left[\frac{\epsilon\psi_0 E_{x,sp}}{\eta}\right]^2\left[\overline{D} + \frac{3}{2}\kappa H\overline{C}^2 - \frac{5}{2}\overline{D}\,\overline{C}\right]\right] \\ & + \frac{2}{\kappa}\left[\frac{p_{,x}}{\eta}\right]\left[\kappa H - \overline{D} + \frac{\left[\frac{p_{,x}}{\eta}\right]^2 2\varepsilon\lambda^2}{\kappa^2}\left(\kappa^3H^3 - 6\overline{D} - 3\kappa^2H^2\overline{D} + 6\kappa H\right)\right] \\ & + 4\kappa\varepsilon\lambda^2\left[\frac{\epsilon\psi_0 E_{x,sp}}{\eta}\right]^2\left[\frac{p_{,x}}{\eta}\right]\left[-\frac{1}{3}\overline{D} + \kappa H\overline{D}^2 - 2\kappa H\overline{C} + \frac{7}{3}\overline{D}\,\overline{C}\right] \\ & + 2\frac{\varepsilon\lambda^2}{\kappa}\left[\frac{\epsilon\psi_0 E_{x,sp}}{\eta}\right]\left[\frac{p_{,x}}{\eta}\right]^2\left[\frac{3}{2}\overline{D} - \kappa^3H^3\overline{C} + 9\kappa H - \frac{21}{2}\kappa H\overline{C}\right] \\ & + 2\frac{\varepsilon\lambda^2}{\kappa}\left[\frac{\epsilon\psi_0 E_{x,sp}}{\eta}\right]\left[\frac{p_{,x}}{\eta}\right]^2\left[3\kappa^2H^2\overline{D} - 12\kappa H\overline{D}^2\right]\end{aligned} \tag{7.43}$$

The electrical conduction current in the channel can now be expressed as:

$$I'_c = 2\sigma_t E_{x,sp} H \tag{7.44}$$

where σ_t is the total electric conductivity. Note that the conduction current can now flow back through both the fluid as well as the channel walls, depending on the corresponding electrical conductivities. The total electrical conductivity can be calculated as $\sigma_t = \sigma_{fluid} + \sigma_{sur}P_{sur}/A_{chan}$, where P_{sur} and A_{chan} are the wetting perimeter and cross section area of the channel, respectively and σ_{fluid} and σ_{sur} are the fluid bulk and wall surface conductivities, respectively. This equation and the condition imposed by equation (7.41) leads finally to the expression that defines the relation between the imposed pressure gradient and the ensuing streaming electric field, $E_{x,sp}$. This ratio is $\Gamma_{sp} = -\frac{H^2}{\epsilon\psi_0}\frac{p_{,x}}{E_{x,sp}}$ and such relation is equation (7.45)

$$\begin{aligned}-2\Upsilon_1 = {} & \overline{\kappa}\overline{D} - \overline{\kappa}^2\overline{C} + 9\frac{\overline{\kappa}^3\varepsilon De_N^2}{\Gamma_{sp}^2}\left(\overline{D} + \frac{3}{2}\overline{\kappa}\overline{C}^2 - \frac{5}{2}\overline{D}\,\overline{C}\right) \\ & - \frac{2}{\overline{\kappa}}\Gamma_{sp}\left[\overline{\kappa} - \overline{D} + \frac{18\varepsilon De_N^2}{\overline{\kappa}^2}\left(\overline{\kappa}^3 - 6\overline{D} - 3\overline{\kappa}^2\overline{D} + 6\overline{\kappa}\right)\right] \\ & - 36\frac{\overline{\kappa}\varepsilon De_N^2}{\Gamma_{sp}}\left[-\frac{1}{3}\overline{D} + \overline{\kappa}\overline{D}^2 - 2\overline{\kappa}\overline{C} + \frac{7}{3}\overline{D}\,\overline{C}\right] \\ & + 18\frac{\varepsilon De_N^2}{\overline{\kappa}}\left[3\overline{\kappa}^2\overline{D} - 12\overline{\kappa}\overline{D}^2 + \frac{3}{2}\overline{D} - \overline{\kappa}^3\overline{C} + 9\overline{\kappa} - \frac{21}{2}\overline{\kappa}\overline{C}\right]\end{aligned} \tag{7.45}$$

with $\Upsilon_1 = \frac{H^2 \eta \sigma_t}{\epsilon^2 \psi_0^2}$. This new dimensionless number quantifies the effect of electric conductivity. Equation (7.45) is a cubic equation in Γ_{sp}, that can be rewritten in compact form as

$$\Gamma_{sp}^3 + a_1 \Gamma_{sp}^2 + a_2 \Gamma_{sp} + a_3 = 0 \tag{7.46}$$

with coefficients

$$\begin{aligned}
a_1 &= -\frac{\bar{\kappa}\Upsilon_1 + 0.5\bar{\kappa}^2\overline{D} - 0.5\bar{\kappa}^3\overline{C}}{\bar{\kappa} - \overline{D} + \frac{18\varepsilon De_N^2}{\bar{\kappa}^2}\left(\bar{\kappa}^3 - 6\overline{D} - 3\bar{\kappa}^2\overline{D} + 6\bar{\kappa}\right)} \\
&\quad - \frac{9\varepsilon De_N^2\left[3\bar{\kappa}^2\overline{D} - 12\bar{\kappa}\overline{D}^2 + \frac{3}{2}\overline{D} - \bar{\kappa}^3\overline{C} + 9\bar{\kappa} - \frac{21}{2}\bar{\kappa}\overline{C}\right]}{\bar{\kappa} - \overline{D} + \frac{18\varepsilon De_N^2}{\bar{\kappa}^2}\left(\bar{\kappa}^3 - 6\overline{D} - 3\bar{\kappa}^2\overline{D} + 6\bar{\kappa}\right)} \\
a_2 &= \frac{18\bar{\kappa}^2\varepsilon De_N^2\left[-\frac{1}{3}\overline{D} + \bar{\kappa}\overline{D}^2 - 2\bar{\kappa}\overline{C} + \frac{7}{3}\overline{D}\,\overline{C}\right]}{\bar{\kappa} - \overline{D} + \frac{18\varepsilon De_N^2}{\bar{\kappa}^2}\left(\bar{\kappa}^3 - 6\overline{D} - 3\bar{\kappa}^2\overline{D} + 6\bar{\kappa}\right)} \\
a_3 &= -\frac{9}{2}\frac{\bar{\kappa}^4\varepsilon De_N^2\left(\overline{D} + \frac{3}{2}\bar{\kappa}\overline{C}^2 - \frac{5}{2}\overline{D}\,\overline{C}\right)}{\bar{\kappa} - \overline{D} + \frac{18\varepsilon De_N^2}{\bar{\kappa}^2}\left(\bar{\kappa}^3 - 6\overline{D} - 3\bar{\kappa}^2\overline{D} + 6\bar{\kappa}\right)}
\end{aligned} \tag{7.47}$$

The solution of equation (7.46) for Γ_{sp} is equation (7.33), but with the coefficients of equation (7.47).

For ($10 \lesssim \bar{\kappa} \lesssim 10^3$), $\cosh(\bar{\kappa}) \gg 1$ and $\overline{D} = \tanh(\bar{\kappa}) \approx 1$, and the above equations simplify to become

$$\begin{aligned}
a_1 &= \frac{-\left(\bar{\kappa}\Upsilon_1 + 0.5\bar{\kappa}^2 + 9\varepsilon De_N^2\left[3\bar{\kappa}^2 - 3\bar{\kappa} + \frac{3}{2}\right]\right)}{\bar{\kappa} - 1 + \frac{18\varepsilon De_N^2}{\bar{\kappa}^2}\left(\bar{\kappa}^3 - 3\bar{\kappa}^2 + 6\bar{\kappa} - 6\right)} \\
a_2 &= \frac{18\bar{\kappa}^2\varepsilon De_N^2\left[\bar{\kappa} - \frac{1}{3}\right]}{\bar{\kappa} - 1 + \frac{18\varepsilon De_N^2}{\bar{\kappa}^2}\left(\bar{\kappa}^3 - 3\bar{\kappa}^2 + 6\bar{\kappa} - 6\right)} \\
a_3 &= -\frac{9}{2}\frac{\bar{\kappa}^4\varepsilon De_N^2}{\bar{\kappa} - 1 + \frac{18\varepsilon De_N^2}{\bar{\kappa}^2}\left(\bar{\kappa}^3 - 3\bar{\kappa}^2 + 6\bar{\kappa} - 6\right)}
\end{aligned} \tag{7.48}$$

As expected, equations (7.46) -(7.47) reduce to the Newtonian fluid solution, as found in (Mala et al., 1997), when $\varepsilon \to 0$:

$$\Gamma_{sp} = \Upsilon_1\left[\frac{1 + \frac{1}{2}\frac{\bar{\kappa}^2}{\Upsilon_1}\left(\frac{\overline{D}}{\bar{\kappa}} - \overline{C}\right)}{1 - \overline{D}/\bar{\kappa}}\right] \tag{7.49}$$

7.1.3.6 *Analytical solutions for the FENE-P model*

For fully developed channel flow there is similarity between the solutions for the PTT and the FENE-P models as found by Oliveira et al. (1998). Comparing equations (7.83) to (7.84) for the PTT model with equations (7.86) and (7.87) for the FENE-P model, and since the momentum equation (7.90) is independent of the constitutive equation, there is an exact equivalence of the solution in the sense of a parameter to parameter match, as explained in detail in Cruz et al. (2005). Hence,

the solution of Section 7.1.3.4 also applies to the flow of FENE-P fluids, provided the following substitutions are made:

$$\begin{aligned} f(\boldsymbol{\tau}_{xx}) &\rightarrow \left(\frac{b+2}{b+5}\right) Z(\boldsymbol{\tau}_{xx}) \\ \lambda &\rightarrow \lambda\left(\frac{b+2}{b+5}\right) \\ \varepsilon &\rightarrow \frac{1}{b+5} \\ \eta &\rightarrow \eta \end{aligned} \tag{7.50}$$

Identically, these same substitutions are valid to provide the pipe solution for the FENE-P model from the corresponding PTT equations in Appendix A.

7.1.4 *Discussion of results*

In the previous section, general equations were derived for fully developed flow of viscoelastic fluids (PTT and FENE-P fluids) under the mixed influence of electrokinetic and pressure gradient forces. The different influences of the driving forces and fluid rheology on the velocity profile have been identified in equation (7.25) and in this section we discuss in detail some limiting cases in order to understand the fluid dynamics. The following limit cases contained in the general solution are: (a) Newtonian fluid with mixed electro-osmotic/pressure driving forces; (b) Viscoelastic fluid under the sole influence of an electro-osmotic driving force; (c) Poiseuille flow of a viscoelastic fluid and (d) Viscoelastic fluid with mixed electro-osmotic/pressure driving forces. Case (c) was studied in detail elsewhere (Oliveira and Pinho, 1999c; Alves et al., 2001a; Cruz et al., 2005), and so was case (a) (Dutta and Beskok, 2001), but this latter situation is revisited here as a starting point.

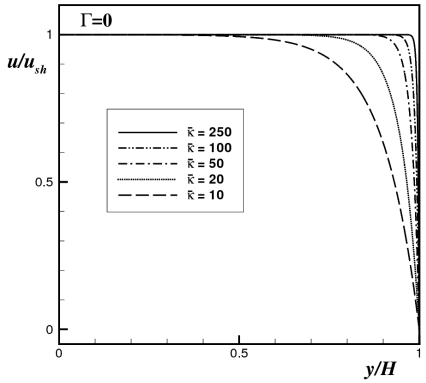

Figure 7.2: Velocity profiles for several relative microchannel ratios, $\bar{\kappa}$, for Newtonian fluids under the sole influence of electrokinetic forces, $\Gamma = 0$.

7.1.4.1 *Newtonian fluid with mixed driving forces*

For a Newtonian fluid the relaxation time is zero and the Deborah number vanishes ($De_\kappa = 0$), thus equation (7.29) becomes

$$\frac{u}{u_{sh}} = 1 - \frac{\cosh(\bar{\kappa}\bar{y})}{\cosh(\bar{\kappa})} - \frac{1}{2}\Gamma\left(1 - \bar{y}^2\right) \tag{7.51}$$

under the mixed influence of electro-osmotic and pressure driving forces, as was also shown by Dutta and Beskok (2001). For $\Gamma \to \infty$, pressure forces dominate the momentum transport for any value of $\bar{\kappa}$, and the classical laminar parabolic velocity profile is recovered. Note that this corresponds to $E_x \to 0$ and $u_{sh} \to 0$, since $u_{sh} \propto E_x$ and $\Gamma \propto E_x^{-1}$. For $\Gamma \to 0$, the last term on the right-hand-side of equation (7.51) vanishes, the flow becomes governed solely by the electro-osmosis and the velocity profile is only a function of the wall distance and the relative microchannel ratio, $\bar{\kappa}$, as shown earlier by Burgreen and Nakache (1964). Figure 7.2 shows the effect of the relative microchannel ratio, $\bar{\kappa}$ (or H/ξ, where ξ is the Debye layer thickness) on the dimensionless velocity profiles for pure electro-osmotic flow, $\Gamma = 0$. As $\bar{\kappa} \to 1$ the double layer thickness becomes of the same order of magnitude as the channel half-height and the region of excess charge is distributed over the entire channel. This situation is not fully compatible with this solution for which the Debye-Hückel approximation was invoked, which requires $\bar{\kappa}_{min} \gtrsim 10$. For $\bar{\kappa} = 100$ the width the Debye layer is about 1% of the channel half-height. Note that for large $\bar{\kappa}$ ($\bar{\kappa} \to \infty$) the size of the EDL or region of excess charge is relatively small, and equation (7.51) reduces to the classical Helmoltz- Smoluchowski equation, $u/u_{sh} = 1$ (von Smoluchowski, 1903), if simultaneously $\Gamma = 0$.

Figure 7.3 shows velocity profiles for various ratios of pressure gradient to electro-osmotic driving forces at $\bar{\kappa} = 20$ and $\bar{\kappa} = 100$. When $\Gamma = 0$ the velocity profiles correspond to a *pluglike flow*. $\Gamma < 0$ and $\Gamma > 0$ correspond to Poiseuille electro-osmotic flows with favorable and adverse pressure gradients, respectively. The velocity profiles shown in Figure 7.3 (b) for $\bar{\kappa} = 100$ are identical to those of Dutta and Beskok (2001). The value of $\bar{\kappa} = 100$ is a typical example for a 0.1 mM buffer solution in a glass channel with ψ_0 of aproximately 25 mV (Dutta and Beskok, 2001).

Equation (7.51) predicts negative velocities at $\bar{y} = 0$ when $\Gamma > 2\frac{\cosh(\bar{\kappa})-1}{\cosh(\bar{\kappa})}$ for all values of $\bar{\kappa}$. For small but finite Debye lengths, $\bar{\kappa} \gtrsim 10$, the velocity becomes negative in the central region of the channel for $\Gamma \gtrsim 2$. As shown in Figure 7.3, the velocity maxima depend on Γ, and this dependency can be expressed by

$$\begin{cases} \left.\frac{u}{u_{sh}}\right|_{max} = 1 - \frac{1}{2}\Gamma & \Gamma \leqslant 0 \bigwedge \bar{\kappa} \gtrsim 10 \\ \left.\frac{u}{u_{sh}}\right|_{max} = 1 - \frac{\cosh(\bar{\kappa}\bar{\delta})}{\cosh(\bar{\kappa})} - \frac{1}{2}\Gamma\left(1 - \bar{\delta}^2\right) & \Gamma > 0 \end{cases} \tag{7.52}$$

where $\bar{\delta}$ is the dimensionless locci of the velocity peaks (or $\tau_{xy\|y=\bar{\delta}} = 0$), given by equation (7.40).

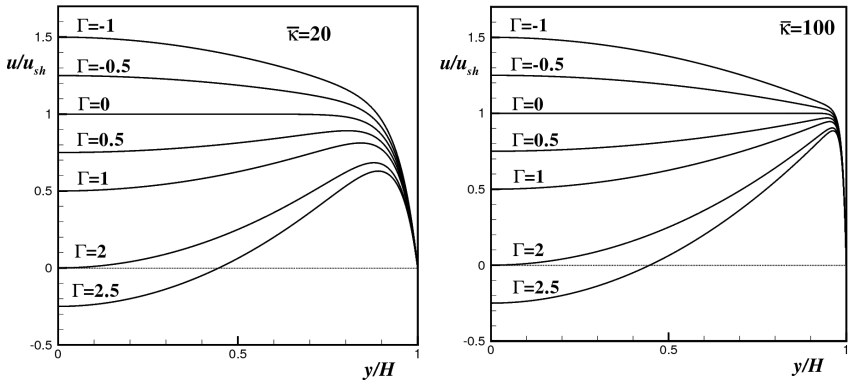

(a) (b)

Figure 7.3: Velocity profiles for various ratios of pressure to electro-osmotic driving forces, Γ, for Newtonian fluids with relative microchannel ratio of (a)$\bar{\kappa} = 20$ and (b)$\bar{\kappa} = 100$.

7.1.4.2 *Viscoelastic fluid with sole electro-osmotic driving force*

The discussion in this paper on viscoelastic flows is for a PTT fluid, but will be identical for a FENE-P model provided the substitutions indicated in Section 7.1.3.6 are made. For a viscoelastic fluid under the sole influence of electro-osmotic driving force, $\Gamma = 0$, equation (7.29) reduces to

$$\frac{u}{u_{sh}} = \left(1 - 2\frac{\varepsilon De_\kappa^2}{\cosh^2(\bar{\kappa})}\right)\left(1 - \frac{\cosh(\bar{\kappa}\bar{y})}{\cosh(\bar{\kappa})}\right) + \frac{2}{3}\varepsilon De_\kappa^2\left[1 - \left(\frac{\cosh(\bar{\kappa}\bar{y})}{\cosh(\bar{\kappa})}\right)^3\right] \tag{7.53}$$

Figure 7.4 (a) shows the corresponding dimensionless velocity profiles as a function of the parameter $\sqrt{\varepsilon}De_\kappa$ for two relative microchannel ratios of $\bar{\kappa} = 20$ and $\bar{\kappa} = 100$ and these profiles should be compared with the profiles in Figure 7.2 for Newtonian fluids. As for Newtonian fluids, the velocity profiles exhibit a *pluglike* shape, but now with the velocity plateau increasing significantly with $\sqrt{\varepsilon}De_\kappa$, for both values of $\bar{\kappa}$. In fact, setting $\bar{y} = 0$ in equation (7.53) leads to the following quadratic relationship between the maximum velocity plateau and $\sqrt{\varepsilon}De_\kappa$,

$$\left.\frac{u}{u_{sh}}\right|_{max} = \left(1 - 2\frac{\varepsilon De_\kappa^2}{\cosh^2(\bar{\kappa})}\right)\left(1 - \frac{1}{\cosh(\bar{\kappa})}\right) + \frac{2}{3}\varepsilon De_\kappa^2\left[1 - \frac{1}{\cosh^3(\bar{\kappa})}\right] \tag{7.54}$$

which for $\bar{\kappa} \gtrsim 10$ reduces to $\left.\frac{u}{u_{sh}}\right|_{max} \approx 1 + \frac{2}{3}\varepsilon De_\kappa^2$.

The influence of $\bar{\kappa}$ on the velocity profiles of Figure 7.4 (a) is restricted to a narrow region, the effective EDL thickness, with the velocity profiles for higher values of $\bar{\kappa}$ exhibiting thinner EDL layers and consequently larger velocity gradients. Figure 7.4 (b) shows the corresponding profiles of dimensionless normal and shear stresses for the viscoelastic fluid as function of De_κ. In order to simplify the analysis of the influence of both De_κ and $\bar{\kappa}$ on the stress profiles, a near-wall variable, $\chi = (1 - \bar{y})\,\bar{\kappa}$, is used. By using χ in Figure 7.4 (b) the stress profiles for different values of $\bar{\kappa}$ collapse, since their magnitudes are determined by the values of $\bar{\kappa}$. The dimensionless shear stress is also independent of De_κ, exhibiting a constant wall value of -1/3 (as predicted by equation (7.35) with $\Gamma = 0$). The normal stresses increase linearly with De_κ regardless of $\bar{\kappa}$ (cf. equation (7.36)).

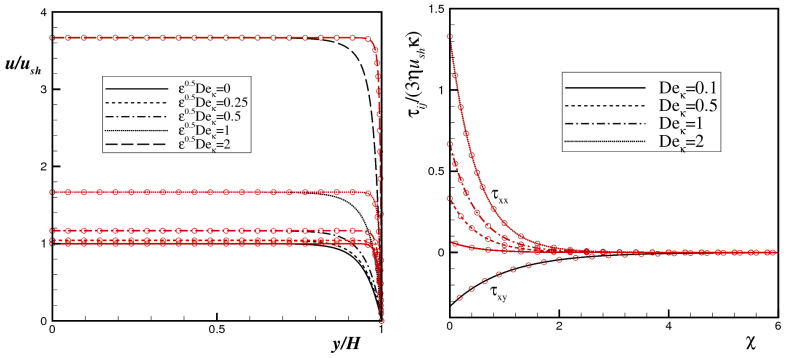

(a) (b)

Figure 7.4: Flow characteristics for electro-osmotic flow ($\Gamma = 0$) of a PTT fluid for relative microchannel ratios of $\bar{\kappa} = 20$ (lines) and $\bar{\kappa} = 100$ (lines and symbols): (a) Dimensionless velocity profiles as function of $\sqrt{\varepsilon}De_\kappa$; (b) Dimensionless normal and shear stress profiles as function of De_κ. $\chi = (1 - \bar{y})\,\bar{\kappa}$ is the near wall variable.

Dimensionless shear viscosity profiles for the PTT fluid in electro-osmotic flow are plotted in Figure 7.5 as function of the near wall variable, χ. There is a decrease in shear viscosity near the wall when $\sqrt{\varepsilon}De_\kappa$ increases, on account of the shear-thinning behavior of the PTT fluid, and consequently the thickness of the EDL is larger than for the equivalent Newtonian flow. By using the modified wall variable the dimensionless shear viscosity profiles, $\bar{\mu}(\dot{\gamma})$, become independent of the relative micro-channel ratio. It is this low wall viscosity at high values of εDe_κ^2 that is responsible for the strong increase in u/u_{sh}.

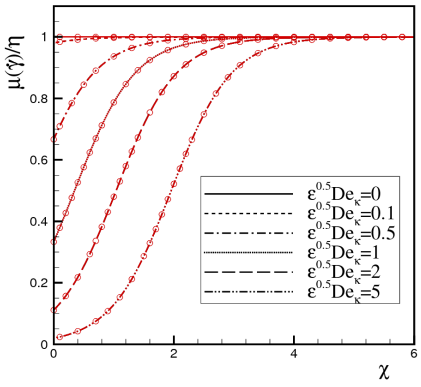

Figure 7.5: Dimensionless viscosity profiles for electro-osmotic viscoelastic flow ($\Gamma = 0$) of a PTT fluid as function of $\sqrt{\varepsilon}De_\kappa$ for relative microchannel ratios of $\bar{\kappa} = 20$ (lines) and $\bar{\kappa} = 100$ (lines and symbols). $\chi = (1 - \bar{y})\,\bar{\kappa}$ is the near wall variable.

7.1.4.3 *Viscoelastic fluid with mixed driving forces*

The viscoelastic flow characteristics under the combined action of electro-osmosis and pressure gradient forcing are discussed here, recalling equation (7.25).

Figures 7.6 (a) and (b) present dimensionless velocity profiles for flows with favorable and adverse pressure gradients, respectively. For $\Gamma < 0$, the velocity profiles increase with $\sqrt{\varepsilon}De_\kappa$, as seen previously in

Figure 7.4, due to shear-thinning effects, leading to correspondingly higher shear rates near the walls. For $\Gamma > 0$, the pressure gradient is against the flow and the velocity profiles show the same double peak seen for Newtonian flows (cf. Figure 7.3). The velocity profiles also increase with $\sqrt{\varepsilon}De_\kappa$, due to increasing levels of shear-thinning, both within the EDL layer and in the bulk zone. For flow with favorable pressure gradients the velocity maximum is given by equation (7.55) (for $\bar{\kappa} \gtrsim 10$) and takes place on the centreplane. For adverse pressure gradients the velocity peaks are at the edge of the EDL and the corresponding velocity maximum depends on Γ as given by equation (7.56).

$$\left.\frac{u}{u_{sh}}\right|_{max} = 1 - \frac{1}{2}\Gamma + \frac{3}{2}\frac{\varepsilon De_\kappa^2}{\bar{\kappa}^2}\Gamma\left[1 - 2\bar{\kappa} + \frac{4}{9}\frac{\bar{\kappa}^2}{\Gamma}\right] \tag{7.55}$$
$$+\frac{3}{2}\frac{\varepsilon De_\kappa^2}{\bar{\kappa}^2}\Gamma\left[\frac{8}{\bar{\kappa}^2}\Gamma\left[1 + \bar{\kappa}\left(\frac{1}{2}\bar{\kappa} - 1\right)\right] - \frac{\Gamma^2}{3}\right] \quad , \Gamma \leqslant 0,\ \bar{\kappa} \gtrsim 10$$

$$\left.\frac{u}{u_{sh}}\right|_{max} = \frac{u(\bar{\delta})}{u_{sh}} \quad , \Gamma > 0,\ \bar{\kappa} \gtrsim 10 \tag{7.56}$$

where $\bar{\delta}$ is the dimensionless locci of the velocity peaks (or the location of a zero shear stress, $\tau_{xy\|y=\bar{\delta}} = 0$) to be calculated from equation (7.40).

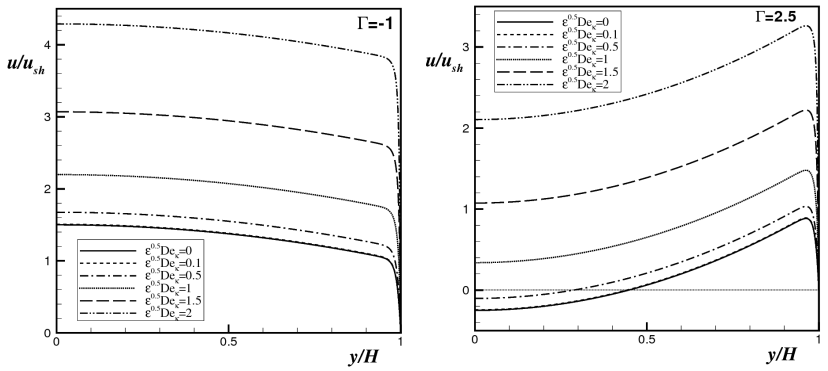

Figure 7.6: Dimensionless velocity profiles for a PTT fluid under the mixed influence of electro-osmotic/pressure driving force as function of $\sqrt{\varepsilon}De_\kappa$ for: (a) $\Gamma = -1$ and $\bar{\kappa} = 100$; (b) $\Gamma = 1$ and $\bar{\kappa} = 20$.

Figure 7.7 shows transverse profiles of the dimensionless normal and shear stresses as function of the near-wall variable, $\chi = (1 - \bar{y})\,\bar{\kappa}$ and Deborah number, for a high value of $\bar{\kappa}$ ($\bar{\kappa} = 100$). The lines represent flows with favorable pressure gradients ($\Gamma = -1$) whereas lines with symbols typify flows with adverse pressure gradients ($\Gamma = 2.5$). In the former case the dimensionless normal stresses decrease sharply near the microchannel walls, within the EDL layer, as shown in detail in Figure 7.8 for $De_\kappa = 2$. In the latter case, as shown in Figure 7.8, the profiles of $\bar{\tau}_{xx}$ also decrease sharply near the microchannel walls within the EDL, followed by an increase to a local maximum near the walls, at the end of the EDL layer. For all flows the magnitude of $\bar{\tau}_{xx}$ increases with De_κ and $\bar{\kappa}$.

As observed in Section 7.1.3.4 in respect to equation (7.25), besides the viscoelastic flow induced by the single contributions from electrical and pressure potentials, there is an extra term that simultaneously

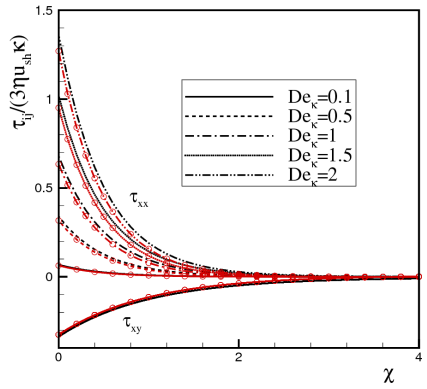

Figure 7.7: Dimensionless normal and shear stresses profiles for viscoelastic fluid under the mixed influence of electro-osmotic/pressure driving force as function of $\sqrt{\varepsilon}De_\kappa$ for $\bar{\kappa} = 100$, $\Gamma = -1$ (lines) and $\Gamma = 2.5$ (lines with symbols).

combines both effects and which is absent from the Newtonian case. This invalidates the superposition principle, and is associated with the non-linearity of the rheological model. These various contributions and the corresponding whole velocity profile are plotted in Figures 7.9 (a) and (b) for two typical cases of favorable and opposed pressure gradient and electric force, $\Gamma = -1$ and $\Gamma = 2.5$, respectively. The combined term u^{EP} acts in the same direction as the Poiseuille contributions, but has a slope like that of the electro-osmotic contribution, i.e, it is a plug like profile except in the wall vicinity. In absolute terms u^{EP} and u^{P} are here of similar magnitude, but u^{EP} can be larger than u^{P} as discussed next.

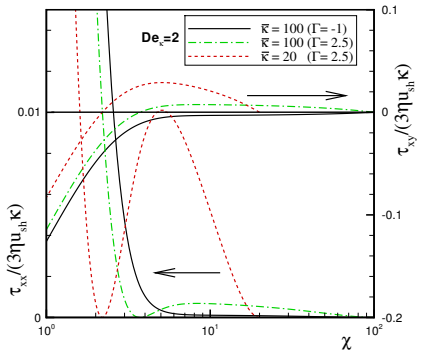

Figure 7.8: Dimensionless normal and shear stresses profiles for viscoelastic fluid under the mixed influence of electro-osmotic/pressure driving force at $De_\kappa = 2$ as function of the near wall variable, for $\bar{\kappa} = 100$ ($\Gamma = -1$ and $\Gamma = 2.5$) and $\bar{\kappa} = 20$ ($\Gamma = 2.5$).

The corresponding flow rates are given by equation (7.30) and the flow rate contributions relative to the total flow rate, $Q_T = Q^E + Q^P + Q^{EP}$, are shown in Figures 7.10 (a) and (b), as function of $\sqrt{\varepsilon}De_N$ for $\Gamma = -1$ and $\Gamma = 2.5$, respectively. The contribution in terms of flow rate are similar to those of the velocity discussed above, but no longer include the effect of position in the channel. In each figure, curves for two relative microchannel ratios of $\bar{\kappa} = 20$ (lines) and $\bar{\kappa} = 100$ (lines and symbols) are presented. At low $\sqrt{\varepsilon}De_N$ the relative contributions

vary quickly from their corresponding Newtonian values to asymptotic values at large $\sqrt{\varepsilon}De_N$ ($\sqrt{\varepsilon}De_N \gtrsim 5$). These asymptotic values at large $\sqrt{\varepsilon}De_N$ are inversely proportional to $\bar{\kappa}$. For $\Gamma = -1$ and $\bar{\kappa} = 20$ the non-linear contribution is actually quite significant, with $Q^{EP}/Q_T \simeq 19\%$, whereas at $\bar{\kappa} = 100$ Q^{EP}/Q_T is only of 4%. At high values of $\sqrt{\varepsilon}De_N$, the non-linear contribution becomes stronger than the pressure potential contribution, because $\overline{Q}^{EP}$ has one term linearly proportional to the pressure gradient and a second term proportional to $p_{,x}^2$, which acts in opposite direction to the linear term for $p_{,x} > 0$. This nonlinear contribution is therefore equivalent to a drag reduction effect when fixing the flow rate and quantifying the required forcings relative to a non-coupled situation. For adverse pressure gradients, the non-linear contribution acts to reduce the total flow rate as shown in Figure 7.10 (b) for $\Gamma = 2.5$, where the non-linear flow reduction, $\overline{Q}^{EP}$, is stronger than the pressure contribution, $\overline{Q}^{P}$. Thus, the coupled term is now acting as a drag increaser. In this situation, the main contribution for the total flow rate is $\overline{Q}^{E}$, with both $\overline{Q}^{P}$ and $\overline{Q}^{EP}$acting to reduce the flow rate. At higher values of $\sqrt{\varepsilon}De_N$ this reduction is again stronger at lower values of $\bar{\kappa}$, with $Q^{EP}/Q_T \simeq -12\%$ and -76% for $\bar{\kappa} = 100$ and $\bar{\kappa} = 20$, respectively (note that $Q^{E}/Q_T \simeq 180\%$ for $\bar{\kappa} = 20$).

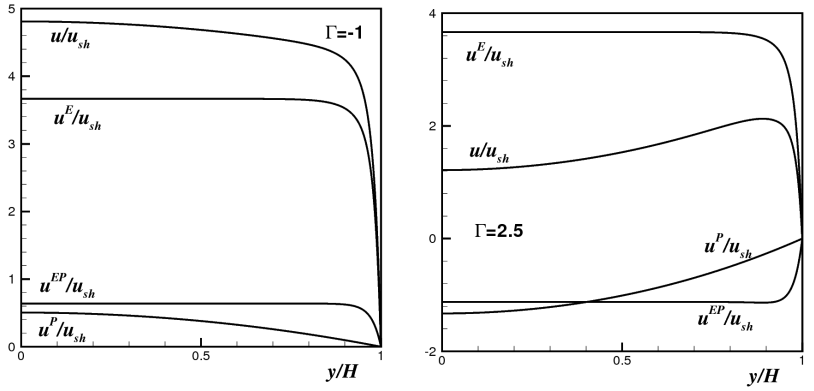

(a) (b)

Figure 7.9: Dimensionless velocity profile components for a PTT fluid under the mixed influence of electro-osmotic/pressure driving force for $\sqrt{\varepsilon}De_\kappa = 2$ and relative microchannel ratio of $\bar{\kappa} = 20$: (a) $\Gamma = -1$ and (b) $\Gamma = 2.5$.

The variation with Γ of the asymptotic values at $\varepsilon De_\kappa^2 = 200$ of the various contributions to the total flow rate are plotted in Figure 7.11 for $\bar{\kappa} = 20$. For very large favorable and adverse pressure gradient the main flow is obviously dominated by the pressure contribution, $\overline{Q}^{P}$. The singularities at $\Gamma \simeq 6.45$ correspond to $\overline{Q} \simeq 0$. Here, the strength of the adverse pressure gradient was sufficient to overcome the strength of the electro-osmotic forcing to reverse the total flow rate.

To discuss the streaming potential problem it is more enlightning to work with the reciprocal of Γ_{sp}, $\Gamma_{sp}^{-1} = -\frac{\epsilon\psi_0}{H^2}\frac{E_{x,sp}}{p_{,x}}$. Figure 7.12 (a) shows that this quantity increases with viscoelasticity, for differents values of $\overline{\kappa}$ and Υ_1. This means that viscoelasticity increases the amount of electrical streaming current, which asymptotes to a constant value at high $\sqrt{\varepsilon}De_N$. In contrast, increasing Υ_1 decreases the value of Γ_{sp}^{-1}

(and the amount of electrical streaming current) for two reasons. The streaming current is directly proportional to $E_{x,sp}$(cf. equation (7.43)) and then with $I_c' = -I_s'$, a higher electrical conductivity implies a lower value of $E_{x,sp}$ as in equation (7.44). So, the combination of these two effects, for a given pressure gradient results in a lower streaming potential therefore a lower value of Γ_{sp}^{-1}. Similarly, if the system has a lower electrical conductivity stronger streaming potentials are required to obtain electrical equilibrium. The necessarily larger electric fields in poor conductors (small Υ_1) lead to stronger effects on the velocity field as is well shown in Figure 7.12 (b). Here, the deviation from pure Poiseuille flow is enhanced by poor electric conductivity. This Figure also confirms that viscoelastic shear-thinning fluids enhance streaming potential effects more than Newtonian fluids. All these effects are enhanced as $\bar{\kappa}$ decreases. Note that the velocity profiles in Figure 7.12 (b) have been normalized by the Newtonian bulk velocity at identical pressure gradient (U_N), instead of u_{sh}, to avoid the singularity in the Helmholtz-Smoluchowski electro-osmotic velocity ($E_{x,sp} = 0$) for pure Poiseuille flow.

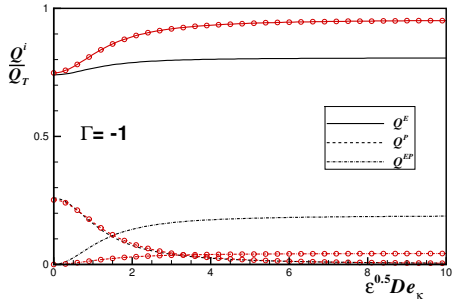

(a)

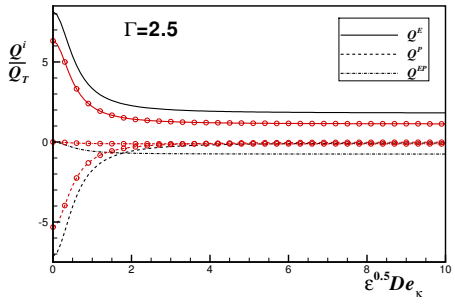

(b)

Figure 7.10: Relative contribution to the flow rate for electro-osmotic flow of a PTT fluid for relative microchannel ratios of $\bar{\kappa} = 20$ (lines) and $\bar{\kappa} = 100$ (lines and symbols) as function of $\sqrt{\varepsilon}De_\kappa$: (a) $\Gamma = 2.5$ (b) $\Gamma = -1$.

The final comment concerns with the skimming layer, the thin layer close to the wall where the fluid essentially behaves as the Newtonian solvent. This can act as a lubrication layer and the real impact on the flow depends on the ratio between its thickness (δ_l) and the EDL thickness (ξ), on the amount of shear-thinning of the bulk fluid, on the applied pressure gradient and on the ratio between the characteristic viscosities of the bulk fluid and solvent. For both $\delta_l = \xi$, and $\delta_l > \xi$,

u/u_{sh} is essentially unchanged in the EDL for the homogeneous and two-fluid model. Outside the EDL, u/u_{sh} does not change much if the flow is purely electro-osmotic regardless of all other parameters, but an intense shear-thinning can lead to differences of up to 20% as can be assessed from Berli and Olivares (2008). In the presence of a skimming layer the sensitivity of u/u_{sh} to pressure gradient is always reduced relative to the homogeneous fluid solution: for $\delta_l = \xi$ this leads to large differences in u/u_{sh} outside the EDL and for $\delta_l > \xi$, say $\delta_l = 5\xi$, this problem is somewhat reduced so that for weak shear-thinning fluids (and Newtonian) the homogeneous solution is a good approximation to the two-fluid model, but for moderate to strongly shear-thinning fluids differences in excess of 70% can be found. This is currently a problem under investigation for viscoelastic fluids.

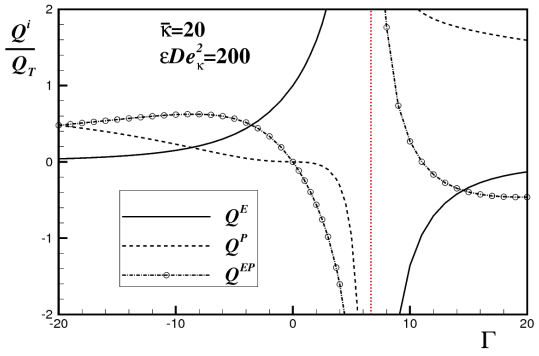

Figure 7.11: Relative contribution to the flow rate for electro-osmotic flow of a PTT fluid for relative microchannel ratios of $\bar{\kappa} = 20$ at large εDe_κ^2 ($= 200$) as a function of Γ.

7.1.5 *Conclusions*

Analytical solutions for channel and pipe flows of viscoelastic fluids under the mixed influence of electrokinetic and pressure forces were obtained. The analysis are restricted to cases with small electric double-layer, where the distance between the walls of a microfluidic device is at least one order of magnitude larger than the EDL. The viscoelastic fluids used are described by the PTT model (Phan-Thien and Tanner, 1977), with linear kernel for the stress coefficient function and zero second normal stress difference (Phan-Thien, 1978), and the FENE-P model (Bird et al., 1980).

In the absence of an imposed pressure gradient, the electro-osmotic flow exhibits a pluglike velocity profile, as found previously for Newtonian fluids, but with the maximum velocity plateau increasing quadraticaly with $\sqrt{\varepsilon}De_\kappa$, for all $\bar{\kappa}$ values.

When the viscoelastic flow is induced by a combination of both electrical and pressure potentials, in addition to the single contributions from these two mechanisms there is an extra term in the velocity profile that simultaneously combines both, which is absent for the Newtonian case where the superposition principle applies. This non-linear term can contribute significantly to the total flow rate, depending on the value of $\bar{\kappa}$. Under conditions of favourable pressure gradient it thus acts as a drag reducer, but for adverse pressure gradients it changes its role to become a drag increaser. Its existence invalidates the superposition

principle and is associated with the non-linearity of the rheological model, with this analitycal solution indicating that for quasi-linear viscoelastic equations the superposition principle still applies.

Under favorable pressure gradients, the velocities increase significantly with $\sqrt{\varepsilon}De_\kappa$, with the profiles at higher values of $\bar{\kappa}$ exhibiting large shear rates within the electric double layer. As for Newtonian fluids, adverse pressure gradients lead to local velocity peaks at the edge of the electric double layer.

Regarding the streaming potential problem, viscoelasticity increases the amount of electrical streaming current, which asymptotes to a constant value at high $\sqrt{\varepsilon}De_N$. The amount of electrical streaming current decreases with the increase of Υ_1, due to the lower $E_{x,sp}$ required to establish the conduction current for good conductors and the consequent lower streaming potential as found for Newtonian fluids.

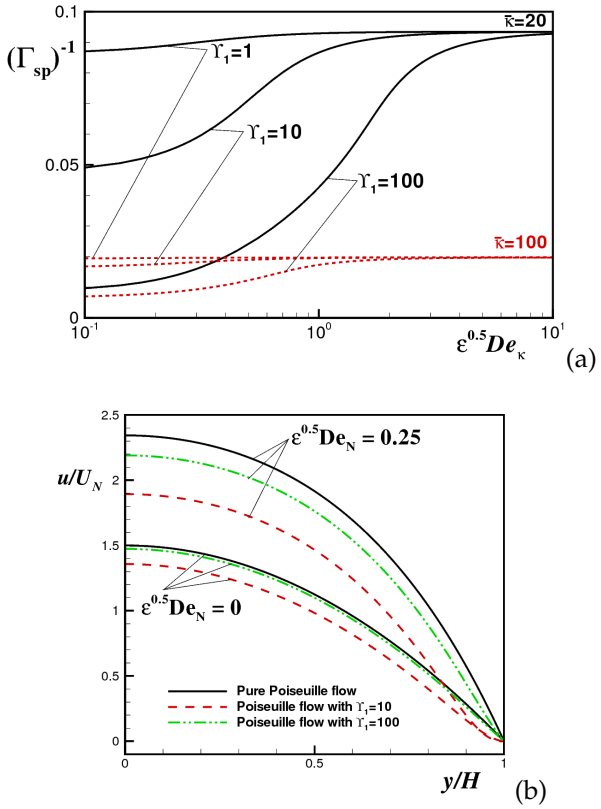

Figure 7.12: Streaming potential: (a) variation of Γ_{sp}^{-1} with $\sqrt{\varepsilon}De_N$ as function of $\bar{\kappa}$ and Υ_1; (b) Normalized velocity profiles for $\bar{\kappa} = 20$ and showing effects of Υ_1 and $\sqrt{\varepsilon}De_N$.

7.1.6 *Acknowledgements*

The authors acknowledge funding from FEDER and Fundação para a Ciência e a Tecnologia (FCT), Portugal, through projects PPCDT/EME/59338/2004, PTDC/EQU-FTT/70727/2006 and PTDC/EQU-FTT/71800/2006. A. Afonso would also like to thank FCT for financial support through the scholarship SFRH/BD28828/2006. The help of Dr. S. Dhinakaran in checking the equations is gratefully acknowledged.

Appendix A: Analytical solution for the PTT and FENE-P models in pipe flow

The momentum equation is given by equation (7.57) where now y denotes the radial coordinate, H is the pipe radius and all other quantities are defined in the main text. The net charge density distribution is given by equation (7.20).

$$\frac{1}{y}\frac{d\left(y\tau_{xy}\right)}{dy} = -\rho_e E_x + p_{,x} \tag{7.57}$$

which can be integrated to obtain

$$\tau_{xy} = \frac{\epsilon\psi_0 E_x \kappa \sinh\left(\kappa y\right)}{\cosh\left(\kappa H\right)} - \frac{\epsilon\psi_0 E_x \cosh\left(\kappa y\right)}{y\cosh\left(\kappa H\right)} + \frac{\epsilon\psi_0 E_x}{y\cosh\left(\kappa H\right)} + \frac{1}{2}p_{,x}y \tag{7.58}$$

Using equation (7.13) the following explicit expression for the normal stress component is obtained for the PTT fluid,

$$\tau_{xx} = 2\frac{\lambda}{\eta}\left(\frac{\epsilon\psi_0 E_x \kappa \sinh\left(\kappa y\right)}{\cosh\left(\kappa H\right)} + \frac{1}{2}p_{,x}y - \frac{\epsilon\psi_0 E_x \cosh\left(\kappa y\right)}{y\cosh\left(\kappa H\right)} + \frac{\epsilon\psi_0 E_x}{y\cosh\left(\kappa H\right)}\right)^2 \tag{7.59}$$

The velocity gradient is,

$$\begin{aligned}\dot{\gamma} \quad \equiv \quad \frac{du}{dy} = &\left[1 + 2\varepsilon\lambda^2\left(\frac{\epsilon\psi_0 E_x \kappa \sinh\left(\kappa y\right)}{\eta\cosh\left(\kappa H\right)} + \frac{1}{2\eta}p_{,x}y - \frac{\epsilon\psi_0 E_x \cosh\left(\kappa y\right)}{\eta y\cosh\left(\kappa H\right)} + \frac{\epsilon\psi_0 E_x}{\eta y\cosh\left(\kappa H\right)}\right)^2\right] \\ &\left(\frac{\epsilon\psi_0 E_x \kappa \sinh\left(\kappa y\right)}{\eta\cosh\left(\kappa H\right)} + \frac{1}{2\eta}p_{,x}y - \frac{\epsilon\psi_0 E_x \cosh\left(\kappa y\right)}{\eta y\cosh\left(\kappa H\right)} + \frac{\epsilon\psi_0 E_x}{\eta y\cosh\left(\kappa H\right)}\right)\end{aligned} \tag{7.60}$$

The integration of equation (7.60) subject to the no-slip boundary condition at the wall ($u_{\|y=H} = 0$) gives the following velocity profile for the PTT fluid:

$$u = u^E + u^P + u^{EP} \tag{7.61}$$

with

$$\begin{aligned}u^E \quad = \quad &\left[\frac{\epsilon\psi_0 E_x}{\eta}\right]\left[\overline{\lambda} - 1 + \sqrt{\overline{c}}\left\{\ln\left(\frac{y}{H}\right) + \mathrm{Chi}\left(\kappa H\right) - \mathrm{Chi}\left(\kappa y\right)\right\}\right] \\ + \quad &\kappa^2 2\varepsilon\lambda^2\left[\frac{\epsilon\psi_0 E_x}{\eta}\right]^3\left[\overline{c}\left(1-\overline{\lambda}\right) + \frac{1}{3}\left(\overline{\lambda}^3 - 1\right) + \overline{c}\left\{\sqrt{\overline{c}}\left(\frac{21}{8}\mathrm{Chi}\left(\kappa y\right) - \frac{21}{8}\mathrm{Chi}\left(\kappa H\right)\right.\right.\right. \\ + \quad &\left.\frac{3}{2}\mathrm{Chi}\left(2\kappa H\right) - \frac{3}{2}\mathrm{Chi}\left(2\kappa y\right) + \frac{3}{8}\mathrm{Chi}\left(3\kappa y\right) - \frac{3}{8}\mathrm{Chi}\left(3\kappa H\right) + \frac{3}{2}\ln\left(\frac{H}{y}\right)\right) \\ + \quad &\left.\frac{3}{2\kappa H}\left[\frac{5}{4}\overline{D}\left(1 - \frac{H}{y}\overline{B}\right) + \sqrt{\overline{c}}\left(\frac{H}{y}\sinh\left(2\kappa y\right) - \sinh\left(2\kappa H\right) - \frac{1}{4}\frac{H}{y}\sinh\left(3\kappa y\right) + \frac{1}{4}\sinh\left(3\kappa H\right)\right)\right] \right. \\ + \quad &\left.\left.\frac{3}{4\kappa^2 H^2}\left[\frac{5}{2}\left(\frac{H^2}{y^2}\overline{\lambda} - 1\right) + \sqrt{\overline{c}}\left(\cosh\left(2\kappa H\right) - \frac{H^2}{y^2}\cosh\left(2\kappa y\right) + \frac{5}{3}\left(1 - \frac{H^2}{y^2}\right)\right.\right.\right. \right. \\ + \quad &\left.\left.\left.\left.\frac{1}{6}\frac{H^2}{y^2}\cosh\left(3\kappa y\right) - \frac{1}{6}\cosh\left(3\kappa H\right)\right)\right]\right\}\right]\end{aligned} \tag{7.62}$$

$$u^P = \frac{1}{2}\left[\frac{p_{,x}}{2\eta}\right]\left(y^2 - H^2\right)\left[1 + \left[\frac{p_{,x}}{2\eta}\right]^2 \varepsilon\lambda^2\left(y^2 + H^2\right)\right] \tag{7.63}$$

$$
\begin{aligned}
u^{EP} \quad = \quad & \frac{3}{2}\varepsilon\lambda^2\left[\frac{\epsilon\psi_0 E_x}{\eta}\right]^2\left[\frac{p_x'}{2\eta}\right]\left[5\left(1-\overline{A}^2\right)+2\kappa\overline{D}\left(y\overline{AB}-H\right)+\kappa^2\overline{C}\left(H^2-y^2\right)\right.\\
& +2\overline{C}\left(4\mathrm{Chi}\left(\kappa H\right)-4\mathrm{Chi}\left(\kappa y\right)+\mathrm{Chi}\left(2\kappa y\right)-\mathrm{Chi}\left(2\kappa H\right)+3\ln\left(\frac{y}{H}\right)\right)\\
& \left.+\,8\sqrt{\overline{C}}\left(\overline{A}-1\right)\right]+12\frac{\varepsilon\lambda^2}{\kappa^2}\left[\frac{\epsilon\psi_0 E_x}{\eta}\right]\left[\frac{p_x'}{2\eta}\right]^2\left[\frac{3}{2}\kappa\overline{D}\left(H-y\overline{B}\right)\right.\\
& \left.+\left(1+\frac{1}{2}\kappa^2 y^2\right)\overline{A}-\left(1+\frac{1}{2}\kappa^2 H^2\right)+\frac{1}{2}\left(\overline{A}-1+\frac{\kappa^2}{2}\sqrt{\overline{C}}\left(y^2-H^2\right)\right)\right]
\end{aligned}
\tag{7.64}
$$

where $\mathrm{Chi}(z)$ is the hyperbolic cosine integral, defined as

$$
\mathrm{Chi}(z)=\gamma+\ln(z)+\int_0^z\frac{\cosh(t)-1}{t}dt \tag{7.65}
$$

and γ is the Euler-Mascheroni constant ($\gamma=0.57721566490...$). $\mathrm{Chi}(z)$ can also be calculated from:

$$
\mathrm{Chi}(z)=\gamma+\ln(z)+\frac{1}{2}\sum_{k=1}^{\infty}\frac{z^{2k}}{k(2k)!} \tag{7.66}
$$

To obtain the solution for pipe flow of FENE-P fluids it suffice to apply the substitutions of section 7.1.3.6 to this set of equations.

For pipe flow, the relation between the electrical streaming current and the electrical conduction current is

$$
I_s=-I_c=\int_0^H 2\pi u(y)\rho_e(y)y\,dy=-\pi\sigma_t E_{x,sp}H^2 \tag{7.67}
$$

For the PTT and FENE-P fluids, equation (7.67) is not integrable, and a numerical approach is required to obtain a solution.

Abstract[2]

This work investigates the flow of viscoelastic fluids between parallel plates under the combined influence of electro-osmotic and pressure gradient forcings with asymmetric boundary conditions, by considering different zeta potentials at the walls. The fluids are z-z symmetric electrolytes. The analytic solutions of the electrical potential, velocity distributions and streaming potential are based on the Debye-Hückel approximation for weak potential. The viscoelastic fluids used are modelled by the simplified Phan-Thien—Tanner constitutive equation, with linear kernel for the stress coefficient function, and the Finitely Extensible Non-linear Elastic dumbbells model with a Peterlin approximation for the average spring force. The combined effects of fluid rheology, electrical double-layer thickness, ratio of the wall zeta potentials and ratio between the applied streamwise gradients of electrostatic potential and pressure on the fluid velocity and stress distributions are discussed.

Keywords: Electro-osmotic/pressure driven flows; asymmetric zeta potentials; simplified Phan-Thien—Tanner model (sPTT); Finitely Extensible Nonlinear Elastic model with Peterlin's approximation (FENE-P); viscoelastic fluids; microchannels.

7.2.1 *Introduction*

Soong and Wang (Soong and Wang, 2003) investigated electro-kinetic effects on flow and heat transfer of Newtonian liquids flowing between two parallel plates under asymmetric boundary conditions including wall-sliding motion, different zeta potentials, and unequal heat fluxes at the walls. They showed that the surface electric condition due to unequal zeta potentials dramatically influences the electric potential distribution with concominant changes in the streaming potential and the Newtonian fluid flow characteristics. Such asymmetries are actually fairly normal because many manufacturing techniques use different materials at different walls (Nguyen and Wereley, 2002). For instance, in soft lithography the channels are often made of polydimethylsiloxane (PDMS) except for the top wall that is often made of glass for optical access or other material for other purpose. In pure electro-osmosis the consequence of this is a linear velocity profile in the bulk instead of a constant front (Kuo et al., 2008). Asymmetric electro-osmosis can also be the outcome of imposed polarization by AC fields in otherwise symmetric geometries (Islam and Wu, 2006; Mansuripur et al., 2009), but this matter is outside of the scope of this work which is related with DC current.

In DC electro-osmosis, recently an investigation was carried out by Afonso et al. (2009c), who presented the analytical solutions for channel and pipe flows of viscoelastic fluids under the mixed influence of electro-osmotic and pressure gradient forcing but only under symmetric boundary conditions. They used the simplified Phan-Thien

2 A.M. Afonso, M.A. Alves, F.T. Pinho (2010). Electro-osmotic flows of viscoelastic fluids in microchannels under asymmetric zeta potential, accepted for publication in the *Journal of Engineering Mathematics.*

and Tanner model (sPTT model, Phan-Thien and Tanner, 1977), with linear kernel for the stress coefficient function and zero second normal stress difference (Phan-Thien, 1978), and the Finitely Extensible Non-linear Elastic dumbbells model (FENE-P model) with a Peterlin approximation for the average spring force (Bird et al., 1980) to describe viscoelasticity. Subsequently, a similar investigation was carried out by Dhinakaran et al. (2010) for PTT fluids with non-zero second normal stress difference coefficient in shear flowing between parallel plates, which identified the conditions for the onset of an instability originated in the constitutive equation. Both analysis were restricted to cases with small electric double-layers, where the distance between the walls of a microfluidic device is at least one order of magnitude larger than the thickness of the electric double layer (EDL). When the viscoelastic flow is induced by a combination of both electrical and pressure potentials, as in the investigations by Afonso et al. (2009c), in addition to the independent contributions from these two mechanisms there is an extra term in the velocity profile that simultaneously combines both, which is absent for the Newtonian case where the superposition principle applies. This non-linear term can contribute significantly to the total flow rate, depending on the value of the EDL thickness and is a consequence of the non-linear nature of the constitutive relation of the fluid. Park and Lee (2008b) derived expressions for the Helmholtz-Smoluchowski velocity for pure electro-osmotic flow of PTT fluids and provided a simple numerical procedure to calculate its value, and Sousa et al. (2010a) considered the effect of a Newtonian skimming layer for the PTT fluid. Note that earlier investigations on pure electro-osmotic flow or combined electro-osmosis with pressure gradient forcing had been carried out in the context of Newtonian fluids, as reviewed by Afonso et al. (2009c). The contributions reviewed in that paper are all for symmetric zeta potentials, though.

This work aims to generalize the study of symmetric $z-z$ electrolyte viscoelastic fluids in electro-osmotic/ pressure gradient driven flows to other pratical relevant flow conditions by presenting the analytical solutions for the flows of sPTT and FENE-P fluids between two parallel plates under asymmetric boundary conditions of unequal zeta potentials at the channel walls. Dilute and semi-dilute polymer solutions can easily be represented by these constitutive equations. Specifically, in Sousa et al. (2010b) the rheology of various aqueous solutions of polyethylene oxide, with molecular weights ranging from $2\text{x}10^6$ to $8\text{x}10^6$ g/mol, and of an $18\text{x}10^6$ g/mol polyacrylamide, all at concentrations not exceeding 0.1% by weight, were investigated. The rheologies of these fluids were very well fit by a single mode form of the PTT model, which is quite adequate for this shear flow.

The paper starts with the set of governing equations including the nonlinear Poisson –Boltzmann equation governing the EDL fields and the momentum equation modified by the body force associated with the applied electrical potential field. The simplifications required to obtain the analytical solution are discussed, the solutions are presented and a discussion of the effects of the various relevant nondimensional parameters upon the flow characteristics closes this work.

7.2.2 *Governing equations*

The basic equations describing the flow are the continuity equation,

$$\nabla \cdot \mathbf{u} = 0 \tag{7.68}$$

and the momentum equation,

$$\rho \frac{D\mathbf{u}}{Dt} = \nabla \cdot \boldsymbol{\tau} - \nabla p + \mathbf{F} \tag{7.69}$$

where $\mathbf{u}$ is the velocity vector, p the pressure, t the time, ρ the fluid density (assumed constant) and $\boldsymbol{\tau}$ the polymeric extra stress contribution. The body force $\mathbf{F}$ in the momentum equation (7.69) is here given as

$$\mathbf{F} = \rho_e \mathbf{E} \tag{7.70}$$

where $\mathbf{E}$ is the applied external electric field and ρ_e is the net electric charge density associated with the spontaneously formed electric double layers, which are assumed here not to be affected by the imposed electric field. The electric field is related to a potential (Φ), by $\mathbf{E} = -\nabla\Phi$, with $\Phi = \psi + \phi$, where ϕ is the applied streamwise potential and ψ is the equilibrium/ induced potential at the channel walls, associated with the interaction between the ions of the fluid and the dielectric properties of the wall. The boundary conditions are no-slip at both walls and asymmetric zeta potentials at the walls, with Figure 7.13 showing schematically the flow channel, coordinate system and type of forcing.

7.2.2.1 *Constitutive equations*

sPTT model

One of the viscoelastic models adopted here to represent viscoelastic effects is the sPTT equation (simplified Phan-Thien and Tanner (Phan-Thien and Tanner, 1977)), which can be expressed by

$$f(\boldsymbol{\tau}_{kk})\boldsymbol{\tau} + \lambda \overset{\nabla}{\boldsymbol{\tau}} = 2\eta \mathbf{D}, \tag{7.71}$$

where $\mathbf{D}$ is the rate of deformation tensor ($\mathbf{D} = \frac{1}{2}\left(\nabla\mathbf{u} + \nabla\mathbf{u}^T\right)$), λ is a relaxation time, η is the constant viscosity coefficient and $\overset{\nabla}{\boldsymbol{\tau}}$ represents the upper-convected derivative, defined by

$$\overset{\nabla}{\boldsymbol{\tau}} = \frac{D\boldsymbol{\tau}}{Dt} - \nabla\mathbf{u}^T \cdot \boldsymbol{\tau} - \boldsymbol{\tau} \cdot \nabla\mathbf{u}. \tag{7.72}$$

The stress coefficient function, $f(\boldsymbol{\tau}_{kk})$, can be expressed in the linearised form, as

$$f(\boldsymbol{\tau}_{kk}) = 1 + \frac{\varepsilon\lambda}{\eta}\boldsymbol{\tau}_{kk}, \tag{7.73}$$

where $\boldsymbol{\tau}_{kk} = \tau_{xx} + \tau_{yy} + \tau_{zz}$ is the trace of the extra stress tensor.

FENE-P model

Another viscoelastic model used in this work is the FENE-P constitutive equation, based on the kinetic theory for finitely extensible dumbbells

with a Peterlin closure for the average spring force (Bird et al., 1980). The coarse grained molecule of the FENE-P model is represented by a single dumbbell, whose connector force follows a non-linear spring law possessing limited extension, without consideration for excluded volume effects and hydrodynamic interaction. The resulting constitutive equation for the polymer stress can be written as

$$Z(\boldsymbol{\tau}_{kk})\boldsymbol{\tau}+\lambda\overset{\nabla}{\boldsymbol{\tau}}-\lambda\left(\boldsymbol{\tau}-\frac{b}{b+2}nk_BT\mathbf{I}\right)\frac{D\ln Z}{Dt}=2\frac{b}{b+2}nk_BT\lambda\mathbf{D} \quad (7.74)$$

where $\overset{\nabla}{\boldsymbol{\tau}}$ represents the upper convected derivative defined by equation (7.71), b is a parameter that measures the extensibility of the dumbbell, k_B is the Boltzmann constant, T is the absolute temperature and n is a parameter of the model (Bird et al., 1980). The stress coefficient function, $Z(\boldsymbol{\tau}_{kk})$ can be expressed as

$$Z(\boldsymbol{\tau}_{kk})=1+3\left(\frac{1}{b+2}+\frac{\lambda}{3\eta}\frac{\boldsymbol{\tau}_{kk}}{(b+5)}\right). \quad (7.75)$$

2.2. Poisson–Boltzmann equation

If a liquid contacts a dielectric surface there are interactions between the ions and the wall, leading to a spontaneous charge distribution at the fluid and the wall. The wall acquires a charge and the counter-ions in the fluid are attracted by the wall while the co-ions are repelled. In this case, an electric layer is formed near the wall, which is called the electric double layer (EDL, see Bruss (2008) for more details). The induced potential field within the electric double layer, can be expressed by means of a Poisson equation:

$$\nabla^2\psi=-\frac{\rho_e}{\epsilon} \quad (7.76)$$

where ψ denotes the EDL potential and ϵ is the dielectric constant of the solution. The net electric charge density in the fluid, ρ_e, can be described by the following Boltzmann distribution

$$\rho_e=-2n_o ez\sinh\left(\frac{ez}{k_BT}\psi\right) \quad (7.77)$$

where, n_o is the ion density, e is the electronic charge and z the valence of the ions. In order to obtain the velocity field, first we need to solve for the net charge density distribution (ρ_e). The charge density field can be calculated by combining equation (7.76), which for fully-developed steady flow reduces to

$$\frac{d^2\psi}{dy^2}=-\frac{\rho_e}{\epsilon}, \quad (7.78)$$

and equation (7.77) to obtain the the well-known Poisson–Boltzmann equation,

$$\frac{d^2\psi}{dy^2}=\frac{2n_o ez}{\epsilon}\sinh\left(\frac{ez}{k_BT}\psi\right). \quad (7.79)$$

The electroosmotic flow is primarily caused by the movement of the charged species adjacent to the channel walls when subjected to an

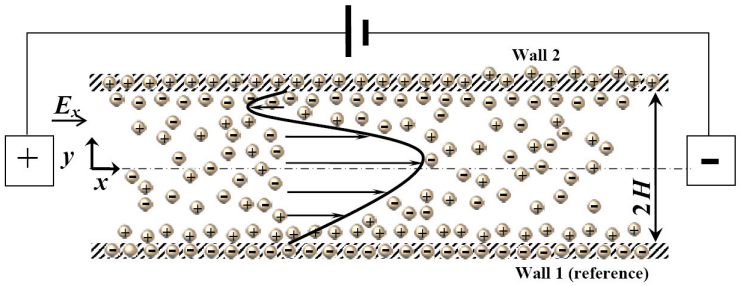

Figure 7.13: Schematic of the flow in a parallel plate microchannel.

externally applied electric field. In general, the distribution of the charged species in the domain is governed by the potential at the walls and by the externally applied electric field. However, when the EDL thickness is small and the charge at the walls is not large, this distribution is essentially governed by the potential at the wall, ψ_0, and is not affected by the externally applied electric field. Thus, the charge distribution near the walls can be determined independently of the applied external electric field. In fact, the effect of fluid motion on the charge redistribution can itself be neglected when the fluid velocity is small, i.e., when the inertial terms in the momentum equation are not dominant or when the EDL thickness is small since the flow is locally uni-directional. In this work with the additional consideration of steady fully-developed channel flow and the inherent symmetry, the charge redistribution is exactly null as is also the inertial term of the momentum equation. Then, for small values of ψ it is also possible to conduct further simplifications because the Debye–Hückel linearization principle ($\sinh x \approx x$) can be invoked. Physically it means that the electrical potential is small compared with the thermal energy of the ions, and the Poisson–Boltzmann equation for the channel flow under investigation becomes:

$$\frac{d^2\psi}{dy^2} = \kappa^2\psi, \tag{7.80}$$

where $\kappa^2 = \frac{2n_0e^2z^2}{\epsilon k_B T}$ is the Debye–Hückel parameter, related with the thickness of the Debye layer, $\xi = \frac{1}{\kappa}$ (normally referred as the EDL thickness). This approximation is valid when the Debye thickness is small but finite, i.e., for $10 \lesssim H/\xi \lesssim 10^3$.

Equation (7.80) can be integrated coupled with boundary conditions for different zeta potential at the walls, $\psi_{\|y=-H} = \zeta_1$ and $\psi_{\|y=H} = \zeta_2$ (cf. Figure 7.13), leading to:

$$\psi(y) = \zeta_1 \left(\Psi_1 e^{\kappa y} - \Psi_2 e^{-\kappa y}\right) \tag{7.81}$$

with $\Psi_1 = \frac{\left(R_\zeta e^{\kappa H} - e^{-\kappa H}\right)}{2\sinh(2\kappa H)}$ and $\Psi_2 = \frac{\left(R_\zeta e^{-\kappa H} - e^{\kappa H}\right)}{2\sinh(2\kappa H)}$, and where $R_\zeta = \zeta_2/\zeta_1$ denotes the ratio of zeta potentials of the two walls. This equation is valid for $-H \leqslant y \leqslant H$ and when $R_\zeta = 1$ the symmetric potential profile of Afonso et al. (2009c) is recovered.

Finally, the net charge density distribution, equation (7.77), in conjunction with equation (7.81) reduces to

$$\rho_e = -\epsilon\kappa^2\zeta_1 \left(\Psi_1 e^{\kappa y} - \Psi_2 e^{-\kappa y}\right) = -\epsilon\kappa^2\zeta_1\Omega_1^-(y), \tag{7.82}$$

where the operator $\Omega_p^{\pm}(y) = \Psi_1^p\,(e^{\kappa y})^p \pm \Psi_2^p\,(e^{-\kappa y})^p$ is a hyperbolic function of the transverse variable y, and depends on the ratio of zeta potentials and on the thickness of the Debye layer.

7.2.3 *Analytical solution*

7.2.3.1 *sPTT Constitutive equation*

The predictions of the sPTT model in this flow, for which $\mathbf{u} = \{u(y), 0, 0\}$, can be obtained from equations (7.72) and (7.73), and leads to

$$f(\tau_{kk})\tau_{xx} = 2\lambda\dot{\gamma}\tau_{xy} \tag{7.83}$$

$$f(\tau_{kk})\tau_{xy} = \eta\dot{\gamma}, \tag{7.84}$$

where $\tau_{kk} = \tau_{xx}$ is the trace of the stress tensor and $\dot{\gamma} = du/dy$ is the velocity gradient. The demonstration that $\tau_{yy} = 0$ for sPTT fluids in fully developed shear flows can be found in Oliveira and Pinho (1999c), so the stress coefficient function becomes an explicit function of the normal stress τ_{xx} only. Upon division of the expressions for the two nonvanishing stresses (equations (7.83) and (7.84)) the specific function $f(\mathbf{fi}_{xx})$ cancels out, and a relation between the non zero normal and shear stresses is obtained,

$$\tau_{xx} = 2\frac{\lambda}{\eta}\tau_{xy}^2 \tag{7.85}$$

7.2.3.2 *FENE-P Constitutive equation*

For the FENE-P fluid in fully developed channel flow, i.e., subjected to $\mathbf{u} = \{u(y), 0, 0\}$, equations (7.74) and (7.75) reduce to

$$Z(\tau_{kk})\tau_{xx} = 2\lambda\dot{\gamma}\tau_{xy} \tag{7.86}$$

$$Z(\tau_{kk})\tau_{xy} = \left(\frac{b+5}{b+2}\right)\eta\dot{\gamma}. \tag{7.87}$$

Again, the trace of the extra-stress tensor becomes $\tau_{kk} = \tau_{xx}$, thus

$$Z(\tau_{xx}) = \left(\frac{b+5}{b+2}\right)\left[1 + \frac{\lambda}{\eta}\frac{(b+2)}{(b+5)^2}\tau_{xx}\right]. \tag{7.88}$$

The relation between the normal and shear stresses is,

$$\tau_{xx} = 2\frac{\lambda}{\eta}\left(\frac{b+2}{b+5}\right)\tau_{xy}^2. \tag{7.89}$$

Inspection of these expressions and those of Section 7.2.3.1 shows similarities between the sPTT and FENE-P stress distributions and this will have consequences as discussed in Section 7.2.3.4.

7.2.3.3 *Analytical solution for the sPTT model*

From the previous simplifications, the momentum equation (7.69), for fully developed channel flow reduces to

$$\frac{d\tau_{xy}}{dy} = -\rho_e E_x + p_{,x}, \tag{7.90}$$

where $p_{,x} \equiv dp/dx$, $E_x \equiv -d\phi/dx$ and ϕ is the electric potential of the applied external field, which is characterized by a constant streamwise gradient. Note that in this flow the external electrical field is positive according to Figure 1, and negative otherwise. Using equation (7.82), Eq. (7.90) can now be integrated to yield the following distribution of shear stress resulting from a linear contribution of the pressure gradient and electric field contributions,

$$\tau_{xy} = \epsilon\kappa\zeta_1 E_x \Omega_1^+(y) + p_{,x} y + \tau_1, \tag{7.91}$$

where τ_1 is a shear stress integration constant to be quantified later from the boundary conditions.

Using the relationship between the normal and shear stresses - equation (7.85), an explicit expression for the normal stress component is also obtained,

$$\tau_{xx} = 2\frac{\lambda}{\eta}\left(\epsilon\kappa\zeta_1 E_x \Omega_1^+(y) + p_{,x} y + \tau_1\right)^2. \tag{7.92}$$

The square term in equation (7.92) introduces a contribution to the normal stress from the combined electro-osmotic and pressure forces. After combining equations (7.84), (7.91) and (7.92) we arrive to the velocity gradient distribution, given by

$$\dot{\gamma} \equiv \frac{du}{dy} = \left[1 + 2\varepsilon\lambda^2\left(\frac{\epsilon E_x \zeta_1}{\eta}\kappa\Omega_1^+(y) + \frac{p_{,x}}{\eta} y + \dot{\gamma_1}\right)^2\right] \left(\frac{\epsilon E_x \zeta_1}{\eta}\kappa\Omega_1^+(y) + \frac{p_{,x}}{\eta} y + \dot{\gamma_1}\right) \tag{7.93}$$

where for compactness we use the *shear rate asymmetry coefficient* defined as $\dot{\gamma_1} = \tau_1/\eta$. We note that this coefficient has no particular physical interpretation.

Equation (7.93) is integrated subject to the no-slip boundary condition at both walls ($u_{\|y=H} = u_{\|y=-H} = 0$) and the resulting velocity profile is

$$\begin{aligned}
u = {} & \dot{\gamma_1}\,(y+H)\left(1+2\varepsilon\lambda^2\dot{\gamma_1}^2\right)+\left[\frac{\epsilon E_x\zeta_1}{\eta}\right]\left(1+6\dot{\gamma_1}^2\varepsilon\lambda^2\right)\Omega^-_{1,1}(y)\\
& +2\varepsilon\lambda^2\left[\frac{\epsilon E_x\zeta_1}{\eta}\right]^2\kappa\dot{\gamma_1}\left(6\Psi_1\Psi_2\kappa\,(y+H)+\frac{3}{2}\Omega^-_{2,1}(y)\right)\\
& +2\varepsilon\lambda^2\left[\frac{\epsilon E_x\zeta_1}{\eta}\right]^3\kappa^2\left(\frac{1}{3}\Omega^-_{3,1}(y)+3\Psi_1\Psi_2\Omega^-_{1,1}(y)\right)\\
& +\frac{1}{2}\left[\frac{p_{,x}}{\eta}\right]\left(y^2-H^2\right)\left(1+6\varepsilon\lambda^2\dot{\gamma_1}^2+\varepsilon\lambda^2\left[\frac{p_{,x}}{\eta}\right]^2\left(y^2+H^2\right)\right)\\
& +2\dot{\gamma_1}\varepsilon\lambda^2\left[\frac{p_{,x}}{\eta}\right]^2\left(y^3+H^3\right)\\
& +12\frac{\varepsilon\lambda^2\left[\frac{\epsilon E_x\zeta_1}{\eta}\right]\left[\frac{p_{,x}}{\eta}\right]}{\kappa}\dot{\gamma_1}\left(\Omega^-_{1,2}(y)-\Omega^+_{1,1}(y)\right)\\
& +6\frac{\varepsilon\lambda^2\left[\frac{\epsilon E_x\zeta_1}{\eta}\right]\left[\frac{p_{,x}}{\eta}\right]^2}{\kappa^2}\left(\Omega^-_{1,3}(y)+2\Omega^-_{1,1}(y)-2\Omega^+_{1,2}(y)\right)\\
& +6\varepsilon\lambda^2\left[\frac{\epsilon E_x\zeta_1}{\eta}\right]^2\left[\frac{p_{,x}}{\eta}\right]\left(\Psi_1\Psi_2\kappa^2\left(y^2-H^2\right)+\frac{1}{2}\Omega^-_{2,2}(y)-\frac{1}{4}\Omega^+_{2,1}(y)\right)
\end{aligned} \tag{7.94}$$

where the operator $\Omega^{\pm}_{p,q}(y)$ is defined as

$$\Omega^{\pm}_{p,q}(y) = (\kappa y)^{(q-1)}\,\Omega^{\pm}_{p}(y) - (-1)^{(q+1)}\,(\kappa H)^{(q-1)}\,\Omega^{\pm}_{p}(-H). \tag{7.95}$$

The no-slip boundary conditions for the velocity at the walls allows the determination of the integration constants. Here we chose to obtain an explicit form for $\dot{\gamma_1}$. The application of the second no-slip boundary condition leads to the following cubic equation:

$$\dot{\gamma_1}^3 + a_1\dot{\gamma_1}^2 + a_2\dot{\gamma_1} + a_3 = 0. \tag{7.96}$$

The Cardan-Tartaglia solution of the cubic equation gives the following explicit expression for the physically meaningful real solution of equation (7.96) (the other two solutions are complex and unphysical),

$$\begin{aligned}
\dot{\gamma_1} &= \sqrt[3]{-\frac{b_1}{2}+\sqrt{\frac{b_1^2}{4}+\frac{a^3}{27}}}+\sqrt[3]{-\frac{b_1}{2}-\sqrt{\frac{b_1^2}{4}+\frac{a^3}{27}}}-\frac{a_1}{3}\\
a &= a_2-\frac{a_1^2}{3}\\
b_1 &= a_3-\frac{a_1a_2}{3}+\frac{2a_1^3}{27}
\end{aligned} \tag{7.97}$$

with coefficients

$$
\begin{aligned}
a_1 &= \frac{3}{2}\frac{\epsilon E_x \zeta_1}{\eta H}\Omega^-_{1,1}(H)\\
a_2 &= \frac{1}{2\varepsilon\lambda^2} + \left(\frac{p_{x,}}{\eta}\right)^2 H^2 + 6\left(\frac{\epsilon E_x \zeta_1}{\eta}\kappa\right)^2 \Psi_1\Psi_2 + \frac{3}{4}\frac{\left(\frac{\epsilon E_x \zeta_1}{\eta}\kappa\right)^2}{\kappa H}\Omega^-_{2,1}(H)\\
&\quad + 3\frac{\left(\frac{\epsilon E_x \zeta_1}{\eta}\kappa\right)\frac{p_{x,}}{\eta}}{\kappa^2 H}\left(\Omega^-_{1,2}(H) - \Omega^+_{1,1}(H)\right) \qquad (7.98)\\
a_3 &= \frac{1}{2}\frac{\epsilon E_x \zeta_1}{\eta}\frac{\Omega^-_{1,1}(H)}{2\varepsilon\lambda^2 H} + \frac{1}{2}\frac{\left(\frac{\epsilon E_x \zeta_1}{\eta}\kappa\right)^3}{\kappa H}\left(\frac{1}{3}\Omega^-_{3,1}(H) + 3\Psi_1\Psi_2\Omega^-_{1,1}(H)\right)\\
&\quad + \frac{3}{2}\frac{\left(\frac{\epsilon E_x \zeta_1}{\eta}\kappa\right)^2\frac{p_{x,}}{\eta}}{\kappa^2 H}\left(\frac{1}{2}\Omega^-_{2,2}(H) - \frac{1}{4}\Omega^+_{2,1}(H)\right)\\
&\quad + \frac{3}{2}\frac{\left(\frac{\epsilon E_x \zeta_1}{\eta}\kappa\right)\left(\frac{p_{x,}}{\eta}\right)^2}{\kappa^3 H}\left(\Omega^-_{1,3}(H) + 2\Omega^-_{1,1}(H) - 2\Omega^+_{1,2}(H)\right).
\end{aligned}
$$

As suggested by equation (7.161) there are terms which are only proportional to E_x, others to $p_{,x}$ and those that are simultaneously proportional to $p_{,x}$ and E_x. Even the terms proportional to $\dot{\gamma}_1$ depend on both forcings. Therefore, as discussed by Afonso et al. (2009c), the superposition principle valid for Newtonian fluids and quasi-linear viscoelastic fluids is no longer valid for the sPTT fluid and suggests that the same applies to other non-linear viscoelastic models.

It is often more convenient to work with the dimensionless form of equation (7.161). Introducing the normalizations $\bar{y} = y/H$ and $\bar{\kappa} = \kappa H$, the dimensionless velocity profile can be written as

$$
\begin{aligned}
\frac{u}{u_{sh}} &= \bar{\dot{\gamma}}_1(\bar{y}+1)\left(1 + 2\bar{\dot{\gamma}}_1^2\frac{\varepsilon De_\kappa^2}{\bar{\kappa}^2}\right) - \left(1 + 6\bar{\dot{\gamma}}_1^2\frac{\varepsilon De_\kappa^2}{\bar{\kappa}^2}\right)\overline{\Omega}^-_{1,1}(\bar{y})\\
&\quad + 2\bar{\dot{\gamma}}_1\frac{\varepsilon De_\kappa^2}{\bar{\kappa}}\left(6\Psi_1\Psi_2\bar{\kappa}(\bar{y}+1) + \frac{3}{2}\overline{\Omega}^-_{2,1}(\bar{y})\right)\\
&\quad - 2\varepsilon De_\kappa^2\left(\frac{1}{3}\overline{\Omega}^-_{3,1}(\bar{y}) + 3\Psi_1\Psi_2\overline{\Omega}^-_{1,1}(\bar{y})\right)\\
&\quad + \frac{1}{2}\Gamma\left(\bar{y}^2-1\right)\left(1 + 6\bar{\dot{\gamma}}_1^2\frac{\varepsilon De_\kappa^2}{\bar{\kappa}^2} + \frac{\varepsilon De_\kappa^2}{\bar{\kappa}^2}\Gamma^2\left(\bar{y}^2+1\right)\right)\\
&\quad + 2\bar{\dot{\gamma}}_1\frac{\varepsilon De_\kappa^2}{\bar{\kappa}^2}\Gamma^2\left(\bar{y}^3+1\right)\\
&\quad - 12\bar{\dot{\gamma}}_1\frac{\varepsilon De_\kappa^2}{\bar{\kappa}^3}\Gamma\left(\overline{\Omega}^-_{1,2}(\bar{y}) - \overline{\Omega}^+_{1,1}(\bar{y})\right)\\
&\quad + 6\frac{\varepsilon De_\kappa^2}{\bar{\kappa}^2}\Gamma\left(\Psi_1\Psi_2\bar{\kappa}^2\left(\bar{y}^2-1\right) + \frac{1}{2}\overline{\Omega}^-_{2,2}(\bar{y}) - \frac{1}{4}\overline{\Omega}^+_{2,1}(\bar{y})\right)\\
&\quad - 6\frac{\varepsilon De_\kappa^2}{\bar{\kappa}^4}\Gamma^2\left(\overline{\Omega}^-_{1,3}(\bar{y}) + 2\overline{\Omega}^-_{1,1}(\bar{y}) - 2\overline{\Omega}^+_{1,2}(\bar{y})\right) \qquad (7.99)
\end{aligned}
$$

where $\overline{\Omega}^\pm_{p,q}(y)$ is the normalization of the operator introduced by equation (7.95), defined as

$$
\overline{\Omega}^\pm_{p,q}(\bar{y}) = (\bar{\kappa}\,\bar{y})^{(q-1)}\,\overline{\Omega}^\pm_p(\bar{y}) - (-1)^{(q+1)}\bar{\kappa}^{(q-1)}\overline{\Omega}^\pm_p(-1). \quad (7.100)
$$

with $\overline{\Omega}^\pm_p(\bar{y}) = \Psi_1^p\left(e^{\bar{\kappa}\,\bar{y}}\right)^p \pm \Psi_2^p\left(e^{-\bar{\kappa}\,\bar{y}}\right)^p$.

The dimensionless shear rate asymmetry coefficient calculated from

$$
\bar{\dot{\gamma}}_1^3 + \bar{a}_1\bar{\dot{\gamma}}_1^2 + \bar{a}_2\bar{\dot{\gamma}}_1 + \bar{a}_3 = 0, \qquad (7.101)
$$

with coeficients

$$\begin{aligned}
\overline{\alpha}_1 &= -\frac{3}{2}\overline{\Omega}^-_{1,1}(1)\\
\overline{\alpha}_2 &= \frac{\overline{\kappa}^2}{2\varepsilon De^2_\kappa} + \Gamma^2 + 6\overline{\kappa}^2\Psi_1\Psi_2 + \frac{3}{4}\overline{\kappa}\overline{\Omega}^-_{2,1}(1) - 3\frac{\Gamma}{\overline{\kappa}}\left(\overline{\Omega}^-_{1,2}(1) - \overline{\Omega}^+_{1,1}(1)\right)\\
\overline{\alpha}_3 &= -\frac{1}{4}\frac{\overline{\kappa}^2\overline{\Omega}^-_{1,1}(1)}{\varepsilon De^2_\kappa} - \frac{1}{2}\overline{\kappa}^2\left(\frac{1}{3}\overline{\Omega}^-_{3,1}(1) + 3\Psi_1\Psi_2\overline{\Omega}^-_{1,1}(1)\right)\\
&\quad + \frac{3}{2}\Gamma\left(\frac{1}{2}\overline{\Omega}^-_{2,2}(1) - \frac{1}{4}\overline{\Omega}^+_{2,1}(1)\right)\\
&\quad - \frac{3}{2}\frac{\Gamma^2}{\overline{\kappa}^2}\left(\overline{\Omega}^-_{1,3}(1) + 2\overline{\Omega}^-_{1,1}(1) - 2\overline{\Omega}^+_{1,2}(1)\right),
\end{aligned} \tag{7.102}$$

where $\overline{\dot{\gamma}}_1 = \frac{\dot{\gamma}_1 H}{u_{sh}}$ and $De_\kappa = \frac{\lambda u_{sh}}{\xi} = \lambda\kappa u_{sh}$ is the Deborah number based on the EDL thickness and on the Helmholtz-Smoluchowski electro-osmotic velocity, defined as $u_{sh} = -\frac{\varepsilon\zeta_1 E_x}{\eta}$ (Park and Lee, 2008b). In Poiseuille flows a different Deborah number is usually defined (Oliveira and Pinho, 1999c) based on the cross-sectional average velocity for the Newtonian flow under the sole influence of pressure gradient and the channel half-height, $De_N = \frac{\lambda U_N}{H}$ with $U_N = -\frac{H^2 p_{,x}}{3\eta}$. A third alternative Deborah number for electro-osmotic flow is based again on u_{sh}, but considers the channel half-height, $De_{sh} = \frac{\lambda u_{sh}}{H}$. These three Deborah numbers are related by $De_\kappa = \bar{\kappa} De_{sh} = -\frac{3}{\Gamma}\bar{\kappa} De_N$, where parameter $\Gamma = -\frac{H^2}{\varepsilon\zeta_1}\frac{p_{,x}}{E_x}$ represents the ratio of pressure to electro-osmotic driving forces. Note that for simplicity the above terms were based on the zeta potential at the bottom wall ($\psi_{\|y=-H} = \zeta_1$), but can be related with the upper wall zeta potential using the ratio of zeta potentials: $u_{sh} = u_{sh2}/R_\zeta$, $\Gamma = R_\zeta\Gamma_2$ and $De_\kappa = De_{\kappa 2}/R_\zeta$. The solution of equation (7.101) is similar to equation (7.97).

The flow rate per unit length can be determined from integration of the velocity profile (7.161). Here, this integration was carried out using the normalized velocity profile, equation (7.162), leading to the following expression

$$\begin{aligned}
\overline{Q} = \frac{Q}{2Hu_{sh}} = \frac{\overline{u}}{u_{sh}} &= \frac{1}{2}\int_{-1}^{1}\frac{u}{u_{sh}}d\bar{y} = \overline{\dot{\gamma}}_1\left(1 + 2\frac{\varepsilon De^2_\kappa}{\overline{\kappa}^2}\overline{\dot{\gamma}}^{-2}_1\right)\\
&- \frac{1}{2}\Gamma\left(\frac{4}{5}\frac{\varepsilon De^2_\kappa}{\overline{\kappa}^2}\Gamma^2 + \frac{2}{3}\left(1 + 6\overline{\dot{\gamma}}^{-2}_1\frac{\varepsilon De^2_\kappa}{\overline{\kappa}^2}\right)\right)\\
&+ 2\overline{\dot{\gamma}}_1\frac{\varepsilon De^2_\kappa}{\overline{\kappa}^2}\Gamma^2 - \frac{1}{2}\left(1 + 6\frac{\varepsilon De^2_\kappa}{\overline{\kappa}^2}\overline{\dot{\gamma}}^{-2}_1\right)\left(\frac{\overline{\Omega}^+_{1,1}(1)}{\overline{\kappa}} - 2\overline{\Omega}^-_1(-1)\right)\\
&+ \frac{\varepsilon De^2_\kappa}{\overline{\kappa}}\overline{\dot{\gamma}}_1\left(12\Psi_1\Psi_2\overline{\kappa} + \frac{3}{2}\left(\frac{\overline{\Omega}^+_{2,1}(1)}{2\overline{\kappa}} - 2\overline{\Omega}^-_2(-1)\right)\right)\\
&- \varepsilon De^2_\kappa\left(\frac{\overline{\Omega}^+_{3,1}(1)}{9\overline{\kappa}} - \frac{2}{3}\overline{\Omega}^-_3(-1) + 3\Psi_1\Psi_2\left(\frac{\overline{\Omega}^+_{1,1}(1)}{\overline{\kappa}} - 2\overline{\Omega}^-_1(-1)\right)\right)\\
&- 6\overline{\dot{\gamma}}_1\frac{\varepsilon De^2_\kappa}{\overline{\kappa}^4}\Gamma\left[\overline{\Omega}^+_{1,2}(1) - 2\overline{\Omega}^-_{1,1}(1) + 2\overline{\kappa}\left(\overline{\kappa}\overline{\Omega}^-_1(-1) + \overline{\Omega}^+_1(-1)\right)\right]\\
&+ 3\frac{\varepsilon De^2_\kappa}{\overline{\kappa}^2}\Gamma\left(\frac{1}{4\overline{\kappa}}\left(\overline{\Omega}^+_{2,2}(1) - \overline{\Omega}^-_{2,1}(1)\right) - \frac{4}{3}\Psi_1\Psi_2\overline{\kappa}^2 + \overline{\kappa}\overline{\Omega}^-_2(-1) + \frac{1}{2}\overline{\Omega}^+_2(-1)\right)\\
&- 3\frac{\varepsilon De^2_\kappa}{\overline{\kappa}^5}\Gamma^2\left(\overline{\Omega}^+_{1,3}(1) - 4\overline{\Omega}^-_{1,2}(1) + 6\overline{\Omega}^+_{1,1}(1)\right)\\
&+ 6\frac{\varepsilon De^2_\kappa}{\overline{\kappa}^4}\Gamma^2\left(\left(\overline{\kappa}^2 + 2\right)\overline{\Omega}^-_1(-1) + 2\overline{\kappa}\overline{\Omega}^+_1(-1)\right).
\end{aligned} \tag{7.103}$$

The decoupling of this total flow rate into its three fundamental contributions (pure electro-osmosis, pure Poiseuille flow and the nonlinear combined forcing contribution) is not attempted here since it leads to extremely complex relations, if at all possible. In fact, the dependence on the *shear rate asymmetry coefficient*, $\overline{\dot{\gamma}}_1$, complicates this task, because

$\bar{\dot{\gamma}}_1$ is the solution of equation (7.102) to the cubic equation (7.101), and each of its various component coefficients ($\bar{a}_1$, $\bar{a}_2$ and $\bar{a}_3$) also contain the same fundamental contributions. However, it is possible to gain insight into this issue by looking at the simpler symmetric case for which Afonso et al. (2009c) quantified the relative flow rate contributions (cf. their Figure 10). For instance, for large viscoelasticity ($\sqrt{\varepsilon}De_\kappa \geqslant 5$), the ratio of flow rates asymptotes and becomes inversely proportional to $\bar{\kappa}$. If the double layer is thick, say $\bar{\kappa} = 20$, and for a favourable pressure gradient, $\bar{Q}_{EP}/\bar{Q}_T$ can be of the order of 19%, decreasing to 4% for a thin EDL. This non-linear contribution becomes stronger than the pure Poiseuille contribution at high values of $\sqrt{\varepsilon}De_\kappa$, even if the pressure gradient is adverse.

The explicit expressions for the dimensionless shear and normal stress components are obtained from normalization of equations (7.91) and (7.92),

$$\frac{\tau_{xy}}{3\eta u_{sh}\kappa} = \frac{1}{3}\left[\Gamma\frac{\bar{y}}{\bar{\kappa}} + \frac{\bar{\dot{\gamma}}_1}{\bar{\kappa}} - \bar{\Omega}_1^+(\bar{y})\right] \tag{7.104}$$

$$\frac{\tau_{xx}}{3\eta u_{sh}\kappa} = \frac{2}{3}De_\kappa\left[\Gamma\frac{\bar{y}}{\bar{\kappa}} + \frac{\bar{\dot{\gamma}}_1}{\bar{\kappa}} - \bar{\Omega}_1^+(\bar{y})\right]^2. \tag{7.105}$$

The normalized shear rate is

$$\frac{\dot{\gamma}}{u_{sh}\kappa} = \left[1 + 2\varepsilon De_\kappa^2\left(\Gamma\frac{\bar{y}}{\bar{\kappa}} + \frac{\bar{\dot{\gamma}}_1}{\bar{\kappa}} - \bar{\Omega}_1^+(\bar{y})\right)^2\right]\left(\Gamma\frac{\bar{y}}{\bar{\kappa}} + \frac{\bar{\dot{\gamma}}_1}{\bar{\kappa}} - \bar{\Omega}_1^+(\bar{y})\right) \tag{7.106}$$

and the viscosity profile can be obtained from

$$\mu(\dot{\gamma}) \equiv \frac{\tau_{xy}}{\dot{\gamma}} \Rightarrow \frac{\mu(\dot{\gamma})}{\eta} = \left[1 + 2\varepsilon De_\kappa^2\left(\Gamma\frac{\bar{y}}{\bar{\kappa}} + \frac{\bar{\dot{\gamma}}_1}{\bar{\kappa}} - \bar{\Omega}_1^+(\bar{y})\right)^2\right]^{-1}. \tag{7.107}$$

7.2.3.4 *Analytical solution for the FENE-P model*

As pointed out at the end of Section 7.2.3.2, for fully developed channel flow there is similarity between the solutions for the sPTT and the FENE-P models (Bird et al., 1980). Comparing equations (7.83) and (7.84) for the sPTT model with equations (7.86) and (7.87) for the FENE-P model, and since the momentum equation (7.90) is independent of the constitutive equation, an exact equivalence in the sense of a parameter to parameter match is obtained, as explained in detail in Cruz et al. (2005). Hence, the solution of Section 7.2.3.3 also applies to the flow of FENE-P fluids provided the following substitutions are made:

$$\begin{aligned} f(\tau_{xx}) &\rightarrow \left(\frac{b+2}{b+5}\right) Z(\tau_{xx}) \\ \lambda &\rightarrow \lambda \left(\frac{b+2}{b+5}\right) \\ \varepsilon &\rightarrow \frac{1}{b+5} \\ \eta &\rightarrow \eta \end{aligned} \tag{7.108}$$

7.2.4 *Discussion of results*

In Section 7.2.3 the solution was obtained for fully developed flow of viscoelastic fluids (sPTT and FENE-P fluids) under the mixed influence of pressure gradient and electro-osmosis induced by asymmetric zeta potentials at the channel walls. The different influences of the driving forces, fluid rheology and zeta potential ratio on the velocity profiled have been identified in equation (7.161) and in this section we discuss in detail some of the various limiting cases in order to better understand the fluid dynamics. The limit cases contained in the general solution are: (a) Newtonian fluid with mixed electro-osmotic/pressure driving forces and asymmetric wall zeta potentials; (b) Pure electro-osmotic flows of viscoelastic fluids with asymmetric wall zeta potentials; (c) Poiseuille flow of a viscoelastic fluid and (d) Viscoelastic fluid with mixed electro-osmotic/pressure driving forces and asymmetric wall zeta potentials. Case (c) was studied in detail elsewhere (Oliveira, 2002; Cruz et al., 2005; Oliveira and Pinho, 1999c; Alves et al., 2001a), and so was case (a) in Soong and Wang (2003), but this latter situation is revisited here as a starting point.

7.2.4.1 *Newtonian fluid with mixed driving forces and asymmetric zeta potentials*

For a Newtonian fluid the relaxation time is zero, so the Deborah number vanishes ($De_\kappa = 0$), and equation (7.162) becomes

$$\frac{u}{u_{sh}} = \bar{\dot{\gamma}}_1 (\bar{y}+1) - \bar{\Omega}_{1,1}(\bar{y}) + \frac{1}{2}\Gamma\left(\bar{y}^2 - 1\right), \tag{7.109}$$

under the mixed influence of electro-osmotic and pressure driving forces, as was also shown by Soong and Wang (2003). As explained in Section 7.2.3.3, the asymmetric boundary conditions for the zeta potential at the channel walls introduces a new constant in the velocity profile, $\bar{\dot{\gamma}}_1$, that depends on the ratio of zeta potentials, R_ζ, on the relative microchannel ratio, $\bar{\kappa}$, on the ratio of pressure gradient to electro-osmotic driving forces, Γ, and on the fluid rheology. For a Newtonian fluid the dimensionless *shear rate asymmetry coefficient* is a linear function of R_ζ, as expressed by $\bar{\dot{\gamma}}_1 = \frac{1}{2}\bar{\Omega}_{1,1}(1) = \frac{1}{2}(R_\zeta - 1)$. For symmetric boundary conditions ($R_\zeta = 1$), $\bar{\dot{\gamma}}_1 = 0$, and the velocity profile is simplified to that of Dutta and Beskok (2001). For $\Gamma \rightarrow \infty$, pressure forces dominate the momentum transport for any value of $\bar{\kappa}$, and the classical laminar parabolic velocity profile is recovered. Note that this corresponds to $E_x \rightarrow 0$ and $u_{sh} \rightarrow 0$, since $u_{sh} \propto E_x$ and $\Gamma \propto E_x^{-1}$. For $\Gamma \rightarrow 0$, the last term on the right-hand-side of equation (7.109)

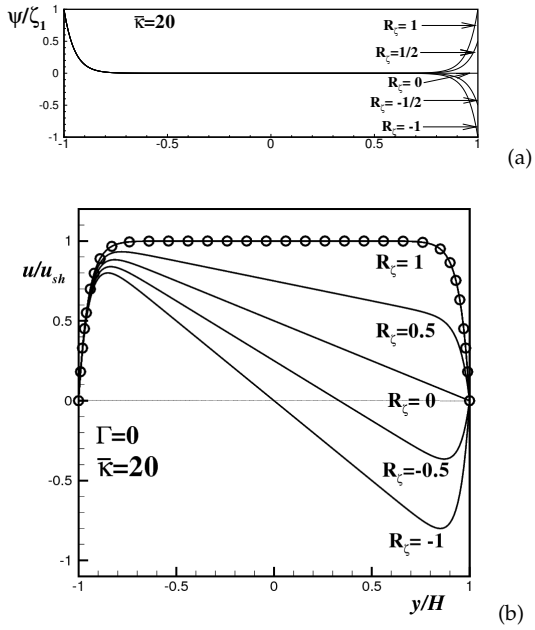

Figure 7.14: Effect of zeta potential ratio on Newtonian flow under pure electro-osmosis ($\Gamma = 0$) and $\bar{\kappa} = 20$: (a) Dimensionless potential and (b) velocity profiles. Symbols in (b) represent the data from Burgreen and Nakache (1964).

vanishes, the flow becomes governed exclusively by electro-osmosis and the velocity profile is a function of the wall distance, the relative microchannel ratio, $\bar{\kappa}$, and the ratio of zeta potentials, R_ζ, as shown by Soong and Wang (2003). So, for symmetric boundary conditions ($R_\zeta = 1$), the velocity profile is only a function of the wall distance and the relative microchannel ratio, $\bar{\kappa}$, as shown earlier by Burgreen and Nakache (1964). Note that for large $\bar{\kappa}$ ($\bar{\kappa} \to \infty$) the size of the EDL, or region of excess charge, is relatively small, and equation (7.109) reduces to the classical Helmoltz- Smoluchowski equation, $u/u_{sh} = 1$ (Park and Lee, 2008b), if simultaneously $\Gamma = 0$.

Figure 7.14(a) shows the effect of the ratio of zeta potentials, R_ζ, on the variation of the dimensionless potential for pure electro-osmotic flow ($\Gamma = 0$) and relative microchannel ratio of $\bar{\kappa} = 20$. When the ratio of zeta potentials decreases from symmetric ($R_\zeta = 1$) to anti-symmetric ($R_\zeta = -1$) the corresponding dimensionless potential profiles varies from fully symmetric to fully anti-symmetric, respectively. This is also observed in the velocity profiles presented in Figure 7.14(b): for symmetric boundary conditions ($R_\zeta = 1$) the velocity profile corresponds to a *pluglike flow*, as shown earlier by Burgreen and Nakache (1964). When $R_\zeta = -1$ the velocity profiles are fully anti-symmetric.

Figure 7.15 shows Newtonian velocity profiles for various ratios of pressure gradient to electro-osmotic driving forces at $\bar{\kappa} = 20$ and for different values of R_ζ. When $\Gamma = 0$ and $R_\zeta = -1$ the velocity profiles are anti-symmetric, as seen in Figure 7.14(b). When $\Gamma \neq 0$, corresponding to mixed Poiseuille electro-osmotic flows, the pressure gradient effect can be observed in the favorable ($\Gamma < 0$) or adverse ($\Gamma > 0$) contributions for the velocity profiles. The velocity profiles shown in Figure 7.15 (b) for $\bar{\kappa} = 20$ and $R_\zeta = 2$, show a *skewed pluglike* profile, due to a higher zeta potential at $\bar{y} = 1$. Equation (7.109) predicts negative velocities

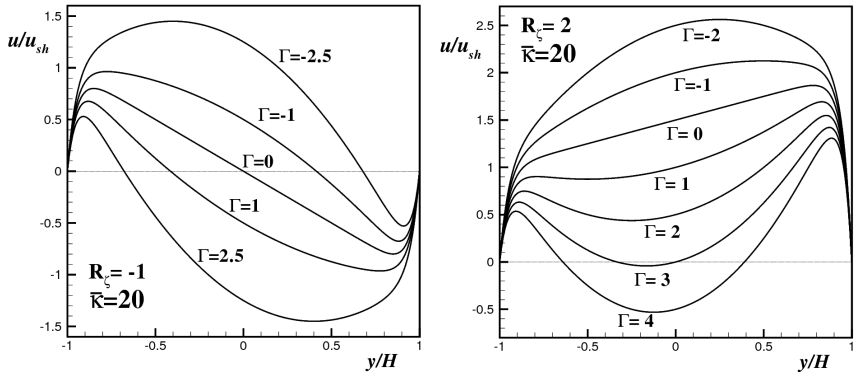

Figure 7.15: Velocity profiles for Newtonian fluids for $\bar{\kappa} = 20$ and different ratios of pressure to electro-osmotic driving forces, Γ, and zeta potential ratios: (a) $R_\zeta = -1$ and (b) $R_\zeta = 2$.

at $\bar{y} = 0$ when $\Gamma > 2\bar{\dot{\gamma}}_1 - \left[\frac{R_\zeta + 1 - 2\cosh(\bar{\kappa})}{\cosh(\bar{\kappa})}\right]$ for all values of $\bar{\kappa}$ and R_ζ. For symmetric boundary conditions, negative velocities at $\bar{y} = 0$ are predicted for $\Gamma > 2$ and small but finite Debye lengths, $\bar{\kappa} \gtrsim 10$, as observed by Afonso et al. (2009c).

7.2.4.2 *Viscoelastic fluid with pure electro-osmosis and asymmetric zeta potential*

For the sPTT fluid under pure electro-osmosis driving force, the solution is derived by setting $\Gamma = 0$, for which equation (7.162) reduces to

$$\begin{aligned}\frac{u}{u_{sh}} = {} & \bar{\dot{\gamma}}_1 (\bar{y}+1)\left(1 + 2\bar{\dot{\gamma}}_1^{-2}\frac{\varepsilon De_\kappa^2}{\bar{\kappa}^2}\right) - \left(1 + 6\bar{\dot{\gamma}}_1^{-2}\frac{\varepsilon De_\kappa^2}{\bar{\kappa}^2}\right)\bar{\bar{\Omega}}_{1,1}(\bar{y}) \\ & + 2\bar{\dot{\gamma}}_1\frac{\varepsilon De_\kappa^2}{\bar{\kappa}}\left(6\Psi_1\Psi_2\bar{\kappa}(\bar{y}+1) + \frac{3}{2}\bar{\bar{\Omega}}_{2,1}(\bar{y})\right) \\ & - 2\varepsilon De_\kappa^2\left(\frac{1}{3}\bar{\bar{\Omega}}_{3,1}(\bar{y}) + 3\Psi_1\Psi_2\bar{\bar{\Omega}}_{1,1}(\bar{y})\right).\end{aligned} \tag{7.110}$$

For symmetric boundary conditions ($R_\zeta = 1$ and $\bar{\dot{\gamma}}_1 = 0$) the above equation reduces to that presented by Afonso et al. (2009c), but for $R_\zeta \neq 1$ the dimensionless *shear rate asymmetry coefficient*, $\bar{\dot{\gamma}}_1$, depends on the fluid rheological properties, as shown in Figure 7.16(a). For $R_\zeta < 1$, $\bar{\dot{\gamma}}_1$ is always negative, decreasing with the increase of $\sqrt{\varepsilon}De_\kappa$, an indication that the shear stress is also decreasing as $\sqrt{\varepsilon}De_\kappa$ increases. For $R_\zeta > 1$, $\bar{\dot{\gamma}}_1$ is always positive and increases with $\sqrt{\varepsilon}De_\kappa$, due to the increasing of the shear-thinning behaviour of the fluid, leading to higher shear stress. All curves asymptote to the same limiting curve when $\sqrt{\varepsilon}De_\kappa \to \infty$, with the absolute value of $\bar{\dot{\gamma}}_1$ increasing when $\bar{\kappa}$ increases ($\bar{\kappa} = 20$, 100, 150 and 200), as observed in Figure 7.16(b). The increase of $\bar{\dot{\gamma}}_1$ with $\bar{\kappa}$ is related with the reduction of the shear layer, leading to high shear stresses near the wall, requiring higher values of $\bar{\dot{\gamma}}_1$ to balance the velocity profile.

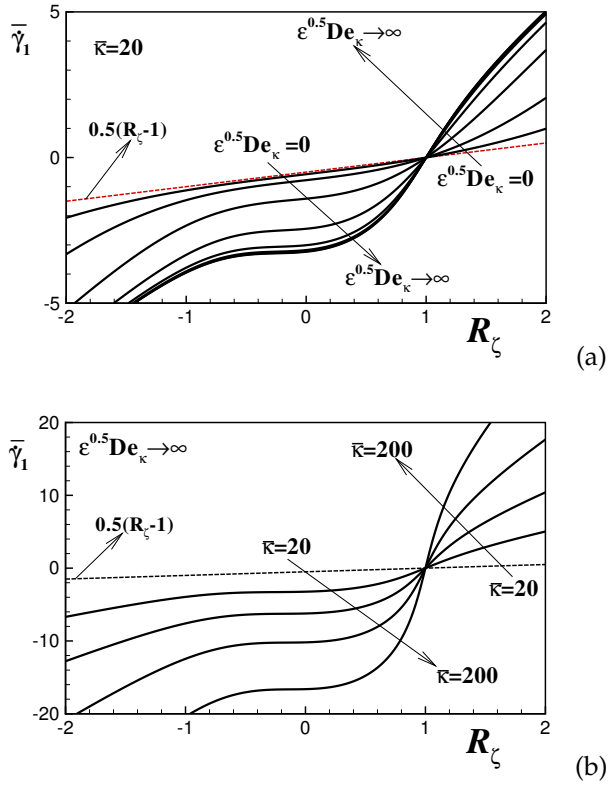

Figure 7.16: Variation of the dimensionless *shear rate asymmetry coefficient*, for pure electro-osmotic viscoelastic flow ($\Gamma = 0$) as a function of the ratio of zeta potentials, R_ζ. (a) increasing $\sqrt{\varepsilon}De_\kappa$ for $\bar{\kappa} = 20$ and (b) assimptotic limit for $\sqrt{\varepsilon}De_\kappa \to \infty$ at several $\bar{\kappa}$.

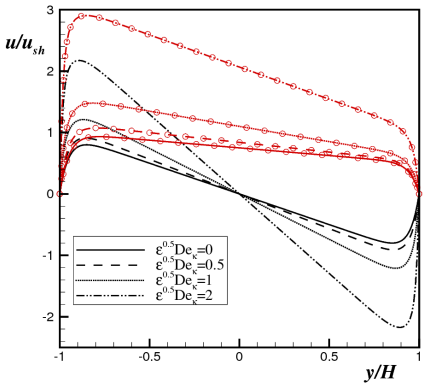

Figure 7.17: Dimensionless velocity profiles as a function of $\sqrt{\varepsilon}De_\kappa$ for electro-osmotic flow ($\Gamma = 0$) of a PTT fluid for $R_\zeta = -1$ (lines) and $R_\zeta = 0.5$ (lines with symbols) at relative microchannel ratios of $\bar{\kappa} = 20$.

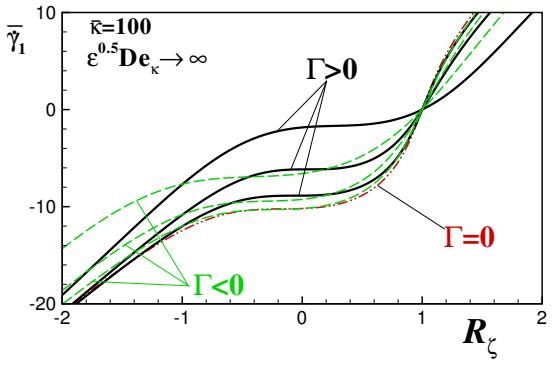

Figure 7.18: Variation of the dimensionless *shear rate asymmetry coefficient*, with R_ζ as a function of Γ (electro-osmotic/pressure drive flow) for the asymptotic limit of $\sqrt{\varepsilon}De_\kappa \to \infty$ and $\bar{\kappa} = 100$.

Figure 7.17 shows the corresponding dimensionless velocity profiles as a function of the parameter $\sqrt{\varepsilon}De_\kappa$ for two ratios of zeta potentials, $R_\zeta = -1$ and $R_\zeta = 0.5$, and a relative microchannel ratio of $\bar{\kappa} = 20$. These profiles should be compared with those in Figure 7.14(b) pertaining to Newtonian fluids. As for Newtonian fluids, the velocity profiles for $R_\zeta = -1$ exhibit an *anti-symmetric pluglike* shape (full lines in Figure 7.17), with the absolute velocites increasing with $\sqrt{\varepsilon}De_\kappa$. For $R_\zeta = 0.5$, increasing $\sqrt{\varepsilon}De_\kappa$ also leads to an increase in the *skewed pluglike* profile, as observed in Figure 7.17. This flow enhancement by increasing $\sqrt{\varepsilon}De_\kappa$ is typical of sPTT fluids and is associated with the increased shear-thinning behaviour of the fluid.

7.2.4.3 *Viscoelastic fluid with mixed driving forces and asymmetric zeta potentials*

The viscoelastic flow characteristics under the combined action of electro-osmosis and a pressure gradient are discussed in this Section, recalling equation (7.161).

The Poiseuille effect on the dimensionless *shear rate asymmetry coefficient*, $\bar{\dot{\gamma}}_1$, is presented in Figure 7.18, here for the asymptotic limit of $\sqrt{\varepsilon}De_\kappa \to \infty$. Increasing the favorable pressure gradient (decreasing Γ), $\bar{\dot{\gamma}}_1$ increases, especially for $R_\zeta < 1$. Increasing Γ for adverse pressure gradient conditions, $\bar{\dot{\gamma}}_1$ also increases, especially for $-1 < R_\zeta < 1$, i.e., $\bar{\dot{\gamma}}_1$ behaves monotonically but non-linearly with R_ζ showing the minimum value for $R_\zeta < 1$ and the maximum for $R_\zeta > 1$. Figures 7.19 (a) and (b) present the dimensionless velocity profiles for the flows with favorable and adverse pressure gradients, respectively. For $\Gamma < 0$ with anti-symetric zeta potentials ($R_\zeta = -1$), the velocity profiles increase with $\sqrt{\varepsilon}De_\kappa$, due to shear-thinning effects, leading to correspondingly higher shear rates near the walls. For $\Gamma > 0$ with $R_\zeta = 0.5$, the velocity profiles show the same double peak seen for Newtonian flows (cf. Figure 7.15(a)), due to the retarding action of the pressure gradient. The velocity profiles also increase with $\sqrt{\varepsilon}De_\kappa$, again due to shear-thinning effects, both within the EDL layer and in the bulk zone.

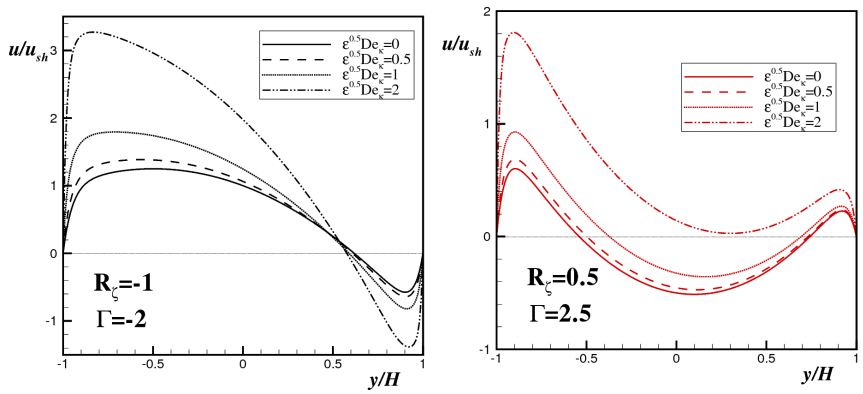

(a) (b)

Figure 7.19: Dimensionless velocity profiles for a PTT fluid under the mixed influence of electro-osmotic/pressure driving force as function of $\sqrt{\varepsilon}De_\kappa$ for relative microchannel ratio of $\bar{\kappa} = 20$: (a) $\Gamma = -2$ and $R_\zeta = -1$ and (b) $\Gamma = 2.5$ and $R_\zeta = 0.5$.

7.2.5 *Conclusions*

Analytical solutions for channel flow of symmetric $z-z$ electrolyte viscoelastic fluids under the mixed influence of electro-osmosis and pressure gradient forcings were obtained for the case of asymmetric wall zeta potentials. This analysis is restricted to cases with small electric double-layers, where the wall-to-wall distance is at least one order of magnitude larger than the thickness of each EDL. The viscoelastic fluids analysed are described by the sPTT model (Phan-Thien and Tanner, 1977), with linear kernel for the stress coefficient function and zero second normal stress difference (Phan-Thien, 1978), and the FENE-P model (Bird et al., 1980).

7.2.6 *Acknowledgements*

The authors acknowledge funding from FEDER and Fundação para a Ciência e a Tecnologia (FCT), Portugal, through projects PTDC/EQU-FTT/70727/2006 and PTDC/EQU-FTT/71800/2006. A.M. Afonso would also like to thank FCT for financial support through scholarship SFRH/BD/28828/ 2006.

7.3 ANALYTICAL SOLUTION OF EO VISCOELASTIC FLUID FLOW: PTT MODEL

Abstract[3]
The electro-osmotic flow of a viscoelastic fluid between parallel plates is investigated analytically. The rheology of the fluid is described by the Phan-Thien-Tanner model. This model uses the Gordon-Schowalter convected derivative, which leads to a non- zero second normal stress difference in pure shear flow. A nonlinear Poisson-Boltzmann equation governing the electrical double-layer field and a body force generated by the applied electrical potential field are included in the analysis. Results are presented for the velocity and stress component profiles in the microchannel for different parametric values that characterize this flow. Equations for the critical shear rates and maximum electrical potential that can be applied to maintain a steady fully developed flow are derived and discussed.

Keywords*:* Electro-osmotic flow, parallel plates, PTT model, viscoelastic fluid, analytical study, constitutive flow instability.

7.3.1 *Introdution*

The theoretical analysis of electro-osmotic flows (EOF) of Newtonian fluids in microchannels has been the subject of several studies. Burgreen and Nakache (1964) studied the effect of the surface potential on liquid transport through ultrafine capillary slits assuming the validity of the Debye-Hückel linear approximation to the electrical potential distribution under an imposed electrical field. Rice and Whitehead (1965) discussed the same problem in a circular capillary. Dutta and Beskok (2001) obtained analytical solutions for the velocity distribution, mass flow rate, pressure gradient, wall shear stress, and vorticity in mixed electro-osmotic/pressure driven flows for a two-dimensional straight channel geometry, for small, yet finite symmetric electrical double layers (EDL), relevant for applications where the distance between the two walls of a microfluidic device is about 1-3 orders of magnitude larger than the EDL thickness. Arulanandam and Li (2000) and Wang et al. (2007a) presented a two-dimensional analytical model for the electro-osmotic flow in a rectangular microchannel. Wang et al. (2007b) derived a semianalytical solution to study the flow behaviour of periodical electro-osmosis in a rectangular microchannel based on the Poisson-Boltzmann and the Navier-Stokes equations. Zade et al. (2007) presented analytical solutions for the heat transfer characteristics of Newtonian fluids under combined pressure and electro-osmotic flow forcing in planar microchannels. Analytical solutions for the two-dimensional, time-dependent as well as time-independent EOF driven by a uniform electric field with non-uniform zeta potential distributions along the walls of a conduit were presented by Qian and Bau (2002). Several other articles can be found in the literature on theoretical studies of EOF with Newtonian fluids in microchannels such as those of Petsev and Lopez (2006), Qian and Bau (2005), among others.

3 S. Dhinakaran, A.M. Afonso, M.A. Alves, F.T. Pinho (2010). Steady viscoelastic fluid flow in microchannels under electrokinetic forces: PTT model, *Journal of Colloid And Interface Science* **344** 513-520.

Biofuids are often solutions of long chain molecules which impart a non-Newtonian rheological behaviour characterized by variable viscosity, memory effects, normal stress effect, yield stress and hysteresis of fluid properties. These fluids are encountered in chips used for chemical and biological analysis or in micro-rheometers.

The theoretical study of electro-osmotic flows of non-Newtonian fluids is recent and has been mostly limited to simple inelastic fluid models, such as the power-law, due to the inherent analytical difficulties introduced by more complex constitutive equations. Examples are the recent works of Das and Chakraborty (2006) and Chakraborty (2007), who presented explicit relationships for velocity, temperature and concentration distributions in electro-osmotic microchannel flows of non-Newtonian bio-fluids described by the power-law model. Other purely viscous models were analytically investigated by Olivares et al. (2009), who considered the existence of a small wall layer depleted of additives and behaving as a Newtonian fluid (the skimming layer), under the combined action of pressure and electrical fields, thus restricting the non-Newtonian behavior to the electrically neutral region outside the electrical double layer. Very recently these studies were extended to viscoelastic fluids by Afonso et al. (2009c), who presented analytical solutions for channel and pipe flows of viscoelastic fluids under the mixed influence of electro-kinetic and pressure forces, using two constitutive models: the Phan-Thien-Tanner model (PTT, Phan-Thien and Tanner (1977)), with linear kernel for the stress coefficient function and zero second normal stress difference Phan-Thien (1978), and the kinetic theory based Finitely Extensible Non-linear Elastic model with a Peterlin closure for the average dumbbell spring force (cf. Bird et al. (1980)) denoted as FENE-P model. Their analysis (Afonso et al., 2009c) was restricted to cases with small electric double-layers, where the distance between the walls of a microfluidic device is at least one order of magnitude larger than the EDL, and the fluid is uniformly distributed across the channel.

Afonso et al. (2009c) also showed that when the viscoelastic flow is induced by a combination of both electric and pressure potentials, in addition to the contributions from these two isolated mechanisms there is an extra term in the velocity profile that simultaneously combines both forcings, which is absent for the Newtonian fluids where the superposition principle applies. This extra term can contribute significantly to the total flow rate, and appears only when the rheological constitutive equation is non-linear. Afonso et al. (2010c) extendedtheir earlier study Afonso et al. (2009c) to the flow of viscoelastic fluids under asymmetric zeta potential forcing, whereas Sousa et al. (2010a) considered the effect of a Newtonian skimming layer for the PTT fluid.

Flow instabilities can occur for a variety of reasons. For instance, they are associated with perturbations to non-linear terms of the governing equations which grow without control. Generally speaking, in electro-osmotic flows in microchannels, flow instabilities can be promoted by oscillating electric fields, as was justified by Boy and Storey Boy and Storey (2007) among others. They can also be promoted by gradients of conductivity as shown in the experimental study of Lin et al. (2004) who also analyzed the problem theoretically and numerically.

In addition to inertial non-linearities, which require high Reynolds number flows, non-Newtonian fluids are also prone to flow instabilities due to non-linearities in their rheological behaviour. For instance, for

viscoelastic fluids constitutive instabilities in Poiseuille and Couette flows were observed when the constitutive equation exhibit a non-monotonic behaviour for the shear stress, as reported by Alves et al. (2001a) for the full PTT model, and by Español et al. (1996) and Georgiou and Vlassopoulos (1998) for the Johnson-Segalman (JS) constitutive equation (Larson, 1998). To the best knowledge of the authors this constitutive instability in microchannels under EOF has not yet been studied. There are other viscoelastic flow instabilities not associated with non-monotonic fluid properties, but these are not considered here.

In this study, we extend the work of Afonso et al. (2009c) considering the full Gordon-Schowalter convective derivative in the PTT model to analyze the steady fully developed flow in the microchannel. We derive expressions for the critical shear rates and Deborah number beyond which constitutive flow instability occurs. The rest of the paper is organised as follows. The physical description of the problem is given in Section 7.3.2 while the equations governing the flow are presented in Section 7.3.3. The analytical solutions are derived in Section 7.3.4. Section 7.3.5 discusses the results of the study and the conclusions are presented in Section 7.3.6.

7.3.2 *Physical description of the problem*

The geometry under consideration is shown schematically in Figure 7.20, where a microchannel is formed between two parallel plates separated by a distance (height) 2H. The length of the channel is L and the width is W, both assumed to be much larger than the height, i.e., $L, W \gg 2H$. The bottom plate is located at $y = -H$ while the top plate is located at $y = H$. A potential is applied along the axis of the channel which provides the necessary driving force for the flow through electro-osmosis. Due to symmetry of the geometry and flow conditions with respect to the channel mid-plane ($y = 0$), only the upper half of the channel ($0 \leqslant y \leqslant H$) is considered in this analysis.

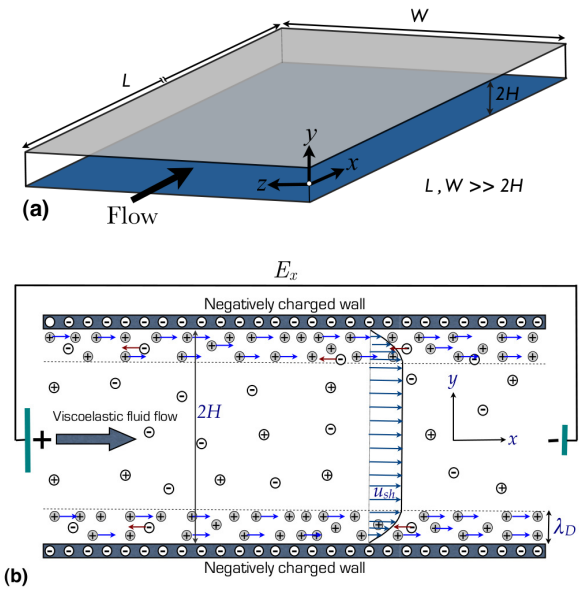

Figure 7.20: (a) Diagram of the microchannel geometry considered in the study; (b) 2D representation of electro-osmotic flow of viscoelastic fluids in the microchannel for a negatively charged wall.

7.3.3 *Governing Equations*

The equations governing the flow of an incompressible fluid between the parallel walls of the microchannel are the continuity and the modified Cauchy equation,

$$\nabla \cdot \mathbf{u} = 0 \tag{7.111}$$

$$\rho \frac{D\mathbf{u}}{Dt} = -\nabla p + \nabla \cdot \boldsymbol{\tau} + \eta_s \nabla^2 \mathbf{u} + \mathbf{F} \tag{7.112}$$

where $\mathbf{u}$ is the velocity vector, t the time, ρ the fluid density, η_s is the Newtonian solvent viscosity and $\boldsymbol{\tau}$ the polymeric contribution to the extra-stress tensor. Here, we consider that the solvent viscosity is negligible in comparison with the polymeric contribution, i.e., $\eta_s = 0$. The term $\mathbf{F}$ in the modified momentum Eqn. (7.112) represents a body force per unit volume, given by

$$\mathbf{F} = \rho_e \mathbf{E} \tag{7.113}$$

where $\mathbf{E} = -\nabla\phi$ is the applied external electric field and ρ_e is the net electric charge density. The potential has two contributions: (a) an applied external field, $\mathbf{E}$ and (b) a spontaneously induced potential that appears near the wall, ψ. The formation of the EDL in a fluid containing charged species occurs spontaneously when the fluid is brought in contact with the microchannel walls, causing a preferential redistribution of the charged species in the fluid and wall (Bruss, 2008; Probstein, 2003). In order to obtain the induced potential field, the net charge density distribution (ρ_e) has to be solved as discussed in Section 7.3.3.2.

7.3.3.1 *Constitutive equation*

The model adopted here to describe the viscoelastic behaviour of the fluid is the PTT model (Phan-Thien and Tanner, 1977), which can be expressed as

$$f(\tau_{kk})\boldsymbol{\tau} + \lambda \overset{\diamond}{\boldsymbol{\tau}} = 2\eta \mathbf{D}, \tag{7.114}$$

where $\mathbf{D} = (\boldsymbol{\nabla}\mathbf{u}^{\mathbf{T}} + \boldsymbol{\nabla}\mathbf{u})/2$ is the rate of deformation tensor, λ is the relaxation time, η is the polymer viscosity coefficient and $\overset{\diamond}{\boldsymbol{\tau}}$ represents the Gordon-Schowalter convected derivative of the stress-tensor, defined as

$$\overset{\diamond}{\boldsymbol{\tau}} = \frac{D\boldsymbol{\tau}}{Dt} - \nabla u^{T} \cdot \boldsymbol{\tau} - \boldsymbol{\tau} \cdot \nabla u + \xi \left(\boldsymbol{\tau} \cdot \mathbf{D} + \mathbf{D} \cdot \boldsymbol{\tau}\right), \tag{7.115}$$

where ε is the extensibility parameter and parameter ξ accounts for the slip between the molecular network and the continuum medium (Phan-Thien and Tanner, 1977). A simplified version of the above model is the so-called simplified Phan-Thien-Tanner (sPTT) equation, where $\xi = 0$. The stress coefficient function, $f(\tau_{kk})$ is given by the linear form,

$$f(\tau_{kk}) = 1 + \frac{\varepsilon\lambda}{\eta}\tau_{kk} \tag{7.116}$$

where $\tau_{kk} = \tau_{xx} + \tau_{yy} + \tau_{zz}$ represents the trace of the extra-stress tensor. As the flow is two dimensional, we have $\tau_{zz} = 0$. When $f(\tau_{kk}) =$

1 (i.e., when $\varepsilon = 0$, but $\xi \neq 0$), the Johnson-Segalman constitutive equation, used for dilute polymeric solutions, is recovered.

7.3.3.2 *Potential field within the electric double layer*

The flow investigated is steady and fully developed and in addition the electric double layers (EDLs) are thin so that there is no interference from one wall into the other. These conditions simplify the Nernst-Planck equations governing the ionic and electric potential field (ψ) distributions. Consequently, the potential field within the electric double layer can be given by the well known Poisson equation:

$$\nabla^2\psi = -\frac{\rho_e}{\epsilon} \tag{7.117}$$

where ϵ is the dielectric constant of the solution. We are here considering standard kinetic theory conditions, where the applied constant potential streamwise gradient ($\Delta\phi/L$, where L is the channel length) is much weaker than the induced transverse ion potential (ψ_o/ξ) so mutual interference is negligible. The distribution of the net electric charge density, ρ_e, in equilibrium near a charged surface, as in a fully developed flow, is described as (Bruss, 2008)

$$\rho_e = -2n_o ez \sinh\left(\frac{ez}{k_B T}\psi\right). \tag{7.118}$$

For small values of ψ, the Debye-Hückel linearization principle ($\sinh x \approx x$) can be used, which means physically that the electrical potential is small compared with the thermal energy of the charged species. Invoking this principle, the Poisson-Boltzmann equation resulting from substitution of Eqn. (7.118) into Eqn. (7.117) takes the following simpler linear form

$$\frac{d^2\psi}{dy^2} = \kappa^2\psi, \tag{7.119}$$

where $\kappa^2 = 2n_o e^2 z^2/(\epsilon k_B T)$ is the Debye-Hückel parameter, related with the thickness of the Debye layer, $\lambda_D = 1/\kappa$ (normally referred as the EDL thickness). This approximation is valid when the Debye thickness is small but finite, i.e., for $10 \leqslant H/\lambda_D \leqslant 10^3$. As a consequence the induced potential is limited so that its energy does not exceed the thermal energy. Equation (7.119) can be solved subjected to the following boundary conditions: zeta potential at the wall, $\psi_{||y=H} = \psi_0$ and symmetry in the centerline, $(d\psi/dy)_{||y=o} = 0$, and can be written in the dimensionless form as

$$\overline{\psi} = \frac{\cosh(\overline{\kappa}\,\overline{y})}{\cosh(\overline{\kappa})}, \tag{7.120}$$

where, the following non-dimensional quantities are defined: $\overline{\psi} = \psi/\psi_0, \overline{\kappa} = \kappa H$ and $\overline{y} = y/H$. Finally, the net charge density distribution Eqn.(7.118) in conjunction with Eqn.(7.120) reduces to

$$\rho_e = -\epsilon\psi_0\kappa^2\frac{\cosh(\overline{\kappa}\,\overline{y})}{\cosh(\overline{\kappa})}. \tag{7.121}$$

7.3.4 *Analytical solution*

7.3.4.1 *PTT constitutive equation*

The predictions of the PTT model in this flow, for which $\mathbf{u}$ ={u(y),0,0}, can be obtained from equations (7.114) - (7.116), and leads to

$$f(\tau_{kk})\tau_{xx} = \lambda(2-\xi)\dot{\gamma}\tau_{xy} \tag{7.122}$$

$$f(\tau_{kk})\tau_{yy} = -\lambda\xi\dot{\gamma}\tau_{xy} \tag{7.123}$$

$$f(\tau_{kk})\tau_{xy} = \eta\dot{\gamma} + \lambda\left(1-\frac{\xi}{2}\right)\dot{\gamma}\tau_{yy} - \frac{\lambda\xi}{2}\dot{\gamma}\tau_{xx} \tag{7.124}$$

where $\tau_{kk} = \tau_{xx} + \tau_{yy}$ is the trace of the extra-stress tensor and $\dot{\gamma}$ is the velocity gradient ($\dot{\gamma} = du/dy$). Upon division of Eqn. (7.122) by Eqn. (7.123) the specific function $f(\tau_{kk})$, $\dot{\gamma}$ and τ_{xy} cancel out, and a relation between the two normal stresses is obtained,

$$\tau_{yy} = -\frac{\xi}{2-\xi}\tau_{xx} \tag{7.125}$$

leading to the following form of the stress coefficient function:

$$f(\tau_{kk}) = 1 + \frac{2\varepsilon\lambda(1-\xi)}{\eta(2-\xi)}\tau_{xx}. \tag{7.126}$$

Division of Eqn. (7.124) by Eqn. (7.122) results in a second order algebraic equation for the streamwise normal stress,

$$\lambda\xi\tau_{xx}^2 - \eta\tau_{xx} + \lambda(2-\xi)\tau_{xy}^2 = 0 \tag{7.127}$$

which leads to the following physical solution for τ_{xx} (note that at the centerline, τ_{xx} and τ_{xy} should be zero)

$$\tau_{xx} = \frac{\eta}{2\lambda\xi}\left[1 - \sqrt{1 - \frac{4\lambda^2\xi(2-\xi)}{\eta^2}\tau_{xy}^2}\right]. \tag{7.128}$$

7.3.4.2 *Analytical flow solution for the PTT model*

From the invoked assumptions and for a zero pressure gradient, the momentum equation (7.112), reduces to

$$\frac{d\tau_{xy}}{dy} = -\rho_e E_x \tag{7.129}$$

where $E_x = -d\phi/dx$ is the streamwise gradient of the applied external electric potential (ϕ). Using equation (7.121) and noting that $\tau_{xy||y=0} = 0$, Eqn. (7.129) can be integrated to yield

$$\tau_{xy} = \epsilon\psi_0 E_x \kappa \frac{\sinh(\kappa y)}{\cosh(\kappa H)} \tag{7.130}$$

Using the relation between the normal and shear stresses - equation (7.128), an explicit expression for the normal stress component is obtained,

$$\tau_{xx} = \frac{\eta}{2\lambda\xi}\left[1 - \sqrt{1 - \left(a\lambda\kappa u_{sh}\frac{\sinh(\kappa y)}{\cosh(\kappa H)}\right)^2}\right] \tag{7.131}$$

with a defined as $a = 2\sqrt{\xi(2-\xi)}$, for compactness and $u_{sh} = -\epsilon\psi_o E_x/\eta$ is the Helmholtz-Smoluchowski velocity based on the zero-shear rate viscosity. After combining Eqns. (7.124), (7.125), (7.126), (7.130) and (7.131) we obtain an expression for the velocity gradient:

$$\dot{\gamma} = \frac{du}{dy} = -\frac{\left[1 + \frac{1}{\chi}\left\{1 - \sqrt{1 - \left(a\lambda\kappa u_{sh}\frac{\sinh(\kappa y)}{\cosh(\kappa H)}\right)^2}\right\}\right]\kappa\, u_{sh}\frac{\sinh(\kappa y)}{\cosh(\kappa H)}}{1 - \frac{1}{2}\left[1 - \sqrt{1 - \left(a\lambda\kappa u_{sh}\frac{\sinh(\kappa y)}{\cosh(\kappa H)}\right)^2}\right]} \tag{7.132}$$

with χ defined as $\chi = \frac{\xi(2-\xi)}{\varepsilon(1-\xi)}$, in order to improve the readability. Integrating Eqn. (7.132) and applying the no-slip boundary condition at the wall (i.e., $u = 0$, at $y = H$) the following velocity profile is obtained:

$$\begin{aligned} u = \; &= \frac{2\cosh(\kappa H)}{a^2\lambda^2\kappa^2 u_{sh}}\left(\frac{2+\chi}{\chi}\right)\left[\frac{1}{2}\ln\left\{\frac{(1+A(H))(1-A(y))}{(1-A(H))(1+A(y))}\right\} - \ln\left\{\frac{\tanh(\frac{\kappa y}{2})}{\tanh(\frac{\kappa H}{2})}\right\}\right. \\ &-\frac{1}{(2+\chi)}\frac{a^2\lambda^2\kappa^2 {u_{sh}}^2}{\cosh(\kappa H)}\left\{1 - \frac{\cosh(\kappa y)}{\cosh(\kappa H)}\right\} - \frac{a\lambda\kappa u_{sh}}{\cosh(\kappa H)} \\ &\left.\left[(\arcsin\{B\cosh(\kappa y)\} - \arcsin\{B\cosh(\kappa H)\}\right)\right] \end{aligned} \tag{7.133}$$

where,

$$A(y) = \frac{\cosh(\kappa y)}{\sqrt{1 - \left[a\lambda\kappa u_{sh}\frac{\sinh(\kappa y)}{\cosh(\kappa H)}\right]^2}}; B = \frac{\frac{a\lambda\kappa u_{sh}}{\cosh(\kappa H)}}{\sqrt{1 + \left[\frac{a\lambda\kappa u_{sh}}{\cosh(\kappa H)}\right]^2}}$$

Equation (7.133) can be written in dimensionless form as

$$\begin{aligned} u/u_{sh} =& \frac{2}{G a De_\kappa}\left(\frac{2+\chi}{\chi}\right)\left[\frac{1}{2}\ln\left\{\frac{(1+\overline{A}(1))(1-\overline{A}(\overline{y}))}{(1-\overline{A}(1))(1+\overline{A}(\overline{y}))}\right\}\right. \\ &-\ln\left\{\frac{\tanh(\frac{\overline{\kappa}\,\overline{y}}{2})}{\tanh(\frac{\overline{\kappa}}{2})}\right\} - \frac{1}{(2+\chi)}G a De_\kappa\left\{1 - \frac{\cosh(\overline{\kappa}\,\overline{y})}{\cosh(\overline{\kappa})}\right\} \\ &\left.-G\left(\arcsin\{\overline{B}\cosh(\overline{\kappa}\,\overline{y})\} - \arcsin\{\overline{B}\cosh(\overline{\kappa})\}\right)\right] \end{aligned} \tag{7.134}$$

with the dimensionless forms of A and B,

$$\overline{A}(\overline{y}) = \frac{\cosh(\overline{\kappa}\,\overline{y})}{\sqrt{1 - G^2\sinh^2(\overline{\kappa}\,\overline{y})}}; \overline{B} = \frac{G}{\sqrt{1+G^2}} \text{ and } G = \frac{aDe_{\lambda}}{\cosh(\overline{\kappa})} \tag{7.135}$$

where $De_\kappa = \lambda\kappa u_{sh}$ is a Deborah number.

Critical shear rate

A physical solution for the transverse profile of velocity, in Eqn. (7.133), only occurs when

$$\left[a\lambda\kappa u_{sh}\frac{\sinh(\kappa y)}{\cosh(\kappa H)}\right]^2 \leqslant 1.$$

Thus, at critical conditions (that occurs at the wall):

$$\sinh(\kappa H) = \frac{\cosh(\kappa H)}{a\lambda\kappa\left|u_{sh}\right|}. \tag{7.136}$$

Substituting Eqn. (7.136) in Eqn. (7.132), we conclude that the critical shear rate $|\dot{\gamma}_c|$ is

$$\lambda|\dot{\gamma}_c| = \frac{\varepsilon(1-\xi)+\xi(2-\xi)}{[\xi(2-\xi)]^{3/2}}. \tag{7.137}$$

This is the same constitutive instability obtained by Alves et al. (2001a) for pressure-driven channel flows, and is related with the existence of a local maximum of the shear stress as a function of the shear rate for the PTT model without a solvent viscosity, and occurs for the condition indicated in Eqn. (7.137), independent of the mechanism used to drive the flow (Alves et al., 2001a). This critical shear rate depends on both ε and ξ, i.e., it is a characteristic of the PTT model and independent of the type of forcing. Above the maximum shear rate given in Eqn.(7.137), the governing equations for the flow between the walls of the microchannel do not have a real solution, and the fully-developed steady solution no longer exists.

Expression for critical Deborah number

Under critical conditions at the wall, multiplying Eqn.(7.132) by λ results in the expression

$$\lambda\dot{\gamma}_c = -2\left[1+\frac{1}{\chi}\right]De_\kappa\tanh(\kappa H)$$

For $\kappa H > 10$, $\tanh(\kappa H) \to 1$ and the previous equation takes the form

$$\lambda\dot{\gamma}_c = -2\left[1+\frac{1}{\chi}\right]De_\kappa \tag{7.138}$$

Equating Eqn.(7.137) and Eqn.(7.138) we get a relation for the critical Deborah number as

$$|De_{\kappa,c}| = \frac{1}{a} \tag{7.139}$$

Beyond this critical value of $De_{\kappa,c}$ the flow cannot be steady and fully developed, as the shear rate near the wall exceeds the critical value. An expression for the corresponding critical electric potential, that can be applied, $E_{x,c}$, can be obtained from Eqn.(7.139) and is given by

$$|E_{x,c}| = \frac{\eta}{a\lambda\kappa\epsilon|\psi_o|} \tag{7.140}$$

This expression is useful in setting the electric field along the channel so as to have a stable flow. If a strong forcing is imposed, the flow must naturally evolve to a different condition, presumably an unsteady flow. Note that an asymmetric steady flow would lead to a shear rate beyond the critical value of Eqn. (7.137) at one of the walls, thus reinforcing the idea that only an unsteady flow is possible. However, the investigation of the flow characteristics above this critical conditions and of the transition process requires the use of various different specific tools.

7.3.5 *Results and Discussion*

The general equations for the flow of viscoelastic fluids in microchannels under the influence of electro-osmosis were derived in Section 7.3.4. The influence of electro-kinetic forcing and fluid rheology on the velocity profile has been identified in Eqn. (7.133). Important limiting cases contained in the general solutions are: (a) Newtonian flow under the sole influence of electrokinetic forces and (b) viscoelastic fluid with zero second normal stress difference, i.e., the simplified Phan-Thien-Tanner (sPTT) equation with $\xi = 0$.

For a Newtonian fluid the relaxation time is zero and the Deborah number vanishes ($De_\kappa = \lambda\kappa u_{sh} = 0$, although also true, it suffices to impose $\lambda = 0$), so the velocity profile is only a function of the wall distance and the relative microchannel ratio, $\overline{\kappa}$, as shown earlier by Burgreen and Nakache (1964). Figure 7.21 shows the effect of the relative microchannel ratio, $\overline{\kappa}$ (or H/λ_D, where λ_D is the Debye layer thickness) on the dimensionless velocity profiles (u/u_{sh}) for pure electro-osmotic flow. As $\overline{\kappa} \to 1$ the double layer thickness becomes of the same order of magnitude as the channel half-height and the region of excess charge is distributed over the entire channel. This situation is not fully compatible with this solution for which the Debye-Hückel approximation was invoked, which requires $\overline{\kappa} \geqslant 10$. As $\overline{\kappa}$ increases, the width of the Debye layer decreases, and the profile becomes sharper near the wall, as illustrated in Figure 7.21.

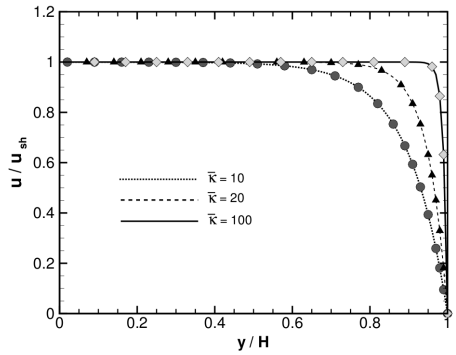

Figure 7.21: Dimensionless velocity profiles for $\overline{\kappa} = 10$, 20 and 100 for pure electro-osmotic flow of a Newtonian fluid. Symbols represent the data from Burgreen and Nakache (1964).

The effect of De_κ on the dimensionless velocity profiles is shown in Figure 7.22 at different Deborah numbers and fixed ϵ and ξ, while $\overline{\kappa} = 20$. At large Deborah numbers, the ratio u/u_{sh} is significantly greater than unity near the centerline due to shear-thinning of the viscosity of the PTT fluid and the consequent lower viscosities at the

wall region. With a decrease in De_κ, shear thinning effects become less important, and below $De_\kappa = 0.1$ the dimensionless velocity profile remains unaltered, and equal to the profile for a Newtonian fluid.

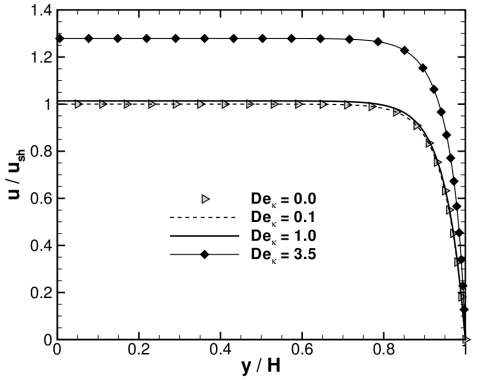

Figure 7.22: Effect of De_κ ($\varepsilon, \xi = 0.01, \bar{\kappa} = 20$) on the non-dimensional velocity profiles for the viscoelastic fluid flow in the microchannel under the influence of electro-osmotic forces.

The flow between the parallel walls of the microchannel depends on rheological and electro-osmotic parameters. The influence of ε and ξ on the dimensionless transverse velocity profiles are plotted in Figure 7.23(a) and 7.23(b), respectively, for $\bar{\kappa} = 20$ at $De_\kappa = 3.0$. Upon fixing De_κ and ξ and decreasing ϵ from 0.2 to 0.001, we find that the dimensionless velocity profiles approach the solution for Johnson-Segalman fluid ($\varepsilon = 0$), which in this case is similar to the Newtonian solution because of the small ξ used, as seen in Figure 7.23(a). The variation of the non-dimensional velocity profiles at $\xi = 0.001, 0.005$ and 0.01 is presented in Figure 7.23(b) for $De_\kappa = 3$ and $\varepsilon = 0.1$. Increasing ξ from 0.001 to 0.01 increases the velocity profile due to enhanced shear-thinning associated with ξ.

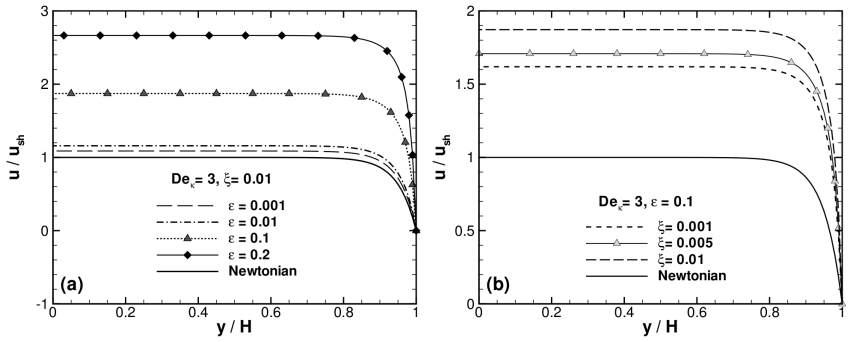

(a) (b)

Figure 7.23: Effect of (a) variation of ε at $De_\kappa = 3$ and $\xi = 0.01$ and (b) variation of ξ at $De_\kappa = 3$ and $\varepsilon = 0.1$ on the non-dimensional velocity profiles for the viscoelastic fluid flow in the microchannel under the influence of electro-osmotic forces. In all cases $\bar{\kappa}$ =20.

The critical Deborah number ($|De_{\kappa,c}|$), predicted from Eqn.(7.139) is presented in Figure 7.24 as a function of ξ. In log-log scale $De_{\kappa,c}$ decreases monotonically and linearly as the parameter ξ increases (with a slope of -1/2) for small values of ξ, and in the limiting case of $\xi = 0$

(sPTT model) the flow is constitutively stable for any De_κ. At any non-zero value of ξ, increasing the value of De_κ (or the electric gradient, E_x) beyond a critical value produces a constitutively unstable flow. From Eqn.(7.139), we find $|De_{\kappa,c}|$ only depends on ξ, when $\overline{\kappa} > 10$.

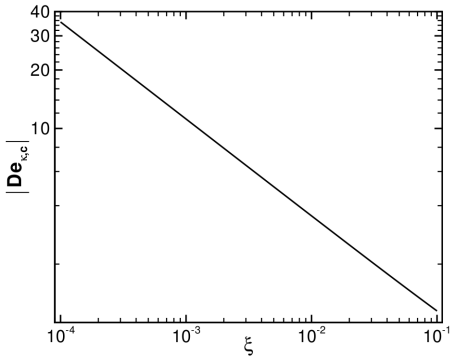

Figure 7.24: Variation of critical Deborah number ($|De_{\kappa,c}|$) with ξ.

The variation of the dimensionless critical shear rate ($\lambda|\dot{\gamma}_c|$) with ε as a function of ξ, is presented in Figure 7.25 for $\xi = 0.001$, 0.01 and 0.1. The plot of critical shear rate versus ε shows a linear relationship for all ξ, as anticipated from Eqn. (7.137). The critical shear rate gradually increases for $\xi = 0.01$ and 0.1, whereas, a steep rise with ε is observed as ξ decreases (cf. Figure 7.25 with $\xi = 0.001$). In the limit, for $\xi = 0$ the curve is vertical, i.e., $\lambda|\dot{\gamma}|_c$ tends to infinity meaning stable flow.

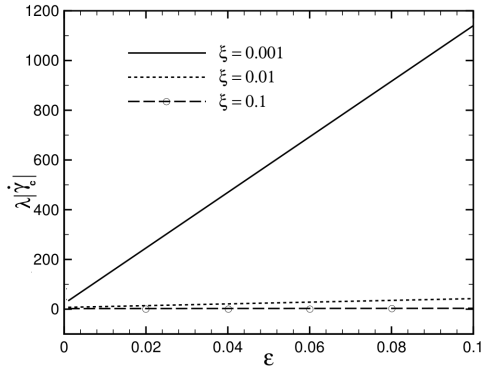

Figure 7.25: Variation of dimensionless critical shear rate ($\lambda|\dot{\gamma}_c|$) with ε at $\xi = 0.001$, 0.01 and 0.1.

Profiles of normal and shear stresses, drawn based on Eqn. (7.130) and (7.131), are shown in Figure 7.26 (a), (b) as a function of y/H at $\overline{\kappa} = 10$ and 20 for different values of De_κ. The normal stress approaches zero for $y/H < 0.75$ and increases rapidly near the wall. At low De_κ the normal stress is almost zero near the wall for both $\overline{\kappa} = 10$ and 20. With increase in De_κ the normal stress increases gradually. The increase in normal stress is gradual for $\overline{\kappa} = 10$ compared to $\overline{\kappa} = 20$ where the rise is sudden in agreement with the corresponding variations of the velocity profile. A similar trend is observed for the shear stress profiles as seen in Figure 7.26.

For the channel flow of viscoelastic fluids with electrokinetic forces, in the absence of Gordon-Schowalter derivative, Afonso et al. (2009c, 2010c) observed that the influences of ε and De_κ can be combined as a single dimensionless quantity, εDe_κ^2. In order to verify whether this

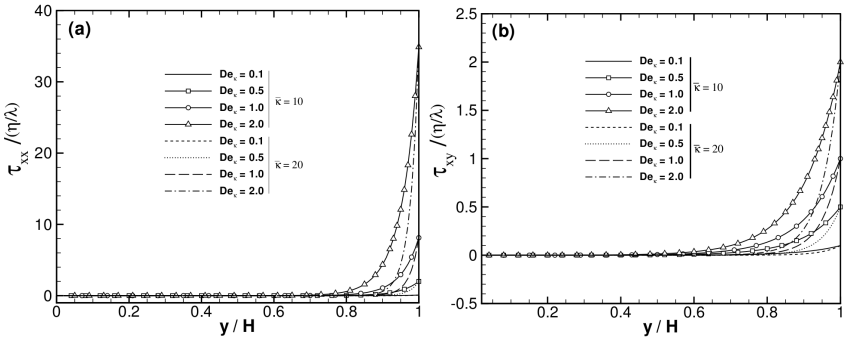

(a) (b)

Figure 7.26: (a) Normal stress (τ_{xx}) and (b) Shear stress (τ_{xy}) as a function of y/H at different Deborah number (De_κ) for $\bar{\kappa} = 10$ and 20.

also occurs here, we considered two sets of data ε and De_κ so that εDe_κ^2 are equal to 0.1 and 0.4, keeping ξ constant and equal to 0.01. Results for the dimensionless transverse velocity profiles in the channel (not shown here) revealed that no such εDe_κ^2 scaling apply here compared to the sPTT model.

7.3.6 *Conclusions*

Analytical solutions in microchannels for the electro-osmotic flow of viscoelastic fluids obeying the full PTT model have been derived. The Gordon-Schowalter convected derivative has been used in this model which leads to non- zero second normal stress difference. Symmetric boundary conditions with equal zeta potentials at the walls were assumed. A nonlinear Poisson-Boltzmann equation governing the electrical double-layer field and a body force generated by the applied electrical potential field were included in the Navier-Stokes equations. Some of the important results can be summarised as follows:

- Comparison of the present result with the analytical solution, for the flow of Newtonian fluids, available in the literature is found to be consistent.
- Profiles of dimensionless velocities in the channel are invariant with De_κ below $De_\kappa = 0.1$.
- When the shear rate and Deborah number exceed a critical value a constitutive flow instability occurs for $\xi \neq 0$. Expressions for these critical values of shear rate and Deborah number are reported. The critical shear rate is found to be dependent of ε and ξ, whereas the critical Deborah number is only dependent on ξ for large $\bar{\kappa}$. The critical Deborah number increases with decrease in ξ tending to infinity as ξ tends to zero.
- Normal and shear stresses are approximately zero near the centerline and rise rapidly near the channel walls. At low Deborah numbers both these quantities are almost negligible. At higher De_κ the values of these quantities rise rapidly with increasing microchannel height ratio.

7.3.7 *Acknowledgments*

The authors are grateful to Fundação para a Ciência e a Tecnologia (FCT) for funding this work through projects PTDC/EME-MFE/70186/2006 and PTDC/EQU-FTT/71800/2006. A. M. Afonso would also like to thank FCT for financial support through the scholarship SFRH/BD/28828/ 2006.

7.4 ANALYTICAL SOLUTION OF TWO-FLUID EO FLOWS OF VISCOELASTIC FLUIDS

Abstract[4]
This paper presents an analytical model that describes a two-fluid electro-osmotic flow of stratified viscoelastic fluids. This is the principle of operation of an EO two-fluid pump, recently presented by Brask et al. (2003), *in which an electrically nonconducting fluid is transported by the interfacial dragging viscous force of a conducting fluid that is driven by electro-osmosis. The electric potential in the conducting fluid and the analytical steady flow solution of the two-fluid electro-osmotic stratified flow in a planar microchannel are presented by assuming a planar interface between the two immiscible fluids with Newtonian or viscoelastic rheological behaviour. The effects of fluid rheology, dynamic viscosity ratio, holdup and interfacial zeta potential are analyzed to show the viability of this technique, where an enhancement of the flow rate is observed as the shear-thinning effects are increased.*

Keywords: Electro-osmotic flows; two-fluid pump; viscoelastic fluids.

7.4.1 *Introduction*

Electro-osmotic flows (EOF) in microfluidic devices have been studied extensively over the past decade (Brask et al., 2003; Gao et al., 2005; Chen and Santiago, 2002; Xuan and Li, 2004; Wang et al., 2009), because they enable precise liquid manipulation and are easily scalable to nanosized systems. The major applications of EO pumps are in micro flow injection analysis, microfluidic liquid chromatography systems, microreactors, microenergy systems and microelectronic cooling systems. Fluid pumps are important elements in such microchannel networks, and promising candidates for miniatuzization are lectro-hydrodynamic pumps using ion-dragging effects via the so-called electro-osmosis, and traveling-wave-induced flow (Brask et al., 2003) due to the inherent simplicity in producing small-sized pumps with these techniques. A comprehensive review on electrokinetic pumps has been recently published by Wang et al. (2009).

Some of the above studies were focused on the transport of fluids with high electrical conductivity, for which a classical EO pump is needed. An overview of fabrication and working principles for such systems was presented by Zeng et al. (2001). For nonpolar fluids, such as oil, traditional EOF pumping cannot be used, due to the low fluid conductivity (Gao et al., 2005). To overcome this limitation, Brask et al. (2003) proposed an idea that allows the use of EOF as a driving mechanism, using an electric fluid with high conductivity to drag the low conductivity nonpolar fluid. Their study (Brask et al., 2003) analyzed the performance of the pump by equivalent circuit theory and computational fluid dynamic simulations.

The theoretical study of electro-osmotic flows of non-Newtonian fluids is recent and has been limited to simple inelastic fluid models, such as the power-law, due to the inherent analytical difficulties introduced

4 A.M. Afonso, F.T. Pinho and M.A. Alves (2010), Two-fluid electro-osmotic flows of viscoelastic fluids, in preparation to submit to *Microfluidics and Nanofluidics.*

by more complex constitutive equations. Examples are the recent works of Das and Chakraborty (2006) and Chakraborty (2007), who presented explicit relationships for velocity, temperature and concentration distributions in electro-osmotic microchannel flows of non-Newtonian bio-fluids described by the power-law model. Other purely viscous models were analytically investigated by Berli and Olivares (2008), who considered the existence of a small wall layer depleted of additives and behaving as a Newtonian fluid (the skimming layer), under the combined action of pressure and electrical fields, thus restricting the non-Newtonian behaviour to the electrically neutral region outside the Electrical Double Layer (EDL). More recently these studies were extended to viscoelastic fluids by Afonso et al. (2009c), who presented analytical solutions for channel and pipe flows of viscoelastic fluids under the mixed influence of electrokinetic and pressure forces, using two constitutive models: the Phan-Thien and Tanner (PTT model (Phan-Thien and Tanner, 1977)), with linear kernel for the stress coefficient function and zero second normal stress difference (Phan-Thien, 1978), and the Finitely Extensible Non-linear Elastic dumbbells model with a Peterlin approximation for the average spring force (FENE-P model, cf. (Bird et al., 1980)). The analysis of Afonso et al. (2009c) was restricted to cases with small electric double-layers, where the distance between the walls of a microfluidic device is at least one order of magnitude larger than the EDL, and the fluid is well mixed and uniformly distributed across the channel. When the viscoelastic flow is induced by a combination of both electric and pressure potentials, in addition to the single contributions from these two mechanisms there is an extra term in the velocity profile that simultaneously combines both forcings, which is absent for the Newtonian fluids where the superposition principle applies. This extra term can contribute significantly to the total flow rate, depending on the value of the relative microchannel ratio and appears only when the rheological constitutive equation is non-linear. Afonso et al. (2010c) later extended this study to the flow of viscoelastic fluids under asymmetric zeta potential forcing.

The analytical solution of the steady two-fluid electro-osmotic stratified flow in a planar microchannel is presented here by assuming a planar interface between the two viscoelastic immiscible liquids. The working principle of the two-fluid pump is described in detail in the begining of Section 7.4.2. The PTT fluids considered (Phan-Thien and Tanner, 1977) obey a simplified model, with a linear kernel for the stress coefficient function (Phan-Thien, 1978) and a zero second normal stress difference in shear. The PTT model also includes the limiting case for Upper-Convected Maxwell (UCM) fluids.

The remaining of the paper starts with the flow problem definition, followed by the presentation of the set of governing equations and a discussion of the assumptions made to obtain the analytical solution. Using this solution, the effects of the various relevant dimensionless parameters upon the flow field characteristics are discussed in detail.

7.4.2 *Flow geometry and definitions*

The flow under investigation is the steady, fully-developed flow of two incompressible and immiscible viscoelastic fluids which also have significantly different condutivities, as shown schematically in Figure 7.27(a). This type of flow can be found in some EOF pumps Brask

et al. (2003), where the nonconducting fluid located at the upper part of the system is dragged by an electrically conducting fluid at the bottom section, as illustrated in Figure 7.27(b). Although the origin of the coordinate system is at the interface between the two fluids, their thickness are not necessarily identical.

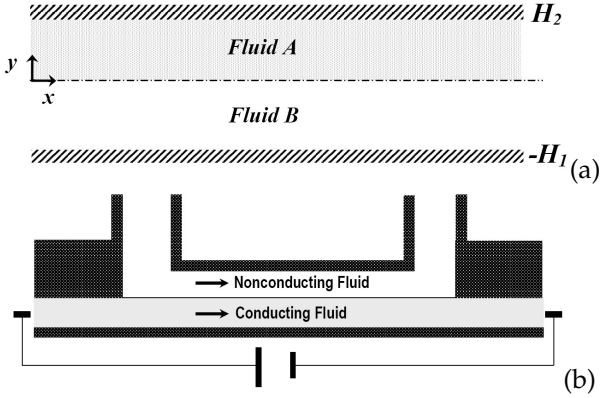

Figure 7.27: (a) Illustration of the coordinate system and (b) schematic of the two-fluid EOF pump.

The migration of ions naturally arises due to the interaction between the dielectric bottom wall and the conducting fluid. Concerning the wall-fluid interface, the charged bottom wall of the channel attracts counter-ions to form a layer of charged fluid near the wall and repels the co-ions. A very thin layer of immobile counter-ions covers the bottom wall, known as the Stern layer, and is followed by a thicker more diffuse layer of mobile counter-ions. These layers near the wall form the EDL. The global charge of the conducting fluid remains neutral, but since the EDL is thin the core of the conducting fluid is essentially neutral. Applying a DC potential difference between the two electrodes at the inlet and outlet of the bottom channel section, generates an external electric field that exerts a body force on the counter-ions of the EDL, which move along the bottom channel dragging the neutral conducting fluid core above by viscous forces.

A similar situation arises at the fluid-fluid interface, where there is also dielectric interaction leading to the formation of a second EDL in the conducting fluid next to the interface. The conducting fluid (Fluid B) drags the nonconducting fluid (Fluid A) by hydrodynamic viscous forces at the interface (cf. Figure 7.27(a)).

The pressure difference that can be independently applied between the inlets and outlets of both the upper and lower channels can act in the same or in the opposite directions of the electric field. Alternatively, the streamwise electric potential difference may not be imposed independently, but results from the accumulation of ions at the end of the channel due to the flow forced by an imposed pressure difference. This particular case is known as the streaming potential and implies a specific relationship between the imposed favorable pressure gradient and the ensuing adverse external electric field (Yang and Li, 1997), a case which will not be analysed in this paper for conciseness.

To analyse this system, a two-dimensional Cartesian orthonormal coordinate system (x, y) is used with the origin located at the fluid-fluid interface, as shown in Figure 7.27(a). We assume a stratified viscoelastic flow and a planar interface, a condition satisfied when the contact angle

between fluids A and B is close to 90° (Gao et al., 2005). The thickness of the conducting fluid is H_1 and that of the non-conducting fluid is H_2. The width w is assumed very large, such that $w \gg H_2 + H_1 = H$.

The holdup of the conducting fluid (Fluid B), R_B, is here defined as the ratio between the cross section area occupied by the conducting fluid and the cross section area of the channel, i.e.,

$$R_B = \frac{H_1}{H_2 + H_1} = \frac{H_1}{H}. \tag{7.141}$$

Similarly, the hold up of nonconducting fluid (Fluid A) is defined as

$$R_A = 1 - R_B = \frac{H_2}{H_2 + H_1} = \frac{H_2}{H}. \tag{7.142}$$

The electrical double layer that forms near the bottom channel wall in contact with the conducting fluid (Fluid B), has a zeta potential denoted by ζ_1. The second EDL in Fluid B, at the interface contact with fluid A, has an interfacial zeta potential (ζ_i) that depends on the properties of the two fluids and varies with the pH value, the concentration of ions in the conducting fluid and the presence of ionic surfactants (Gao et al., 2005). This interfacial zeta potential influences the potential distribution in the two EDLs, hence the electroosmotic force distribution and therefore the flow.

7.4.3 *Theoretical model of the two-fluid electroosmotic viscoelastic flow*

The basic field equations describing this fully-developed laminar flow of incompressible fluids are the continuity equation,

$$\nabla \cdot \mathbf{u} = 0 \tag{7.143}$$

and the modified Cauchy equation,

$$-\nabla p + \nabla \cdot \boldsymbol{\tau} + \rho_e \mathbf{E} = 0 \tag{7.144}$$

where $\mathbf{u}$ is the velocity vector, p is the pressure and $\boldsymbol{\tau}$ is the polymeric extra-stress tensor.

The $\rho_e \mathbf{E}$ term of equation (7.144) represents a body force per unit volume, where $\mathbf{E}$ is the applied external electric field and ρ_e is the net electric charge density in the fluid. This term is null for the non-polar fluid A, but needs to be quantified for the polar fluid B.

The main simplifying assumptions and considerations in the current analysis are: (i) the two fluids are viscoelastic (but the Newtonian fluid is also included as a limiting case when the relaxation time is negligible); (ii) fluid properties are assumed to be independent of local electric field, ion concentration and temperature (this is certainly true for dilute solutions (Gao et al., 2005), but we make this assumption for our fluids); (iii) the flow is steady and fully developed with no-slip boundary conditions at the channel walls; (iv) the two fluids are immiscible and there is stratification with a planar interface between fluids where a second EDL can form; (v) a pressure gradient can simultaneously be imposed along the channel and (vi) the standard electrokinetic theory conditions apply (Probstein, 2003).

7.4.3.1 *PTT model constitutive equations*

The polymer extra-stress $\boldsymbol{\tau}$ is described by an appropriate constitutive equation, and in this work we consider the viscoelastic model of Phan-Thien and Tanner (Phan-Thien and Tanner, 1977; Phan-Thien, 1978) (PTT model) of equation (7.145) derived from network theory arguments

$$f(\boldsymbol{\tau}_{kk})\boldsymbol{\tau} + \lambda \overset{\nabla}{\boldsymbol{\tau}} = 2\eta \mathbf{D}. \tag{7.145}$$

Here, $\mathbf{D} = \left(\bigtriangledown \mathbf{u}^{T} + \bigtriangledown \mathbf{u}\right)/2$ is the rate of deformation tensor, λ is the relaxation time of the fluid, η is the viscosity coefficient and $\overset{\nabla}{\boldsymbol{\tau}}$ represents the upper-convected derivative of $\boldsymbol{\tau}$, defined as

$$\overset{\nabla}{\boldsymbol{\tau}} = \frac{D\boldsymbol{\tau}}{Dt} - \bigtriangledown \mathbf{u}^{T}.\boldsymbol{\tau} - \boldsymbol{\tau}.\bigtriangledown \mathbf{u}\,. \tag{7.146}$$

The stress coefficient function, $f(\boldsymbol{\tau}_{kk})$, is given by the linear form (Phan-Thien and Tanner, 1977)

$$f(\boldsymbol{\tau}_{kk}) = 1 + \frac{\varepsilon\lambda}{\eta}\boldsymbol{\tau}_{kk}, \tag{7.147}$$

where $\boldsymbol{\tau}_{kk}$ represents the trace of the extra-stress tensor. The extensibility parameter, ε, imposes a maximum of the steady state elongational viscosity, which is inversely proportional to ε, for small ε. For $\varepsilon = 0$ the UCM model is recovered which has an unbounded elongational viscosity above a critical strain rate $\dot{\varepsilon} = 1/(2\lambda)$. For fully-developed flow conditions, for which $\mathbf{u} = \{u(y), 0, 0\}$, the extra-stress field for the PTT model can be obtained from equations (7.145–7.147), leading to

$$f(\boldsymbol{\tau}_{kk})\tau_{xx} = 2\lambda\dot{\gamma}\tau_{xy} \tag{7.148}$$

$$f(\boldsymbol{\tau}_{kk})\tau_{xy} = \eta\dot{\gamma} \tag{7.149}$$

where $\boldsymbol{\tau}_{kk} = \tau_{xx}$, since $\tau_{yy} = 0$ (Pinho and Oliveira, 2000; Alves et al., 2001a), and $\dot{\gamma}$ is the transverse velocity gradient ($\dot{\gamma} \equiv du/dy$). Then, upon division of equation (7.148) by equation (7.149) the specific function $f(\tau_{xx})$ cancels out, and a relation between the normal and shear stresses is obtained,

$$\tau_{xx} = 2\frac{\lambda}{\eta}\tau_{xy}^{2}. \tag{7.150}$$

7.4.3.2 *Electric double layers in the conducting fluid (Fluid B)*

The potential field within the conducting fluid B, can be expressed by means of a Poisson equation:

$$\nabla^{2}\psi = -\frac{\rho_{e}}{\epsilon}, \tag{7.151}$$

where ψ denotes the electric potential and ϵ is the dielectric constant of the fluid. In equilibrium conditions near a charged wall, the net electric charge density, ρ_e, can be described as

$$\rho_e = -2n_o ez \sinh\left(\frac{ez}{k_B T}\psi\right), \tag{7.152}$$

where n_o is the ion density, e is the elementary electric charge, z is the valence of the ions, k_B is the Boltzmann constant, and T is the absolute temperature. In order to obtain the velocity field for fluid B, we first need to determine the net charge density distribution (ρ_e). The charge density field can be calculated by combining equations (7.151) and (7.152) under fully developed flow conditions, to obtain the well-known Poisson–Boltzmann equation

$$\frac{d^2\psi}{dy^2} = \frac{2n_o ez}{\epsilon}\sinh\left(\frac{ez}{k_B T}\psi\right). \tag{7.153}$$

The electroosmotic flow is primarily caused by the action of an externally applied electric field on the charged species that exist near the bottom channel wall and in the vicinity of the interfacial surface. The distribution of the charged species in the domain is governed by the potentials at the wall and at the interface, and then by the externally applied electric field. When the Debye thicknesses are small and the charges at the wall and at the interface are not large, the distribution of the charged species is governed mainly by the ζ_1 potential at the wall and by ζ_i at the interface, and negligibly affected by the externally DC electric field (standard electrokinetic theory). Thus, the charge distribution across fluid B, can be determined independently of the externally applied electric field. Indeed, the effect of fluid motion on the charge redistribution can be neglected when the fluid velocity is small, i.e., when the inertial terms in the momentum equation are not dominant (they are null under fully developed conditions) or when the Debye thickness is small. Additionally, for small values of ψ the Debye–Hückle linearization principle ($\sinh x \approx x$) can also be used, which means physically that the electric potential energy is small compared with the thermal energy of ions, and the Poisson–Boltzmann equation simplified to:

$$\frac{d^2\psi}{dy^2} = \kappa^2\psi, \tag{7.154}$$

where $\kappa^2 = \frac{2n_o e^2 z^2}{\epsilon k_B T}$ is the Debye–Hückel parameter, related with the thickness of the Debye layer as $\xi = \frac{1}{\kappa}$ (normally referred to as the EDL thickness). This approximation is valid when the Debye thickness is small but finite, i.e., for $10 \lesssim H_1/\xi \lesssim 10^3$.

Equation (7.154) can be integrated subjected to the following boundary conditions: zeta potential at the bottom wall $\psi_{\parallel y=-H_1} = \zeta_1$ and zeta potential at the interface $\psi_{\parallel y=0} = \zeta_i$. The potential field becomes

$$\psi(y) = \zeta_1\left(\Psi_1 e^{\kappa y} - \Psi_2 e^{-\kappa y}\right) \tag{7.155}$$

for $-H_1 \leqslant y \leqslant 0$. Denoting $R_\zeta = \zeta_i/\zeta_1$ as the ratio of zeta potentials, then $\Psi_1 = \frac{R_\zeta e^{\kappa H_1}-1}{e^{\kappa H_1}-e^{-\kappa H_1}}$ and $\Psi_2 = \frac{R_\zeta e^{-\kappa H_1}-1}{e^{\kappa H_1}-e^{-\kappa H_1}}$. When $R_\zeta = 1$ a symmetric potential profile obtained as by Afonso et al. (2009c) for the whole

channel, whereas for vanishing zeta potential at the interface, $R_\zeta = 0$, one obtains a special case of that obtained by Afonso et al. (2010c). Finally the net charge density distribution, equation (7.152), together with the Debye–Hückle linearization principle leads to

$$\rho_e = -\epsilon\kappa^2\zeta_1\left(\Psi_1 e^{\kappa y} - \Psi_2 e^{-\kappa y}\right) = -\epsilon\kappa^2\zeta_1\Omega_1^-(y) \tag{7.156}$$

where the operator $\Omega_i^\pm(y) = \Psi_1^i e^{(\kappa y)^i} \pm \Psi_2^i e^{(-\kappa y)^i}$ is a hyperbolic function of the transverse variable y, and depends on the ratio of zeta potentials, R_ζ, and on the thickness of the Debye layer.

7.4.3.3 *Momentum equation of the two-fluid flow*

Conducting fluid (Fluid B)

For the conducting fluid (Fluid B), the momentum equation (7.144), reduces to,

$$\frac{d\tau_{xy}^B}{dy} = p_{,x} - \rho_e E_x = p_{,x} + \epsilon\kappa^2\zeta_1 E_x\Omega_1^-(y) \tag{7.157}$$

where $E_x \equiv -d\phi/dx$ and $p_{,x} \equiv dp/dx$. The electric potential of the applied external field, ϕ, is characterized by a constant streamwise gradient. Equation (7.157) is integrated to yield the following shear stress distribution

$$\tau_{xy}^B = p_{,x}y + \epsilon\kappa\zeta_1 E_x\Omega_1^+(y) + \tau_B \tag{7.158}$$

where τ_B is a stress integration coefficient related to the stress at the fluid-fluid interface. It is clear that in contrast to pure Poiseuille flow the shear stress distribution is no longer linear on the transverse coordinate. Using the relationship between the normal stress and the shear stress, equation (7.150), an explicit expression for the normal stress component is also obtained,

$$\tau_{xx}^B = 2\frac{\lambda}{\eta}\left(p_{,x}y + \epsilon\kappa\zeta_1 E_x\Omega_1^+(y) + \tau_B\right)^2. \tag{7.159}$$

For simplicity subscript B will be removed from the rheological parameters of Fluid B ($\eta_B = \eta$, $\varepsilon_B = \varepsilon$ and $\lambda_B = \lambda$). Combining (7.149), (7.158) and (7.159) we come to the expression for the velocity gradient

$$\begin{aligned}\frac{du^B}{dy} &= \left[1 + 2\varepsilon\lambda^2\left(\frac{\epsilon E_x\zeta_1}{\eta}\kappa\Omega_1^+(y) + \frac{\tau_B}{\eta} + \frac{p_{,x}}{\eta}y\right)^2\right] \\ &\left(\frac{\epsilon E_x\zeta_1}{\eta}\kappa\Omega_1^+(y) + \frac{\tau_B}{\eta} + \frac{p_{,x}}{\eta}y\right).\end{aligned} \tag{7.160}$$

Equation (7.160) can be integrated subject to the no-slip boundary condition at the lower wall ($u^B_{\|y=-H_1}=0$) leading to

$$\begin{aligned}
u^B = {}& \frac{\tau_B}{\eta}(y+H)\left(1+2\varepsilon\lambda^2\left(\frac{\tau_B}{\eta}\right)^2\right)+\left[\frac{\epsilon E_x\zeta_1}{\eta}\right]\left(1+6\left(\frac{\tau_B}{\eta}\right)^2\varepsilon\lambda^2\right)\Omega^-_{1,1}(y)\\
&+2\varepsilon\lambda^2\left[\frac{\epsilon E_x\zeta_1}{\eta}\right]^2\kappa\frac{\tau_B}{\eta}\left(6\Psi_1\Psi_2\kappa(y+H)+\frac{3}{2}\Omega^-_{2,1}(y)\right)\\
&+2\varepsilon\lambda^2\left[\frac{\epsilon E_x\zeta_1}{\eta}\right]^3\kappa^2\left(\frac{1}{3}\Omega^-_{3,1}(y)+3\Psi_1\Psi_2\Omega^-_{1,1}(y)\right)\\
&+\frac{1}{2}\left[\frac{p_{,x}}{\eta}\right]\left(y^2-H^2\right)\left(1+6\varepsilon\lambda^2\left(\frac{\tau_B}{\eta}\right)^2+\varepsilon\lambda^2\left[\frac{p_{,x}}{\eta}\right]^2\left(y^2+H^2\right)\right)\\
&+2\frac{\tau_B}{\eta}\varepsilon\lambda^2\left[\frac{p_{,x}}{\eta}\right]^2\left(y^3+H^3\right)\\
&+12\frac{\varepsilon\lambda^2\left[\frac{\epsilon E_x\zeta_1}{\eta}\right]\left[\frac{p_{,x}}{\eta}\right]}{\kappa}\frac{\tau_B}{\eta}\left(\Omega^-_{1,2}(y)-\Omega^+_{1,1}(y)\right)\\
&+6\frac{\varepsilon\lambda^2\left[\frac{\epsilon E_x\zeta_1}{\eta}\right]\left[\frac{p_{,x}}{\eta}\right]^2}{\kappa^2}\left(\Omega^-_{1,3}(y)+2\Omega^-_{1,1}(y)-2\Omega^+_{1,2}(y)\right)\\
&+6\varepsilon\lambda^2\left[\frac{\epsilon E_x\zeta_1}{\eta}\right]^2\left[\frac{p_{,x}}{\eta}\right]\left(\Psi_1\Psi_2\kappa^2\left(y^2-H^2\right)+\frac{1}{2}\Omega^-_{2,2}(y)-\frac{1}{4}\Omega^+_{2,1}(y)\right)
\end{aligned}\tag{7.161}$$

where the operator $\Omega^{\pm}_{i,j}(y)\equiv(\kappa y)^{(j-1)}\,\Omega^{\pm}_i(y)-(-1)^{(j+1)}\,(\kappa H_1)^{(j-1)}\,\Omega^{\pm}_i(-H_1)$ is now defined for compactness. This equation is valid for $-H_1\leqslant y<0$.

It is often more convenient to work with the dimensionless form of equation (7.161). Introducing the normalizations $\bar{y}=y/H_1=y/(R_BH)$ and $\bar{\kappa}=\kappa R_BH$, the dimensionless velocity profile in the conducting fluid can be written as

$$\begin{aligned}
\frac{u^B}{u_{sh}} = {}& \overline{\tau}_B(\bar{y}+1)\left(1+2\overline{\tau}_B^2\frac{\varepsilon De_\kappa^2}{\overline{\kappa}^2}\right)-\left(1+6\overline{\tau}_B^2\frac{\varepsilon De_\kappa^2}{\overline{\kappa}^2}\right)\overline{\Omega^-_{1,1}}(\bar{y})\\
&+2\overline{\tau}_B\frac{\varepsilon De_\kappa^2}{\overline{\kappa}}\left(6\Psi_1\Psi_2\overline{\kappa}(\bar{y}+1)+\frac{3}{2}\overline{\Omega^-_{2,1}}(\bar{y})\right)\\
&-2\varepsilon De_\kappa^2\left(\frac{1}{3}\overline{\Omega^-_{3,1}}(\bar{y})+3\Psi_1\Psi_2\overline{\Omega^-_{1,1}}(\bar{y})\right)\\
&+\frac{1}{2}\Gamma\left(\bar{y}^2-1\right)\left(1+6\overline{\tau}_B^2\frac{\varepsilon De_\kappa^2}{\overline{\kappa}^2}+\frac{\varepsilon De_\kappa^2}{\overline{\kappa}^2}\Gamma^2\left(\bar{y}^2+1\right)\right)\\
&+2\overline{\tau}_B\frac{\varepsilon De_\kappa^2}{\overline{\kappa}^2}\Gamma^2\left(\bar{y}^3+1\right)\\
&-12\overline{\tau}_B\frac{\varepsilon De_\kappa^2}{\overline{\kappa}^3}\Gamma\left(\overline{\Omega^-_{1,2}}(\bar{y})-\overline{\Omega^+_{1,1}}(\bar{y})\right)\\
&+6\frac{\varepsilon De_\kappa^2}{\overline{\kappa}^2}\Gamma\left(\Psi_1\Psi_2\overline{\kappa}^2\left(\bar{y}^2-1\right)+\frac{1}{2}\overline{\Omega^-_{2,2}}(\bar{y})-\frac{1}{4}\overline{\Omega^+_{2,1}}(\bar{y})\right)\\
&-6\frac{\varepsilon De_\kappa^2}{\overline{\kappa}^4}\Gamma^2\left(\overline{\Omega^-_{1,3}}(\bar{y})+2\overline{\Omega^-_{1,1}}(\bar{y})-2\overline{\Omega^+_{1,2}}(\bar{y})\right)
\end{aligned}\tag{7.162}$$

where $\overline{\tau}_B=\frac{\tau_B}{\eta}\frac{R_BH}{u_{sh}}$ and $De_\kappa=\frac{\lambda u_{sh}}{\xi}=\lambda\kappa u_{sh}$ is the Deborah number based on the relaxation time of the conducting fluid (Fluid B), on the EDL thickness and on the Helmholtz-Smoluchowski electro-osmotic velocity near the bottom wall, defined as $u_{sh}=-\frac{\epsilon\zeta_1E_x}{\eta}$. The dimensionless parameter $\Gamma=-\frac{(R_BH)^2}{\epsilon\zeta_1}\frac{p_{,x}}{E_x}$ represents the ratio of pressure to electro-osmotic driving forces. Note that for simplicity the above terms were based on the zeta potential at the bottom wall ($\psi_{\|y=H_1}=\zeta_1$), but could be based on the interfacial zeta potential using the ratio of zeta potentials: $u_{sh}=u_{shi}/R_\zeta$, $\Gamma=R_\zeta\Gamma_i$ and $De_\kappa=De_{\kappa i}/R_\zeta$.

The normalized flow rate of the pumping fluid B, can be determined from integration of the velocity profile

$$\begin{aligned}
\overline{Q}^{B} = \frac{\overline{u}^{B}}{u_{sh}} = \int_{-H_1}^{0} \frac{u^{B}}{u_{sh} H_1} d\bar{y} = \overline{\tau}_B \left(1 + 2\frac{\varepsilon De_\kappa^2}{\overline{\kappa}^2}\overline{\tau}_B^2\right) \\
- \frac{1}{2}\Gamma\left(\frac{4}{5}\frac{\varepsilon De_\kappa^2}{\overline{\kappa}^2}\Gamma^2 + \frac{2}{3}\left(1 + 6\overline{\tau}_B^2\frac{\varepsilon De_\kappa^2}{\overline{\kappa}^2}\right)\right) \\
+ 2\overline{\tau}_B\frac{\varepsilon De_\kappa^2}{\overline{\kappa}^2}\Gamma^2 - \frac{1}{2}\left(1 + 6\frac{\varepsilon De_\kappa^2}{\overline{\kappa}^2}\overline{\tau}_B^2\right)\left(\frac{\overline{\Omega}_{1,1}^{+}(1)}{\overline{\kappa}} - 2\overline{\Omega}_1^{-}(-1)\right) \\
+ \frac{\varepsilon De_\kappa^2}{\overline{\kappa}}\overline{\tau}_B\left(12\Psi_1\Psi_2\overline{\kappa} + \frac{3}{2}\left(\frac{\overline{\Omega}_{2,1}^{+}(1)}{2\overline{\kappa}} - 2\overline{\Omega}_2^{-}(-1)\right)\right) \\
- \varepsilon De_\kappa^2\left(\frac{\overline{\Omega}_{3,1}^{+}(1)}{9\overline{\kappa}} - \frac{2}{3}\overline{\Omega}_3^{-}(-1) + 3\Psi_1\Psi_2\left(\frac{\overline{\Omega}_{1,1}^{+}(1)}{\overline{\kappa}} - 2\overline{\Omega}_1^{-}(-1)\right)\right) \\
- 6\overline{\tau}_B\frac{\varepsilon De_\kappa^2}{\overline{\kappa}^4}\Gamma\left[\overline{\Omega}_{1,2}^{+}(1) - 2\overline{\Omega}_{1,1}^{-}(1) + 2\overline{\kappa}\left(\overline{\kappa}\overline{\Omega}_1^{-}(-1) + \overline{\Omega}_1^{+}(-1)\right)\right] \\
+ 3\frac{\varepsilon De_\kappa^2}{\overline{\kappa}^2}\Gamma\left(\frac{1}{4\overline{\kappa}}\left(\overline{\Omega}_{2,2}^{+}(1) - \overline{\Omega}_{2,1}^{-}(1)\right) - \frac{4}{3}\Psi_1\Psi_2\overline{\kappa}^2 + \overline{\kappa}\overline{\Omega}_2^{-}(-1) + \frac{1}{2}\overline{\Omega}_2^{+}(-1)\right) \\
- 3\frac{\varepsilon De_\kappa^2}{\overline{\kappa}^5}\Gamma^2\left(\overline{\Omega}_{1,3}^{+}(1) - 4\overline{\Omega}_{1,2}^{-}(1) + 6\overline{\Omega}_{1,1}^{+}(1)\right) \\
+ 6\frac{\varepsilon De_\kappa^2}{\overline{\kappa}^4}\Gamma^2\left(\left(\overline{\kappa}^2 + 2\right)\overline{\Omega}_1^{-}(-1) + 2\overline{\kappa}\overline{\Omega}_1^{+}(-1)\right). \qquad (7.163)
\end{aligned}$$

Nonconducting fluid (Fluid A)

The derivation of the analytical solution for this fluid layer follows the same steps as for the conducting fluid, with the necessary adaptations. For the nonconducting fluid (Fluid A), the momentum conservation equation (7.144), reduces to

$$\frac{d\tau_{xy}^{A}}{dy} = p_{,x}, \qquad (7.164)$$

since, as explained, there no external electrical field forcing, due to low condutivity. Equation (7.164) can be integrated to yield the following shear stress distribution

$$\tau_{xy}^{A} = p_{,x}y + \tau_A \qquad (7.165)$$

where τ_A is the shear stress at the fluid-fluid interface, to be quantified in the next section. Using the relationship between the normal and shear stresses - equation (7.150), the following explicit expression for the normal stress component is obtained,

$$\tau_{xx}^{A} = 2\frac{\lambda_A}{\eta_A}\left(p_{,x}y + \tau_A\right)^2 \qquad (7.166)$$

Combining equations (7.149), (7.165) and (7.166) the velocity gradient distribution in fluid A is given by

$$\frac{du^{A}}{dy} = \left[1 + 2\varepsilon_A\lambda_A^2\left(\frac{p_{,x}}{\eta_A}y + \frac{\tau_A}{\eta_A}\right)^2\right]\left(\frac{p_{,x}}{\eta_A}y + \frac{\tau_A}{\eta_A}\right) \qquad (7.167)$$

Equation (7.167) is integrated subject to the no-slip boundary condition at the upper wall ($u^A_{\|y=H_2} = 0$) and leads to

$$u^A = \frac{\tau_A}{\eta_A}(y - H_2)\left(1 + 2\varepsilon_A\lambda_A^2\left(\frac{\tau_A}{\eta_A}\right)^2\right) + 2\varepsilon_A\lambda_A^2\frac{\tau_A}{\eta_A}\left[\frac{p_{,x}}{\eta_A}\right]^2\left(y^3 - H_2^3\right) + \frac{1}{2}\left[\frac{p_{,x}}{\eta_A}\right]\left(y^2 - H_2^2\right)\left(1 + 6\varepsilon_A\lambda_A^2\left(\frac{\tau_A}{\eta_A}\right)^2 + \varepsilon_A\lambda_A^2\left[\frac{p_{,x}}{\eta_A}\right]^2\left(y^2 + H_2^2\right)\right) \tag{7.168}$$

valid for $0 < y \leqslant H_2$. Introducing the normalizations $\bar{y} = y/H_2 = y/R_A H$ and $\bar{\kappa}_A = \kappa R_A H$, the dimensionless velocity profile can be written as

$$\frac{u^A}{u_{sh}} = \overline{\tau}_A(\bar{y} - 1)\left(1 + 2\overline{\tau}_A^2\frac{\varepsilon_A De_{\kappa A}^2}{\bar{\kappa}_A^2}\right) + 2\overline{\tau}_A\frac{1}{\beta^2}\frac{\varepsilon_A De_{\kappa A}^2}{\bar{\kappa}_A^2}\Gamma_A^2\left(\bar{y}^3 - 1\right) + \frac{1}{2}\frac{1}{\beta}\Gamma_A\left(\bar{y}^2 - 1\right)\left(1 + 6\overline{\tau}_A^2\frac{\varepsilon_A De_{\kappa A}^2}{\bar{\kappa}_A^2} + \frac{1}{\beta^2}\frac{\varepsilon_A De_{\kappa A}^2}{\bar{\kappa}_A^2}\Gamma_A^2\left(\bar{y}^2 + 1\right)\right) \tag{7.169}$$

where $\overline{\tau}_A = \frac{\tau_A}{\eta_A}\frac{R_A H}{u_{sh}}$, $\beta = \eta_A/\eta_B$ is the dynamic viscosity ratio and $De_{\kappa A} = \frac{\lambda_A u_{sh}}{\xi} = \lambda_A u_{sh}\kappa$ is the Deborah number based on the relaxation time of fluid A, on the EDL thickness and on the Helmholtz-Smoluchowski electro-osmotic velocity. The parameter $\Gamma_A = -\frac{(R_A H)^2}{\epsilon\zeta_1}\frac{p_{,x}}{E_x}$ represents the ratio of pressure to electro-osmotic driving forces. The expression for the normalized volumetric flow rate of the pumped fluid A in the upper part of the channel is

$$\overline{Q}^A = \left(\frac{\overline{u}^A}{u_{sh}}\right)\frac{R_A}{R_B} = \frac{\int_0^{H_2} u^A dy}{u_{sh}H_2} = -\frac{\overline{\tau}_A}{2}\left(1 + 2\frac{\varepsilon_A De_{\kappa A}^2}{\bar{\kappa}_A^2}\overline{\tau}_A^2\right) - \frac{3}{2}\overline{\tau}_A\frac{\varepsilon_A De_{\kappa A}^2}{\beta^2\bar{\kappa}_A^2}\Gamma_A^2 - \frac{2}{5}\frac{\Gamma_A^3}{\beta^3}\frac{\varepsilon_A De_{\kappa A}^2}{\bar{\kappa}_A^2} - \frac{1}{3}\frac{\Gamma_A}{\beta}\left(1 + 6\overline{\tau}_A^2\frac{\varepsilon_A De_{\kappa A}^2}{\bar{\kappa}_A^2}\right). \tag{7.170}$$

Fluid A- Fluid B interface conditions

In deriving the shear stress profiles, equations (7.158) and (7.165), and all the subsequent quantities like velocity and flow rates, two integration coefficients appeared, $\overline{\tau}_A$ and $\overline{\tau}_B$, which have to be determined from the boundary conditions at the fluid-fluid interface namely: $\tau_{xy}{}^A_{\|y=0} = \tau_{xy}{}^B_{\|y=0}$ and $u^A_{\|y=0} = u^B_{\|y=0}$.

Using the relationships between the shear stresses at the interface, equations (7.158) and (7.165), and those for the dimensionless velocity profiles, equations (7.162) and (7.169), we can determine the variables $\overline{\tau}_A$ and $\overline{\tau}_B$,

$$\begin{cases} \overline{\tau}_A = \frac{R_A}{R_B}\frac{1}{\beta}\overline{\tau}_B - \frac{\overline{\kappa}_A}{\beta}\Omega_1^+(0) \\ \overline{\tau}_B = \sqrt[3]{-\frac{b_1}{2} + \sqrt{\frac{b_1^2}{4} + \frac{a^3}{27}}} + \sqrt[3]{-\frac{b_1}{2} - \sqrt{\frac{b_1^2}{4} + \frac{a^3}{27}}} - \frac{a_1}{3} \end{cases} \tag{7.171}$$

where $a = a_2 - a_1^2/3$, $b_1 = a_3 - a_1 a_2/3 + 2a_1^3/27$, the coefficients a_1, a_2 and a_3 are obtained from the manipulation of equation (7.162) to obtain an explicit expression for $\overline{\tau}_B$. In that coefficients appears a dimensionless number that relates the rheological properties of the two fluids, $R_\varepsilon = \sqrt{\frac{\varepsilon}{\varepsilon_A}\frac{\lambda^2}{\lambda_A^2}}$.

7.4.4 *Results and discussion*

In the previous section, general equations were derived for steady fully developed two-fluid electro-osmotic stratified flow of PTT viscoelastic fluids under the mixed influence of electrokinetic and pressure gradient forces. The different influences of the driving forces (Γ), fluid rheology (R_ε), dynamic viscosity ratio (β), fluids holdup (R_B) and of the ratio of zeta potentials (R_ζ) on the velocity profile have been explicitly incorparated in equations (7.168), (7.161) and (7.171) and in this section we discuss in detail some limiting cases in order to understand the system fluid dynamics.

The following set of two-fluid systems is included in the general solution where: (a) Newtonian-Newtonian fluid system; (b) viscoelastic-Newtonian fluid system; (c) Newtonian-viscoelastic fluid system; and (d) viscoelastic - viscoelastic fluid system. Cases (b) and (d) are not discussed in this work, due to space limitations, althougth the derived equations also include these cases. Case (a) was studied in detail elsewhere (Gao et al., 2005), but this situation is revisited here as a starting point and for comparison with case (c), i.e., in the following we analyse in detail the pumping of a Newtonian fluid by another Newtonian fluid, and, alternatively, by a viscoelastic fluid.

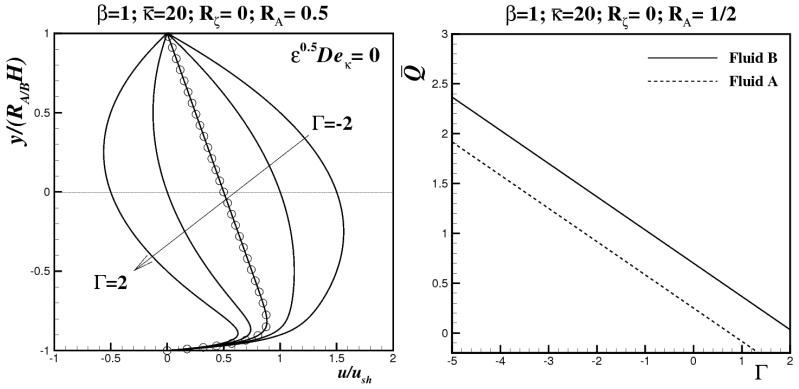

Figure 7.28: Effect of the driving forces ($\Gamma = -2, -1, 0, 1$ and 2) on dimensionless (a) velocity profiles and (b) volumetric flow rate for Newtonian-Newtonian flow configuration. Symbols represent the data from Afonso et al. (2009c) for ($\beta = 1$, $R_\zeta = 0$ and $\Gamma = 0$).

7.4.4.1 *Newtonian-Newtonian EOF pump configuration*

For the Newtonian-Newtonian flow configuration, both the conducting and nonconducting fluids are Newtonian ($De_\kappa = De_{\kappa A} = 0$). The velocity profile system equations and the dimensionless boundary condition coefficients, provided by equation (7.171), simplify to

$$\begin{cases} \dfrac{u^A}{u_{sh}} = \overline{\tau}_A\left(\overline{y}-1\right) + \frac{1}{2\beta}\Gamma_A\left(\overline{y}^2-1\right) & \text{for} \quad 0 \leqslant \overline{y} \leqslant 1 \\ \dfrac{u^B}{u_{sh}} = \overline{\tau}_B\left(\overline{y}+1\right) - \Omega^-_{1,1}(y) + \frac{1}{2}\Gamma\left(\overline{y}^2-1\right) & \text{for} \quad -1 \leqslant \overline{y} \leqslant 0 \end{cases} \tag{7.172}$$

For small relative microchannel ratio, $\bar{\kappa} \to 1$, the double layer thickness is of the same order of magnitude as the Fluid B thickness and the region of excess charge is distributed over the entire fluid. This situation is not compatible with this solution for which the Debye-Hückel approximation was invoked, which requires $\bar{\kappa}_{min} \gtrsim 10$. In this work and as a typical example, we set $\bar{\kappa} = 20$ in all figures.

For $\Gamma = 0$, i.e., when the flow is driven only by electro-osmosis, the velocity profile is a function of the wall distance, of the relative microchannel ratio, $\bar{\kappa}$, of the ratio of zeta potentials, R_ζ, and of the dynamic viscosity ratio as shown earlier by Gao et al. (2005). Also, for a single fluid situation ($\beta = 1$) and in the absence of interface zeta potential ($R_\zeta = 0$) the solution simplifies to a particular case obtained by Afonso et al. (2009c) (no zeta potential in the upper wall and no pressure gradient, symbols in Figure 7.28a). The corresponding effect of the ratio of pressure gradient to electro-osmotic driving forces on the dimensionless flow rate is obvious (cf. Figures 7.28(b)), increasing with favorable pressure gradients ($\Gamma < 0$), and decreasing for flows with adverse pressure gradients ($\Gamma > 0$). Obviously, the flow rate for fluid B is higher because for identical fluids heights fluid B is being forced also by electro-osmosis.

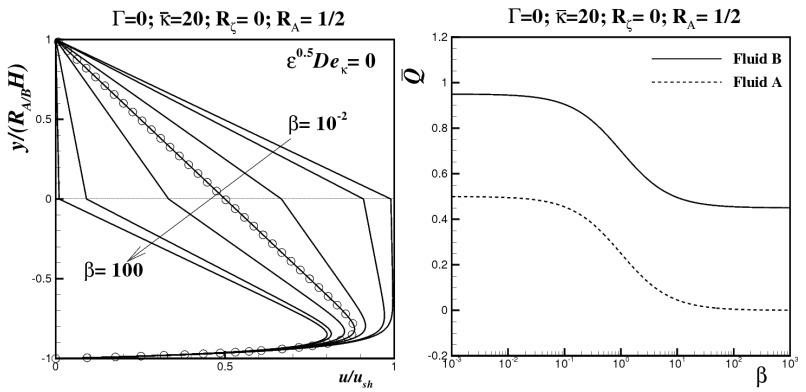

Figure 7.29: Effect of the dynamic viscosity ratio ($\beta = 10^{-2}$, 10^{-1}, 1, 10 and 100) on dimensionless (a) velocity profiles and (b) volumetric flow rate for Newtonian-Newtonian flow configuration.

Figure 7.29 shows the influence of the dynamic viscosity ratio ($\beta \equiv \eta_A/\eta_B$) on the dimensionless velocity profile (a) and on the volumetric flow rate (b). When the dynamic viscosity ratio decreases the dimensionless velocity increases (cf. Figure 7.29(a)). So, if the viscosity of the conducting fluid is much higher than the viscosity of the nonconducting fluid, an increase in the dimensionless volumetric flow rate is expected, as can be observed in Figure 7.29(b). However, a higher viscosity implies a lower Helmholtz-Smoluchowski electro-osmotic velocity consequently the dimensional flow rate may actually decrease.

A major effect on the velocity profile is that due to non-zero interfacial zeta potential, as presented in the profiles of Figures 7.30. When $\zeta_i > 0$, a favorable *extra* drag forcing term arises in the velocity profile at the interface of the two-fluids, leading to a significant increase in the volumetric flow rate, even for $\zeta_i < \zeta_1$. When $\zeta_i < 0$, the adverse localized electrostatic force decreases the pumping action and the corresponding dimensionless flow rate (cf. Figure 7.30(b)).

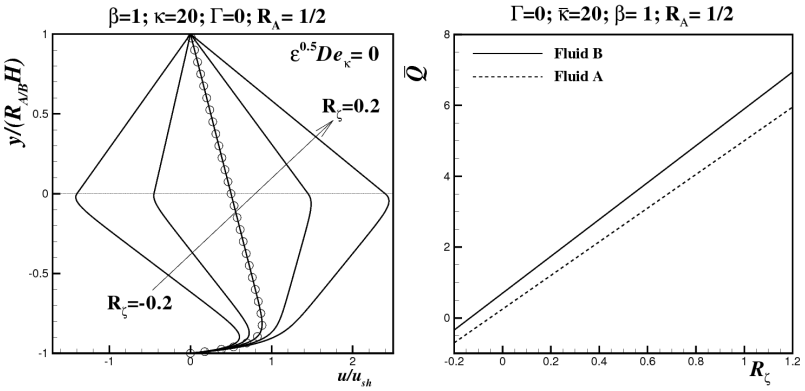

(a) (b)

Figure 7.30: Effect of the ratio of zeta potentials ($R_\zeta = -0.2$, -0.1, 0, 0.1 and 0.2) on dimensionless (a) velocity profiles and (b) volumetric flow rate for Newtonian-Newtonian flow configuration.

Another important effect is due to the holdup of the nonconducting fluid. When the height of the nonconducting fluid is larger than the height of the conducting fluid ($R_A > R_B$), the normalized velocities of both fluids increase, as observed in Figure 7.31(a). This suggests that to obtain higher volumetric flow rates in fluid A, the holdup of the conducting fluid B should be kept small (cf. Figure 7.31(b)). In fact, as the Helmholtz-Smoluchowski electro-osmotic velocity is independent of the thickness of fluid B, as $R_A \to 1$ the fluid interface plane will tend to coincide with the regions of higher velocity. This conclusion also suggests that a better configuration for an EOF pump would be a three layer fluid flow, with the conducting fluid in contact with both the upper and lower walls, and the non conducting fluid in the middle being dragged like a solid body, i.e., a solid lubrificated by thin layers of conducting fluid in motion.

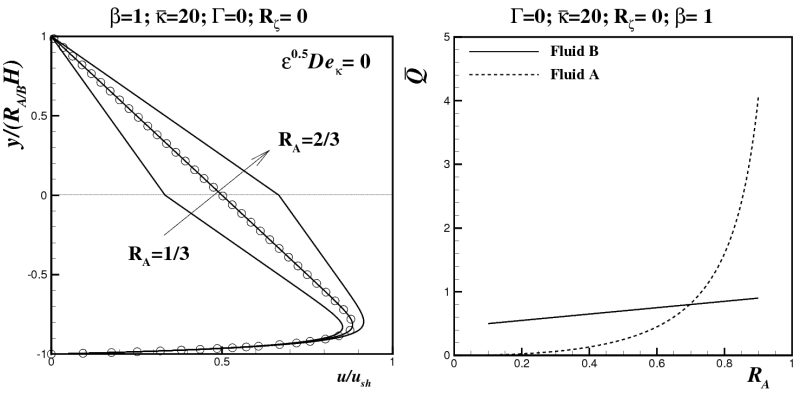

(a) (b)

Figure 7.31: Effect of the nonconducting fluid holdup on dimensionless (a) velocity profiles ($R_A = 1/3$, $1/2$ and $2/3$) and (b) volumetric flow rate for Newtonian-Newtonian flow configuration.

7.4.4.2 *Newtonian-Viscoelastic EOF pump configuration*

For the Newtonian-Viscoelastic flow configuration, the conducting fluid is viscoelastic dragging the nonconducting Newtonian fluid. The Deborah number of the conducting fluid is non-zero ($De_\kappa \neq 0$ and $De_{\kappa A} = 0$), and the velocity profile and the nondimensional boundary condition coefficients are given by

$$\begin{cases} \frac{u^A}{u_{sh}} = \bar{\tau}_A\,(\bar{y}-1) + \frac{1}{2\beta}\Gamma_A\,(\bar{y}^2-1) & \text{for} \quad 0 \leqslant \bar{y} \leqslant 1 \\ \text{Eq. (7.162)} & \text{for} \quad -1 \leqslant \bar{y} \leqslant 0 \end{cases} \tag{7.173}$$

Figures 7.32 (a) and (b) present the dimensionless velocity and volumetric flow rate profiles as a function of $\sqrt{\varepsilon}De_\kappa$, respectively. We can see that increasing the elasticity of the conducting fluid, more than doubles the velocities due to shear-thinning effects within the EDL layer thus raising the velocity value of the bulk transport in the core of the channel. This also helps to increase the shear rates near the bottom wall and at the two fluids interface, increasing the dragging of the nonconducting fluid by the hydrodynamic viscous forces at the interface. Consequently there is a significant increase in the dimensionless volumetric flow rate (cf. Figure 7.32b).

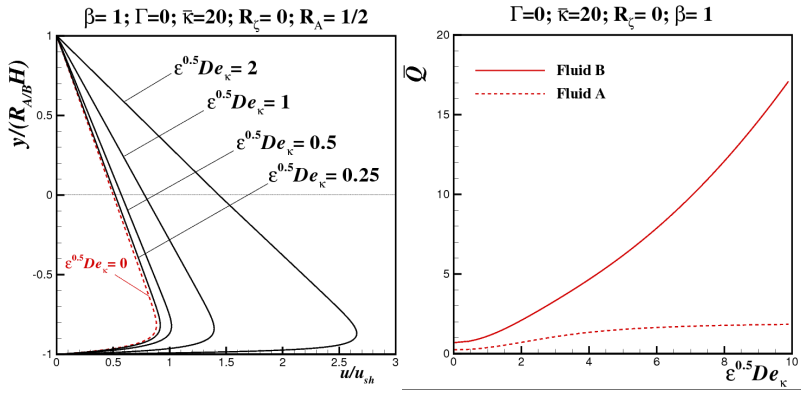

Figure 7.32: Dimensionless profiles of (a) velocity and (b) volumetric flow rate as function of $\sqrt{\varepsilon}De_\kappa$.

As we can also see in Figure 7.32 (a), in the absence of pressure gradient the EDL acts like a plate in pure Couette flow, transmitting a constant shear stress across the channel.

Figure 7.33 shows the dimensionless velocity profiles (a) and volumetric flow rate (b) at $\sqrt{\varepsilon}De_\kappa = 2$ (for comparison the Newtonian results of Figures 7.28 are also presented) to illustrate the effect of Γ. A favorable pressure gradient ($\Gamma < 0$) helps increase the flow rate and makes velocity profiles fuller. By using pressure, the dragging effect at the interface is helped by the pressure forcing which affects directly the two fluids. The beneficial shear-thinning effect is clear in the large increase in the flow rate of Figure 7.33(b).

As for the Newtonian-Newtonian flow configuration, decreasing β leads to an increase in velocity profiles and the volumetric flow rate, which is further increased by shear-thinning effects (cf. Figure 7.34(a) and (b) and compare with Figure 7.29). When using a viscoelastic fluid as conducting fluid it is natural to have a more viscous fluid than

the Newtonian nonconducting fluid, which leads to an *optimal* flow situation.

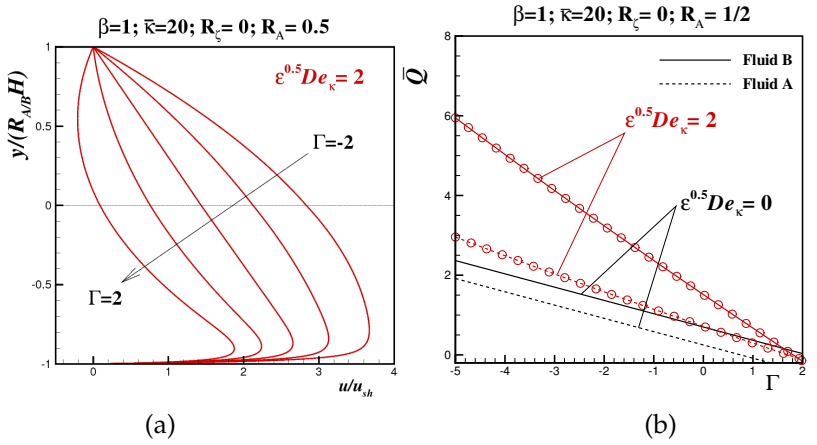

(a) (b)

Figure 7.33: Effect of the driving forces ($\Gamma = -2, -1, 0, 1$ and 2) on dimensionless (a) velocity profiles and (b) volumetric flow rate for Newtonian-Viscoelastic flow configuration.

The effects of the fluid A holdup (R_A) and of the ratio of zeta potentials (R_ζ) are similar to what was seen before, but now the viscoelastic flow exhibits a shear-thinning viscosity and the velocities have increased significantly near the bottom wall (see the higher values of u/u_{sh}) leading to higher volumetric flow rates of Figures 7.35 and 7.36, than in the corresponding constant viscosity case.

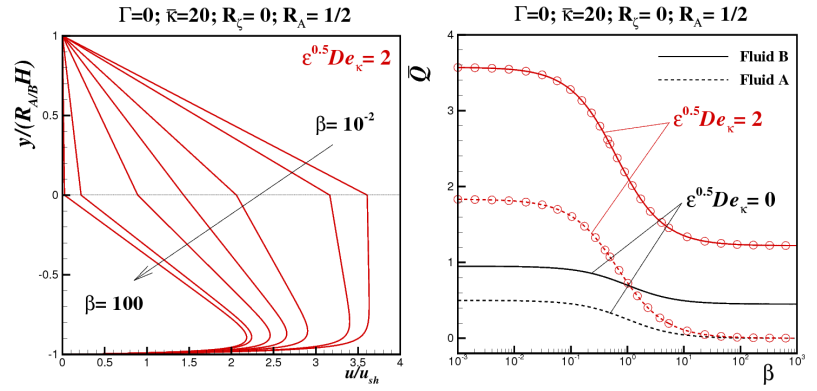

(a) (b)

Figure 7.34: Effect of the dynamic viscosity ratio ($\beta = 10^{-2}$, 10^{-1}, 1, 10 and 100) on dimensionless (a) velocity profiles and (b) volumetric flow rate for Newtonian-Viscoelastic flow configuration.

7.4.5 *Conclusions*

An analytical solution of the steady two-fluid electro-osmotic stratified flow in a planar microchannel is presented by assuming a planar interface between the two viscoelastic immiscible fluids. The PTT fluid model was used, and the effects of fluid rheology, viscosity ratio, fluid holdup and interfacial zeta potential were analyzed to show the viability of this technique.

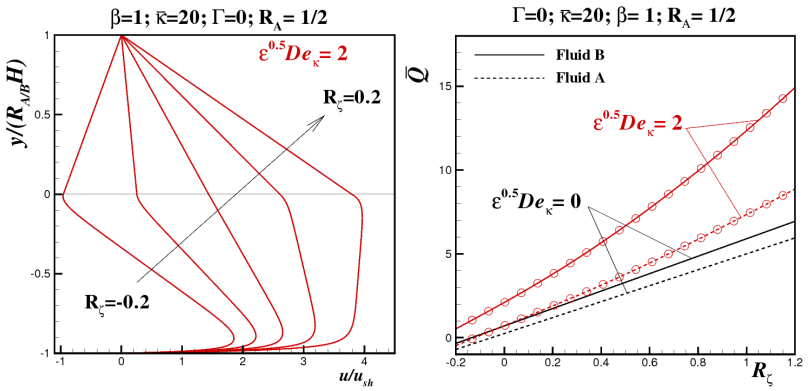

(a) (b)

Figure 7.35: Effect of the ratio of zeta potentials ($R_\zeta = -0.2, -0.1, 0, 0.1$ and 0.2) on dimensionless (a) velocity profiles and (b) volumetric flow rate for Newtonian-Viscoelastic flow configuration.

The flow can be induced by a combination of both electrical and pressure potentials, but in addition to the single contributions from these two mechanisms, when the conducting fluid is viscoelastic, there is an extra term in the velocity profile that simultaneously combines both effects, which is absent from conducting Newtonian fluids where the linear superposition principle applies. Hence, for non-linear viscoelastic fluids the superposition principle is not valid.

This work demostrated that higher volumetric flow rates of a non-conducting Newtonian fluid can be acheived in EOF pumping when the conducting fluid is viscoelastic rather than Newtonian, due to the increasing of the shear-thinning effects.

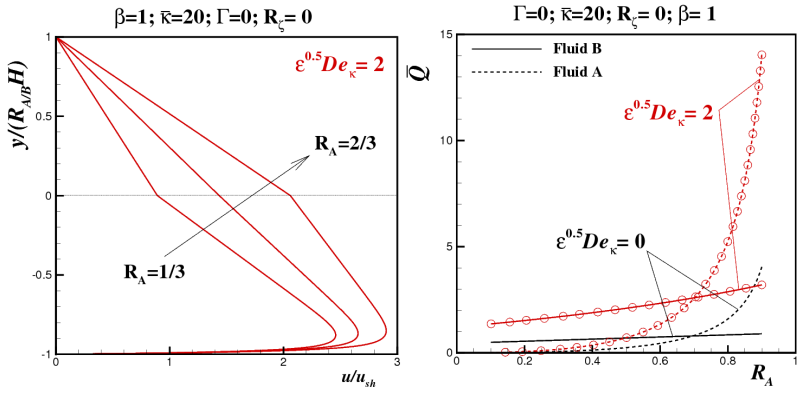

(a) (b)

Figure 7.36: Effect of the nonconducting fluid holdup on dimensionless (a) velocity profiles ($R_A = 1/3, 1/2$ and $2/3$) and (b) volumetric flow rate for Newtonian-Viscoelastic flow configuration.

7.4.6 *Acknowledgments*

The authors would like to acknowledge financial support of FCT through projects PTDC/ EQU-FTT/ 71800/ 2006, PTDC /EQU-FTT/70727/2006 and scholarship SFRH/BD/28828 /2006 (A. M. Afonso).

Abstract[5]
In this work we present a finite volume method (FVM) used to solve the relevant coupled equations for electro- osmotic flows (EOF) of viscoelastic fluids, using the Upper-Convected Maxwell (UCM) and the simplified Phan-Thien—Tanner (sPTT) models. Studies were undertaken in the cross-slot geometry, to investigate the possible appearance of purely-elastic instabilities, by considering the effect of the electric field. We found that even for pure electro-osmotic flow, i.e., in absence of an imposed pressure gradient, we were able to capture the onset of an asymmetric flow above a critical Deborah number, which is lower than the corresponding value for pressure gradient forcing.

Keywords: Electro-osmosis, Viscoelastic fluids, Finite-Volume Method.

7.5.1 *Introduction*

Accurate flow control in microfluidic devices requires techniques that can easily be miniaturized and an obvious candidate is electrokinetic forcing through such mechanisms as electro-osmosis or electrophoresis. An overview of these and other electrokinetic techniques can be found in (Bruss, 2008).

Electro-osmosis is an electrokinetic phenomenon, first demonstrated by Reuss (1809) early in the 19th century, where the channel flow of a polar fluid is forced by an external electric field applied between the inlet and outlet and acting on ions existing near the channel walls. von Helmholtz (1879) proposed the electric double layer (EDL) theory that relates the electrical and flow parameters for electrokinetic transport in 1879. Subsequently, von Smoluchowski (1903) generalized von Helmholtz's double layer theory by taking into account the actual charge/ potential distributions in a capillary channel. A more realistic concept of these distributions in the fluid adjacent to the capillary wall was introduced by Gouy (1910) in 1910. Debye and Hückel (1923) determined the ionic number concentration in a solution of low ionic energy, by means of a linearization of the exponential Boltzmann ion energy distribution.

For Newtonian fluids, rigorous modeling of the electro-osmotic flow in microchannels has been the subject of several studies (Burgreen and Nakache, 1964; Rice and Whitehead, 1965; Arulanandam and Li, 2000; Dutta and Beskok, 2001), and a thorough review on various other aspects of electro-osmosis can be found in Karniadakis et al. (2005). The theoretical study of electro-osmotic flows of non-Newtonian fluids is recent and most works have been limited to simple inelastic fluid models, such as the power-law, due to the inherent analytical difficulties introduced by more complex constitutive equations (Das and Chakraborty, 2006; Park and Lee, 2008b; Berli and Olivares, 2008; Zhao et al., 2008). Recently these studies were extended to viscoelastic fluids by Afonso et al. (2009c), who presented analytical solutions for

5 A.M. Afonso, F.T Pinho and M.A Alves (2010). Electro-osmotic flows of viscoelastic fluids: a numerical study, *Proceedings of the 3rd National Conference on Fluid Mechanics, Thermodynamics and Energy*, Bragança, Portugal.

channel and pipe flows of viscoelastic fluids under the mixed influence of electrokinetic and pressure forces, using two constitutive models: the simplified Phan-Thien—Tanner model (sPTT) (Phan-Thien and Tanner, 1977), with linear kernel for the stress coefficient function and zero second normal stress difference (Phan-Thien, 1978), and the FENE-P model, based on the kinetic theory for Finitely Extensible Non-linear Elastic dumbbells with a Peterlin approximation for the average spring force (cf. Bird et al. (1987a)). Their analysis (Afonso et al., 2009c) was restricted to cases with small electric double-layers, where the distance between the walls of a microfluidic device is at least one order of magnitude larger than the EDL, and the fluid had a uniform distribution across the channel. Afonso et al. (2010c) extended this study to the flow of viscoelastic fluids under asymmetric zeta potential forcing.

In the recent years the efforts for numerical modeling and simulation of EOF has also increased, especially when applied to Newtonian fluids. Yang and Li (1998) developed a numerical algorithm for elecrokinetically driven Newtonian liquid flows, using the Debye-Hückel approximation (Debye and Hückel, 1923). The same approximation was used by Patankar and Hu (1998) in the numerical simulation of microfluidic injection of Newtonian fluids, with electro-osmotic forces through the intersection of two channels. Ermakov et al. (1998) developed a finite difference method (FDM) for electro-osmotic and electrophoretic transport and species diffusion for two-dimensional complex geometry flows of Newtonian fluids. Using the Gouy-Chapman approximation (Gouy, 1910), Bianchi et al. (2000) developed a finite-element method (FEM) to study electro-osmotically driven microflows of Newtonian fluids in T-junctions. Dutta et al. (2002b) used a spectral element method (SEM) for solution of the Poisson–Boltzmann and incompressible Navier–Stokes equations, to analyze mixed electro-osmotic/pressure driven flows of Newtonian fluids in two-dimensional geometries, such as straight channels and T-junction geometry. The previous work was later extended to complex microgeometries (cross-flow and Y-split junctions) by Dutta et al. (2002a). Lin et al. (2002) solved the Nernst–Planck and the full Navier–Stokes equations using FDM to model the EOF of Newtonian fluids in microfluidic focusing chips.

For non-Newtonian fluids the efforts for numerical modeling of EOF are now gathering momentum, with limited advance having been made, still for very simple geometries such as straight microchannels. Recently, Park and Lee (2008a) calculated numerically the electro-osmotic velocity of viscoelastic fluids in a square microchannel with and without externally imposed pressure gradient, using a generalized constitutive equation, which encompasses the upper-convected Maxwell (UCM) model, the Oldroyd-B model and the PTT model. Very recently, Tang et al. (2009), presented a numerical study of EOF in microchannels of non-Newtonian purely viscous fluids described by the power law model, using the lattice Boltzmann method. Zimmerman et al. (2006) presented two-dimensional FEM simulations of EOF in a microchannel T-junction of a purely viscous fluid described by a Carreau-type nonlinear viscosity. The motion within the electrical double layer at the channel walls was approximated by velocity wall slip boundary conditions.

In this work, and for the first time to our best knowledge, we perform numerical EOF simulations of viscoelastic fluids in more complex

geometries. We use an FVM to solve the relevant coupled equations for electro-osmotic flows of viscoelastic fluids, namely the nonlinear Poisson– Nernst–Planck equation that governs the electrical double-layer field, the Cauchy equation with a body force due to the applied electrical potential field and a variety of constitutive equations for the viscoelastic fluids, in particular the UCM and sPTT models. In addition to the simulations in a complex geometry (Cross-Slot geometry), and in order to test the implementation of the numerical method, some predictions are compared with existing analytical solutions for the flow in a two-dimensional microchannel under symmetric and asymmetric boundary conditions for the zeta potential at the walls (Afonso et al., 2009c, 2010c).

The remaining of the paper is organized as follows: in sections 7.5.2 and 7.5.3 we briefly present the governing equations and outline the numerical method used to simulate the EOF of the viscoelastic fluids, respectively. In section 7.5.4, the main results of the numerical implementation tests and of the EOF in a cross-slot geometry are presented, respectively. A summary of the main findings closes the paper in section 7.5.5.

7.5.2 *Governing equations*

The flow is assumed to be steady, laminar and the fluid is incompressible. The governing equations describing the flow are the continuity equation,

$$\nabla \cdot \mathbf{u} = 0 \tag{7.174}$$

and the Cauchy equation:

$$\rho \left[\frac{\partial \mathbf{u}}{\partial t} + \nabla \cdot \mathbf{u}\mathbf{u} \right] = -\nabla p + \beta \eta_0 \nabla^2 \mathbf{u} + \frac{\eta_0}{\lambda} (1-\beta) \nabla \cdot \mathbf{A} + \mathbf{F} \tag{7.175}$$

where $\mathbf{u}$ is the velocity vector, p the pressure, t the time, ρ the fluid density, η_s the Newtonian solvent viscosity and $\mathbf{A}$ is the conformation tensor. The polymer solution either obeys the UCM or the sPTT models, hence the total fluid extra stress is the sum of the solvent and polymer stress contributions. The equations are written in general form. The polymer has a relaxation time λ and a viscosity coefficient η_p, defining a zero-shear rate total viscosity $\eta_0 = \eta_p + \eta_s$. The coefficient β in equation (7.175) is the ratio between the solvent viscosity and η_0 ($\beta = \eta_s/\eta_0$) and is a measure of the concentration of polymer additive ($\beta = 0$ implies no solvent and $\beta = 1$ means that the fluid is Newtonian and there is no polymer additive).

The polymer extra-stress $\boldsymbol{\tau}$ can be related to the conformation tensor $\mathbf{A}$ using

$$\boldsymbol{\tau} = \frac{\eta}{\lambda} (\mathbf{A} - \mathbf{I}) \tag{7.176}$$

which requires the solution of an evolution equation of the form,

$$\lambda \left[\frac{\partial \mathbf{A}}{\partial t} + \nabla \cdot \mathbf{u}\mathbf{A} \right] + Y(\mathrm{tr}\mathbf{A})\,\mathbf{A} = Y(\mathrm{tr}\mathbf{A})\,\mathrm{I} + \lambda \left(\mathbf{A} \cdot \nabla \mathbf{u} + \nabla \mathbf{u}^{\mathrm{T}} \cdot \mathbf{A} \right) \tag{7.177}$$

where $\mathbf{I}$ is the unitary tensor. When $Y(\mathrm{tr}\mathbf{A}) = 1$ we recover the Oldroyd-B model which further simplifies to the UCM equation if $\beta = 0$. Oth-

erwise, we are in the presence of the sPTT model with a Newtonian solvent and $Y(\mathrm{tr}\mathbf{A})$ imparts to the fluid shear-thinning behavior and bounds the extensional viscosity as explained in the original papers of Phan-Thien and Tanner (1977) and Phan-Thien (1978).

In its general form function $Y(\mathrm{tr}\mathbf{A})$ is exponential, but in this work we use its linear form

$$Y(\mathrm{tr}\mathbf{A}) = 1 + \varepsilon(\mathrm{tr}\mathbf{A} - 3) \tag{7.178}$$

The $\mathbf{F}$ term in the Cauchy equation (7.175) represents a body force per unit volume, given as

$$\mathbf{F} = \rho_e \mathbf{E} \tag{7.179}$$

where $\mathbf{E}$ is the applied external electric field and ρ_e is the net electric charge density. The electric field intensity is related to the electric potential, Φ, by

$$\mathbf{E} = -\nabla\Phi \tag{7.180}$$

while the electric potential is governed by,

$$\nabla^2\Phi = -\frac{\rho_e}{\epsilon} \tag{7.181}$$

where ϵ is the electrical permittivity of the solution. Two types of electric fields can be identified in EOF flows, depending on their origin. One is the applied electric field generated by the electrodes at the inlet and the outlet of the flow geometry, ϕ. The other electric field is due to the net charge distribution in the EDL, due to the charge acquired at the wall, ψ. The total electric field is simply a linear superposition of these two contributions, and this can be written as

$$\Phi = \phi + \psi \tag{7.182}$$

Consequently, equation (7.181) can be rewritten as two separate equations,

$$\nabla^2\phi = 0 \tag{7.183}$$

and

$$\nabla^2\psi = -\frac{\rho_e}{\epsilon} \tag{7.184}$$

Finally, we need to quantify the electric charge density in order to have a closed-form equation. For a symmetric electrolyte the ions and the counter-ions have the same charge valence, $z^+ = -z^- = z$, and the net electric charge density is given by:

$$\rho_e = ez\left(n^+ - n^-\right) \tag{7.185}$$

where n^+ and n^- are the concentrations of the positive and negative ions, respectively, and e is the elementary electric charge. In order to find the net charge density ρ_e, the distributions of ionic concentra-

tions n^+ and n^- must be determined. This is achieved by solving the following transport equation, known as the Nernst-Planck equations:

$$\frac{\partial n^{\pm}}{\partial t} + \mathbf{u}\cdot\nabla n^{\pm} = \nabla\cdot\left(D^{\pm}\nabla n^{\pm}\right) \pm \nabla\cdot\left[D^{\pm}n^{\pm}\frac{ez}{k_B T}\nabla\left(\phi+\psi\right)\right] \quad (7.186)$$

where D^+ and D^- are the diffusion coefficients of the positive and negative ions, respectively. The set of equations (7.183) to (7.186) is usually called the Poisson-Nernst-Planck equations (PNP).

Another way to quantify the electric charge density is using the widely adopted Poisson–Boltzmann equation derived from the Nernst–Planck equations. From the ionic transport equations (7.186), when the ionic distribution is stationary, the electric double layer does not overlap at the center of the channel and significant variations of $n^{\pm}$ and ψ occur only in the normal direction to the channel walls, the stable Boltzmann distribution of ions in the electric double layer can be assumed, that according to Bruss (2008) is given by

$$\rho_e = -2n_o ez \sinh\left(\frac{ez}{k_B T}\psi\right) \quad (7.187)$$

where $n_o = CN_A$ is the bulk number concentration of ions in the electrolyte solution, C is the molar concentration of ions, N_A is Avogadro's number, T is the temperature and k_B is the Boltzmann constant. The set of equations (7.183), (7.184) and (7.187) is usually called the Poisson-Boltzmann equations (PB).

For small values of $ez\psi_0/k_B T$, synonymous of a small ratio of electrical to thermal energies, equation (7.187) can also be linearized, $\sinh x \approx x$, using the so-called Debye-Huckel approximation. Then, the electric charge density equation, becomes

$$\rho_e = -\epsilon\kappa^2\psi \quad (7.188)$$

where $\kappa^2 = \frac{2n_o e^2 z^2}{\epsilon k_B T}$ is the Debye-Huckel parameter, related to the thickness of the Debye layer, (also referred to as the EDL thickness). The set of equations (7.183), (7.184) and (7.188) is usually called the Poisson- Boltzmann-Debye-Huckel equations (PBDH).

Finally, we can rewrite the Cauchy equation (7.175) as,

$$\frac{D\mathbf{u}}{Dt} = -\nabla p + +\beta\eta_0\nabla^2\mathbf{u} + \frac{\eta_0}{\lambda}\left(1-\beta\right)\nabla\cdot\mathbf{A} + \rho_e\nabla\left(\phi+\psi\right) \quad (7.189)$$

keeping in mind that the electric charge density equation can be obtained by equations (7.185), (7.187) or (7.188), depending on the desired level of approximation.

7.5.3 *Numerical method*

In the past, our group adapted a Newtonian FVM to calculate pressure driven flows of viscoelastic fluids. The method is based on a time marching pressure-correction algorithm formulated with the collocated variable arrangement and is explained in detail in Oliveira et al. (1998) and Alves et al. (2003a). For improved convergence, the FVM was modified with the matrix logarithmic of the conformation tensor (Fattal and Kupferman, 2004), and details of that implementation have been previously given by Afonso et al. (2009b).

Here, the existing method was extended to mixed electro-osmotic/pressure driven flows, and the modifications are explained below. As observed in the previous section, the new set of equations depends on the approximations applied to the closed-form equation for the electric charge density, i.e., the PNP, PB or PBDH equations. This fact also reflects on the numeric implementation, and we chose to implement all the three approximations. Briefly, the PNP, PB or PBDH equations are transformed first to a non-orthogonal system (σ_l), but keeping the Cartesian velocity and stress components. This is advantageous from a numerical point of view, because the equations are written in a strong conservation form which helps to ensure that the final algebraic equations retain conservativeness. Then, the equations are integrated in space over the control volumes (cells with volume V_P) forming the computational mesh, and in time over a time step (δt), so that sets of linearised algebraic equations are obtained, having the general form:

$$a_P^\Theta \Theta_P = \sum_{F=1}^{6} a_F^\Theta \Theta_F + S^\Theta \tag{7.190}$$

to be solved for all variables ($\Theta = u$, v, w, θ, ψ, n^+ or n^-). The equations for the pressure and extra stress components (or the Log-conformation tensor) are similar to equation (7.190) and are the same used in the pressure driven flow version of the code (see Oliveira et al., 1998; Alves et al., 2003a), and so they are not included in this description. In these equations a_F are coefficients accounting for convection and diffusion, S^Θ are source terms encompassing all contributions not included in the coefficients, the subscript P denotes the cell under consideration and subscript F its corresponding neighbouring cells. The coefficients of the PNP equations are given by:

$$\phi \Rightarrow \left\{ a_F^\phi = D_f; \quad a_P^\phi = \textstyle\sum_{F=1}^{6} a_F^\phi; \quad S^\phi = 0 \right.$$

$$\psi \Rightarrow \left\{ a_F^\psi = D_f; \quad a_P^\psi = \textstyle\sum_{F=1}^{6} a_F^\psi; \quad S^\psi = \frac{ez}{\epsilon}\,(n^+ - n^-)\,V_P \right.$$

$$n^\pm \Rightarrow \begin{cases} a_F^{n^\pm} = D_f + C_f; \quad a_P^{n^\pm} = \frac{V_P}{\delta t} + \sum_{F=1}^{6} a_F^{n^\pm} \\ S^{n^\pm} = S_{HRS}^{n^\pm} + \left[\frac{n^\pm}{\delta t} \pm \left(\frac{D^\pm n^\pm}{2} \kappa^2 \,(n^- - n^+) \right.\right. \\ \qquad \left.\left. + \sum_{i=1}^{3} \frac{\partial \left(D^\pm n^\pm \frac{ze}{k_B T} \right)}{\partial x_i} \frac{\partial (\phi + \psi)}{\partial x_i} \right) \right] V_P \end{cases}$$

$$u,\, v,\, w \Rightarrow \left\{ S_E^{uvw} = ez\,(n^+ - n^-)\,\nabla\,(\phi + \psi)\,V_P \right. \tag{7.191}$$

where D_f and C_f are the diffusive and convective conductance, respectively. The term S_E^{uvw} is the electric body force term in the momentum equations (7.189), and is added to the other source terms in the mo-

mentum equation (see Oliveira et al., 1998; Alves et al., 2003a). The coefficients of the PB equations are given by:

$$\phi \Rightarrow \begin{cases} a_F^{\phi} = D_f; & a_P^{\phi} = \sum_{F=1}^{6} a_F^{\phi}; \quad S^{\phi} = 0 \end{cases}$$

$$\psi \Rightarrow \begin{cases} a_F^{\psi} = D_f; \quad a_P^{\psi} = \sum_{F=1}^{6} a_F^{\psi} + \kappa^2 \cosh\left(\frac{ez}{k_B T}\psi\right) V_P \\ S^{\psi} = \left[\kappa^2 \psi \cosh\left(\frac{ez}{k_B T}\psi\right) - 2\frac{n_o ez}{\epsilon} \sinh\left(\frac{ez}{k_B T}\psi\right)\right] V_P \end{cases}$$

$$u, v, w \Rightarrow \begin{cases} S_E^{uvw} = 2n_o ez \sinh\left(\frac{ez}{k_B T}\psi\right) \nabla(\phi + \psi) V_P \end{cases} \tag{7.192}$$

In the coefficients for the potential ψ, especial attention was given to the hyperbolic function $\sinh(ez\psi/k_B T)$, especially at high values of $ez\psi/k_B T$, due to the exponential behavior of the function. So, a linearization of the source term, S^{ψ} was introduced in equation (**??**). Finally, the coefficients of the PBDH equations are given by:

$$\phi \Rightarrow \begin{cases} a_F^{\phi} = D_f; & a_P^{\phi} = \sum_{F=1}^{6} a_F^{\phi}; \quad S^{\phi} = 0 \end{cases}$$

$$\psi \Rightarrow \begin{cases} a_F^{\psi} = D_f; & a_P^{\psi} = \sum_{F=1}^{6} a_F^{\psi} + \kappa^2 V_P; \quad S^{\psi} = 0 \end{cases} \tag{7.193}$$

$$u, v, w \Rightarrow \begin{cases} S_E^{uvw} = \epsilon \kappa^2 \psi \nabla(\phi + \psi) V_P \end{cases}$$

The CUBISTA high-resolution scheme (Alves et al., 2003a) was used in the discretization of the convective terms of the momentum, of the Log-conformation tensor and of the ionic transport equations (7.186) (see term $S_{HRS}^{n^{\pm}}$ in equations (7.193)). This scheme is formally of third-order accuracy and was especially designed for differential constitutive relations (see Alves et al. 2003a). Due to the lack of space and because we will use small EDL thickness (and so the electric double layer does not overlap at the center of the channels), and we also assume that significant variations of $n^{\pm}$ and ψ occur only in the normal direction to the channel walls, then only the PB version of the code is used in the present work.

7.5.4 *Results and discussion*

7.5.4.1 *Accuracy tests*

To test the implementation of the numerical method some predictions are compared with existing analytical solutions for the flow in a two-dimensional microchannel under symmetric and asymmetric boundary conditions for the zeta potential at the walls (Afonso et al., 2009c, 2010c). In those works the so-called standard electrokinetic model assumptions were used, along with the sPTT model for the viscoelastic fluid. When the flow is fully-developed the velocity and stress fields only depend on the transverse coordinate y, and on some dimensionless parameters, such as the ratio of microchannel to Debye layer thicknesses $\bar{\kappa} = \kappa H$, the

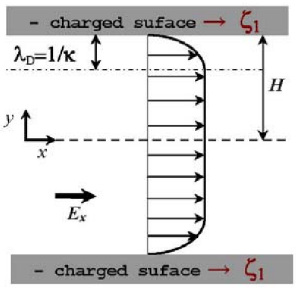

(a) Channel geometry.

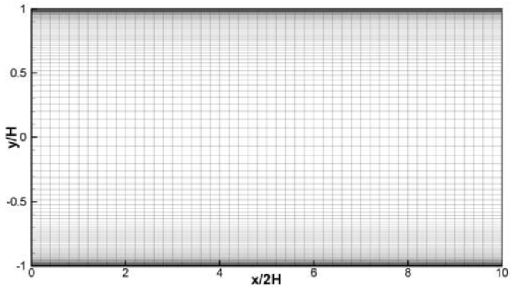

(b) mesh M3.

Figure 7.37: Schematic representation of the channel geometry and computational mesh.

Table 7.1: Mesh details.

	NC	Δx_{min}	Δy_{min}
M1	1800	0.2	$8.0x10^{-4}$
M2	3600	0.2	$4.0x10^{-4}$
M3	7200	0.2	$2.0x10^{-4}$
MCS	12801	$4.0x10^{-4}$	$4.0x10^{-4}$

Helmholtz-Smoluchowski electro-osmotic velocity $u_{sh} = -\epsilon\zeta_i E_x/\eta$, the rheological properties of the fluid via a Deborah number based on the EDL thickness and u_{sh}, $De_k = \lambda u_{sh}/\lambda_D = \lambda u_{sh}\kappa$ (or based in the channel length, $De_H = \lambda u_{sh}/H$ as in Afonso et al., 2009c) and the fluid extensibility parameter ε. To account for the combined forcing of pressure gradient and electro-osmosis, the non-dimensional ratio between these two forcings is given by $\Gamma = -\left(H^2/\varepsilon\zeta_i\right)(p_{,x}/E_x)$.

The channel geometry is represented in Figure 7.37(a). At the walls the no-slip condition applies ($u = 0$ at $y = \pm H$), along with $\partial\phi/\partial y_{|wall} = 0$ and $\psi = \zeta_i$. Depending on the value of ζ_i on the walls, we can determine if the flow is symmetric ($R_\zeta = \zeta_1/\zeta_2 = 1$, i.e. $\zeta_1 = \zeta_2$) or asymmetric ($R_\zeta = \zeta_1/\zeta_2 \neq 1$, i.e. $\zeta_1 \neq \zeta_2$). At the inlets fully-developed velocity and stress profiles are imposed and at the outlet planes Neumann boundary conditions are applied, i.e. $\partial\theta/\partial x = 0$).

The main characteristics of the three meshes used in this work for the accuracy test are given in Table 7.1, including the total number of cells (NC) and the minimum cell spacing (Δx_{min} and Δy_{min}). Note that the refinement in the transverse direction is very high, in order to obtain accurate results in the sharp zone of the EDL. This high refinement is shown in Figure 7.37(b), here for mesh M3.

The results for the accuracy tests are presented in Figure 7.38. When $R_\zeta = 1$, i.e., for symmetric conditions, Figure 7.38(a), presents the

fully-developed dimensionless velocity profiles obtained with $\epsilon = 0.25$,$De_k = 1$, $\bar{\kappa} = 200$ and $\Gamma = 0$ (pure EOF). As observed, both the analytical and numerical results collapse, showing excellent accuracy, even at a very sharp EDL ($\bar{\kappa} = 200$). For complete asymmetric flow ($R_\zeta = -1$), with $\varepsilon = 0.25$,$De_k = 1$, $\bar{\kappa} = 50$ and in the presence of a favourable pressure gradient (with $\Gamma = -2$), the comparison between the analytical and numeric results is also excellent, as observed in Figure 7.38(b). These results show that the refinement near the wall for mesh M2 is sufficient to obtain accurate results, even for very small EDL thickness.

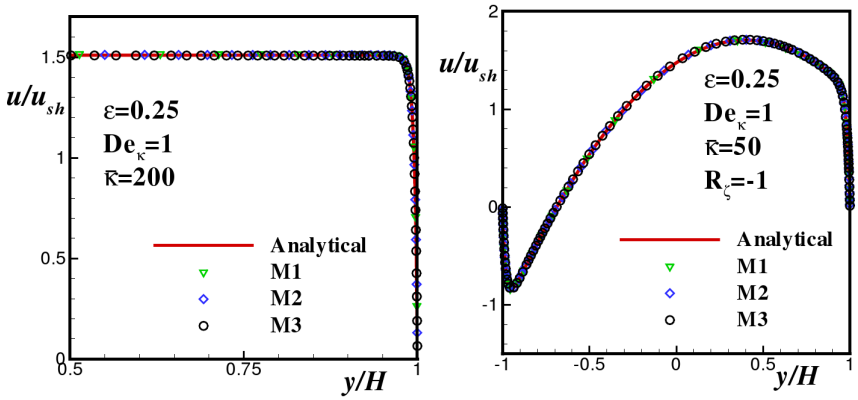

(a) (b)

Figure 7.38: Dimensionless velocity profiles for (a) symmetric zeta potential for pure EOF ($\Gamma = 0$) and (b) asymmetric zeta potential for favourable pressure gradient ($\Gamma = -2$).

7.5.4.2 *Cross-Slot flow results*

Further studies were undertaken in a more complex geometry, usually described as cross-slot geometry (see Figure 7.39). We are particularly interested in investigating the possible appearance of purely-elastic instabilities, as observed recently in a three-dimensional cross-slot microchannel flow by Arratia et al. (2006), under pure Poiseuille flow. Poole et al. (2007c) simulated the two-dimensional cross-slot flow of an UCM fluid under creeping-flow conditions, and were able to capture qualitatively the onset of a bistable steady asymmetric flow above a first critical Deborah number followed by a later transition to a time dependent flow, in agreement with the experimental findings of Arratia et al. (2006). Poole et al. (2007b) extended the earlier study of Ref. Poole et al. (2007c) by considering the three-dimensional nature of a real microfluidic cross slot flow and investigated in detail the effect of the aspect ratio of the geometry, by varying the depth of the cross slot from low values (quasi-Hele Shaw flow) up to very large values (quasi-two dimensional flow). Later, Poole et al. (2007a) incorporated the effect of solvent viscosity ($\beta \neq 0$ in the Oldroyd-B) and finite extensibility ($\varepsilon \neq 0$ in the sPTT model), presenting some $\beta - Re - De$ and $\varepsilon - Re - De$ maps of flow pattern types, showing the existence of a narrow region where steady asymmetric flow can emerge, and identified the limiting De for onset of time-dependent flow. The effect of finite extensibility was also studied by Rocha et al. (2009), using FENE models. Afonso et al. (2010b) presented a numerical study of the creeping flow of an UCM fluid in a

three-dimensional cross-slot geometry with six arms and studied the influence of the different types of extensional flow near the stagnation point. They found that the uniaxial extension flow configuration is prone to the onset of steady flow asymmetries, while in the biaxial extension flow configuration the flow was perfectly symmetric.

In this work we further extend the previous investigations by considering the effect of the electric field in the appearance of the flow instabilities. The cross-slot geometry is shown schematically in Figure 7.39 together with the mesh used in this work. All branches have the same width (H) and the inlet and outlet branches have lengths of twenty channel widths (20H). At the inlets fully-developed velocity and stress profiles are imposed and the inlet length is more than sufficient for the flow at the junction to be independent of the inlet condition. Similarly, the outlets are sufficiently long to avoid any effect of the outflow boundary condition upon the flow in the central region. At the outlet planes vanishing axial gradients are applied to all variables (Neumann boundary conditions, i.e. $\partial\psi/\partial y = 0$), and no-slip conditions are imposed at all channel walls. For the potential at the walls, we assume $\partial\phi/\partial n_{|wall} = 0$ and $\psi = \zeta_i$. The mesh used in these calculations has the same refinement near the walls as mesh M2 of the accuracy tests, and the main characteristics of that mesh are also given in Table 7.1. Near the central square, and as observed in Figure 7.39(b), the mesh in the axial direction is also very refined, with both minimum cell spacings equal $\Delta x_{min} = \Delta y_{min} = 4.0x10^{-4}$. All the calculations were carried out at a vanishing Reynolds number, $Re = \rho UH/\eta = 0$ (creeping flow conditions – imposed by dropping out the convective term in the momentum equation).

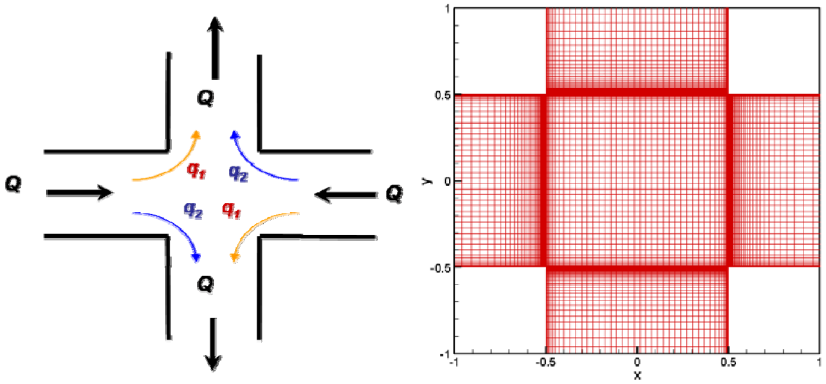

(a) Cross-slot geometry.

(b) mesh MCS.

Figure 7.39: Schematic representation of the Cross-slot geometry and computational mesh.

As already described, we are particularly interested in the effect of the electric field in the possible appearance of asymmetries in the cross-slot flow. We start presenting the effect of the combined forcing by pressure gradient and electro-osmosis in the flow characteristics. Theoretically, for Newtonian fluid flow in a straight channel, when the non-dimensional ratio between these two forcings is $\Gamma = 2$, the dimensionless velocity at the center line is zero (due to the adverse effect of both forcing terms, i.e., pressure is driving the flow in one direction while electric potential drives it in the opposite direction). Figure 7.40(a), shows the streamlines superimposed with the u-velocity

contours for this situation. We can observe that near the walls the EOF is driving the flow towards the central square while in the center line of the channel the backpressure drives the flow out in the channel. This is also evident if the adverse pressure gradient is increased, as observed in Figure 7.40(b), here for $\Gamma \approx 2.5$.

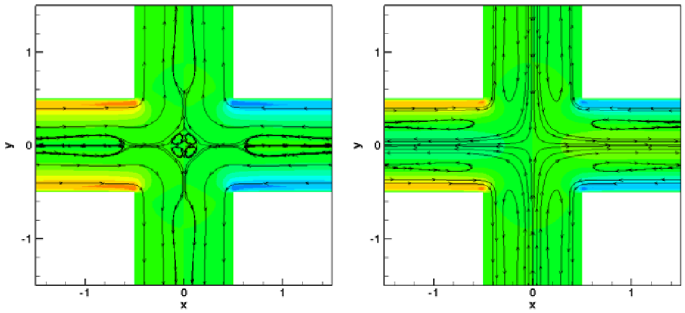

(a) (b)

Figure 7.40: Streamlines superimposed over axial velocity field for Newtonian flow for adverse pressure gradients: (a) $\Gamma \approx 2$ and (b) $\Gamma \approx 2.5$.

For viscoelastic fluids we performed additional simulations with $\Gamma \approx 0$, i.e., for pure EOF, and $\bar{\kappa} = 20$ using the UCM model. Figure 7.41 presents the streamlines superimposed over u-velocity contour maps for UCM flow for several Deborah numbers, showing that above a critical Deborah number ($De_H = 0.275$) the flow becomes asymmetric. The differences between the results for the cross slot with pure EOF and pure pressure gradient flows may be understood from the role of the amount of stabilizing shear flow in the stagnation point region which is less in the case of EOF. This difference may also be important for understanding the appearance of the purely-elastic instabilities in the cross slot geometry. At higher Deborah numbers the flow becomes unsteady, with the formation of vortical structures in the central square, but these flow conditions require further studies, to be undertaken in the future.

7.5.5 *Conclusions*

In this work we present a finite volume method that can be used to solve the relevant coupled equations for electro-osmotic flows of viscoelastic fluids, namely the nonlinear Poisson–Boltzmann equation that governs the electrical double-layer field, the Cauchy equation with a body force due to the applied electrical potential field and the constitutive equations for the viscoelastic fluids.

To describe the rheological behavior of viscoelastic fluids we use the Upper-Convected Maxwell (UCM) model and the simplified Phan-Thien—Tanner model (sPTT) (Phan-Thien and Tanner, 1977). We tested the implementation of the numerical method against existing analytical solutions for the flow in a two-dimensional microchannel under symmetric and asymmetric boundary conditions for the zeta potential at the walls (Afonso et al., 2009c, 2010c), and the comparison between the analytical and numeric results collapsed within numerical uncertainty, even for very small EDL thickness.

In this work we further extend the previous investigations in the cross-slot geometry by considering the effect of the electric field in

the appearance of the flow instabilities, and found that even for pure electro-osmotic flow (in absence of any imposed pressure gradient) we were able to capture the onset of an asymmetric steady flow above a critical Deborah number, $De_H = 0.275$, which was lower than for pure pressure gradient forcing.

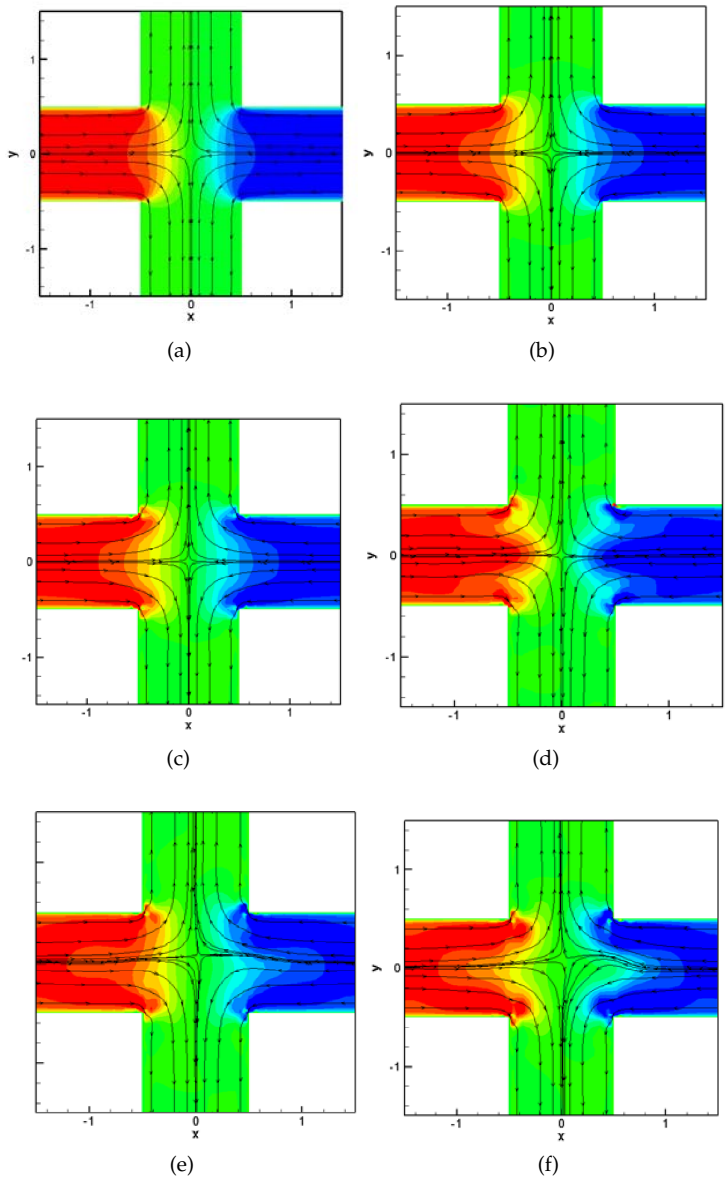

Figure 7.41: Streamlines superimposed over u-velocity field for pure EO flow of UCM fluid: (a) steady symmetric flow at $De_H = 0$; (b) $De_H = 0.1$, (c) $De_H = 0.2$; (d) $De_H = 0.25$ and steady asymmetric flow at (e) $De_H = 0.275$ and (f) $De_H = 0.3$.

7.5.6 *Acknowledgments*

The authors acknowledge funding from FEDER and Fundação para a Ciência e a Tecnologia (FCT), Portugal, through projects PTDC/EQU-FTT/70727/2006 and PTDC/EQU-FTT/71800/2006. A.M. Afonso would

also like to thank FCT for financial support through the scholarship SFRH/BD28828/2006.

Part IV

CONCLUSIONS AND OUTLOOK

8

CONCLUSIONS

I don't know!
I don't know why I did it,
I don't know why I enjoyed it,
and I don't know why I'll do it again!

— Bart Simpson

Who would also think that the simplicity of Heraclitus of Ephesus (540–475 BC) philosophical statement "Panta rhei" (everything flows), could lead into this PhD thesis? So let us ascend (or descend, following again Heraclitus's ideas "The road up and the road down is one and the same") to the closing conclusions of this dissertation.

The present thesis, was aimed to increasing the current knowledge about several distinct, but complementary, subjects. This was accomplished by a numerical and theoretical investigation, with four main objectives/questions introduced in Part I, Section 1.2 (on page 15). The following answers resume the main conclusions:

OBJ. 1 Is it possible to development robust and highly accurate numerical schemes to overcome the HIGH WEISSENBERG NUMBER PROBLEM?

ANS. 1 Not completely, but the developments of this thesis albeit small were a firm step into the possible solution of the HIGH WEISSENBERG NUMBER PROBLEM. This was accomplished within the framework of finite volume method, with the incorporation into the in-house code of the numerical stabilization methodology recently proposed by Fattal and Kupferman (2004). After this implementation, the code was able to obtain very precise results in computational rheology benchmark flows (cylinder and contraction flows), with the calculations at very high Weissenberg numbers showing the tendency to become unsteady.

In the computational rheology benchmark flow around a confined cylinder with a blockage ratio of 0.5 the results obtained in the most refined mesh (with a minimum cell size of the order $O(10^{-3}, 10^{-4})$), presented no limiting bound for the attained Deborah number, although only simulations up to $De = 1.9$ were performed. This represents an increase of about 90% in the maximum attainable De when compared with the actual literature, and an outstanding step into the HIGH WEISSENBERG NUMBER PROBLEM solution.

The achievements were even more impressive in the results obtained in the 4:1 contraction benchmark flow. For this flow, again

no limiting bound for the attained Deborah number was observed, with stable solutions obtained up to $De = 100$ in the 2D case with the Oldroyd-B model and up to $De \approx 10,000$ in the 3D square/square contraction flow with the PTT model. A rich succession of dynamical transitions, from steady to unsteady flow with lip and corner vortex enhancement, and from symmetric to asymmetric patterns with alternating vortex pulsation, up to almost chaotic regime of back-shedding upstream of the contraction plane, were also presented, to the author's best knowledge, for the first time in the literature.

The energy losses in the flow of the Oldroyd-B fluid through the abrupt contraction, evaluated by the Couette correction coefficient (C_{corr}) that represents a dimensionless extra pressure drop due to flow redevelopment at the entrance of the smaller channel, presented a non-monotonical variation with elasticity. The increase in C_{corr} occurred for $De > 20$, as had been seen in earlier studies for the PTT fluid (Alves et al., 2003b) and in close agreement with the experimental findings of McKinley et al. (1991b) and Rothstein and McKinley (2001).

OBJ. 2 Is it possible to use these robust and highly accurate numerical schemes to simulate complex flows of complex fluids that originate purely elastic FLOW INSTABILITIES?

ANS. 2 Yes. Here this was accomplished by the application of the log-conformation method for the three-dimensional cross-slot flow and in the mixing-separating geometries, in which purely elastic instabilities are present.

In the three-dimensional cross-slot geometries, the uniaxial extensional flow configuration (a configuration with four inlets and two outlets) is prone to the onset of steady flow asymmetries and at a higher Deborah number there is a second transition from steady asymmetric to unsteady flow, as in the corresponding two-dimensional cross slot geometry.

On the other hand, for the biaxial extensional flow configuration (a configuration with two inlets and four outlets) a perfectly symmetric flow was observed up to a critical Deborah number, at which the flow becomes unsteady and asymmetric without transitioning through a steady asymmetric flow. Inertia was found to stabilize the first type of transition (for the uniaxial extensional flow) and to destabilize the second transition in both flow configurations, although to a much lesser degree in the biaxial extensional flow configuration.

In the mixing-separating geometry, and for a combination of critical flow parameters, it was possible to identify a new steady and stable bifurcation in the flow patterns at low inertia and high elasticity.

For large dimensionless gap sizes, but below a critical value ($\theta \leqslant 1.6$), the reversed flow is initially slightly enhanced with elasticity, followed by a significant decrease towards zero when the Deborah number further increases. This behaviour is characterized by a

significant departure from streamline parallelism in the mixing-separating gap region, although with the fluid still tending to flow unidirectionally in agreement with experiments (Cochrane et al., 1981; Walters and Webster, 1982).

For a supercritical dimensionless gap size ($\theta \geqslant 1.84$), elasticity is responsible for a continuous increase of flow reversal relative to the unidirectional flow with Deborah number. This type of supercritical pattern has not yet been observed experimentally primarily due to the stabilising effect of inertia.

At an intermediate gap width range ($1.6 \leqslant \theta \leqslant 1.84$), a steady bifurcation flow pattern emerges, with a sudden jump between two widely different flow configurations, ranging from almost unidirectional to almost fully reversed, at Deborah numbers slightly higher than the critical Deborah number. The bifurcation between these two flow patterns is due to a purely-elastic instability since inertia has no role ($Re = 0$) in the present simulations (we have also observed such purely elastic instabilities in the works of Poole et al., 2007c,a and Rocha et al., 2009). Further stability analysis suggested that in this bifurcation flow pattern, and although both flow configurations are steady and stable, the unidirectional configuration is preferred.

OBJ. 3 Is it possible to use these robust and highly accurate numerical schemes to simulate complex flows of complex fluids driven by NEW FORCING TERMS, such as electro-osmosis, and do these flows lead to elastic FLOW INSTABILITIES?

ANS. 3 Yes. Here this was accomplished by the application of the log-conformation method in electro-osmostic flows (EOF). Up to the beginning of this thesis, numerical investigations on modelling of EOF were nonexistent. Meanwhile, these are now gathering momentum, with limited advance having been made, still for very simple geometries such as in straight microchannels.

Three different implementations of physical models were carried out, which depend on the desired level of approximation. In the first implementation, the Poisson-Nernst–Planck (PNP) equations were incorporated into the code and the electric charge distribution required to quantify the electric field forcing of the momentum equation is calculated from the most fundamental equations. The second implementation is realy an approximation in which a stable Boltzmann distribution of ions is assumed to occur in the electric double layer. Here, the Poisson-Boltzmann equations were implemented. Finally, the so-called Debye-Hückel approximation was also implemented in the Poisson-Boltzmann-Debye-Hückel (PBDH) model, which is valid for cases with a small ratio of electrical to thermal energies. To test each numerical implementation, some predictions are compared with existing analytical solutions for the flow in a two-dimensional microchannel under symmetric and asymmetric boundary conditions for the zeta potential at the walls (Afonso et al., 2009c, 2010c).

New types of flow instabilities, a combination of electrokinetic and elastic instabilities, were obtained in the electro-osmosis flow

of viscoelastic fluids, such as the observed in the cross-slot flow. For the UCM fluid flow above a critical Deborah number ($De_H = 0.275$) the flow becomes asymmetric, and the differences between the results for the cross slot with pure EOF and pure pressure gradient flows by Poole et al. (2007c), were related with the role of the amount of stabilizing shear flow in the stagnation point region which is less significant in the case of EOF. This difference may also be important for understanding the onset of the purely-elastic instabilities. At higher Deborah numbers the flow becomes unsteady, with the formation of vortical structures in the central square.

OBJ. 4 Is it possible to obtain analytical solutions for simple flows of complex fluids driven by NEW FORCING TERMS, such as electro-osmosis?

ANS. 4 Yes. Up to the beginning of this thesis, there were no analytical solutions for fully-developed electro-osmotic flows of non-linear viscoelastic fluids. The present dissertation aimed at fulfilling this gap in the literature, and various analytical solutions were presented for combined pressure/electro-osmosis forced flows of viscoelastic fluids in a channel under a variety of boundary conditions of practical relevance, such as those observed in the case of electro-osmotic pumps.

An analytical solution for the flow of viscoelastic fluids in micron sized ducts, namely between parallel plates and pipes under the combined influence of electrokinetic and pressure forces using the Debye–Hückel approximation was presented. This study also included the limit case of pure electro-osmotic flow. Using the simplified Phan-Thien–Tanner and the FENE-P models, the presented solution was non-linear with a significant contribution arising from the coupling between the electric and pressure potentials. This new term acts as a drag reducer and a drag increaser under favourable and adverse pressure gradients, respectively and contrasts with the Newtonian flow case, for which it does not exist, demonstrating that the superposition principle valid for Newtonian fluids no longer applies when non-linear viscoelastic fluid models are considered.

The solution for the mixed pressure/EO flows was extended assuming asymmetric boundary conditions, in which different zeta potentials at the walls were considered. This situation can be found, for instance, in soft lithography where the channels are often made of polydimethylsiloxane (PDMS) except for the top wall that is often made of glass for optical access, or other material for other purpose. The fluids were $z-z$ symmetric electrolytes, and again the simplified Phan-Thien–Tanner and the FENE-P models were used. The combined effects of fluid rheology, electrical double-layer thickness, ratio of the wall zeta potentials and ratio between the applied streamwise gradients of electrostatic potential and pressure on the fluid velocity and stress distributions were discussed.

Analytical studies of electro-osmotic flow of a viscoelastic fluid described by the complete Phan-Thien-Tanner model was also

presented. This PTT model uses the Gordon-Schowalter convected derivative, which leads to a non- zero second normal stress difference in pure shear flow. Equations for the critical shear rates and maximum electrical potential required to maintain a steady fully developed flow were derived and discussed. When the shear rate and Deborah number exceed a critical value a constitutive flow instability occurs for $\xi \neq 0$, and this critical shear rate is found to be dependent of ε and ξ, whereas the critical Deborah number is only dependent on ξ for large $\overline{\kappa}$. The critical Deborah number increases with decrease in ξ tending to infinity as ξ tends to zero.

An applied theoretical study of practical relevance in the transport of non-polar fluids was also presented. The theoretical study of a two-fluid electro-osmotic pump, in which the work fluid is viscoelastic. This is the principle of operation of an EO two-fluid pump, presented by Brask et al. (2003), in which an electrically nonconducting fluid is transported by the interfacial dragging viscous force of a conducting fluid that is directly driven by electro-osmosis. The effects of fluid rheology, dynamic viscosity ratio, holdup and interfacial zeta potential are analysed to show the viability of this technique, where a higher volumetric flow rate of a nonconducting Newtonian fluid can be achieved in EOF pumping when the conducting fluid is viscoelastic rather than Newtonian, due to lower wall viscosities of the shear-thinning fluids.

These analytical solutions were also of significant importance in order to test the proposed code implementations and demonstrate their high stability and accuracy, as described in Ans. 3.

9

OUTLOOK

How often I found where I should be going
only by setting out for somewhere else.

Whenever I draw a circle,
I immediately want to step out of it.

— Buckminster Fuller

If some of the questions posed in this work were fully answered, there are even more open questions that are still waiting for a solution or even to be formulated. Let us close this dissertation by addressing the expectations for possible future outcomes.

- There are plenty of new clever ideas to be tested in the numerical solution of the High Weissenberg Number Problem.

  In the mid-term outlook, a more detailed investigation on the new *square-root* formalism introduced by Balci et al. (2010) (See Section 2.1, on page 22) should be carried out. We have implemented this *square-root* formalism in our code (Afonso et al., 2010a), and a comparative study with the log-conformation will be performed, using the cylinder flow problem.

  In order to optimize the mesh refinement near critical zones, such as near walls and other singular points, some numerical techniques need to be implemented. An adaptive-grid method is planned for implementation in the near term in the same in-house code.

  The adoption of fine-grain constitutive equations will be also implemented, in order to improve the physical level of approximation of the numerical methods. The parallelization of the code will be very helpful for this purpose.

- Viscoelastic flow instabilities are still a stimulating and provocative subject.

  Numerical investigation of viscoelastic instabilities in multiphase flows and in flows with electrokinetic forcing in microfluidic systems will also be carried out. For such endeavour, the Level-Set method, to compute liquid-gas and liquid-liquid flows, with viscoelastic continuous phase, will be implemented in the near future.

- Explore the gathering momentum of electro-osmotic flow of complex fluids.

  Even though electro-osmotic flow of complex fluids in microfluidics is still in a state of exploratory research, there are industrial applications where its advantages stand out clearly, such as in screening for protein crystallization, bio-analyses or the manipulation of multiphase flows. Electrokinetic forcing can lead to the onset of flow instabilities, called electrokinetic instabilities (EKI). When used in combination with viscoelastic fluids, new phenomena arise, as recently discovered Bryce and Freeman (2010) and a sound understanding of the instability driving mechanism needs to be obtained.

Part V

BIBLIOGRAPHY AND REFERENCES

BIBLIOGRAPHY

Confucius (551–479 BC). *Lunyu (Analects)*. Trans. D. C. Lau, Middlesex, penguin books edition, 1979. (Cited on page 3.)

M. Aboubacar and M. F. Webster. A cell-vertex finite volume/element method on triangles for abrupt contraction viscoelastic flows. *J. Non-Newtonian Fluid Mech.*, 98(2-3):83–106, 2001. (Cited on pages 43, 44, 114, 121, 122, 125, and 132.)

A. Acrivos, M. J. Shah, and E. E. Petersen. Momentum and heat transfer in laminar boundary-layer flows of non-newtonian fluids past external surfaces. *AIChE Journal*, 6(2):312–317, June 1960. (Cited on page 8.)

A. Afonso and F. T. Pinho. Numerical investigation of the velocity overshoots in the flow of viscoelastic fluids inside a smooth contraction. *J. Non-Newtonian Fluid Mech.*, 139:1–20, 2006. doi: 10.1016/j.jnnfm.2006.05.012. (Cited on pages 39 and 41.)

A. Afonso, M. A. Alves, F. T. Pinho, and P. J. Oliveira. Uniform flow of viscoelastic fluids past a confined cylinder. *Rheologica Acta*, 47: 325–348, 2008. doi: 10.1007/s00397-007-0234-3. (Cited on pages xi, 26, 29, 36, 65, 70, 71, 74, 75, 81, 83, 84, and 87.)

A. Afonso, J. M. Miranda, and J. B. L. M. Campos. Numerical study of bsa ultrafiltration in the limiting flux regime - effect of variable physical properties. *Desalination*, 249(3):1139–1150, 2009a. doi: 10.1016/j.desal.2009.05.012. (Cited on page 23.)

A. Afonso, P. J. Oliveira, F. T. Pinho, and M. A. Alves. The log-conformation tensor approach in the finite volume method framework. *J. Non-Newtonian Fluid Mech.*, 157:55–65, 2009b. doi: 10.1016/j.jnnfm.2008.09.007. (Cited on pages xi, 26, 29, 30, 31, 32, 33, 65, 67, 116, 118, 145, 146, 159, and 249.)

A. M. Afonso, M. A. Alves, and F. T. Pinho. Analytical solution of mixed electro-osmotic pressure driven flows of viscoelastic fluids in microchannels. *J. Non-Newtonian Fluid Mech.*, 159:50–63, 2009c. doi: 10.1016/j.jnnfm.2009.01.006. (Cited on pages xi, 14, 59, 61, 65, 171, 197, 198, 201, 205, 207, 210, 216, 217, 225, 230, 234, 239, 240, 245, 246, 247, 251, 252, 255, and 263.)

A. M. Afonso, M. A. Alves, and F. T. Pinho. Report on the implementation of the oldroyd-b and sptt constitutive equations based on the sqrt-conformation tensor. Technical report, Centro de Estudos de Fenómenos de Transporte (CEFT) internal report, 2010a. (Cited on pages 24 and 267.)

A. M. Afonso, M. A. Alves, and F. T. Pinho. Purely-elastic flow instabilities in a 3d six arms cross slot geometry. *J. Non-Newtonian Fluid Mech.*, 165:743–751, 2010b. doi: 10.1016/j.jnnfm.2010.03.010. (Cited on pages xi, 48, 51, 65, 143, 163, and 253.)

A. M. Afonso, M. A. Alves, and F. T. Pinho. Electro-osmotic flows of viscoelastic fluids in microchannels under asymmetric zeta potential, in press. *Journal of Engineering Mathematics, Special issue Complex Flows and Complex Fluids*, 2010c. doi: 10.1007/s10665-010-9384-x. (Cited on pages xi, 59, 60, 61, 65, 197, 216, 225, 230, 235, 246, 247, 251, 255, and 263.)

A. M. Afonso, M. A. Alves, R. J. Poole, P. J. Oliveira, and F. T. Pinho. Viscoelastic flows in mixing-separating cells, in press. *Journal of Engineering Mathematics, Special issue Complex Flows and Complex Fluids*, 2010d. doi: 10.1007/s10665-010-9384-x. (Cited on pages xi, 48, 54, 65, 143, 155, and 157.)

A. M. Afonso, P. J. Oliveira, F. T. Pinho, and M. A. Alves. Dynamics of high deborah number entry flows - a numerical study, submited to. *Journal of Fluid Mechanics*, 2010e. URL paginas.fe.up.pt/~mmalves/jfm2010/. (Cited on pages xi, 39, 44, 45, 65, and 113.)

A. M. Afonso, F. T. Pinho, and M. A. Alves. Two-fluid electro-osmotic flows of viscoelastic fluids, in preparation to submit to. *Microfluidics and Nanofluidics*, 2010f. (Cited on pages xi, 59, 61, 66, and 229.)

A. M. Afonso, F. T. Pinho, and M. A. Alves. Electro-osmotic flows of viscoelastic fluids: a numerical study, in preparation to submit to. *J. Non-Newtonian Fluid Mech.*, 2010g. (Cited on pages xi, 59, 61, 66, and 245.)

M. A. Alves. *Escoamentos de fluidos viscoelásticos em regime laminar: análise numérica, teórica e experimental*. PhD thesis, FEUP, Porto, Portugal, 2004. (Cited on pages 15, 22, 29, and 31.)

M. A. Alves and R. J. Poole. Divergent flow in contractions. *J. Non-Newtonian Fluid Mech.*, 144(2-3):140–148, 2007. (Cited on pages 39, 129, and 148.)

M. A. Alves, F. T. Pinho, and P. J. Oliveira. Effect of a high-resolution differencing scheme on finite-volume predictions of viscoelastic flows. *J. Non-Newtonian Fluid Mech.*, 93(2-3):287–314, 2000. (Cited on pages 43, 70, 71, 92, 96, 118, 121, and 135.)

M. A. Alves, F. T. Pinho, and P. J. Oliveira. Study of steady pipe and channel flows of a single-mode Phan-Thien-Tanner fluid. *J. Non-Newtonian Fluid Mech.*, 101:55–76, 2001a. (Cited on pages 172, 185, 208, 217, 222, and 233.)

M. A. Alves, F. T. Pinho, and P. J. Oliveira. The flow of viscoelastic fluids past a cylinder: finite-volume high-resolution methods. *J. Non-Newtonian Fluid Mech.*, 97(2-3):207–232, 2001b. (Cited on pages 22, 26, 29, 30, 32, 33, 67, 70, 71, 74, 76, 77, 78, 79, 87, 88, 92, 93, 96, 97, 99, and 105.)

M. A. Alves, P. J. Oliveira, and F. T. Pinho. A convergent and universally bounded interpolation scheme for the treatment of advection. *Int. J. Numer. Meth. Fluids*, 41:47–75, 2003a. (Cited on pages 15, 23, 43, 70, 71, 73, 92, 96, 118, 146, 159, 160, 249, 250, and 251.)

M. A. Alves, P. J. Oliveira, and F. T. Pinho. Benchmark solutions for the flow of Oldroyd-B and PTT fluids in planar contractions. *J. Non-Newtonian Fluid Mech.*, 110(1):45–75, 2003b. (Cited on pages 43, 44, 46, 114, 116, 118, 119, 121, 132, 135, and 262.)

M. A. Alves, F. T. Pinho, and P. J. Oliveira. Visualizations of Boger fluid flows in a 4: 1 square-square contraction. *AIChE journal*, 51(11): 2908–2922, 2005. (Cited on pages 41, 114, and 134.)

M. A. Alves, F. T. Pinho, and P. J. Oliveira. Viscoelastic flow in a 3d square-square contraction: Visualizations and simulations. *J. Rheol.*, 52(6):1347–1368, November/December 2008. doi: 10.1016/j.jnnfm.2008.09.007. (Cited on pages 38, 41, 113, 114, 118, 134, 136, 140, and 143.)

M. T. Arigo and G. H. McKinley. An experimental investigation of negative wakes behind spheres settling in a shear-thinning viscoelastic fluid. *Rheologica Acta*, 37(4):307–327, 1998. (Cited on pages 34, 89, and 90.)

P. E. Arratia, C. C. Thomas, J. D. Diorio, and J. P. Gollub. Elastic instabilities of polymer solutions in cross-channel flow. *Physical Review Letters*, page 144502, 2006. (Cited on pages 49, 50, 54, 144, 149, 152, 153, 158, 162, and 253.)

S. Arulanandam and D. Li. Liquid transport in rectangular microchannels by electro-osmotic pumping. *Colloids Surf., A*, 161:29–102, 2000. (Cited on pages 173, 215, and 245.)

G. Astarita and G. Marrucci. *Principles of non-Newtonian fluid mechanics*. McGraw-Hill Companies, 1974. (Cited on page 8.)

F. P. T. Baaijens. Mixed finite element methods for viscoelastic flow analysis: a review. *J. Non-Newtonian Fluid Mech.*, 79(2-3):361–385, 1998. (Cited on pages 25, 38, 92, and 113.)

F. P. T. Baaijens, H. P. W. Baaijens, G. W. M. Peters, and H. E. H. Meijer. An experimental and numerical investigation of a viscoelastic flow around a cylinder. *Journal of Rheology*, 38:351–351, 1994. (Cited on pages 28, 68, and 74.)

F. P. T. Baaijens, S. H. A. Selen, H. P. W. Baaijens, G. W. M. Peters, and H. E. H. Meijer. Viscoelastic flow past a confined cylinder of a LDPE melt. *J. Non-Newtonian Fluid Mech*, 68:173–203, 1997. (Cited on pages 28 and 29.)

F. P. T. Baaijens, M. A. Hulsen, and P. D. Anderson. The use of mixed finite element methods for viscoelastic fluid flow analysis, Chapter 14 in Encyclopedia of Computational Mechanics, E. Stein, R. de Borst and T.J.R. Hughes, 2004. (Cited on pages 25 and 28.)

H. P. W. Baaijens, G. W. M. Peters, F. P. T. Baaijens, and H. E. H. Meijer. Viscoelastic flow past a confined cylinder of a polyisobutylene solution. *Journal of Rheology*, 39:1243, 1995. (Cited on pages 28 and 29.)

M. Bajaj, M. Pasquali, and J. R. Prakash. Coil-stretch transition and the breakdown of computations for viscoelastic fluid flow around a confined cylinder. *Journal of Rheology*, 52:197, 2008. (Cited on page 79.)

N. Balci, B. Thomases, M. Renardy, and C. R. Doering. Symmetric factorization of the conformation tensor in viscoelastic fluid models. Preprint submitted to. *J. Non-Newtonian Fluid Mech.*, Arxiv preprint arXiv:1006.3488, 2010. (Cited on pages 24 and 267.)

A. Baloch, P. Townsend, and M. F. Webster. On the simulation of highly elastic complex flows. *J. Non-Newtonian Fluid Mech.*, 59(2-3):111–128, 1995. (Cited on pages 53 and 157.)

P. Becherer, A. N. Morozov, and W. Saarloos. Scaling of singular structures in extensional flow of dilute polymer solutions. *J. Non-Newtonian Fluid Mech.*, 153(2-3):183–190, 2008. (Cited on pages 51, 52, 144, 149, 152, and 154.)

A. A. Becker. *The boundary element method in engineering*. McGraw-Hill, London, 1992. (Cited on page 11.)

F. Belblidia, I. J. Keshtiban, and M. F. Webster. Stabilised computations for viscoelastic flows under compressible implementations. *J. Non-Newtonian Fluid Mech.*, 134(1-3):56–76, 2006. (Cited on pages 43 and 121.)

C. L. A. Berli and M. L. Olivares. Electrokinetic flow of non-newtonian fluids in microchannels. *J. Colloid Interface Sci.*, 320:582–589, 2008. (Cited on pages 59, 173, 177, 193, 230, and 245.)

D. Bernoulli. *Hydrodynamica*. Typs Joh. Henr. Deckeri, 1738. (Cited on pages 3, 4, and 7.)

F. Bianchi, R. Ferrigno, and H. H. Girault. Finite element simulation of an electroosmotic-driven flow division at a T-junction of microscale dimensions. *Anal. Chem*, 72(9):1987–1993, 2000. (Cited on page 246.)

P. Biller and F. Petruccione. The flow of dilute polymer solutions in confined geometries: A consistent numerical approach. *J. Non-Newtonian Fuid Mech.*, 25(3):347–364, 1987. (Cited on page 11.)

R. B. Bird and C. F. Curtiss. Fascinating polymeric liquids. *Physics Today*, 37:36, 1984. (Cited on pages 9 and 10.)

R. B. Bird, P. J. Dotson, and N. L. Johnson. Polymer solution rheology based on a finitely extensible bead-spring chain model. *J. Non-Newtonian Fluid Mech*, 7:213–235, 1980. (Cited on pages 11, 21, 53, 115, 158, 172, 173, 175, 193, 198, 200, 207, 213, 216, and 230.)

R. B. Bird, R. C. Armstrong, and O. Hassager. *Dynamics of Polymeric Liquids. Vol. 1- Fluid Mechanics*. John Wiley & Sons, New York, 2nd edition, 1987a. (Cited on pages 6, 8, 67, 91, 151, and 246.)

R. B. Bird, C. F. Curtiss, R. C. Armstrong, and O. Hassager. *Dynamics of Polymeric Liquids. Vol. 2- Kinetic Theory*. John Wiley & Sons, New York, 2nd edition, 1987b. (Cited on pages 6 and 8.)

R. B. Bird, W. E. Stewart, and E. N. Lightfoot. *Transport Phenomena*. John Wiley & Sons, New York, 2nd edition, 2002. (Cited on page 6.)

H. Blasius. Grenzschichten in flüssigkeiten mit kleiner reibung. *Z. Math. Phys.*, page 56:137, 1908. (Cited on page 8.)

D. V. Boger. Highly elastic constant-viscosity fluid. *J. Non-Newtonian Fluid Mech.*, 3:87–91, 1977. (Cited on pages 26, 53, and 157.)

D. V. Boger. Viscoelastic flows through contractions. *Annu. Rev. Fluid Mech.*, 19:157–182, 1987. (Cited on pages 38, 40, 113, and 125.)

D. V. Boger and K. Walters. *Rheological phenomena in focus*. Elsevier, Amsterdam, 1993. (Cited on page 9.)

D. V. Boger and K. Walters. Experimental dilemmas in non-Newtonian fluid mechanics and their theoretical resolution. *Korea-Australia Rheology Journal*, 12(1):27–38, 2000. (Cited on page 21.)

D. V. Boger, D. U. Hur, and R. J. Binnington. Further observations of elastic effects in tubular entry flows. *J. Non-Newtonian Fuid Mech.*, 20: 31–49, 1986. (Cited on page 40.)

L. Boltzmann. Zur theorie der elastichen nachwirkung. *Sitz. Kgl. Akad. Wiss. Wien (Math-Naturwiss Klasse)*, 70:275–306, 1874. (Cited on pages 8 and 14.)

D. A. Boy and B. D. Storey. Electrohydrodynamic instabilities in microchannels with time periodic forcing. *Phys. Rev. E: Stat. Nonlinear Soft Matter Phys.*, 76(2):026304, 2007. (Cited on page 216.)

A. Brask, G. Goranovic, and H. Bruus. A novel electro-osmotic pump design for nonconducting liquids: theoretical analysis of flow rate–pressure characteristics and stability. *Tech. Proc. Nanotech.*, 1:190–193, 2003. (Cited on pages 61, 229, 230, and 265.)

R. Bringhurst. *The Elements of Typographic Style*. Version 2.5. Hartley & Marks, Publishers, Point Roberts, WA, USA, 2002. (Cited on page 299.)

J. M. Broadbent and B. Mena. Slow flow of an elastico-viscous fluid past cylinders and spheres. *The Chemical engineering Journal*, 8(1):11–19, 1974. (Cited on page 87.)

R. A. Brown and G. H. McKinley. Report on the VIIIth international workshop on numerical methods in viscoelastic flows. *J. Non-Newtonian Fluid Mech.*, 52(3):407–413, 1994. (Cited on pages 25, 26, and 73.)

H. Bruss. *Theoretical Microfluidics, Oxford Master Series in Condensed Matter Physics*. Oxford University Press, Oxford, UK, 2008. (Cited on pages 172, 176, 200, 218, 219, 245, and 249.)

R. M. Bryce and M. R. Freeman. Abatement of mixing in shear-free elongationally unstable viscoelastic microflows. *Lab Chip*, 10:1436–1441, 2010. (Cited on pages 59 and 268.)

D. Burgreen and F. R. Nakache. Electrokinetic flow in ultrafine capillary slits. *J. Phys. Chem.*, 68:1084–1091, 1964. (Cited on pages 172, 186, 209, 215, 223, and 245.)

M. B. Bush. The stagnation flow behind a sphere. *J. Non-Newtonian Fluid Mech.*, 49(1):103–122, 1993. (Cited on pages 34 and 87.)

M. B. Bush. On the stagnation flow behind a sphere in a shear-thinning viscoelastic liquid. *J. Non-Newtonian Fluid Mech.*, 55(3):229–247, 1994. (Cited on pages 89 and 90.)

J. A. Byars. *Experimental characterization of viscoelastic flow instabilities*. PhD thesis, Cambridge: Massachusetts Institute of Technology, 1995. (Cited on page 28.)

J. A. Byars, R. C. Armstrong, R. A. Brown, and G. H. McKinley. Viscoelastically-driven instabilities in polymer processing. *ANTEC'95.*, I–Processing:1101–1105, 7-11 May 1995. (Cited on page 28.)

P. J. Cable and D. V. Boger. A comprehensive experimental investigation of tubular entry flow of viscoelastic fluids. part i - vortex characteristics in stable flow. *AIChE J.*, 24:869–879, 1978a. (Cited on pages 13, 39, 44, 113, and 114.)

P. J. Cable and D. V. Boger. A comprehensive experimental investigation of tubular entry flow of viscoelastic fluids. part ii - the velocity field in stable flow. *AIChE J.*, 24:992–999, 1978b. (Cited on pages 13, 39, 44, 113, and 114.)

P. J. Cable and D. V. Boger. A comprehensive experimental investigation of tubular entry flow of viscoelastic fluids. part iii - unstable flow. *AIChE J.*, 25:152–159, 1979. (Cited on pages 13, 39, 44, 48, 113, and 114.)

O. Cadot and A. Kumar. Experimental characterization of viscoelastic effects on two- and three- dimensional shear instabilities. *Journal of Fluid Mechanics*, 416:151–172, 2000. (Cited on page 48.)

A. E. Caola, Y. L. Joo, R. C. Armstrong, and R. A. Brown. Highly parallel time integration of viscoelastic flows. *J. Non-Newtonian Fluid Mech.*, 100(1-3):191–216, 2001. (Cited on pages 29, 87, and 88.)

U. Cartalos and J. M. Piau. Creeping flow regimes of low concentration polymer solutions in thick solvents through an orifice die. *J. Non-Newtonian Fluid Mech.*, 45(2):231–285, 1992. (Cited on page 40.)

A. Cauchy. De la pression ou tension dans un corps solide. *Exercices de Mathématiques*, 2:42, 1827. (Cited on page 4.)

S. Chakraborty. Dynamics of capillary flow of blood into a microfluidic channel. *Lab on a Chip*, 5(4):421–430, 2005. (Cited on page 173.)

S. Chakraborty. Electro-osmotically driven capillary transport of typical non-Newtonian biofluids in rectangular microchannels. *Anal. Chim. Acta*, 605:175–184, 2007. (Cited on pages 173, 216, and 230.)

C. H. Chen and J. G. Santiago. A planar electroosmotic micropump. *Journal of Microelectromechanical Systems*, 11(6):672–683, 2002. (Cited on page 229.)

K. Chiba, T. Sakatani, and K. Nakamura. Anomalous flow patterns in viscoelastic entry flow through a planar contraction. *J. Non-Newtonian Fluid Mech.*, 36:193–203, 1990. (Cited on pages 44, 113, 114, and 125.)

K. Chiba, I. Yoshida, S. Sako, and N. Mori. Anomalous Entry Flow Patterns in the Transition Regime to Global Flow Instability Generated after Vortex Enhancement. *Journal of the Society of Rheology*, 32 (5):303–311, 2004. (Cited on pages 48 and 130.)

M. D. Chilcott and J. M. Rallison. Creeping flow of dilute polymer solutions past cylinders and spheres. *J. Non-Newtonian Fluid Mech.*, 29:381–432, 1988. (Cited on pages 21, 24, and 91.)

K. S. Cho. Vector decomposition of the evolution equations of the conformation tensor of Maxwellian fluids. *Korea-Australia Rheology Journal*, 21(2):143–146, 2009. (Cited on page 24.)

A. Chow, A. Keller, J. A. Müller, and J. A. Odell. Entanglements in polymer solutions under elongational flow: a combined study of chain stretching, flow velocimetry and elongational viscosity. *Macromolecules*, 21:250–256, 1988. (Cited on pages 13, 49, 54, 143, and 158.)

P. J. Coates, R. C. Armstrong, and R. A. Brown. Calculation of steady-state viscoelastic flow through axisymmetric contractions with the EEME formulation. *J. Non-Newtonian Fluid Mech.*, 42(1-2):141–188, 1992. (Cited on page 101.)

T. Cochrane, K. Walters, and M. F. Webster. On newtonian and non-newtonian flow in complex geometries. *Phil. Trans. R. Soc. Lond. A*, 301(1460):163–181, May 1981. doi: 10.1098/rsta.1981.0103. (Cited on pages 42, 53, 54, 157, 163, 164, 168, and 263.)

P. M. Coelho and F. T. Pinho. Vortex shedding in cylinder flow of shear-thinning fluids:: I. Identification and demarcation of flow regimes. *J. Non-Newtonian Fluid Mech.*, 110(2-3):143–176, 2003a. (Cited on pages 27 and 48.)

P. M. Coelho and F. T. Pinho. Vortex shedding in cylinder flow of shear-thinning fluids: II. Flow characteristics. *J. Non-Newtonian Fluid Mech.*, 110(2-3):177–193, 2003b. (Cited on pages 27 and 48.)

P. M. Coelho and F. T. Pinho. Vortex shedding in cylinder flow of shear-thinning fluids. III:: Pressure measurements. *J. Non-Newtonian Fluid Mech.*, 121(1):55–68, 2004. (Cited on pages 27 and 48.)

F. N. Cogswell. Converging flow and stretching flow: a compilation. *J. Non-Newtonian Fuid Mech.*, 4:23–38, 1978. (Cited on page 48.)

O. M. Coronado. *Finite element methods for viscoelastic fluid flow simulations: Formulations and applications*. PhD thesis, Rice University, 2009. (Cited on page 25.)

O. M. Coronado, D. Arora, M. Behr, and M. Pasquali. A simple method for simulating general viscoelastic fluid flows with an alternate log-conformation formulation. *J. Non-Newtonian Fluid Mech.*, 147(3):189–199, 2007. (Cited on pages 29, 30, 68, 69, 74, 76, 77, 78, 116, 119, and 145.)

M. J. Crochet and K. Walters. Numerical methods in non-newtonian fluid mechanics. *Annu. Rev. Fluid Mech.*, 15:241–260, 1983. (Cited on pages 12 and 38.)

M. J. Crochet, A. R. Davies, and K. Walters. *Numerical Simulation of Non-Newtonian Flow*. Elsevier, Amsterdam, 1984. (Cited on page 8.)

D. O. A. Cruz and F. T. Pinho. Skewed poiseuille-couette flows of sptt fluids in concentric annuli and channels. *J. Non-Newtonian Fluid Mech.*, 121(1):1–14, 2004. (Cited on page 172.)

D. O. A. Cruz and F. T. Pinho. Fully-developed pipe and planar flows of multimode viscoelastic fluids. *J. Non-Newtonian Fluid Mech.*, 141 (2-3):85–98, 2007. (Cited on page 172.)

D. O. A. Cruz, F. T. Pinho, and P. J. Oliveira. Analytical solutions for fully developed laminar flow of some viscoelastic liquids with a newtonian solvent contribution. *J. Non-Newtonian Fluid Mech.*, 132 (1-3):28–35, 2005. (Cited on pages 172, 184, 185, 207, and 208.)

H. Damanik, J. Hron, A. Ouazzi, and S. Turek. A monolithic FEM approach for the log-conformation reformulation (LCR) of viscoelastic flow problems. *in press J. Non-Newtonian Fluid Mech.*, 2010. (Cited on pages 29, 30, 32, and 33.)

S. Das and S. Chakraborty. Analytical solutions for velocity, temperature and concentration distribution in electroosmotic microchannel flows in a non-Newtonian bio-fluid. *Anal. Chim. Acta*, 559:25–24, 2006. (Cited on pages 59, 173, 216, 230, and 245.)

J. M. Dealy. Weissenberg and deborah numbers - their definition and use. *Rheology Bulletin (Soc. of Rheol.)*, 79(2):14–18, 2010. (Cited on page 12.)

B. Debbaut and M. J. Crochet. Further results on the flow of a viscoelastic fluid through an abrupt contraction. *J. Non-Newtonian Fuid Mech.*, 20:173–185, 1986. (Cited on pages 38 and 42.)

P. Debye and E. Hückel. Zur Theorie der Elektrolyte II Physik. *Z*, 24:15, 1923. (Cited on pages 245 and 246.)

M. M. Denn. Boundary layer flows for a class of elastic fluids. *Chemical Engineering Science*, 22(3):395–405, March 1967. (Cited on page 8.)

M. M. Denn. Extrusion instabilities and wall slip. *Annual Review of Fluid Mechanics*, 33:265–287, January 2001. (Cited on pages 13 and 47.)

M. M. Denn. Fifty years of non-newtonian fluid dynamics. *AIChE Journal*, 50 10:2335–2345, 2004. (Cited on pages 4, 5, and 9.)

S. A. Dhahir and K. Walters. On non-Newtonian flow past a cylinder in a confined flow. *Journal of Rheology*, 33:781, 1989. (Cited on pages 27 and 29.)

S. Dhinakaran, A. M. Afonso, M. A. Alves, and F. T. Pinho. Steady viscoelastic fluid flow in microchannels under electrokinetic forces: Ptt model. *Journal of Colloid And Interface Science*, 344:513–520, 2010. doi: 10.1016/j.jcis.2010.01.025. (Cited on pages xi, 59, 60, 66, 198, and 215.)

D. Doraiswamy. The origins of rheology: a short historical excursion. *Rheology Bulletin*, 71:7–17, 2002. (Cited on page 4.)

H. S. Dou and N. Phan-Thien. The flow of an Oldroyd-B fluid past a cylinder in a channel: adaptive viscosity vorticity (DAVSS-ω) formulation. *J. Non-Newtonian Fluid Mech.*, 87(1):47–73, 1999. (Cited on pages 26 and 29.)

H. S. Dou and N. Phan-Thien. Negative wake in the uniform flow past a cylinder. *Rheologica Acta*, 42(5):383–409, 2003. (Cited on pages 35, 36, 37, 81, 89, 90, 91, 94, 95, 96, 97, 98, 99, 102, 104, 105, 106, and 111.)

H. S. Dou and N. Phan-Thien. Criteria of negative wake generation behind a cylinder. *Rheologica Acta*, 43(3):203–209, 2004. (Cited on pages 34, 35, 88, 90, 99, 102, and 104.)

H. S. Dou and N. Phan-Thien. An instability criterion for viscoelastic flow past a confined cylinder. *Korea-Australia Rheology Journal*, 20(1): 15–26, 2008. (Cited on pages 28 and 48.)

D. Drikakis. *Uniformly high-order methods for unsteady incompressible flows. Godunov Methods: Theory and Applications*. Kluwer Academic Publishers, e.f. toro edition, 2001. (Cited on page 23.)

F. Dupret and J. M. Marchal. Loss of evolution in the flow of viscoelastic fluid. *J. Non-Newtonian Fluid Mech.*, 20:143–171, 1986. (Cited on pages 22, 38, 42, and 94.)

P. Dutta and A. Beskok. Analytical solution of combined electro-osmotic/pressure driven flows in two-dimensional straight channels: finite debye layer effects. *Anal. Chem.*, 73:1979–1986, 2001. (Cited on pages 172, 185, 186, 208, 215, and 245.)

P. Dutta, A. Beskok, and T. C. Warburton. Electroosmotic flow control in complex microgeometries. *Microelectromechanical Systems, Journal of*, 11(1):36–44, 2002a. (Cited on page 246.)

P. Dutta, A. Beskok, and T. C. Warburton. Numerical simulation of mixed electroosmotic/pressure driven microflows. *Numerical Heat Transfer, Part A: Applications*, 41(2):131–148, 2002b. (Cited on page 246.)

R. Edgeworth, B.J. Dalton, and T. Parnell. The pitch drop experiment. *Eur. J. Phys*, pages 198–200, 1984. URL `www.physics.uq.edu.au/physics_museum/pitchdrop.shtml`. (Cited on page 5.)

M. El Hadj and P. A. Tanguy. A finite element procedure coupled with the method of characteristics for simulation of viscoelastic fluid flow. *J. Non-Newtonian Fluid Mech.*, 36:333–349, 1990. (Cited on pages 125 and 131.)

S. V. Ermakov, S. C. Jacobson, and J. M. Ramsey. Computer simulations of electrokinetic transport in microfabricated channel structures. *Anal. Chem*, 70(21):4494–4504, 1998. (Cited on page 246.)

P. Español, X. F. Yuan, and R. C. Ball. Shear banding flow in the Johnson-Segalman fluid. *J. Non-Newtonian Fluid Mech.*, 65:93–109, 1996. (Cited on page 217.)

L. Euler. Continuation des recherches sur la théorie du mouvement des fluides. *Mémoires de l'académie des sciences de Berlin*, 11:316–361, 1755. (Cited on pages 3, 4, and 7.)

R. E. Evans and K. Walters. Flow characteristics associated with abrupt changes in geometry in the case of highly elastic liquids. *J. Non-Newtonian Fuid Mech.*, 20:11–29, 1986. (Cited on page 40.)

R. E. Evans and K. Walters. Further remarks on the lip-vortex mechanism of vortex enhancement in planar-contraction flows. *J. Non-Newtonian Fuid Mech.*, 32(1):95–105, 1989. (Cited on page 40.)

V. M. Falkner and S. W. Skan. Some approximate solutions of the boundary layer equations. *Philos. Mag.*, 12:865–896, 1931. (Cited on page 8.)

H. Fam, J. T. Bryant, and M. Kontopoulou. Rheological properties of synovial fluids. *Biorheology*, 44(2):59–74, 2007. (Cited on page 173.)

Y. Fan, R. I. Tanner, and N. Phan-Thien. Galerkin/least-square finite-element methods for steady viscoelastic flows. *J. Non-Newtonian Fluid Mech.*, 84(2-3):233–256, 1999. (Cited on pages 26, 29, 32, 74, 76, 77, 78, 87, and 88.)

R. Fattal and R. Kupferman. Constitutive laws for the matrix-logarithm of the conformation tensor. *J. Non-Newtonian Fluid Mech.*, 123(2-3): 281–285, November 2004. doi: 10.1016/j.jnnfm.2004.08.008. (Cited on pages 15, 22, 23, 24, 29, 30, 43, 45, 67, 68, 71, 72, 85, 113, 116, 118, 140, 145, 146, 159, 249, and 261.)

R. Fattal and R. Kupferman. Time-dependent simulation of viscoelastic flows at high Weissenberg number using the log-conformation representation. *J. Non-Newtonian Fluid Mech.*, 126(1):23–37, 2005. (Cited on pages 24, 29, 43, 68, and 116.)

J. H. Ferziger. *Numerical methods for engineering application*. Wiley New York, 1981. (Cited on page 162.)

N. Fiétier. *Numerical simulation of viscoelastic fluid flows by spectral element methods and time-dependent algorithms*. PhD thesis, FACULTE DES SCIENCES ET TECHNIQUES DE L'INGENIEUR, LAUSANNE, 2002. (Cited on pages 53, 157, and 158.)

M. Fortin and D. Esselaoui. A finite element procedure for viscoelastic flows. *International Journal for Numerical Methods in Fluids*, 7(10):1035–1052, 1987. (Cited on pages 125 and 131.)

G. G. Fuller and L. G. Leal. Flow birefringence of dilute polymer solutions in two-dimensional flows. *Rheologica Acta*, 19(5):580–600, 1980. (Cited on page 151.)

G. G. Fuller, C. A. Cathey, B. Hubbard, and B. E. Zebrowski. Extensional viscosity measurements for low viscosity fluids. *Journal of Rheology*, 31:235–249, 1987. (Cited on page 49.)

R. B. Fuller. Buckminster fuller: Thinking out loud. American Masters TV Documentary, 1996. (Cited on pages 65 and 267.)

M. M. Fyrillas, G. C. Georgiou, and D. Vlassopoulos. Time-dependent plane poiseuille flow of a johnson-segalman fluid. *J. Non-Newtonian Fluid Mech.*, 82(1):105–123, 1999. (Cited on page 172.)

Y. Gao, T. N. Wong, C. Yang, and K. T. Ooi. Two-fluid electroosmotic flow in microchannels. *Journal of colloid and interface science*, 284(1): 306–314, 2005. (Cited on pages 229, 232, 239, and 240.)

K. Gardner, E. R. Pike, M. J. Miles, A. Keller, and K. Tanaka. Photon-correlation velocimetry of polystyrene solutions in extensional flow fields. *Polymer*, 23:1435–1442, 1982. (Cited on pages 13, 48, and 49.)

P. H. Gaskell and A. K. C. Lau. Curvature-compensated convective transport: SMART, a new boundedness-preserving transport algorithm. *International Journal for Numerical Methods in Fluids*, 8(6):617–641, 1988. (Cited on page 92.)

G. C. Georgiou and D. V. Vlassopoulos. On the stability of the simple shear flow of a Johnson-Segalman fluid. *J. Non-Newtonian Fluid Mech.*, 75:77–97, 1998. (Cited on page 217.)

M. I. Gerritsma. Direct minimization of the discontinuous least-squares spectral element method for viscoelastic fluids. *Journal of Scientific Computing*, 27(1):245–256, 2006. (Cited on pages 29, 87, and 88.)

H. Giesekus. Strömungen mit konstantem geschwindigkeitsgradienten und die bewegung von darin suspendierten teilchen teil i: Räumliche strömungen. *Rheol. Acta*, 2(2):101–112, 1962. (Cited on pages 13 and 48.)

H. Giesekus. Nicht-lineare effekte beim strömem viskoelasticher flüssigkeiten durch schlitz- und lochdüsen. *Rheol. Acta*, 7:127–138, 1968. (Cited on pages 13 and 48.)

H. Giesekus. A simple constitutive equation for polymer fluids based on the concept of deformation-dependent tensorial mobility. *J. Non-Newtonian Fluid Mech.*, 11(1-2):69–109, 1982. (Cited on pages 21 and 91.)

G. Gouy. Sur la Constitution de la Charge Électrique à la Surface dun Électrolyte. *J. Phys.*, 9:457–468, 1910. (Cited on pages 245 and 246.)

M. D. Graham. Interfacial hoop stress and instability of viscoelastic free surface flows. *Physics of Fluids*, 15:1702–1710, 2003. (Cited on pages 13 and 48.)

A. Groisman and V. Steinberg. Elastic turbulence in a polymer solution flow. *Nature*, 405(6782):53–55, 2000. (Cited on pages 47 and 144.)

A. Groisman and V. Steinberg. Elastic turbulence in curvilinear flows of polymer solutions. *New Journal of Physics*, 6:29, 2004. (Cited on page 144.)

R. Guénette, A. Fortin, A. Kane, and J. F. Hétu. An adaptive remeshing strategy for viscoelastic fluid flow simulations. *J. Non-Newtonian Fluid Mech.*, 153(1):34–45, 2008. (Cited on pages 29, 30, 68, 69, 76, 77, and 120.)

S. Gulati, S. J. Muller, and D. Liepmann. Direct measurements of viscoelastic flows of DNA in a 2: 1 abrupt planar micro-contraction. *J. Non-Newtonian Fuid Mech.*, 155(1-2):51–66, 2008. (Cited on page 42.)

J. Hadamard. Sur les problèmes aux dérivées partielles et leur signification physique. *Princeton University Bulletin*, 13(1):49–52, 1902. (Cited on pages 22 and 23.)

O. G. Harlen. The negative wake behind a sphere sedimenting through a viscoelastic fluid. *J. Non-Newtonian Fluid Mech.*, 108(1-3):411–430, 2002. (Cited on pages 34, 35, 89, 90, 102, and 104.)

O. Hassager. Negative wake behind bubbles in non-Newtonian liquids. *Nature*, 279:402–403, 1979. (Cited on pages 33, 88, and 89.)

O. Hassager. Working group on numerical techniques. In *Proceedings of the Vth Workshop on Numerical Methods in Non-Newtonian Flow, J. Non-Newtonian Fluid Mech*, volume 29, pages 2–5, 1988. (Cited on pages 25, 37, 38, 42, and 113.)

H. S. Hele-Shaw. The flow of water. *Nature*, 58(1489):33–36, 1898. (Cited on page 39.)

O. L. Hemminger, P. E. Boukany, S. Q. Wang, and L. J. Lee. Flow pattern and molecular visualization of DNA solutions through a 4: 1 planar micro-contraction. *J. Non-Newtonian Fuid Mech.*, 2010. (Cited on page 42.)

C. W. Hirt, A. A. Amsden, and J. L. Cook. An arbitrary lagrangian eulerian computing method for all flow speeds. *Journal of Computational Physics*, 14(3):227–253, 1974. (Cited on page 11.)

T. C. Ho and M. M. Denn. Stability of plane Poiseuille flow of a highly elastic liquid. *J. Non-Newtonian Fluid Mech.*, 3(2):179–195, 1977. (Cited on page 158.)

R. Hooke. *De Potentia Restitutiva (of Spring Explaining the Power of Springing Bodies)*, page 23. London, 1678. (Cited on page 4.)

K. D. Housiadas and A. N. Beris. An efficient fully implicit spectral scheme for DNS of turbulent viscoelastic channel flow. *J. Non-Newtonian Fluid Mech.*, 122(1-3):243–262, 2004. (Cited on page 23.)

K. D. Housiadas, L. Wang, and A. N. Beris. A new method preserving the positive definiteness of a second order tensor variable in flow simulations with application to viscoelastic turbulence. *Computers & Fluids*, 39(2):225–241, 2010. (Cited on page 23.)

J. S. Howell. Computation of viscoelastic fluid flows using continuation methods. *Journal of Computational and Applied Mathematics*, 225(1): 187–201, 2009. (Cited on page 127.)

C. C. Hsieh, S. J. Park, and R. G. Larson. Brownian dynamics modeling of flow-induced birefringence and chain scission in dilute polymer solutions in a planar cross-slot flow. *Macromolecules*, 38(4):1456–1468, 2005. (Cited on page 49.)

H. H. Hu and D. D. Joseph. Numerical simulation of viscoelastic flow past a cylinder. *J. Non-Newtonian Fluid Mech.*, 37(2-3):347–377, 1990. (Cited on pages 29 and 87.)

P. Y. Huang and J. Feng. Wall effects on the flow of viscoelastic fluids around a circular cylinder. *J. Non-Newtonian Fluid Mech.*, 60(2-3): 179–198, 1995. (Cited on pages 29, 35, 87, 88, and 89.)

R. R. Huilgol and N. Phan-Thien. *Fluid mechanics of viscoelasticity*. Elsevier, Amsterdam, 1997. (Cited on page 8.)

M. A. Hulsen. Some properties and analytical expressions for plane flow of Leonov and Giesekus models. *J. Non-Newtonian Fluid Mech*, 30:85–92, 1988. (Cited on pages 32, 71, 75, 79, and 93.)

M. A. Hulsen, R. Fattal, and R. Kupferman. Flow of viscoelastic fluids past a cylinder at high Weissenberg number: stabilized simulations using matrix logarithms. *J. Non-Newtonian Fluid Mech.*, 127(1):27–39, 2005. (Cited on pages 26, 29, 30, 32, 33, 68, 69, 74, 76, 77, 78, 81, 109, 116, 119, 123, and 145.)

J. A. C. Humphrey and S. Li. Tilting, Stretching, Pairing and Collapse of Vortex Structures in Confined Counter-Current Flow. *Journal of Fluids Engineering*, 103:466, 1981. (Cited on pages 53, 54, 157, and 158.)

J. A. C. Humphrey, J. L. Rosales, L. A. Legendre, J. P. LeDuc, and J. P. Landers. Vortex dynamics in confined counter-current shearing flows with applications to mixing. *International Journal of Heat and Fluid Flow*, 29(4):1089–1102, 2008. (Cited on pages 53, 54, 157, and 158.)

F. Ilinca, J. F. Hétu, and D. Pelletier. A unified finite element algorithm for two-equation models of turbulence. *Computers & Fluids*, 27(3): 291–310, 1998. (Cited on pages 23 and 68.)

N. Islam and J. Wu. Microfluidic transport by AC electroosmosis. In *Journal of Physics: Conference Series*, volume 34, page 356. IOP Publishing, 2006. (Cited on page 197.)

F. Jacon and D. Knight. A navier-stokes algorithm for turbulent flows using an unstructured grid and flux difference splitting, 1994. (Cited on page 23.)

A. Jafari, N. Fiétier, and M. O. Deville. A new extended matrix logarithm formulation for the simulation of viscoelastic fluids by spectral elements. *Computers & Fluids*, 39:1425–1438, 2010. (Cited on pages 29 and 30.)

G. Jaumann. *Grundlagen der Bewegungslehre*. Springer, Leipzig, 1905. (Cited on page 8.)

R. M. Jendrejack, E. T. Dimalanta, D. C. Schwartz, M. D. Graham, and J. J. de Pablo. Dna dynamics in a microchannel. *Physical review letters*, 91(3):38102, 2003. (Cited on page 172.)

H. Jin, N. Phan-Thien, and R. I. Tanner. A finite element analysis of the flow past a sphere in a cylindrical tube: PTT fluid model. *Computational Mechanics*, 8(6):409–422, 1991. (Cited on page 89.)

Y. L. Joo and E. S. G. Shaqfeh. A purely elastic instability in Dean and Taylor-Dean flow. *Phys. Fluids A*, 4(3):524–543, 1992. (Cited on pages 144 and 158.)

D. D. Joseph. *Fluid Dynamics of Viscoelastic Liquids*. Springer-Verlag, New York, 1990. (Cited on pages 8, 22, and 23.)

D. D. Joseph and J. C. Saut. Change of type and loss of evolution in the flow of viscoelastic fluids. *J. Non-Newtonian Fuid Mech.*, 20:117–141, 1986. (Cited on pages 38 and 42.)

S. L. Josse, K. C. Lee, and B. A. Finlayson. False bifurcations and instability of a maxwell fluid in fully developed flow. *J. Non-Newtonian Fuid Mech.*, 20:257–269, 1986. (Cited on pages 38 and 42.)

A. Kane, R. Guénette, and A. Fortin. A comparison of four implementations of the log-conformation formulation for viscoelastic fluid flows. *J. Non-Newtonian Fluid Mech.*, 164(1-3):45–50, 2009. (Cited on pages 29, 30, 116, and 145.)

G. Karniadakis, A. Beskok, and N. Aluru. *Microflows and nanoflows. Fundamentals and Simulation*, volume 29 of *Interdisciplinary Applied Mathematics Series*. Spinger Verlag, 2005. (Cited on pages 14, 59, 173, and 245.)

W. Thomson (Lord Kelvin). On the elasticity and viscosity of metals. *Proc. Roy. Soc. London*, 14:289–297, 1865. (Cited on page 8.)

R. Keunings. On the high weissenberg number problem. *J. Non-Newtonian Fluid Mech.*, 20:209–226, 1986. (Cited on pages 13, 22, 38, and 42.)

R. Keunings. Simulation of viscoelastic fluid flow. *Fundamentals of computer modeling for polymer processing*, 1989. (Cited on pages 37, 38, 42, and 113.)

R. Keunings. Micro-macro methods for the multiscale simulation of viscoelastic flow using molecular models of kinetic theory. *Rheology Reviews*, pages 67–98, 2004. (Cited on pages 11 and 115.)

J. H. Kim, A. Öztekin, and S. Neti. Instabilities in viscoelastic flow past a square cavity. *J. Non-Newtonian Fluid Mech.*, 90:261–281, 2000. (Cited on pages 13 and 48.)

J. M. Kim, C. Kim, K. H. Ahn, and S. J. Lee. An efficient iterative solver and high precision solutions of the Oldroyd-B fluid flow past a confined cylinder. *J Non-Newtonian Fluid Mech*, 123:161–173, 2004. (Cited on pages 26, 29, 32, 35, 76, 77, 78, 87, 88, and 89.)

J. M. Kim, C. Kim, C. Chung, K. H. Ahn, and S. J. Lee. Negative wake generation of fene-cr fluids in uniform and poiseuille flows past a cylinder. *Rheol Acta*, 44:600–613, 2005a. (Cited on pages 35, 36, 37, 87, 89, 90, 91, 94, 96, 97, 102, 103, and 111.)

J. M. Kim, C. Kim, J. H. Kim, C. Chung, K. H. Ahn, and S. J. Lee. High-resolution finite element simulation of 4: 1 planar contraction flow of viscoelastic fluid. *J. Non-Newtonian Fluid Mech.*, 129(1):23–37, 2005b. (Cited on pages 43, 94, and 121.)

A. P. Koppol, R. Sureshkumar, A. Abedijaberi, and B. Khomami. Anomalous pressure drop behaviour of mixed kinematics flows of viscoelastic polymer solutions: a multiscale simulation approach. *Journal of Fluid Mechanics*, 631:231–253, 2009. (Cited on pages 45, 115, and 140.)

A. T. Kuo, C. H. Chang, and H. H. Wei. Transient currents in electrolyte displacement by asymmetric electro-osmosis and determination of surface zeta potentials of composite microchannels. *Applied Physics Letters*, 92:244102, 2008. (Cited on page 197.)

A. Kurganov and E. Tadmor. New high-resolution central schemes for nonlinear conservation laws and convection-diffusion equations. *Journal of Computational Physics*, 160(1):241–282, 2000. (Cited on page 23.)

Y. Kwon. Finite element analysis of planar 4: 1 contraction flow with the tensor-logarithmic formulation of differential constitutive equations. *Korea-Australia Rheology Journal*, 16(4):183–191, 2004. (Cited on pages 29, 30, 43, 68, 69, 116, and 145.)

Y. Kwon. Numerical analysis of viscoelastic flows in a channel obstructed by an asymmetric array of obstacles. *Korea–Australia Rheol. J*, 18:161–167, 2006. (Cited on pages 68, 69, and 116.)

R. R. Lagnado, N. Phan-Thien, and L. G. Leal. The stability of two-dimensional linear flows. *Physics of Fluids*, 27:1094–1101, 1984. (Cited on page 143.)

H. Lamb. *Hydrodynamics*. Cambridge University Press, Cambridge, UK, 6th edition, 1932. (Cited on page 171.)

R. G. Larson. *Constitutive Equations for Polymer Melts and Solutions*. Butterworths, Boston, 1998. (Cited on pages 8 and 217.)

R. G. Larson. *The structure and rheology of complex fluids*. Oxford University Press, 1999. (Cited on page 8.)

R. G. Larson. Turbulence without inertia. *Nature*, 405:27, 2000. (Cited on page 47.)

R. G. Larson, E. S. G. Shaqfeh, and S. J. Muller. A purely elastic instability in Taylor–Couette flow. *Journal of Fluid Mechanics*, 218: 573–600, 2006. (Cited on pages 13, 143, and 144.)

J. S. Lee, R. Dylla-Spears, N. P. Teclemariam, and S. J. Muller. Microfluidic four-roll mill for all flow types. *Applied Physics Letters*, 90:074103, 2007. (Cited on pages 119 and 151.)

Y. J. Lee and J. Xu. New formulations, positivity preserving discretizations and stability analysis for non-Newtonian flow models. *Computer methods in applied mechanics and engineering*, 195(9-12):1180–1206, 2006. (Cited on page 24.)

A. I. Leonov and A. N. Prokunin. *Nonlinear phenomena in flows of viscoelastic polymer fluids*. Kluwer Academic Publishers, London, UK, 1st edition, 1994. (Cited on page 8.)

S. Levine, J. R. Marriott, G. Neale, and N. Epstein. Theory of electrokinetic flow in fine cylindrical capillaries at high zeta-potentials. *Journal of Colloid and Interface Science*, 52(1):136–149, 1975. (Cited on page 172.)

G. Lielens, R. Keunings, and V. Legat. The FENE-L and FENE-LS closure approximations to the kinetic theory of finitely extensible dumbbells. *J. Non-Newtonian Fluid Mech.*, 87:179–196, 1999. (Cited on pages 11 and 115.)

H. Lin, B. D. Storey, M. H. Oddy, C. H. Chen, and J. G. Santiago. Instability of electrokinetic microchannel flows with conductivity gradients. *Phys. Fluids*, 16(6):1922–1935, 2004. (Cited on page 216.)

J. Y. Lin, L. M. Fu, and R. J. Yang. Numerical simulation of electrokinetic focusing in microfluidic chips. *Journal of micromechanics and microengineering*, 12:955, 2002. (Cited on page 246.)

A. W. Liu, D. E. Bornside, R. C. Armstrong, and R. A. Brown. Viscoelastic flow of polymer solutions around a periodic, linear array of cylinders: comparisons of predictions for microstructure and flow fields. *J. Non-Newtonian Fluid Mech.*, 77(3):153–190, 1998. (Cited on pages 25, 26, 29, 87, and 88.)

A. Lozinski and R. G. Owens. An energy estimate for the Oldroyd B model: theory and applications. *J. Non-Newtonian Fluid Mech.*, 112 (2-3):161–176, 2003. (Cited on page 23.)

M. E. Mackay and D. V. Boger. An explanation of the rheological properties of Boger fluids. *J. Non-Newtonian Fuid Mech.*, 22(2):235–243, 1987. (Cited on page 40.)

G. M. Mala, D. Li, and J. D. Dale. Heat transfer and fluid flow in microchannels. *International Journal of Heat and Mass Transfer*, 40(13): 3079–3088, 1997. (Cited on page 184.)

O. Manero and B. Mena. On the slow flow of viscoelastic liquids past a circular cylinder. *J. Non-Newtonian Fluid Mech.*, 9(3-4):379–387, 1981. (Cited on page 87.)

P. Manneville. *Instabilities, Chaos and Turbulence*. Imperial College Press, World Scientific, London, UK, 2004. (Cited on pages 13 and 47.)

T. S. Mansuripur, A. J. Pascall, and T. M. Squires. Asymmetric flows over symmetric surfaces: capacitive coupling in induced-charge electro-osmosis. *New Journal of Physics*, 11:075030, 2009. (Cited on page 197.)

J. M. Marchal and M. J. Crochet. Hermitian finite elements for calculating viscoelastic flow. *J. Non-Newtonian Fuid Mech.*, 20:187–207, 1986. (Cited on pages 38 and 42.)

H. Matallah, P. Townsend, and M. F. Webster. Recovery and stress-splitting schemes for viscoelastic flows. *J. Non-Newtonian Fuid Mech.*, 75(2-3):139–166, 1998. (Cited on page 43.)

J. C. Maxwell. On the dynamical theory of gases. *Phil. Trans. R. Soc. Lond.*, A157:49–88, 1867. (Cited on pages 3 and 8.)

G. H. McKinley. Dimensionless groups for understanding free surface flows of complex fluids. *Rheol Bulletin (Soc. of Rheol.)*, 72(2):6–9,18–19, 2005. (Cited on page 12.)

G. H. McKinley, J. A. Byars, R. A. Brown, and R. C. Armstrong. Observations on the elastic instability in cone-and-plate and parallel-plate flows of a polyisobutylene boger fluid. *J. Non-Newtonian Fluid Mech.*, 40(2):201–229, 1991a. (Cited on page 13.)

G. H. McKinley, W. P. Raiford, R. A. Brown, and R. C. Armstrong. Nonlinear dynamics of viscoelastic flow in axisymmetric abrupt contractions. *Journal of Fluid Mechanics*, 223:411–456, 1991b. (Cited on pages 38, 40, 44, 45, 46, 113, 114, 115, 116, 125, and 262.)

G. H. McKinley, R. C. Armstrong, and R. A. Brown. Ldv measurements of viscoelastic flow instabilities in the wake of confined circular cylinders. *Theoretical and Applied Rheology*, 1:27–32, 1992. (Cited on pages 26, 27, and 28.)

G. H. McKinley, R. C. Armstrong, and R. A. Brown. The wake instability in viscoelastic flow past confined circular cylinders. *Philosophical Transactions: Physical Sciences and Engineering*, 344(1671):265–304, 1993. (Cited on pages 25, 26, 27, 28, 29, 34, 68, 74, 79, 87, 89, 99, 101, 104, and 109.)

G. H. McKinley, P. Pakdel, and A. Öztekin. Rheological and geometric scaling of purely elastic flow instabilities. *J. Non-Newtonian Fluid Mech.*, 67:19–47, 1996. (Cited on pages 13, 28, 48, 52, 144, 149, 154, and 158.)

G. R. McNamara and G. Zanetti. Use of the boltzmann equation to simulate lattice-gas automata. *Phys. Rev. Lett.*, 61:2332–2335, 1988. (Cited on page 11.)

S. Meng, X. K. Li, and G. Evans. Numerical simulation of oldroyd-b fluid in a contraction channel. *The Journal of Supercomputing*, 22(1): 29–43, 2002. (Cited on page 43.)

A. B. Metzner and R. E. Otto. Agitation of non-newtonian fluids. *AIChE Journal*, 3(1):3–10, March 1957. (Cited on page 8.)

A. B. Metzner and J. C. Reed. Flow of non-newtonian fluids - correlation of the laminar, transition, and turbulent-flow regions. *AIChE Journal*, 1(4):434–440, December 1955. (Cited on page 8.)

O. E. Meyer. Theorie der elastischen nachwirkung. *Annalen der Physik*, 227(1):108–119, 1874. (Cited on page 8.)

J. M. Miranda and J. B. L. M. Campos. An improved numerical scheme to study mass transfer over a separation membrane. *Journal of Membrane Science*, 188(1):49–59, 2001. (Cited on pages 23 and 68.)

M. Mirzazadeh, M. P. Escudier, F. Rashidi, and S. H. Hashemabadi. Purely tangential flow of a ptt-viscoelastic fluid within a concentric annulus. *J. Non-Newtonian Fluid Mech.*, 129(2):88–97, 2005. (Cited on page 172.)

E. Mitsoulis and S. G. Hatzikiriakos. Modelling PTFE paste extrusion: The effect of an objective flow type parameter. *J. Non-Newtonian Fluid Mech.*, 159(1-3):41–49, 2009. (Cited on page 151.)

H. K. Moffatt. Viscous and resistive eddies near a sharp comer. *Journal of Fluid Mechanics*, 18:1–18, 1964. (Cited on pages 39 and 137.)

J. J. Monaghan. An introduction to sph. *Computer Physics Communications*, 48:88–96, 1988. (Cited on page 11.)

A. N. Morozov and W. van Saarloos. An introductory essay on subcritical instabilities and the transition to turbulence in visco-elastic parallel shear flows. *Physics Reports*, 447(3-6):112–143, August 2007. (Cited on pages 13, 158, and 163.)

M. Moyers-Gonzalez, R. G. Owens, and J. Fang. A non-homogeneous constitutive model for human blood. Part 1. Model derivation and steady flow. *Journal of Fluid Mechanics*, 617:327–354, 2008. (Cited on page 173.)

S. J. Muller, R. G. Larson, and E. S. G. Shaqfeh. A purely elastic transition in Taylor-Couette flow. *Rheologica Acta*, 28(6):499–503, 1989. (Cited on pages 13 and 143.)

S. J. Muller, E. S. G. Shaqfeh, R. G. Larson, et al. Experimental studies of the onset of oscillatory instability in viscoelastic Taylor-Couette flow. *J. Non-Newtonian Fluid Mech.*, 46(2-3):315–330, 1993. (Cited on pages 13 and 143.)

C. L. M. H. Navier. Mémoire sur les lois du mouvement des fluides. *Mém. Acad. Sci. Inst. France*, 6:389–440, 1822. (Cited on pages 3 and 7.)

W. Nernst. Uber die Berechnung chemischer Gleichgewichte aus thermischen Messungen. *Nachr. Kgl. Ges. d. Wiss. Gottingen*, 6:1–40, 1906. (Cited on page 14.)

S. I. Newton. *Philosophiae Naturalis Principia Mathematica*. Bk2, 1st edition, 1687. (Cited on pages 3, 4, 6, and 19.)

H. Nguyen and D. V. Boger. The kinematics and stability of die entry flows. *J. Non-Newtonian Fluid Mech.*, 5:353–368, 1979. (Cited on pages 39 and 40.)

N. T. Nguyen and S. T. Wereley. *Fundamentals and applications of microfluidics*. Artech House Publishers, 2002. (Cited on page 197.)

S. Nigen and K. Walters. Viscoelastic contraction flows: comparison of axisymmetric and planar configurations. *J. Non-Newtonian Fluid Mech.*, 102(2):343–359, 2002. (Cited on page 41.)

J. A. Odell, A. J. Muller, K. A. Narh, and A. Keller. Degradation of polymer solutions in extensional flows. *Macromolecules*, 23(12):3092–3103, 1990. (Cited on page 49.)

Heraclitus of Ephesus. Die fragmente der vorsokratiker - dk22b12, 540–475 BC. (Cited on pages 3, 4, and 261.)

Archimedes of Syracuse. *Archimedes Palimpsest*. 200 BC. URL www.archimedespalimpsest.org. (Cited on page 3.)

J. G. Oldroyd. On the formulation of rheological equations of state. *Proceedings of the Royal Society of London. Series A, Mathematical and Physical Sciences*, 200(1063):523–541, 1950. (Cited on pages 8 and 117.)

M. L. Olivares, L. V. Candiotti, and C. L. A. Berli. The eof of polymer solutions. *Electrophoresis*, 30:921–929, 2009. (Cited on page 216.)

M. S. N. Oliveira, L. E. Rodd, G. H. McKinley, and M. A. Alves. Simulations of extensional flow in microrheometric devices. *Microfluidics and Nanofluidics*, 5(6):809–826, 2008. (Cited on page 42.)

M. S. N. Oliveira, F. T. Pinho, R. J. Poole, P. J. Oliveira, and M. A. Alves. Purely elastic flow asymmetries in flow-focusing devices. *J. Non-Newtonian Fluid Mech.*, 160(1):31–39, 2009. (Cited on pages 143, 147, 155, and 168.)

P. J. Oliveira. Method for time-dependent simulations of viscoelastic flows: vortex shedding behind cylinder. *J. Non-Newtonian Fluid Mech.*, 101(1-3):113–137, 2001a. (Cited on pages 29, 80, and 167.)

P. J. Oliveira. On the numerical implementation of nonlinear viscoelastic models in a finite-volume method. *Numerical Heat Transfer, Part B: Fundamentals*, 40(4):283–301, 2001b. (Cited on pages 92 and 96.)

P. J. Oliveira. Time-dependent simulations of shear-thinning elastic flows through contractions. *Proceedings of 2001 ASME - IMECE, New York*, 2001c. (Cited on page 125.)

P. J. Oliveira. An exact solution for tube and slit flow of a fene-p fluid. *Acta Mechanica*, 158(3):157–167, 2002. (Cited on pages 172 and 208.)

P. J. Oliveira and A. I. P. Miranda. A numerical study of steady and unsteady viscoelastic flow past bounded cylinders. *J. Non-Newtonian Fluid Mech.*, 127(1):51–66, 2005. (Cited on pages 29, 70, 71, 79, 83, 87, 96, and 102.)

P. J. Oliveira and F. T. Pinho. Plane contraction flows of upper convected maxwell and phan-thien-tanner fluids as predicted by a finite-volume method. *J. Non-Newtonian Fluid Mech.*, 88:63–88, 1999a. (Cited on pages 15, 38, 43, 113, 116, 118, and 121.)

P. J. Oliveira and F. T. Pinho. Numerical procedure for the computation of fluid flow with arbitrary stress-strain relationships. *Numer. Heat Transfer B*, 35:295–315, 1999b. (Cited on page 15.)

P. J. Oliveira and F. T. Pinho. Analytical solution for fully developed channel and pipe flow of phan-thien–tanner fluids. *Journal of Fluid Mechanics*, 387:271–280, 1999c. (Cited on pages 172, 180, 185, 202, 206, and 208.)

P. J. Oliveira, F. T. Pinho, and G. A. Pinto. Numerical simulation of non-linear elastic flows with a general collocated finite-volume method. *J. Non-Newtonian Fluid Mech.*, 79:1–43, 1998. (Cited on pages 15, 35, 70, 71, 72, 73, 74, 83, 87, 88, 89, 92, 96, 99, 118, 159, 184, 249, 250, and 251.)

C. W. Oseen. Uber die Stokessche Formel und uber eine verwandte Aufgabe in der Hydrodynamik. *Ark. Mat. Astron. Fys*, 6(29):1–20, 1910. (Cited on page 27.)

R. G. Owens. A new microstructure-based constitutive model for human blood. *J. Non-Newtonian Fluid Mech.*, 140(1-3):57–70, 2006. (Cited on page 173.)

R. G. Owens and T. N. Phillips. *Computational Rheology*. Imperial College Press, London, 2002. (Cited on pages 8, 13, 25, 38, 39, 44, 68, 113, and 114.)

R. G. Owens, C. Chauvière, and T. N. Philips. A locally-upwinded spectral technique (LUST) for viscoelastic flows. *J. Non-Newtonian Fluid Mech.*, 108(1-3):49–71, 2002. (Cited on pages 26, 29, 78, 87, and 88.)

A. Öztekin, B. Alakus, and G. H. McKinley. Stability of planar stagnation flow of a highly viscoelastic fluid. *J. Non-Newtonian Fuid Mech.*, 72(1):1–29, 1997. (Cited on page 49.)

P. Pakdel and G. H. McKinley. Elastic instability and curved streamlines. *Physical Review Letters*, 77(12):2459–2462, 1996. (Cited on pages 13, 28, 48, and 144.)

T. W. Pan and J. Hao. Numerical simulation of a lid-driven cavity viscoelastic flow at high Weissenberg numbers. *Comptes Rendus Mathematique*, 344(4):283–286, 2007. (Cited on pages 68 and 116.)

H. M. Park and W. M. Lee. Effect of viscoelasticity on the flow pattern and the volumetric flow rate in electroosmotic flows through a microchannel. *Lab on a Chip*, 8(7):1163–1170, 2008a. (Cited on page 246.)

H. M. Park and W. M. Lee. Helmholtz-smoluchowski velocity for viscoelastic electroosmotic flows. *Journal of colloid and interface science*, 317(2):631–636, 2008b. (Cited on pages 57, 59, 173, 180, 198, 206, 209, and 245.)

B. Pascal. *Traité de l'équilibre des liqueurs*. G. Desprez, Paris, 1663. (Cited on page 3.)

N. A. Patankar and H. H. Hu. Numerical simulation of electroosmotic flow. *Anal. Chem*, 70(9):1870–1881, 1998. (Cited on page 246.)

S. V. Patankar. *Numerical Heat Transfer and Fluid Flow*. Hemisphere Publishing Corporation, 1980. (Cited on pages 11 and 15.)

A. T. Patera. A spectral element method for fluid dynamics: laminar flow in a channel expansion. *J. Comput. Phys.*, 54:468–488, 1984. (Cited on page 11.)

J. A. Pathak and S. D. Hudson. Rheo-optics of equilibrium polymer solutions: wormlike micelles in elongational flow in a microfluidic cross-slot. *Macromolecules*, 39(25):8782–8792, 2006. (Cited on page 49.)

J. R. A. Pearson. Instabilities in non-newtonian flow. *Annual Review of Fluid Mechanics*, 8:163–181, 1976. (Cited on page 47.)

F. Petruccione and P. Biller. A consistent numerical analysis of the tube flow of dilute polymer solutions. *Journal of Rheology*, 32:1, 1988. (Cited on page 11.)

D. N. Petsev and G. P. Lopez. Electrostatic potential and electroosmotic flow in a cylindrical capillary filled with symmetric electrolyte: Analytic solutions in thin double layer approximation. *J. Colloid Interface Sci.*, 294(2):492–498, 2006. (Cited on page 215.)

N. Phan-Thien. A nonlinear network viscoelastic model. *Journal of Rheology*, 22:259, 1978. (Cited on pages 21, 67, 70, 81, 91, 117, 172, 173, 175, 193, 198, 213, 216, 230, 233, 246, and 248.)

N. Phan-Thien and H. S. Dou. Viscoelastic flow past a cylinder: drag coefficient. *Computer Methods in Applied Mechanics and Engineering*, 180(3-4):243–266, 1999. (Cited on pages 29, 81, 87, 88, and 105.)

N. Phan-Thien and R. I. Tanner. A new constitutive equation derived from network theory. *J. Non-Newtonian Fluid Mech.*, 2(4):353–365, 1977. (Cited on pages 21, 53, 67, 70, 81, 91, 117, 157, 172, 173, 175, 177, 193, 198, 199, 213, 216, 218, 230, 233, 246, 248, and 255.)

T. N. Phillips and A. J. Williams. Comparison of creeping and inertial flow of an Oldroyd B fluid through planar and axisymmetric contractions. *J. Non-Newtonian Fuid Mech.*, 108(1-3):25–47, 2002. (Cited on page 43.)

F. T. Pinho and P. J. Oliveira. Axial annular flow of a nonlinear viscoelastic fluid–an analytical solution. *J. Non-Newtonian Fluid Mech.*, 93(2-3):325–337, 2000. (Cited on pages 172, 180, and 233.)

M. Planck. On the law of distribution of energy in the normal spectrum. *Annalen der Physik*, 4(553):1, 1901. (Cited on page 14.)

J. L. Poiseuille. Recherches expérimentales sur le mouvement des liquides dans les tubes de très-petits diamètres. *Comptes Rendus*, Académie des Sciences(12):112, 1841. (Cited on page 3.)

S. D. Poisson. Mémoire sur la propagation du mouvement dans les milieux élastiques. *Mémoires de l'Académie Royale des Sciences de l'Institut de France*, 10:549–606, 1831. (Cited on page 7.)

R. J. Poole and M. A. Alves. Velocity overshoots in gradual contraction flows. *J. Non-Newtonian Fuid Mech.*, 160(1):47–54, 2009. (Cited on page 41.)

R. J. Poole, M. A. Alves, A. Afonso, F. T. Pinho, and P. J. Oliveira. Purely elastic instabilities in a cross-slot flow. In *The Society of Rheology 79th Annual Meeting, Salt Lake City, USA*, 2007a. (Cited on pages 50, 51, 54, 144, 147, 158, 164, 253, and 263.)

R. J. Poole, M. A. Alves, A. M. Afonso, F. T. Pinho, and P. J. Oliveira. Purely-Elastic flow instabilities in a microfluidic cross-slot geometry. In *AIChE 2007 Annual Meeting, Salt Lake City, USA*, 2007b. (Cited on pages 50, 51, 144, 147, 149, 152, 153, and 253.)

R. J. Poole, M. A. Alves, and P. J. Oliveira. Purely elastic flow asymmetries. *Physical review letters*, 99(16):164503, 2007c. (Cited on pages 50, 51, 52, 54, 62, 74, 143, 144, 147, 149, 152, 153, 154, 155, 158, 164, 165, 168, 253, 263, and 264.)

R. J. Poole, M. P. Escudier, A. Afonso, and F. T. Pinho. Laminar flow of a viscoelastic shear-thinning liquid over a backward-facing step preceded by a gradual contraction. *Physics of Fluids*, 19(093101):1–17, 2007d. doi: 10.1063/1.2769380. (Cited on pages 39 and 41.)

L. Prandtl. Über flüssigkeitsbewegung bei sehr kleiner reibung. *Verhandlungen d. III. Internat. Math. Kongr. Heidelberg*, pages 485–491, 8-13. Aug 1904. (Cited on pages 7 and 8.)

R. F. Probstein. *Physicochemical Hydrodynamics: An Introduction*. Hoboken, New Jersy, USA, Wiley Interscience, 2nd edition, 2003. (Cited on pages 218 and 232.)

I. Proudman and J. R. A. Pearson. Expansions at small Reynolds numbers for the flow past a sphere and a circular cylinder. *Journal of Fluid Mechanics*, 2(03):237–262, 1957. (Cited on page 27.)

S. Qian and H. H. Bau. A chaotic electroosmotic stirrer. *Anal. Chem.*, 74 (15):3616–3625, 2002. (Cited on page 215.)

S. Qian and H. H. Bau. Theoretical investigation of electro-osmotic flows and chaotic stirring in rectangular cavities. *Appl. Math. Modell.*, 29(8):726–753, 2005. (Cited on page 215.)

L. M. Quinzani, G. H. McKinley, R. A. Brown, and R. C. Armstrong. Modeling the rheology of polyisobutylene solutions. *Journal of rheology*, 34:705, 1990. (Cited on pages 26, 28, and 40.)

J. M. Rallison and E. J. Hinch. Do we understand the physics in the constitutive equation? *J. Non-Newtonian Fluid Mech.*, 29:37–55, 1988. (Cited on page 144.)

V. V. Ramanan and M. D. Graham. Stability of viscoelastic shear flows subjected to parallel flow superposition. *Physics of Fluids*, 12:2702–2710, 2000. (Cited on pages 13 and 48.)

M. Reiner. The deborah number. *Physics Today*, 17(1):62, 1964. (Cited on page 5.)

J. Remmelgas, P. Singh, and L. G. Leal. Computational studies of nonlinear elastic dubbell models of boger fluids in a cross-slot flow. *J. Non-Newtonian Fuid Mech.*, 88:31–61, 1999. (Cited on page 49.)

M. Renardy. Current issues in non-Newtonian flows: a mathematical perspective. *J. Non-Newtonian Fluid Mech.*, 90(2-3):243–259, 2000. (Cited on page 22.)

M. Renardy. A comment on smoothness of viscoelastic stresses. *J. Non-Newtonian Fluid Mech.*, 138(2-3):204–205, 2006. (Cited on pages 81 and 144.)

F. F. Reuss. Sur un novel effet de l'électricité galvanique. *Mémoires de la Société Impériale des Naturalistes de Moskou*, 2:327–337, 1809. (Cited on pages 14, 58, 172, and 245.)

O. Reynolds. An experimental investigation of the circumstances which determine whether the motion of water shall be direct or sinuous and of the law of resistance in parallel channel. *Phil. Trans. of the Royal Soc.*, 174:935–982, 1883. (Cited on pages 6, 7, 13, and 47.)

C. L. Rice and R. Whitehead. Electrokinetic flow in a narrow cylindrical capillary. *J. Phys. Chem.*, 69:4017–4024, 1965. (Cited on pages 172, 215, and 245.)

P. J. Roache. *Computational Fluid Dynamics*. Hermosa Publishers, Denver, Colorado, 1972. (Cited on page 11.)

G. N. Rocha, R. J. Poole, M. A. Alves, and P. J. Oliveira. On extensibility effects in the cross-slot flow bifurcation. *J. Non-Newtonian Fluid Mech.*, 156(1-2):58–69, 2009. (Cited on pages 51, 52, 54, 74, 144, 147, 152, 154, 164, 168, 253, and 263.)

L. E. Rodd, T. P. Scott, D. V. Boger, J. J. Cooper-White, and G. H. McKinley. The inertio-elastic planar entry flow of low-viscosity elastic fluids in micro-fabricated geometries. *J. Non-Newtonian Fuid Mech.*, 129(1):1–22, 2005. (Cited on pages 38, 39, and 41.)

L. E. Rodd, J. J. Cooper-White, D. V. Boger, and G. H. McKinley. Role of the elasticity number in the entry flow of dilute polymer solutions in micro-fabricated contraction geometries. *J. Non-Newtonian Fluid Mech.*, 143(2-3):170–191, 2007. (Cited on pages 42 and 173.)

J. P. Rothstein and G. H. McKinley. Extensional flow of a polystyrene Boger fluid through a 4: 1: 4 axisymmetric contraction/expansion. *J. Non-Newtonian Fluid Mech.*, 86(1-2):61–88, 1999. (Cited on pages 40 and 115.)

J. P. Rothstein and G. H. McKinley. The axisymmetric contraction-expansion: the role of extensional rheology on vortex growth dynamics and the enhanced pressure drop. *J. Non-Newtonian Fluid Mech.*, 98 (1):33–63, 2001. (Cited on pages 40, 46, 48, 130, and 262.)

M. Sahin and H. J. Wilson. A semi-staggered dilation-free finite volume method for the numerical solution of viscoelastic fluid flows on all-hexahedral elements. *J. Non-Newtonian Fluid Mech.*, 147(1-2):79–91, 2007. (Cited on pages 29 and 32.)

J. C. B. Saint-Venant. Note a joindre au memoire sur la dynamique des fluides. *Comptes-rendus hebdomadaires des Seances de l'Acadamie des Sciences*, 17, 1843. (Cited on page 7.)

T. Sato and S. M. Richardson. Explicit numerical simulation of time-dependent viscoelastic flow problems by a finite element/finite volume method. *J. Non-Newtonian Fluid Mech.*, 51:249–275, 1994. (Cited on pages 11 and 43.)

J. V. Satrape and M. J. Crochet. Numerical simulation of the motion of a sphere in a Boger fluid. *J. Non-Newtonian Fluid Mech.*, 55(1):91–111, 1994. (Cited on pages 35, 89, 102, and 104.)

G. Schleiniger and R. J. Weinacht. Steady poiseuille flows for a giesekus fluid. *J. Non-Newtonian Fluid Mech.*, 40(1):79–102, 1991. (Cited on page 172.)

W. R. Schowalter. The application of boundary-layer theory to power-law pseudoplastic fluids: Similar solutions. *AIChE Journal*, 6(1):24–28, March 1960. (Cited on page 8.)

W. R. Schowalter. *Mechanics of Non-Newtonian Fluids*. Pergamon Press, New-York, 1978. (Cited on page 8.)

E. S. G. Shaqfeh. Purely elastic instabilities in viscometric flows. *Annual Review of Fluid Mechanics*, 28:129–185, 1996. (Cited on pages 13, 47, 130, and 158.)

A. H. Shiang, J. C. Lin, A. Öztekin, and D. Rockwell. Viscoelastic flow around a confined circular cylinder: measurements using high-image-density particle image velocimetry. *J. Non-Newtonian Fluid Mech.*, 73 (1-2):29–49, 1997. (Cited on pages 28, 68, 74, and 79.)

A. H. Shiang, A. Ozkekin, J. C. Lin, and D. Rockwell. Hydroelastic instabilities in viscoelastic flow past a cylinder confined in a channel. *Experiments in fluids*, 28(2):128–142, 2000. (Cited on pages 28, 68, 74, and 79.)

D. Sigli and M. Coutanceau. Effect of finite boundaries on the slow laminar isothermal flow of a viscoelastic fluid around a spherical obstacle. *J. Non-Newtonian Fluid Mech.*, 2(1):1–21, 1977. (Cited on pages 88 and 89.)

I. Sirakov, A. Ainser, M. Haouche, and J. Guillet. Three-dimensional numerical simulation of viscoelastic contraction flows using the pom-pom differential constitutive model. *J. Non-Newtonian Fluid Mech.*, 126(2-3):163–173, 2005. (Cited on pages 41, 114, and 136.)

A. H. P. Skelland. *Non-Newtonian Flow and Heat Transfer*. John Wiley & Sons, New York, 1967. (Cited on page 171.)

C. Y. Soong and S. H. Wang. Theoretical analysis of electrokinetic flow and heat transfer in a microchannel under asymmetric boundary conditions. *Journal of colloid and interface science*, 265(1):202–213, 2003. (Cited on pages 197, 208, and 209.)

J. Soulages, M. S. N. Oliveira, P. C. Sousa, M. A. Alves, and G. H. McKinley. Investigating the stability of viscoelastic stagnation flows in T-shaped microchannels. *J. Non-Newtonian Fluid Mech.*, 163(1-3): 9–24, 2009. (Cited on pages 143 and 155.)

J. J. Sousa, A. M. Afonso, F. T. Pinho, and M. A. Alves. Effect of skimming layer on electro-osmotic - poiseuille flows of viscoelastic fluids: Ptt model, in press. *Microfluidics and Nanofluidics*, 2010a. (Cited on pages 59, 198, and 216.)

P. C. Sousa, P. M. Coelho, M. S. N. Oliveira, and M. A. Alves. Three-dimensional flow of Newtonian and Boger fluids in square-square contractions. *J. Non-Newtonian Fluid Mech.*, 160(2-3):122–139, 2009. (Cited on pages 41, 48, 114, 130, 134, 136, and 143.)

P. C. Sousa, F. T. Pinho, M. S. N. Oliveira, and M. A. Alves. Efficient microfluidic rectifiers for viscoelastic fluid flow. *J. Non-Newtonian Fluid Mech.*, 165:652–671, 2010b. (Cited on page 198.)

T. M. Squires and S. R. Quake. Microfluidics: Fluid physics at the nanoliter scale. *Reviews of modern physics*, 77(3):977–1026, 2005. (Cited on pages 14, 49, and 144.)

G. G. Stokes. On the theories of the internal friction of fluids in motion, and of the equilibrium and motion of elastic solids. *Transactions of the Cambridge Philosophical Society*, 8, 1845. (Cited on pages 3 and 7.)

G. G. Stokes. On the effect of the internal friction of fluids on the motion of pendulums. *Transactions of the Cambridge Philosophical Society*, 9:8–106, 1851. (Cited on pages 7 and 27.)

H. A. Stone, A. D. Stroock, and A. Ajdari. Engineering flows in small devices, microfluidics toward a lab-on-a-chip. *Annual Review of Fluid Mechanics*, 36:381, 2004. (Cited on pages 165 and 172.)

A. D. Stroock, S. K. W. Dertinger, A. Ajdari, I. Mezic, H. A. Stone, and G. M. Whitesides. Chaotic mixer for microchannels. *Science*, 295 (5555):647, 2002. (Cited on page 49.)

J. Sun, M. D. Smith, R. C. Armstrong, and R. A. Brown. Finite element method for viscoelastic flows based on the discrete adaptive viscoelastic stress splitting and the discontinuous Galerkin method: DAVSS-G/DG. *J. Non-Newtonian Fluid Mech.*, 86(3):281–307, 1999. (Cited on pages 87 and 88.)

R. Sureshkumar and A. N. Beris. Effect of artificial stress diffusivity on the stability of numerical calculations and the flow dynamics of time-dependent viscoelastic flows. *J. Non-Newtonian Fluid Mech.*, 60 (1):53–80, 1995. (Cited on page 23.)

G. H. Tang, X. F. Li, Y. L. He, and W. Q. Tao. Electroosmotic flow of non-newtonian fluid in microchannels. *J. Non-Newtonian Fluid Mech.*, 157(1-2):133–137, 2009. (Cited on page 246.)

R. I. Tanner and K. Walters. *Rheology: An Historical Perspective*. Elsevier, Amsterdam, 1998. (Cited on page 8.)

B. Thomases and M. Shelley. Emergence of singular structures in Oldroyd-B fluids. *Physics of Fluids*, 19:103103, 2007. (Cited on page 144.)

B. Thomases and M. Shelley. Transition to mixing and oscillations in a Stokesian viscoelastic flow. *Physical review letters*, 103(9):94501, 2009. (Cited on page 144.)

G. B. Thurston and H. Greiling. Viscoelastic properties of pathological synovial fluids for a wide range of oscillatory shear rates and frequencies. *Rheologica Acta*, 17(4):433–445, 1978. (Cited on page 173.)

T. Vaithianathan, A. Robert, J. G. Brasseur, and L. R. Collins. An improved algorithm for simulating three-dimensional, viscoelastic turbulence, 2006. (Cited on page 23.)

J. P. Van Doormaal and G. D. Raithby. Enhancements of the SIMPLE method for predicting incompressible fluid flows. *Numerical Heat Transfer, Part A: Applications*, 7(2):147–163, 1984. (Cited on page 160.)

A. P. G. Van Heel, M. A. Hulsen, and B. Van den Brule. On the selection of parameters in the FENE-P model. *J. Non-Newtonian Fluid Mech.*, 75(2-3):253–271, 1998. (Cited on pages 11 and 115.)

J. J. Van Schaftingen and M. J. Crochet. Analytical and numerical solution of the poiseuille flow of a johnson-segalman fluid. *J. Non-Newtonian Fluid Mech.*, 18(3):335–351, 1985. (Cited on page 172.)

A. Vissink, H. A. Waterman, E. J. Gravermade, A. K. Panders, and A. Vermey. Rheological properties of saliva substitutes containing mucin, carboxymethyl cellulose or polyethylenoxide. *Journal of Oral Pathology and Medicine*, 13:22–28, 1984. (Cited on page 173.)

W. Voigt. Ueber die beziehung zwischen den beiden elasticitätsconstanten isotroper körper. *Annalen der Physik*, 274(12):573–587, 1889. (Cited on page 8.)

H. von Helmholtz. Studien über electrische grenzschichten. *Ann Physik*, pages 337–82, 1879. (Cited on pages 14, 58, 172, and 245.)

M. von Smoluchowski. Contribution à la théorie lÂŽendosmose électrique et de quelques phénomènes corrélatifs. *Krak Anz*, pages 182–99, 1903. (Cited on pages 14, 58, 172, 180, 186, and 245.)

K. Walters. Lessons from history. *Korea-Australia Rheology Journal*, 11 4: 265–268, 1999. (Cited on page 8.)

K. Walters and M. F. Webster. On dominating elasto-viscous response in some complex flows. *Phil. Trans. R. Soc. Lond. A*, 308:199–218, 1982. (Cited on pages 40, 42, 53, 54, 157, 158, 163, 164, and 263.)

K. Walters and M. F. Webster. The distinctive CFD challenges of computational rheology. *International Journal for Numerical Methods in Fluids*, 43(5):577–596, 2003. (Cited on pages 38 and 113.)

K. Walters, M. F. Webster, and H. R. Tamaddon-Jahromi. The numerical simulation of some contraction flows of highly elastic liquids and their impact on the relevance of the Couette correction in extensional rheology. *Chemical Engineering Science*, 64(22):4632–4639, 2009. (Cited on pages 147 and 151.)

C. Wang, T. N. Wong, C. Yang, and K. T. Ooi. Characterization of electro-osmotic flow in rectangular microchannels. *Int. J. Heat Mass Transfer*, 50:3115–3121, 2007a. (Cited on pages 173 and 215.)

X. Wang, B. Chen, and J. Wu. A semianalytical solution of periodical electro-osmosis in a rectangular microchannel. *Phys. Fluids*, 19(12): 127101, 2007b. (Cited on page 215.)

X. Wang, C. Cheng, S. Wang, and S. Liu. Electroosmotic pumps and their applications in microfluidic systems. *Microfluidics and nanofluidics*, 6 (2):145–162, 2009. (Cited on page 229.)

W. E. Weber. Ueber die elasticitaet der seidenfaeden. *Ann. Phys. Chem.*, 34:247–257, 1835. (Cited on page 8.)

W. E. Weber. Ueber die elasticitaet fester koerper. *Ann. Phys. Chem.*, 54: 1, 1841. (Cited on page 8.)

K. Weissenberg. A continuum theory of rheological phenomena. *Nature*, 159:310–311, 1947. (Cited on page 12.)

F. M. White. Viscous fluid flow. 1991, 1991. (Cited on page 134.)

J. L. White. Dynamics of viscoelastic fluids, melt fracture, and the rheology of fiber spinning. *J. Appl. Polym. Sci.*, 8:2339–2357, 1964. (Cited on page 12.)

S. A. White, A. D. Gotsis, and D. G. Baird. Review of the entry flow problem: experimental and numerical. *J. Non-Newtonian Fluid Mech.*, 24(2):121–160, 1987. (Cited on page 38.)

C. H. K. Williamson. Vortex dynamics in the cylinder wake. *Annual Review of Fluid Mechanics*, 28(1):477–539, 1996. (Cited on page 130.)

B. Xia and D. W. Sun. Applications of computational fluid dynamics (CFD) in the food industry: a review. *Computers and Electronics in Agriculture*, 34(1-3):5–24, 2002. (Cited on page 25.)

X. Xuan and D. Li. Analysis of electrokinetic flow in microfluidic networks. *Journal of Micromechanics and Microengineering*, 14:290, 2004. (Cited on page 229.)

S. Xue, N. Phan-Thien, and R. I. Tanner. Numerical investigations of Lagrangian unsteady extensional flows of viscoelastic fluids in 3-D rectangular ducts with sudden contractions. *Rheologica Acta*, 37(2): 158–169, 1998a. (Cited on page 43.)

S. C. Xue, N. Phan-Thien, and R. I. Tanner. Three dimensional numerical simulations of viscoelastic flows through planar contractions. *J. Non-Newtonian Fuid Mech.*, 74(1-3):195–245, 1998b. (Cited on page 43.)

C. Yang and D. Li. Electrokinetic effects on pressure-driven liquid flows in rectangular microchannels. *Journal of colloid and interface science*, 194(1):95–107, 1997. (Cited on pages 174 and 231.)

C. Yang and D. Li. Analysis of electrokinetic effects on the liquid flow in rectangular microchannels. *Colloids and Surfaces A: Physicochemical and Engineering Aspects*, 143(2-3):339–353, 1998. (Cited on page 246.)

Z. Yang and H. T. Shih. A gallilean and tensorial invariant k-ω model for near-wall turbulence, 1993. (Cited on page 23.)

B. Yesilata, A. Öztekin, and S. Neti. Instabilities in viscoelastic flow through an axisymmetric sudden contraction. *J. Non-Newtonian Fluid Mech.*, 85(1):35–62, 1999. (Cited on page 113.)

Y. J. Yoo and Y. Na. A numerical study of the planar contraction flow of a viscoelastic fluid using the SIMPLER algorithm. *J. Non-Newtonian Fuid Mech.*, 39(1):89–106, 1991. (Cited on page 43.)

S. Yoon and Y. Kwon. Finite element analysis of viscoelastic flows in a domain with geometric singularities. *Korea-Australia Rheology J*, 17: 99–110, 2005. (Cited on pages 43, 68, 69, and 116.)

T. Young. *A Course of Lectures on Natural Philosophy and the Mechanical Arts*. republished 2002 by Thoemmes Press, 1807. (Cited on page 4.)

A. Q. Zade, M. T. Manzari, and S. K. Hannani. An analytical solution for thermally fully developed combined pressure - electroosmotically driven flow in microchannels. *Int. J. Heat Mass Transfer*, 50(5-6):1087–1096, 2007. (Cited on page 215.)

S. Zaremba. Correlation of dynamic and steady ow viscosities. *Bull. Acad. Sci. Cracovie*, 594-614, 614-621, 1903. (Cited on page 8.)

S. Zeng, C. H. Chen, J. C. Mikkelsen, and J. G. Santiago. Fabrication and characterization of electroosmotic micropumps. *Sensors and Actuators B: Chemical*, 79(2-3):107–114, 2001. (Cited on page 229.)

C. Zhao, E. Zholkovskij, J. H. Masliyah, and C. Yang. Analysis of electroosmotic flow of power-law fluids in a slit microchannel. *Journal of colloid and interface science*, 326(2):503–510, 2008. (Cited on pages 59 and 245.)

R. Zheng, N. Phan-Thien, and R. I. Tanner. The flow past a sphere in a cylindrical tube: effects of intertia, shear-thinning and elasticity. *Rheologica Acta*, 30(6):499–510, 1991. (Cited on page 89.)

Q. Zhou and R. Akhavan. A comparison of FENE and FENE-P dumbbell and chain models in turbulent flow. *J. Non-Newtonian Fluid Mech.*, 109(2-3):115–155, 2003. (Cited on pages 11 and 115.)

O. C. Zienkiewicz and R. L. Taylor. *The finite element method: basic formulation and linear problems*. McGraw-Hill College, 1989. (Cited on page 11.)

W. B. Zimmerman, J. M. Rees, and T. J. Craven. Rheometry of non-Newtonian electrokinetic flow in a microchannel T-junction. *Microfluidics and Nanofluidics*, 2(6):481–492, 2006. (Cited on page 246.)

COLOPHON

This thesis was typeset with LaTeX 2ε using Hermann Zapf's *Palatino* and *Euler* type faces (Type 1 PostScript fonts *URW Palladio L* and *FPL* were used). The listings are typeset in *Bera Mono*, originally developed by Bitstream, Inc. as "Bitstream Vera". (Type 1 PostScript fonts were made available by Malte Rosenau and Ulrich Dirr.)

The typographic style was inspired by Bringhurst's genius as presented in *The Elements of Typographic Style* (Bringhurst, 2002). It is available for LaTeX via CTAN as "`classicthesis`".